Subsurface deformation micromechanisms induced during machining of titanium alloys at low temperatures, and a novel testing methodology to examine their machining behaviour

Maureen Idalia Aceves López

Department of Materials Science and Engineering

The University of Sheffield

Summary

The aerospace industry's drive towards higher productivity has led manufacturers to strive for higher surface speeds in metal cutting. Machining of titanium alloys leads to high temperatures attributed to their low thermal properties, resulting in high tool wear rates. To counter this, large amounts of coolants are used. These contain toxic chemicals, which are harmful to both people and the environment. To reduce these hazards, near-dry strategies such as cryogenic cooling and minimum quantity lubrication (MQL) are investigated in this thesis. A fundamental knowledge gap in the literature was identified, which is the characterisation of the subsurface microstructural evolution during plastic deformation in the machining of titanium alloys. Besides, its impact on surface integrity needs to be investigated in detail.

The aims of this PhD research were (1) To determine the "machinability" of titanium alloys by designing a novel and straightforward cutting test. (2) To determine the effect of low temperatures (LTs) on the underlying deformation mechanisms during plastic deformation in the machining of aero-structural Ti-6Al-4V. In particular, during the application of a cryogen media such as LN_2 and CO_2. (3) To build a constitutive model to predict the experimental flow behaviour. (4) To analyse the imparted subsurface deformation and relate to its subsurface integrity. A material's inherent mechanical, physical and thermal properties strongly influence its machining behaviour. In the uniaxial compression test, it was determined that β annealed Ti-6Al-4V ELI: undergoes shear localisation even at quasi-static strain rates, has a high sensitivity to temperature and a lower sensitivity to strain rate. The higher the temperature, the higher the strain rate sensitivity. Plastic deformation at LTs exhibited higher flow stresses vs ambient temperature. The true strain at the onset of thermal instability (softening) and at fracture was identified, it was c30% smaller at LTs vs room temperature, leading to a reduction in c20% energy for cutting at LTs. The strain-hardening rate during plastic deformation decreases linearly with further imparted strain and decreases faster at LTs.

Machining generates a graded subsurface microstructure. Four different regions were identified in this investigation. (1) Severe plastic deformation region (SPD), where a nanocrystalline grain structure was observed through electron microscopy from cryogenic machining under CO_2, resulting in a significant increase in strength. (2) Gross plastic deformation region. (3) Twinned region. (4) Undeformed bulk.

In conclusion, machining of titanium alloys at cryogenic temperatures is easier as a lower strain is required for shearing, leading to lower energy spent for chip generation. Nevertheless, a larger microstructural damage depth is introduced into the subsurface, leading to more potential sites for crack nucleation. The main challenges that lie ahead are: (1) to determine the extent of the effect the microstructural damage has on the fatigue life during dynamic loading, and (2) to determine whether easy diffusion is allowed to occur under thermal exposure, which would negatively affect their mechanical properties.

Contents

Acknowledgements

I would like to express my gratitude to my supervisor, Dr. Martin Jackson, for his guidance, support and encouragement during the development of this project. He was fundamental to the successful completion of this research. I would like to thank Professor Brad Wynne for the enriching discussions, which improved the quality of the microstructural analysis significantly. I am grateful to Dr. Pete Crawforth for providing me very valuable guidance and for allowing me the possibility of undertaking an experiment at the AMRC with Boeing. I am thankful to Dr. Christopher Taylor, Dr. Ian Cook and Dr. Nikolaos Tapoglou for allowing me to work collaboratively on high-speed cryogenic machining of titanium alloys and for providing me with the material for subsequent examination. I also thank Dr. Adrian Leyland for his many constructive suggestions. I thank CONACYT for the financial support they kindly provided for this project.

I am very lucky for having great officemates in D1, and I appreciate their friendship. First of all, I am grateful to Dr. Ben Thomas for the stimulating discussions, which greatly enriched the project, for kindly explaining to me some concepts and motivating me to learn new skills, to Dr. Nick Weston for his help on the compression testing and enriching discussions, and to Dr. Luke Marshall for his guidance and support on the ASP as well as for providing me some material for testing. I would like to extend my gratitude to Emma Calvert for her suggestions on the use of the electron microscope, Daniel Suarez for helping me on the ASP, Kyle Marshall and Joshua Baines for his collaboration on the CAD drawing of the workpiece holder. And to all my colleagues in D1, who made studying in the UK such a great experience, as well as for all the tea and coffee.

I thank the technical staff who supported me while undertaking the experimental work: Joanna Sharp, Ian Ross, Le Ma, Mike Bell and Dean Haylock.

I am very grateful to my friend Rob Mahan, who always listened and discussed with me the project, believed in me and kept encouraging me to work hard.

I dedicate this thesis to my parents Obdulia and Roberto, who influenced me towards my interest in science, to my siblings Roberto, Claudia, Marlon and Cristian, and my family, especially my aunt Rosa and uncle Fernando Rivera, who always have supported and encouraged me, and for that, I am very grateful. I also appreciate the encouragement and support from my friends.

Preface

The original aim of this research was to investigate the processing parameters to generate reliable surface integrity on the surface and subsurface of machined components of titanium alloys at high surface speeds. Improved surface integrity leads to enhanced fatigue resistance during in-service operation, especially for high-reliability structural components. Nanocrystalline or ultrafine microstructures provide higher strengths and higher ductility. These properties are highly valuable for structural components as they could support higher loads, resulting in longer operational lifetimes. On the other hand, microstructural features imparted to the subsurface during plastic deformation such as mechanical twinning and intense slip bands are potential sites for crack initiation in cyclic loading [1]–[5]; consequently, these features are considered to be deleterious during cyclic loading and are classified as imparted "damage" in the subsurface.

The second phase of the project consisted of establishing a testing methodology to determine the machinability of titanium alloys. Chip formation is produced by shear deformation. According to Merchant [6], the main parameter to influence the direction of shear is the compressive stress on the shear plane. This led to the use of a simple uniaxial test to obtain this information. Microstructural composition and stress state are determined by the thermomechanical processing history of an alloy. This strongly influences the plastic behaviour during deformation. Thus, a simple axisymmetric compression test of a cylinder, which directly considers the material physical properties and stress state was considered. Factors such as tool geometry, the tool's coating, depth of cut, surface speed and cooling or lubricating conditions should also be taken into consideration to determine the plastic behaviour of the material. Thus, an orthogonal cut in an arbitrary strain path (ASP) machine was undertaken. The plastic behaviour is determined by the workpiece material physical properties, and the geometry of chip formation is dictated by the system of forces acting on the workpiece material.

Smaller chips during high-speed precision machining of titanium alloys are desired in order to flush them away from the cutting area efficiently. This prevents workpiece or tool wear damage. Consequently, the application of liquefied gases or cryogenic coolants was investigated.

Finally, a full-scale trial was undertaken to correlate the subsurface microstructural evolution during machining in β annealed Ti-6Al-4V. A transmission electron microscopy analysis was performed to determine the microstructural effect of high-speed milling under CO_2 cryogenic cooling conditions on the subsurface closest to the machined edge. The immediate area below the cutting edge has suffered the highest shear stresses, shear strains and shear strain rates, therefore a nanocrystalline or ultra-fine grained size microstructure was expected.

Chapter 1. Introduction. It presents an overview of the titanium alloys industry and provides an insight into the current trend "towards dry cutting" due to environmental, occupational safety concerns and high rates of heat removal.

Chapter 2. Literature review. It includes a summary of the types of titanium alloys, the deformation mechanisms, features of plastic deformation such as the formation of adiabatic shear banding, dynamic recrystallization, mechanics of cutting, general types of coolants, mechanical and thermal properties of titanium alloys at low temperatures and some of the microstructural features induced in the workpiece during machining at low temperatures.

Chapter 3. Experimental methodology. It describes the approach for the design of a bespoke small-scale cutting test to determine the machinability of titanium alloys. It also explains the procedures for the characterisation of the machined workpieces, such as high-resolution electron microscopy and cross-polarised light microscopy.

Chapter 4. Thermo-mechanical testing: quasi-static uniaxial compression. The effect of temperature and strain rate during instability in plastic deformation was investigated through the application of simple uniaxial mechanical testing (also known as axisymmetric compression testing) for Ti-6Al-4V in a β annealed condition. Three materials models were built: one for plastic deformation at room temperature, one for two intermediate low temperatures, and the third, for the lowest achieved temperature in the uniaxial compression testing.

Chapter 5. Orthogonal cut or near Plane Strain Machining. The effect of temperature and cutting speed was investigated on the designed small-scale cutting test, with the introduction of additional parameters: tool geometry, and depth of cut. The investigation included the following alloys: β annealed Ti-6Al-4V ELI, CP-Ti and mill annealed Ti-6Al-4V. Subsurface damage introduced in the form of severe plastic deformation (SPD) and mechanical twinning was correlated to the aforementioned parameters.

Chapter 6. CO_2 cryogenic cooling β annealed Ti-6Al-4V ELI face milling. It corroborates, through a high-speed test, the effects of cutting temperature on the subsurface deformation generated by machining. Different coolant and/or lubricants were applied directly to the cutting edge through spindle tool delivery. Coolants and lubricants were: conventional flood coolant, atomization of Minimum Quantity Lubrication (MQL), different percentage delivery of CO_2 (25, 75 and 100%) and the combined effect of CO_2 plus MQL. Bright-field transmission electron microscopy was utilised to determine the nature of the region immediately below the machined edge, which could be considered part of the adiabatic shear band formation during metal cutting.

The inter-relationship of the parameters investigated in this work between chapters 4, 5 and 6 is illustrated in Figure 1 (next page).

Chapter 7. Conclusions and future work. A summary of the main findings in this investigation. The relationship between the involved parameters and the evaluation of this new small scale and bespoke testing to relate machinability to the subsurface microstructural evolution and the mechanical properties, which result from this. Additionally, future work is suggested to improve understanding of the impact of the generated microstructural modification during in-service operation.

Uniaxial Compression

Simple stress state deformation to study the material's strength, strain and energy for the onset of failure by shear band formation.

Quasi-static test (0.01 to 10 s⁻¹)

Input
$\dot{\varepsilon}$ (s⁻¹)
ε (mm.mm⁻¹)
T (°C)

Platens

Cylinder

F

F

ho

Do

Df

hf

Load & friction → σ
Displacement → ε
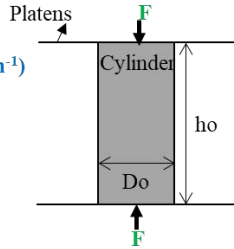
Fracture occurs by **catastrophic shear**
Shear instability by thermal softening, localization of def., void nucleation and fracture.

Onset of softening, ε_{OS}
0.2% offset Yield Stress (MPa)

True Stress, σ (MPa)
True strain, ε (mm.mm⁻¹)
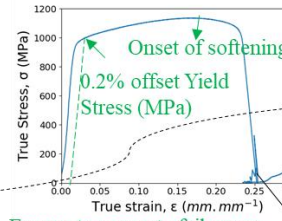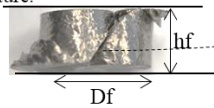
Energy to generate failure or Workability (J.m⁻³) $= \int_0^{\varepsilon_f} \frac{d\sigma}{d\varepsilon}$

Shear Stress (MPa)

Build a Model

Underlying deformation mechanisms

SB (μm)
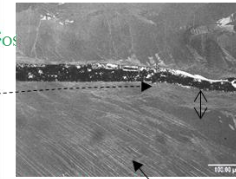
Crystallographic reorientation towards the shear direction.

SB to SPD comparison

Output

(1) Flow stress
(2) Strain onset of instability and fracture
(3) Energy for PD
(4) Temperature rise
(5) Micro-mech. for PD
(6) ASB thickness
(7) Likelihood for ASB formation

Model to predict:

(1) Peak and trough loads
(2) Strain in chip & subsurface
(3) Strain rate in chip & subsurface
(4) Temperature rise
(5) Type of chip formation
(6) Tool wear

Plane Strain Machining (PSM) 2D

Biaxial stress state.

Input

(1) V_c (m/min)

(2) Coolant (mL/min), T (C)
(3) Tool geometry, coating
(4) Alloy chemistry

α(°)

SBA (°)

h₁ (mm)

Deformation front in a **compressive stress state**, leading to **catastrophic shear**.

Peak Load (kN) → τ
Displacement (mm) → SB spacing
$\dot{\varepsilon}$ estimation
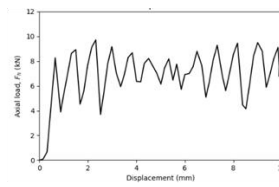
Shear Stress (MPa)
Shearing energy
Friction energy

Axial load, Fₐ (kN) — Displacement (mm)
Shear Stress, τ (MPa) — Displacement (mm)

SPD (μm)

Mech. twinning (μm)
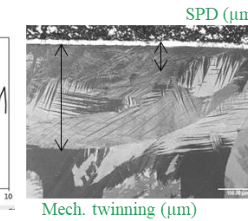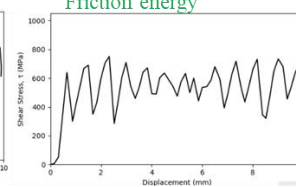
Output

(1) Peak, trough loads (force fluctuation)-> vibration
(2) Temperature rise
(3) Micro mechanism of chip formation
   (1) Segmented or homogeneous
   (2) ASB angle
   (3) BUE formation
(4) Surface generation. Likelihood of notch generation
(5) Subsurface damage
(6) Tool wear depths; contact length with the tool's flank & rake face

Milling 3D

Input
Coolant
$\dot{V}$ (mL/min)

ADoC (mm)
RDoC (mm)
LoC (mm)

V_c (m/min)

Deformation front in a **compressive stress state**, leading to **catastrophic shear**.
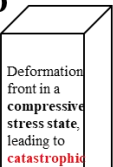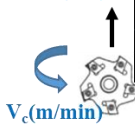
Fracture by **catastrophic shear**.

Multiaxial stress state.

Energy during cutting
Higher friction → higher tool wear

Flank Wear Average (mm) — Cutting time (min)
— Coolant type
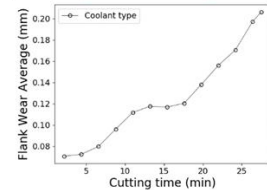
SPD region. Crystalline structure of dynamically recrystallized Nano equiaxed grains

SPD (μm)

Mech. twinning (μm)

Crystallographic reorientation towards the cutting tool.
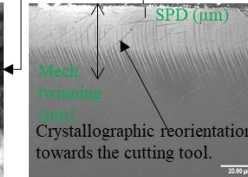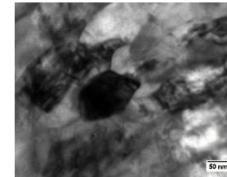
Output

(1) Subsurface microstructural evolution
(2) Type of chip formation
(3) Tool wear

Figure 1. Inter-relationship between variables analysed in each testing methodology.

Table of figures

1. Introduction

The aerospace industry is the biggest global consumer of titanium alloys. In 2016, 65% of all mill products (150 000 tons) were used by the aerospace industry [7]. Civil airframes and engines represented 75% of this market. It is estimated that there will be a 5% annual increase in titanium consumption in the aerospace industry until the year 2026. The percentage of titanium alloys usage in civil aircraft has increased considerably, see Figure 1-1. For instance, Boeing's 787 contains 15% in fly-weight and Airbus's A320/A350 between 12 -14% in comparison with 4-8% in previous aircraft models [7]. This increase in titanium alloys usage in airframes in the aerospace industry has served as a catalyst for manufacturing engineers to find ways to improve the material removal rate and thus to improve the machinability of titanium alloys.
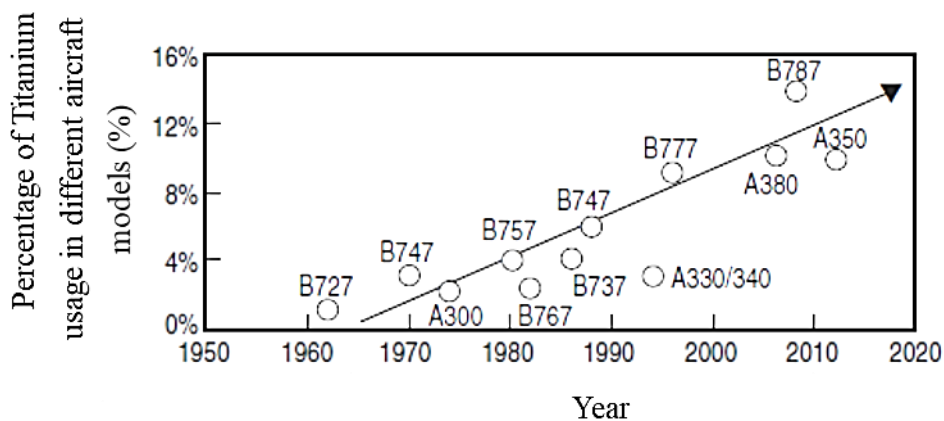
Figure 1-1. Percentage of Titanium usage in commercial airframes [8].

Ti-6Al-4V has a market share of about 50% of all titanium alloys [9]. The demand for titanium continues to grow, and the aerospace sector will continue to grow beyond 2020 [10]. For aerospace OEM Airbus, the increase in production rates and the introduction of new aircraft designs (i.e. A350XWB and A320neo (Ti pylon)) has greatly increased titanium demand. 43,000 new aircraft will be built in the next 20 years [10], [11], 44% will replace current aircraft. There is good compatibility of titanium with carbon fibre composites, which also has contributed to the increase in demand for titanium alloys. Original Equipment Manufacturers (OEMs) are looking to improve material usage by increasing the "buy-to-fly" ratio and use it in new products. Safran uses more than 2,000 tons of metastable beta titanium alloys for its landing gears due to their superior properties: mechanical (strength, fatigue, weight) and chemical (corrosion), which provides low maintenance. CFRP is increasingly used on LEAP engines (30% more on fan blades and case) leading to weight savings of nearly 272 Kg [10].

Figure 1-2 a) shows the forecast for the number of commercial engines grouped into next generation and legacy engines. A substantial increase in the production of next-generation engines is expected by the year 2030, reaching a yearly production of about 5,000 engines in 2030 from 3,500 in 2018. Next-generation engines will require between 2 to 3 times more titanium compared to legacy engines. Some of the new models are A320 NEO, 737 MAX, A330 NEO and 777X. Figure 1-2 b) shows that by 2030, nearly 25,000 metric tonnes will be demanded for the production of commercial jet engines, from nearly 15,000 in 2018. From 2024, growth will start to accelerate. By 2020, titanium demand is expected to grow fastest among metals, at a 4.3% CAGR (compound annual growth rate).
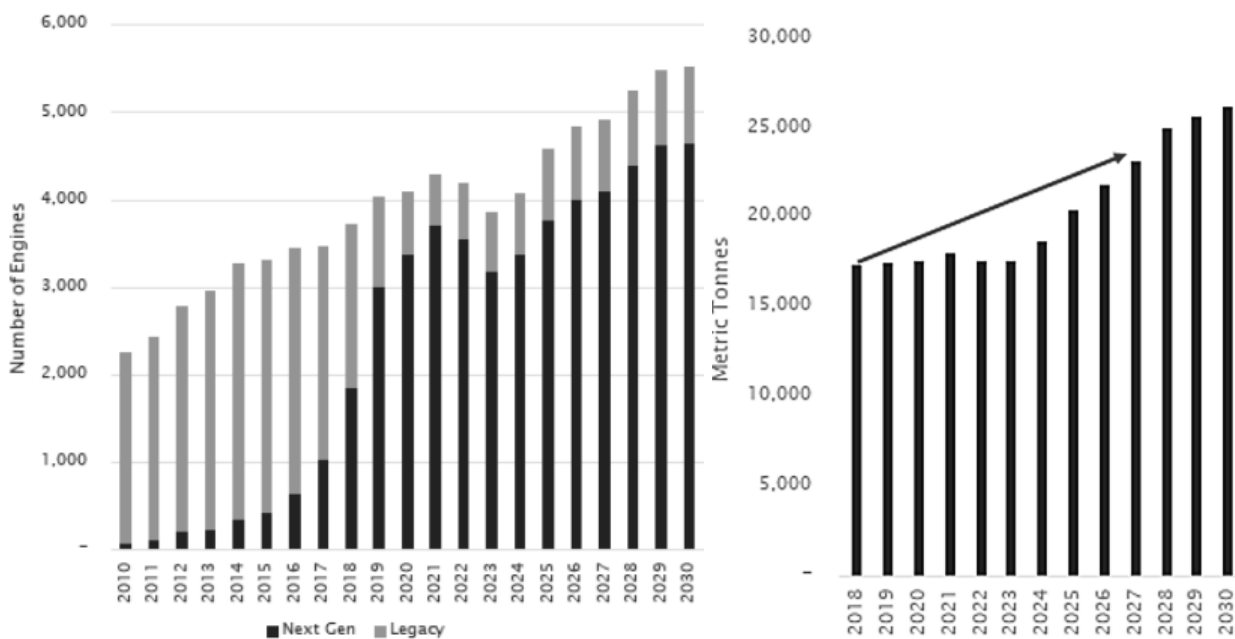
Figure 1-2. a) Forecast for the demand of commercial engines b) demand of titanium for engine components (including spare parts for current engines) [10].

Figure 1-3 shows the expected demand for titanium alloys classified by OEM. It is observed that Rolls Royce is expected to increase its demand and to be the largest user by 2030. The second largest user will be CFM (a joint venture between GE Aviation and Safran Aircraft); however, they may reduce titanium consumption in comparison with previous years. Pratt & Whitney shows growth in consumption but at a much lower level. General Electric (GE) will slightly reduce its usage.
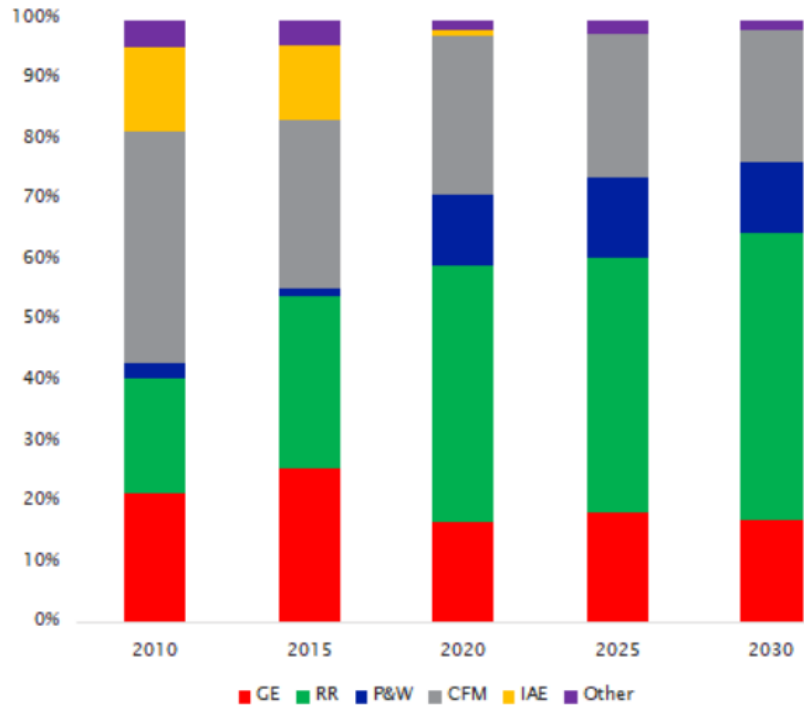
Figure 1-3. Future demand for titanium alloys by OEM by the year 2030. General Electric (GE), Rolls Royce (RR), Pratt & Whitney (P&W), a joint venture between GE Aviation and Safran Aircraft Engines (CFM) and International Aero Engines (IAE) [10].

Evaluation of machinability historically has been based on a mechanical engineering approach, in terms of three main factors. The first factor is classified as tool wear rates, which are strongly influenced by cutting temperatures generated in the cutting zone, the chemical processes and mechanical stresses experienced by the cutting tool leading to tool damage and eventual failure or fracture. The second is based on cutting forces, power consumption and the efficiency of chip removal and clearance from the cutting zone. The third parameter is related to the machined workpiece quality in terms of surface roughness and dimensional stability. Unfortunately, the damage generated on the subsurface of the machined workpiece has been ignored by scientists studying machinability. It can have severe effects on workpiece fatigue life during operation. Therefore, a detailed study of the subsurface damage generated on machined components is necessary. Its operational life depends on the microstructural features with which the workpiece is brought into service. Severe plastic deformation processes have been known to generate nanocrystalline or ultrafine grain sizes after the deformation process has taken place. In the case of machining, where a cut is generated with a tool tip, deformation is highly localised. This has generated a graded microstructure, producing very fine grains (in the nanoscale) in the immediate subsurface layer of the cut, where higher strain rates, strain and stresses were experienced on the workpiece material.

Taking a hollistic approach, machinability depends on three main groups of factors. The first includes the workpiece and cutting tool material's intrinsic properties such as mechanical, thermal, physical and chemical, as well as its microstructure, which is dictated by the thermo-

mechanical processing history, grain size, inclusions, second phase particles (such as β-phase in α+β titanium alloys), tool physical properties such as grain size, coating, thickness and chemical affinity of the tool with the workpiece material. The second group of factors refer to the cutting parameters such as surface speed, depth of cut, feed rate and the method of cooling and lubrication to remove the heat away from the cutting zone in order to reduce thermally activated processes such as solid diffusion between the tool and workpiece material. The third group is linked to the cutting tool and workpiece fixtures such as machining operations (turning, milling), rigidity (as this will reduce tool deflection), available power from the cutting lathe, tool geometry and tool roundness. As titanium alloys have a low modulus of elasticity, the tool tends to deflect, which could generate a non-uniform depth of cut. A fourth is the tool life. Keeping the tool integrity for longer means the tool stays sharp, so the cut can maintain higher dimensional accuracy and work more efficiently.

1.1. Sustainability

Currently, conventional flood cooling is the dominant cooling methodology used in aerospace machining. The use of near-dry strategies such as cryogenic cooling and MQL is at an early stage of research, and its application in the industry remains limited. The aerospace industry is moving towards the use of cryogenic media to machine aero engine components.

In the last decade, there has been a strong tendency towards the elimination of fluid coolants and lubricants for machining, known as "near dry". There are three main driving forces for this tendency. The first is the increased incidence of occupational health related issues related to human exposure to fluid coolants and additives. The second is an attempt to reduce costs relating to cooling and lubrication, which represent nearly 15% of the total cost of the manufactured workpiece. The third reason is special requirements where the workpiece cannot be in contact with chemicals or contain chemical residues due to their damaging influence and degradation of the mechanical properties.

In accordance with the Air Transport Action Group (ATAG) and Climate Change Act 2008 in the UK [12] there is an aim to improve fuel efficiency 1.5% each year up to the year 2020 and to reduce greenhouse gas emissions to 50% of these emitted in 2005 by the year 2050. Light materials such as Carbon Fibre Reinforced Polymers (CFRP) or metal composites are increasingly being used within the aerospace industry in order to reduce aircraft weight [13].

CFRP requires machining to create the precise shape of the final product within dimensional tolerances. CFRP are difficult to machine due to their anisotropic properties, fibres are abrasive and have low thermal conductivity [14]; therefore, to machine CFRP a coolant and/or lubricant medium is required. During machining, the use of conventional coolants in metal composites may lead to chemical or moisture absorption, which subsequently degrades mechanical

properties by reducing adhesive bonding strength. In addition, delamination, fibre pull out, break out and matrix cracking may potentially occur [15]. To reduce the residual damage generated by the high heat generation, a cryogenic cooling methodology may be applied.

Cutting fluids and its chemical additives have proven to cause environmental and occupational health problems. Primary reasons are microbial growth (bacterial and fungal cells and its by-products: endotoxins, exotoxins and mycotoxins) [16], the toxicity from the biocides to control it, small metal particles generated during metal cutting and chemicals to prevent corrosion and foam generation [17], [18]. Typical routes of exposure are through breathing in minute aerosol particles and via skin contact. In the USA the National Institute for Occupational Safety (NIOSH) gathered evidence that the occupational exposure risk to hazardous working fluids generates a higher risk of carcinoma and illnesses in the respiratory tracts such as asthma and hypersensitivity pneumonitis [16]. In the USA alone, approximately 1.2 million workers in metal cutting operations are potentially at occupational risk [16]. The Occupational Safety and Health Administration (OSHA) established an exposure limit of 0.5 $mg.m^{-3}$ up to 10 hours per day assuming a 40-hour week to prevent occupational risks.

The cost of metal cutting fluids during a machining operation accounts for nearly 15% of the total cost [19][20]. This involves the acquisition, maintenance and disposal of potentially hazardous wastes.

Besides these occupational, contamination issues and the reduction in tool wear rates, an important factor has been identified, which refers to the generation of much smaller grain sizes (from the ultra-fine to the nanoscale) through SPD leading to high strength. By considering the Zener-Hollomon mechanism for the prediction of recrystallized grain size, the reduction in temperature and/or the increase in strain rate allows for the generation of smaller grain sizes. Thus, it is estimated that through the application of cryogenic coolants such as CO_2 and LN_2 improved mechanical properties (such as higher strength and higher toughness) can be achieved. For these reasons, the manufacturing community is moving towards a more sustainable approach to metal cutting.

The use of titanium alloys in the aerospace industry requires higher speed rates to reach production goals. As a result, the research community is searching for ways to improve the machinability of titanium alloys. Additionally, ductile alloys generate continuous and tangled chips as shown in Figure 1-4. These tangled chips remain in the machining zone; they could potentially damage the structural integrity of the workpiece or damage the machine components. The machine operator has to remove these chips manually. Thus, a methodology to generate smaller chips or improve chip breakability is the drive of this investigation. By locally modifying the material properties, only to the uncut chip thickness depth, could aid to reduce the size of the chips and consequently enhance the chip removal from the machining zone.
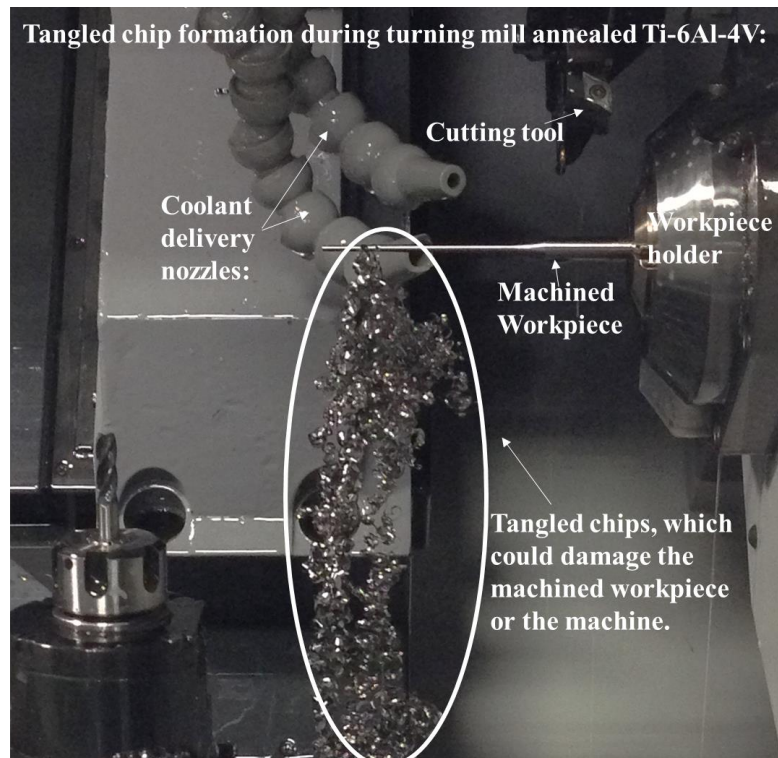
Figure 1-4. Formation of tangled chips inside the machine during turning ductile mill annealed Ti-6Al-4V at 80 m.min^{-1} and t_1=0.8 mm, after semi-finishing turning.

Usually, titanium is machined from forged components where more than 90 percent of the material is removed as swarf, known as the "buy to fly ratio" [21], resulting in final complex and lightweight components. This results in nearly 60% of the total cost of the component [22]. Normally, the cost of coolant/lubricant fluids is 15% of the cost of a machining operation [19]; however, it was reported that in "difficult to cut materials" it reaches 20-30% [23]. Thus, besides the improvement in subsurface properties, reduction in workers' exposure to hazardous chemicals and the prevention of contamination to the environment, a cryogenic coolant might lead to a reduction in operational costs.

During machining, a local region is heavily strained until fracture. Titanium alloys have a strong tendency to plastically deform in a non-homogeneous mode. This leads to the formation of segmented chips with narrow zones of concentrated heat and imparted shear strain also called adiabatic shear bands (ASB), hence temperature reduction in the cutting zone is of paramount importance for five reasons. The first reason is that the titanium alloys tend to build up heat during machining due to their low thermal conductivity. Also, the chips generated may ignite during machining. The second reason is the tendency for tensile residual stresses to be imparted into the machined workpiece relating to thermal expansion as a direct effect of high temperatures, leading to a reduction in crack initiation toughness under dynamic loading. A third reason is the solid-state diffusional processes, which degrades tool integrity. Intimate contact between the hot chip and ASBs of concentrated heat with the tool cause a significant rise in temperature. This enhances the diffusion of substitutional and interstitial elements. The

fourth reason is the high tendency to build up edge (BUE) formation at higher temperatures, in which a part of a chip welds to the cutting tool and is subsequently removed; however, this causes material particles from the cutting tool to also be removed, degrading it or causing premature failure. The fifth reason is that at higher temperatures, softening in the machined subsurface might readily occur to such an extent that either it only recovers by dislocation annihilation (climb and cross-slip) or it dynamically recrystallizes. It may lead to a high grain size growth, which may locally reduce the yield strength (due to the Hall-Petch relation), therefore preventing improvements to its mechanical properties.

Strategies for the optimisation of resource consumption are currently under research. Near dry approaches such as the application of liquefied industrial gases or cryogens and minimum quantity lubrication (MQL) have been widely accepted in the machinability of titanium alloys and are considered as environmentally friendly and non-toxic. It has been regarded as beneficial, especially regarding tool life as it brought increases of up to three times that of conventional flood cooling [24], [25]. This approach is adopted mainly by mechanical and industrial engineers. However, a fundamental knowledge gap exists regarding the ultimate goal of machining - workpiece integrity. Although current surface integrity parameters such as residual stress, surface roughness, hardness, surface tearing and smearing have been investigated, a higher level of detail and the characterisation of the microstructural evolution of subsurface layers are needed in the literature. This thesis aims to examine some of these issues.

During this research work, the generation of a graded subsurface layer during machining CP-Ti under LN_2 and β annealed Ti-6Al-4V ELI under CO_2 has been studied through high-resolution electron backscatter microscopy, transmission electron microscopy and cross-polarised light microscopy. The first layer or the immediate area below the cutting edge is composed of an equiaxed nanocrystalline structure followed by a strain-hardened layer and finishing with the undisturbed bulk microstructure. The generation of this microstructure gives rise to an improvement in the mechanical properties of machined components such as yield strength and resistance to wear.

The increased use of CFRP in the aerospace industry to reduce aircraft weight leads to a reduction in fuel consumption. Consequently, it leads to a reduction in greenhouse emissions, resulting in increased use of titanium alloys needed to be machined to generate the final component. However, the machining of CFRP with conventional cutting fluids has a negative impact on their mechanical properties. For example, shear strength between laminates in the event of contamination or even simply absorption of water. Additionally, medical components that are in contact with the human body must not be contaminated by chemicals due to the hazard they represent to human health. Therefore, the application of a coolant/lubricant, which evaporates to the atmosphere and does not contaminate the workpiece is essential. The use of cryogenic coolants such as CO_2 and LN_2 has been proven to improve workpiece mechanical

properties. The application of MQL vegetable oils also reduces friction during cutting and prevents chemical contamination.

The current approach to determine machinability is through the study of tool wear. Unfortunately, the machinability of a material is strongly influenced by its inherent mechanical, physical and thermal properties, which are determined by its stress state, thermomechanical processing history, and processing parameters (imparted shear strain, shear strain rate and temperature). Axisymmetric compression exposes the specimen to a stress state close to a simple shear, leading to the rise to concentrated shear bands, similar to that encountered in machining. The compressive stress imparted on the shear plane is the primary parameter which influences the direction of shear [6]. Based on this fact, the simple unidirectional shear imparted in the axisymmetric compression test could predict the shear stress imparted to the workpiece during orthogonal cutting. In this way, shear stresses generated in metal cutting can be predicted from flow stress behaviour in pure shear.

With the aim to determine more efficiently the machinability of an alloy, a novel small-scale test was developed where any cutting shank and tool insert could be studied. Effects of the most important parameters: strain, strain rate and temperature, depth of cut, feed and surface speed can be analysed in this small-scale testing, as well as strain and energy to generate fracture by catastrophic shear.

Tailored graded subsurfaces with different mechanical properties could be engineered by modifying the deformation process parameters such as shear strain, shear strain rate and temperature. Low-temperature deformation introduces a higher amount of lattice defects. These defects provide the driving force for dynamic recrystallization.

2. Literature review

As outlined previously, the main objectives of this research were (1) to investigate the effect of temperature on the underlying plastic deformation micro-mechanisms and the microstructure evolution during cutting titanium alloys. (2) To design a simple and versatile cutting rig to determine the machinability of titanium alloys, to estimate the shear stresses experienced by the workpiece material and the tool. (3) To validate the effect of temperature on the underlying microstructural modification in high-speed machining of titanium alloys. This review describes the deformation characteristics of the hcp unit cell.

2.1.   Titanium crystal structure and phase diagrams

Titanium is the fourth most abundant structural element [22] extracted by the Kroll process (invented in 1940) from the oxide minerals rutile (TiO_2) and ilmenite ($FeTiO_3$). Titanium has a low density, nearly 60 % that of steel and that of nickel superalloys. It can be strengthened by solid-solution alloying or by imparting plastic deformation. It has a strong corrosion resistance which stems from its ability to passivate itself.

At room temperature, pure titanium occurs as α phase (hexagonal close-packed; hcp) and undergoes an allotropic phase transformation to β phase (body centred cubic; bcc) at 882°C [21]. The transformation from the high-temperature β phase to the low-temperature α phase occurs by diffusional nucleation and growth processes, strongly influenced by cooling rate. The transformation temperature strongly depends on interstitial and substitutional content. The unit cell of the hcp or α phase is illustrated in Figure 2-1 a); the a lattice measures 0.295 nm, the c lattice 0.468 nm and this gives a c/a ratio of 0.158, less than the hcp ideal. It shows the three most densely packed planes; the basal (0002) plane, one corresponding to the three $\{10\bar{1}0\}$ prismatic planes and one which belongs to the six pyramidal $\{10\bar{1}1\}$ planes. The close-packed directions $< 11\bar{2}0 >$ are represented by a_1, a_2 and a_3 axes. The unit cell of the bcc (β phase) is depicted in Figure 2-1 b); it shows one of the $\{110\}$ close-packed planes, the close-packed directions $< 111 >$ and the lattice measures 0.332 nm.
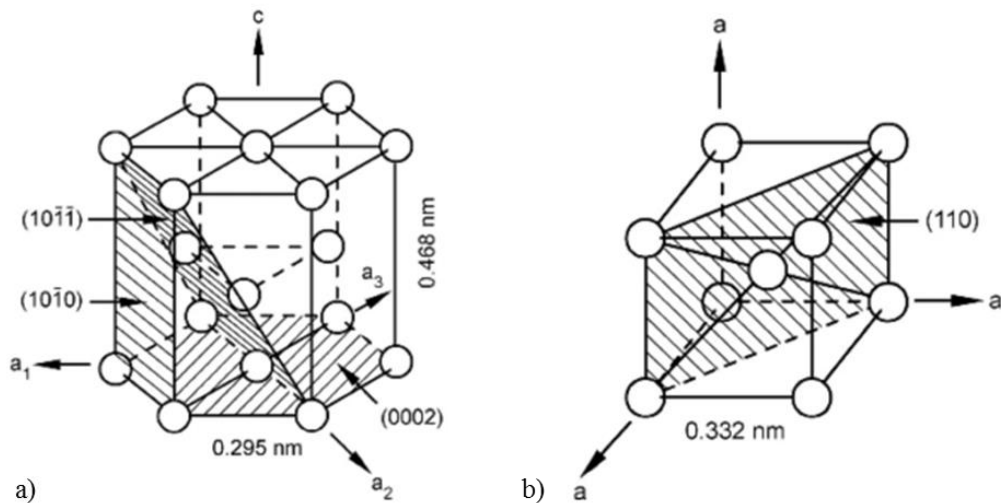
Figure 2-1.Unit cell of a) the hcp or α phase and b) the bcc or β phase [21].

Burgers described the relationship between the β and the α phase crystallographic orientation, and it is known as the Burger relationship:

$$(110\,)\beta \parallel (\,0002\,)\alpha$$
$$[\,111\,]\beta \parallel [1120\,]\alpha$$

There are 12 hexagonal variations from which the β phase can transform to α phase, generating different orientations in relation to the parent β grain.

The alloying constituents of titanium are categorised as α or β stabilisers as illustrated in Figure 2-2. This depends on their effect on the α➔β transformation temperature; increase or decrease from the 882°C of pure titanium. Strong alpha stabiliser elements are interstitial O, N and C and substitutional Al and they increase the transformation temperature α➔β. The most important and commonly used substitutional element is aluminium as it has high solubility in the α and β phases. Oxygen is the interstitial element most used to improve strength, especially for CP titanium. β stabilisers are classified as β-isomorphous and β eutectoid. Most common β isomorphous elements are V, Mo and Nb and for the β eutectoid are Cr, Fe and Si. Zr and Sn are classified as neutral elements as they do not have a strong influence on the transformation temperature.
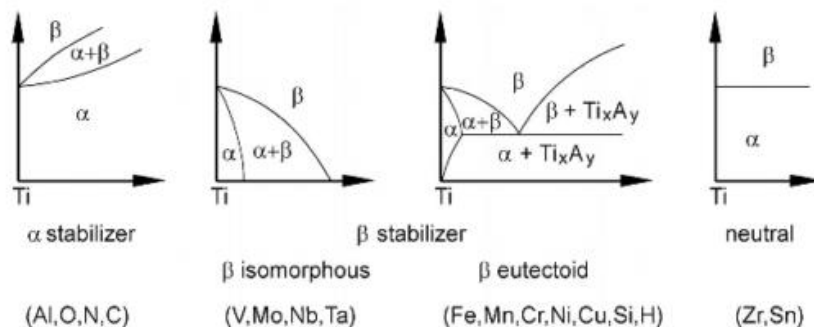
Figure 2-2. Schematic representation of phase diagrams of titanium depending on alloying element content [21].

There are five types of commercial titanium alloys: α, near α, α+β, near β and β. These classifications correspond to the location in the pseudo-binary phase diagram from a β isomorphous class as shown in Figure 2-3.
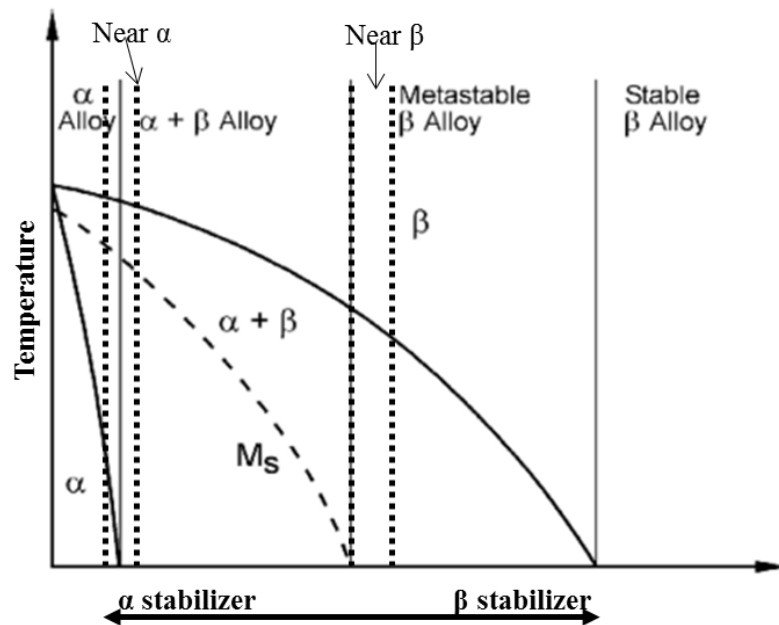
Figure 2-3. Pseudo phase diagram showing the effect of α and β stabilising elements [21].

2.2. Titanium alloys classification

2.2.1. α alloys

At room temperature, the α phase is the major component. α alloys can be strengthened by the addition of interstitial elements O, N and C and substitutional Al. These type of alloys have excellent corrosion resistance properties, being commercially pure (CP-Ti) the main one. Yield strength varies from 170 MPa to 480 MPa by the difference in impurity content level. They possess good welding capabilities as they do not react to heat treatment due to the lack of phase transformation to β. They are highly resistant to creep at high temperatures. "Extra-low interstitial content" (ELI; 0.12% Oxygen) alloys maintain good ductility and toughness at cryogenic temperatures up to -250°C. Ti-5Al-2.5Sn-ELI is used for applications exposed to cryogenic environments.

2.2.2. near α alloys

In this alloy type, the α phase (hcp) is the main constituent, and at room temperature, they contain a small volume fraction of β phase (2-5% vol), which is stabilised by Fe. They contain substitutional elements such as Al or Sn, interstitial elements such as O, N or C and may contain

limited elements of Fe, V and Mo. They have excellent workability and weldability because they have low element content and therefore, they do not respond to heat treatment. They can be used in-service up to 480°C.

Ti-8Al-1Mo-1V, Ti-6Al-2Nb-1Ta-0.8Mo and Ti-5Al-4Sn-3.5Zr-0.7Nb-0.5Mo-0.3Si-0.06C (Timetal® 834) are examples of near α alloys. Timetal® 834 is classified as an advanced alloy used at high temperature, providing excellent creep resistance, fatigue, fracture toughness, crack propagation resistance, ductility and good temperature stability properties [3]. Its microstructure is composed of 15% primary α, and 85% transformed beta (a matrix of lamellar alpha and beta).

2.2.3.   α + β alloys

This class of alloys contain the addition of α and β stabilising chemical elements. The formation of the higher volume fraction of β phase, allows the alloy to be strengthened by solid solution treating and ageing. The mechanical properties depend on the amount of β stabilisers present. By the addition of higher concentration of β stabilising elements, a more balanced chemistry of α and β phases results, and a wider range of microstructural characteristics are seen. The resulting microstructure, and consequently the mechanical properties can be tailored by adjusting the thermomechanical processing parameters [22]. The main type of microstructures developed in this alloys is fully lamellar, fully equiaxed and bi-modal. The main alloy belonging to this class is Ti-6Al-4V, which accounts for more than 50% of the market share [21]. β transus of Ti-6Al-4V and its comparison to α alloy CP-Ti is shown in Table 1.

β annealing is a heat treatment in the β phase field given to α + β alloys in the final steps of the primary processing route, and it generates a lamellar type of microstructure. This process is also known as β recrystallization and is schematically shown in Figure 2-4. The first step during primary working is a homogenization heat treatment in the β phase field. The second step undertakes deformation either in the β phase field or α + β phase field by forging or rolling. Commonly, it is deformed first in the β phase field because lower flow stress is required, followed by deformation in the α + β phase field to prevent large β grain sizes. The third step, recrystallization heat treatment, is kept between 30 to 50°C above the β transus to prevent excessive β grain growth. The prior β grain size results in sizes near 600 μm. The cooling rate in step III is the most important parameter as it determines the characteristics of the lamellar microstructure such as the α colony size, the thickness of the α lamellae, and the thickness of α at prior β grain boundaries. All these parameters decrease by increasing the cooling rate. Cooling rates vary from slow cooling in a furnace, typically 1°C.min^{-1} to fast cooling 8000°C.min^{-1} by water quenching thin components [21].

The main change in microstructural dimensions occurs in a small cooling rate range. For instance, the width of the α lamellae reduces from 5 μm at slow cooling rates to near 0.5 μm at

a cooling rate of 100°C.min^{-1}. An increase in cooling rate leads only to a reduction of nearly 0.2 µm. The slow cooling rate could lead to an α colony size of about half of the prior β grain size, about 300 µm. Increasing the cooling rate to 100°C.min^{-1} leads to a small decrease in size of nearly 100 µm. The largest reduction in α colony size occurs between 100°C.min^{-1} and 8000°C.min^{-1}. The presence of α phase in the prior β grain cannot be avoided. At slow cooling rates, the size is similar to the α lamellae in the colonies.
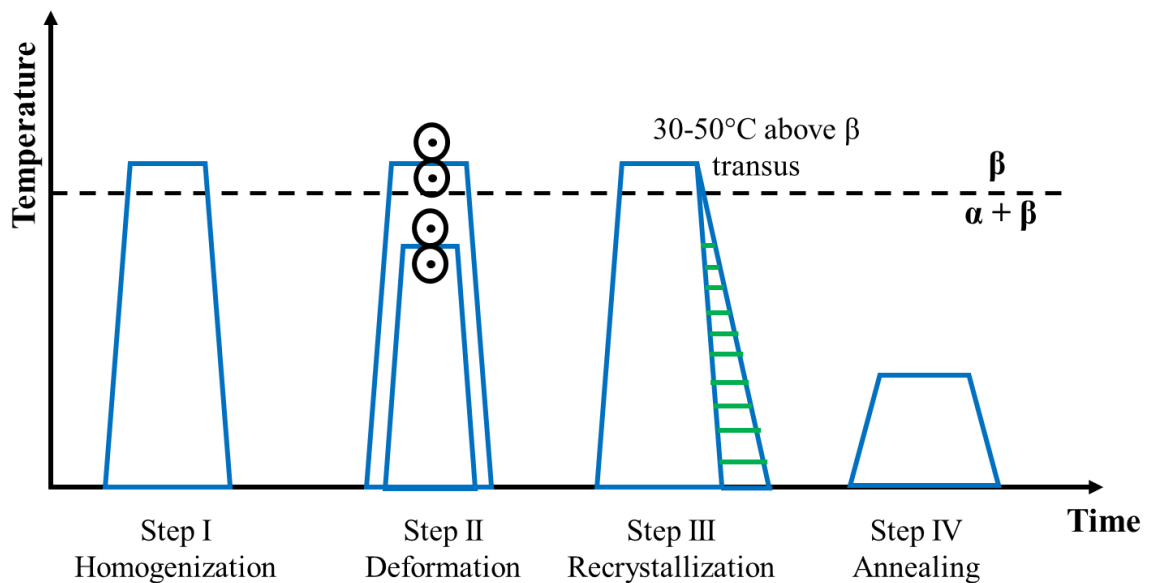
β annealing

Figure 2-4. Processing steps to generate a lamellar microstructure in α + β alloys (β annealing)- after Lütjering and Williams [21].

Mill annealing is a common heat treatment but is not very well defined. The recrystallization (step III) is not undertaken, see Figure 2-5. As a result, parameters used in step II during deformation determine the characteristics of the microstructure, particularly the amount of recrystallization. Processing parameters may vary between producers or between lots. The annealing treatment, step IV, is usually done at temperatures higher than the Ti$_3$Al solvus, resulting in a stress relieving treatment.

Mill annealing
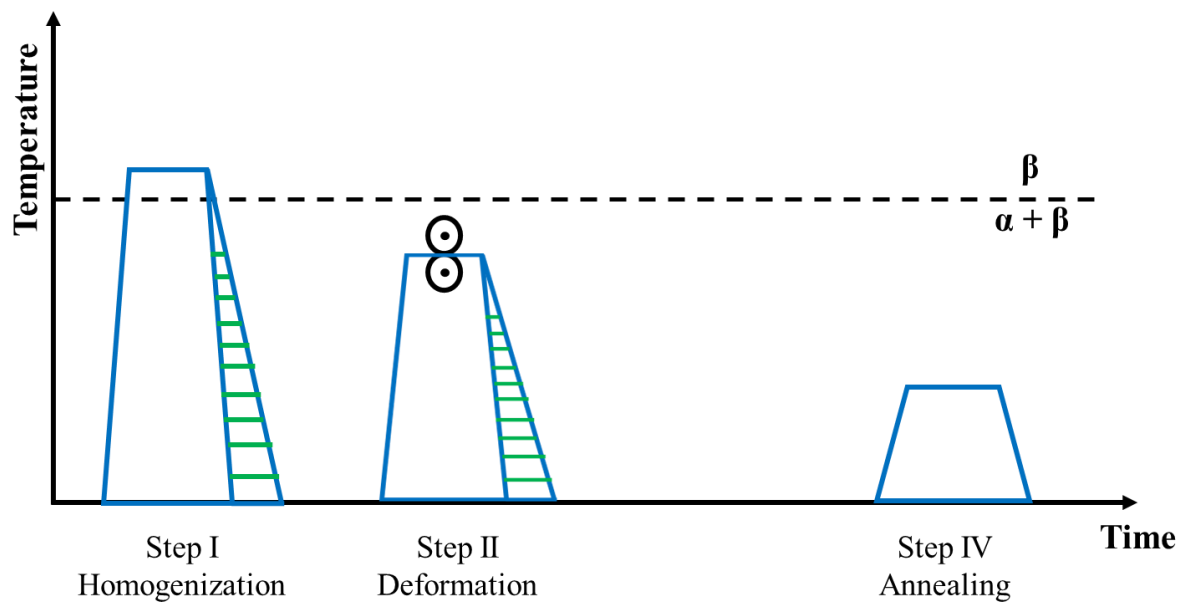
Figure 2-5. Processing steps for mill annealing α+β alloys - after Lütjering and Williams [21].

Table 1. β transus of CP-Ti and Ti-6Al-4V [21].

Alloy	β transus (°C)
CP-Ti	915
Ti-6Al-4V	995
Ti-6Al-4V ELI	975

2.2.4. Metastable β alloys

This type of alloy contains a higher content of β stabilising elements, the β transus is lowered, and this allows a higher volume fraction of β phase at room temperature. They possess high hardenability and have excellent forgeability and good cold formability attributed to the bcc crystal structure. β alloys are metastable, consequently upon heating to slightly high temperatures or cold working at room temperature they could return to the equilibrium condition by transforming to α.

High strengths can be reached with this type of alloy by forming finely dispersed α particles in the retained β. If sufficient β stabilising elements are added, the martensite start/finish (M_s/M_f) temperature can be suppressed and upon quenching the alloy does not transform [26]. Consequently, 100% β could be retained at room temperature in the solution-treated state. This state exhibits low strength, leading to outstanding formability. They precipitate α at elevated

14

temperatures. Thus their microstructure is unstable in service at high temperatures without stabilisation treatment.

Some disadvantages are their higher density, low creep strength and low tensile ductility. However, they exhibit high fracture toughness.

2.2.5. Fully lamellar microstructure

This microstructure is obtained through an annealing treatment in the β-phase field, known as β annealing. It is applied after work by forging in the β phase or α +β phase field. The critical parameter in this annealing is the cooling rate from the β phase field. It determines the size of the α colony, α lamellae, and thickness of α layers at prior β grain boundaries; all decrease by increasing cooling rate. The effect of cooling rate from the β phase field in Ti-6246 is shown in Figure 2-6. Figure 2-6 a) shows cooling at a slow rate, allowing solid-state diffusional processes to take place and Figure 2-6 b) shows a high cooling rate at 8000 °C.min^{-1}. Small α colonies and small α lamellae in comparison to coarse dimensions commensurately decrease the slip length, therefore increases the yield strength, increases high cycle fatigue and strain to fracture [21]. These types of microstructure are used in applications where high fracture toughness and high crack growth resistance under cyclic fatigue is required. The prior β grain size strongly influences these mechanical properties; with coarse prior β grain size, an improvement in fracture toughness and creep resistance is reached, while with a small prior β grain size strength and ductility are achieved.
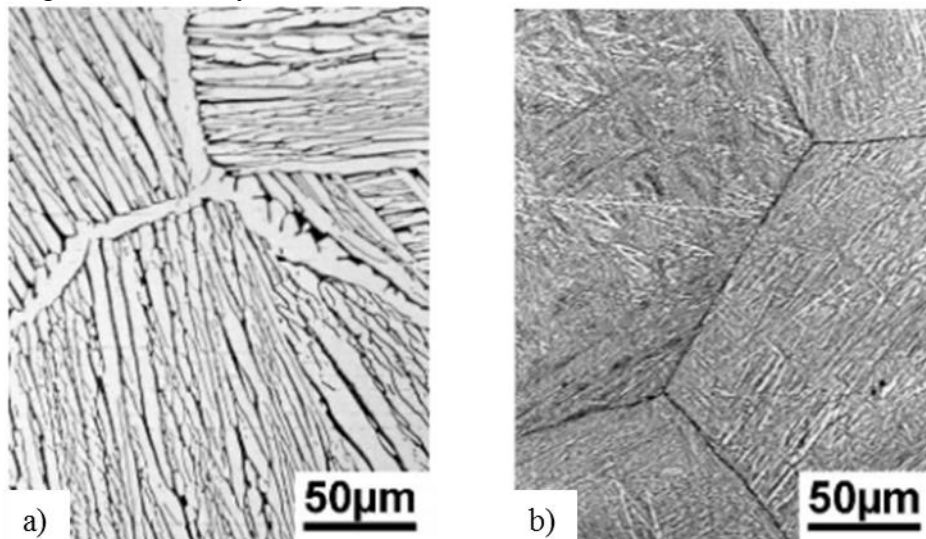
Figure 2-6. Microstructural effect as a dependency on cooling rate on Ti-6242 light micrographs at : a) 1°C.min^{-1}, b) 8000 °C.min^{-1} [21].

2.2.6. Bimodal (duplex) microstructure

The thermomechanical processing to generate a bi-modal microstructure involves four steps. (1) Homogenization in the β phase, (2) deformation in the α + β phase field, (3) recrystallization in the α + β phase field and (4) annealing in the α + β phase field. The most critical parameter in this type of microstructure is the cooling rate from step I (homogenization) from the β phase. It determines the width of α lamellae, which is then deformed and recrystallized (see Figure 2-7). The temperature during the recrystallization anneal controls the volume fraction of recrystallized primary α (α_p) situated at recrystallized β grains, triple points. A bimodal microstructure exhibits improved yield strength, higher strain to fracture, HCF strength, slower crack propagation rate of microcracks during fatigue, and higher LCF in comparison to fully lamellar microstructures [21]. The crack nucleation resistance during HCF is reduced by increasing the volume fraction of α_p.
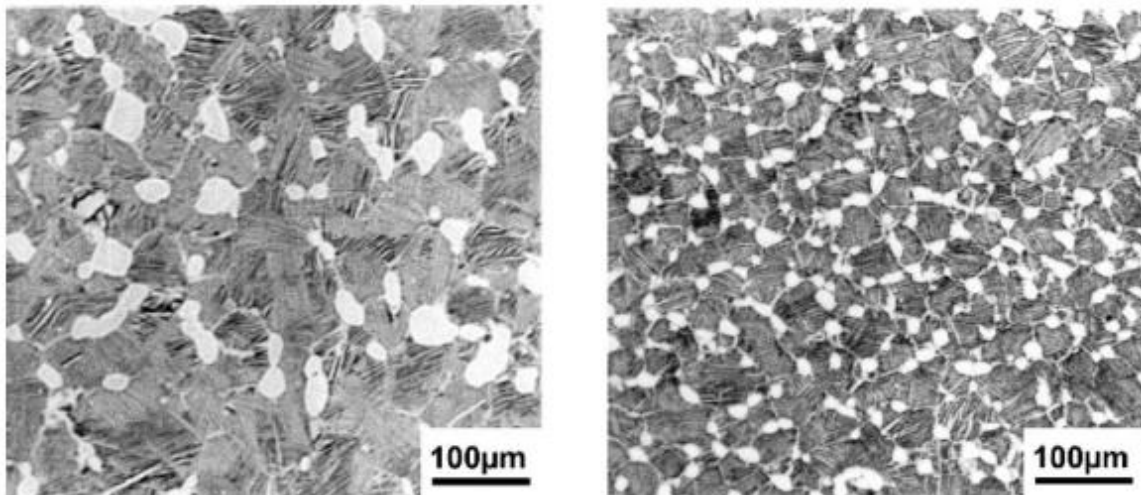
Figure 2-7. Bimodal microstructure of IMI 834 alloy. Different cooling rates from the β phase in the homogenization step I at a) slow cooling rate and b) high cooling rate [21].

2.2.7. Equiaxed microstructure

The processing steps to form an equiaxed microstructure are similar to the bi-modal process up to recrystallization, where the cooling rate is lower to allow diffusional processes to only grow α_p, and α lamellae. This results in an equiaxed microstructure with a small volume fraction of β phase remaining at triple points of the α grains. An example of an equiaxed microstructure is shown in Figure 2-8. The cooling rate from the homogenization step dictates the size of the α grains.

The mechanical properties of a fully equiaxed microstructure are strongly influenced by the grain size α since it determines the slip length. The smaller the grain size, the higher the HCF strength, the higher the yield strength and the higher the ductility under tension [21].
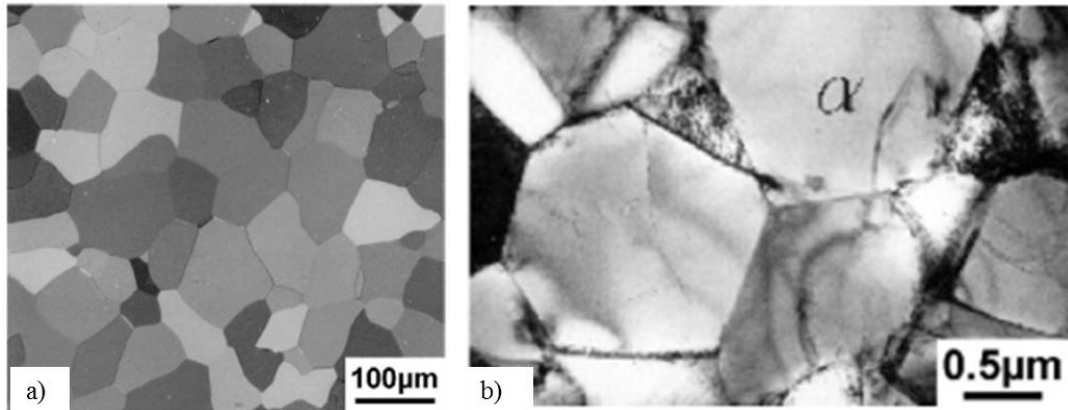
Figure 2-8. Equiaxed microstructure: a) CP-Ti with 0.03% Fe under light microscopy and b) Ti-6Al-4V recrystallized at 800°C observed under TEM [21].

This work involved the study of the deformation mechanisms of the fully lamellar microstructure of α + β phases, β annealed Ti-6Al-4V ELI, the fully equiaxed mill annealed Ti-6Al-4V, and equiaxed CP-Ti.

2.3.   Deformation mechanisms

The deformation of the α phase is highly anisotropic, and it is attributed to the inherent low symmetry of this type of crystal structure. The α phase titanium exhibits ductile behaviour even at low temperatures. This results from the operation of mechanical twins additionally to slip systems. Although Lütjering et al. [21] states that mechanical twinning is nearly suppressed in α+β alloys, in this investigation mechanical twins have been widely observed under ambient and low-temperature deformation.

Hcp metals undergo both dislocation slip and mechanical twinning during plastic deformation [21], [27]. The glide usually consists of a-type, a+c –type or c-type dislocation slip. Hcp α titanium, with a c/a ratio 1.587 principally deforms by prismatic glide of the a-type dislocations. Bcc β phase undergoes twinning and slip. However, the incidence of twinning occurs only in the single phase and decreases by the addition of solute content.

2.3.1.   Slip

The slip systems (planes and directions) of hcp α titanium have been previously described in section 2.2.1., and are shown in Figure 2-9. The slip systems with the different Burgers vectors are shown in Table 2-2. Only the pyramidal plane with a Burgers vector $\bar{c} + \bar{a}$ has 5 independent slip systems.
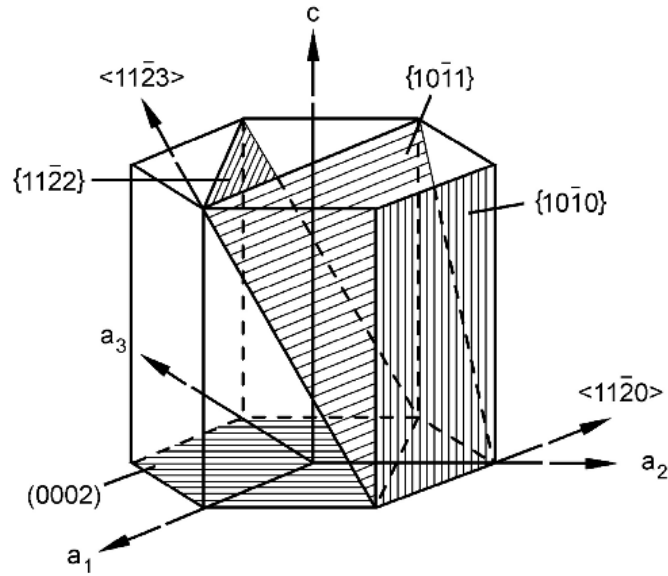
Figure 2-9. Slip planes and directions in the hcp phase [21].

Table 2-2. Slip systems in hcp α titanium [21].

Slip system type	Burgers vector type	Slip direction	Slip plane	No. of slip systems Total	No. of slip systems Independent
1	$\bar{a}$	$<11\bar{2}0>$	(0002)	3	2
2	$\bar{a}$	$<11\bar{2}0>$	$\{10\bar{1}0\}$	3	2
3	$\bar{a}$	$<11\bar{2}0>$	$\{10\bar{1}1\}$	6	4
4	$\bar{c}+\bar{a}$	$<11\bar{2}3>$	$\{11\bar{2}2\}$	6	5

The critical resolved shear stress CRSS for the operation of slip is strongly dependent on the temperature of deformation as observed in Figure 2-10. As the temperature decreases, there is a higher increase in CRSS between the different slip modes. Although the basal slip with $\bar{a}$ Burgers vector shows a small increase in the CRSS with respect to prism slip with a reduction in temperature, the slip with $\bar{c} + \bar{a}$ Burgers vector shows a much higher increase with respect to the basal slip. As von Mises stated, for homogeneous plastic deformation to occur in polycrystalline materials, a minimum of five independent slip systems is required [28]. This is as 6 stress tensors define a system and due to the constancy of volume, the requirement is reduced to 5 [2]. Only the $\bar{c} + \bar{a}$ Burgers vector system has 5 independent slip systems. The CRSS at lower temperature greatly increases and the twinning CRSS is nearly temperature independent (Figure 2-11), consequently, mechanical twinning will be the leading deformation mechanism at lower temperatures.
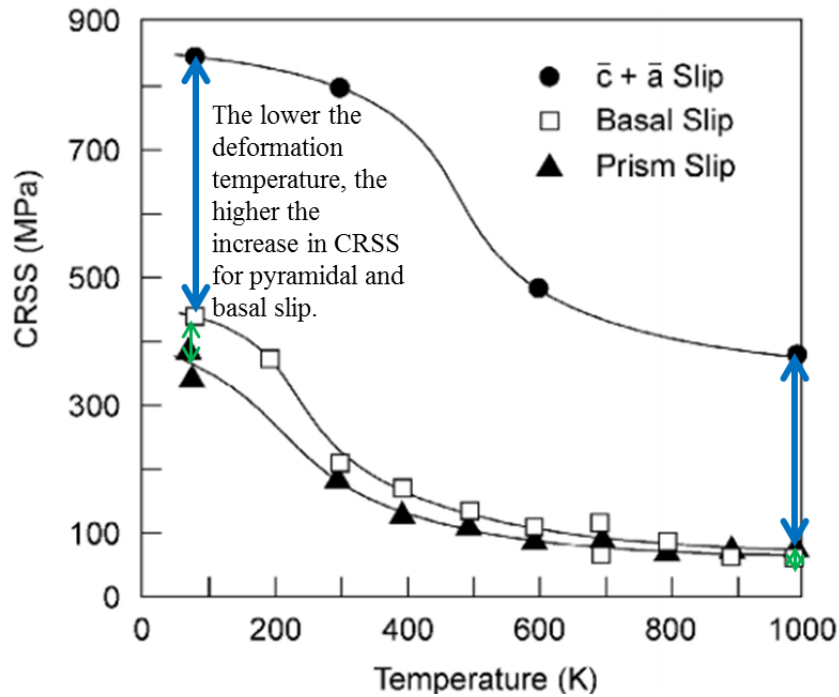
Figure 2-10. The effect of temperature on the Critical Resolved Shear Stress (CRSS) (MPa) for basal, prism and pyramidal slip in Ti-6.6Al single crystals[21].

Meyers et al. [29] show that while the CRSS for slip is temperature dependent, the CRSS for twinning is insensitive to temperature as illustrated in Figure 2-11. It also points out that the slip-twin intersection is substantially dependent on strain rate; at 120K (-153 °C) at a strain rate of 10^{-3} s^{-1} and 200K (-76°C) at a strain rate of 10^3 s^{-1}.
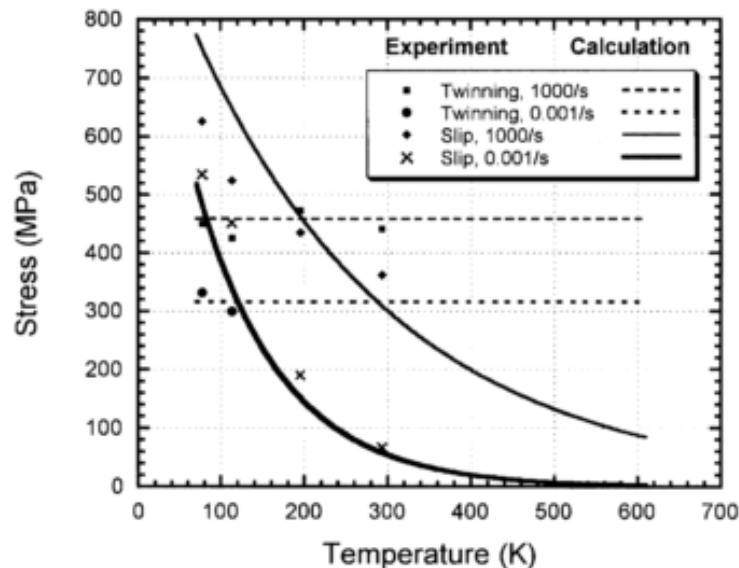
Figure 2-11. Effect of temperature on the CRSS of slip and twinning under quasistatic strain rate and dynamic strain rate in single crystals of iron [29].

2.3.2.　　　Mechanical twinning

Twinning is the predominant deformation mechanism in low stacking fault (SFE) metals [30]. At an imparted strain into the crystal lattice, the limited number of slip systems promotes the activation of deformation twinning. The nucleation of a mechanical twin occurs at a site of stress concentration, and it is not thermally activated. As discussed in § 2.3.1, the $\bar{c} + \bar{a}$ Burgers vector is the only type with 5 independent slip systems and its CRSS strongly increases by reducing temperature or reducing interstitial content, thus mechanical twinning becomes the dominant deformation mechanism.

In plastic deformation, twinning plays a significant role in grains that have their <c> axis in the same direction to the loading direction. These grains are likely not to undergo slip as their Schmidt factor for dislocation glide is equal to zero.

A single crystal deformed sphere can illustrate the nucleation process of a twin, as shown in Figure 2-12, where the upper half exhibits the twinned material, and the lower part portrays the parent material. By application of uniform shear, the upper part is distorted into the twinned location and is represented by an ellipsoid shape. This ellipsoid intersects the sphere in 2 circles, which represent the undistorted planes K_1 and K_2*. K_1 is the twinning plane. The shear direction in represented by η_1 and is shown as the line through the sphere. K_2 is the undistorted plane after shear has occurred and before the material has twinned. The shear strain γ can be estimated knowing the angle between the K_1 and K_2 undistorted planes. [3], [31]. A twin formation produces a change in the shape of the sphere. However, this does not translate into an increase in dimensions of material [31].

There are two significant effects of mechanical twinning in plastic deformation. The first, it subdivides the grains; therefore there are more barriers to slip and work hardening. The second, it contributes to plastic deformation by the twinning shear, which produces a reduction in the work hardening rate [29]. A grain has a high Schmidt factor when the principal stress direction along the c-axis is in tension (twinning modes T1 or T2) or compression (twinning modes C1 or C2). It also shows the misorientation angle of the twinned plane with respect to its original parent.
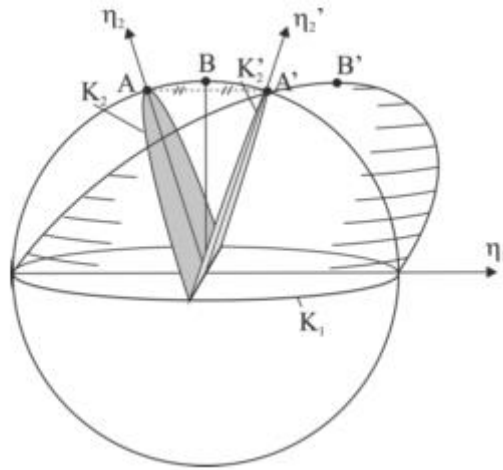
Figure 2-12. Schematic illustration of the representation by an analogy of the parent grain and a twin with a sphere and a twin ellipsoid sharing K_1, the common plane [31].

The angle of Misorientation (determined by TEM) and their correspondent axis is given in Table 2-3. These relations allow identification of shear misorientation between the twin and the parent grain. The twinning type in Table 2-3 indicates whether, during the occurrence of twinning, an extension or compression along the <c> axis is accommodated in the hcp unit cell. Di Iorio et al. [32], [33] found the existence of $\{5\bar{6}1\bar{3}\}$ during quasi-static tensile testing of powder metallurgy Ti-6Al-4V ELI at 20 K (-273.15°C) with a lamellar microstructure composed of α lamellae colonies orientated in the same direction and retained β. The leading deformation mechanism was twinning attributed to the low-temperature plastic deformation and the specimen's low interstitial content. Its K_1 plane was considered to be irrational "i" by being of a high order. "i" twins were considered to be a major damage precursor at the microscopic scale. $\{10\bar{1}1\}$ twins were identified in the interior of $\{5\bar{6}1\bar{3}\}$ as secondary twinning and accommodating 10% plastic strain. These secondary twins were attributed to the increase of internal stresses, leading to the nucleation of cavities and promoting the $\{5\bar{6}1\bar{3}\}$ twin, resulting in debonding from the matrix.

Table 2-3. Twinning in α titanium [3], [21], [32].

Twin Plane	Shear direction	Misorientation θ about <uvtw>	Twin type	Twinning shear
$\{10\bar{1}2\}$	$\langle\bar{1}011\rangle$	84.78° $\langle2\bar{1}\bar{1}0\rangle$	Tension	0.167
$\{11\bar{2}1\}$	$\langle\bar{1}\bar{1}26\rangle$	35.1° $\langle10\bar{1}0\rangle$	Tension	0.638
$\{11\bar{2}2\}$	$\langle\bar{1}\bar{1}23\rangle$	64.62° $\langle10\bar{1}0\rangle$	Compression	0.225
$\{10\bar{1}1\}$	$\langle\bar{1}012\rangle$	57.42° $\langle2\bar{1}\bar{1}0\rangle$	Compression (>400°C)	-
$\{5\bar{6}1\bar{3}\}$	$\langle41\bar{5}3\rangle$	65°$\langle3\bar{3}6\bar{3}\rangle$	Irrational "i" twin tension	-

21

Di Iorio et al. [32] studied the plastic deformation and damage of Powder Metallurgy (PM) Ti-6Al-4V Extra Low Interstitial (ELI) at cryogenic cooling conditions (20K) under tensile loading. This alloy contains 90 % α and 10 % β crystallographic phases. It was found that twinning $\{5\bar{6}1\bar{3}\}$ type is the precursor to the nucleation of cavities by twinning plane debonding process as shown in Figure 2-13. The first twins appear after 3 to 4 % of strain, then the number of twinned grains grows with increasing strain. Then secondary twins are detected at high strain. The twin type $\{10\bar{1}1\}$ was found inside the twin type $\{5\bar{6}1\bar{3}\}$ at 10 % strain. It led to an increase in internal stresses, which favoured the $\{5\bar{6}1\bar{3}\}$ twin plane, resulting in debonding.
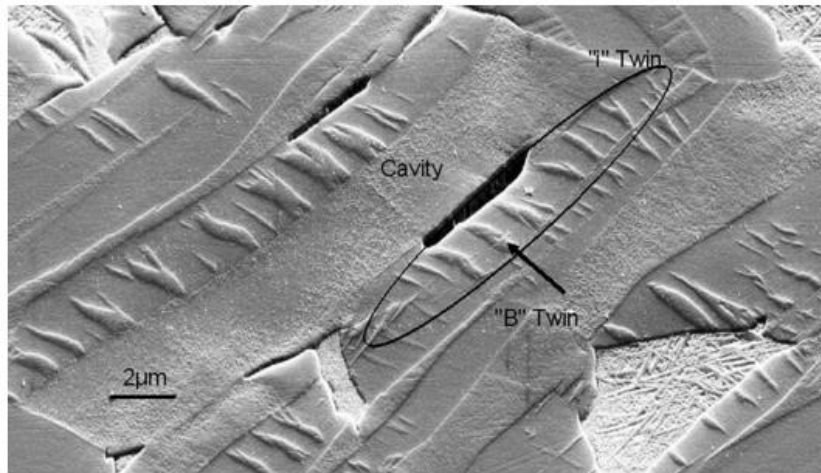
Figure 2-13 Cavities generated at the end of secondary twins [32].

The underlying microstructure plays a key role during plastic deformation as it determines the type of mechanisms operating during deformation. Process parameters are also closely connected with the resulting deformation features. The effect of process parameters such as strain, strain rate and temperature on the resulting deformation features in the microstructure is still not well defined. This investigation will concentrate a section of the work in investigating the role of these process parameters on the underlying microstructure evolution during uniaxial quasi-static compression testing.

There is a high tendency for the occurrence of mechanical twinning in BCC and HCP metals under low temperatures and high strain rates since at these conditions the flow stress can be increased to the required level for twinning [29]. Meyers et al. [29] generated a constitutive twinning model for BCC, in which deformation transfers across a grain boundary are owing to the presence of a dislocation source. Since pile-ups create stress concentrations due to the activation of the Frank-Read or Koehler source, the distance between the source and the barrier as well as the applied stress determines the number of dislocations that pile up. If the energy for twin nucleation is lower than that required to pass the grain boundary, the dislocation pile-

up provides the energy necessary for the nucleation of a twin. That required energy strongly depends on the crystallographic orientation of the specific grain.

2.3.3. Influence of Subsurface Damage features during crack initiation in fatigue

Slip and twinning are plastic deformation mechanisms which are not thermally activated, and they have a high influence in the mechanisms of failure by fatigue [34]. The reason is the fact that fatigue failures have occurred in a workpiece at 4 K [34]. Therefore it is believed that thermal energy is not necessary to cause fatigue; thus diffusion is not necessarily operative in the process. In many metals, near room temperature, slip systems are the deformation mechanisms operative, and at low temperatures, mechanical twinning is predominant as the CRSS is lower than other operating mechanisms.

In alloys, slip bands (groups of slip lines which are closely spaced) form prior to fracture and below the fatigue limit. These slip bands are formed on planes of high resolved shear stress, and the number of slip bands rises as the number of cycles increases. The number and the length depending on the applied stress. Under cyclic load, they form into groups known as striations, and these compose persistent slip bands (PSBs). In polycrystalline materials, PSBs, as shown in Figure 2-12, are common nucleation sites, especially in alloys that are prone to strain localisation. The cracks leading to fatigue failure have been found in the PSBs, where there is the highest local strain. Thus sites of high strain localisation could give rise to PSB's.
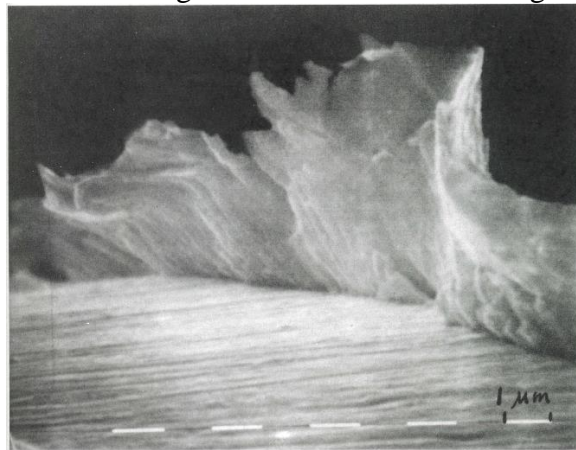
Figure 2-14. Persistent slip band (PSB) in a single crystal of copper at a plastic strain amplitude 2 X 10^{-3} during 30,000 cycles [34].

2.4.   Effect of temperature during plastic deformation

2.4.1.   Dislocation structure

During plastic deformation, the dislocation distribution is strongly influenced by (1) the underlying crystallographic structure of the deforming workpiece, (2) the temperature during deformation, (3) imparted strain, and (4) the imparted strain rate. Likewise, features such as the distribution of phases (in this case α and β), grain size, stacking fault energy, grain boundaries and precipitates influence the distribution of the dislocations.

The temperature experienced by the workpiece metal during plastic deformation has a strong influence on the underlying dislocation behaviour. An example is illustrated by Hull [35]; he shows the contrasting difference of accommodation of the imparted plastic strain into the subsurface of iron in Figure 2-15. Figure 2-15 a) shows the development of tangled dislocation arrangements surrounding dislocation-free cells in the sample subjected to 9 percent strain at 20°C; reaching a specific cell size at low strains which only changes slightly on the application of higher strains. Figure 2-15 b) shows the underlying dislocations uniformly distributed. Although iron is an allotropic material usually composed of bcc and fcc, it has different properties. This example shows the contrast differences in dislocation behaviour under plastic deformation at different temperatures. This high dislocation introduction allows the strain hardening of the underlying crystals by the interaction of dislocation strain fields, forest dislocations, interaction with "debris" such as point defects and loops, generated during the movement of dislocations and any other obstacle present in the material. In order to predict the work hardening response at a specific temperature and strain rate, it is necessary to know the distribution of dislocations and their change by additional imparted strain.
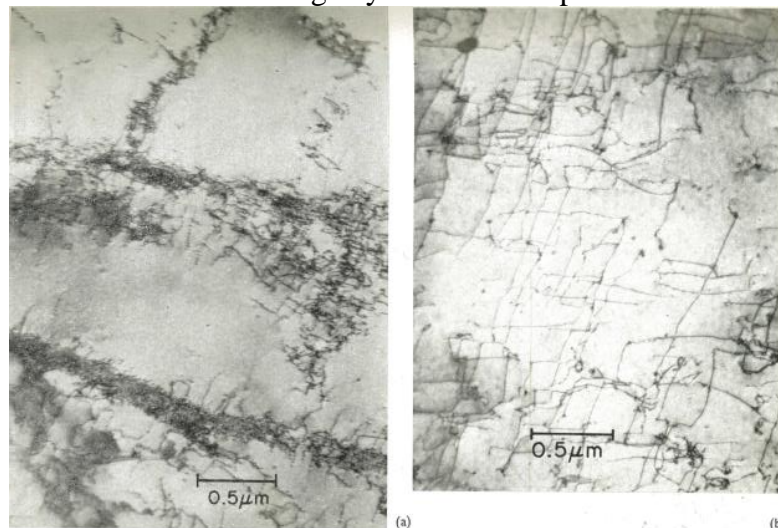
Figure 2-15. Dislocation distribution by strain imparted during plastic deformation in iron; a) dislocations tangled in dense arrays surrounded by dislocation-free cells at an imparted

strain of 9 percent at 20°C and b) dislocations distributed uniformly in 7 percent imparted strain at -135°C [35].

Figure 2-16 shows further evidence of the uniform distribution of dislocations during plastic deformation at low temperatures to a strain of 14% in iron.

0.3 µm
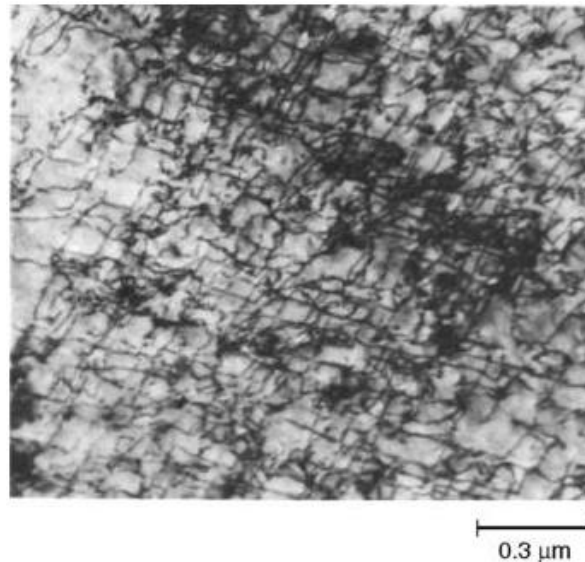
Figure 2-16. A bright field TEM micrograph showing a uniform distribution of dislocations in 14% iron, deformed at a temperature of -195°C [36].

Williams et al. [37] studied the temperature dependence on the thermally activated flow stress (τ^*) and internal stress (τ_{int}) on α titanium with a 25-30 µm grain size, using both high and low oxygen concentration. They found a strong temperature dependence on the long-range internal stress. At a higher oxygen concentration, a dislocation arrangement transition occurs at low temperatures from wavy to planar slip giving rise to an increase in internal stress and thermally activated stress. The transition from wavy to planar slip denotes the difficulty of cross slip at lower temperatures and higher oxygen content. At a high oxygen content, the maximum thermally activated stress arises at the temperature where the onset of planar glide occurs. At a low oxygen concentration, a uniform distribution of dislocations at low temperatures is observed as shown in Figure 2-17 d) and e). They observed twin thickness and frequency to decrease with increasing temperature and oxygen content. Slip accompanied the deformation twins in the matrix and the twin.
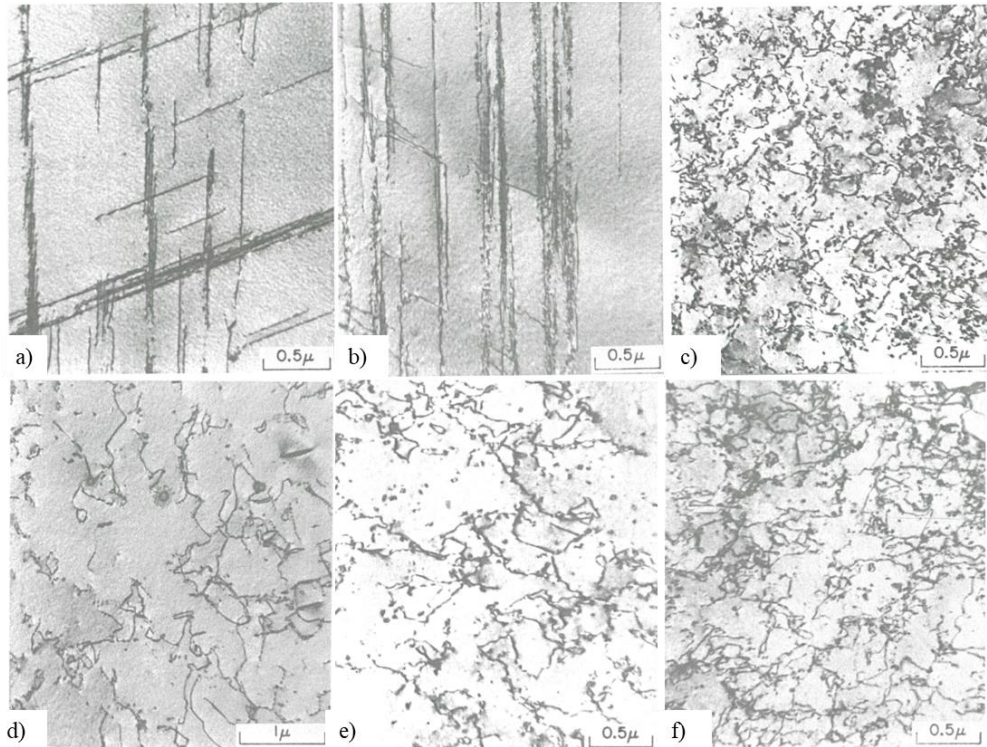
Figure 2-17. α titanium: a)-c) high oxygen interstitial content (5200 ppm), d-f) low oxygen interstitial content (475 ppm), at temperatures: a) and d) 77K, b) and e) 300K and c) and d) 500 K. Adapted from Williams et al. [38].

A c/a ratio close to 1.6 has been identified as a reference for good ductility [39]. As Ti is close to this ideal ratio with a value of 1.587, it has become an important metal, which exhibits a good level of ductility, especially at low temperatures.

HCP metals yield stress dependency on temperature reaches a plateau with the increase of temperature, at a temperature range between 0.25 to 0.5 Tm (melting temperature) [40], showing a similar behaviour to the bcc metals. The range in bcc metals is lower; from 0.2 to 0.25 Tm. Additionally, the effect of temperature on the flow stress has a dependency on interstitial content. As observed in Figure 2-18, the increase in purity content in titanium generated a greater thermal component of the yield strength (τ^*), which is similar to the bcc metals. On the other hand, if the purity is increased (Figure 2-17 d)–f)), the thermal component of the flow stress has a much lower dependence on temperature and much lower values, similar to those of the fcc.
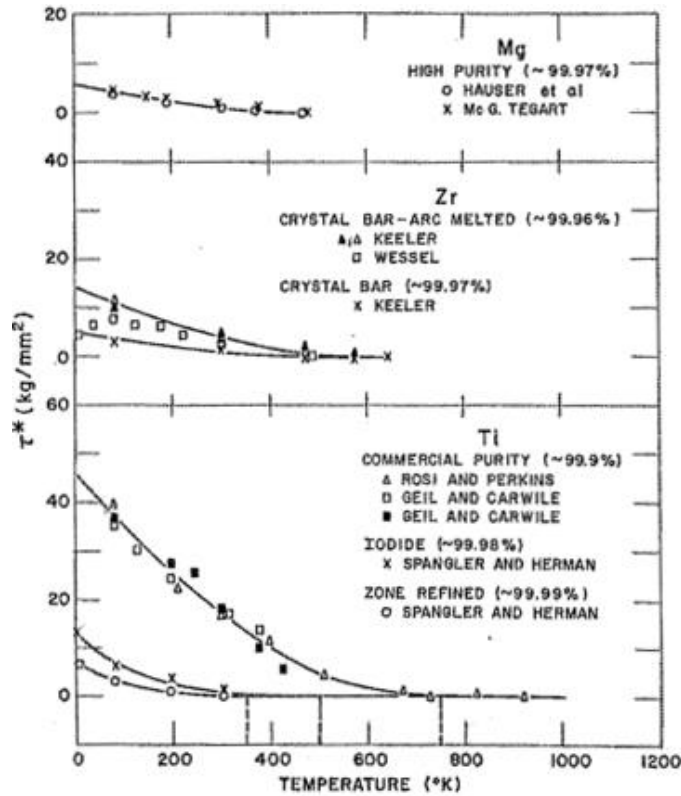
Figure 2-18. Influence of temperature on the thermal component of the flow stress [40].

The strain-rate sensitivity parameter, "m", for CP-Ti is shown in Figure 2-19. It shows an increase with increasing temperature, up to nearly 230°C. A further increase in temperature leads to a decrease in "m". At room temperature, CP-Ti in Figure 2-19 gives a value of nearly 0.03, whereas β annealed Ti-6Al-4V ELI has a value of 0.021. This suggests that the increase in substitutional element content leads to a lower sensitivity to strain rate. This implies that increasing the surface speed when cutting CP-Ti, will show a much higher increase in force in comparison to the increase in Ti-6Al-4V, leading to a higher increase in subsurface damage in comparison to the CP-Ti at lower surface speeds.

The activation energy for plastic flow (H) for α titanium is shown in Figure 2-20 a). 1eV equals 1.60218E-19 J. It follows a straight line, indicating the operation of one rate-controlling mechanism [40]. This graph indicates that by lowering the temperature, lower activation energy is required for plastic flow. At -196°C, H is nearly 0.15 eV or 2.4E-20 J, whereas at room temperature nearly 0.7 eV or 1.12E-19 J. Nearly 4.6 times lower energy is required at low temperatures to activate plastic deformation.

The dependency of stress on the activation volume in 99.7% Ti is shown in Figure 2-20 b). It is observed that higher stresses lead to lower activation volume values. Plastic deformation at low temperatures requires higher stresses for plastic flow; this suggests that lower activation volume is required at low temperatures. This means a lower volume of dislocation structures is involved in the plastic deformation process.

27
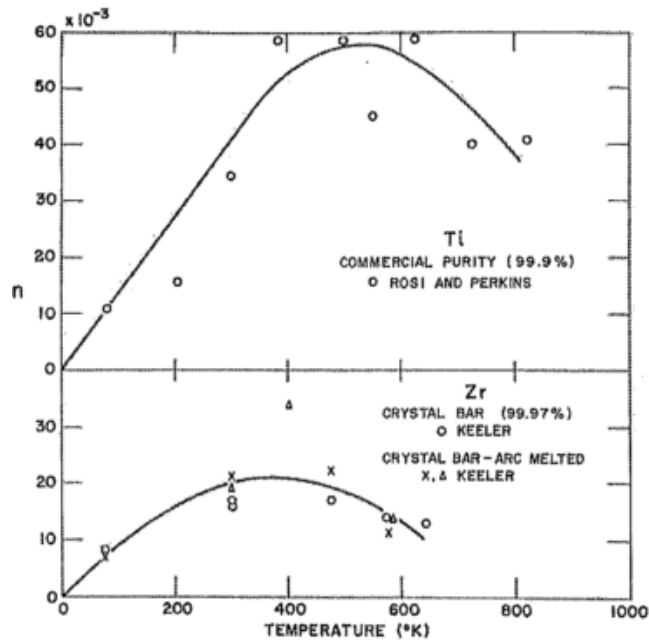
Figure 2-19. Dependence of the strain-rate sensitivity on temperature [40].
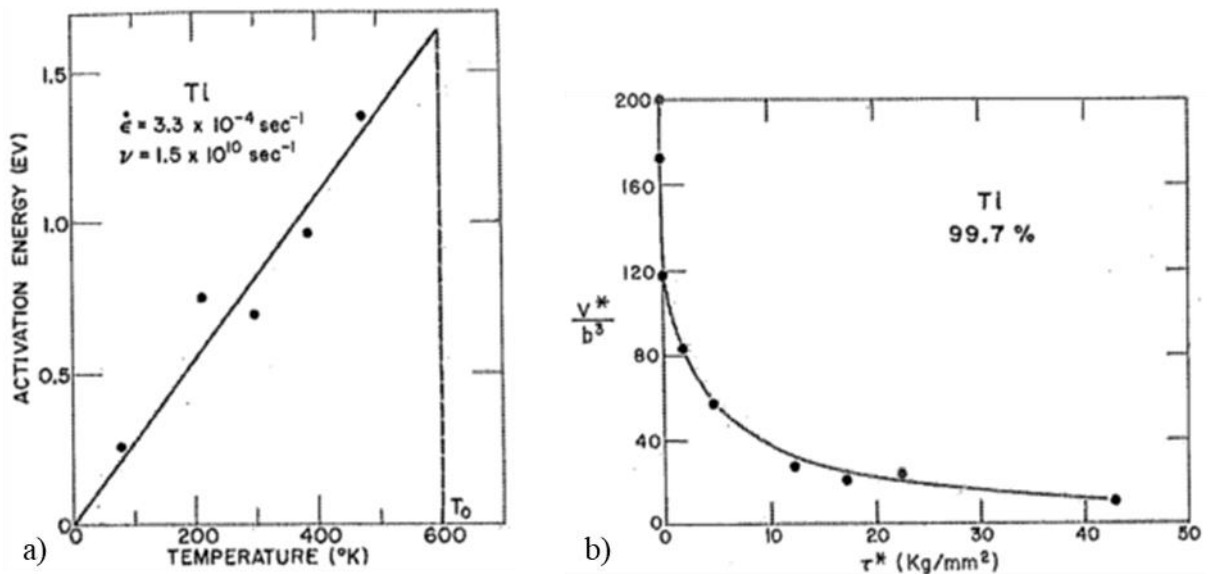
Figure 2-20. a) Temperature dependence of the activation energy for Ti and b) dependence of stress on the activation volume for plastic deformation [40].

The activation volume is not dependent on the applied strain. This is in agreement with the operation of (1) overcoming the lattice stresses opposing deformation (Peierls-Nabarro force), overcoming impurity atoms and cross slip. The activation volume values were similar for high impurity content titanium and for high purity Zr, which leads to the suggestion that the stress overcoming impurities is not the most influential mechanism at low temperatures.

28

2.4.2.   Deformation mechanisms at low temperatures

The mechanism of plastic deformation of titanium at room temperature is both by slip and twinning [41]. The predominant slip system is in the plane $\{10\bar{1}0\}$ in the $[11\bar{2}0]$ direction. Slip on $\{10\bar{1}1\}$ in the same direction is less prevalent. Slip on the $\{0001\}$ plane has seldom been found in CP-Ti. The CRSS is $\{10\bar{1}0\} < \{10\bar{1}1\} < \{0001\}$. Williams et al. [42] found a relationship of the CRSS for slip and twinning $C_{s(0001)} = 1.1C_{s\{10\bar{1}1\}} = 1.02C_{s\{10\bar{1}0\}} = C_{t\{10\bar{1}2\}} = C_{s\{1122\}}$.

Rosi et al. [43] determined the effect of deformation temperature on the micromechanism of plastic deformation by studying the plastic deformation in coarse-grained specimens of iodide titanium (99.975 % purity) and sponge Ti (99.77 % purity) on tensile testing specimens with coarse grain size. They also provided evidence of the predominant occurrence of slip on the $\{10\bar{1}0\}$ plane in a $\langle11\bar{2}0\rangle$ direction over a wide range of temperatures (from -196°C to 500°C), with an incidence of secondary slip on the $\{10\bar{1}1\}$ plane predominantly at higher temperatures. The incidence of mechanical twinning was determined to be more predominant at lower temperatures; thus the operating system during twinning depends on the testing temperature. They did not provide an accurate grain size. Unfortunately, the effect of grain size on deformation twinning cannot be accurately predicted with this data.

Five different twin systems were observed at -196°C; $\{11\bar{2}4\}, \{11\bar{2}2\}, \{11\bar{2}1\}, \{10\bar{1}2\}$ and $\{11\bar{2}3\}$ [43]. The $\{11\bar{2}4\}$ twin plane was the predominant twin as shown in Figure 2-21, making it the highest contributor to the accommodation of plastic strain. The other types of systems occurred on regions of complex stress systems as they occurred at the edge of the specimen or near grain boundaries, thus having a low contribution to the accommodation of plastic deformation. At room temperature, they also observed the occurrence of the same type of twins, however at much lower density and $\{11\bar{2}1\}$ occurred preferentially over the $\{11\bar{2}4\}$ twin planes. The contribution of twinning to plastic deformation increases as the deformation temperature is lowered, thus increasing the number of operational twinning systems and increasing the occurrence of $\{11\bar{2}4\}$ reducing $\{10\bar{1}0\}$ slip. At 500°C and 800°C, no evidence of mechanical twins was observed.

At -196°C, plastic deformation accommodated by slip occurred only on $\{10\bar{1}0\}$ prismatic planes on a $\langle11\bar{2}0\rangle$ direction. Contrarily, at room temperature, slip occurred on $\{10\bar{1}0\}, (0001)$ and $\{10\bar{1}1\}$ planes with $\{10\bar{1}0\}$ being the predominant plane. Figure 2-22 shows the nucleation of slip bands at -196°C at a minimal applied strain (<1%) and do not entirely traverse the grains. With the introduction of higher strain, deformation proceeds by the creation of new bands, reducing the average spacing, thus giving rise to an increase in slip density with increase in strain. The slip direction was always the same, corresponding to the close-packed direction.

Rosi et al. [43] showed that there is only a small dependency of the crystal orientation with the tensile axis and its influence on slip density. By increasing this angle, only a small increase in slip band density was observed (Figure 2-23).
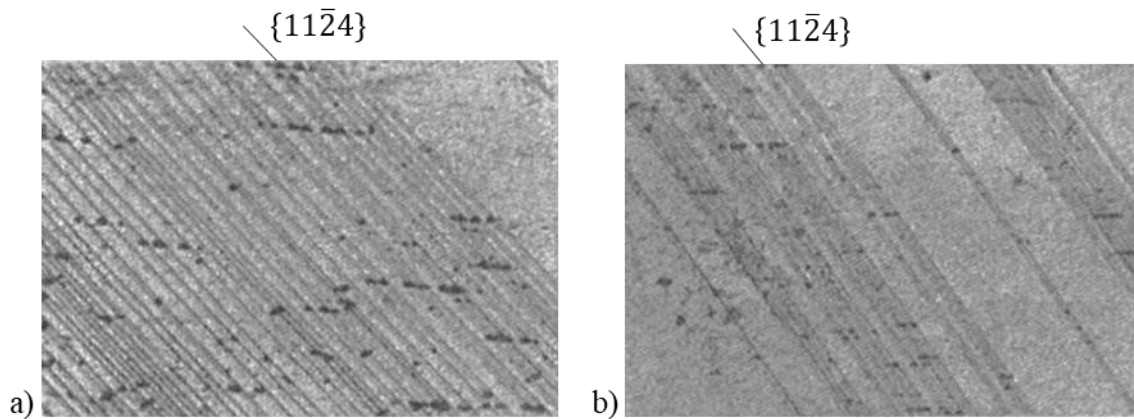
Figure 2-21. Profuse mechanical twinning at -196°C on $\{11\bar{2}4\}$ planes a) X100, b) X60 [43].
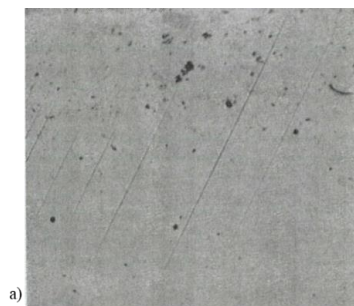
Figure 2-22. $\{10\bar{1}0\}$ prismatic slip bands at -196°C in specimen deformed under tension a) duplex slip b) at a low imparted strain ($< 1\%$) [43].
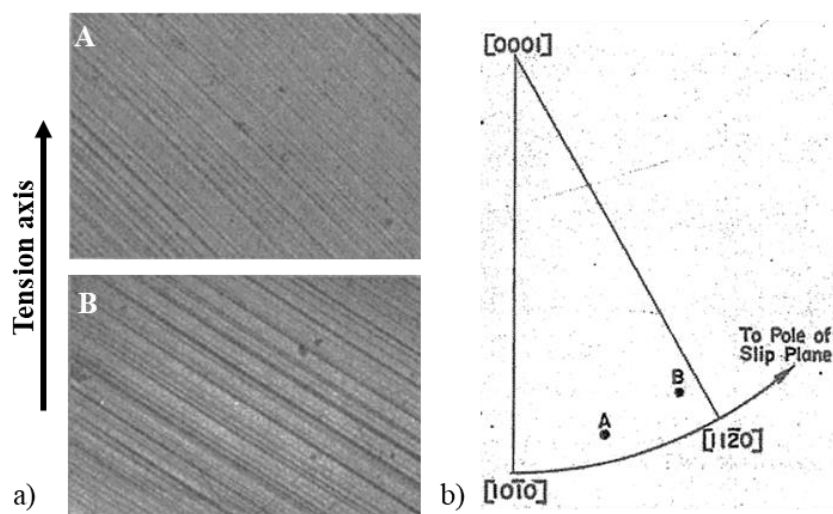
Figure 2-23. Low temperatures -196°C, the influence of the crystal orientation a) at an angle of (A) 44° and (B) 56° to the stress axis b) on the occurrence of prismatic slip bands [43].

2.5. Effect of strain rate during plastic deformation

Chichili et al. [27] studied the deformation mechanisms of hcp α-titanium by quasi-static and dynamic high strain rate compression testing. At low strain rates, twinning density increased slowly with strain. At high strain rate, twin density increased rapidly at low strains and reached saturation at high strains. Additionally, they correlated the twin density to the flow stress. A linear correlation was found where an increase in twin density corresponds to the increase in flow stress.

Chichili et al. [27] reported a correlation on the increase in mechanical twin density as a function of strain rate on CP- titanium deformation. They did not report mechanical twinning penetration depths. Mechanical twinning was measured as a percentage of the number of grains twinned and the number of twins per grain (twin density). The twin density is also a function of the imparted strain; the higher the strain, the higher the mechanical twin density on the subsurface as higher strain was accommodated into the lattice.

A linear correlation of the percentage of twinned grains as a function of stress was established: the higher the imparted stress, the higher the mechanical twin density (see Figure 2-24 b)). In this correlation, the effect of strain rate and the temperature is implicit in the flow stress as shown in Figure 2-24 a). Also, the higher the grain size, the higher the mechanical twin density is expected.
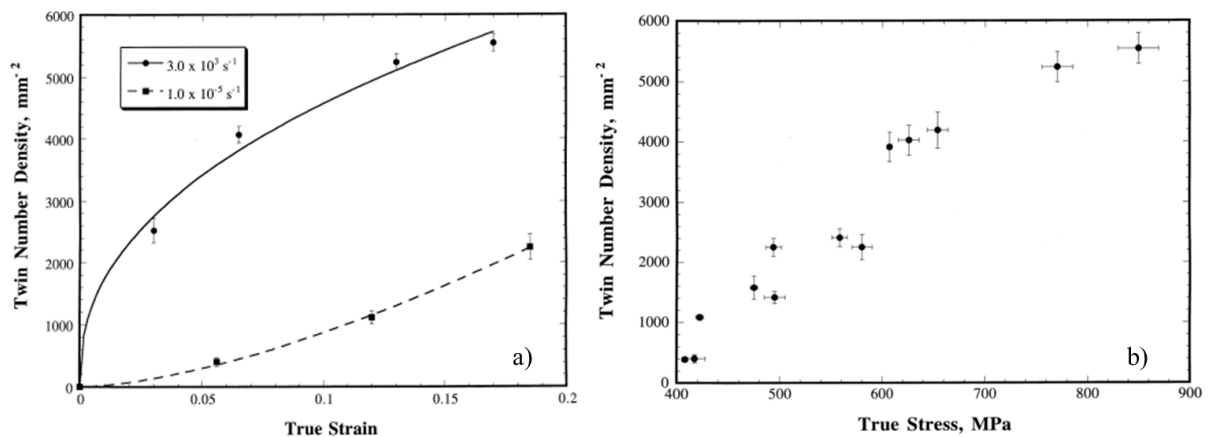
Figure 2-24. Twin density dependency on: a) imparted strain and strain rate and b) true stress [27].

This correlation implies that the higher the imparted stress into the material during deformation, the more strain energy is accommodated by the lattice.

Twin density is a strong function of imparted stress [27], [31]. However, stress is not a function of twins in the subsurface of the workpiece material. This has been corroborated by quasi-static deformation at a low temperature of -196°C, which generated a high density of twins. Then, the specimen was unloaded and reloaded at an ambient temperature of 25°C. The

flow stress did not reach the same level as at a lower temperature. Plastic deformation of α-Ti is strongly influenced by the mobility of dislocations, which depend on the temperature and strain rate. The lower the temperature, or the higher the strain rate, the higher the stress required for yielding. This implies that the low temperatures hamper dislocation motion. During high-temperature deformation, dislocations are assisted by the thermal energy, thus requiring lower stress to yield.

After reloading at low temperatures, the strain hardening followed the same rate as the initial low-temperature deformation test. Thus, the interaction of the high density of mechanical twins with dislocations made it harder to impart more plastic strain deformation.
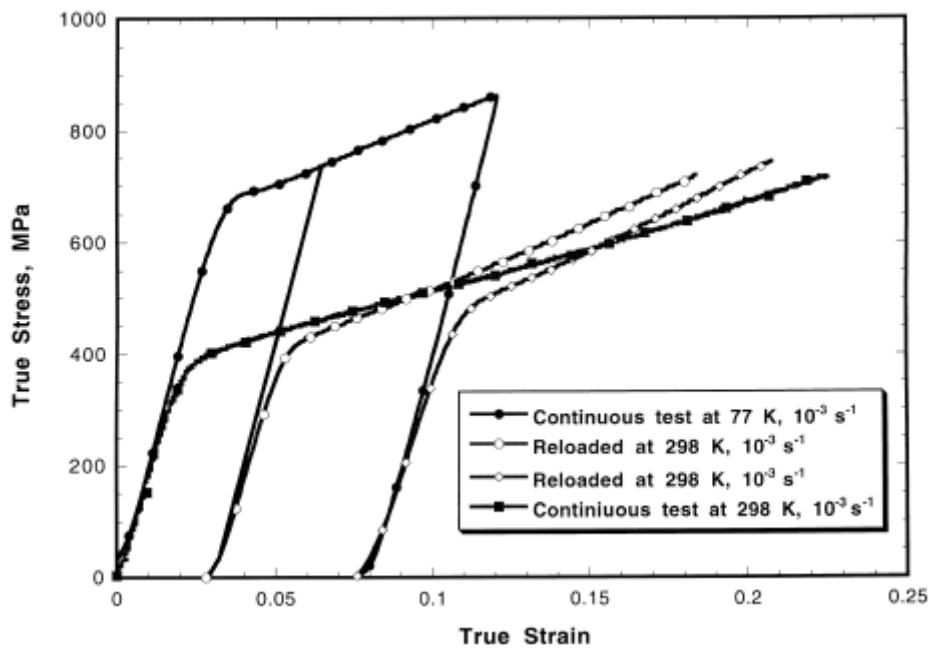
Figure 2-25.Flow stress dependence on pre-strained and twinned microstructure. Reload at room temperature and low temperatures [27].

2.6. Work hardening

During plastic deformation, a high density of dislocations is being introduced into the lattice. It could be of the order of 10^5 to 10^6 new dislocations [2]. As the plastic deformation proceeds, dislocations interact with each other, generating dislocation tangles and forests, making the motion of other dislocations harder thus requiring higher stresses for an increment of imparted strain. Higher dislocation introduction is enhanced at lower temperatures and higher strain rates.

An analysis performed by Salem et al. [44] on simple compression, plane strain compression and simple shear of a high purity titanium alloy correlated the deformation twinning with the strain hardening behaviour shown in Figure 2-26. It was found that the onset of deformation

twinning was linked with a sudden increase in strain hardening rate in a simple and plane strain compression test. The work hardening behaviour also presented a falling rate, which was associated with the saturation of twin volume fraction. In simple shear, the strain hardening was much lower. This is linked to a lower density of deformation twinning.
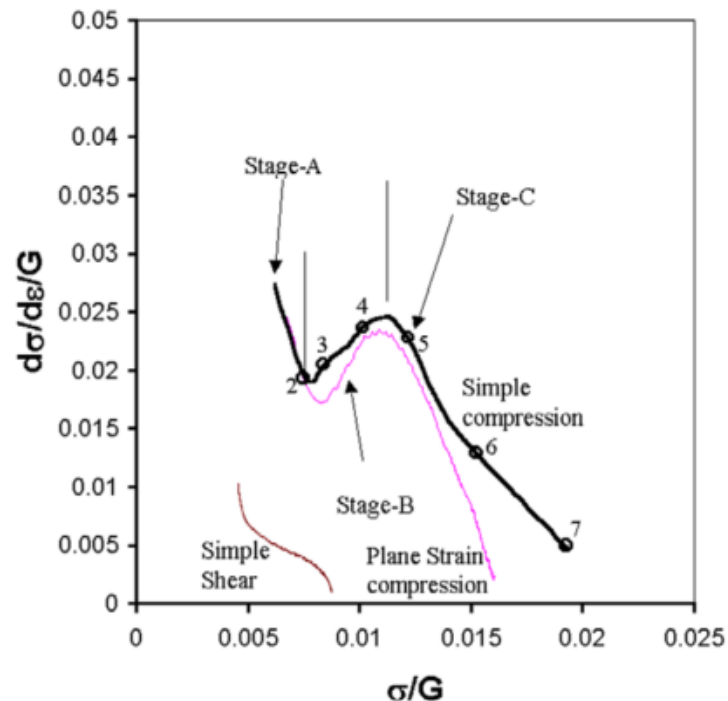
Figure 2-26. Strain hardening behaviour of high purity α-titanium under simple, plane strain compression and simple shear [44].

2.7.   Adiabatic Shear Band (ASB) formation

Narrow bands of localised intense shear strain are formed in materials being plastically deformed; especially low symmetry crystal structures, such as hcp. The adiabatic term is attributed to Zener and Hollomon (1944), and it is a thermomechanical phenomenon. During plastic deformation, more than 90% of the work imparted is transformed into heat [2], [45], which in turn will increase the temperature of the deformation zone, especially if the material has low thermal conductivity. If the strength reduction is higher than the strength increase due to applied strain and strain hardening, there will be localised thermal softening in a narrow region. Then, plastic deformation will become unstable, and the homogenous plastic deformation will lead to a localised zone of deformation, which is known as the adiabatic shear band (ASB).

The shear band formation occurs in two stages. The first stage is the shear instability caused by thermal softening, and the temperature increase enhances dislocation motion. The second stage, known as localisation, is where microstructural changes such as recovery and

33

recrystallization take place. It corresponds to the initiation and propagation phenomenon, where stress concentration sites or microstructural in-homogeneities are the initiation sites [46]. If microvoids are formed, they contribute to softening, which accelerates shear localisation.

There are two types of shear bands, deformed bands and transformed bands. The former corresponds only to zones of intense plastic shear, and the transformed are also zones of intense shear where phase transformation has taken place. Figure 2-27 illustrates transformed ASBs in titanium alloys. However, Bai and Dodd [47] stated that not all shear bands occurring in titanium alloys are transformed; Meyers and Pak [48] examined the shear bands formed in projectile impact of CP-Ti, small equiaxed grains were found, which indicate that recrystallization may have occurred, and the material next to the shear band contained a high dislocation density. As there was no evidence of β-phase present, it was implied that the temperature would not have been higher than 882°C.
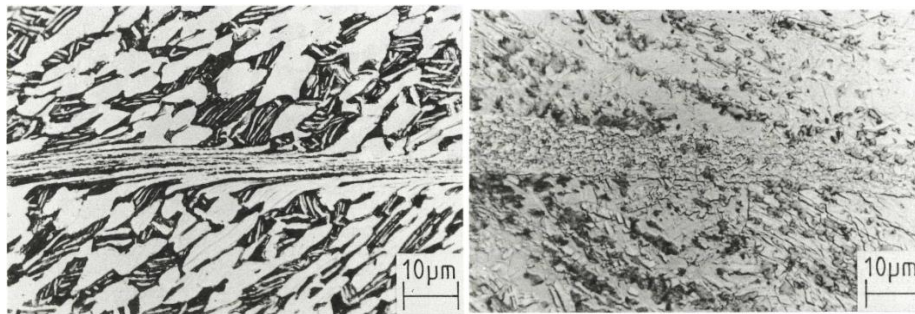
Figure 2-27. Transformed bands in titanium alloys a) hot rolled Ti-4Al-4Mo-2Sn-0.5Si and b) hot rolled CP-Ti. After Timothy and Hutchings in 1984 [47].

There are four main variables which strongly influence shear band formation [47]. Firstly, the workpiece material characteristics such as density (ρ), specific heat of heat transfer (c), thermal conductivity (k), thermal diffusion (α), strain hardening rate (θ) and thermal softening rate. Secondly, the material stress state such as shear stress (τ), shear strain (γ), shear strain rate ($\dot{\gamma}$), temperature, hydrostatic pressure (p) and characteristics of multi-axis stress state. Thirdly, the microstructure of the specimen including size, texture, shape, second phase particles, etc. Finally, the external loading conditions such as disturbances.

The strain hardening rate decreases when the yield strength increases, thus the critical parameter in determining the susceptibility to shear localisation is the strain-hardening exponent. This suggests that titanium at low temperatures should have a low strain hardening exponent as they exhibit higher flow stresses at cryogenic temperature.

In low thermal conductivity materials, shear banding occurs even at low strain rates; such is the case of pure α Ti ($\lambda = 19 W.m^{-1}K^{-1}$) compared to copper ($\lambda = 400 W.m^{-1}K^{-1}$).

The formation of ASB is a process driven by several stages. First of all, there is homogeneous plastic deformation, which drives to instability causing inhomogeneous

deformation, then a localised shear zone appears, which follows the complete development of the shear band and finally fracture along the shear zone occurs [47]. Bai and Dodd [47] reported that ASB widths are not highly sensitive to the stress state.

Dynamic compression may suppress voids in nucleation, growth and cracking stages, but the tensile state favours fracture by this mechanism, as this stress state prevents the necessary accumulation of strain for ASB to occur.

The morphology of the void generated during localisation is strongly dependent on the stress state under which the void was created and the temperature inside the shear band. The centre of the shear band is subjected to higher shear strain; therefore, higher microdamage might be found there. It is of the opinion of the author that Bai and Dodd [47] did not consider the property enhancement in this localised zone attributed to the creation of nanocrystalline or ultra-fine grains by the introduction of a high grain boundary area.

The development of a shear band in Ti-6Al-4V is shown in Figure 2-28. The author observes a region of high lattice curvature reaching the edges of the shear band. A refers to the area of shear strain concentration. The author thinks that further straining was required to create instability in shear by thermal softening to reduce the load-carrying capacity, allowing further deformation more easily and generating areas of shear stress and shear strain concentration, leading to the nucleation of voids, then growth and finally coalescence to cause a fracture. According to Sagapuram et al. [49], it has the appearance of a viscous fluid; however, they did not provide any detail of the lattice disturbance. B refers to a high angle of lattice reorientation or a region of sharp lattice curvature. In A, a reduction in α plates or reduction in retained β spacings is observed. This microstructure appears similar to the microstructure observed in this investigation; however, Sagapuram et al. [49] do not show evidence nor mention mechanical twinning.
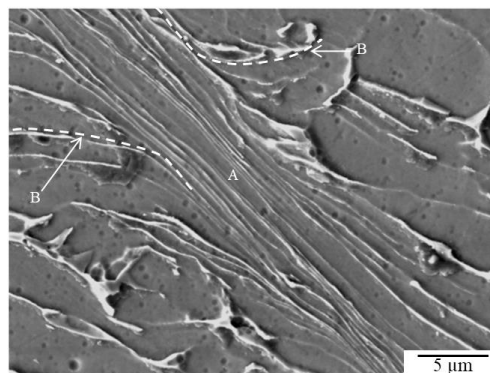
Figure 2-28. Shear band development in Ti-6Al-4V – adapted from [49].

2.7.1.   Dynamic recrystallization inside the ASB

Bright field TEM images from hat-shaped specimens of Ti-6Al-4V subjected to dynamic plastic deformation, to high strain rates of 1500-2500 s^{-1} at ambient temperature revealed a

nanocrystalline grain structure inside an ASB [50] see Figure 2-29. Regions adjacent to the ASB show elongated grains. There is a graded microstructure reducing grain size towards the centre of the ASB. The circle-like diffraction pattern (1) corresponds to the centre of the band and specifies several crystallographic orientations. (2) indicates the overlapping between the ASB and the adjacent region. (3) shows separated spots, which indicates a single grain adjacent to the ASB.
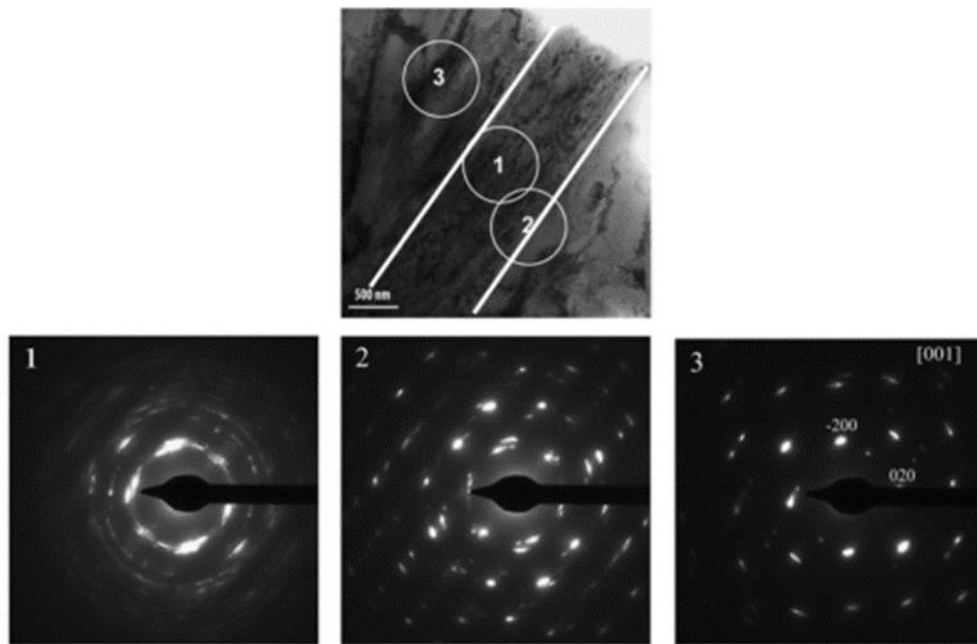
Figure 2-29. Transmission electron micrograph of the inside of an ASB, the near region and the boundary during compression of Ti-6Al-4V at high strain rate in a split-Hopkinson pressure bar –After Peirs et al. [50].

2.8.   Recrystallization during Severe Plastic Deformation Processes

During plastic deformation at low temperatures (T < 0.4 Tm), nearly 10% of the energy expended in the deformation process is stored in the lattice, and it represents the driving force for other mechanisms such as recovery and recrystallization. Additionally, during deformation, high strains are accumulated into the lattice and with it, the introduction of a high dislocation density, which is fundamental for the increase in the grain boundary area.

Recrystallization is defined as the formation of a strain-free region with a high degree of misorientation which has been transformed by the high energy and strain stored in the lattice during plastic deformation [51]. Nucleation of recrystallization occurs at heavily deformed regions inside the grains.

Grain refinement requires an enormous amount of grain boundary area to increase [52]. Prangell et al. [52] have identified two mechanisms. The first is the extension of the existing

boundaries by the application of strain. The second is the generation of new HAGB by grain subdivision, being an effect of the crystallographic essence of plastic deformation.

At high strain accumulation in the lattice, slip concentration can appear inside the shear bands, leading to the rotation of the grains within it, which also contributes to the generation of additional HAGB's. In metals where slip systems are limited, twinning strongly contributes to plastic deformation, and due to the crystallographic change orientation, new grains of high misorientation angles are created.

There are two mechanisms known to trigger recrystallization. One is known as strain-induced boundary migration, which uses the existing grain boundaries to form nuclei. The second is through sub-grain growth in regions of high lattice curvature. There are two mechanisms. The first is polygonization in which LAB merge into HAGB by growth. The second is sub-grain rotation and coalescence.

It has been reported that nuclei have been found in deformation bands, in the boundary adjacent to mechanical twinning which has suffered higher strain, twin intersections and grain boundaries [53]. Figure 2-30 illustrates a case of sub-grain rotation and coalescence in a 3%Si-Fe alloy, which was cold rolled to a reduction of 70% and heated to 600°C inside the electron microscope.
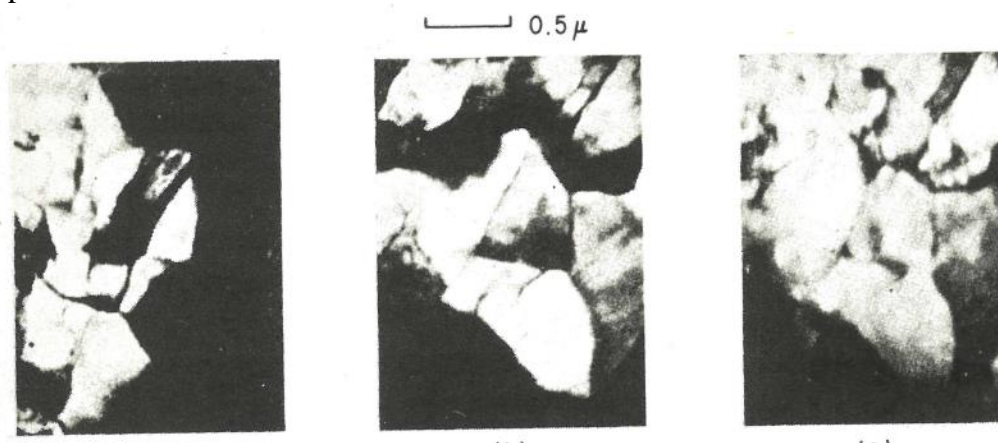
Figure 2-30. Electron micrographs showing sub-grain coalescence in situ on annealing a Fe-Si thin foil at 720°C for a) 30 s, b) 2 min, c) 3min [53].

Sub-grain rotation or coalescence during recrystallization has been observed in titanium, copper, aluminium and low carbon steel alloys [53]. Figure 2-31 a) shows the mechanism for the formation of HAGB by sub-grain rotation and coalescence and Figure 2-31 b) shows recrystallization by grain coalescence.

37
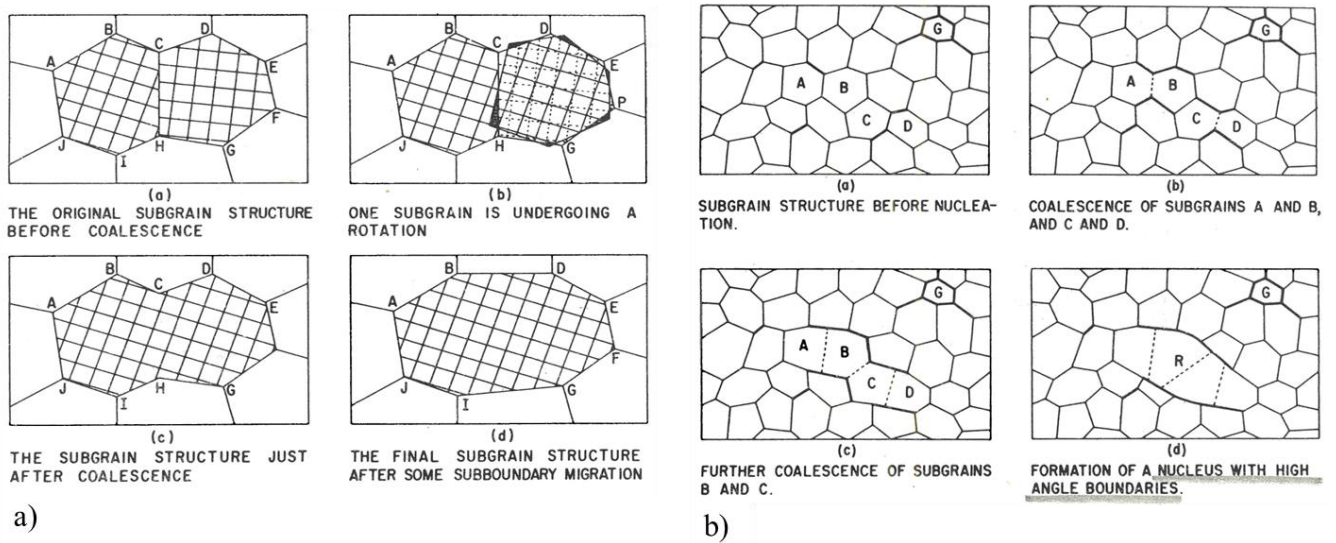
Figure 2-31. Schematic diagram of a) sub-grain coalescence and formation of HAGBs by rotation of a sub-grain, b) recrystallization by sub-grain coalescence [53].

2.8.1.   Influence of deformation temperature

Plastic deformation at lower temperatures, introduces an increased dislocation density, thus providing higher strain energy into the lattice, which is available for subsequent processes such as recovery and recrystallization. The reduction in deformation temperature leads to a reduction in the activation energy to start the primary recrystallization [53]. The increase in imparted strain and reduction of temperature during plastic deformation leads to uniformly distributed and smaller grain sizes of high angle misorientations [35], [53].

2.8.2.   Influence of twinning during recrystallization

Cotterill [53] reports that in materials that deform by slip and twinning, neighbouring regions to isolated twins represent potential sites for nucleation of recrystallization as shown in Figure 2-32. Twin intersections represent potential sites for nucleation for recrystallization of new grains, as it is a region of severe strain because the twin shear is not continuous.

Figure 2-32. Recrystallization nuclei in the intersection of mechanical twins [53].

Grains size in the nanoscale level has become a topic of high interest in the last decade as they exhibit similar behaviour to that of the Hall-Petch strengthening mechanism while maintaining substantial ductility as well thermal stability [54]. Mechanical twins at the nanoscale were observed through a severe plastic deformation process during metal cutting under cryogenic cooling conditions [54]. Figure 2-33 illustrates the high density and homogenous nano-twinned subsurface generated on copper at a $\dot{\varepsilon} \sim 10^3$ s^{-1} and $\gamma \sim 1.6$ with twin widths near 20 nm. This region has a much higher hardness than those of the bulk.
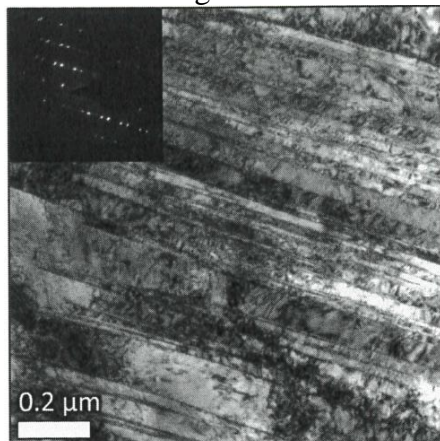
Figure 2-33. Bright field TEM micrograph of copper cryogenic machining (-196°C) at a γ ~1.6 and $\dot{\varepsilon} \sim 10^3$ s^{-1} showing a high density of nanoscale twinning [54].

2.9. Mechanical and thermal properties of titanium alloys at low temperatures

CP titanium, α alloy Ti-5Al-2.5Sn and $\alpha+\beta$ alloys Ti-6Al-4V and Ti-8Al-1Mo-1V remain ductile while at low temperatures, however β alloys such as Ti-13V-11Cr-3Al transit from ductile to brittle plastic deformation when at cryogenic temperatures [55]. Interstitial element content strongly increases strength; however, they reduce the fracture properties [55].

Ti-6Al-4V deforms in a ductile manner from room temperature to -196°C [56], [57], being nearly temperature insensitive. Nevertheless, below -196°C, it abruptly drops until near -253°C, approaching a ductility of 1 to 2 %. The ductility of the annealed Ti-6Al-4V is nearly twice as high than the solution treated and aged (STA). This behaviour is illustrated in Figure 2-34. Reducing the interstitial content in an Extra Low Interstitial (ELI) grade, Ti-6Al-4V ELI exhibits an improvement in 130% fracture toughness at room temperature and 40% at -253°C. Likewise, β annealed Ti-6Al-4V is characteristic of maximum damage tolerance as compared to mill annealed; it presents an improvement in fracture toughness, fatigue crack growth resistance and high cycle fatigue strength [55] (see section 2.10).
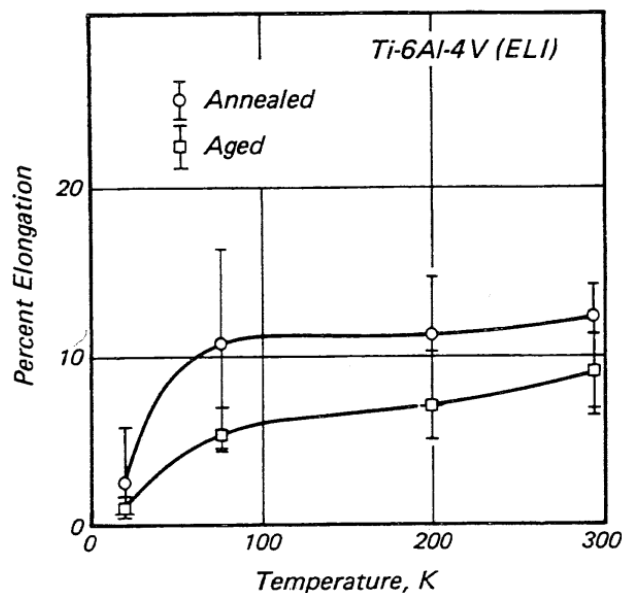
Figure 2-34. Ductility of Ti-6Al-4V ELI grade from room temperature to cryogenic temperatures [55].

The reduction of deformation temperature has a strong influence on the mechanical properties of titanium alloys. Figure 2-35 a) shows the effect of deformation temperature on the yield strength, UTS and % of elongation of Ti-6Al-4V annealed at normal interstitial content [58]. By lowering the temperature, there is a marked increase in yield strength as well as the ultimate tensile strength. Ductility keeps constant up to a temperature just below -200°C, then by further lowering temperature, it drastically decreases. Thus, for metal cutting, it would be ideal to reach a level of a temperature lower than -200°C during machining, in order to reach very low ductility and to break the chip at a much lower strain, thus spending much lower energy for chip formation. However, the drawback by the reduction in temperature is the introduction of high density and depth of mechanical twinning at these temperatures. Consequently, it may introduce much further damage to the subsurface.

An advantage of the reduction in temperature is the increase in modulus of elasticity as shown in Figure 2-35 b), reducing the workpiece deflection during cutting [55], [59]. This would generate more accurate dimensional workpieces. Also, dimensional stability increases

40

owing to its lower coefficient of thermal expansion. It has been reported that compressive residual stresses are generated on the subsurface of a machined component. It will be discussed in section 2.14.3.
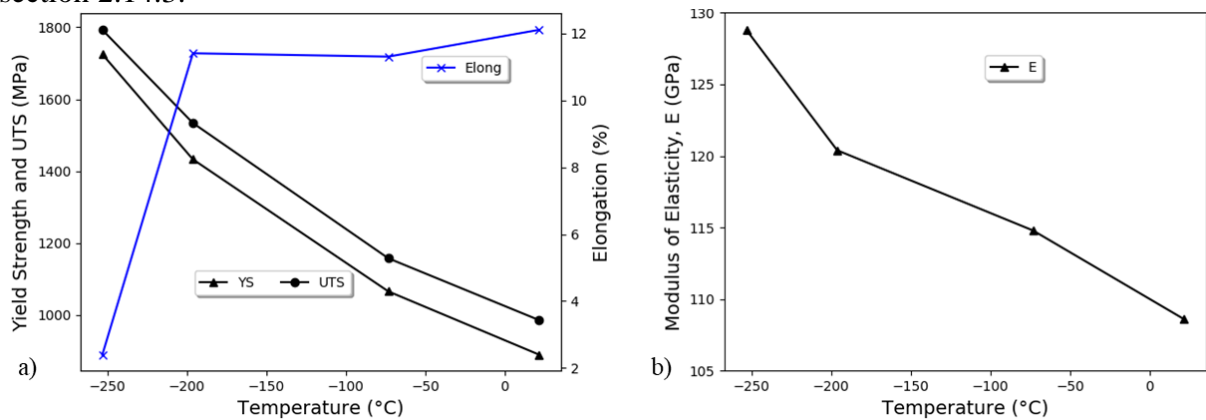
Figure 2-35. Effect of temperature in Ti-6Al-4V annealed at normal interstitial content on a) yield strength, UTS and elongation, and b) on the modulus of elasticity. Adapted from the National Physical Laboratory [58].
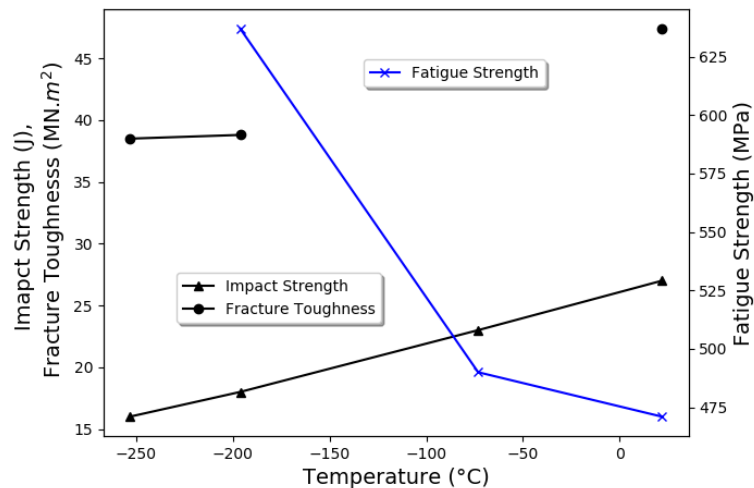
Figure 2-36. Effect of temperature on impact strength, fracture toughness and fatigue strength on Ti-6Al-4V annealed at normal interstitial content. Adapted from the National Physical Laboratory [58].

The impact strength steadily decreases by reducing the temperature as shown in Figure 2-40. This suggests that any reduction in temperature during machining Ti-6Al-4V under normal interstitial content may be beneficial, as it would reduce the energy spent in the shear band formation and fracture. In this investigation, Ti-6Al-4V at normal interstitial content was machined by near orthogonal cutting in section 5.9 and nearly a third of the energy required for cutting at room temperature was required at -150°C. This shows an improvement in the machinability in terms that it is easier to generate the chips. However, the subsurface damage

41

introduced is higher, resulting in the introduction of higher potential sites for crack nucleation under in-service cyclic stresses.

Figure 2-37 shows the mechanical properties of Ti-6Al-4V Extra Low Interstitial under different conditions: (1) as forged, (2) sheet, annealed and test specimen in a longitudinal orientation, (3) sheet, annealed and test specimen in a transversal orientation, (4) plate, annealed and test specimen in a longitudinal orientation and (5) forged and recrystallized annealed. The yield stress increases linearly by reducing temperature under all these conditions. Likewise, regarding elongation, the reduction of temperature generates a linear decrease. The sheet, annealed and test specimen in a longitudinal orientation exhibits the lowest ductility under all temperatures. Figure 2-37 b) suggests nearly a 50% reduction in elongation in this condition from RT to -150°C.
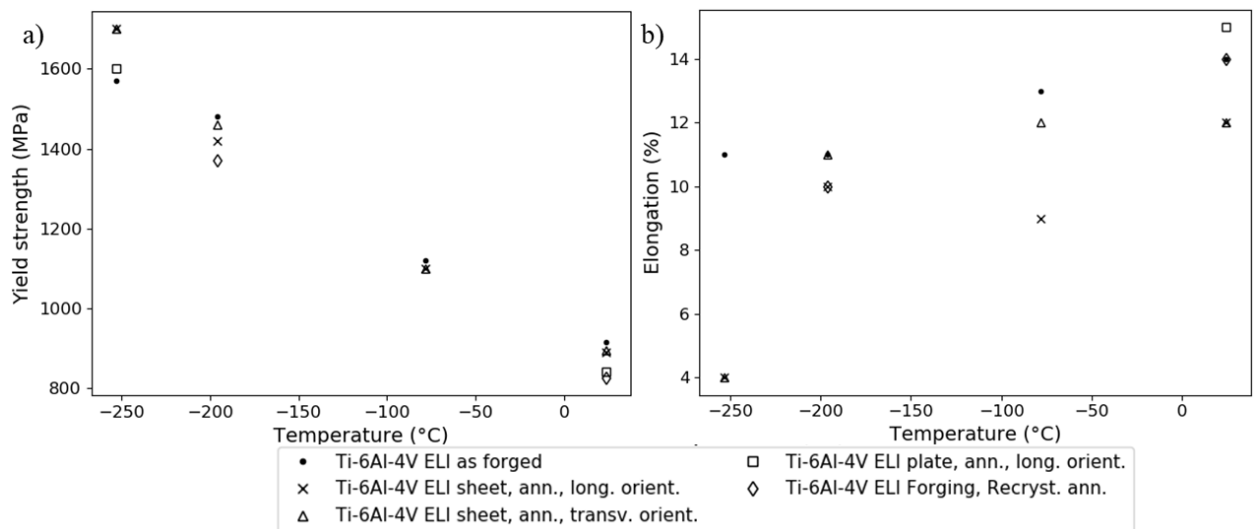
Figure 2-37. Effect of temperature on Ti-6Al-4V ELI on a) Tensile yield strength and b) Elongation [60].

The effect of temperature on thermal conductivity of Ti-6Al-4V solution treated and annealed (STA) Extra Low Interstitial (ELI) is shown in Figure 2-38 a). Figure 2-38 b) shows the effect of temperature on the heat capacity in the same alloy. It is evident that the reduction in deformation temperature reduces the thermal properties of this alloy. Although mechanical properties are improved, lowering the temperature lowers both thermal conductivity and heat capacity, resulting in higher temperatures in the machining zone and build up in the workpiece.
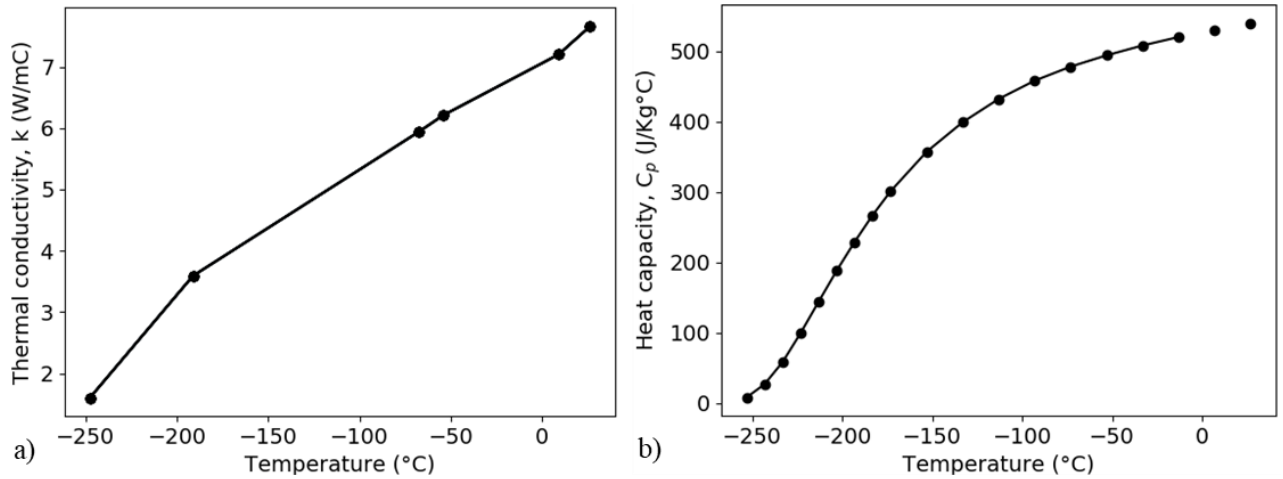
Figure 2-38. Ti-6Al-4V STA Extra Low Interstitial (ELI) Effect of temperature on a) the thermal conductivity and b) the heat capacity. Adapted from the National Physical Laboratory [58].
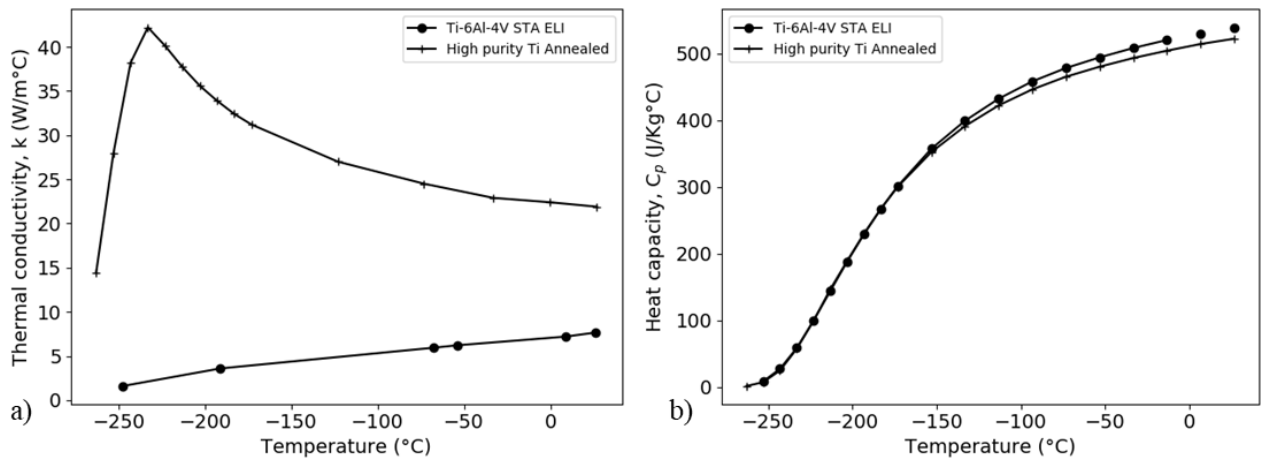
Figure 2-39. Thermal properties of High purity titanium, Ti-6Al-4V STA ELI as a function of temperature. Adapted from the National Physical Laboratory [58].

Figure 2-39 illustrates the thermal conductivity differences between the high purity α titanium and the Ti-6Al-4V STA ELI as a function of temperature. High purity α-Ti exhibits much higher thermal conductivity, and it is increased by the lowering of the test temperature, reaching a maximum at -233°C and then decreasing further. This improvement in thermal conductivity at lower temperatures is ideal for increasing the conduction and dissipation of heat generated during machining. At LN_2 temperatures, this value increases 55% from room temperature (21.9 to 33.9 $W.m^{-1}°C^{-1}$). On the contrary, Ti-6Al-4V STA ELI exhibits a much lower thermal conductivity value in the order of 7.66 $W.m^{-1}°C^{-1}$ at room temperature. Not only the thermal conductivity is low, but also it continually decreases by the lowering of the temperature. This leads to a higher concentration of heat in the cutting zone, leading to higher temperature build up and thermal softening by adiabatic heating. Although the cryogen media is physically at low temperatures, there may be higher heat accumulation in a narrow zone

43

(ASB) during cutting (attributed to the low thermal conductivity and its reduction when subjected to low temperatures). In a continuous operation such as turning, the increase in operational time may lead to higher temperatures in the cutting zone, higher diffusional processes between the tool and workpiece, and therefore the need for higher volumetric flow rates to keep the cutting zone at low temperatures. On the other hand, in an intermittent operation, not much heat may build up as it may transfer to the environment in the time the tool disengages.

The thermal conductivity in pure metals is transported mainly by electrons, while that for alloys is carried by mainly by phonons or due to lattice conduction and in lower grades by electron conduction [61]. Both phonon and electron conductivities are limited by scattering, leading to thermal resistance. Defects in the lattice such as impurity atoms, vacancies, stacking faults and dislocations will impose a thermal resistivity for electron conduction and lattice thermal vibrations introduce a thermal resistivity due to electron scattering. At low temperatures, there are not sufficient phonons of high intensity; thus electrons cannot be transferred; they can only be scattered, and thus only phonon wavelengths are involved in heat transport at low temperatures.

Impurity elements reduce the electron heat transport, making the phonon conductivity more important in metallic alloys [61]. Dislocations and defects in the lattice generate phonon resistivity. Impurity atoms and point defects do not influence the low-temperature conductivity because they are smaller than the wavelength of the phonons; thus phonons are not scattered.
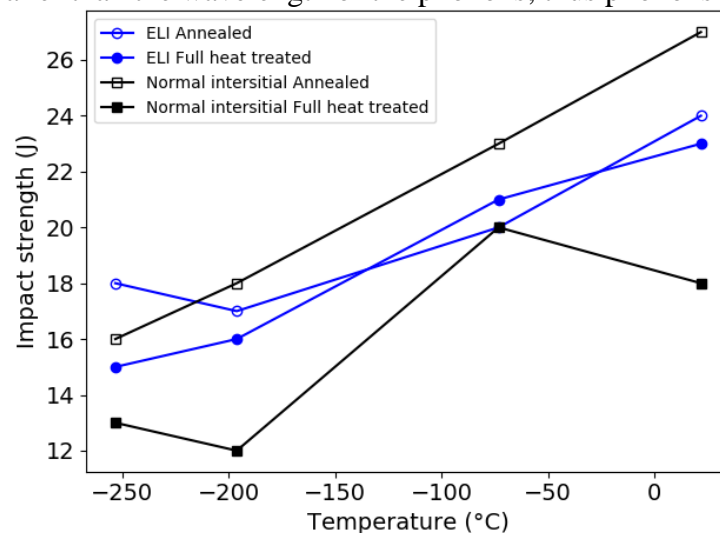
Figure 2-40. Effect of temperature on the impact strength of Ti-6Al-4V at extra-low interstitial (ELI) content and normal interstitial content. Adapted from the National Physical Laboratory [58].

Figure 2-40 shows the effect of low temperatures on the impact strength of Ti-6Al-4V ELI and at normal interstitial content. It shows a linear reduction in the energy absorbed during fracture. For an ELI annealed grade, it shows a reduction of 30% from room temperature to -

160°C, improving the machinability at low temperatures in terms of energy spent to generate chips. This is in agreement with experimental evidence in section 4.2.
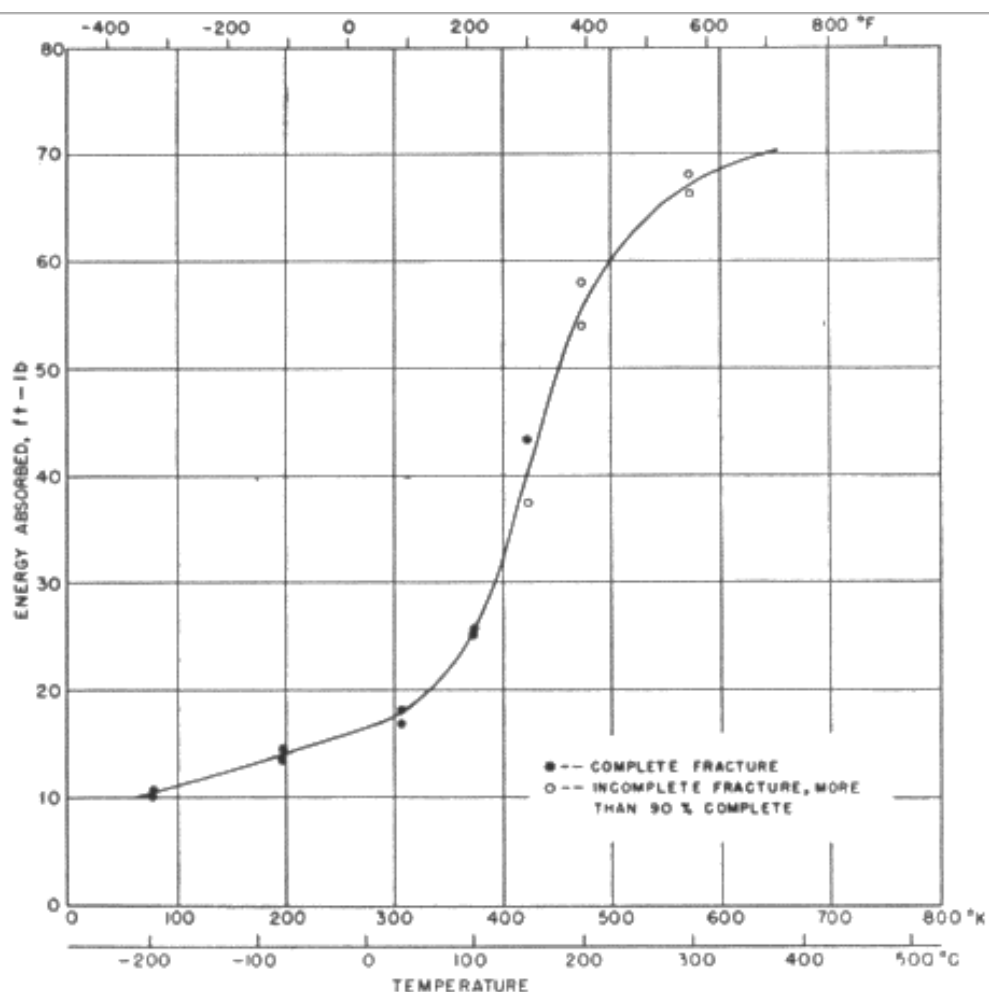
Figure 2-41. Energy absorbed in Charpy impact test as a function of test temperature on a CP-Ti alloy [62].

Figure 2-41 shows the impact energy absorbed dependency on temperature of CP-Ti. From high temperatures, there is a sharp decrease in energy absorbed by decreasing the temperature. However, from room temperature to lower temperatures, the energy absorbed decreases linearly and steadily. However, it still generates a reduction in the energy required for chip formation, which is beneficial for machinability. However, subsurface damage must be taken into account to prevent a reduction in fatigue properties by the introduction of higher damage.

The fracture toughness (K_{IC}) significantly reduces by lowering temperature in Ti-6Al-4V normal interstitial grade. The ELI grade possesses a much higher K_{IC}; however, it shows a decrease by reduction of temperature.

The fracture toughness of different materials as a function of temperature is shown in Figure 2-43. Ti-6Al-4V ELI has a higher fracture toughness than normal interstitial. The ELI grade at -153°C exhibits a sharp and continuous decrease with lowering the temperature from nearly

45

100 MPa.m$^{1/2}$ to 60 MPa.m$^{1/2}$ at -173°C. The normal interstitial grade has a much smaller difference with temperature as previously shown in Figure 2-42.
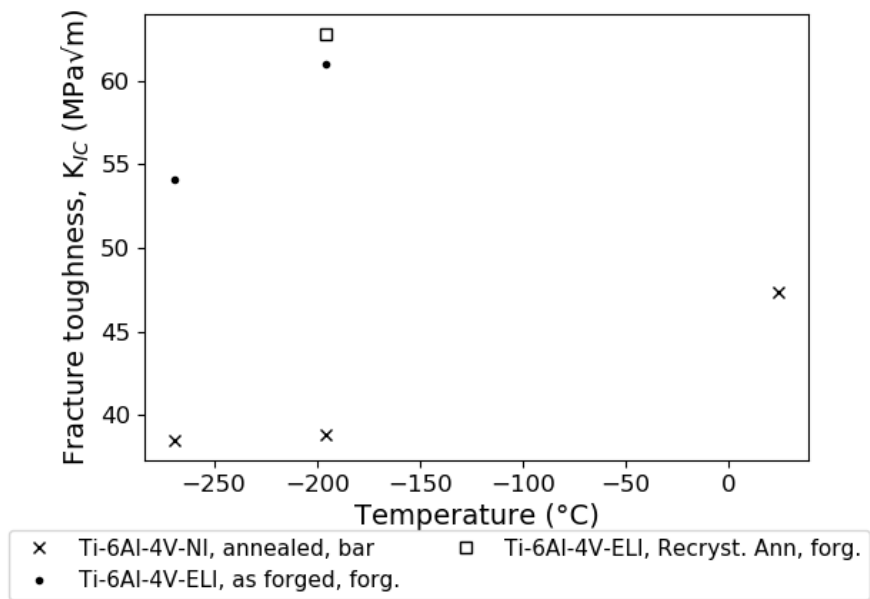
Figure 2-42. Effect of temperature on the plane strain fracture toughness (K_{IC}) [22].
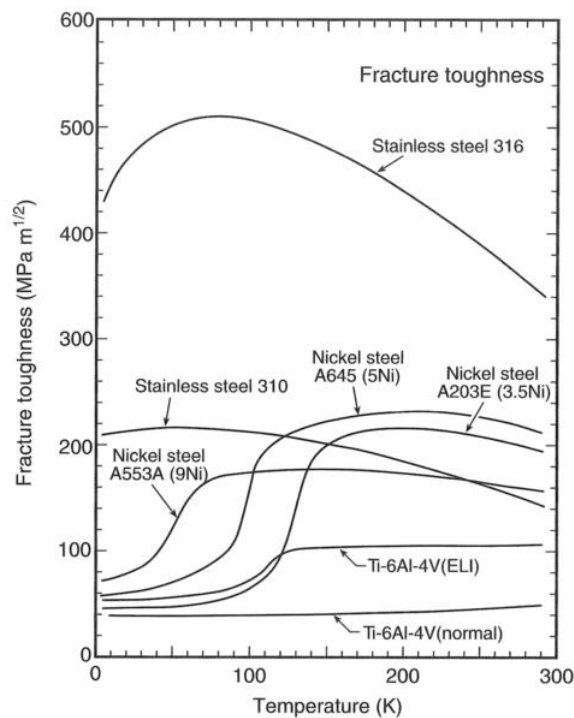
Figure 2-43. Effect of temperature on fracture toughness (K_{IC} is the plane strain stress intensity factor) [63].

On the other hand, the reduction in temperature generates a contraction rather than expansion in both NI and ELI as illustrated in Figure 2-44. This aspect may improve the dimensional tolerances during precision machining at low temperatures.
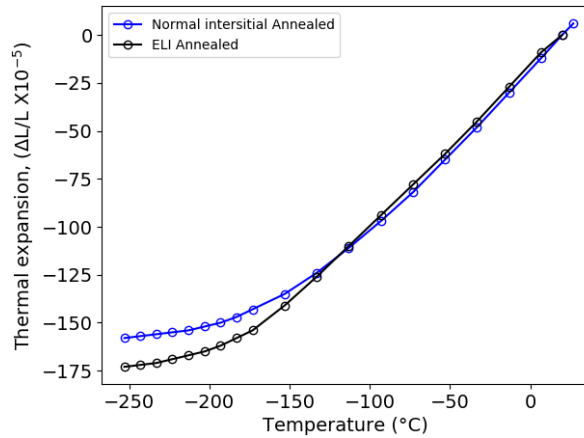
Figure 2-44. Effect of temperature on the thermal expansion (ΔL/L X10^{-5}) of Ti-6Al-4V annealed at normal interstitial content and ELI. Adapted from the National Physical Laboratory [58].

With regards to yield strength, Ti-6Al-4V exhibits a high increase from room temperature 21°C (70 F) to -150°C (- 238 F) from 135 ksi to 185 ksi respectively as shown in Figure 2-45. Figure 2-45 illustrates that Ti-6Al-4V absorbs less energy at low temperatures than at high temperature, which means there is less work required to cause a fracture. It also shows that other titanium alloys are either less (Ti-13V-11Cr-3Al) or more (Ti-4Al-3Mo-1V) sensitive to temperature. Ti-4Al-3Mo-1V has the lowest yield at all temperatures, absorbs the highest energy during impact but shows the highest reduction in energy with lowering the temperature.
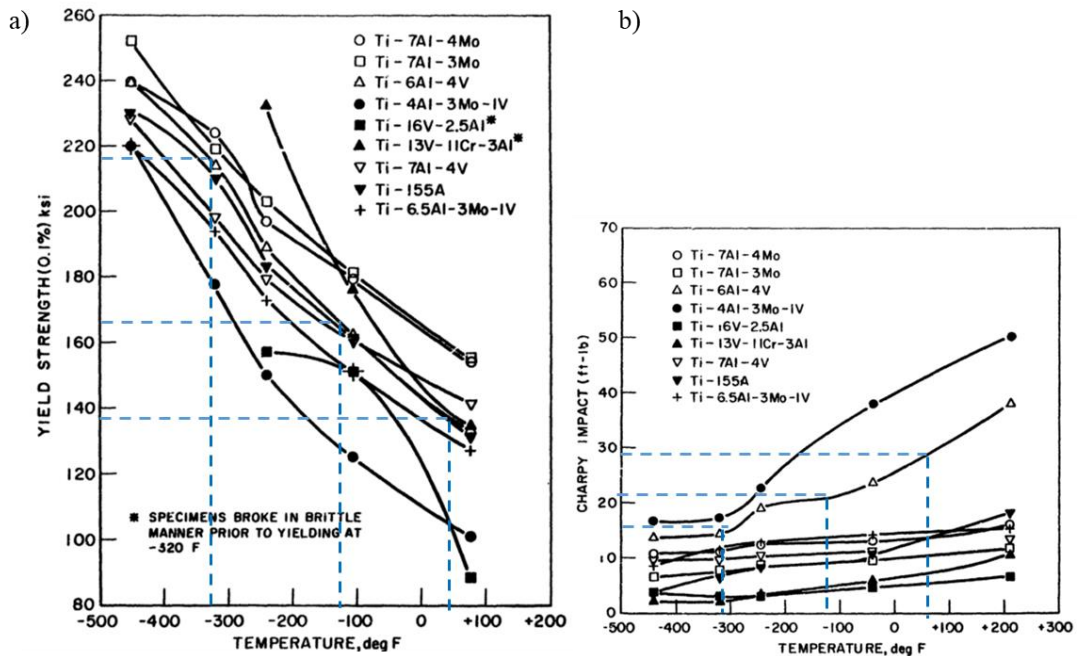
Figure 2-45. a) Yield strength of titanium alloys at cryogenic temperatures [64], b) impact energy on Charpy impact tests on titanium alloys at cryogenic temperatures [64].

2.10. β annealed Ti-6Al-4V ELI

A typical microstructure of β annealed Ti-6Al-4V Extra Low Interstitial (ELI) under cross-polarised light is shown in Figure 2-46 a), and at higher magnification from an etched specimen, a prior β grain boundary joining three different colonies is shown in Figure 2-46 b). The mechanical properties of Ti-6Al-4V under annealed and β annealed heat treatments are observed in Table 2-4. 38.4% increase in fracture toughness and 6.5% increase in yield is achieved by a heat treatment in the β phase field. However, the elongation has slightly decreased from 15 % to 11 %. This heat treatment also improves the fatigue crack growth resistance, the high cycle fatigue strength and resistance to aqueous stress corrosion [55].
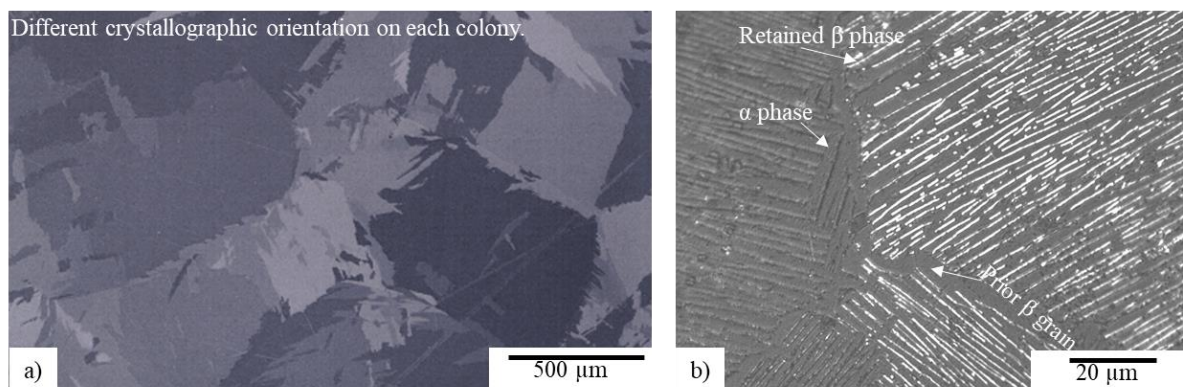
Figure 2-46. β annealed Ti-6Al-4V ELI: a) cross-polarised light micrographs and b) etch and light micrograph.

Table 2-4. Mechanical properties of Ti-6Al-4V ELI at room temperature under different heat treatments [55].

Alloy	Fracture Toughness (MPa√m)	YS (MPa)	UTS (MPa)	Elongation (%)
Ti-6Al-4V annealed	65	930	860	15
Ti-6Al-4V β annealed	90	990	910	11

Figure 2-47 shows the yield and ultimate tensile strength of β annealed Ti-6Al-4V NI content. Figure 2-47 a) shows a marked increase in yield and UTS at a cryogenic temperature of -269°C in comparison to RT. Figure 2-47 b) shows the strain at fracture. Reducing the testing temperature provides a marked reduction in strain. In the fast cooled specimen, the strain reduced from 10 % to 4 % from room temperature to -269°C. However, LN_2 reaches -196°C, and even if the strain would be 7 % at that temperature, it still represents an improvement in the machinability in terms of lower strain at fracture and lower energy for chip formation. This would represent a 30% improvement in machinability, as aforementioned from Figure 2-40.
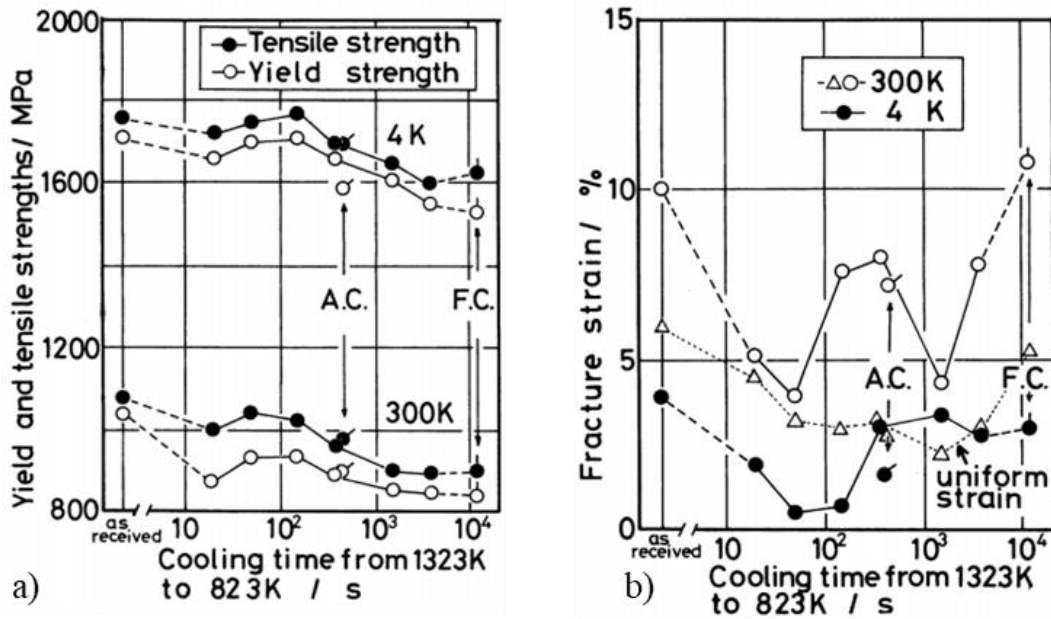
Figure 2-47. β annealed Ti-6Al-4V normal interstitial properties after different cooling rates from the β-phase field [65].

2.11. Cutting mechanics

2.11.1. Types of chip formation

Metal cutting is a chip generation process [66]. The study of chip formation is a good indicator of the understanding of machining behaviours such as temperatures, forces and plastic deformation. There are several types of chips formed during metal cutting, as seen in Figure 2-48. The type of chip depends on the material properties such as thermal conductivity, heat capacity, density, thermal diffusivity, flow stress, material microstructure and crystallographic orientation. For example, most steels generate a continuous chip; stainless steel leads to lamellar chipping swarf, cast irons result in short chipping swarf, superalloys generate high force chipping swarf, aluminium soft and long chipping swarf, hard steels form high pressure – high-temperature chips and titanium alloys a segmented type of chip.

| Steel | Stainless steel | Cast-iron | Heat resistant alloys | Aluminium | Hard steels | Titanium |
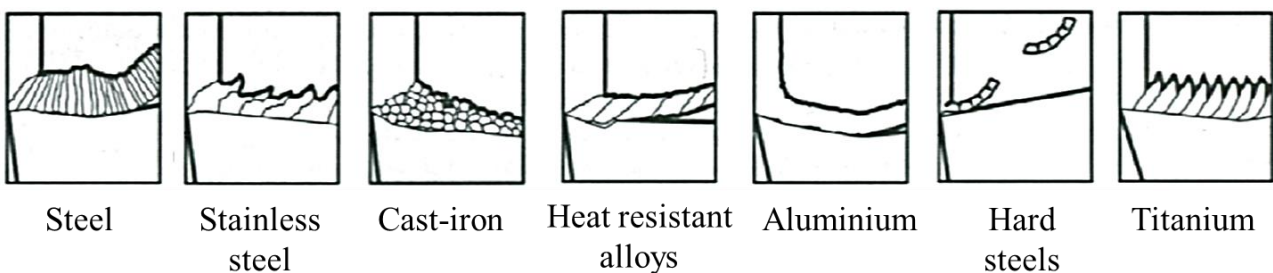
Figure 2-48. Types of chips formed depending on the material being cut [66].

49

Figure 2-49 shows the relationship between the type of chip formation and the force fluctuation during metal cutting. Figure 2-49 a) shows a more homogeneous chip formation in steel, leading to a low force fluctuation; this also leads to a lower vibration and surface roughness in comparison to Figure 2-49 b) stainless steel. Figure 2-49 b) generated a wider spacing between the segments; this leads to a higher force fluctuation.
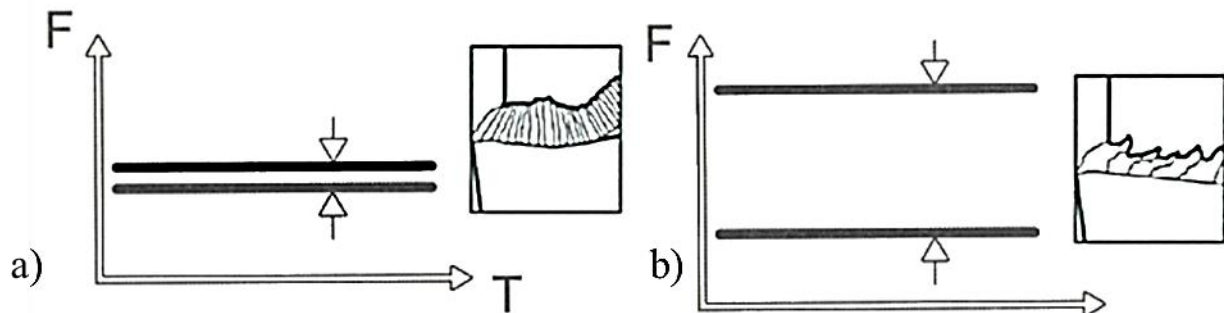
Figure 2-49. Force fluctuation dependence on the type of chip formation a) steel and b) stainless steel [66].

2.11.2.   Chip formation in machining of titanium alloys

Metal cutting is a localised shear straining process in a region known as the uncut chip thickness, involving fracture by the movement of the tool in relation to the workpiece. Figure 2-50 is a schematic illustration that represents the mechanisms taking place in a simple orthogonal cutting process. A tool with a single point is used, characterised by the rake angle (α) and the relief angle (θ). The rake face of the tool is the region where the material is leaving the shear zone slides. Two shear zones are generated as the tool advances in relation to the workpiece; the primary shear zone (PSZ) and the secondary shear zone (SSZ). The PSZ is the region where the highest shear strain and the highest temperatures are experienced, resulting in a near adiabatic region. This results in an inhomogeneous deformation that localises into a narrow zone called an adiabatic shear band (ASB). It is attributed to the high heat generation during metal cutting (plastic deformation and friction), the low thermal conductivity, the low thermal capacity and the low density of titanium alloys. The SSZ has two regions, one of sticking friction and the other of sliding friction. The chip slides on the rake face of the tool, as schematically illustrated in Figure 2-50, and it is the primary source of friction forces. The chip generation process imparts large plastic strains into the metal (γ 2 to 4) at strain rates higher than 10^3 s^1 [2], [67].

The grains that are near the PSZ are subjected to a high reorientation and high elongation in the direction of the shear strain, including the grains in the subsurface that remains in the machined component.

The material ahead of the cutting tool experiences a compressive stress state and the material just behind the cutting tool a tensile stress state. The instability in uniaxial compression testing

occurs as inhomogeneous localised shear deformation caused by thermal softening, and it fractures by void nucleation, elongation and coalescence. Consequently, there is a close approximation of micro-mechanisms, material behaviour and properties taking place in a uniaxial compression test to the orthogonal cutting process.
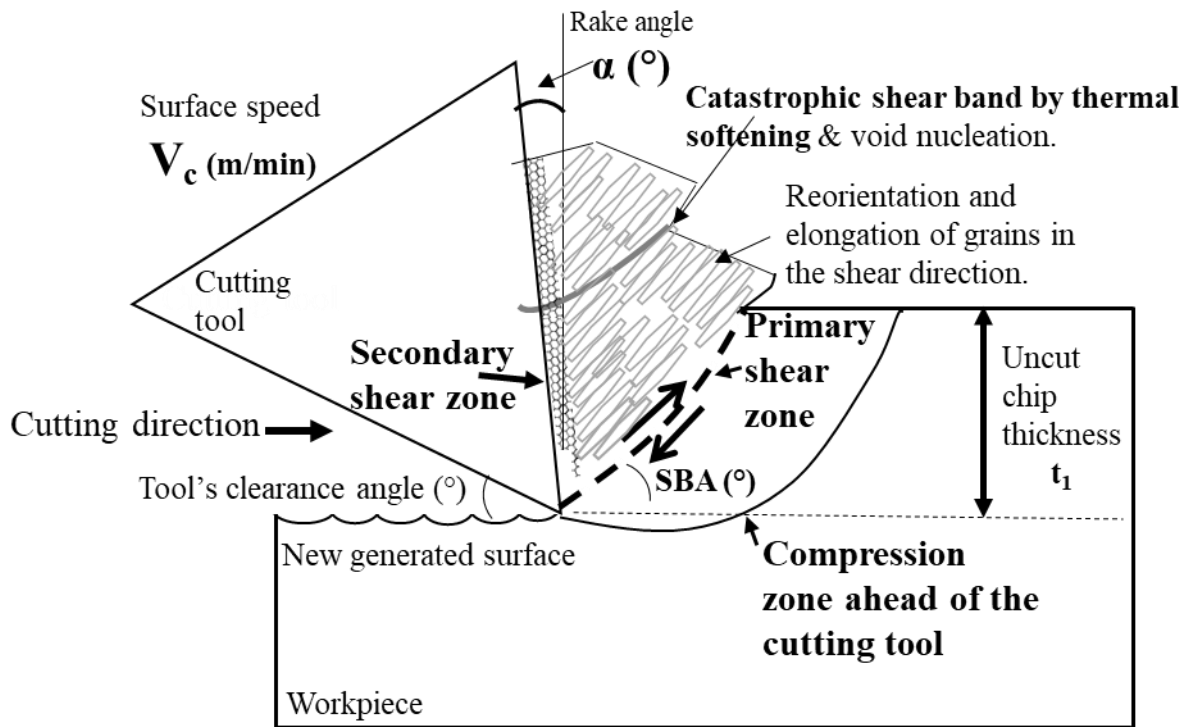
Figure 2-50. Schematic illustration of orthogonal cutting of titanium alloys.

Kommanduri and Turkovich [68] provided a detailed mechanism for the formation of saw-tooth chip formation. They described two stages for formation. The first is the plastic instability by thermal softening leading to strain localisation. The crack initiates in front of the cutting tool and progressively curves until fracture in the free surface. The second stage is the gradual flattening of the shear-failed segment, allowing minimal plastic deformation during its compression. This renders the chip thickness the same size as the uncut chip thickness, which leads them to believe that the shear angle is very high, about 45°.

The strain localisation along a shear surface is created from the tooltip in a direction parallel to the cutting direction. It gradually curves, creating an upward concave surface as shown in Figure 2-51.

The initial contact of the tool with the segment is short but increases as the flattening of the segment advances. From the start of the flattening of the segment up to strain localisation, there is almost no motion between the back surface of the chip and the rake face of the tool [68]. This allows rapid heat conduction, providing the conditions for chemical reactions to take place. After localisation, the segment slides along the tool faster.

Heat remains in the shear-failed region, and this is in direct contact with the cutting tool, allowing more heat transfer to it (due to the tool's higher thermal conductivity).

During the compression stage, the cutting force increases, and this deflects the tool from the cutting area. Once instability and fracture occur, the force decreases and the tool springs back rapidly. This causes vibrations and mechanical fatigue in the tool.
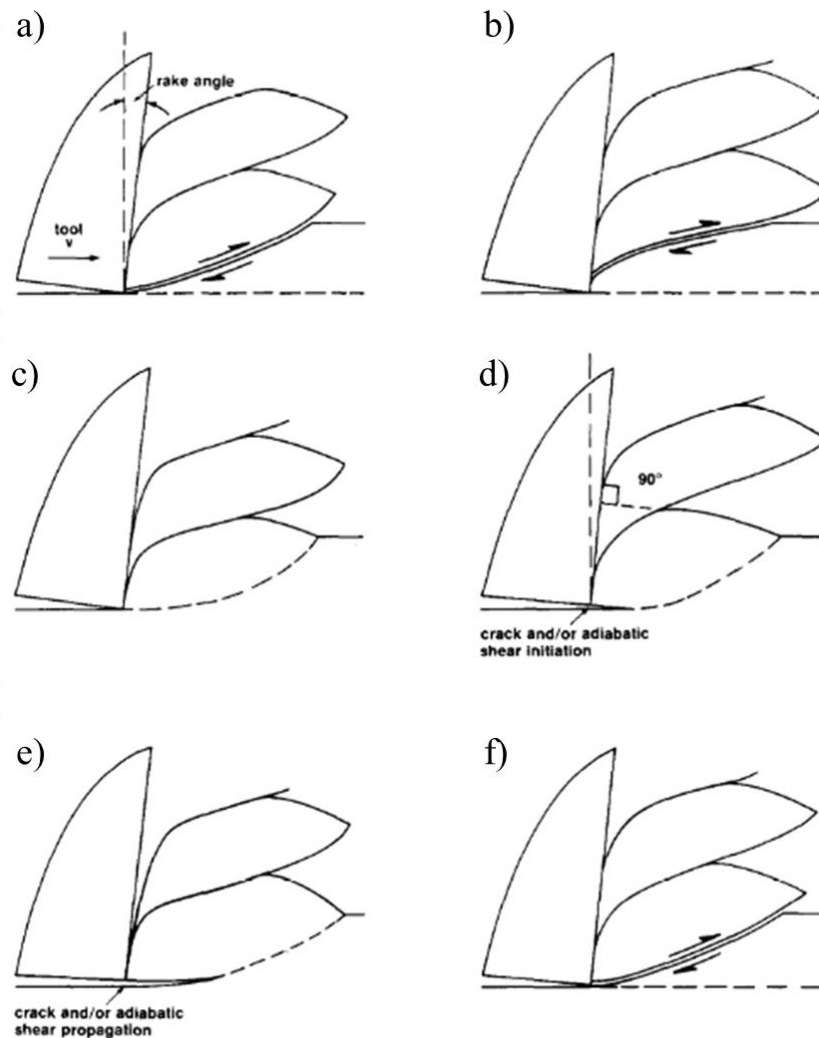
Figure 2-51. Mechanics of chip formation of segmented chips in titanium alloys-after Komanduri and Turkovich [68].

Komanduri and Turkovich [68] described a plasticity problem involving both plane strain and plane stress. In-plane strain, the rupture is prevented by the adjacent material. As the chip is unconstrained on the sides (plane stress), the segments can crack near the surface. Sagapuram et al. [69] were able to suppress the fracture along the shear bands by imposing a constraint, removing the plane stress condition. If the tool manufacturers find a way to introduce this constraint during machining, the tool may last for long times as the chip formed would be homogeneous, there would not be a high-temperature concentration along the shear bands and

vibration may be minimized, leading to a lower fluctuation in cutting shear stresses. This may lead to longer tool life and a reduction in surface roughness.

Bayoumi and Xie [70] report that there is a critical value (a combination of the surface speed, V_c, times the feed, f) for the formation of shear localised chips. This correlates with Shaw et al. [71] who by changing these parameters obtained a homogeneous chip formation during machining of an α+β titanium alloy (Ti-140A), see Figure 2-57. This may be influenced by a higher rate of thermal softening over strain hardening by the increase in surface speed and feed. Bayoumi and Xie [70] observed non-diffusional phase transformation in the chips of machined Ti-6Al-4V workpieces. This corresponds to the β to α phase change. They attributed the chip serration to the material flow, which concentrated in a narrow band, rather than in a plane. This was also observed at the bottom of the chips.
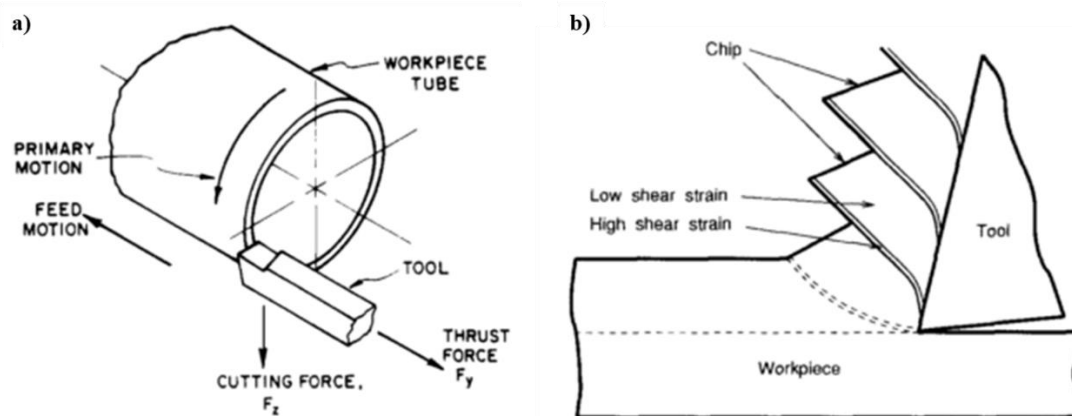
Figure 2-52. Orthogonal cutting of Ti-6Al-4V a) experimental set up and b) chip formation .-After Bayoumi and Xie [70].

Semiatin and Rao [72] determined the susceptibility of shear band localisation during metal cutting by using a parameter depending on material properties such as strain hardening, and flow stress depending on temperature and strain rate and the heat transfer. Estimating this parameter, they estimated the maximum surface speed for homogeneous chip formation. This was close to experimental values.

2.11.3.   Heat generation and tool wear during machining of titanium alloys

Tool wear rates are higher during machining of titanium alloys. This is attributed to their poor thermal properties and the intimate contact between the tool and the concentrated shear, which are known as adiabatic shear bands due to the significant increase in temperature in these narrow bands (appearing as white in a light microscope due to being chemically etched). As the tool has a higher thermal conductivity than titanium alloys, heat is transported to it, and as a result, most of the heat generated is transported to it. On the contrary, as iron alloys have

much higher thermal properties, the heat is not concentrated and is carried away on the chip. Thus less heat is transferred to the cutting tools, allowing for longer cutting times. Figure 2-53 a) shows a continuous and inhomogeneous or catastrophic shear localised chip formation where the imparted strain was not uniformly distributed. Figure 2-53 b) shows a continuous and homogeneous type of chip. It corresponds to the cutting of steel, in it, the plastic deformation was accommodated uniformly, and the chip thickness is much greater than the uncut chip thickness.
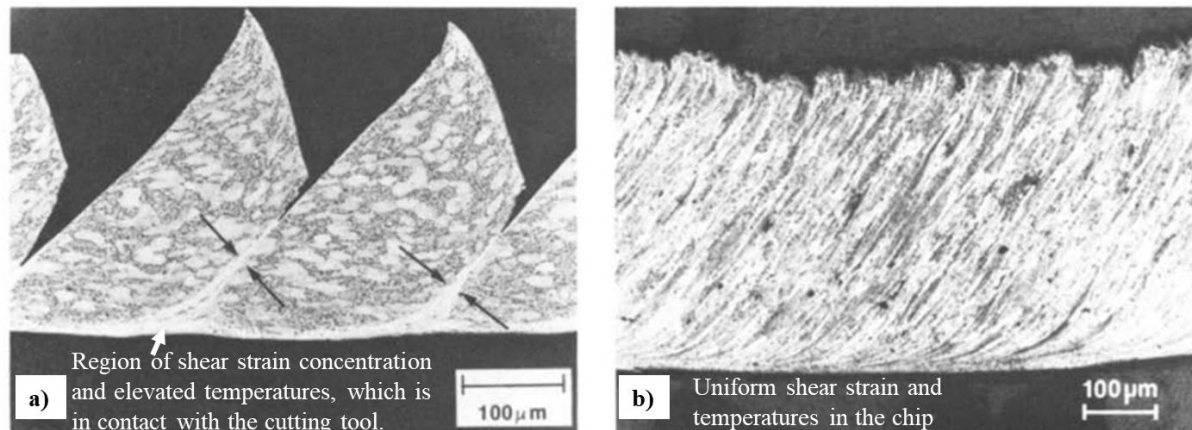
Figure 2-53. Etched microstructures of different types of chip formation a) inhomogeneous or segmented chip formation with concentrated shear in narrow bands in Ti-6Al-4V, b) homogeneous chip formation in steel.-After Komanduri and Turkovich [68].

Plastic deformation caused by the tool front and friction between the tool/workpiece and tool/chip causes high heat generation. This heat is concentrated in a shear zone ahead of the tool, thus causing thermal softening and with it comes to the formation of a shear band. The deformation in this zone is of primary importance as it accounts for near 80 % of the total cutting energy [73], [74]. Ezugwu et al. [75] estimated that nearly 80% of the heat produced during the cutting operation remains in the tool and only the other 20% is removed by the chip (as shown in Figure 2-54). It is estimated that nearly 75% of the energy is spent on the shearing process, while 25% on friction [59]. Pervaiz et al. [76] estimated an increase in temperature of 663°C in the chip which is in contact with the cutting tool, just in a fraction of a second (3.9E-4 s). The surface speed was 150 m.min^{-1} and the feed rate 0.2 mm.rev^{-1}. With longer cutting times, the temperatures would increase exponentially, accelerating the wear process of the tool, especially the solid-state diffusional processes, as shown in Figure 2-58.

Rake Angle

Chip
Sliding
on Tool
②

Heat in Chip
[2]

Catastrophic Shear
in a Narrow Band

Tool →

[1]
Heat to Tool

Chip Segment
(Negligible
Deformation)

④

① Intense Localized
Deformation

[3]
Heat to Work Piece

③ Flank Rubbing on the
Machined Surface

Work Piece
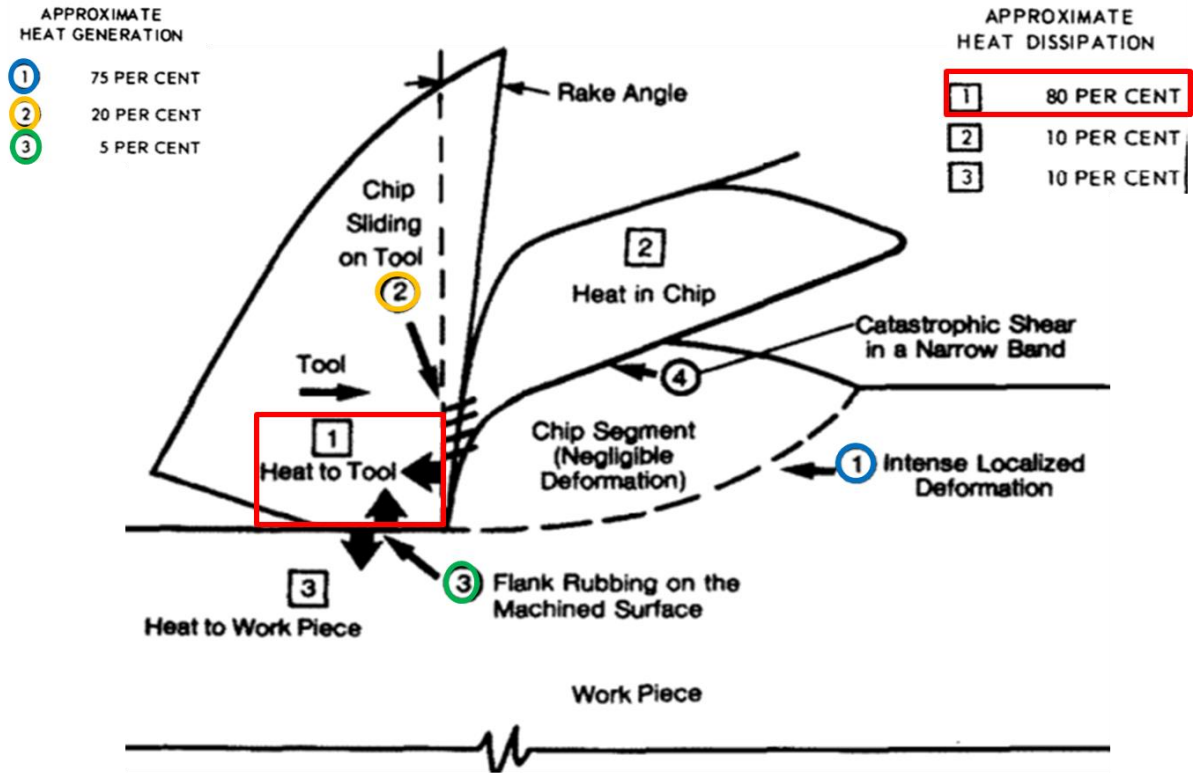
Figure 2-54. Heat generation during machining titanium alloys [75], [77].
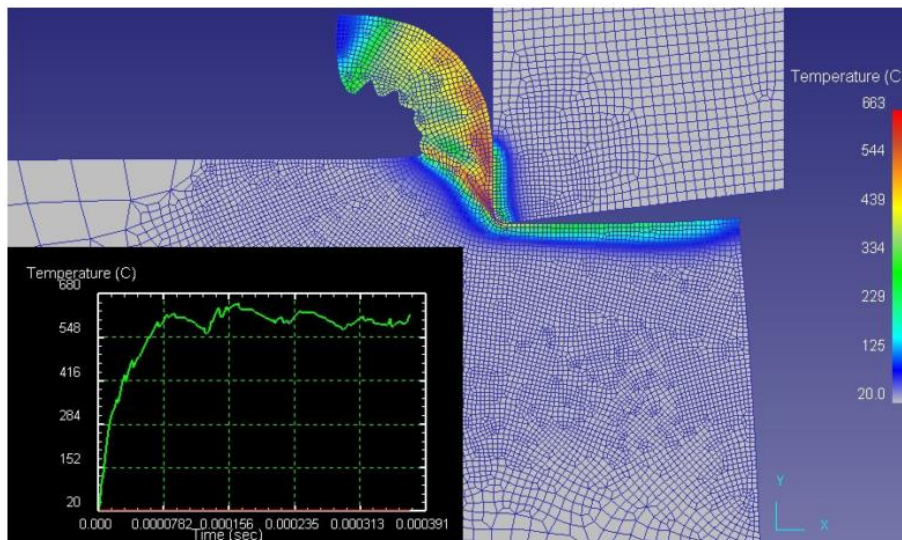
Figure 2-55. Finite element simulation of the temperature distribution during machining Ti64 at 150 m.min^{-1} and feed 0.2 mm.rev^{-1} [76].

Shaw et al. [78] found out that varying the cutting parameters during machining of titanium alloys can give rise to different mechanisms of chip formation; from saw-tooth to continuous and homogeneous type. They precision turned Ti-140A at 45.7 m.min^{-1} at a feed rate of 0.264 mm.rev^{-1} obtaining a segmented chip formation, see Figure 2-57 a). Reducing the surface speed to 30.48 m.min^{-1} and the feed rate to half the previous value - to 0.132 mm.rev^{-1} gave rise to

homogeneous chip formation; see Figure 2-57 b). They also precision turned 1045 Steel under the same cutting conditions as in Ti-140. In both testing conditions, during machining SAE 1045 Steel, they obtained a continuous and homogeneous type of chip. Also, in both cases, the chip thickness generated from steel SAE 1045 is much higher than during machining of Ti-140 (Figure 2-57). This may be the result of a larger number of operating slip systems in the 1045 steel workpiece material, allowing for more easy accommodation of plastic strain. This may distribute the temperature homogeneously throughout the chip material, reducing the large temperature rise in localised areas. Thus, reducing the high-temperature exposure to the cutting tool, leading to longer tool lives during cutting. Ti-140A is an $\alpha+\beta$ alloy and its composition in wt.% is: 94.3 Ti, 0.14 N, 2.04 Fe, 0.04 C, 1.80 Cr and 1.70 Mo [78]. Steel SAE 1045 composition in wt.% is: C 0.44, Mn 0.70, P 0.053, S 0.039, Si 0.24 and Fe remaining [79].

The chip-cutting ratio, r, (uncut chip thickness t over the chip thickness t_c), equation (2.1), is higher for titanium alloys. This is because the chip thickness does not increase as much as in steels, such as SAE 1045.

$$r = \frac{t}{t_c} \tag{2.1}$$
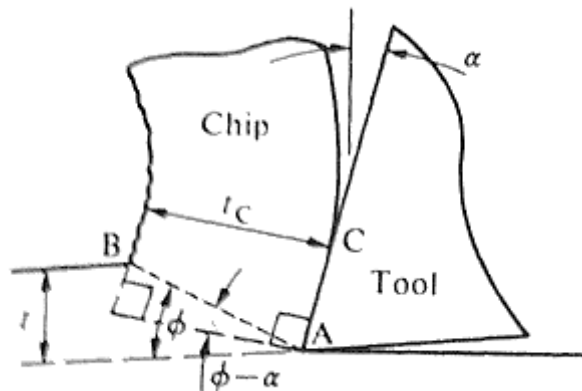
Figure 2-56. The relationship between the shear angle (ϕ) and the cutting ratio (r) – After Shaw [59].

The shear band angle should not be higher than 45°. In Figure 2-56 it is observed that the $\tan(\phi) = t/AB$; $\tan(45) = 1$, AB will always be larger than t; therefore, t/AB is always lower than 1. The shear angle is higher for titanium alloys as in Ti-140A, in comparison to SAE 1045 steel. It is related to the large chip cutting ratio and lower strain imposed on the chip during cutting and to higher chip velocities [78]. Shaw et al. [78] estimated a higher friction energy per unit volume during machining Ti-140A, close to 40%, and a lower value for SAE 1045, nearly 20%.

The inhomogeneous type of chips should be avoided [78]. This is because of the inhomogeneous strain accommodation, and the strong increase in temperature in the

concentrated shear strain regions, which are in direct contact with the cutting tool. This is unfavourable because the chip maintains contact with the tool and it almost does not advance while the chip is being compressed. When the strain localises, the chip advances at higher velocity generating friction and a stress fluctuation leading to tool fatigue stress. The tool usually has a higher thermal conductivity than titanium alloys; thus most of the heat transfers to it, subjecting the tool to thermal stresses. The tool life in SAE 1045 steel was much higher than in Ti-140A. This is the result of the homogeneous plastic deformation and the uniform temperature distribution, leading to a lower increase in temperatures in the tool. For Ti-140A, the low speed (Figure 2-57 b) allows a cutting time of 250 min, whilst the higher speed (Figure 2-57 a) only 30 min. For steel SAE 1045, the low speed (Figure 2-57 d) allowed 800 min of cutting time, whilst the higher speed (Figure 2-57 c) allowed more than 1000 min.
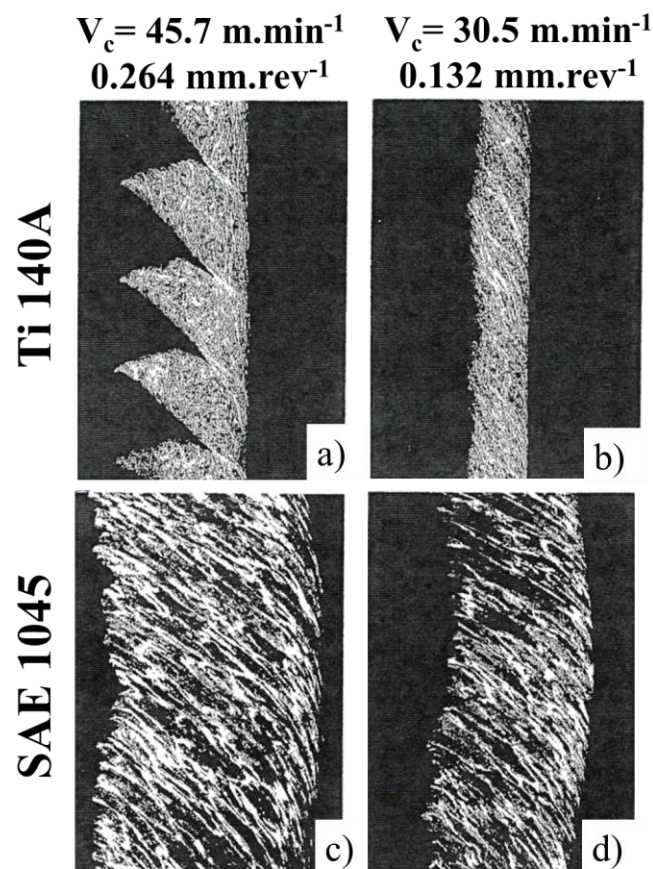
Figure 2-57. Cross-sectional light micrographs of the chip formation of Ti-140 a)-b) and Steel SAE 1045 c)-d) at surface speeds of 45.7 m.min^{-1} and 30.48 m.min^{-1} at feeds of 0.264 mm.rev^{-1} and 0.132 mm.rev^{-1}. After Shaw et al. [78], no length scale was provided.

Table 2-5. Properties of Titanium and other structural alloys, for comparison. –The first four columns are after Shaw et al. [78], and the data was converted to the International System of Units, data is added for other titanium alloys for comparison.

Properties at ambient Temperature	75A Titanium	SAE 1020 Steel	18-8 Stainless Steel	75ST Aluminium	SAE 1045 Steel	Ti-6Al-4V @ 20°C	Ti-6Al-4V @ -140°C
Crystal Structure	HCP	BCC	FCC	FCC	BCC	HCP + BCC	HCP + BCC
Specific weight $(Kg.m^{-3})$	4,429	7,750	7,750	2,768	7,850	4430	4460
UTS (MPa)	207	345	621	565	565	900	1365
Young Modulus, E (GPa)	110	207	207	71	200	113.8	117.5
Shear Modulus, G (GPa)	41.4	79.3	79.3	26.9	80.0	44.0	45.5
Melting point (°C)	1760	1427	1427	557		1660	1660
Coefficient of linear expansion (per °C) $*10^{-6}$	9	11.88	16.2	23.4	11.7	0	-1350
Thermal conductivity, k $(W\ m^{-1}\ K^{-1}\ )$	20.56	56.08	16.45	119.63	16.45	6.6	4.26
Specific heat, C_p $(J\ Kg^{-1}\ K^{-1})$	502	544	502	879	515	526.3	388.87
Volume specific heat, ρC_p $(GJ.m^{-3}.\ K^{-1})$	2.22	4.22	3.89	2.43	4.04	2.33	1.73
Thermal diffusivity $\alpha = (k/\rho C_p)$ $(cm^2\ s^{-1})$	0.090	0.135	0.045	0.490	0.490	0.028	0.025
Thermal combination $= k\ \rho\ C_p$ $(\ J.m^{-2}\ K^{-1})^2.s^{-1}\ x10^6$	**45.71**	236.43	**64.00**	291.06	66.50	15.39	**7.39**

Before titanium alloys were used as structural materials, stainless steel was heavily used due to its high strength. Stainless steel was the alloy with the greatest difficulty to machine, attributed to its low thermal combination, as seen in Table 2-5 [78]. The thermal combination of stainless steel is 64.0 x 10^6 (J m^{-2} K^{-1})^2 s^{-1} and other alloys such as steel and aluminium generated higher values such as 236.4 x 10^6 (J m^{-2} K^{-1})^2 s^{-1} and 291 x 10^6 (J m^{-2} K^{-1})^2 s^{-1}, respectively. This was the reason to machine stainless steel at low cutting speeds. When titanium alloys were developed, they were even harder to machine due to very high temperatures and prohibitive tool wear rates. The thermal combination value reduced nearly a quarter from that of stainless steel, resulting in an even higher reduction in cutting speeds. Commercially pure or low element content titanium alloys have higher thermal conductivity, such as 20 W m^{-1} K^{-1}. Higher element content alloys, such as Ti-6Al-4V have a much lower thermal conductivity, nearly 7 W m^{-1} K^{-1}, attributed to electron scattering. This results in a nearly 66% reduction in the thermal combination number 15.4 x 10^6 (J m^{-2} K^{-1})^2 s^{-1} from that of CP-Ti. Lowering the deformation temperature of Ti-6Al-4V leads to a reduction in both thermal conductivity and heat capacity with a slight increase in density. This leads to a further reduction in the thermal combination number to nearly half of Ti-6Al-4V at room temperature or nearly 84% reduction vs CP-Ti.

Shaw et al. [78] obtained much higher experimental temperatures during machining of Ti-140A in comparison to steel SAE 1045; 740°C and 415.5°C, respectively under the same cutting parameters; surface speed 30.5 m.min^{-1} and 0.132 mm.rev^{-1}. It was attributed predominantly to the low thermal combination number (kρC$_p$).

There is a critical temperature where solid-state diffusional processes start to operate, and these accelerate tool wear as shown in Figure 2-58. The cryogenic coolant may retard the occurrence of that temperature, allowing extra operational cutting time with a higher integrity cutting edge.
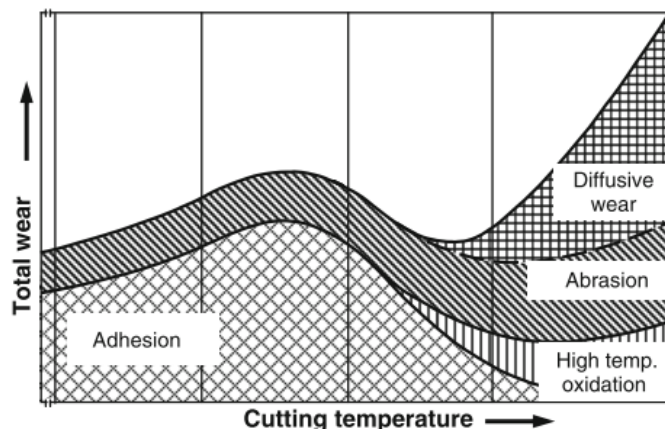
Figure 2-58. Temperature dependence on tool wear mechanisms [80].

Deformation maps, which correlate deformation parameters such as shear strain, shear strain rate and temperature to microstructural evolution characteristics during machining, have been developed, such as that shown in Figure 2-59. Figure 2-59 shows different shear strain rates (from 10^1 s^{-1} to 10^5 s^{-1}) and shear strains (1 to 15) during machining high purity copper (99.999%) and their microstructural characteristics in the SPD region.
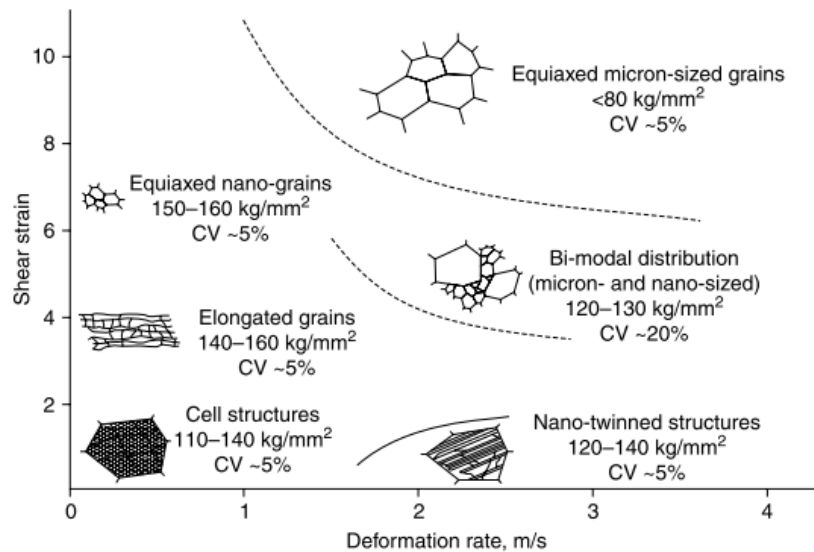
Figure 2-59. Deformation map of machining of copper correlating deformation parameters such a shear strain and strain rate to microstructural effects [54].

2.12. Cooling-lubricating strategies during machining operations

The cooling and lubricating fluids are an essential part of the machining system as they enhance tool life, the finish of the machined piece, dimensional stability and help to evacuate the chips from the cutting zone. The cooling and lubrication methodology usually accounts for nearly 15% of the total cost of manufacturing a component [67]. The use of water-based coolants has a high capital cost expenditure in advance, as not only the cost of the coolants is involved, but also maintenance and disposal are involved. Additionally, the risk of occupational exposure to operators is a hazard.

The industry generates millions of barrels of hazardous waste, which are contaminating the land. Thus, a strategy needs to be generated, where the reduction of hazardous waste is created. Additionally, the mist generated by cutting fluids has been classified as dangerous for personnel working directly with them, through skin and inhalation exposure. Cancer, lung illnesses and skin irritation problems have been reported [19], [67], [81]. Therefore

OSHA [82] has reduced the exposure limit of these fluids from 5 mg.m^3 to less than 0.5 mg.m^3.

Components such as knee and hip replacements must not be contaminated with oils or chemicals as they will be in direct contact with human tissue, thus the use of metalworking fluids during its manufacture it is prohibited. Cryogen media such as CO_2 and LN_2 leaves no residues, thus is beneficial to the machinability of these components.

Lubricating oils represents mineral, vegetable, animal and synthetic oils, which are not diluted in water. Petroleum mineral oils are frequently used due to their low cost.

Vegetable oils are better lubricants attributed to their dipolar inherent characteristics and have a high flash point, a property which prevents smoke formation. They cost more than mineral oils, but they are more effective in specific applications as they can improve tool life. However, a drawback is its short shelf life related to bacterial degradation and hydrolyzation.

2.12.1.   Minimum Quantity Lubrication (MQL)

It refers to the application of a fine aerosol mist (a mixture of neat oil droplets in compressed air). Typical flow rates are in a range between 5 and 200 mL.h^{-1}, which is influenced by the workpiece material and cutting operation parameters. In this type of application, the oil is consumed during the process, there is no need to collect, and it cannot be reused.

During MQL application, frictional heating and build up edge (BUE) is reduced as better lubrication in the cutting zone is provided in comparison to conventional cutting fluids, however, cooling and dimensional stability are not significantly improved as MQL is not highly effective in the heat reduction, nor the removal of the chips out of the cutting zone. The friction during metal cutting could be reduced by increasing the viscosity of the oils used as lubricants, which is influenced by the temperature [83].

The fact that the oil dissolves into the supersaturated cryogenic coolant may improve the lubrication of the machining operation, as the particles will have the kinetic energy to reach the cutting edge and therefore lubricate.

2.12.2.   Cryogenic cooling

The strict definition of cryogenic refers to temperatures lower than -150°C, defined by standards institutions [84]. However, in industry and research, it is usually referred to as temperatures below 0°C or sub-zero temperatures. The most commonly liquefied industrial

gases used are liquid nitrogen (LN_2), and it is the most common cryogen, as it is readily available and carbon dioxide snow (CO_2) or dry ice at 194.5 K (-78.6°C). Both are considered as industrial cryogens thanks to their physical states cooling capacity. CO_2 is stored in a liquid state in pressurised tanks (near 57 bar) at room temperature, LN_2 has to be kept cooled in insulated tanks.

The Young's modulus of titanium alloys decreases with increase in temperature [77]. Machai et al. [85] reported a decrease of 50% by a temperature increase from room temperature to 204 °C. Thus, the cryogenic cooling effect of carbon dioxide would be expected to prevent a decrease in modulus during machining, therefore preventing rubbing of the tool instead of cutting action and therefore avoiding tool deflection, thus generating higher accuracy surfaces.

2.12.3.   Carbon Dioxide (CO_2) and Liquid Nitrogen (LN_2)

CO_2 is usually stored in pressurised containers at a pressure near 57 bar and ambient temperature as a liquid phase state, as schematically illustrated in Figure 2-60. It is heavier than air, resulting in the requirement for ventilation systems. For application in metal cutting processes, CO_2 is delivered through high-pressure nozzles directly to the cutting zone. In 1862, Joule and Thompson discovered that in a gas expanding through a valve and experiencing a decrease in pressure, there was a temperature reduction, a process known as "cooling on adiabatic expansion" [86]. When the liquid CO_2 experiences atmospheric pressure, it undergoes the Joule-Thompson effect, producing a phase change to approximately 40% solid or CO_2 snow and 60% gas with a temperature of -78.5 °C [85].

CO_2 in the supercritical phase (scCO_2) has significant solubility for aromatic and aliphatic hydrocarbons [67]. This ability makes CO_2 carry the lubricants in a liquid solution, and thus it is an excellent medium to reach the deepest part of the cutting zone acting as both a coolant and a lubricant. An MQL-scCO_2 system would provide excellent cooling and lubrication capabilities. In a system like this, CO_2 is brought to high pressure, compressing it, then it is warmed up to a supercritical temperature in a chamber, which also contains lubricant oil. When the mixture leaves the delivery pipe it reaches atmospheric pressure and the cooling effect is provided by the expansion from liquid to gas and the dissolved oil separates from the CO_2 and thus it provides lubrication.

The oxidation wear during CO_2 cooling is expected to be prevented. Additionally, it is expected to enhance the chemical stability of workpiece and tool materials, as the lower temperature will deter chemical reactions between the elements of the cutting tool and workpiece materials.

N$_2$ is a colourless, inert, odourless, non-hazardous and nontoxic gas. It is found in the environment at nearly 79% volume fraction. It has a lower density than air; therefore, it releases into the atmosphere readily. This results in a lower requirement for ventilation during its usage. LN$_2$ is stored in insulated containers at atmospheric pressure. Its boiling point is -196°C. Upon contact with the atmosphere, it boils and transforms into a gas state, see Figure 2-60. When LN$_2$ contacts hotter surfaces, it forms a vapour blanket layer, surrounding the hotter material. This hot vapour blanket has an insulating effect, known as the Leidenfrost effect, resulting in a slow cooling rate and heat transfer occurs mainly by radiation. LN$_2$ reduces the friction coefficient during cutting, and there is a reduction in the contact length between the chip and the tool.
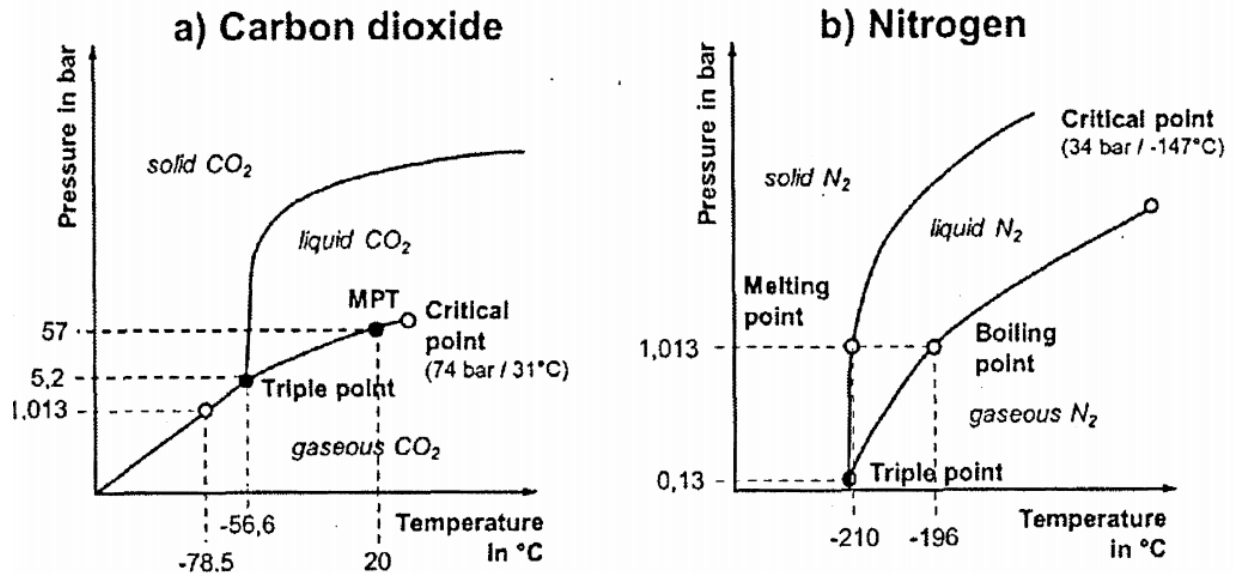
Figure 2-60. Schematic phase change diagrams for: a) CO$_2$ [87], [88], b) LN$_2$ [88].

Cryogen media under super-critical condition absorbs more heat and releases to the atmosphere by evaporation [89]. Tao Lu [89] reported that the dominant heat transfer mechanism in cryogenic machining is boiling, resulting in high values of heat transfer coefficients up to 10^5 W.°C^{-1}m^{-2}. This mechanism initiates as film boiling and turns into boiling. In the nucleation boiling stage, there is a substantial increase in the cooling rate, see Figure 2-61 a). Boiling comprises three stages: (1) nucleate boiling, (2) transition boiling and (3) film boiling [90]. The heat transfer coefficient reaches a maximum in this stage, see Figure 2-61 b). Thus, a high flow rate should be maintained to allow boiling to occur during cutting.
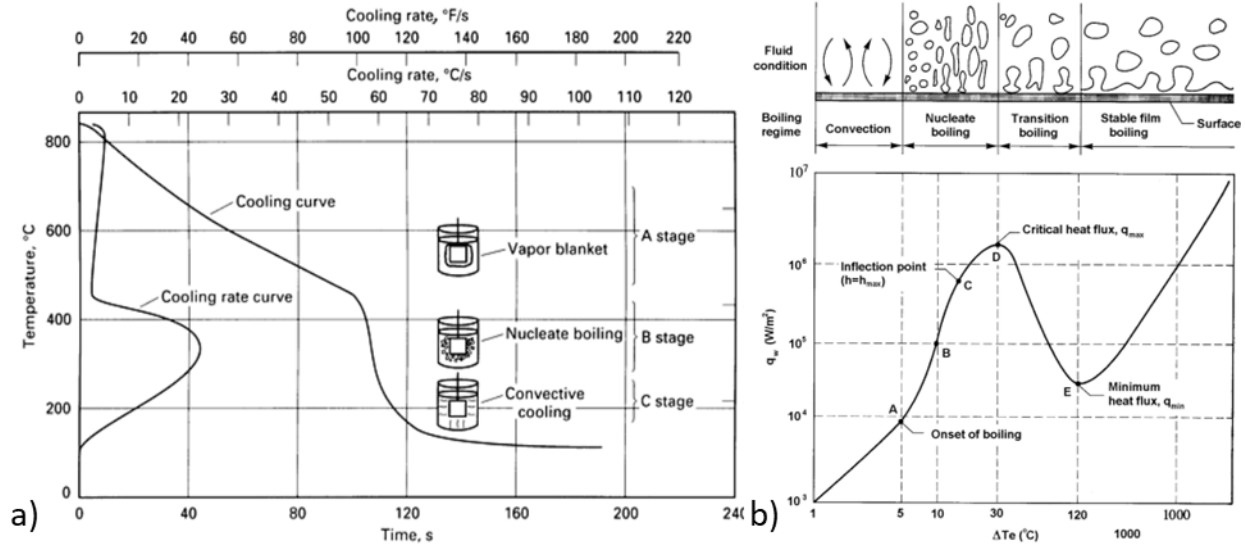
Figure 2-61. a) Change in temperature vs time and the cooling rate during quenching a 25 mm diameter specimen with water at 95°C [91] and b) heat transfer coefficient dependence on the operative mechanism for water boiling at atmospheric pressure [90].

Stahl et al. [92] report that the generated higher yield strengths of the workpiece material cause the height of stagnation point (Y_s) to decrease, and consequently better control of burr formation [85]. Additionally, a rapid reduction in the fracture toughness of the workpiece material results in brittle material separation rather than ductile [92]. This fact is highly beneficial as localised cooling in the cutting edge region could help cut material in a brittle way while maintaining material properties below the machined edge.

Besides, other advantages are that cryogens do not generate hazardous waste, they pose fewer health risks, and there is no chip contamination; therefore this technology is easier to apply to the tightly restricted machining of biomedical components. Also, CO_2 can be collected from waste processes such as fractional distillation instead of sending it to the atmosphere. This is known as resource-efficient and environment neutral [88].

The enthalpy of sublimation of CO_2 snow is almost three times as high as the enthalpy of vaporisation of LN_2 (see Table 2-6 and Table 2-7). However, the water at ambient temperature has a much higher enthalpy of vaporisation, more than four times that of sublimation of CO_2 (Table 2-7). The boiling points of different cryogenic media are shown in Table 2-8. The heat transfer coefficient between air and water in free and forced convection is shown in Table 2-9. Forced convection in water provides the highest values. This may be one of the reasons for the improvement in convection under high-pressure flood cooling in comparison to conventional flood cooling.

Table 2-6. Thermal properties of cryogen gases and air [93].

Gas	ρ $(Kg.m^{-3})$	Cp $(KJ.Kg^{-1}°C^{-1})$	μ $(Kg.m^{-1}s^{-1})$	k $(W.m^{-1}C^{-1})$	ν $(cm^2.s^{-1})$	Pr	Hv $(KJ.Kg^{-1})$
Dry Air	1.164	1.007	1.86E-05	0.0263	0.160	0.72	
CO_2	1.773	0.852	1.51E-05	0.0166	0.085	0.78	574
N_2	1.138	1.041	1.78E-05	0.0259	0.156	0.72	

Table 2-7. Thermal properties of liquids [93], [94].

Liquid	ρ $(Kg.m^{-3})$	Cp $(KJ.Kg^{-1}°C^{-1})$	μ $(Kg.m^{-1}s^{-1})$	k $(W.m^{-1}C^{-1})$	ν $(cm^2.s^{-1})$	Pr	Hv $(KJ.Kg^{-1})$
N_2, -196 °C	808	1.04	1.80E-05	0.138	0.0020	0.849	199
Water, 20°C	998	4.183	8.90E-04	0.597	0.0089	7.56	2,264
Graphite oil-based nanofluids, 20°C				0.16			

Table 2-8. The boiling point of cryogen media [95].

Gas	T (°C)
Helium	-269
Hydrogen	-253
Neon	-246
Nitrogen	**-196**
Argon	-186
Oxygen	-183
Carbon dioxide	**-78.5**

Table 2-9. Typical heat transfer coefficient of free and forced convection values [95].

Fluid flow mode	C $(W.m^{-2}K)$
Free convection in air	5-20
Forced convection in air	20-200
Free convection in water	20-100
Forced convection in water	50-10,000

Figure 2-62 shows the conventional flood emulsion as the coolant with the highest potential for heat removal; however, it is not the lubricant, which generates the lowest tool wear. scCO$_2$-DL (dissolved lubricant 4-40 ml.hr^{-1}) shows the second highest potential for heat removal and the lowest tool wear damage average. This may be as the lubricant is dissolved in the CO_2 it can reach deeper into the cutting zone, even under conditions of high pressure and temperature (such as the region of contact between the tool and the workpiece).
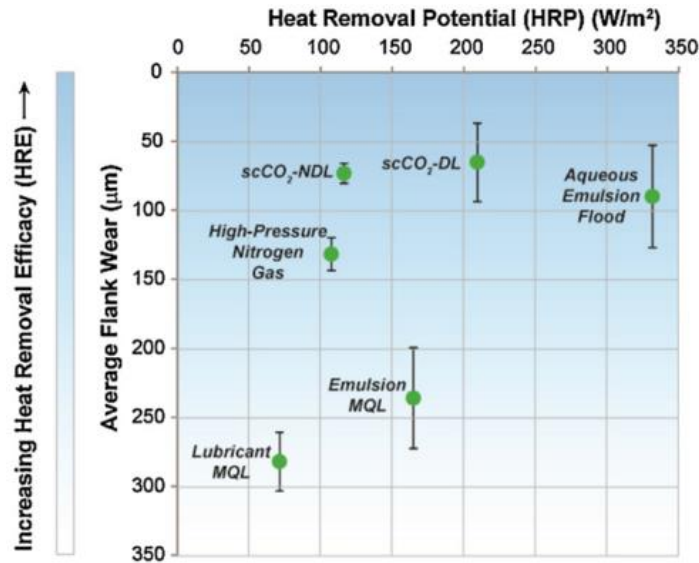
Figure 2-62. Heat removal efficiency of different coolants in metal cutting. DL means dissolved lubricant 4-40 ml.hr^{-1} and NDL non dissolved lubricant [81].

2.12.4.   Advantages

The application of a cryogen fluid during metal cutting changes the material properties in both the workpiece and the cutting tool materials and improves dissipation of the heat generated during metal cutting.

   Material strength (yield strength, hardness, and tensile strength) is increased at low temperatures as previously shown in section 2.9. Some of the advantages of cryogenic machining are the following:

1) Low-temperature increases the Young's Modulus of Elasticity
2) Longer tool life due to slower tool wear rates and reduction in temperature thus slowing down solid-state diffusional processes.
3) Lower elongation at lower temperatures.
4) Less energy per unit volume required to break a chip.
5) Lower strain to fracture.
6) A decrease in the stagnation point or the zone of dead material.

2.12.4.1.   Increase in tool life

Tool life has been reported to improve more than two times during metal cutting using a cryogen fluid such as CO_2 or LN_2 compared to conventional flood cooling. Sadik et al. [24] reported an increase in tool life of over three times when applying CO_2 as a

coolant/lubricant through a tool nozzle in comparison to flood cooling in a two flute milling operation. The material was Ti-6Al-4V in a mill annealed condition using a PVD coated cutting insert at a speed of 80 m.min^{-1} at a depth of cut of 2 mm. Three CO_2 volumetric flow rates were applied: 0.65 Kg.min^{-1}, 0.19 Kg.min^{-1} and 0.15 Kg.min^{-1}. Both CO_2 and flood was applied at the same pressure 50 bar. The limiting wear rate being notch wear. They reported longer operational tool life, which was heavily influenced by the volumetric flow rate of the CO_2. Reduction of thermal cracks propagating laterally was attributed to higher CO_2 flow rates. The author believes the ability to remove a higher amount of energy from the cutting zone reduces the thermally activated mechanisms of tool wear such as diffusion (also shown in Figure 2-58). Although the tool shows deeper cracks under CO_2, they were generated vertically. This might take a longer time to damage the rake face of the tool as by cracking longitudinally, the flank face of the tool might fail earlier. Even though there are higher thermal stresses during cooling with CO_2, the thermal fatigue cracks might get localised. Although much longer tool lives are generated under CO_2, they do not provide any evaluation of the most important result of machining, the workpiece integrity. When the tool wear is high, tensile stresses are imparted into the workpiece [96]. High-temperature loads lead to tensile residual stresses [84].

2.12.4.2.   Cutting forces

Lower cutting forces have been misreported during metal cutting under cryogenic cooling conditions [97], [98]. Titanium alloys exhibit higher forces during deformation at low temperatures as previously described in section 2.9 and experimental work presented in chapter 5. According to scientific evidence and review of the literature, it is the author's belief that in these studies that report lower cutting forces, the cryogenic coolant could not have reached the cutting edge, therefore could not have had an effect on both the workpiece material and the cutting tool, thus lower cutting forces were recorded.

Even with higher cutting forces experienced at low cutting temperatures, a lower strain is required to bring the onset of failure of shear localisation to generate the shear band (See chapter 5). Dilip et al. [98] reported lower cutting forces during machining Ti-6Al-4V under CO_2 and LN_2 compared to dry and conventional cooling. Lower forces under CO_2 than LN_2 are reported [98] which agree with experimental evidence, as the CO_2 temperatures reached are higher than LN_2. However, they reported higher cutting forces under conventional cooling and dry machining than cooling under both cryogens. This is in disagreement with previous reported scientific evidence. Cutting forces should be lower under dry machining, and conventional cooling as there is more heat built up and Ti-6Al-

4V has a low thermal conductivity. Thus the material should soften and generate lower cutting forces.

2.13. Subsurface deformation levels: Severe Plastic Deformation Induced grain refinement (nanostructured) and twinning

The subsurface of a machined component could be engineered by tailoring the subsurface machining-induced plastic deformation desired levels and generating a microstructure that provides the required mechanical properties for in-service applications. This could be achieved by tailoring the plastic deformation through modifying the imparted strain, strain rate, temperature and friction conditions that could generate the required grain size such as nano or ultra-fine size. Different tool rake angles generate a wide range of plastic strains imparted into the chip and the workpiece. The surface speed directly influences the strain rate and the higher the speed, the higher the generated temperature. The temperature and friction mechanisms could be modified by the cooling and lubrication methodology such as cryogenic cooling, high-pressure cooling, MQL or cooled air. Additionally, the flow stress is influenced by the variation of any of these factors.

During machining, a graded subsurface microstructural modification is generated on the workpiece. Although three different subsurface regions (featureless zone, twinned subsurface and bulk undeformed region) are reported in the literature [99], such as in Figure 2-63, the author has classified it into four areas. The first area is the SPD, where the microstructural features are not resolvable by light, nor electron microscopy (backscattered electron) BSE nor secondary electron (SE), only through TEM. This SPD layer belongs to a region of the ASB formation that had failed through instability by thermal softening and strain localisation thus by void nucleation, growth and coalescence. The second area corresponds to gross plastic deformation where the deformation-imparted features are resolvable but are highly distorted, showing that the deformation features imparted ahead of the tool may have been affected by the passing of the tool, generating a disordered structure, also corresponding to a strain-hardened area. The third region is the mechanical twinning area, where they subdivide and completely reorientate parts of the grains. The fourth area is the undistorted bulk microstructure.

The mechanical twinning imparted on the β annealed Ti-6Al-4V in this investigation does not traverse the grain. This is because the material has a high grain size (of the order of 600 µm to 1200 µm) and the cutting action may not have provided enough strain energy to traverse the entire grain. The author believes that not fully traversing the grains is

beneficial as there would not be as many easy slip systems available for plastic deformation during operation and there is less damage introduction to the subsurface.
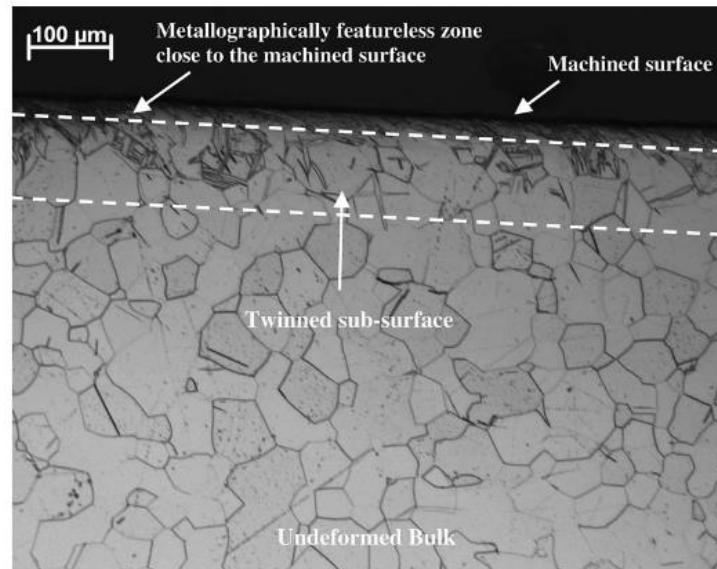
Figure 2-63. Subsurface microstructural regions during plane strain machining CP-Ti with a grain size of 60 µm using an HSS tool with $\alpha = 20°$, uncut chip thickness of 0.3 mm at a $V_s =$ of 10 mm.s^{-1}, dry cutting, at room temperature [99].

Shankar et al. [99] studied the effect of the rake angle (positive, zero and a negative) during orthogonal cutting of CP-Ti (initial grain size of 60 µm) at a surface speed of 10 mm.s^{-1}, and uncut chip thickness of 0.3 mm, under dry cutting, on the strain imparted microstructure refinement in the chip formed. They estimated a higher strain in the chip using a negative rake angle. The strain in the chip using a 20° rake angle was estimated to be ~ 1.4 and at using a rake angle of -20°, a strain of ~ 3.5. Through bright field TEM micrographs (Figure 2-64), they observed dynamic recrystallization in the chips. Figure 2-64 a) shows a bright field transmission electron micrograph (BF-TEM) of a chip generated with a +20° rake angle, it shows a grain size near 100 nm (UFG) and elongated subgrain structures. Figure 2-64 b) shows a BF-TEM of a chip generated with a -20° rake angle. It shows a nanocrystalline grain structure with a higher level of grain refinement, which corresponds to the negative rake angle. They suggested that the ring-like pattern from the SAD is related to a higher misorientation degree between the grains. However, no evidence of the distribution of misorientation angles is provided. They reported a 7.3% higher increase in hardness in the chip deformed at lower rake angle (corresponding to more than double the imparted strain) in comparison to the positive rake angle; 247 Kg.mm^2 vs 230 Kg.mm^2 respectively. Both values are much higher than the bulk: 144 Kg.mm^2, corresponding to a high strain hardening imparted to the chip during cutting.

69
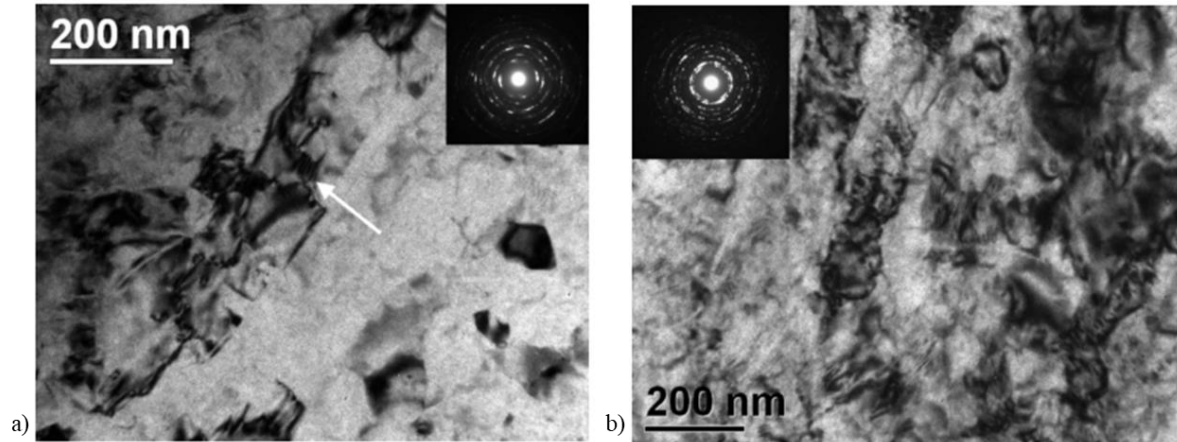
Figure 2-64. Bright field TEM micrographs corresponding to the chip microstructure of CP-Ti orthogonally cut with HSS tools at: a) $\alpha = +20°$, b) $\alpha = -20°$ [99].

Pu et al. [100] have reported the generation of a white layer under cryogenic machining in AZ31 Mg. Although they have called it a white layer, it corresponds to the SPD region, and the author thinks that it should be referred to as SPD layer. White layers are typically generated in steel, and they correspond to a martensitic phase transformation [67]. As previously seen, plastic deformation at lower temperatures generates a higher density of dislocations, which provides more material for the formation of new high angle grain boundary (HAGB) misorientations by dynamic recrystallization. This may be the reason for the generation of an SPD layer composed probably of UFG in the uppermost layer. The use of a lower cutting tool edge radius generated a lower SPD layer. This may be because the deformation concentrates in a smaller region in comparison to a higher tool edge radius.

Tao [101] observed nanocrystalline grain sizes attributed to dynamic recrystallization due to the imparted strain on a nickel workpiece. The generation of high dislocation density allowed the formation of subgrain boundaries of small misorientation, which by further strain imparting resulted in high angle grain boundaries.
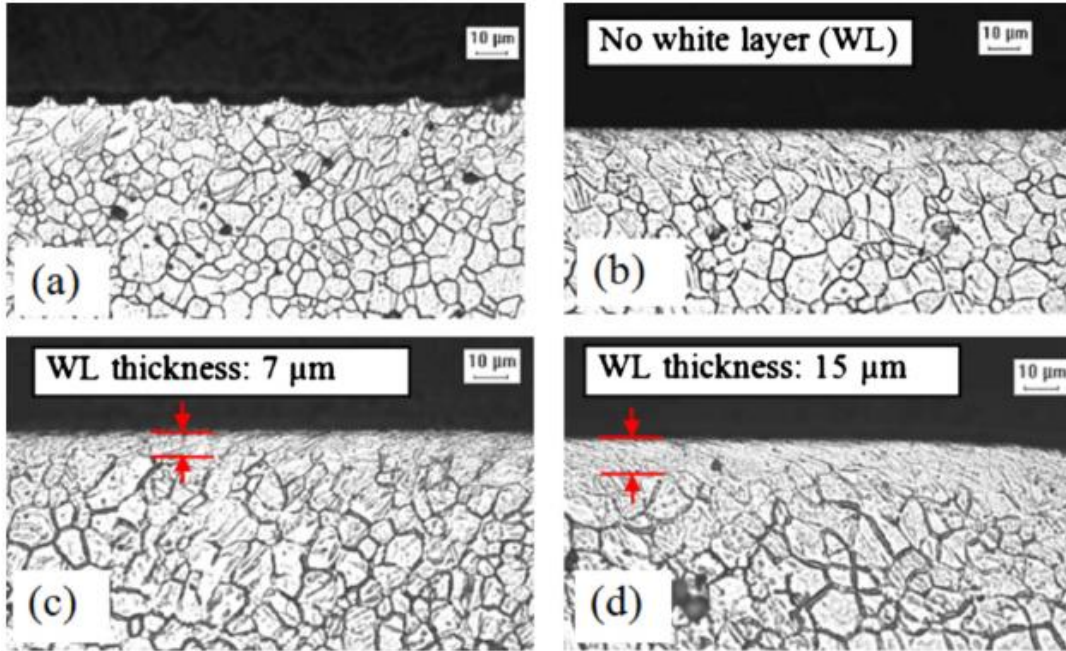
Figure 2-65. Machining-induced grain refinement to a nanostructured grain size of AZ31 Mg alloy; a) undeformed, b) dry machining with an edge radius 30 µm, c) cryogenic machining with an edge radius = 30 µm and d) cryogenic machining with an edge radius = 70 µm [100], [102].

Figure 2-66 shows the effect of tool wear on the imparted subsurface deformation. Figure 2-66 a) shows the deformation with a new tool and b) with a worn tool. This image shows the β phase grain boundary rotation towards the cutting direction. However, the authors did not provide information about the deformation of the α phase.

(a)   (b)
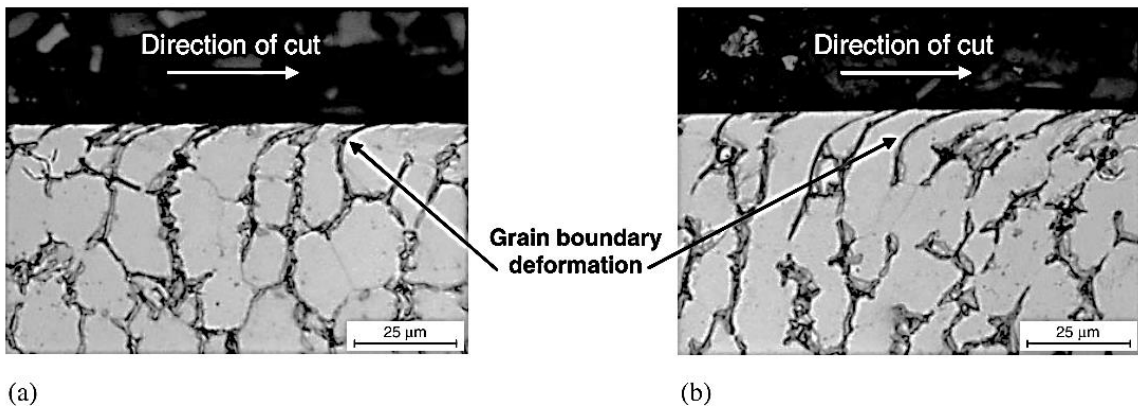
Figure 2-66. Effect of tool wear damage on the imparted subsurface microstructural modification of annealed Ti-6Al-4V with a) new tool and b) worn tool [103].

The lattice rotation in down milling of a Ti-4wt.% Al alloy characterised by Marshall [5] is observed in Figure 2-67. It is observed that the crystal lattice in the nearest region to the surface undergoes a reorientation. In the uppermost surface, mechanical twins appear dragged towards the direction of the tool. This represents the development of a strain-hardened region and the introduction of crystal defects into the lattice. The level of reorientation in the twins is much higher than the reorientation of the matrix.
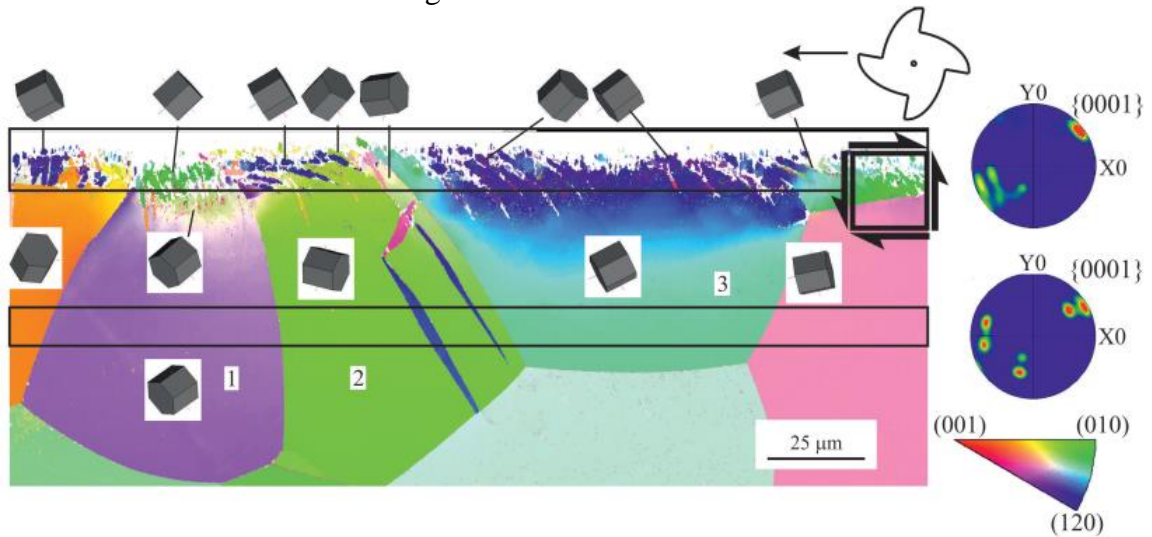
Figure 2-67. Lattice rotation in a down milling operation in Ti-wt.4% Al at 188 m.min^{-1} observed in an Inverse Pole Figure (IPF) using EBSD. After Marshall [5].

2.13.1.   Effect of surface speed on subsurface deformation levels

Through the application of Electron Backscatter Diffraction (EBSD), Crawforth et al. [104] demonstrated an increased level of introduced subsurface damage (mechanical twins and dislocation slip) by increasing surface speed during precision turning of near α Ti-834 using a tool geometry of $\alpha = 7°$ and clearance angle of 6°, as illustrated in Figure 2-68. Crawforth et al. [104] suggested that the best condition is 70 m.min^{-1} as it generates the lowest maximum level. However, the lowest arithmetic average is found at 80 m.min[-1,] and there is not a marked difference in the maximum damage at 70 m.min^{-1}.

On the other hand, by assessing the subsurface damage as the depth of the β-phase dragged towards the cutting tool (by BSE), Crawforth et al. [104] reported a reduction in the level of damage observed; from 10 µm at 50 m.min^{-1} to 3 µm at 120 m.min^{-1}.
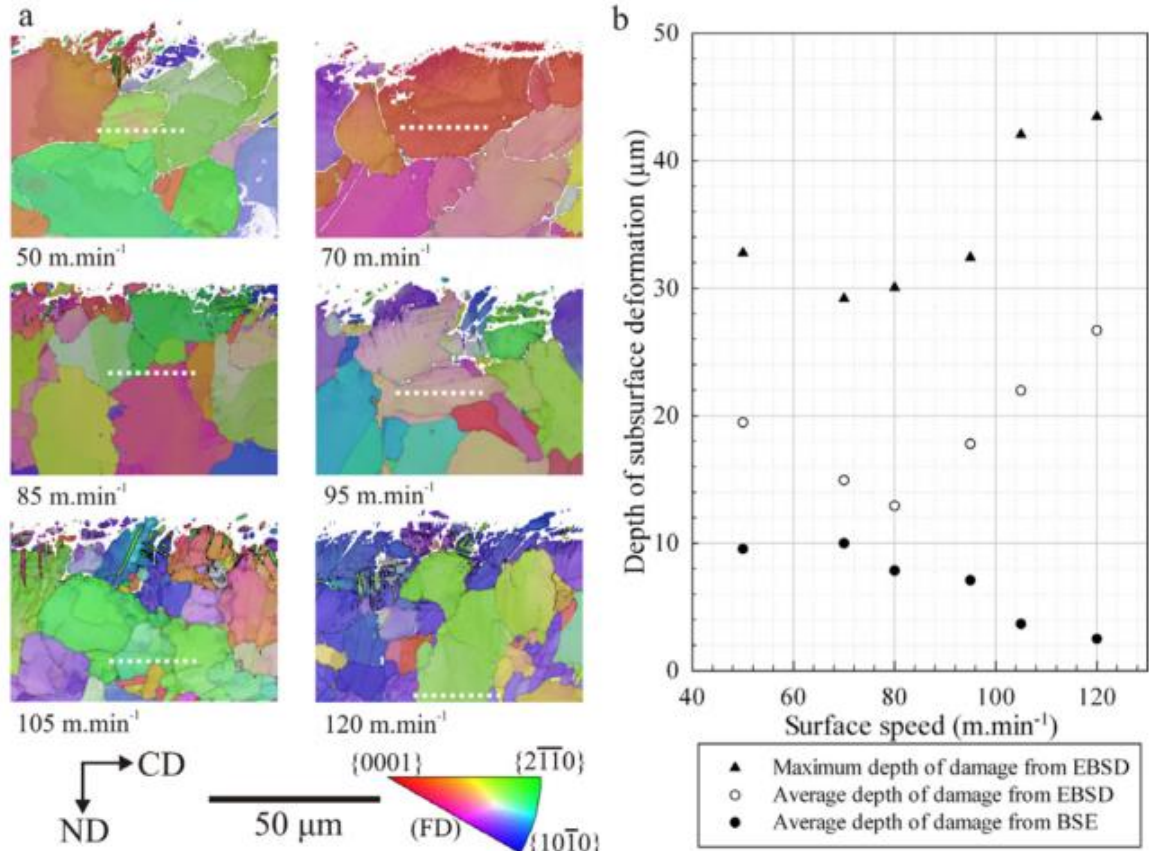
Figure 2-68. Electron Backscatter Diffraction, Inverse Pole Figure (EBSD-IPF) of near α Ti-834 illustrating the effect of surface speed on the subsurface damage imparted during precision turning. The white line represents the maximum measured damage After Crawforth [104].

The author believes that the subsurface microstructural damage should be evaluated using techniques that resolve clearly the highest level of imparted damage, such as EBSD, cross-polarised light or assuring a good contrast in the SEM under BSE. Considering only the depth of the β phase dragged may disregard mechanical twinning, which may be detrimental during cyclic fatigue. Also, measuring cross-polarised light micrographs results in a higher statistical significance of the measured average values. This is because a higher number of micrographs can be obtained, in comparison to EBSD, which may take over 12 hours to generate one scan. Alternatively, SEM, which not only takes slightly more time but is more costly to use. The subsurface damage should be evaluated on workpieces machined using tools with the highest level of wear. This would assure the reliability of machined workpieces with lower levels of tool wear.

The residual plastic deformation of the α phase may provide a more direct relationship to the mechanical properties of machined components during in-service applications.

73

During cyclic loading, deformation is stressed at the twinning interfaces; twins break up into segments, leaving a high density of dislocation debris composed of dipole loops and crack nucleates in these segments [1].

Relating to high-pressure cooling and dry conditions, Dargusch et al. [105] investigated the subsurface damage during slot milling of titanium grade 2 from low to medium surface speeds (29.6, 39.6, 48.3, 55.7 m.min^{-1}) to demonstrate that titanium alloys can be milled without the use of a lubricant. They reported an SPD layer between 5-10 µm, followed by a region in the subsurface containing mechanical twinning. At a speed of 48.3 m.min^{-1}, they reported more than double compressive residual stress under dry condition (90 MPa) and (40 MPa) under a lubricant and a better surface roughness (0.9 ± 0.2 µm) under dry conditions in comparison to a cut using lubricants (1.9 ± 0.3 µm). This result is at odds with other literature sources [106] as heat has been identified to give rise to tensile residual stresses. However, much higher twin depth was found under dry conditions (180 µm dry and 75 µm using a coolant) and twin density (2700 mm^{-2} dry and 1900 mm^{-2} with coolant; 29 % higher twin density under dry condition) as it is observed in Figure 2-69. Even though they found higher compressive residual stress under dry conditions, higher twin depth and density are seen in the optical microstructures. As is well known, mechanical twins have been found to provide sites of crack initiation under cyclic fatigue, and with the competitive environment of the actual market conditions, higher productivity is trying to be reached, giving rise to higher surface speeds during machining. This leads to the idea that machining under dry conditions at higher speeds might not be feasible, as more twin features will be generated even though higher compressive residual stresses and surface roughnesses are obtained, as titanium alloys are mainly used for structural components and higher twin depth and density would lead to lower operational fatigue life.
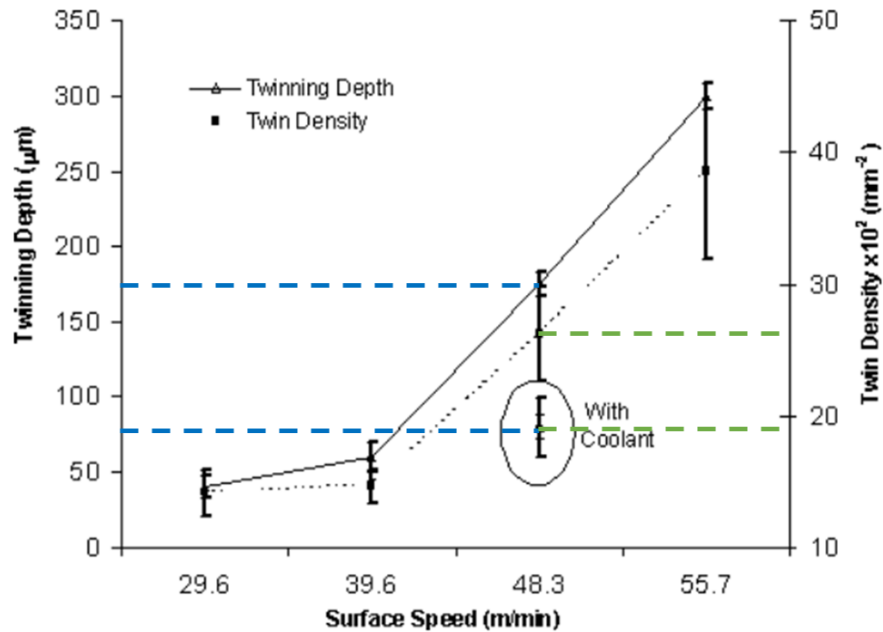
Figure 2-69. Effect of surface speed during slot milling of Ti grade 2 on twin depth and twin density [105].

Figure 2-70 illustrates the twins generated during slot milling of CP-Ti grade 2 at a surface speed of 48 m.min^{-1} a) with a water-soluble oil lubricant at a medium pressure of 40 bar and a flow rate 23 L.min^{-1} and b) under dry conditions. It can be observed that there is a higher twin depth and twin density in the dry machined sample, however, the authors reported a higher compressive residual stress on the dry machined sample.
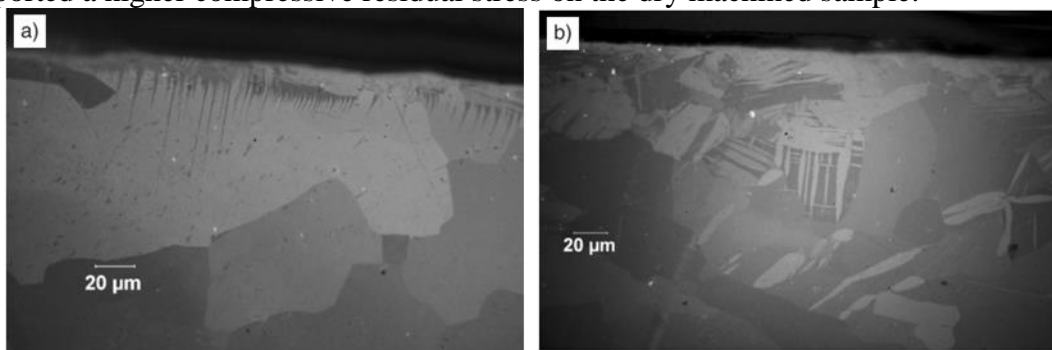
Figure 2-70. CP-Ti slot machined at a surface speed of 48.3 m/min a) with lubricant, b) dry [105].

The subsurface microstructure modification depths of machined components under cryogenic cooling conditions reported in the literature are contradicting. Some authors argue that a smaller machining-induced depth [107], [108] is generated, while others report a deeper [100], [109] affected layer.

A deeper machining-induced affected subsurface layer under cryogenic LN_2 orthogonally cut in comparison to the dry cutting of TiNi shape memory alloys (shown in Figure 2-71) was reported by Kaynak et al. [109]. Highly twinned grains are observed in both conditions but at a higher depth in cryogenic cooling. They claim the increase in temperature under dry cutting resulted in recovery thus producing a thin affected layer. The author considers that if dynamic recovery has occurred on the machining-induced top layer, a lower density of deformation features should be observed, along with lower dislocation density, which does not correspond with the bright-field TEM images shown in Figure 2-72. Figure 2-72 a) the initial microstructure shows a low dislocation density, whilst the dry machined (Figure 2-72 b) shows a higher dislocation content along with some mechanical twins. Figure 2-72 c) shows the microstructure of a workpiece machined under LN_2 composed of a high density of nanometre size mechanical twins. Their corresponding diffraction patterns are shown. The diffraction pattern corresponding to LN_2 shows a ring-like pattern, suggesting the presence of recrystallized grains. This larger subsurface deformation depth of TiNi under LN_2 corresponds to the results obtained in Ti-6Al-4V under CO_2, see Figure 6-10. Higher forces are required to plastically deform Ti-6Al-4V at low temperatures, see Figure 4-7, this leads to higher shear stresses, which are imparted into the material microstructure. Also, the strain is more concentrated in a narrow zone, and the surrounding regions may deform more uniformly; this may lead to larger depths below the shear band. The strain may be accommodated more easily than at ambient temperatures.
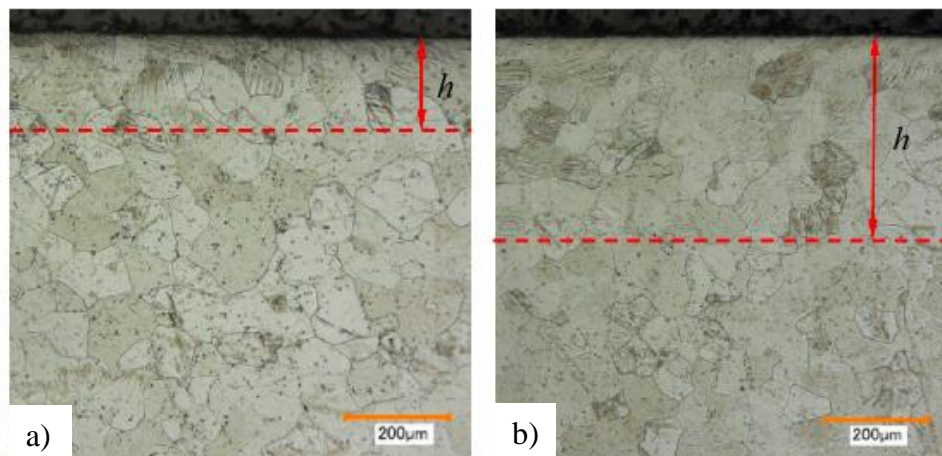
Figure 2-71. Cross section of the machining-induced subsurface deformation in TiNi shape memory alloy orthogonally cut at 6.25 m.min^{-1}, DoC 0.05 mm under a) dry and b) precooled to -185C for 30 min following cutting with cryogenic LN_2 [109].
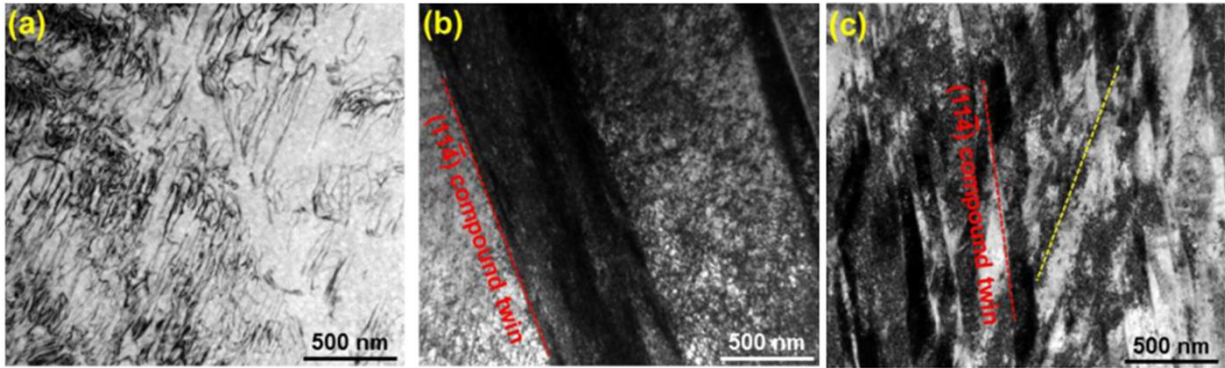
Figure 2-72. Bright field TEM microstructures of TiN a) as received, b)machined without a coolant, c) LN$_2$ cryogenically machined.– After Kaynak et al. [109].

Machai and Bierman [85] have investigated turning of β-titanium alloy Ti-10V-2Fe-3Al cooled with cryogenic CO$_2$ snow. β alloys exhibit the highest strength of the titanium alloys, which leads to the following challenges during machining: (1) high temperatures, (2) high mechanical loads and (3) rapid tool wear. The flank wear under CO$_2$ snow cooling was uniformly spread, and tool life increased two times even at higher cutting velocities, in comparison to flood cooling. This increase in tool life may be attributed to the tendency of β alloys to embrittle at low temperatures as discussed in section 2.9.

2.14. Surface and subsurface microstructural features induced by machining and their influence on fatigue life

The microstructural features remaining on the subsurface (such as intense slip bands and mechanical twins) after a machining operation has been undertaken have a significant influence on the fatigue life of components.

Crawforth [3] reported that the most common mechanism for fatigue crack initiation is slip band intersection with grain boundaries or the specimen surface. In agreement with this fact are the results reported by Taplin [110], who stated that crack nucleation has occurred where two mechanical twins intersect or between the intersection of a twin and a grain boundary.

According to Hull [111], a significant mechanism for crack nucleation is the intersection of mechanical twins in bcc metals. As the hcp crystal structure has less operative slip systems, more mechanical twin systems will be operative, especially at low temperatures. If during further straining, an hcp metal cannot accommodate the imparted strain as the mechanical twin boundaries represent barriers to dislocation motion, the only

77

way to accommodate it, would be through the nucleation of a crack. Therefore, the author considers this mechanism a significant mode of crack nucleation in hcp metals.

Microstructural features such as slip bands and mechanical twins are inherent features of the plastic deformation process. The incidence of any of these features strongly depends on the type of crystal lattice, the grain's crystallographic orientation and the relative CRSS for basal, prism or pyramidal slip versus shear stress required for twinning to occur. These features are found to be detrimental during in-service operation and strongly active in the failure mechanisms during fatigue [2], [34], [112].

Fatigue failures are usually initiated at the surface, thus the importance of generating a smooth surface during machining without V-notches nor surface tears or laps.

Slip band impingement on a microstructural discontinuity such as twin boundaries, grain boundaries, second phase particles, inclusions and v-notches generate a stress concentration and a crack initiation.

The structure of the slip band might affect fracture activity. For instance, the ability to cross slip generates a broadening of the slip band, hampering the cracking of a particle if the slip band impinges upon that particle.

The observation of slip bands in deformed specimens is the result of a build-up of many small slip movements of a size of near 1 nm. The incidence or accumulation of many slip lines gives rise to the generation of slip bands of the order of 100 to 1000 nm [34].

In components that operate under cyclic stresses, the direction of imparted strain changes continuously. This is reflected by the nature of the slip lines intersecting the surface. If the stress is imparted only in one direction, simple slip lines appear as in Figure 2-73 a). If the stress is alternating, the slip bands agglomerate giving rise to striations as observed in Figure 2-73 b). These striations are composed of persistent slip bands. Small localised strains (due to the movement of dislocations during cyclic loading) appear in the PSB, called extrusions (ridges) and intrusions (grooves) as observed in Figure 2-73 and its presence strongly depends on the crystallographic orientation of the grain. Extrusions and intrusions have been observed to be crack initiation sites [2] [34].

Persistent slip bands (PSB) are observed in an interrupted fatigue test. The deformed surface is removed by electropolishing. Usually, there are some slip bands more persistent remaining visible, while the polishing step has removed the others. These PSB's have been detected at very early stages of the fatigue testing (~5%) and represent embryonic cracks due to extensive opening behaviour under small tensile strains.

Partridge [1] reported that fatigue cracks nucleate commonly along mechanical twin interfaces. Findings from Xiaoli et al. [113] are in agreement in the fact that the deformation twin boundaries are preferential sites for crack nucleation during fatigue.

In high purity titanium, sites of fatigue crack initiation have been found along persistent slip bands where holes and microcracks were found [113].

Cracks have been initiated at mechanical twins [114]. In hcp and bcc crystal structures, mechanical twinning turns into the leading plastic deformation mechanism. Twin intersection with other twins and with grain boundaries are significant sites for crack initiation [2][115].
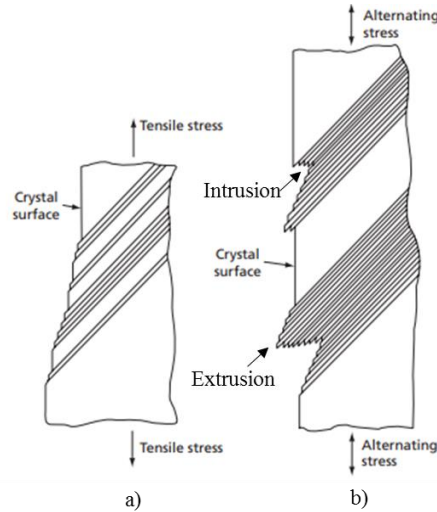
Figure 2-73. Slip band intersection with the surface of a specimen under a) unidirectional deformation and b) cyclic loading [34].

Hull [115] observed mechanical twins close to the area of brittle fracture in specimens tested under tensile loads at sub-zero temperatures in 3%wt silicon iron.

Dieter [2] reported void nucleation in the intersection of mechanical twin boundaries and intersection between grain boundaries and twin boundaries. During high cycle fatigue, the principal mechanism for crack initiation is the intersection of slip bands with the surface or grain boundaries [4]. Therefore, the damage imparted during machining may be deleterious to the integrity. Twins and slip bands are nucleation sites for silicide precipitation: creep & fatigue strength are locally reduced.

In traditional industry-practices, after a machining operation, a surface treatment to introduce compressive residual stresses such as shot peening or surface burnishing is performed. Structural high-strength titanium alloys are exposed to high thermal environments during operation. Ti-834 is a structural alloy being used in the intermediate stage of turbine engines. Components made of this alloy are first machined, then a shot peening process is performed to impart compressive residual stresses as it is believed these compressive stresses would prevent crack initiation during high cycle fatigue. Generation of nanograin size on the upper layer of the subsurface has been observed after shot peening

[55]. It is beneficial as it may improve the strength of the surface. However, Thomas [4] reported silicide precipitation during thermal exposure of shot peened components of Ti-834. He concluded that the result of high grain boundary area in non-equilibrium and high misorientation, generated during peening, serve as easy diffusion paths during thermal exposure. This allows the O_2 and N_2 to diffuse easily into the subsurface. Silicides were precipitated in the regions near the twin boundary areas and on the SPD layer, generating potential sites for crack nucleation. During machining, a similar uppermost surface layer is created. It is composed of nanocrystalline or ultra-fine grain size. For this investigation, a high-temperature thermal exposure study would be beneficial to determine the potential of the interstitial elements to diffuse into the subsurface during in-service operation as the non-equilibrium HAGB generated may represent easy diffusion paths too.

The Widmanstätten or colony microstructure of the β annealed Ti-6Al-4V ELI condition provides higher fatigue resistance. The reason is the creation of many colonies in different crystallographic orientations to prevent the growth of nucleated cracks. The most influential factor in the mechanical properties of a lamellar microstructure is the α colony size as it regulates the effective slip length [21] which consequently determines the strength, ductility and the crack growth resistance. The cooling rate from the β phase field determines the α colony size, α lamellae thickness and β lamellae or retained β. An increase in cooling rate provides a smaller α colony size and smaller α lamellae width which at the same time improves its mechanical properties. A slip band grows along a colony but does typically not traverse to other colonies.

Wanhill et al. [116] illustrated some of the crack initiation sites in a lamellar β annealed Ti-6Al-4V. These sites where slip bands across an α colony (traversing all α lamella and retained β lamellae), and α-β interfaces especially in the α of a prior β grain boundary as shown in Figure 2-74 a). Figure 2-74 b) illustrates the crack path of a β annealed Ti-6Al-4V ELI under low cycle fatigue. It is observed that the microcracks traverse the colony boundary and after passing the boundary there is not a change in the crystallographic orientation of the crack as would have been expected. They concluded that prior β grain boundaries and changes in orientation of different colonies are not always strong barriers to slip movement. They did not comment on the mechanical twinning influence on the fatigue, this mode of plastic deformation being critical in cyclic fatigue. The microstructure appears close to that of martensite. They may not have considered twinning due to the lack of α phase plates in a martensitic microstructure.
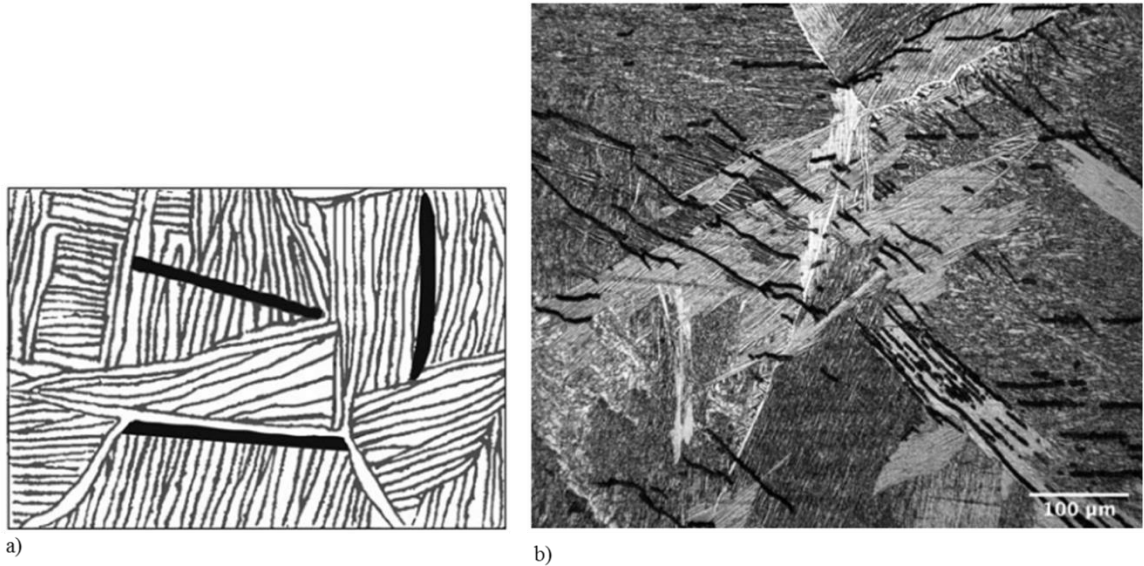
Figure 2-74. Ti-6Al-4V β annealed a)Typical crack initiation sites under cycle fatigue b) cracks generated in a fatigued specimen [116].

2.14.1.   White layer

The formation of a white layer on the near surface of machined components has been identified as a stress raiser, which considerably decreases the fatigue life of the component. It is characterised as having undergone a microstructural modification by high temperatures and oxygen hardening. After chemical etching, it appears white under the optical microscope and featureless in the SEM. It shows a significant increase in hardness, has a similar chemical composition as the bulk; however, there are differences in the microstructure, which relates to different mechanical properties.

White layers have been mainly observed in the cutting of ferrous materials [67] due to high temperatures in the cutting zone and insufficient cooling. For these reasons, a white layer should be avoided, and if present, it should be removed. Field and Kahles [117] show the presence of cracks in the white layer corresponding to an untampered martensitic phase transformation after machining steels. This phase transformation leads to different lattice parameters of the unit cell (expansion or contraction), and this may lead to microcrack generation. This will negatively affect fatigue life.

Extreme tool wear promotes white layer development in the subsurface of the machined components [106]. This may be counteracted by applying a cryogenic coolant which reduces tool wear rates reducing cutting temperatures and subsequently lessening the white layer formation.

Detrimental layers comparable to a white layer have been observed in titanium, nickel, brass and copper alloys. In titanium, it represents a severe plastic deformation region and has been exposed to thermal damage such as differential thermal contraction upon cooling.

In this investigation, during β annealed Ti-6Al-4V ELI milling with a worn tool (200 um wear) no white layer was detected in optical microscopy nor electron microscopy.

During machining of Ti-6Al-4V alloys, no white layer development was observed in the subsurface. CO_2 cryogenically machined Ti-6Al-4V lead to the generation of a nanostructured layer below the surface of the workpiece, which is beneficial for in-service properties (higher strength and higher ductility), however, in the subsurface nearly 2-3 µm wide strain localised regions were observed. As these regions have already been localised, they do not have the same load-carrying capacity as the rest of the layer to carry a load and to exceed its load carrying capacity may lead to microcrack nucleation.

2.14.2. Surface integrity

Surface integrity refers to the machining-induced mechanical, thermal and chemical property changes in the surface and subsurface of the machined component and is one of the most critical properties generated during metal cutting. For critical components subjected to cyclic loading, residual stress is of prime concern as it may prolong its fatigue life. A literature gap has been identified in the investigation of subsurface microstructural modification of components machined under cryogenic cooling fluids such as LN_2 or CO_2. The ultimate goal of manufacturing processes should be the integrity of workpiece components, especially in critical structural applications that are subjected to cyclic loading such as in turbine compressor disks or blades, which are exposed to high temperatures of nearly 600°C under cyclic stresses.

In 1951, Henriksen [118] was one of the pioneers in studying the surface and subsurface integrity generated in machined workpieces by analysing their residual stresses. It was 1964 when Field and Kahles [119] introduced the concept of surface integrity, and it was defined as: "*the inherent or enhanced condition of a surface produced in a machining or other surface generation processes*". It is the opinion of the author that this definition may not be highly accurate as in some cases, the surface and subsurface generated may not be an enhanced surface condition, such as in abusive conditions in which the subsurface may represent a stress raiser region which may easily induce crack initiation or propagation. On the other hand, under more gentle conditions, enhanced strength capacity is generated attributed to the generation of a high grain angle boundary, nanocrystalline grain structure. Below this, there is a strain-hardened region.

Surface integrity comprises two areas; one is surface roughness or topography, and the other is metallurgical alterations in the subsurface. These include plastic deformation, restorative mechanisms such as dynamic recrystallization or recovery, phase transformations, residual stress distribution, microcracking, hardness, tears and laps associated with BUE and embrittlement by chemical absorption. These characteristics are very significant in determining the reliability of structural components subjected to cyclic dynamic/static loading. The principal sources of the surface or metallurgy alterations in machining are:

- High temperatures generated in the cutting zone.
- Plastic deformation.
- Chemical reactions between the cutting tool, workpiece and the coolant fluid. Absorption of chemical elements into the subsurface, which may cause embrittlement.

The surface and subsurface modifications after a machining operation have a substantial effect on fatigue life and stress corrosion properties. For example, it has been reported that shot peening may increase the endurance limit under dynamic loading and enhance stress corrosion resistance. Thomas [4] results conflicted with this argument as he found out that on shot peened Ti-834 specimens after machining, exposed to elevated temperature in air, lead to surface embrittlement due to oxygen uptake and the precipitation of silicides in regions of high dislocation density such as twin boundaries. An investigation of finish-machined components under thermal exposure under atmospheric air should be undertaken to evaluate the effect on fatigue. This is because the structural titanium alloys used in the aircraft' engines are exposed to elevated temperatures and these may provide the conditions for easy diffusion, therefore, locally reducing the load-carrying capacity.

Machining conditions have a strong influence on the fatigue life of structural components. Milling Ti-6Al-4V under abusive conditions strongly decreased the fatigue strength or endurance limit to almost half of that of gentle conditions, from 482 MPa to 220 MPa respectively [117]. Abusive conditions develop higher temperatures and more plastic deformation.

Similarly to steels, a white layer in the region nearest to the surface may be generated in machined titanium workpieces under abusive conditions. Field and Kahles [117] presented evidence of an overheated white layer formation by face milling Ti-6Al-4V under abusive conditions, see Figure 2-75 b) considered to be overheated. Figure 2-75 a) shows a very shallow white layer formed under gentle machining conditions. The gentle condition did not show a change in hardness; on the other hand, the abusive condition has reported a decrease of nearly half the hardness in comparison to the bulk. The authors

reported a white layer of about 100 µm, however with the evidence they show, it appears that the white layer is much smaller, in the order of 13 µm. They did not provide details of the microstructure conditions such as grain morphology, grain size or phase distribution. It appears to be an α phase equiaxed grain structure with β grain boundaries.
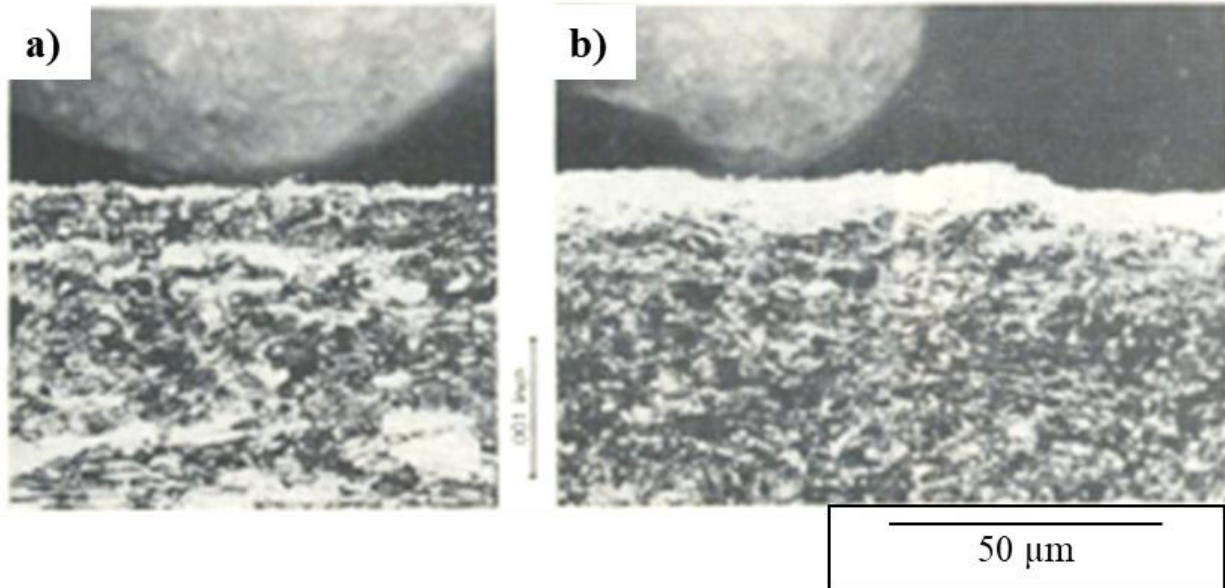
Figure 2-75. Subsurface integrity in face milling Ti-6Al-4V under a) gentle conditions and b) abusive conditions [117].

In face milling, the residual stresses tend to be tensile in the surface and change into compression in the subsurface [117]. The more worn the tool is, the deeper the compressive residual stress in the subsurface and deeper distortion results.

Jawahir et al. [102] presented a comprehensive review of experimental studies of surface integrity in metal cutting. They stated that the residual stress distribution of machined components is one of the most critical response variables as they affect fatigue life, the fracture behaviour and wear behaviour. Jawahir et al. [102] provide evidence of the effect of coolant on the grain refinement in the SSZ within the chip during orthogonal cutting of copper with an initial grain size of 47.1 µm. The grains refined and resulted as nanocrystalline with 364 nm size using water as a coolant. Whilst dry cutting, the grains refined to a lesser extent, to 1.2 µm. This shows the importance of using an efficient coolant fluid during metal cutting, which may lead to grain refinement and resulting in an increase in strength via the Hall-Petch mechanism. Jawahir et al. [102] also present a FEM simulation to determine the grain size evolution of AISI 52100 in orthogonal cutting. It was achieved using the Zener-Hollomon parameter. A sub-micron size grain structure was

obtained in the near subsurface, which correlates with experimental observations under the same conditions.

Crawforth et al. [120] reported that in alloys with a low molybdenum equivalent or higher hcp α content, the cutting edge radius has a higher impact on the subsurface deformation damage introduced during machining. This is due to the low symmetry of the α phase and the low available slip systems for plastic deformation. Thus, higher damage is introduced in the form of mechanical twins. As a result, machining of a higher volume fraction of α phase content alloys should be undertaken with sharp tools. The author believes there should be a correlation with the residual stress introduced during cutting. Dargush et al. [105] report an increase in the compressive residual stress in machined workpieces where there was a large increase in twin depth and density.

2.14.3.   Residual stress

Residual stresses refer to internal stresses imparted to a workpiece after being exposed to thermal and mechanical loads [121]. It represents distortions in the microstructure and strain remains in the lattice due to the cutting action. Compressive residual stresses are generated by plastic deformation or are mechanically induced. Tensile residual stresses are by surface thermal gradients and may be associated with phase transformations and chemical reactions. Residual stress on the subsurface is a critical property during the service life of the component. Compressive and tensile residual stress formation is represented in Figure 2-76. Plastic deformation at the subsurface initiates imparting tensile residual stresses behind the tool due to overstraining, which results in compressive residual stress after elastic recovery. Compressive residual stresses left in the surface and subsurface of a workpiece during machining are valuable during in-service applications as they counteract the tensile stresses experienced in exposure to cyclic loads [121] therefore extending its fatigue lifetime. Additionally, there could be detrimental residual stresses, such as tensile, which are mainly generated by high heat generation or thermal loading during metal cutting [106]. This drawback is even more prominent in hard-to-cut metals due to the high heat generation in the cutting zone and especially in low thermal conductivity metals such as titanium alloys. This distortion imparted into the workpiece represents a concern in aircraft structures, structural components, turbine blades and discs, which are subjected to cyclic loads. The use of coolants results in reduced temperatures leading to a reduction in frictional heating, temperature gradients and plastic deformation, which ultimately lower the tensile residual stresses in machined components.

85
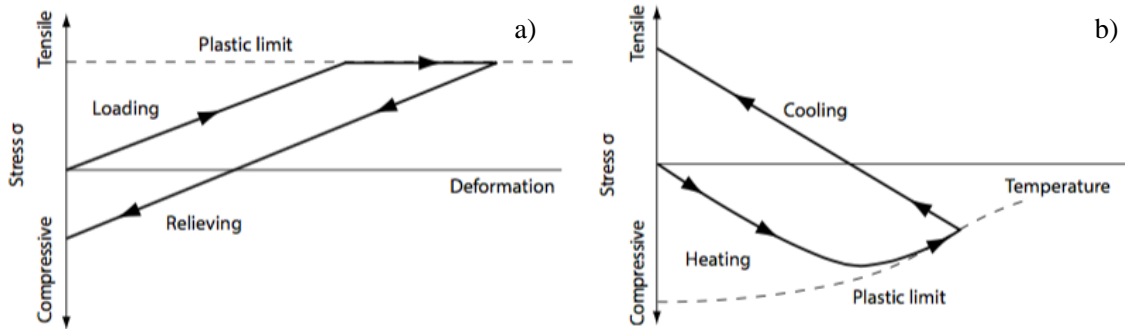
Figure 2-76. Schematic representation of residual stress formation during metal cutting a) plastic deformation results in compressive residual stress and b) thermal gradients results in tensile residual stresses [67].

With the increase in tool wear, there is an increase in frictional heating between the cutting tool and the workpiece as well as an increase in forces. Thus higher temperatures are generated in the cutting zone leading to more tensile surface residual stresses. Pusavec et al. [106] report that the tool wear increases the tensile residual stress and also increases the compressive residual stress in the subsurface. They also reported that a large edge radius results in higher temperatures and larger stress fields. It has been reported that a sharp tool would generate a subsurface residual stress of nearly 50 μm, while a worn tool could generate from 5 to 10 times that value. Machining with uncoated tools results in compressive residual stresses [83], [122].

Henriksen and Ithaca [118] report that during cutting of a ductile metal, the surface undergoes a massive distortion and heating, leading to residual tensile stress. This stress is maximum in the direction parallel to the cutting tool; thus they suggest that tension depends on a great extent to the mechanical deformation and to a lesser extent to the local heating.

By the application of cryogenic fluids as cooling media, there is a temperature reduction in the cutting edge during metal cutting, especially in metals with low thermal conductivity such as titanium alloys.

Negative rake angle promotes compressive residual stresses [122]. It has previously been reported that compressive stresses remaining in workpiece materials imparted during machining enhance fatigue life [123]. One method is retarding the crack initiation and reducing the speed of crack propagation [124]. Compressive residual stresses resulted after machining age hardened Inconel 718 under a conventional flood coolant, whereas tensile residual stresses were generated during dry cutting [122]. Tensile stresses resulted only on the surface of the machined workpiece. The compressive residual stresses generated into the subsurface may be the result of the effect of the generated mechanical twinning imparted into the subsurface, which may be compressive in the c-axis parallel to the loading

direction. There is a literature gap in the understanding of microstructural evolution on the subsurface of components induced by machining operations.
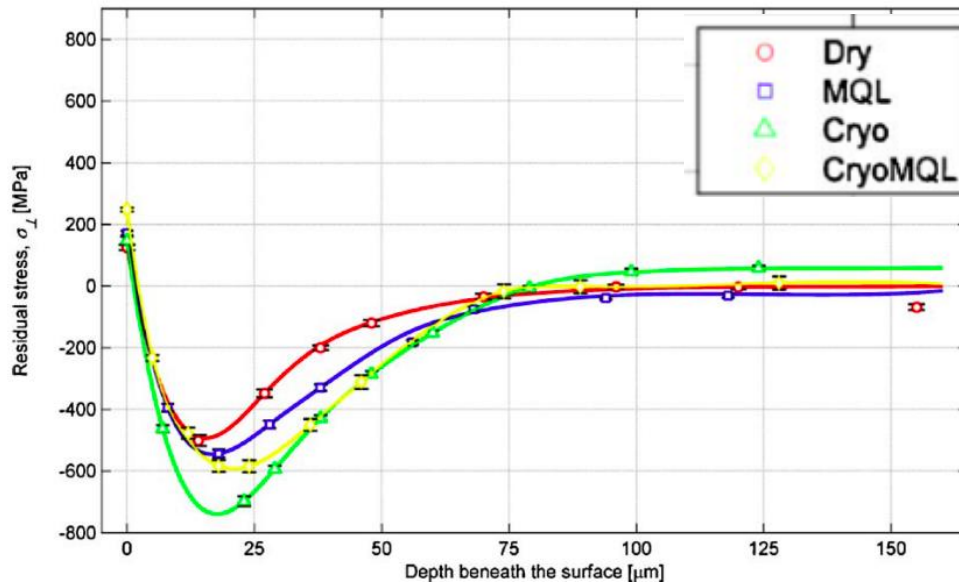
Figure 2-77. Residual stress in the axial direction generated in the subsurface of turned components of Inconel 718 at a speed of 60 m.min^{-1}, DoC= 0.63 mm, f = 0.05 mm.rev^{-1} [106].

Figure 2-77 shows that cryogenic machining generated more compressive residual stresses in comparison to other cooling methods, in Inconel 718 at a speed of 60 m.min^{-1}, DoC= 0.63 mm, f = 0.05 mm.rev^{-1}.

2.14.4.   Surface Roughness

Machining using liquefied industrial gases or cryogenic coolants, lead to the generation of smoother surfaces, or lower surface roughness (R_a). A machined edge with a low surface roughness may inhibit crack initiation during cyclic loading. The reason lies behind the lower amount of discontinuities (or stress raisers) on the surface. Thus stress may spread homogeneously across the surface area without any stress concentration, thus allowing lower tool's cutting time.

The mean surface roughness of Ti-6Al-4V with an equiaxed microstructure and a mean grain size of 20 µm, orthogonally cut under LN_2 cryogenic coolant generated lower R_a values in comparison to MQL and dry at speeds of 70 and 110 m.min^{-1} at a feed rate of 0.05 mm.rev^{-1} as shown in Figure 2-78. On the other hand, it generated a similar value at a higher cutting speed of 150 m.min^{-1}. The cutting tool used is a Kennametal® KCU10 with a PVD TiAlN coating with a rake angle 7° and clearance 11° and edge radius 8 to 10 µm.

The MQL flow rate was of 60 mL.h^{-1} and pressure of 4 bar. The LN$_2$ flow rate was not provided, only that it was delivered through a 2 mm nozzle with a 12 bar pressure. Higher surface speeds may have generated higher friction. Therefore R$_a$ under LN$_2$ was not better than MQL as the lubricant action of the vegetable oil might have lowered the friction forces, giving rise to low values of R$_a$. Vegetable oils have better lubricity properties than synthetic oils [83]. The use of a higher lubricity lubricant might have given rise to a smoother machined surface. At lower speeds of 70 and 110 m.min^{-1}, LN$_2$ might have been more effective in removing the generated heat at the cutting edge, thus allowing lower thermal expansion of both the cutting tool material and workpiece material, leading to lower R$_a$ values. On the other hand, dry cutting would have generated high temperatures giving rise to a high thermal expansion of both materials and therefore higher surface roughness.
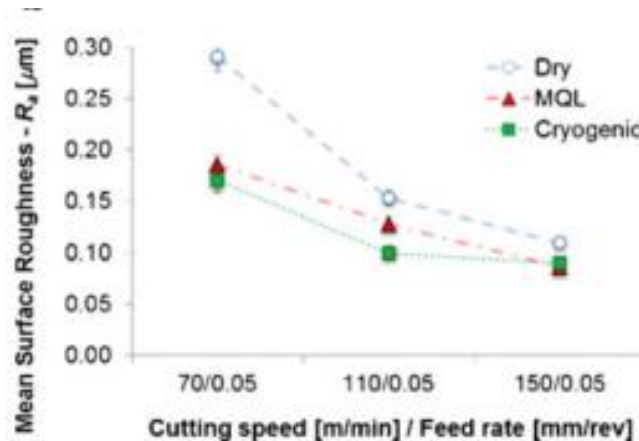
Figure 2-78. Surface roughness of Ti-6Al-4V orthogonal cutting at 70, 110 and 150 m.min^{-1} at a feed rate of 0.05 mm.rev^{-1} [125].

2.14.5.   Hardness

The temperature of plastic deformation strongly influences the hardness values of the surface and subsurface. A very high increase in surface hardness has been obtained by the application of a cryogenic coolant [123]. The hardness values obtained after orthogonal cutting of Ti-6Al-4V of an equiaxed grain microstructure significantly increased ~ 19% in the uppermost region, near the machined surface, at a surface speed of 150 m.min^{-1} and a feed rate of 0.1 mm.rev^{-1} in comparison to MQL and dry conditions as shown in Figure 2-79 a). The high increase in hardness is associated with the high introduction of dislocations during plastic deformation at low temperatures and its resultant nanocrystalline grain structure due to dynamic recrystallization during the cutting process.

The low temperatures may have also prevented dynamic recovery and grain growth of the subsurface layers. The low stacking fault inherent from the hcp crystal structure does not allow easy climb of dislocations, therefore leading to higher clusters of dislocations giving rise to strain hardening.

Additionally, the introduction of mechanical twinning in the subsurface also gives rise to higher strain hardening as twin boundaries are found to follow a Hall-Petch relationship type as the higher the number of boundaries, the higher the strength. The higher temperatures generated by MQL and dry may have led to a thermal softening effect by dynamic recovery by dislocation annihilation; thus the lower strain-hardened surface and subsurface or the lower hardness. Figure 2-79 b) shows that by increasing surface speed higher hardness is generated and much higher hardness at the LN_2 cryogenic temperature. This effect may be related to higher strain rate sensitivity of the workpiece material Ti-6Al-4V and slightly higher at lower temperatures.

Figure 2-80 shows a much higher hardness generated into the subsurface when cryogenically machining the shape memory alloy NiTi under LN_2 cooling. Their results suggest a higher strain-hardened subsurface in comparison to dry machining.
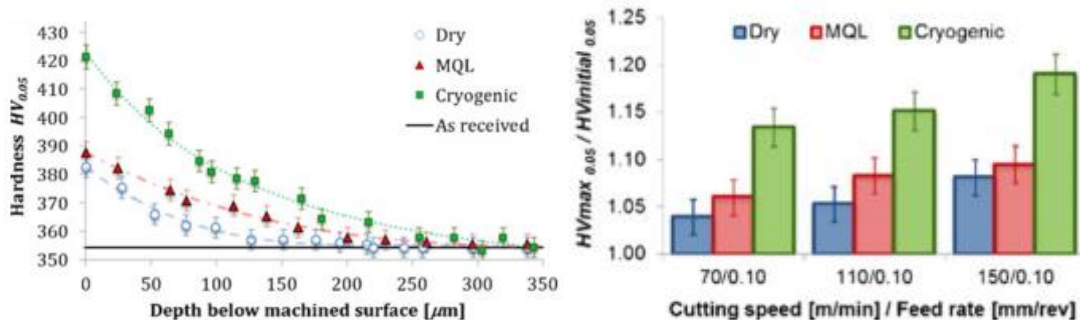
Figure 2-79. Hardness of a Ti-6Al-4V orthogonally cut a) at a surface speed of 150 m.min^{-1} b) surface speed of 70, 100 and 150 m.min^{-1} and 0.1 mm.rev^{-1} [125].
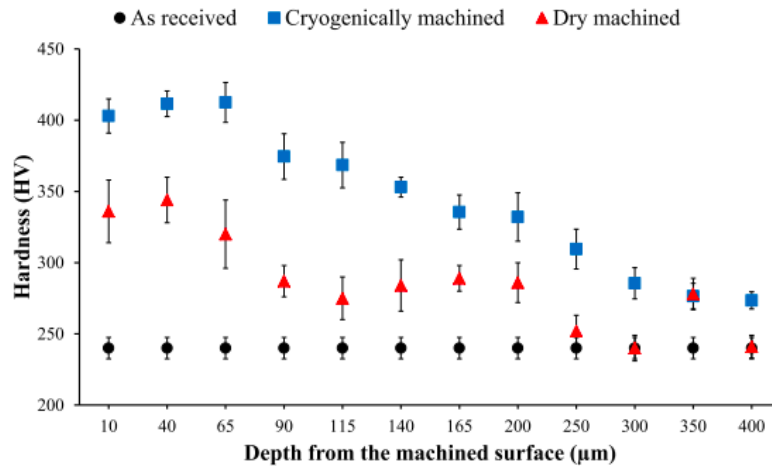
Figure 2-80. Hardness below the orthogonally cut edge in TiNi shape memory alloy under dry and LN$_2$ cryogenic cooling [109].

2.15. Plastic deformation under high strain rates

Kuhn and Medlin [126] suggested that to accurately predict the mechanical behaviour of metals during plastic deformation in shear at large strains should be tested directly in shear at the corresponding levels of strain, strain rate and temperature. Shear and torsion tests are preferred as the Poisson ratio effect is eliminated; necking in tension and barrelling in compression does not occur. The following tests are suggested depending on the required strain rate (in s^{-1}):

1. Conventional shear (< 0.1)
2. Servo-hydraulic machines (0.1-100)
3. Torsional impact (10 to 10^3)
4. Hopkinson bar in torsion ($10^2 – 10^4$)
5. Double-notch shear and punch ($10^3 – 10^4$)
6. Pressure-shear plate impact ($10^4 -10^7$).

Above at a strain rate of 10^4 s^{-1}, the flow stress rises more rapidly directly as a function of strain rate [127]. This statement correlates with the results reported by Chichili et al. [27] which are shown in Figure 2-81. This is attributed to the following dynamic factors. (1) Inertia, which opposes uniform plastic deformation. (2) Elastic and plastic wave propagation, which is transmitted and reflected within the specimen at the speed of sound. (3) Shock wave. (4) Thermal effects, and (5) the difficulty of strain measurement [127].

90
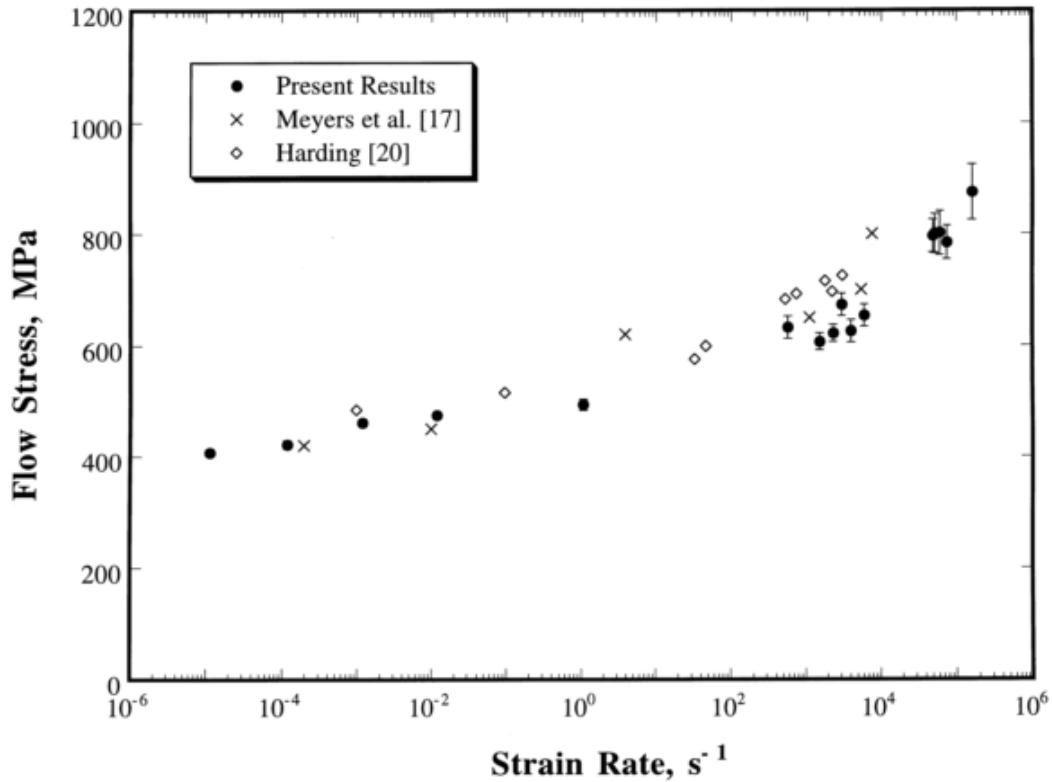
Figure 2-81. Effect of strain rate on the yield stress of CP-TI.-After Chichili et al. [27].

The split-Hopkinson pressure bar in compression and tension is the most widely used to study the mechanical effect of materials subjected to high strain rates. An example of a compression split-Hopkinson pressure bar is shown in Figure 2-82. A striker bar impacts the incident bar, and an elastic compressive wave is generated and measured with the strain gage A. The wave is partially transmitted to the specimen and somewhat reflected in the specimen. A percentage of the incident wave is reflected in the incident bar (as a tensile wave). This is the strain measured in the strain gage A. The stress-strain flow behaviour is determined from the strain measurements. Two conditions must be met to be valid. (1) Wave propagation is one dimensional and (2) the specimen deforms uniformly [127].
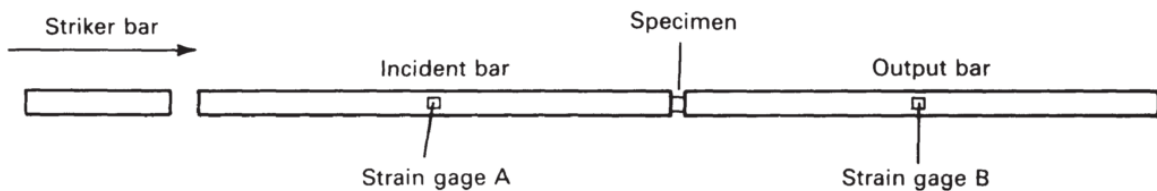
Figure 2-82. Split Hopkinson pressure bar, the specimen is placed between two elastic pressure bars, each bar has a strain gage in the centre. – After Kuhn and Medlin [127].

91

Hat shaped specimens have been used to determine plastic deformation directly in shear. Peirs et al. [128] used a hat shaped specimen (as shown in Figure 2-83) to study the plastic deformation process in the concentrated shear strain in the corners of the specimen under high strain rate in a compression spit-Hopkinson pressure bar. A disadvantage is that the reproducibility of testing is low; it strongly depends on accurate specimen dimensions. The interpretation of the results is difficult to attribute to the complex stress state and only in limited cases can the shear stresses in the shear direction be determined from the measured force [128].
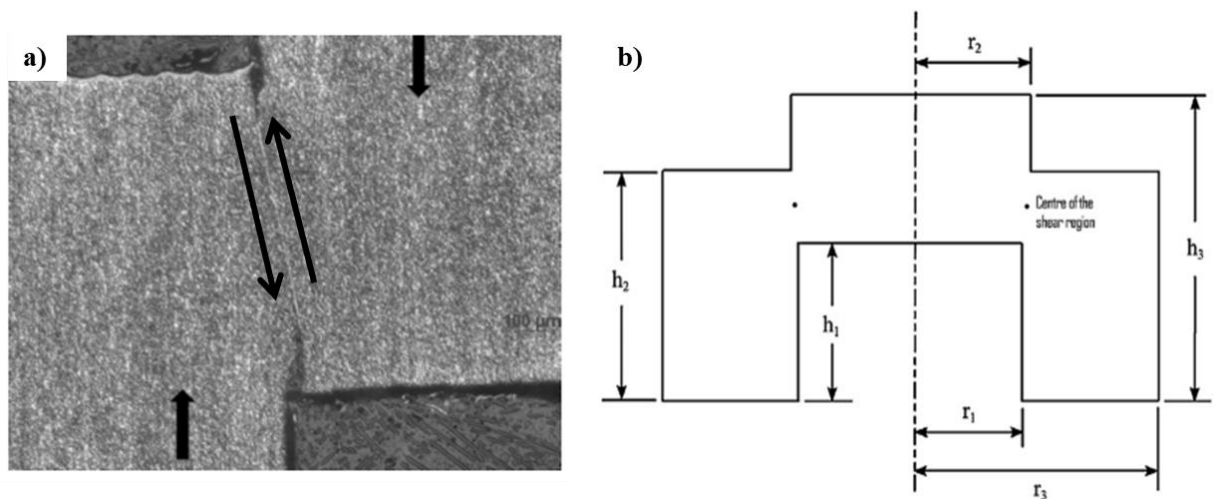
Figure 2-83. Hat-shaped specimen for high strain rate shear deformation a) microstructure and b) specimen dimensions are r_1 4.0 mm, r_2 = 4.1 mm, r_3 = 8 mm, h_1 = 4.0 mm, h_2 = 5.0 mm and h_3 = 8.0 mm –After Peirs [128].

2.16. Summary

In this section, the effect of alloying elements and thermomechanical processing on metallurgical microstructure was described. The effect of temperature on plastic deformation characteristics was presented. The main parameters to evaluate surface and subsurface integrity of machined titanium alloys were described. Finally, a method to determine high strain rates, to the corresponding to high-speed machining was introduced. This investigation will concentrate on the effect of temperature on the underlying deformation mechanisms in the subsurface of β annealed Ti-6Al-4V ELI, mill annealed Ti-6Al-4V and commercially pure titanium (CP-Ti).

3.   Experimental Methodology

This section outlines the methodology utilised during this research program. It includes material characterisation techniques such as optical imaging, scanning electron microscopy and transmission electron microscopy as well as focused ion beam thinning sample preparation. It goes on to describe the simple uniaxial and shear test in axisymmetric compression. It follows by detailing the approach taken in building a materials constitutive equation. It then describes the stages for the design of an orthogonal cutting rig. It finishes by describing the methodology used in the high-speed milling trial.

3.1.   Material characteristics

3.1.1.   β annealed Ti-6Al-4V ELI

β annealed Ti-6Al-4V Extra Low Interstitial (ELI) was employed as the research material to investigate the effect of temperature on the plastic deformation response. The Advanced Manufacturing Research Centre with Boeing (AMRC) supplied it. The reason for the selection of this material is due to its common usage in the aerospace industry as a structural material because of its ability to tolerate damage. The drawback of this is a slight loss of ductility [55]. The material's chemical composition is shown in Table 3-1. β annealed Ti-6Al-4V ELI grain size average was 590.05 ± 65.45 µm (with 95% CI), with a colony size of 318 ± 48 µm (with 95% CI), α plates of 2.53 ± 0.34 µm (with 95% CI), α phase at prior grain boundaries 8.25 µm and retained β thickness of 0.23 ± 0.11 µm (with 95% CI). The mechanical and thermal properties of this alloy were described in Section 2.10.

Table 3-1. Chemical composition of β annealed Ti-6Al-4V ELI (wt.%).

C	Si	Mg	Mo	Ti	Al	V	Fe	O	Cu	B	Zr	Y	Cr	Ni	H
0.0100	0.0100	0.0100	0.0100	Bal.	6.4100	4.0800	0.1500	0.1300	0.0200	0.0010	0.0100	0.0010	0.0100	0.0100	0.0014

3.1.2. Mill annealed Ti-6Al-4V and CP-Ti

Other materials analysed in the Arbitrary Strain Path machine (ASP) were CP-Ti and Ti-6Al-4V in a mill annealed condition. Their chemical composition is presented in Table 3-2 and Table 3-3 respectively. The grain size estimated through the linear intercept method was: mill annealed Ti-6Al-4V a grain size average of 18.19 ± 0.638 µm and CP-Ti an average grain size of 104.93 ± 5.91 µm.

Table 3-2. Chemical composition ($\pm 0.05\%$wt) of CP-Ti (ASTM Grade II) [21].

Element	Fe	O	C	N	Ti
Weight %	0.3	0.25	0.08	0.03	Bal

Table 3-3. Chemical composition (%wt) of Ti-6Al-4V in a mill annealed treatment [21].

Element	Al	V	Fe	Cu	O	Ti
Weight %	6.41	4.08	0.15	0.02	0.18	Bal

3.2. Material characterisation

First of all, all the samples were precision sectioned to obtain a cross-section of the subsurface immediately below the machine edge. A 10 mm length of cut, along the machined edge, was sectioned for analysis. This was done with an automatic cut-off Secotom 50 machine. This used a silicon carbide blade and a blade speed of 2500 rev.min^{-1}. A circulating cooling fluid was used to minimise workpiece heating and prevent microstructural distortion.

3.2.1. Microstructural preparation

After sectioning the workpiece to a 1 cm^3 size (see Figure 3-1), it was then mounted in a 32 mm diameter Bakelite resin. An automatic Streuers Abramin polishing machine was used. The microstructural preparation consisted of conventional methods [21] as described in Table 3-4. The first stage consisted of grinding the workpiece to a planar finish through

the use of silicon carbide paper of different grid sizes. The second stage consisted of an initial polishing step lasting 6 min using a 9-µm diamond suspension applied every 45 seconds to keep the surfaces well lubricated. The final polishing step consisted of two stages of 5 minutes each with a solution composed of 85% 0.05-µm colloidal silica (silco), 5% H_2O_2 at a 30% w/v and 10% water. After the first 5 minutes of polishing, a flow of water is passed to wash both the samples and the pad. After the first 5 minutes, the polishing pad and the sample are cleaned with water to prevent silco's crystallization. Finally, the samples are cleaned with soap and water, then alcohol and are hair dried to prevent fast oxidation during exposure to air. A force of 20 N was applied to the samples. The head speed was set at 50 rev.min^{-1} and the silicon carbide grinding pad at 249 rev.min^{-1}. For the polishing stages, the pad speed was reduced to 150 rev.min^{-1} to prevent the solution from being expelled during turning.

Table 3-4. Microstructural polishing preparation for optical and SEM observation.

Procedure:	Grinding paper/polishing pad.	Conditions	Processing time
Grinding	P800 grit silicon carbide	Constant water flow for cooling and lubrication.	1 min.
	P1200 grit silicon carbide	Constant water flow for cooling and lubrication.	Each grinding paper was used for only 1 min. It is usually done three times.
Initial polishing	MD-Largo from Streuers.	9 µm diamond water-based suspension.	6 mins, adding diamond suspension every 45 seconds to keep it well lubricated.
Polishing	MD-Chem porous neoprene disc from Streuers.	0.05 µm colloidal silica suspension (Silco) 85%. 5% lab reagent grade H_2O_2 (30% w/v). 10 % tap water.	5 min silco without additional water. Pad and samples cleaned with water. 5 min silco without additional water.
Cleaning	NA	Clean with water and soap. Then add isopropanol on the surface. Dry at 45° on a hand drier. Might need a careful cleaning with cotton wool after being dried.	NA

3.2.2. Optical microstructure imaging

The polished samples were observed under optical microscopy on a Nikon Eclipse LV150, cross-polarised filters were used to distinguish the crystallographic structure which otherwise would have needed to be attacked chemically (via chemical etching) to be revealed. For obtaining the images, the software Buehler Omni Met Cross was utilised. Maximum magnification obtained was 100x. Different crystallographic orientations reflected the light in different directions. This meant the plastic deformation could be captured with a high level of detail at the maximum magnification, which is 100x.

3.2.3. Scanning Electron Microscopy (SEM)

To obtain images of the microstructures at much higher magnifications an FEI Inspect F-50 a Field Emission Gun Scanning Electron Microscope (FEGSEM) was utilised. The parameters used during this investigation are presented in Table 3-5. During imaging, the backscatter detector was utilised to show more contrast between the phases present in the material (α and β). The detector also showed the presence of deformation induced mechanical twins and slip bands via channelling contrast.

Table 3-5. Operating parameters used on the SEM.

Parameter	Value
Accelerating voltage (keV)	10
Spot size	3
Working distance (mm)	7 -8
Detector Mode	Secondary electron (SE) and Backscatter detector (BSE).

3.2.4. Specimen milling for Transmission Electron Microscopy

Figure 3-1 schematically illustrates how the workpiece was precision sectioned for subsurface microstructural examination under cross-polarised light microscopy and scanning electron microscopy. In the shoulder milling trial, two surfaces were generated: one corresponding to the face milling (shown in green) and another corresponding to the shoulder. For this investigation, only the face surface and subsurface were analysed.

Figure 3-2 schematically illustrates the place where the TEM foil was sectioned inside the SEM through the Focused Ion Beam. The specimen shown in Figure 3-2 was precision-sectioned from the centre of the face milling in the Y-axis as shown in Figure 3-1.

a_p = 6 mm
a_e = 1 mm
LoC = 100 mm
MRR = 600 mm³ per pass
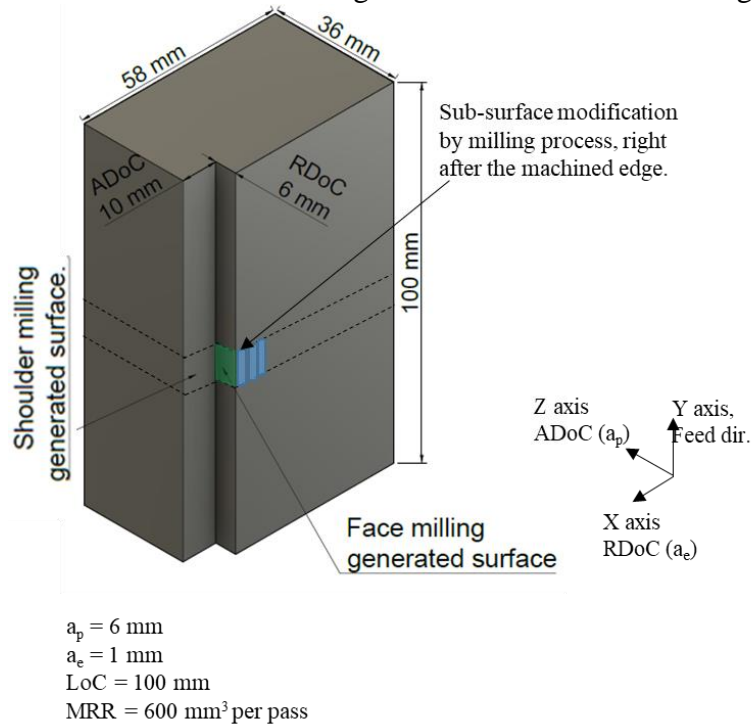
Figure 3-1. Schematic diagram illustrating precision sectioning of the face milling during shoulder milling of β annealed Ti-6Al-4V ELI. This image shows ten passes.
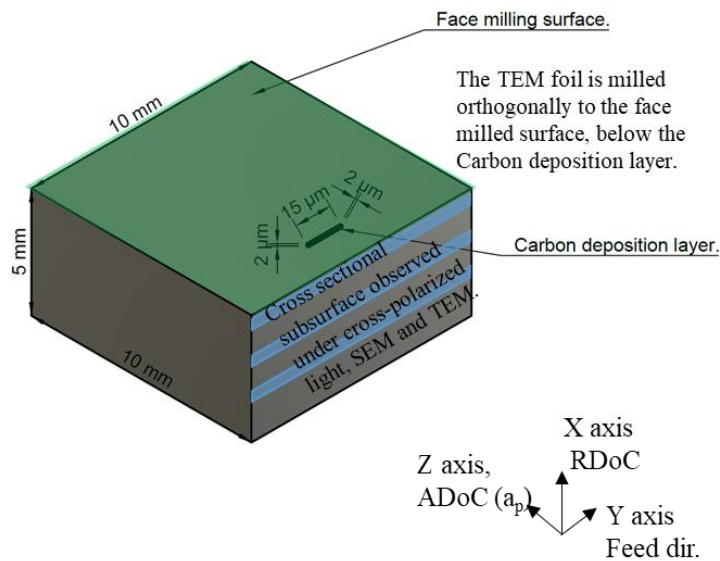
Figure 3-2. Schematic diagram illustrating the precision sectioning of the TEM foil under the SEM through Focused Ion Beam.
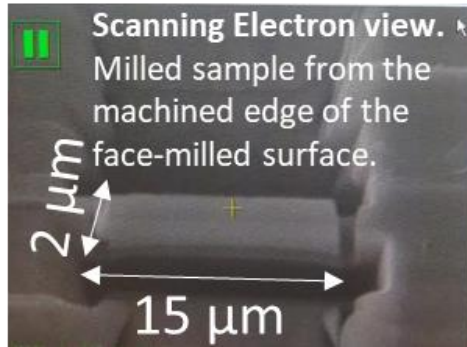
Figure 3-3. Carbon deposition on top of the generated face milled surface and trench cut to lift only the foil for final thinning.
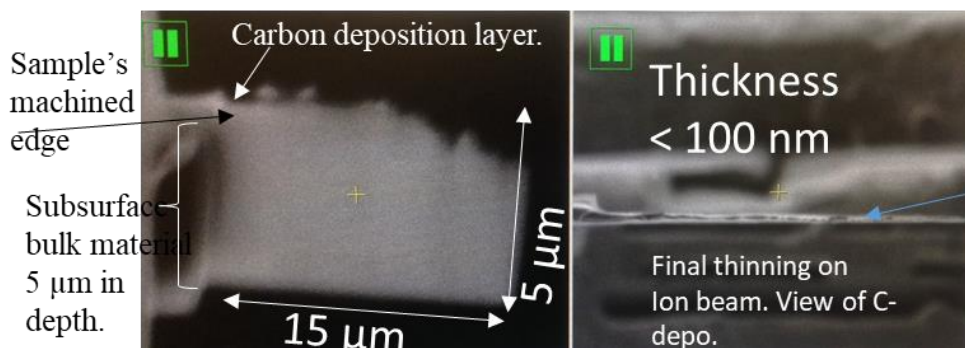
Figure 3-4. TEM foil observed under the SEM and the FIB imaging milled down to a thickness less than 100 nm.

3.2.5.   Focused Ion Beam (FIB)

To characterise the microstructure of machined samples after the machined edge, a lift out procedure on a specific sample location was performed. The 1 cm^3 sample was mounted on a stub and adhered to it with silver paint for high electrical conduction. For this, an FEI Quanta 3D SEM/FIB was utilised.

On the machined surface, a carbon coating of (2 X 15 X 2) µm was deposited. Two trenches at high current were milled on the sides of the carbon layer, then two more at lower current were milled. A "j-cut" was performed to release the free material, just leaving a corner attached, to be milled away after being attached to the copper grid with another layer of carbon deposition, see Figure 3-3.

98

A thin foil of thickness < 100 nm, height ~ 8 µm and width of ~ 16 µm was obtained from a direction perpendicular to the cutting edge, see Figure 3-4.

Table 3-6 shows the typical parameters used for the final stage of foil thinning.

Table 3-6. Parameters used during the final thinning procedure of foil generation for TEM analysis.

Stage	Current		Tilt stage	Expected thickness (nm) after milling
1	0.5 nA	Front	53.2°	-
2	0.5 nA	Back	50.8°	500
3	100 pA	Front	53°	-
4	100 pA	Back	51°	150
5	30 pA	Front	52.5°	-
6	30 pA	Back	51.5°	<100

3.3. Axisymmetric Compression Test

3.3.1. Thermomechanical compression testing

Determination of the stress state is essential for the study of plastic deformation [129]. A traditional metal cutting operation such as turning or milling creates a complex three-dimensional stress state. A simple uniaxial compression test approaches a two-dimensional state. This test can be used to predict the stress state and the deformation mechanisms or microstructural evolution during cutting under similar process parameters.

In this work, the effect of temperature and strain rate on the stress state experienced in the internal structure and on the deformation mechanisms of β annealed Ti-6Al-4V in a uniaxial thermomechanical compression test was performed. These tests were undertaken in a thermomechanical compression testing machine (TMC). This machine has a load capacity of up to 500 kN and a maximum displacement rate of 3000 mm.s^{-1}.

Cylindrical specimens were manufactured to dimensions of 15 mm in height and 10 mm diameter. An aspect ratio (h0/d0) of 1.5 was used as recommended by Roebuck et al. [130]. An N-type thermocouple inserted in the centre of the cylinders to measure the starting

deformation temperature and its evolution during the progression of the test. Each specimen was covered with a boron nitride (BN) lubricant to reduce friction between the platens and the specimen during compression.

For the cryogenic axisymmetric compression tests, liquid nitrogen was used. Different techniques were tested. First, a funnel with an attached hose was used to deliver the LN_2 directly to the cylinder in the compression area between the platens, Figure 3-5 b). As this technique did not prove successful in keeping the temperature at a cryogenic level, it was decided to soak the cylindrical specimen in LN_2 until reaching thermal equilibrium at a temperature of nearly -165°C as observed in Figure 3-5 c). It took nearly 10 s from placing the specimen on the robot arms until the test occurred, Figure 3-5 c) temperature increased by nearly 10°C.
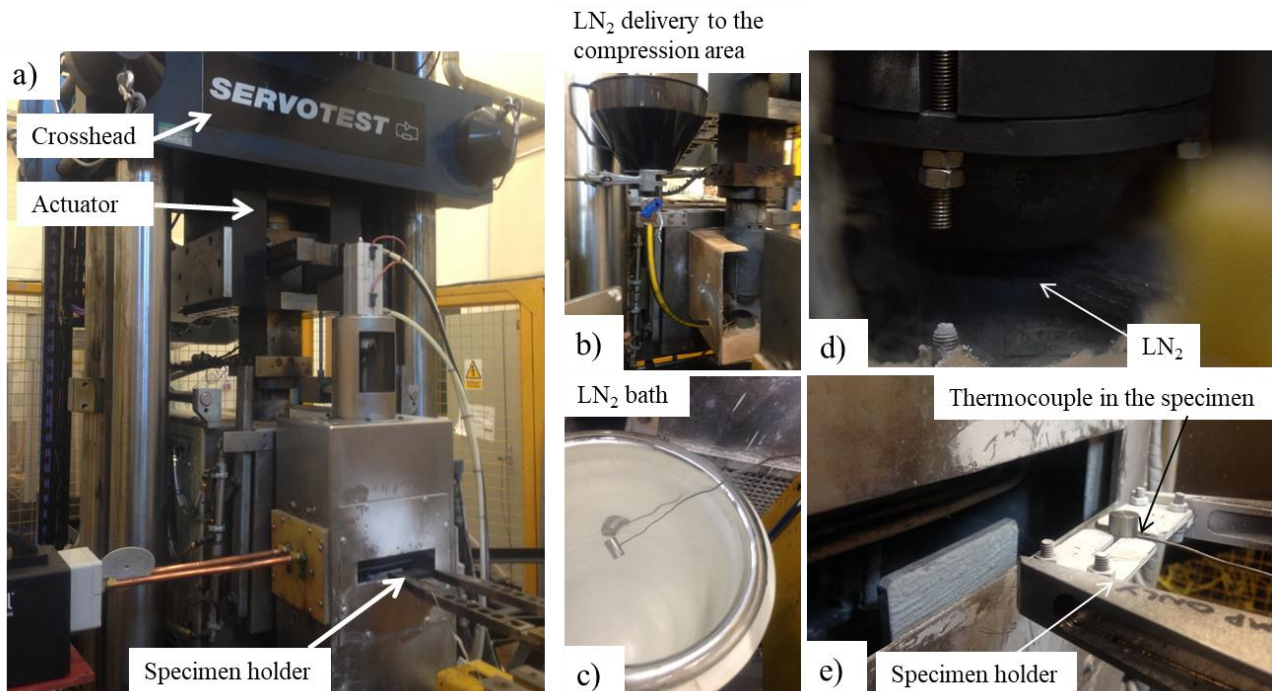
Figure 3-5. Uniaxial compression testing: a) TMC machine, b) Delivery of LN_2 through a funnel directly to the compression platens (see image d), c) Soaking the specimen cylinder in a LN_2 bath until it reaches thermal equilibrium then placing it on the robot arm grips, d) LN_2 flow to the compression area and e) shows the thermocouple in the specimen on the robot grips, ready for testing.

3.3.2.   Flow stress estimation

The data obtained from the uniaxial compression test was load, displacement, time and temperature. That information was used to determine the flow stress of the material under

certain temperatures and strain rates. True strain was estimated by equation (3.1) by considering the instantaneous height during deformation. The flow stress was estimated by calculating the measured compressive axial force dived by the instantaneous area of the cylindrical specimen. The analysis was carried out according to Roebuck's [129] methodology.

$$\varepsilon = \ln(\frac{h}{h_0}) \tag{3.1}$$

$$\sigma = \frac{F}{A_i} \tag{3.2}$$

By plotting the true stress vs true strain the 0.2% compressive yield strength was estimated. For this, the intercept of the best fit relation in the elastic area was calculated, then this gradient was offset by 0.002 strain and the intercept with the true stress provided the 0.2% proof yield strength.

3.3.3. Work required for catastrophic shear failure

The estimation of the work done to cause the onset of failure by shear bands during axisymmetric compression (as was first suggested by Marshall [5]) was calculated by working out the area under the curve produced by the flow stress equation (3.3) up to the point of maximum stress. This also provides the strain imparted to the onset of failure and zero strain hardening. This equation corresponds to the Cockcroft-Latham damage criterion. It is a phenomenological based criterion, it captures the idea of damage accumulation or workability, and this is dependent on the amount of plastic deformation and the principal stress.

Workability is described as the energy required to cause the onset of instability in ASB generation and represents the area under the curve of true stress vs true strain during mechanical testing. σ is the true stress and ε_f the true strain up to the point of the onset of instability.

$$W = \int_0^{\epsilon_f} \sigma d\varepsilon \tag{3.3}$$

3.3.4.   Strain hardening

Strain hardening represents the change in the true stress vs true strain curve and is estimated through finding the derivative or the change in stress with respect to the change in strain.

$$\theta = \frac{\delta\sigma}{\delta\varepsilon} \tag{3.4}$$

3.3.5.   Shear Stress Calculation

Dieter [2] presents three different equations to estimate the shear stress, which correspond to Von Mises, Octahedral and Tresca.

$$K_{Von\ Mises} = \frac{1}{\sqrt{3}}\sigma_0 \tag{3.5}$$

$$K_{Octahedral} = \frac{\sqrt{2}}{3}\sigma_0 \tag{3.6}$$

$$K_{Tresca} = \frac{\sigma_0}{2} \tag{3.7}$$

3.3.6.   Strain rate sensitivity (m)

It was determined by plotting the yield strength of the material versus the strain rate and estimating the gradient through a best-fit approach. The gradient represents the strain rate sensitivity.

3.3.7.   Zener-Hollomon Parameter (Z)

The combined effect of temperature and strain rate on the evolution of the microstructure was calculated through estimation of the Zener-Hollomon parameter (Z), equation (3.8). Where Q is the activation energy for deformation processes to start. In this case, the activation energy for grain boundary diffusion was used. A prediction of the grain size can be made using this parameter using equation (3.9), a and b are material constants.

$$Z = \dot{\varepsilon}\ exp\left(\frac{Q}{RT}\right) \tag{3.8}$$

$$d^{-1} = a + b\ lnZ \tag{3.9}$$

3.4.   Materials Deformation Modelling

3.4.1.   Power-Law (Norton-Hoff) Constitutive Equation

This constitutive equation assumes perfect viscoplasticity; therefore it fails to examine the effect of the elastic behaviour. $\dot{\varepsilon}$ is the strain rate (in s^{-1}), ε is the strain imparted into the specimen, Q is the activation energy, T is the absolute temperature in Kelvin.

$$\sigma = K\varepsilon^n\dot{\varepsilon}^m\left(\frac{Q}{RT}\right) \tag{3.10}$$

Where K is a constant, n is the strain-hardening exponent, m the strain rate sensitivity parameter, Q the activation energy, R the ideal gas constant and T temperature.

To obtain the K, n, m, and Q/R parameters, a multiple linear regression was used.

3.5.   Orthogonal cut rig design

3.5.1.   Tool rig design methodology

The idea to generate an orthogonal cut was to study the plastic deformation process in a simple plane strain, approximating a 2D process. The angle of the shear band formation and plastic deformation characteristics are determined by the process parameters such as tool geometry, surface speed, cooling/lubricating characteristics, workpiece material flow stress under specific strain, strain rate and temperature as well as the tribology interaction between tool, workpiece and chip surfaces.

A new, simple, versatile small-scale testing technique was designed to mount any tool shank with specific tool insert geometry as illustrated in Figure 3-13. For this investigation, a Seco shank tool holder with code DTGNL-3232P22-M was used to study the generation of a near true strain or orthogonal cut. This tool holder has an inclination angle of -6 degrees and -6 degrees rake angle. As the aim was to generate an orthogonal cut with a rake angle of -6°, the -6° inclination angle was removed through electro-discharge machining (EDM) for an accurate and precise cut. The design of the SECO cutting tool was followed by Marshall's work [5]. As Marshall previously generated two chips, in this work it was aimed to measure the load required for only one chip to determine the shear stresses needed for the generation of every chip. The design process took several stages.

The first stage involved modifying the design of the workpiece holder to prevent its deflection during cutting. This stage was crucial, as the modulus of elasticity of titanium alloys is very low. As a result, the stiffer the holder, the more accurate and precise cuts can be achieved. Initially, the workpiece contained a hole through its centre all the way along. It was held by a solid metal bar and was not tightly held during cutting – allowing it to move. Therefore, a more robust rig was designed to hold the workpiece in place during plastic deformation and to prevent it from deflection during tool engagement. For that, a cylindrical rig insert that could be tightly mounted to the hydraulic actuator was designed, and it is illustrated in Figure 3-7 a). At first, a hole was created where the workpiece sits which would have traversed it. This design proved to be inadequate as there was too much workpiece movement. Therefore, two-screw patterns were created in a corner edge of the square where the workpiece sits. The workpiece was moved to a corner, and the screws were tightened to prevent movement during cutting. This was successfully achieved; however, during the next cutting trial, the whole axis of the actuator moved during the cut operation as illustrated in Figure 3-10. Movement of the main hydraulic cylinder occurred as the area that supports its load is highly reduced at the bottom or where it is supported (Figure 3-6). The ASP has this reduction in area at the bottom of the actuator cylinder so that torsion tests can be undertaken there. This area reduction helps to rotate the central hydraulic cylinder during torsion tests. However, for the orthogonal cutting test, it proved to be non-beneficial.

The second stage involved the design of a simple rig plate to mount in the fixed lower tool post. This plate contains four mounting holes to attach it to the fixed lower post and in its centre a square free area to allow the workpiece to pass freely during cutting. The tool shank and plate were simulated in Autodesk Fusion 360 to determine the exact dimensions of the cut.

The first attempt to generate an orthogonal cut (as illustrated in Figure 3-9) was ineffective as the uncut chip thickness, t_1, was not uniform due to tool deflection, see Figure 3-11 and Figure 3-12. There are two reasons for this. The first reason is that as the cut was only placed on one corner of the rectangular prism workpiece, the force needs to be balanced on the opposite corner. The second reason is that due to the ASP's torsional capability, the bottom part of it is reduced to a small area (see Figure 3-6). This generates the movement of the vertical axis, which means that the horizontal or thrust force makes the shank tool holder move towards the left-hand side, causing less engagement with the workpiece as the workpiece advances downwards during the cutting process.

Figure 3-10 and Figure 3-11 show the initial tool deflection caused by the workpiece thrust force during cutting and due to the lower part of the axial column, being reduced

(Figure 3-6). The red squares refer to the initial tool position, where its movement during the cutting operation is clearly illustrated. This fact led to the design of a long block (arm extension) to translate the horizontal force from the tool shank to this new block, as illustrated in Figure 3-13.

The workpiece geometry is depicted schematically in Figure 3-8 a). Figure 3-8 b) and Figure 3-8 c) also shows the geometry of two aluminium blocks to transfer the load and prevent tool and workpiece deflection.
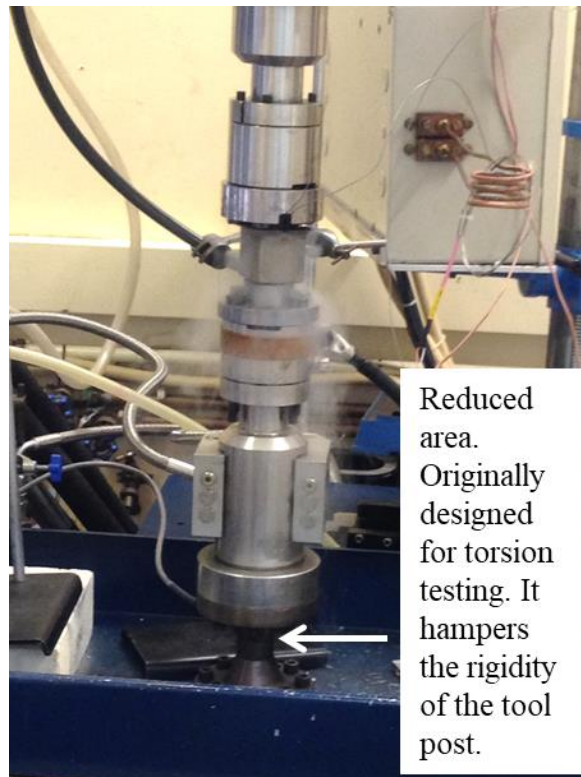
Figure 3-6. ASP's central cylinder reduced area for torsion capability. This caused the cutting tool in PSM to deflect from the cutting zone.

a) **Workpiece holder**

Top view

Mounting points to the ram driven upper.

Side view

Workpiece sits in this space.

Workpiece secured by tightening two screws.

Bottom view

Holder lip to be inserted into the upper tool.

b) **Rig plate**

Top view

4 Fixed lower post mounting points

2 Mounting points for the aluminium block.

Side view

Mounting point for the tool.
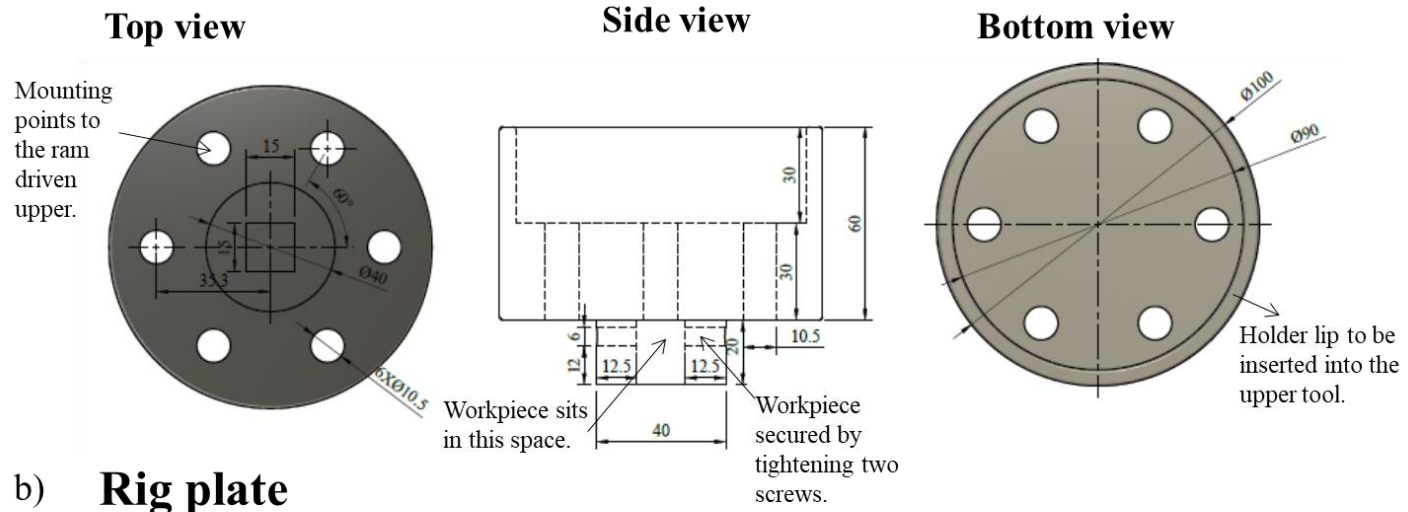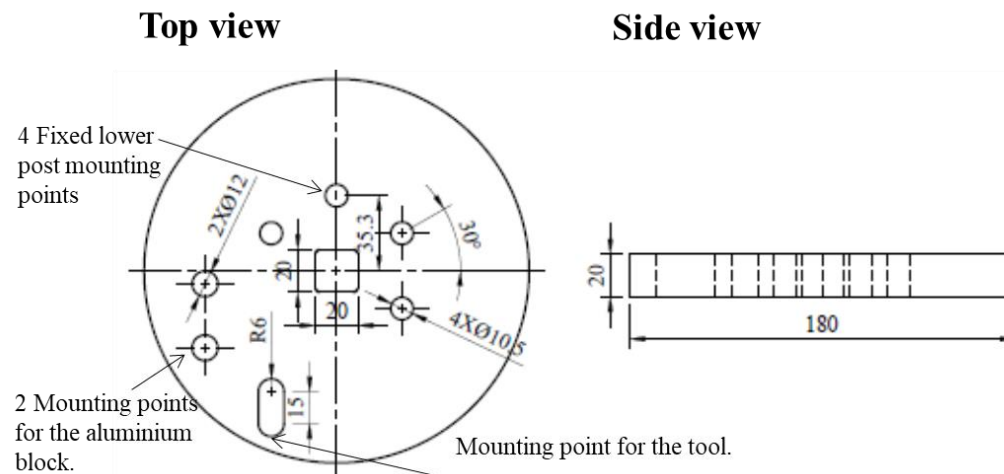
Figure 3-7. Engineering drawings corresponding to a) Workpiece holder and b) tool rig plate.

a) Workpiece geometry.

$15^{0}_{-0.1}$

$15^{0}_{-0.1}$

60 ± 11

b) Aluminium block

Rig plate mounting points.

90

30

Ø8

30

30

60

c) Aluminium block

Rig plate mounting points.

51.3

R5.25

45

10.5

51.3

8

43.3
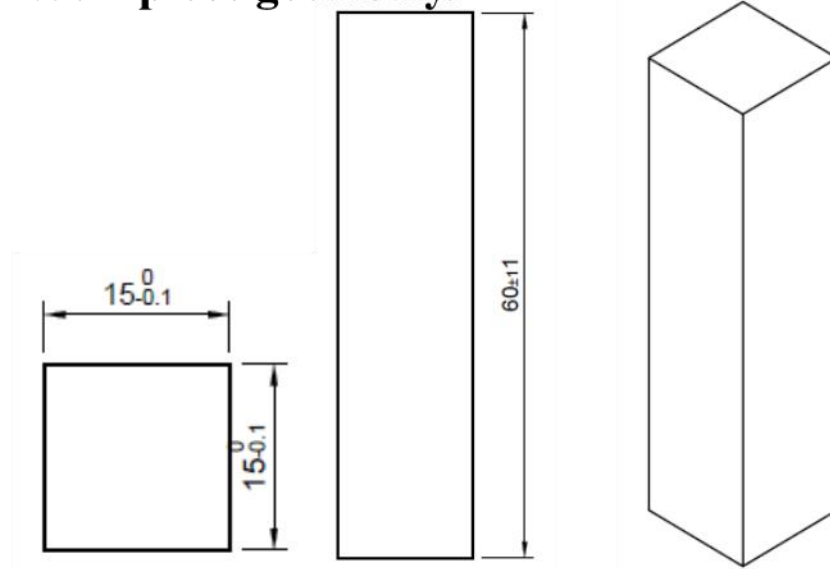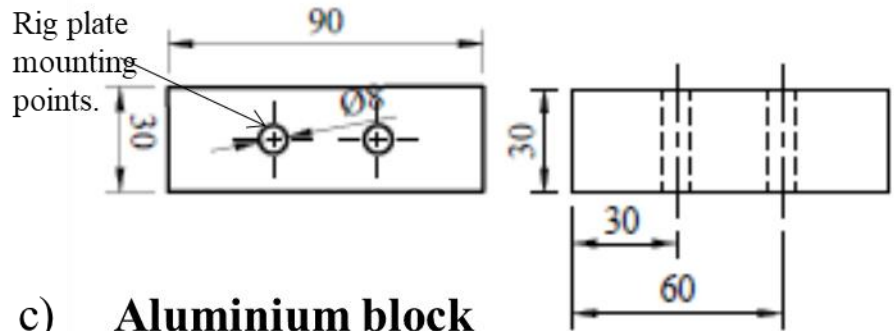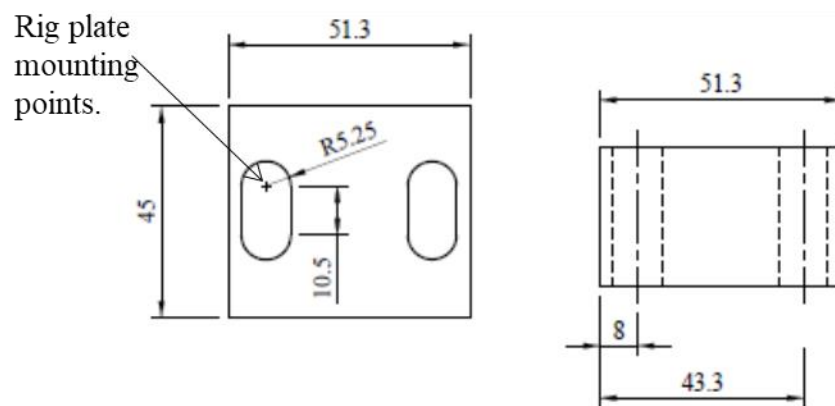
Figure 3-8. Engineering drawings relating to a) workpiece, b) and c) aluminium blocks for tool and workpiece deflection respectively.

a)

Aluminium block to prevent the tool shank holder movement during cutting.

Workpiece

Steel rig

Seco tool shank holder: DTGNL 3232P22-M

Seco cutting tool: TNMA220416, 263

Shim to prevent the shank holder to plastically deform.

b)

β annealed Ti-6Al-4V workpiece

5 mm

LoC Length of cut

1.3 mm

t_1 Uncut chip thickness

α -6°

Cutting tool. The edge radius was sectioned to cut with a flat surface.

Figure 3-9. a) Second stage tool rig design, b) magnified facing the cutting direction.
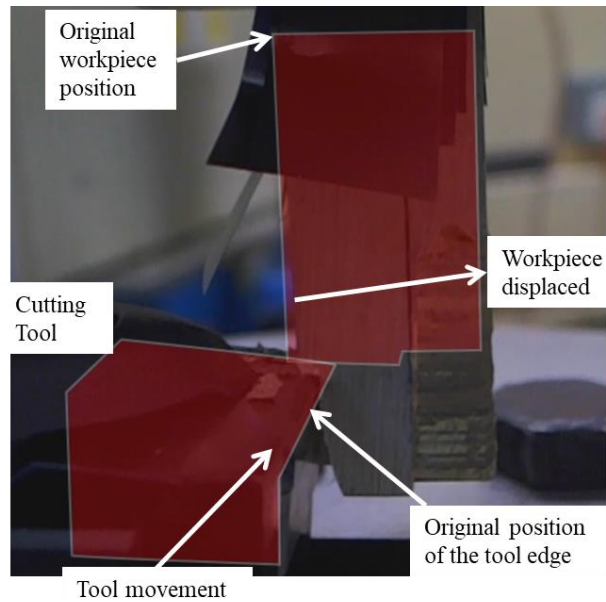
Figure 3-10. Initial tool deflection due to the thrust force applied by the workpiece.
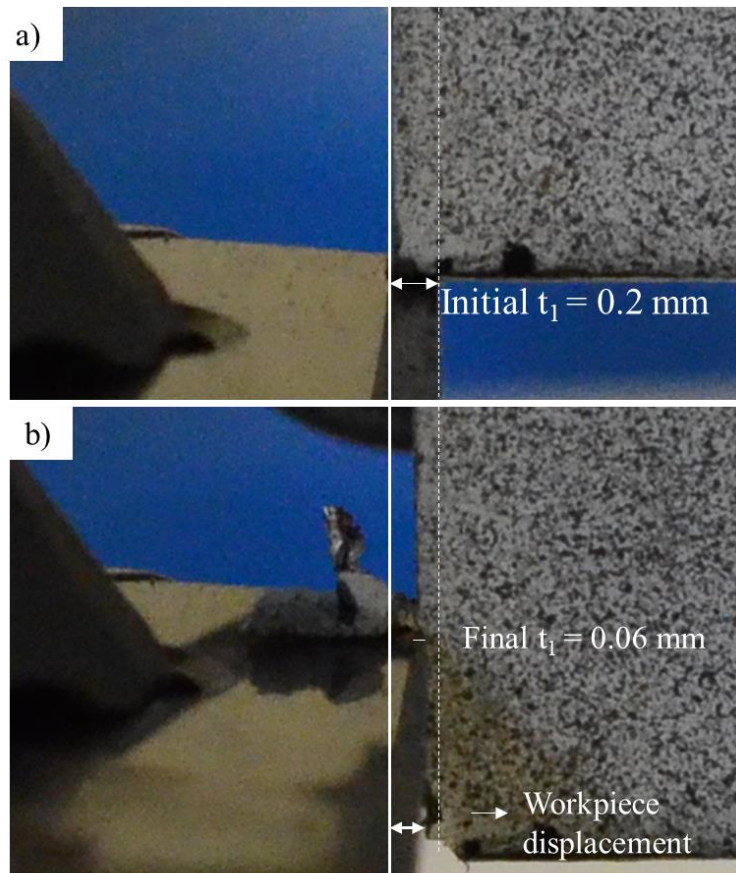
Figure 3-11. Tool displacement during PSM: a) Initial uncut chip thickness 0.2 mm, b) after lateral displacement is reduced to only 0.06 mm.

A test with a higher t_1 was undertaken to reach the desired value of t_1 as shown in Figure 3-12. This resulted in a high level of workpiece displacement; therefore, it was decided to add the arm extension to reduce the workpiece deflection and get the required t_1 uniformly along the edge of the workpiece.
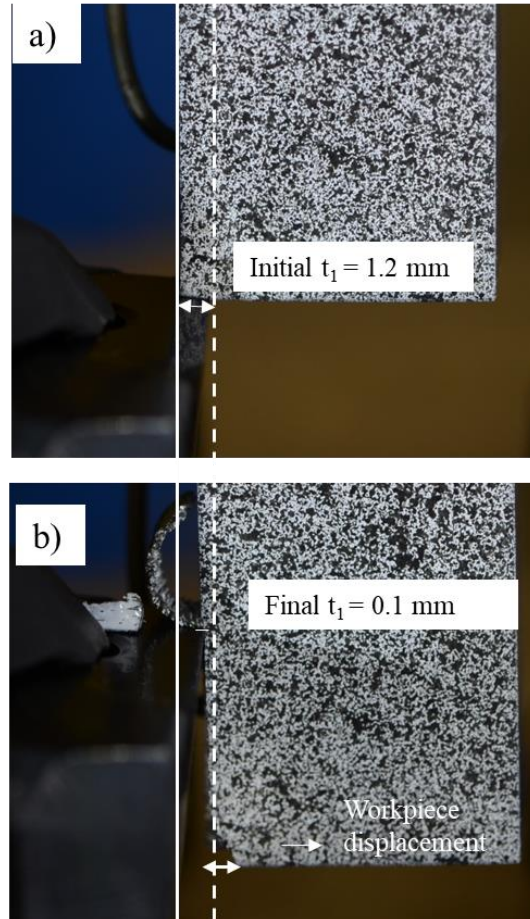
Figure 3-12. Test with a higher initial uncut chip thickness, t_1, to get the required t_1.

After adding the arm's extension, the cut in the transversal direction was uniformly created. However, the workpiece continued deflecting as it did not provide sufficient support in the longitudinal direction. As a result, it was decided to place an aluminium block to the side of the workpiece to restrict its deflection to the right during the cutting operation. Lubricant oil was added to the aluminium block to reduce friction forces as much as possible. In the end, there was still a slight tool deflection in the direction of the uncut chip, but it was more uniform.

The data obtained from each test is time, load, displacement and torque. The lower tool post has a load cell where forces are estimated through the measurement of a specimen strain, and the axial displacement is measured through a Linear Variable Differential Transformer (LVDT) fixed on the upper tool.
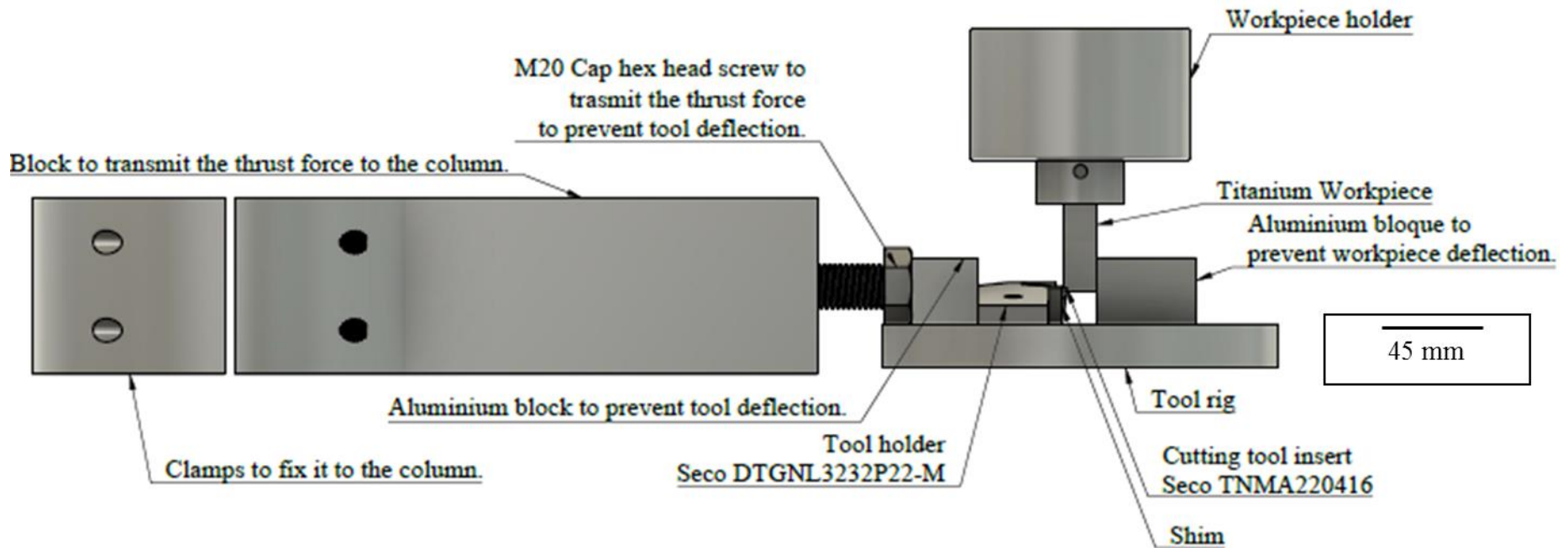
Figure 3-13. Front view of the final tool-rig assembly using both Seco shank holder and Seco tool cutting insert.

3.6.   Orthogonal cutting in an Arbitrary Strain Path (ASP) machine

3.6.1.   Cutting Tool Insert

The selected tool for orthogonal cutting was Seco TNMA220416, 890. This is a triangular 60° shape of 20 mm length (l). The substrate is predominantly a fine-grained tungsten carbide with low binder phase content (WC-6%Co) uncoated.

A negative rake angle of -6° was selected as larger strains are imparted into the subsurface of machined components and the chips [131]. This leads to easily recrystallization of the subsurface (SPD layer) and improves the strength of this layer. A negative rake angle also imparts compressive residual stresses [106].

Table 3-7. Seco's tool used in PSM testing of β annealed Ti-6Al-4V ELI, insert characteristics.

Grade	Image	Dimensions	Substrate	Coating
TNMA220416		 Rake angle -6° r_ε is the corner radius	WC-6%CO	None
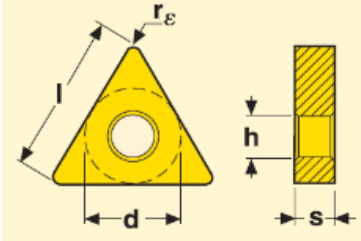
The corner radius of this tool was sectioned to prevent a triaxial stress state during cutting. A high-resolution Nikon camera was used to take a series of pictures during the cutting process to study the chip formation process; 4 frames per second were taken, as observed in Figure 3-16.

For CP-Ti and mill annealed Ti-6Al-4V, Sandvik Coromant grade H13A cutting tools were used, as shown in Figure 3-17. Two cutting tools were used to balance the forces during cutting.

3.6.2.   Orthogonal cutting on an Arbitrary Strain Path Machine, Servotest

The Servotest is a machine capable of performing compression, torsion or tension tests and measures the load and displacement applied. It has two adjustable hydraulic cylinders that support the actuator as seen in Figure 3-14. During testing, only the actuator moves. The ASP ram driven upper has a capacity of movement of $\pm$ 30 mm displacement at a maximum speed of 100 mm.s^{-1} and a load capacity up to 100 kN.
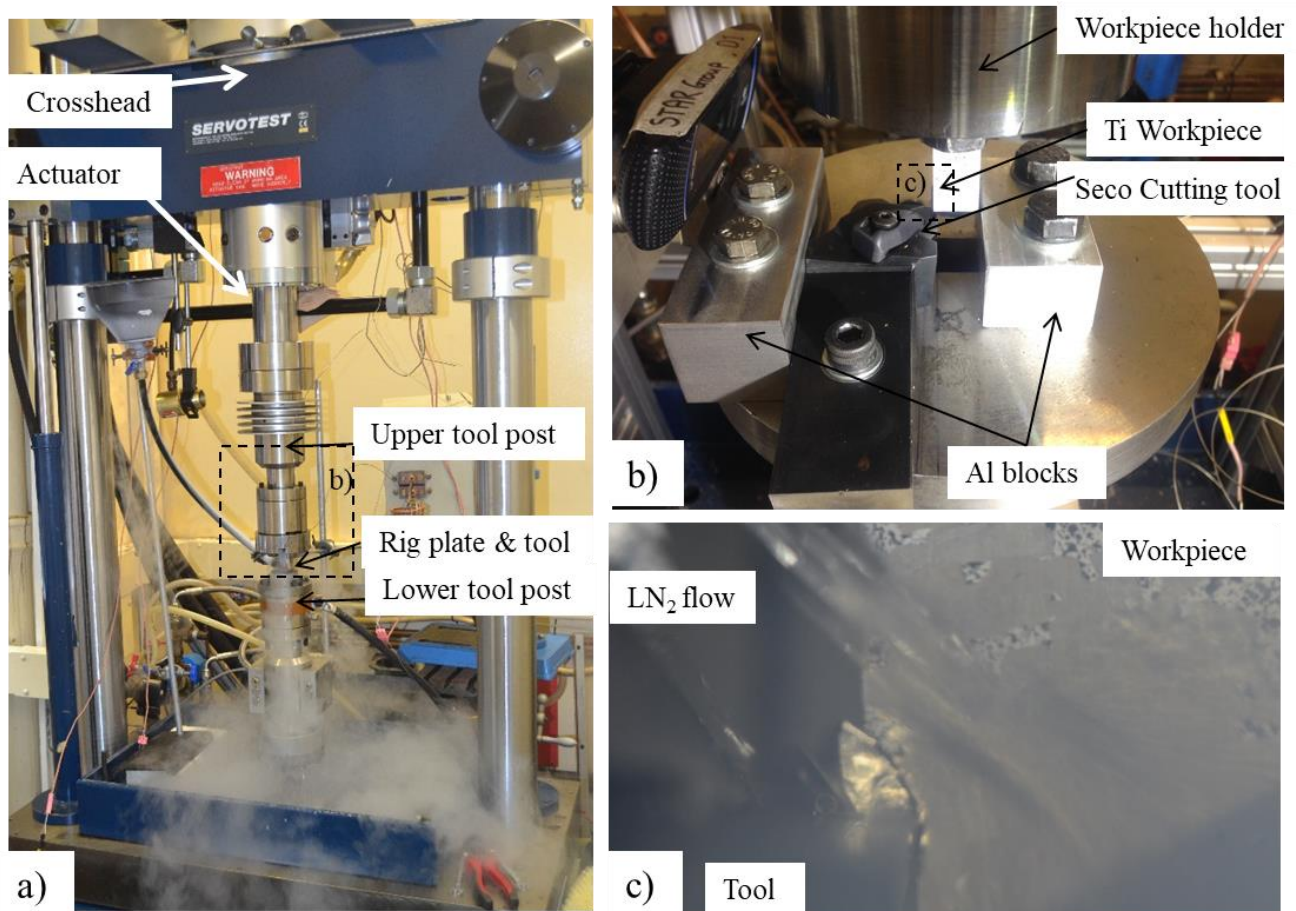
Figure 3-14. a) Arbitrary Strain Path (ASP) Machine, b) Magnification of the cutting section with the rig plate and Seco tool, c) Magnification of the cutting region under LN$_2$.

Figure 3-15 shows the experimental set up during PSM of β annealed Ti-6Al-4V ELI under LN$_2$. It also shows the place where the thermocouple was inserted to measure the near region temperature during machining.
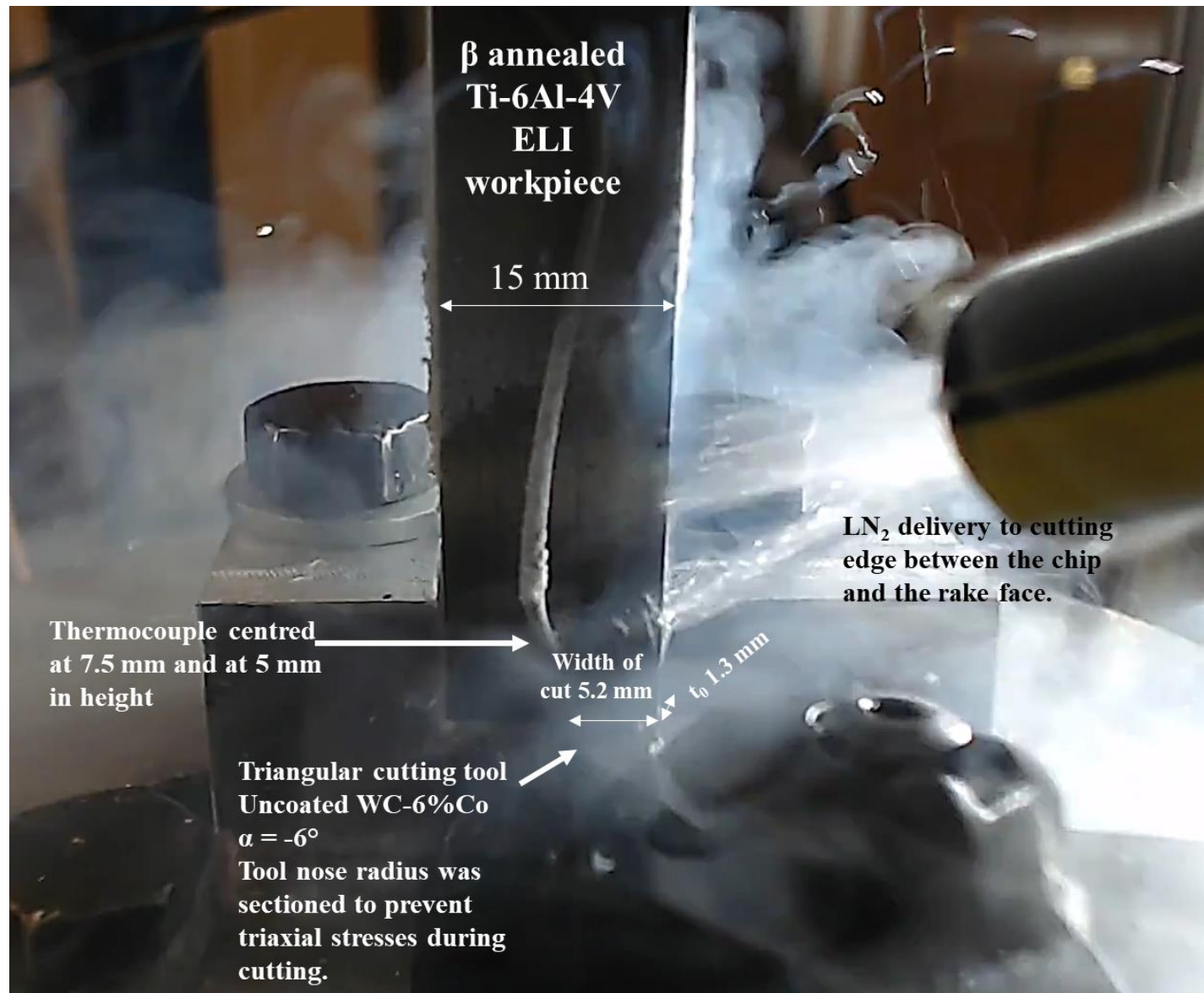
Figure 3-15. Cryogenic LN$_2$ application between the rake face of the tool and chip formation during orthogonal cutting and point of temperature measurement embedded in the workpiece.
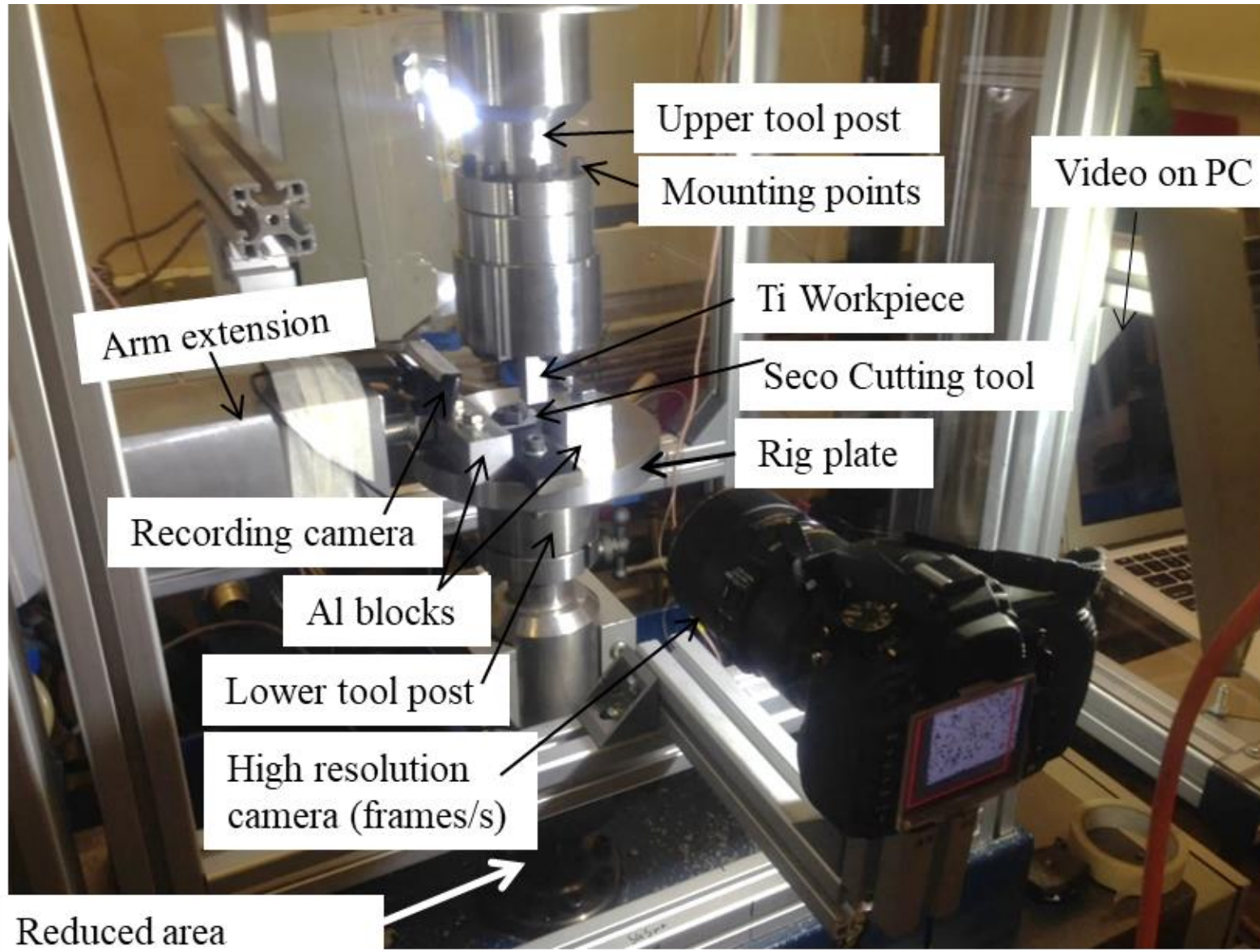
Figure 3-16. Camera set up for the acquisition of serial pictures during the cutting process.
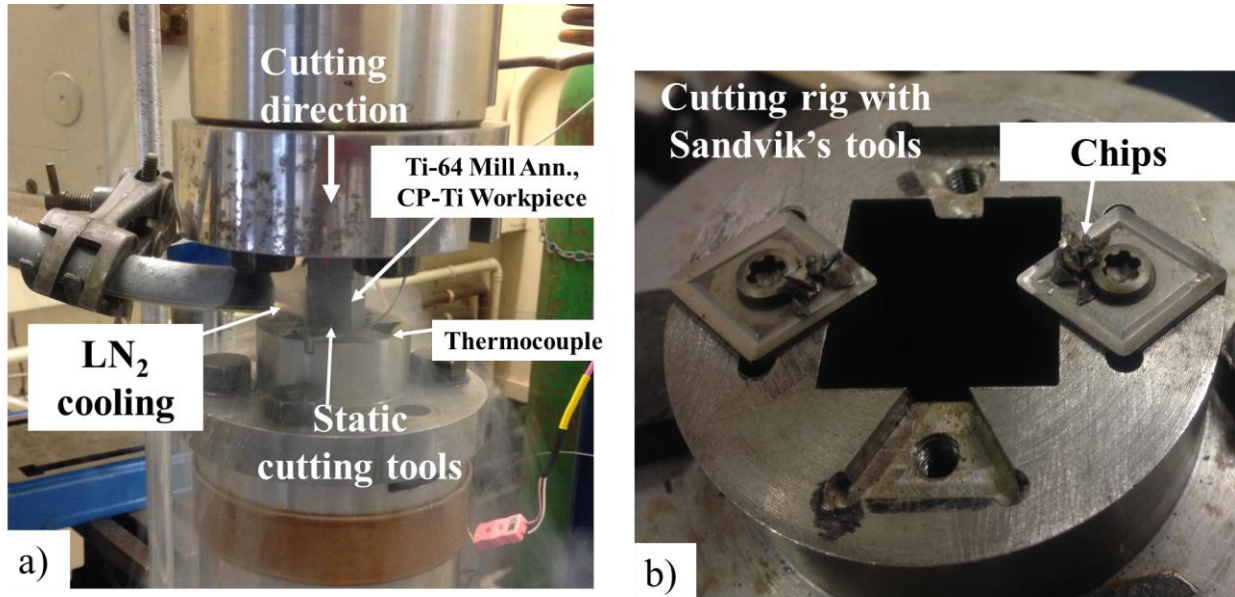
Figure 3-17. Near PSM of CP-Ti and Mill annealed Ti-6Al-4V using Sandvik Coromant grade H13A cutting tools.

3.6.3. Force system and shear stress estimation

The shear stress was estimated through the Merchant's force circle analysis [132] in 1945. Force in the cutting direction (F_h) and displacement was obtained from the plane strain machining tests. F_t is the tangential and F_n is the normal force to the tool's rake face; however, they are not determined directly. The force was measured by a strain gage toolpost, which measured the horizontal cutting force F_h. F_v the tangential force, also known as thrust force, needs to be estimated, as it was not able to measure it directly. This force can be obtained by knowing the coefficient of friction on the tool surface, μ, which can be estimated using the friction angle β. In this work, β was estimated through the assumption made by Merchant that the shear band would assume a value, which minimises the energy (equation (3.13)). F_s represents the force in the shear direction and is estimated through equation (3.15). F_{ns} is the normal force from the shear direction and is calculated by equation (3.16). A_s is the area where shearing has taken place and is estimated through equation (3.17). In this equation, t represents the uncut chip thickness, and b the width of the cut. The shear stress in orthogonal cutting was estimated through the equation (3.18).

$$F_n = F_h cos\ \alpha - F_v cos\ \alpha \tag{3.11}$$

116

$$F_t = F_h \sin \alpha + F_v \cos \alpha \tag{3.12}$$

$$\beta = \left(\frac{\pi}{4} + \frac{\alpha}{2} - \phi\right) * 2 \tag{3.13}$$

$$\mu = \tan \beta = \frac{F_t}{F_n} = \frac{F_v + F_h \tan \alpha}{F_h - F_v \tan \alpha} \tag{3.14}$$

$$F_s = F_h \cos \phi - F_v \sin \phi \tag{3.15}$$

$$F_{ns} = F_h \sin \phi + F_v \cos \phi \tag{3.16}$$

$$A_s = \frac{tb}{\sin\phi} \tag{3.17}$$

$$\tau_s = \frac{F_s}{A_s} \tag{3.18}$$
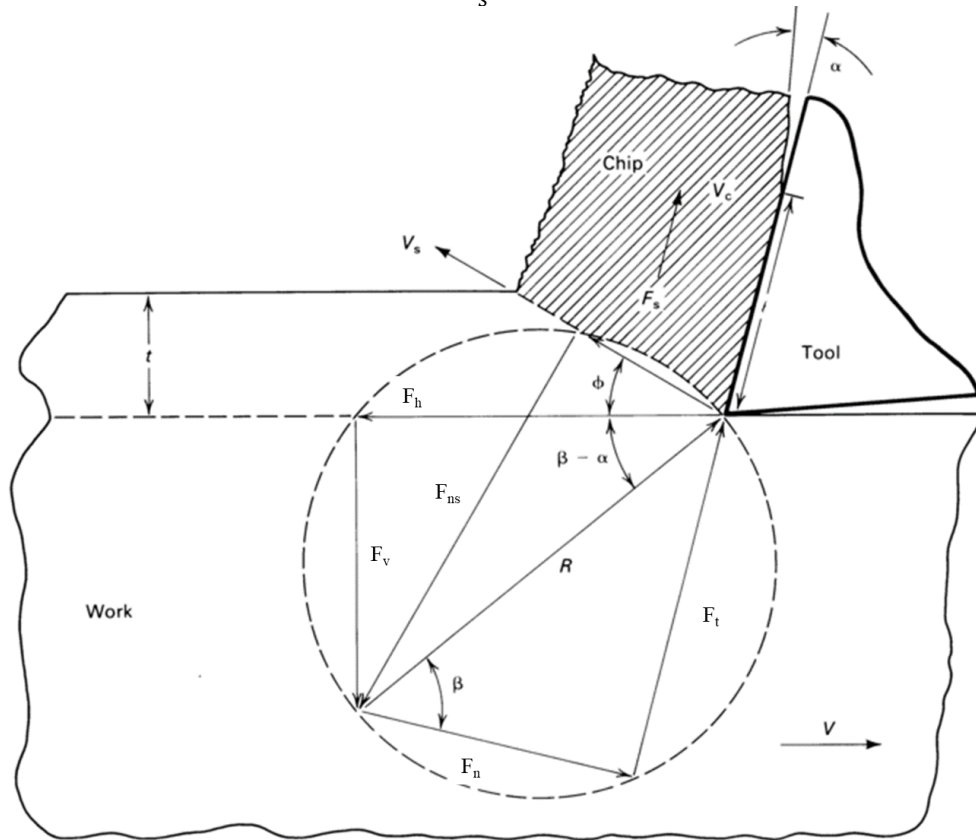
Figure 3-18. Analysis of cutting forces through a Merchant's force circle diagram [132][59][67]. The nomenclature used was obtained from Dieter [2].

117

Merchant's model assumptions [59]:

- The tool's cutting edge is perfectly sharp. There is no contact between the flank face and the workpiece material.
- The shear area is a linear plane originating from the cutting edge.
- There is no build-up edge formation.
- Chip formation is continuous, and plastic deformation in the chip is homogeneous.
- The plane strain is kept when the chip does not flow to either side.
- The depth of cut is kept constant.
- The stresses along the shear plane (shear and normal) are uniform.
- The cutting velocity is constant and uniform.

The shear strain imposed on the chip in the shear plane can be estimated through the shear angle and the rake angle by equation (3.19). In this system, there are three critical velocities. (1) The velocity of cutting V_c, which is the relative velocity of the workpiece to the tool. (2) The chip velocity V_{ch}, the velocity of the chip in relation to the tool in the direction of the tool edge. (3) The shear velocity V_s referring to the velocity of the chip in relation to the workpiece in the direction of shear. V_{ch} and V_s can be estimated by equations (3.20) and (3.21) respectively. The strain rate is estimated through equation (3.22) where Δy represents the thickness of the shear band. Shaw [59] reports that an approximate value is ~ 25 μm.

$$\gamma = \frac{\cos \alpha}{\sin \phi \cos(\phi - \alpha)} \tag{3.19}$$

$$V_{ch} = \frac{\sin \phi}{\cos(\phi - \alpha)} V_c \tag{3.20}$$

$$V_s = \frac{\cos \alpha}{\cos(\phi - \alpha)} V_c \tag{3.21}$$

$$\dot{\gamma} = \frac{\cos \alpha}{\cos(\phi - \alpha)} \frac{V_c}{\Delta y} \tag{3.22}$$

In an orthogonal cut, the total energy spent per unit time is $U = F_c V_c$, and the energy per unit volume is $u = F_c/bt$, where b and t represent width and depth of cut, respectively. Shaw [59] predicted that four different processes generate the total energy. The first is the shear energy on the shear plane u_s equation (3.23). The second is the energy spent on friction on

118

the tool surface as per equation (3.24). The third is the surface energy referring to the formation of two new surface areas. The fourth is related to energy due to the change in momentum when passing the shear plane. Even though there are many forces associated with metal cutting, Shaw [59] calculated that most of the energy is spent on plastic deformation and friction and this energy is then transformed into thermal energy. A plane strain cutting operation requires at least five times that distance of the depth of cut [2].

$$u_s = \frac{F_s V_s}{V_c bt} \tag{3.23}$$

$$u_F = \frac{FV_{ch}}{V_c bt} \tag{3.24}$$

3.6.4.   Energy Dispersive X-Ray Spectroscopy (EDX)

To determine the chemical elements in the tool insert after the diffusion test, an EDX line scan was performed in an SEM F-50 with an X-ray detector.

3.7.   High-speed milling

This section describes the methodology undertaken in a full-scale, high-speed machining trial with the objective of underpinning the deformation mechanisms during plastic deformation of titanium alloys with dependency on deformation temperature and cooling/lubrication conditions.

The analysis of a climb milling trial on β annealed Ti-6Al-4V ELI at high speed of 80 m.min^{-1} was undertaken to evaluate the effect of different cooling and lubrication conditions on the subsurface microstructural modification. These were: conventional flood cooling, Medium Pressure Through Tool (MPTT), Minimum Quantity Lubrication (MQL) and CO_2 cryogenic cooling.

3.7.1.   Equipment

Machining trials were undertaken at the Advanced Manufacturing Research Centre in a Starrag's high precision machining centre with integrated CO_2 cryogenic, MQL, air, flood

and medium/high pressure through tool cooling technologies. Three axes: "X", "Y" and "Z" were used from the five available axes.
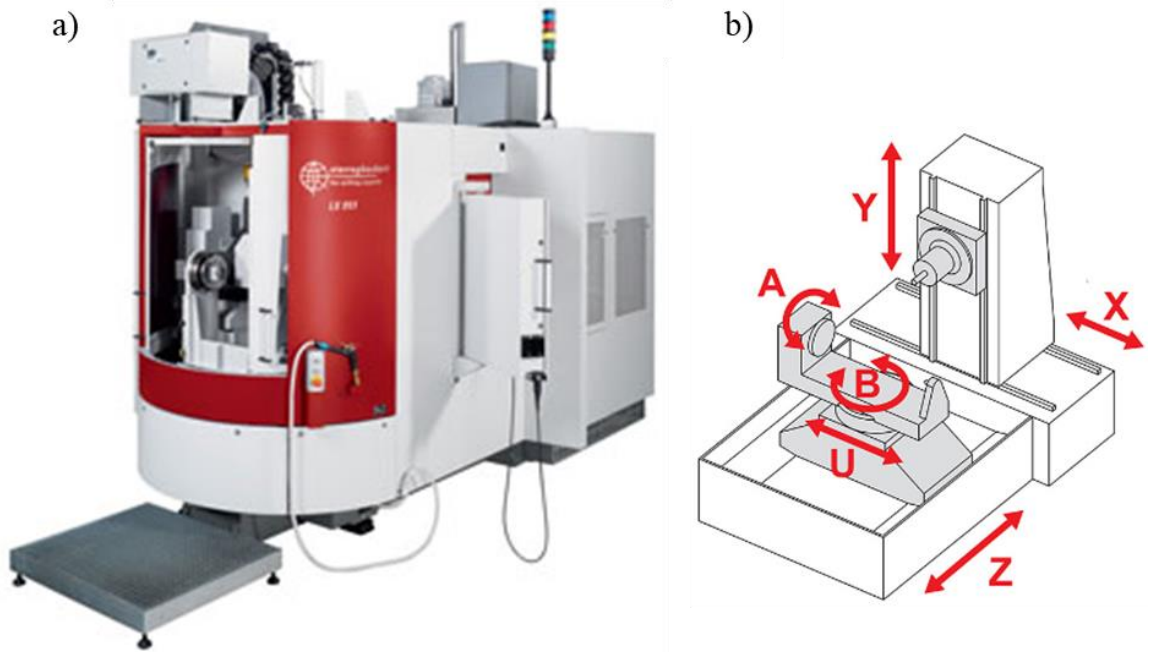
Figure 3-19. a) Starrag machining centre LX 051, b) axes available in the machining centre [133].

3.7.2. Optical microscope for tool wear measurement

A portable, digital, optical microscope InSize® was used for flank and rake wear measurements shown in Figure 3-20.

Figure 3-20. InSize® digital, optical microscope to measure tool wear on site [134].

3.7.3. Climb milling using a round insert

The parameters utilised during the first full-scale milling trial are illustrated in Table 3-8, and the experimental set up is shown in Figure 3-21.

Table 3-8. Operational parameters during the climb milling trial.

Parameter	Value		
Cutting operation	Face Milling		
Axial depth of cut, (mm)	2		
Radial depth of cut, (mm)	10		
Length of cut, (mm)	105		
Surface speed, Vc (m/min)	60, 80, 100	Flow rate	Units
	Conventional flood	20	$L.min^{-1}$
	25% CO_2	1.9	$Kg.hr^{-1}$
	50% CO_2	10.3	$Kg.hr^{-1}$
Cooling/Lubricating conditions	75% CO_2	10.9	$Kg.hr^{-1}$
	100% CO_2	11.8	$Kg.hr^{-1}$
	MQL	35	mL/hr^{-1}
	CO_2 plus MQL	35	mL/hr^{-1}
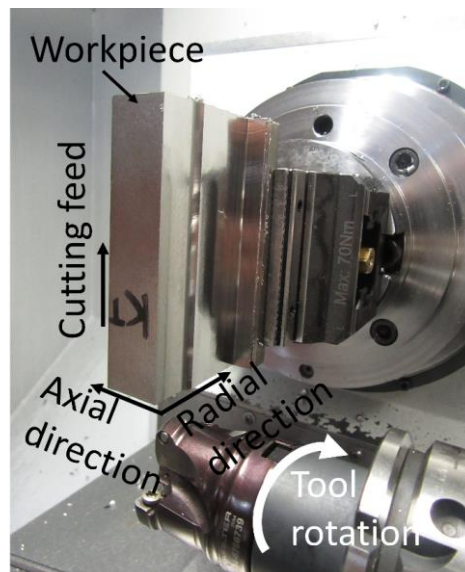
Figure 3-21. Face milling β annealed Ti-6Al-4V, using one Walter's round insert at a_p = 2 mm (axial depth of cut), a_e = 10 mm (radial depth of cut), LoC = 105 mm (length of cut).

At the end of each cutting test, the workpiece was precision sectioned using a Secotom 50 machine. Along the feed direction, the central region of 10 mm was sectioned (Figure 3-22 a), parallel to the radial direction. Then, it was sectioned again along the axial direction, at a distance of 0.5 mm, see Figure 3-22 c). The subsurface corresponding to the feed and axial direction was examined under cross-polarised and electron microscopy.
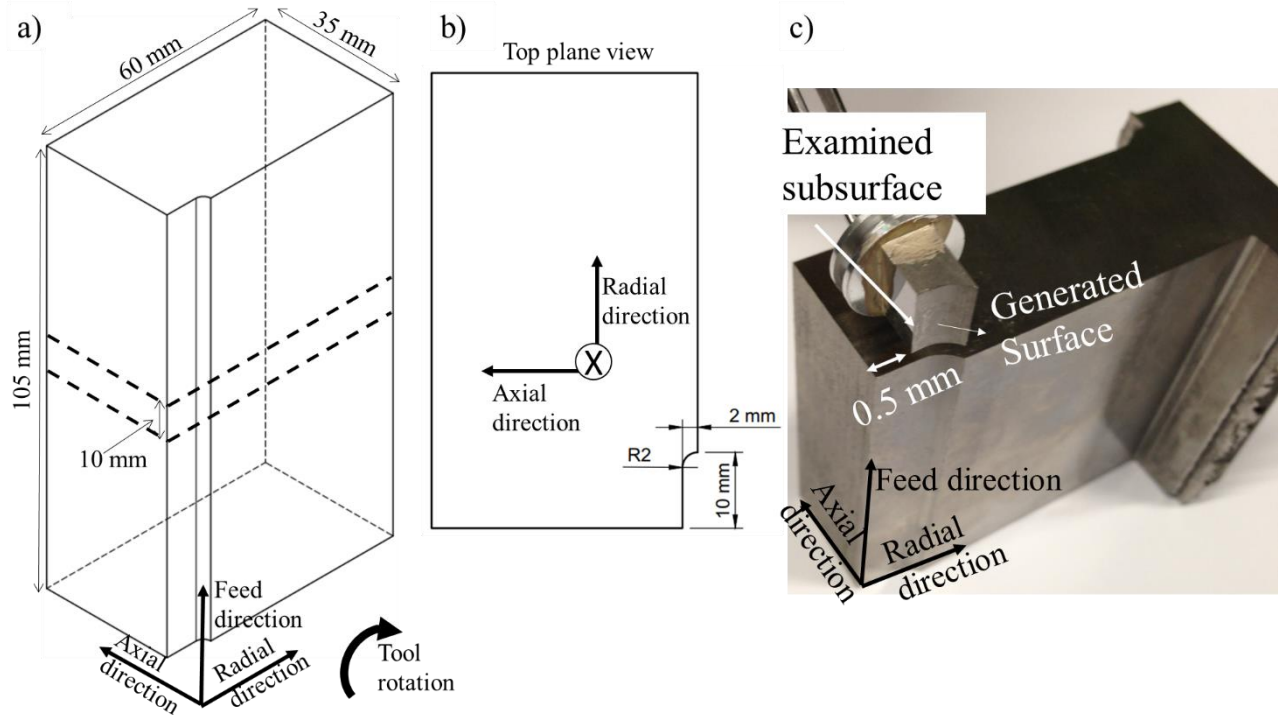
Figure 3-22. Sectioned β annealed Ti-6Al-4V workpiece after face milling at 80 m.min^{-1}, a_p = 2 mm (axial depth of cut), a_e = 10 mm (radial depth of cut), LoC = 105 mm (length of cut).

The operational parameters, which were kept constant during all tests, are shown in Table 3-8 except for cutting speed and cooling-lubrication methodology, which were used as variables during the trials.

For the coolant technologies, the following fluids were selected. For the flood and MPTT cooling conditions, Hocut 795B-eu, a water-soluble fluid with high lubricity attributed to its constituent mineral oils and polar additives, was employed. For the MQL the Aerosol master lubricant c-st Figure 3-23 a) with a density of 0.96 g.cm^{-3} at 15°C, kinematic viscosity (at 40°C) of 20 mm^2.s^{-1} was used. It contains 5-10% weight of di-tert-dodecyl polysulfide (a high active sulphur content substance used in the manufacture of lubricants and metalworking fluids used as anti-wear and extreme pressure additive). This was applied through the Rother technology lubrication system and created a fine aerosol

with micron-sized lubricant particles with the aim of preventing heat instead of cooling it. This system is shown in Figure 3-23 b). For the cryogenic carbon dioxide (CO_2), 12 high-pressure cylinders (near 62 bar) connected in a circuit were used as illustrated in Figure 3-24. Liquid carbon dioxide is contained in each of these cylinders at high pressure. It is then transported as a liquid through a high-pressure internal nozzle into the machine arriving at the tool spindle nozzle outlet. At the exit there is a pressure drop of nearly 61 bar, it expands into a mixture of 60% solid CO_2 snow and 40% CO_2 gas [85].

Figure 3-23. Minimum Quantity Lubrication (MQL) system used in this trial a) Aerosol Master® lubricant c-st oil b) internal system to generate the oil aerosol for the MQL application.

Figure 3-24. Twelve high-pressure (near 62 bar) cylinders connected in series containing liquid carbon dioxide.
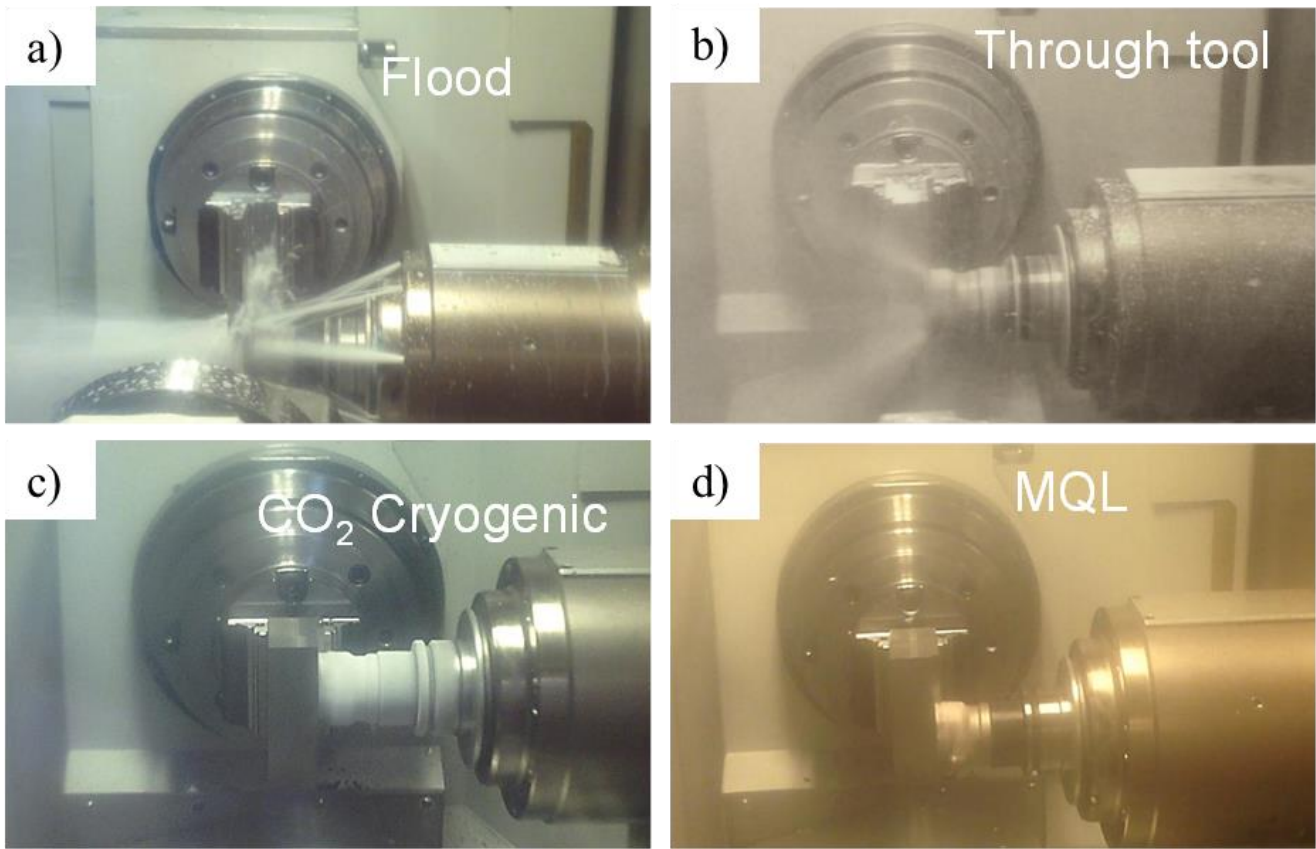
Figure 3-25. a) Flood and b) through tool cooling operation using Hocut 795B-eu, c) CO_2 leaving from each of the flute nozzles and d) Aerosol master lubricant c-st MQL during climb milling of β annealed Ti-6Al-4V ELI.

4. Thermo-mechanical testing: quasi-static uniaxial compression

There are a number of aims for this chapter. Firstly, to describe the effect of temperature on the plastic deformation process during axisymmetric compression testing. This includes flow stress, strain to reach instability by thermal softening, strain for fracture, and energy required for catastrophic shearing and its associated microstructure evolution. Secondly, to correlate the shear stresses generated in uniaxial compression testing to the shear stresses generated during plane strain machining. This enables prediction of the machinability of the material during chip formation by catastrophic shear failure. Thirdly, to generate a model to predict cutting forces during metal cutting. Finally, to examine the underlying microstructure to determine the dominant deformation mechanisms during plastic deformation. A range of strain rates, $\dot{\varepsilon}$, were used: from 10^{-2} to 50^1 s^{-1} at different temperatures from -140°C to 300°C. β annealed Ti-6Al-4V ELI was the focus of this investigation. Mill annealed Ti-6Al-4V and commercially pure titanium (CP-Ti) were also investigated.

4.1. Flow stress determination

The flow stresses experienced during uniaxial compression at different strain rates and temperatures were estimated using the methodology described in Section 3.3.2 based on best guidelines [130] and are shown in Figure 4-1. Several observations were made. (1) Plastic deformation at cryogenic temperatures generated higher compressive yield stress in comparison to deformation at room temperature. (2) At cryogenic temperatures, the strain to the onset of instability by thermal softening (determined by Recht [135] as the point where dσ.dε^{-1} = 0) decreased. (3) The strain to final failure was reduced, which provided a benefit of nearly a third less energy of that required at room temperature for catastrophic shear failure resulting from adiabatic shear banding (ASB).
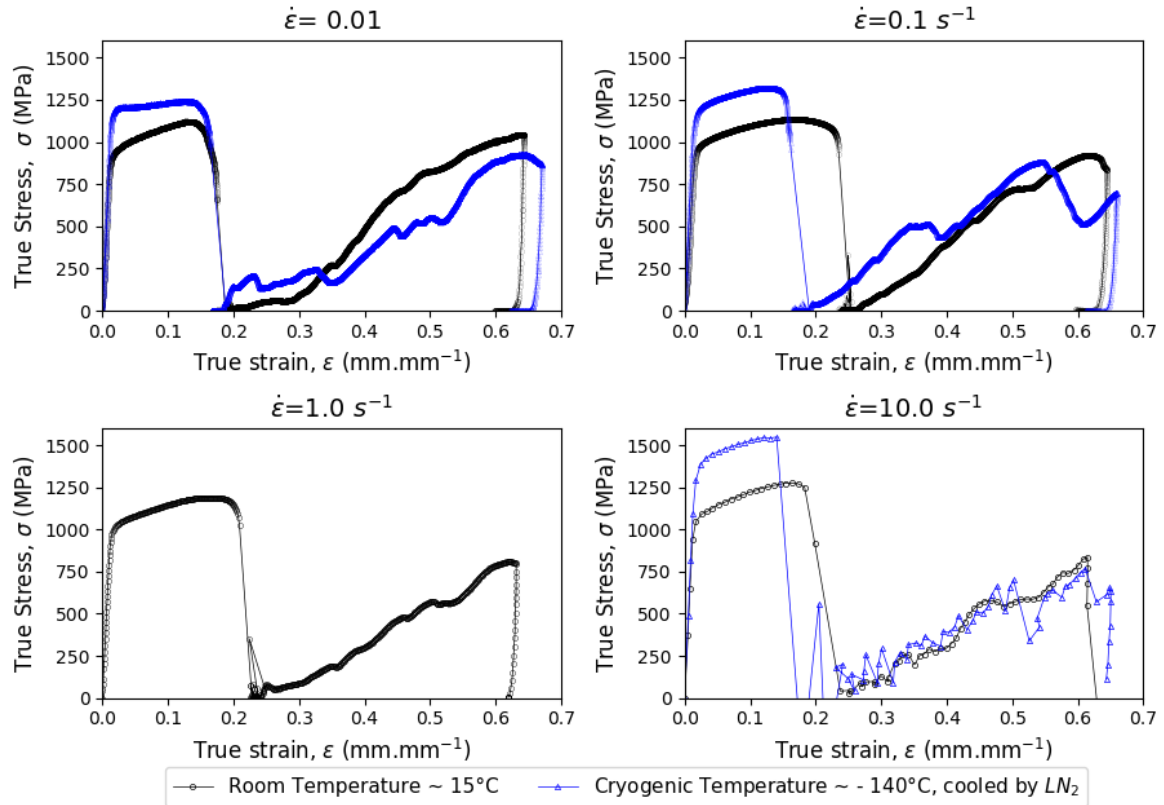
Figure 4-1. Flow stress data from axisymmetric compression cylinders of β annealed Ti-6Al-4V ELI to a true strain of 0.7 at $\dot{\varepsilon} = 10^{-2}$, 10^{-1}, 10^0, 10^1 s^{-1} at a room temperature of 15°C and at a cryogenic temperature of -140°C provided by LN$_2$.

4.2. The effect of deformation temperature on the energy required for the onset of shear instability

The mechanical properties of polycrystalline materials are strongly influenced by their deformation temperature and dislocation structure. For example, their density and distribution, crystal structure (hcp, bcc or fcc), crystallographic orientation, stacking fault energy (SFE) and grain size [2], [34]. The deformation temperature has a strong influence on the deformation mechanisms taking place during plastic deformation, which are strongly dependent on the internal dislocation structure. In high SFE metals, a cell structure composed of areas free of dislocations, surrounded by areas of high dislocation density is usually generated when loaded during plastic deformation [35]. This is due to the ease of cross-slip and climb. Titanium alloys have a low SFE, where cross-slip and climb are hindered by the dissociation of dislocations into partials [21]. Figure 4-2 shows the effect

126

of deformation temperature on the flow stress behaviour for cryogenic and room temperatures at different strain rates. Three main observations taken from this figure are:

1. Generation of higher compressive yield stress after initial rapid work hardening at low temperatures.
2. Lower strain to fracture during failure by catastrophic shear banding
3. Lower energy (i.e. area under the curve of true stress and true strain up to the strain at failure) at low temperatures.

The effect of the deformation temperature (-130°C, 15°C and 300°C) in axisymmetric compression specimens is clearly illustrated in Figure 4-3 at a constant strain rate of $\dot{\varepsilon} = 10^{-1}$ s^{-1} to a true strain $\varepsilon = 0.7$. It can be inferred that different mechanisms should be operative during plastic deformation as it is reflected in the flow stress and on the energy to cause fracture by localised strain. During compression, dislocations are introduced into the lattice. Via interaction with other dislocations and other microstructural features such as grain boundaries, substitutional atoms or interstitials, generate an increased level of internal stress. This results in a greater number of dislocation tangles, which impede dislocation motion, thus giving rise to a strain-hardened structure. Several results are observed by comparing these three flow stress curves. Firstly, the lower the temperature, the higher the compressive yield strength, which is strongly influenced by the strain hardening rate. This indicates that an increase in dislocation density is introduced into the lattice of specimens at low temperatures and more dislocation tangles may be generated, making it harder for further accommodation of plastic strain. Secondly, the strain to failure is generated at a lower level of strain at low temperatures. Thirdly, the area under the flow curve (also known as a workability criterion as suggested by Cockcroft and Latham [136]), which represents the energy required to cause failure by localised shear banding, is greater at higher temperatures, such as 300°C.

The low-temperature specimen, at -130°C, appears to have experienced more strain hardening in the initial stage of deformation; therefore a higher yield strength was obtained. The higher strain hardening also implies higher internal energy in the lattice, which could lead to a higher tendency towards recrystallisation during plastic deformation. At low temperatures the CRSS for slip becomes much higher [21] which hampers its operation during deformation; however, the CRSS for deformational twinning is temperature insensitive [29]. This leads deformation twinning to become the dominant mechanism during plastic deformation. Mechanical twinning introduces a high density of dislocations surrounding the twin boundaries, introducing more sites which hamper dislocation movement. If dislocations cannot move with further application of strain, the lattice can

accommodate the strain only by nucleation of voids, which eventually could lead to fracture.

For the 300°C specimen, the flow curve indicates that the dominant operational mechanism may be dislocation slip. There is a higher degree of softening which suggests a higher degree of dislocation annihilation. This occurs during a longer strain range, which reduces the stress required for continuing plastic deformation and allows it to impart further plastic deformation without causing fracture.
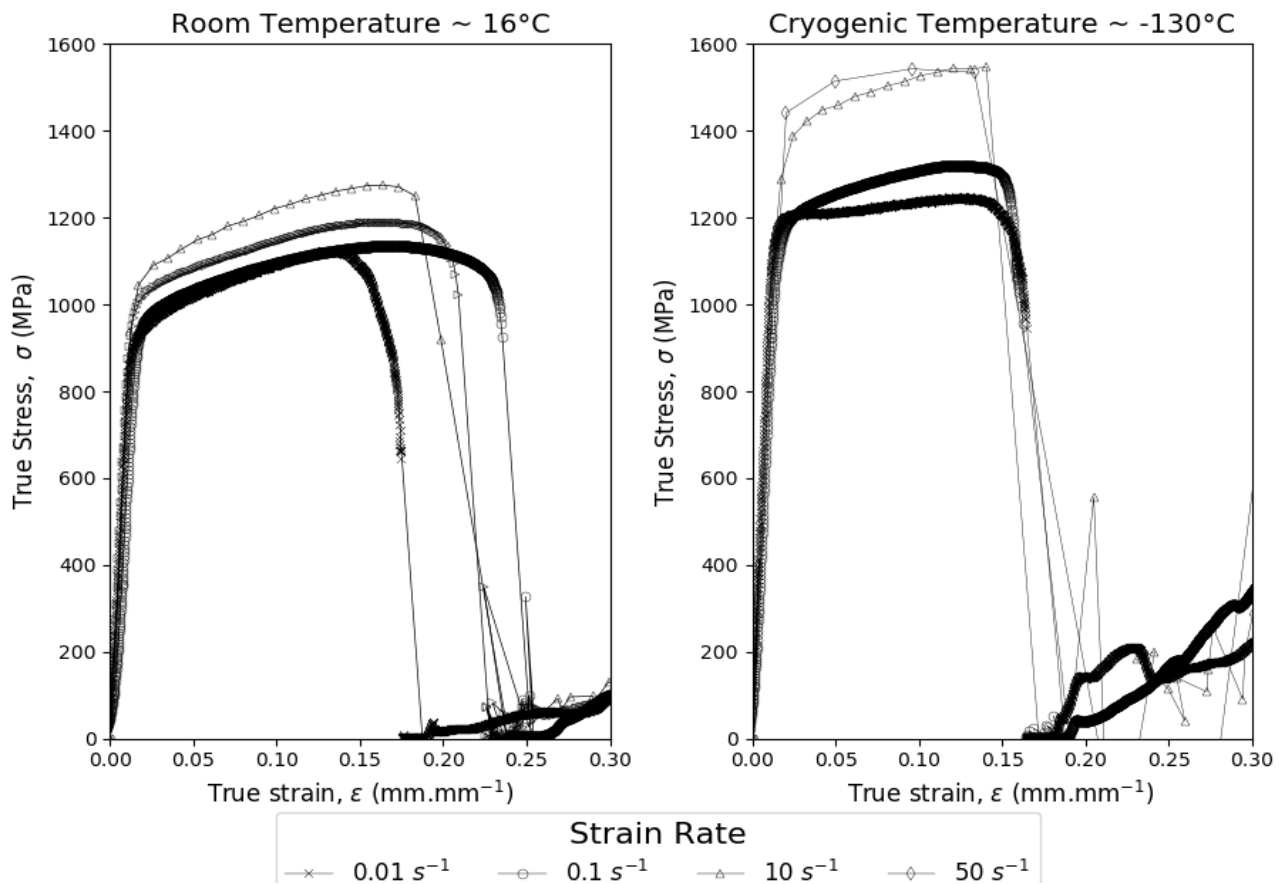
Figure 4-2. Effect of deformation temperature and strain rate on the flow stress of β annealed Ti-6Al-4V ELI.
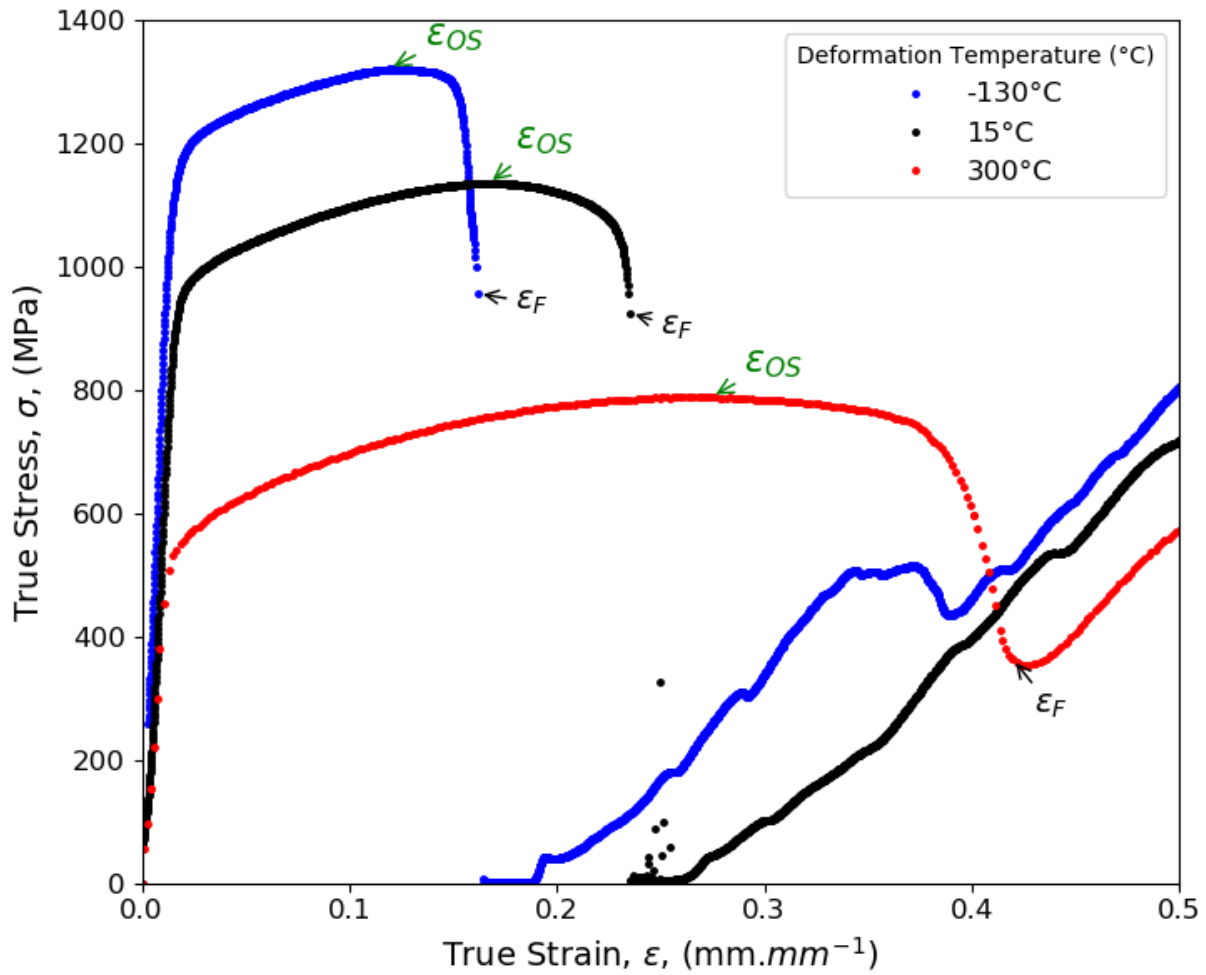
Figure 4-3. Effect of temperature on the flow curves on axisymmetric compression testing at a strain rate $\dot{\varepsilon} = 10^{-1}$ s^{-1} to a true strain $\varepsilon = 0.7$ on β annealed Ti-6Al-4V ELI; ε_{OS} signifies the strain to the onset of thermal softening and ε_F signifies the strain to catastrophic failure.
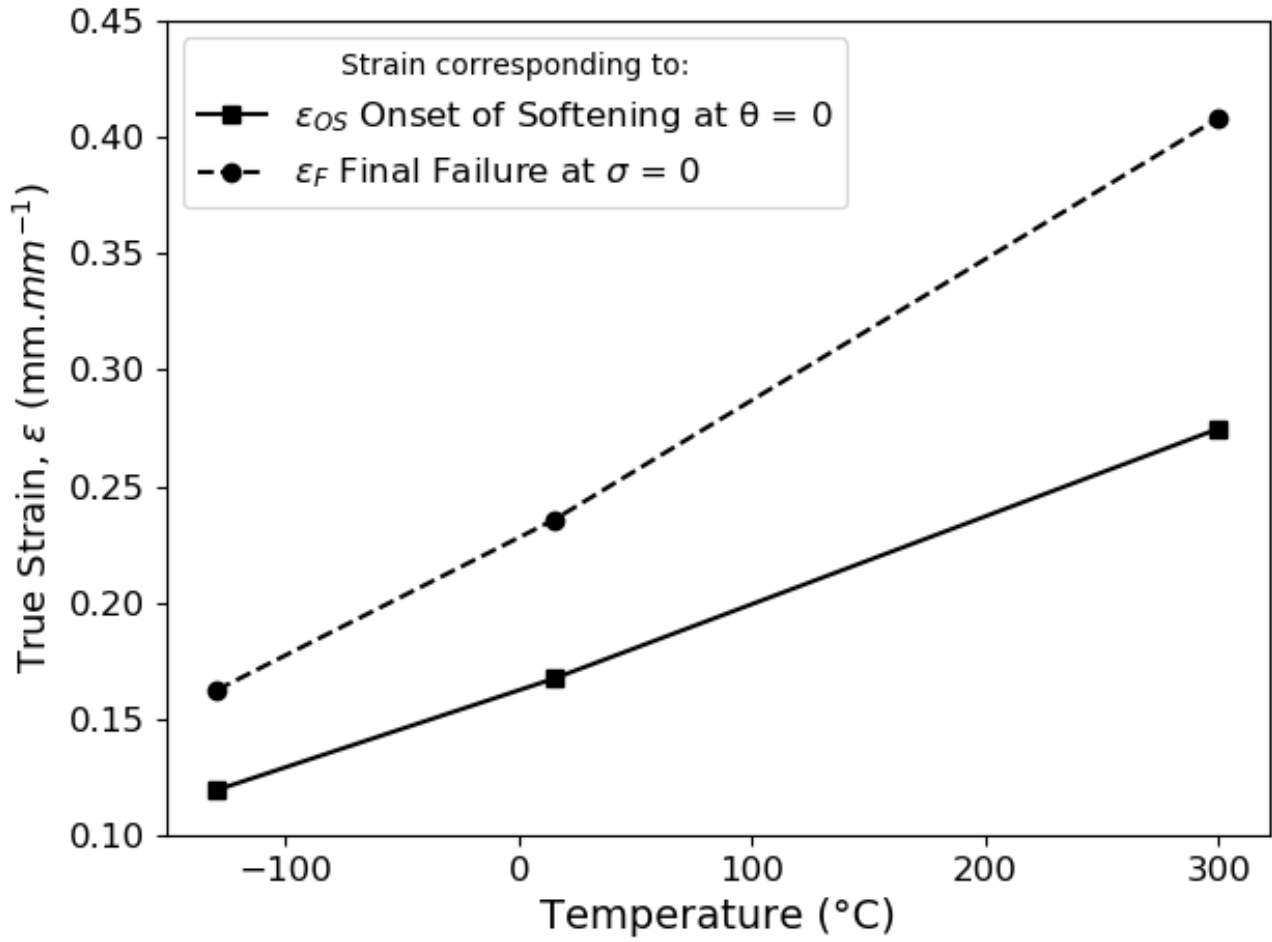
Figure 4-4. Strain at the onset of softening and fracture, this corresponds to Figure 4-3.
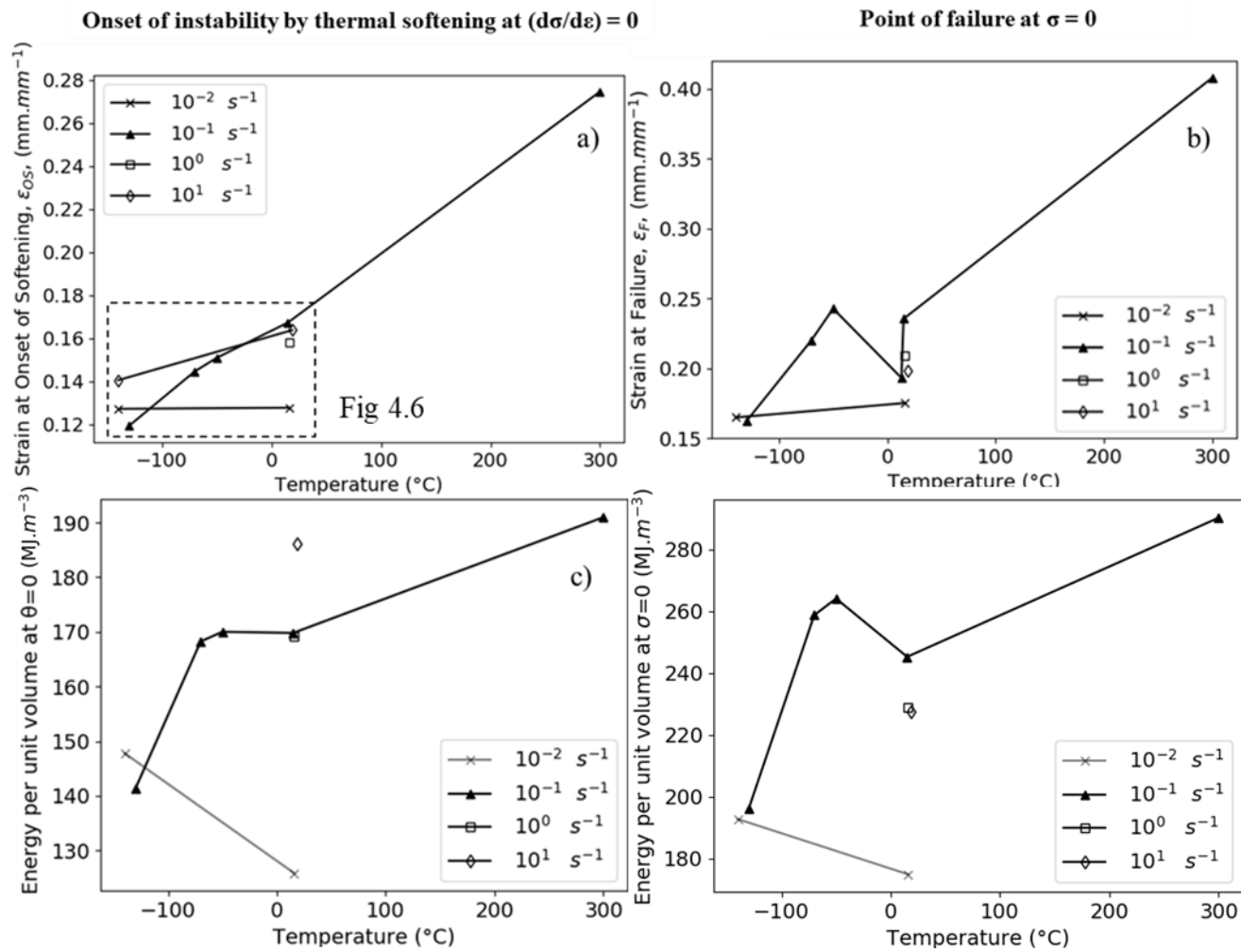
Figure 4-5. Temperature and strain rate dependence on β annealed Ti-6Al-4V ELI to a true strain of ε = 0.7: a) the strain at the onset of instability by thermal softening ε_{OS}, b) strain at fracture ε_F, c) the energy per unit volume or Cockcroft-Latham parameter at the onset of softening and d) Cockcroft-Latham parameter at failure.

At 10^{-1} s^{-1}, higher temperatures show a longer distance between the onset of shear instability and fracture, suggesting higher ductility at higher temperatures, and consequently, a higher energy per unit volume requirement for fracture and chip formation, see Figure 4-4.

Figure 4-5 a) shows the strain at the onset of instability by thermal softening (as indicated in Figure 4-3) and its dependence on temperature. At strain rates of 10^{-1} s^{-1}, it follows a linear trend; increasing by the increase in deformation temperature. At this strain rate (10^{-1} s^{-1}), at -130°C a strain for the onset of failure of 0.12 mm.mm^{-1} is observed versus at 20 °C a strain of 0.165 mm.mm^{-1}, imparting 37% higher strain to generate the onset of instability by thermal softening or onset of fracture at 20°C. A similar tendency occurs at the higher strain rate of 10^{1} s^{-1}, where 14% higher strain is required for the onset of thermal instability (0.14 mm.mm^{-1} versus 0.16 mm.mm^{-1}) see Figure 4-5 a). A magnification of the temperature 140°C to 20°C is shown in Figure 4-6. At a strain rate of 10^{-2} s^{-1}, minimal dependence is observed; however, there are not enough data points to generate a definite conclusion at this strain rate.
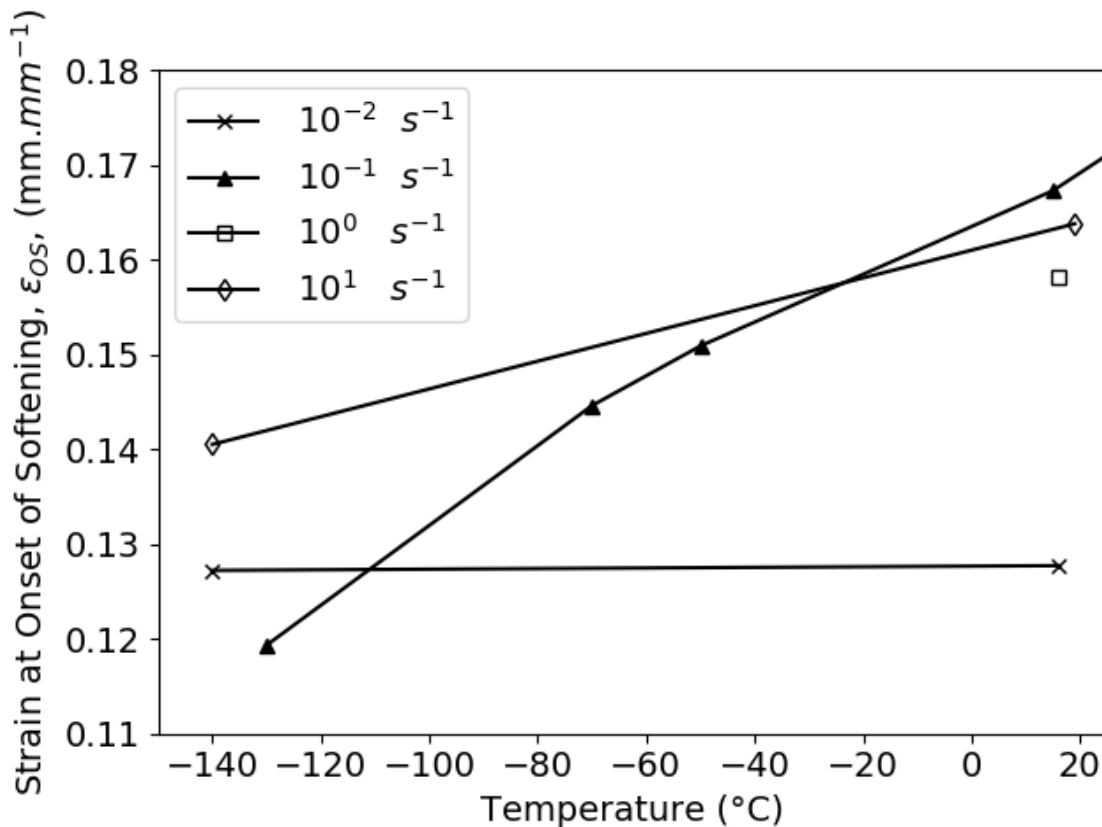
Figure 4-6. The temperature dependence on the strain at the onset of thermal softening $d\sigma.d\varepsilon^{-1} = 0$.

132

The estimated energy to cause failure during axisymmetric compression is strongly dependent on temperature, as is illustrated in Figure 4-5 d). Compared to room temperature, it was estimated that 28% less energy is required to cause failure at a cryogenic temperature near -130°C and 44 % more energy is required to cause failure at higher temperatures of 300°C, as shown in Figure 4-3 (the area under the flow stress curve). Likewise, the energy required for the onset of instability by thermal softening is increased by increasing the deformation temperature.

Orthogonal cutting tests at variable surface speeds and variable uncut chip thickness were generated and are presented in section 5.2. A microstructural analysis is presented to demonstrate the different plastic deformation mechanisms concerning temperature. A TEM analysis was undertaken in the uppermost subsurface layer (i.e. the SPD, which belongs to the shear band region in the primary deformation zone). Metallurgical evidence of the formation of a nanocrystalline grain structure by the process of continuous dynamic recrystallisation at low temperatures was obtained, as shown in Figure 5-59 in section 5.11 and Figure 6-18 in section 6.4.

The effect of temperature and strain rate on the energy required for shear band formation and failure was investigated through axisymmetric compression testing. The energy was calculated by estimating the area under the flow curve up to the point of failure. Metal cutting at low temperatures, and likewise at lower strain rates, results in an energy reduction of nearly 30 %, see Figure 4-3, Figure 4-5 c) and Figure 4-5 d). These images show the estimation of the energy required during plastic instability and failure by shear band formation and fracture during axisymmetric compression to a global true strain of 0.7. They clearly illustrate that at the same strain rate, higher temperatures require more energy to generate the shear band and cause failure. Low temperatures require less energy to cause shear band failure as dislocations accumulate, generating a higher dislocation density through interaction with themselves and other obstacles in the crystal lattice. By taking an average of the energy spent at -125°C at a 10^{-1} s^{-1} strain rate, it is estimated 208 MJ.m^{-3} of energy is spent on fracture, while at 300°C the energy was estimated to be 267 MJ.m^{-3}, which equates to approximately 30% more energy required to form a chip at 300°C compared to -125°C.

At constant temperature, increasing the strain rate increases the amount of energy required to generate a catastrophic shear failure. At room temperature (~18°C), whereas at a strain rate of 10^1 s^{-1} it required 210 MJ.m^{-3}, at a strain rate of 10^{-1} s^{-1} it required 156 MJ.m^{-3}, which equates to a 35% less energy required at the lower strain rate. At cryogenic temperature, achieved by soaking the workpiece in an LN$_2$ bath (reaching a stable temperature of -140°C) at strain rate 10^{-1} s^{-1} it required 237 MJ.m^{-3}, and at a 10 times lower

strain rate 10^{-2} it required 180 MJ.m^{-3}, giving rise to a reduction of 32% energy required for fracture. These results lead to the conclusion that at cryogenic temperatures, the increase in strain rate has a lower impact on the energy required to cause instability in shear than at room temperature. This suggests that the machinability at cryogenic temperatures requires less energy. By increasing the surface speed, it has a low impact on the energy required to generate chips.

After the occurrence of thermal softening, localisation of deformation starts to occur, then sites of stress and strain concentration are created by the formation of a shear band. As a result of the introduction of additional strain, the first voids nucleate, and with further straining, more voids are created. These are then realigned and the ligaments that connect them tear the material completely.

4.3.   The effect of temperature on 0.2% compressive yield strength

The flow stress has a thermal and an athermal component. The thermal component strongly influences the yield strength and is highly sensitive to impurities in the metal. The athermal component is strongly dependent on strain hardening behaviour [56], [137]. According to Conrad [138], the overcoming of interstitial elements by passing dislocations is the factor controlling deformation at low temperatures. The author believes this also applies to substitutional content as they represent obstacles to dislocation motion. An increase in impurities reduces the number of operative slip systems available for plastic deformation. This leads to higher operation of deformation twinning and the introduction of more defects, causing instability to occur at lower levels of imparted strain.

Yielding is attributed to operational systems during deformation, such as slip and mechanical twinning as well as the distribution and density of dislocations. These depend on the strain, strain rate and temperature. Figure 4-7 illustrates the effect of temperature and strain rate on 0.2% compressive yield strength. At a constant strain rate, the reduction in deformation temperature generates a higher yield strength. An important observation is that at a constant strain rate, the yield strength has an inverse linear relationship with temperature. For example, at a strain rate of 10^{-1} s^{-1}; at a temperature of 300°C, its value was 535 MPa, whereas at cryogenic temperature of -140°C it reached 1220.8 MPa, more than twice the value, representing an increase of 130%. At room temperature of 16°C, it generated an intermediate value of $\sigma_{0.2\%}$ = 941 MPa. A fitted equation at this strain rate generated $\sigma_{0.2\%}$ (MPa)= -1.35 * T(°C) + 948.6 with a R^2 = 0.9951. For every one degree Celsius increase in temperature, a reduction of -1.35 times the strength (MPa) is obtained.

In this graph, it is evident that the temperature has a greater impact than the strain rate. For instance, at room temperature, the variation in strain rate form 10^{-2} to 10^{1} s^{-1} resulted in an increase of only 10% (from 1037 to 941 MPa respectively) and at cryogenic temperature an increase of 12.9% (from 1284 to 1138 MPa respectively).
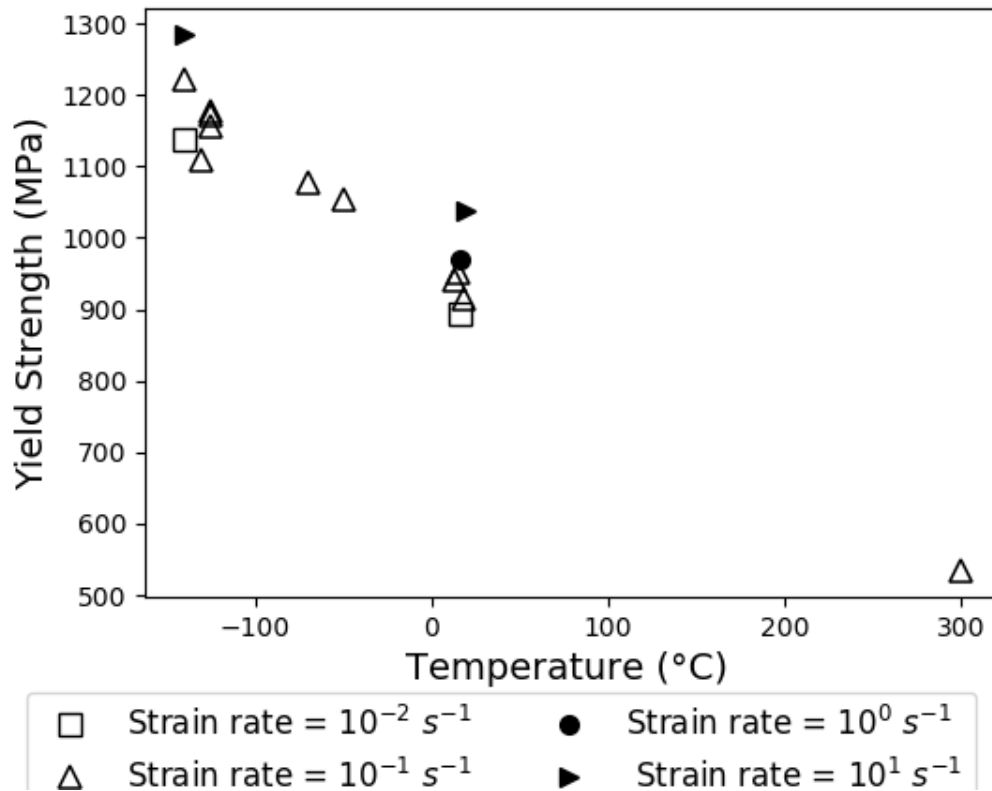
Figure 4-7. Effect of temperature and strain rate on yield strength during axisymmetric compression testing of Ti-6Al-4V β annealed to a true strain of 0.7.

4.4. Ultimate Compressive Strength

The deformation temperature and the strain rate have a significant effect on the ultimate compressive strength (UCS); the lower the temperature, the higher the UCS. Likewise, the higher the strain rate, the higher the UCS. However, the temperature has a more significant influence, in a similar way to the yield strength behaviour. This effect is displayed in Figure 4-8. The deformation temperature influences the strain at which this UCS occurs; however, strain rate seems not to have a substantial impact on this variable.
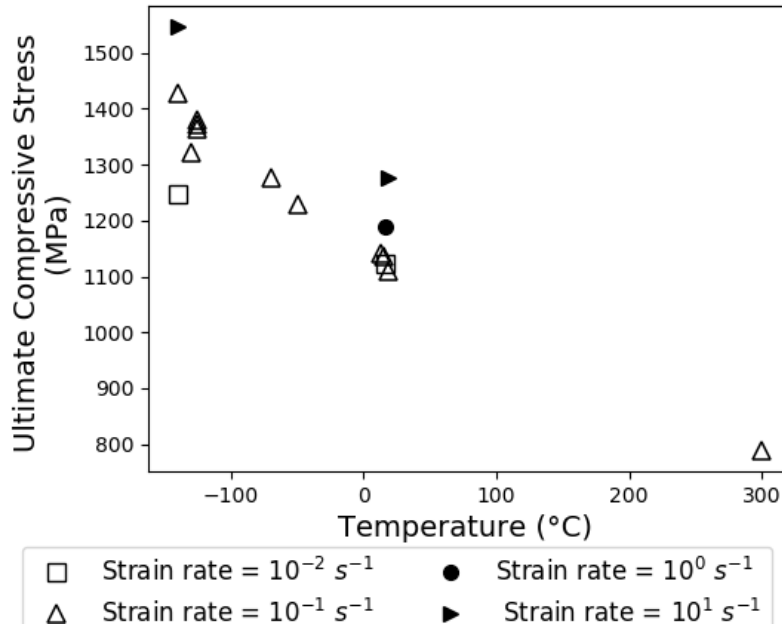
Figure 4-8. Maximum compressive strength in uniaxial compression testing and its dependence on temperature and strain rate.

4.5. The effect of temperature on uniaxial axisymmetric compression of Mill annealed Ti-6Al-4V
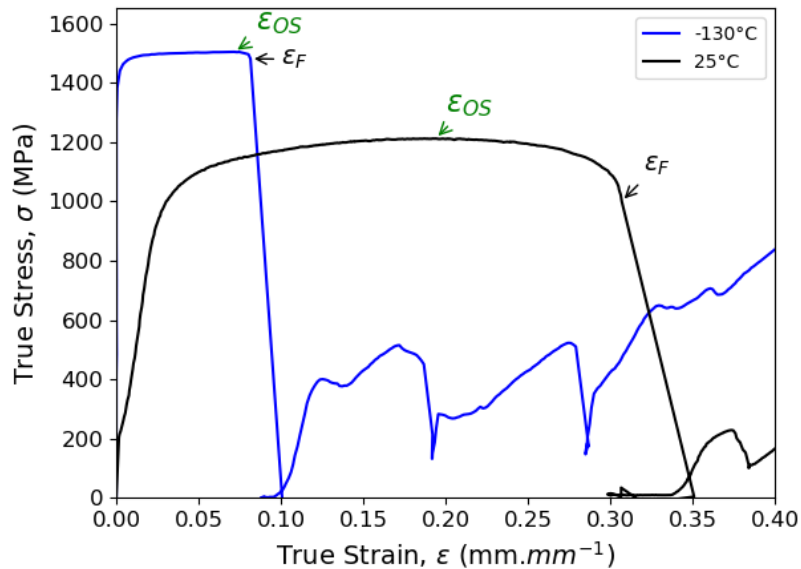
Figure 4-9. Effect of temperature on the true stress and true strain on axisymmetric compression of mill annealed Ti-6Al-4V at strain rate 10^{-1} s^{-1} to a true strain of 0.7. ε_S signifies the strain to the onset of instability by thermal softening and ε_F the strain to failure.

Figure 4-9 illustrates the effect of deformation temperature on mill annealed Ti-6Al-4V during axisymmetric compression. It clearly shows a much smaller area under the flow stress curve. The yield stress was 54% higher at a cryogenic temperature of -130°C in comparison with 25°C (1467 MPa vs 950 MPa respectively). The energy for the generation of shear bands, and the catastrophic failure which resulted was only a third of that at room temperature, as shown in Figure 4-10 a). The strain at the onset of failure at cryogenic temperature was also nearly a third of that at room temperature. The difference in strain from the onset of softening to ultimate failure (Figure 4-10 b)) is higher at room temperature, suggesting that higher friction was experienced when the chip slid over the rake face of the tool and the final shearing of the material.
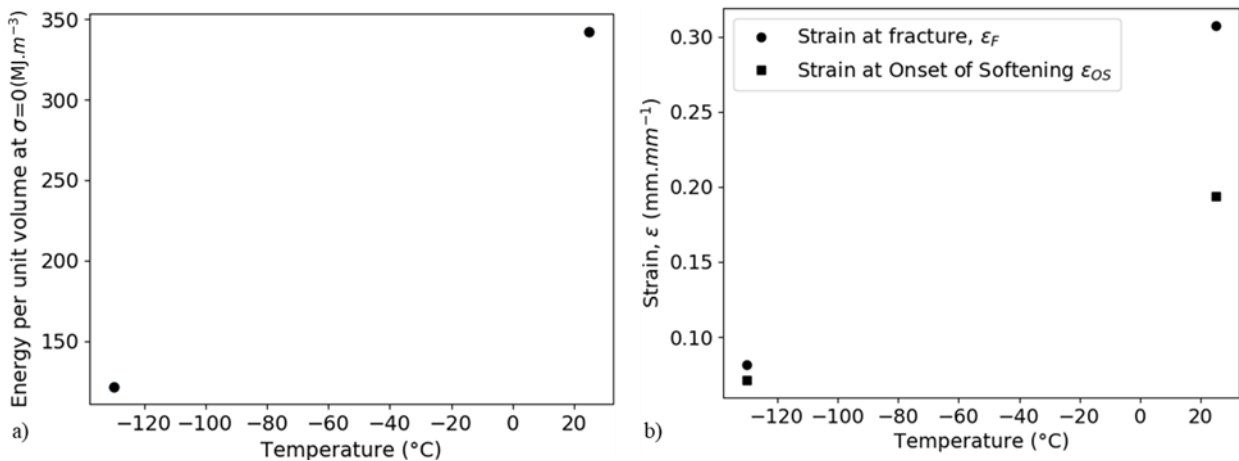
Figure 4-10. Effect of temperature on mill annealed Ti-6Al-4V on axisymmetric compression at a strain rate of 10^{-1} s^{-1} to a true strain of 0.7 on a) Energy at failure $\sigma = 0$ and b) strain at the onset of softening ε_{OS} and strain at failure ε_{F}.

4.6. The effect of temperature on uniaxial axisymmetric compression of CP-Ti

Orthogonal cutting tests were generated with this material under both cryogenic and room temperatures. The microstructural analysis is presented in section 5.10. CP-Ti did not fail as a result of strain localisation during the axisymmetric compression testing to a true strain of 0.7 and strain rate of 10^{-1} s^{-1} as illustrated in Figure 4-11.
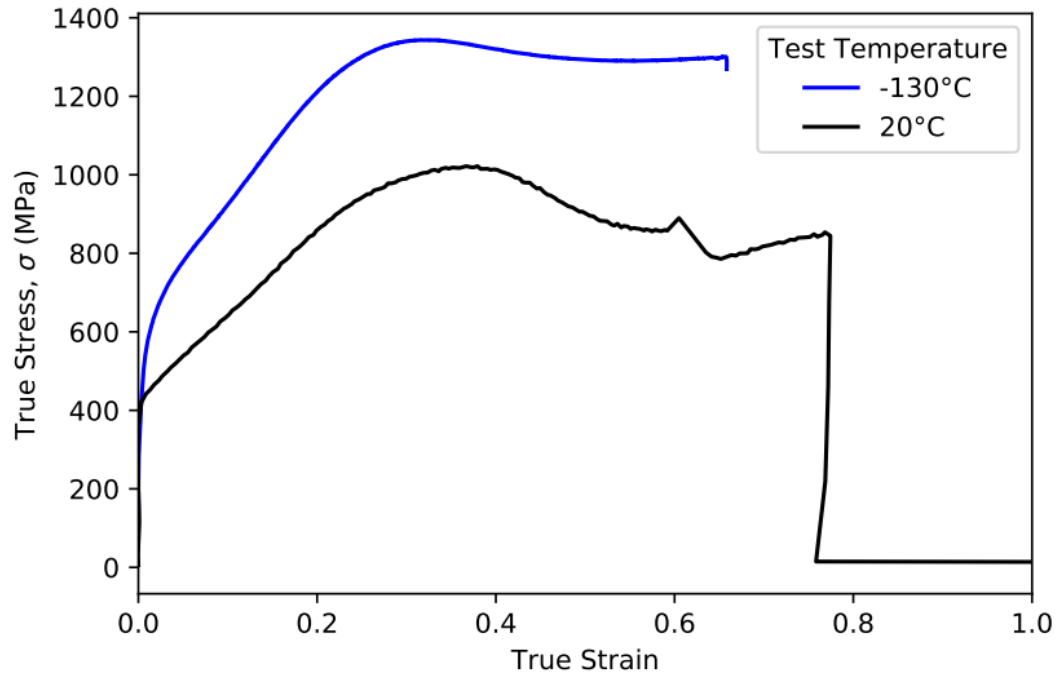
Figure 4-11. Flow curve showing axisymmetric compression of CP-Ti at a strain rate $\dot{\varepsilon}$ $= 10^{-1}$ s^{-1} to a true strain $\varepsilon = 0.7$ at a cryogenic temperature of -130°C and at a room temperature of 20°C.

Comparison of the 0.2% compressive yield strength at a constant strain rate of 10^{-1} s^{-1} as a function of deformation temperatures in different chemistries: β annealed Ti-6Al-4V ELI, mill annealed Ti-6Al-4V and CP-Ti, is depicted in Figure 4-12. It can be observed that different strain hardening rates are dependent on chemistry and heat treatment. Mill annealed Ti-6Al-4V shows a higher strain hardening rate. This is in agreement with Dieter [2] who stated that the rate of strain hardening is lower for hcp than bcc metals, as Ti-6Al-4V has a higher % vol bcc phase content, compared to CP-Ti.
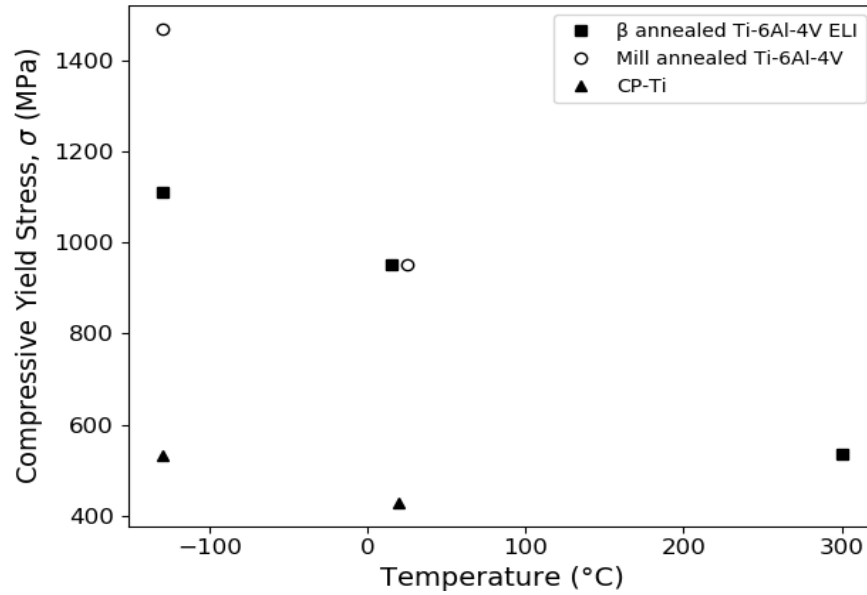
Figure 4-12. Compressive yield stress dependence on deformation temperature under uniaxial compression at 10^{-1} s^{-1} to a true strain of 0.7 of different heat treatment and chemistry.

4.7.   Strain hardening

During plastic deformation, titanium alloys undergo strain hardening. This implies an increase in the required force to impart further strain into the specimen. This is described by equation 4.1 and refers to the change in flow stress resulting from the increase in imparted true strain. Dislocations are introduced into the lattice and these as well as previous dislocations' stress fields interact with each other, giving rise to the formation of more dislocations and clusters which hamper its movement. In low SFE metals, cross-slip is not favourable, leading to a more uniform distribution of dislocations as the partials have a wider distance of separation.

$$\theta = \frac{d\sigma}{d\varepsilon} \hspace{4cm} (4.1)$$

It is essential to investigate the dislocation distribution and density as a function of imparted strain to understand and predict the work hardening response during plastic deformation.   These parameters are sensitive to the type of crystal structure, SFE, temperature and strain rate.

139

At a constant strain rate, low temperatures provide a higher strain-hardening rate, see Figure 4-13. This argument is in agreement with the literature, as material deforming at low temperatures results in higher shear stresses. These higher stresses lead to a higher dislocation density, which during interaction with other dislocations form clusters, forests, or cell arrangements. This makes it more difficult for dislocations to move through the crystal lattice. Additionally, at low temperatures, thermal fluctuations cannot assist of dislocations to move through the crystal lattice.

The rate of strain hardening remains high up to the point where dynamic recrystallization (DRX) occurs. This is the point where the dislocation density is reduced, through the nucleation of new, strain-free grains. It is in agreement with the fact that dynamic recrystallization is favoured over dynamic recovery (DRV) in low stacking fault energy (LSFE) materials [34]. Also, the rate of strain-hardening influences void nucleation [2]; reducing the strain hardening rate. This increases the stress required to nucleate a void and to, therefore, cause fracture.
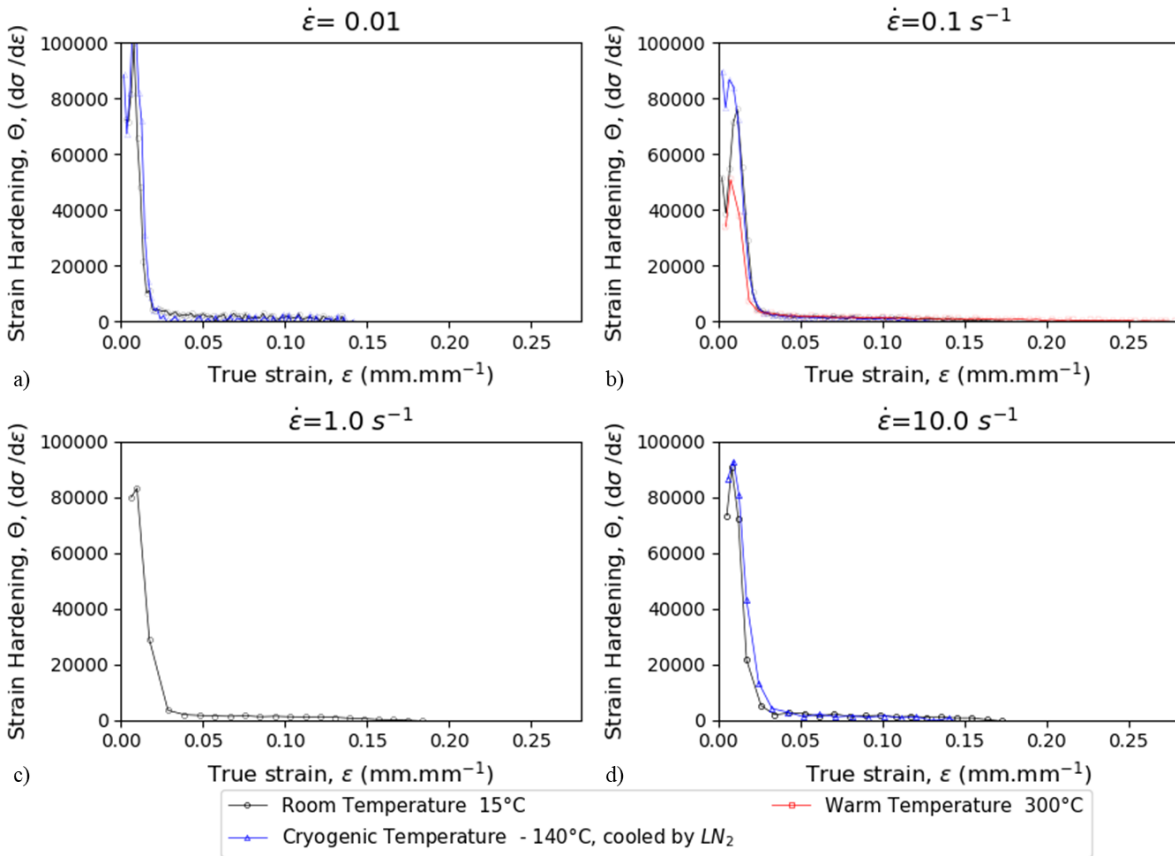
Figure 4-13. Strain hardening θ (dσ.dε^{-1}) of β annealed Ti-6Al-4V ELI during axisymmetric compression testing at different strain rates: a) 10^{-2}, b) 10^{-1}, c) 10^{0} and d) 10^{1} s^{-1}.

Figure 4-13 shows that only the initial part of the plastic deformation process, during uniaxial compression testing (at strains ~ lower than 0.03) corresponding to the initial gradient in Figure 4-2 and Figure 4-3 is where the strain hardening is increasing. This is related to the generation of dislocations in the lattice and the multiplication of the dislocations already in the material by its stress fields up to the yielding point. After this point, the strain hardening gradient shows a constant decrease up to the point of thermal softening and onset of failure as shown in Figure 4-14. The reason behind this continuous decrease may be that mechanical twinning is the dominant deformation mode in operation. As a result, the increase in the number of twin boundaries act as barriers to dislocation slip and provide a Hall-Petch type strengthening mechanism. Figure 4-14 b) compares three different temperatures (-130°C, 15°C and 300°C) at a constant strain rate of 10^{-1} s^{-1}; a much lower gradient is observed, the higher the temperature. This fact is attributed to the activation of dynamic recovery mechanisms such as cross slip and dislocation climb, taking place at higher temperatures. Therefore they impart higher strains into the lattice during deformation before catastrophic shear failure. Indeed, in the microstructure observed in Figure 4-21 at 300°C, the leading deformation mechanism at this temperature was dislocation slip. There was a low incidence of mechanical twinning.

On the other hand, at cryogenic temperatures, deformation twinning is operational at much lower levels of strain, thus leading the decrease in the strain hardening rate to start earlier. This occurs due to the introduction of twin boundaries, which work as barriers to dislocation motion as shown in Figure 4-21 at low temperatures. Higher dislocation accumulation may be generated at lower applied strain, pinning the dislocations to the twin and grain boundaries. This again hampers dislocation motion and leads to high friction stress in addition to the low thermal conductivity and low heat capacity of the specimen. Higher temperatures give rise to thermal softening, and as a consequence, catastrophic failure at smaller applied strains.

Additionally, any slip system in operation inside the twin, due to the lattice reorientation, would generate shorter slip distances. This also contributes to stress concentration sites at twin boundaries, as the dislocation slip could be stopped at these boundaries. Also, in the microstructural analysis from section 4.10 and 4.11, at a constant strain rate, the lower the deformation temperature, the greater the incidence of deformation twinning.

Figure 4-13 also suggests that for the workpiece material exposed to lower strain rates, higher levels of work hardening is experienced. This may be due to low temperatures generated during plastic deformation, which leads to lower levels of recovery by dislocation annihilation.

141

The use of negative rake angles leads to higher cutting forces [66]. This may be attributed to a deeper strain-hardened region by using negative rake angles during machining, as reported by Henriksen and Ithaca [118].

Salem reported that the strain rate continuously decreases in simple shear [44]. The fact that the strain rate only continuously decreases in Figure 4-14 may be related to the stress state generated, as the imparted plastic strain increases and leads to failure in simple shear.
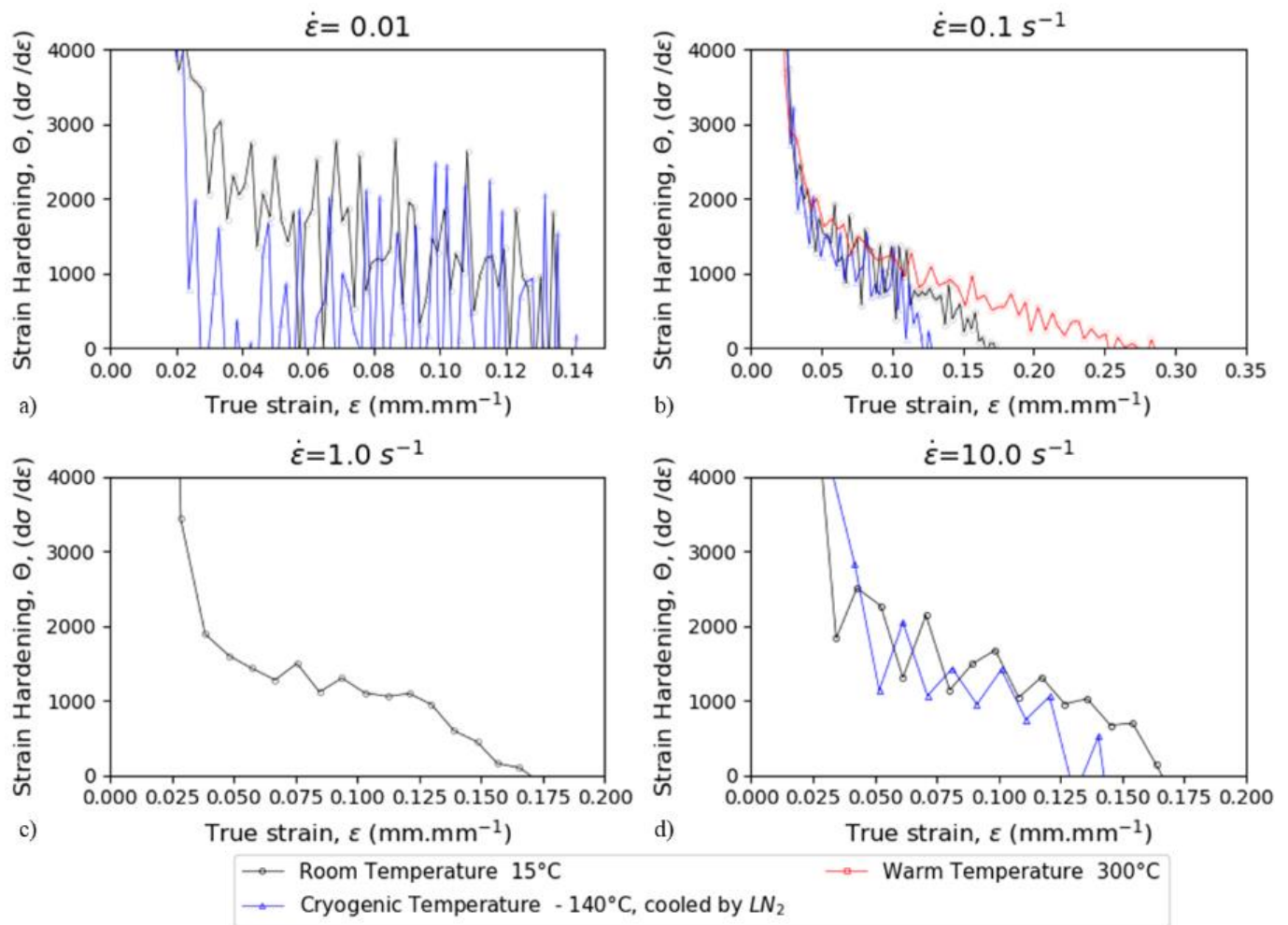
Figure 4-14. Close up from Figure 4-13after the initial strain-hardening region up to the point of $d\sigma.d\varepsilon^{-1} = 0$ or thermal softening at different strain rates: a) 10^{-2}, b) 10^{-1}, c) 10^0 and d) 10^1 s^{-1}.
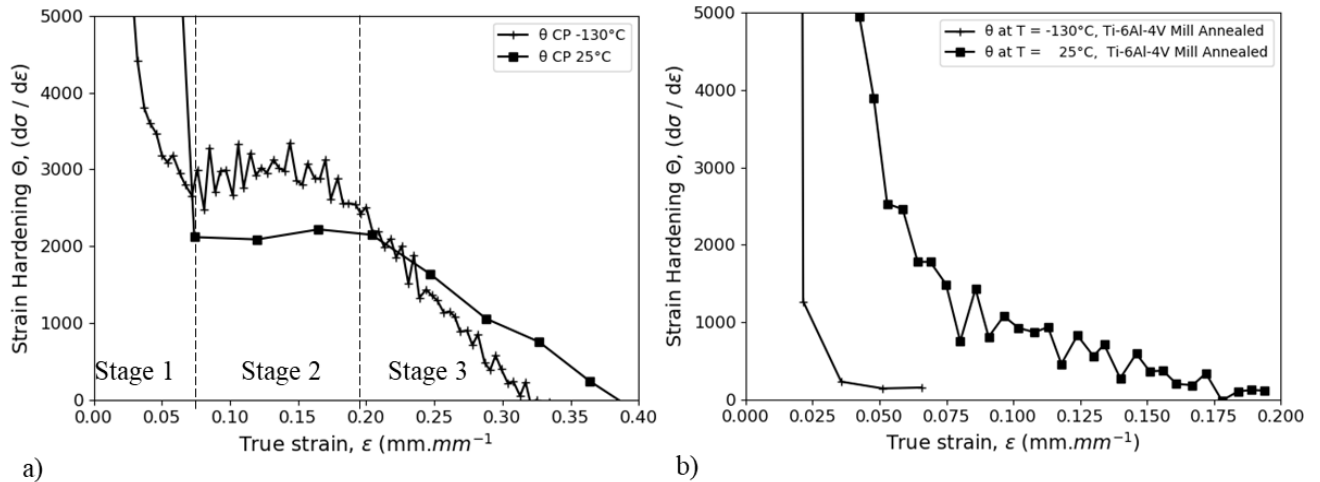
Figure 4-15. Effect of temperature on the strain hardening behaviour as a function of imparted strain on a) CP-Ti and b) Mill Annealed Ti-6Al-4V, in uniaxial compression at 10^{-1} s^{-1}.

The effect of temperature on the strain hardening behaviour of CP-Ti during axisymmetric compression is illustrated in Figure 4-15 a). Three stages are observed, in agreement with Marshall [5] and Salem et al. [44]. The first stage corresponds to a decrease in strain hardening, attributed to dynamic recovery taking place at the start of deformation. This stage operated up to levels of strain lower than 0.07. The second stage which occurred up to a strain of 0.2, is directly linked to the onset of mechanical twinning, allowing the accommodation of high strain in the lattice. A constant decrease in strain hardening characterises the third stage. This is believed to be related to the high density of twin boundaries generated in the second stage. These represent barriers to dislocation motion, leading to shorter slip lengths. The CP-Ti deformed at 25°C shows nearly a third lower strain hardening rate during stage 2. This fact may be related to more dynamic recovery processes taking place at higher temperatures than the -130°C specimen. Also, a lower volume fraction of deformation twinning is taking place. By correlating this behaviour with its microstructural evolution during orthogonal cutting (see section 4.11), it is observed that at -130°C the microstructure is highly refined (much more than at 25°C). The twin thickness appears much smaller, giving rise to a higher density of twin boundaries. On the other hand, at 25°C, the microstructure shows a lower density of mechanical twins and their thickness is much higher. This refines the grains to a lesser extent than at -130°C. Because the microstructure is less refined in stage 2, it allows longer slip distances to operate at 25°C in stage 3, allowing higher strains to be imparted. During stage 3, dynamic recovery may also take place, annihilating dislocations.

143

The strain hardening of CP-Ti is higher than that of higher content of β phase. This result is in agreement with results reported by Froes [39].

At cryogenic temperatures and at a quasi-static strain rate of 10^{-2} s^{-1}, CP-Ti can plastically deform (up to θ = 0) almost three times more than β annealed Ti-6Al-4V ELI (0.32 versus 0.12 true strain, respectively) and, at room temperature, slightly more than 2 times (0.17 versus 0.38 true strain, respectively). At cryogenic temperatures and at a quasi-static strain rate of 10^{-1} s^{-1}, β annealed Ti-6Al-4V ELI allowed the accommodation of 40.4% higher strain than mill annealed Ti-6Al-4V (0.119 versus 0.071 strain, respectively) to the point of θ = 0. This gives a great advantage to Ti-6Al-4V in a mill-annealed state over β annealed at cryogenic temperatures, as it is easier to machine, requiring lower levels of energy to generate the shear band. On the contrary, at room temperature, the β annealed condition allowed 16% lower strain accommodation in comparison with mill annealed, implying that mill annealed is more ductile at ambient temperatures than β annealed. However, it should be considered that there is a significant difference in grain size between the two heat treatments. Mill annealed Ti-6Al-4V had a grain size of 18.19 +/- 0.638 μm and β annealed Ti-6Al-4V ELI a grain size of 590.05 ± 65.45 μm with a colony size of 318 ± 48 μm (with 95% CI), α plates of 2.53 ± 0.34 μm, α phase at prior grain boundaries 8.25 μm and retained β thickness of 0.23 ± 0.11 μm. The SPD layer had a reduced α lamellae thickness of 0.086 ± 0.018 μm and the retained β thickness of 0.035 ± 0.006 μm.

The friction stress or the Peierls-Nabarro stress to move dislocations in the lattice, increases by increasing the impurity content [35] and lattice strain, resulting in an increase in stress required to move dislocations. Then, the dislocations can only move by getting out of the impurities atmosphere or unpinning the dislocations by dragging the impurities with them during their movement. Besides, the impurities can form clusters. Dislocations would then require a much higher force to move and pass these clusters. Because of the increased levels of internal energy by strain hardening and an increase in its internal stress state, the chemical reactivity in this strain-hardened microstructural region increases [2]. This may lead to enhanced diffusional processes, the subgrains providing easy diffusion paths for chemical elements.

4.8.   Strain hardening exponent, "n" parameter

The strain-hardening coefficient, n, has a strong sensitivity to the deformation temperature as shown in Figure 4-16. This parameter is represented in equation (4.2), and it is calculated by obtaining the gradient between the natural logarithm of stress vs natural logarithm of

strain, see equation (4.3). As seen in equation (4.4), it has a different meaning from the strain-hardening rate (θ). The higher the temperature, the higher the coefficient. The relationship is shown in equation 4.4, obtained from equation 4.2 and 4.3. Thus at lower values of n, higher strain rate hardening occurs in the specimen lattice during plastic deformation. Whereas at room temperature, the strain rate appears to have a much lower effect on the coefficient. At cryogenic temperatures, a slightly higher effect, especially comparing the lower strain rate 10^{-2} to 10^{-1} s^{-1} is observed. Only quasi-static strain rates were used in this investigation. However, study at much higher strain rates or dynamic deformation is highly desirable to more closely approach the behaviour which will be experienced during metal cutting (high strain rates from 10^{3} to 10^{5} s^{-1} [2], [45]). This will also allow phenomenological equations to be applied, which will obtain better predictions via FEM modelling.

$$\sigma = K\varepsilon^{n} \tag{4.2}$$

$$n = \frac{d(log\sigma)}{d(log\varepsilon)} = \frac{d\,ln\sigma}{d\,ln\varepsilon} \tag{4.3}$$

$$n = \frac{\varepsilon}{\sigma}\frac{d\sigma}{d\varepsilon} \tag{4.4}$$
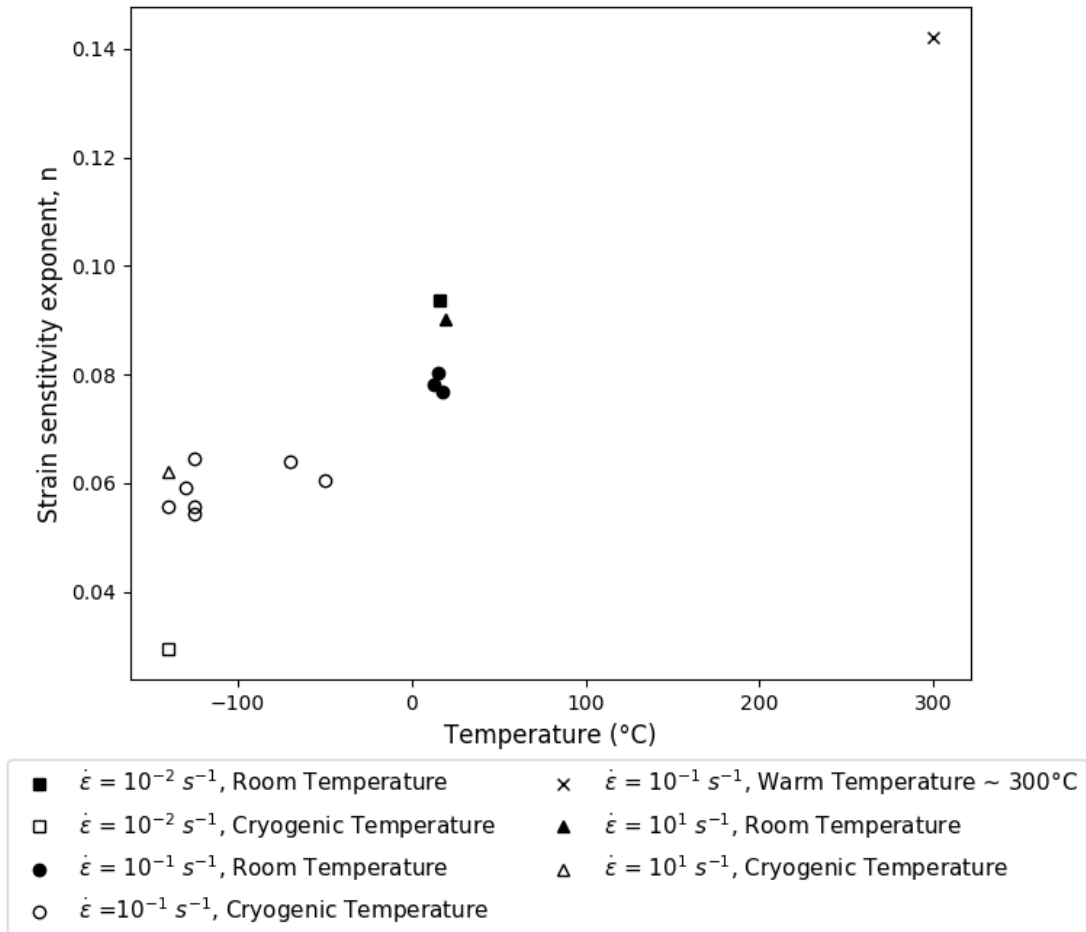
Figure 4-16. Strain sensitivity exponent as a function of test temperature and strain rate.

4.9. Strain rate sensitivity, "m" parameter

According to Dieter et al. [45] the strain rate sensitivity parameter (m)'s influence on yield strength strongly increases with temperature. This effect has been observed by comparing room temperature and cryogenic temperature. A 33% increase in m value was observed at 15°C in comparison to -140°C, Figure 4-17. With the increase of m, there is a reduced tendency for localised deformation; it allows higher elongations without causing plastic instability. Dieter et al. [45] report that strain localisation from shear banding can be delayed at higher m values and that m=1 corresponds to the ideal superplastic behaviour. Indeed, metal cutting in conditions where m values are high would increase the ductility of the metal and lower its flow stress, delaying the fracture process in shear. Metal cutting

146

conditions with lower m values are preferred, as they require lower energy to reach instability in shear. The values obtained in this investigation are very low, indicating a low sensitivity to strain rate in terms of cutting forces.

   The lower m value at low temperatures, suggests that increasing the surface speed and consequently the strain rate, would have a lesser effect compared to room temperature on the cutting forces during shearing.
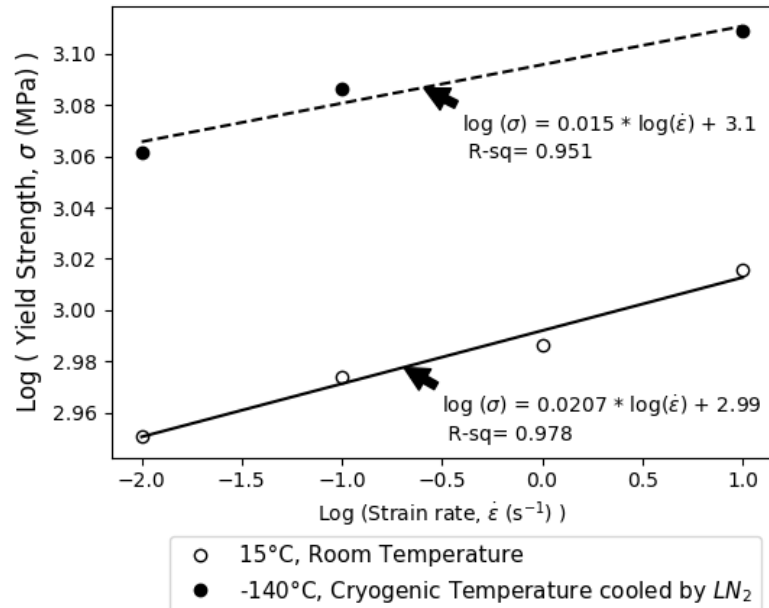
Figure 4-17. Influence of temperature on the strain rate sensitivity parameter, m.
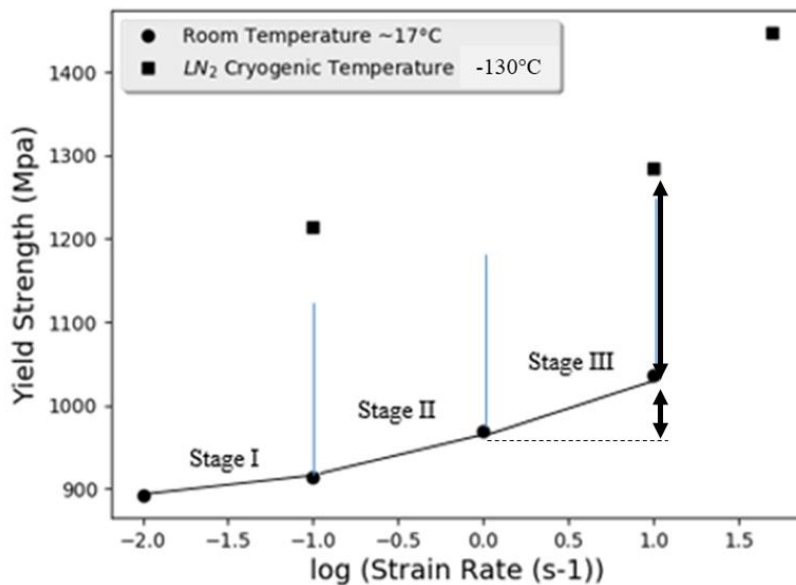
Figure 4-18. Compressive yield strength as a function of strain rate at 17°C and -130°C.

147

The flow behaviour as a function of strain rate was as reported by Bai and Dodd [47] who described the occurrence of three stages in the flow behaviour by varying strain rate. Figure 4-18 shows:

- Stage I: It represents an insensitive flow. However, in this alloy, there is a slight dependence on strain rate at low strain rates. Plastic flow has only a small thermal dependence in this region.
- Stage II: It is a thermally activated region. Thermal energy is required to enable dislocations to overcome obstacles via cross slip.
- Stage III: Characterized by phonon drag on dislocations. It is a dislocation rate controlling mechanism with rapid increase as strain rate increases.

Marshall [5] suggested the correlation of the Cockcroft-Latham parameter to other deformation parameters such as yield strength to determine the machinability of an alloy. Concerning yield strength, it does follow an inverse linear relationship, as observed in Figure 4-19 a). In terms of the degree of strain for the onset of thermal softening (Figure 4-19 b), it follows a positive linear relationship. With increasing energy for catastrophic shear failure, an increase in strain is required to reach the onset of instability or thermal softening. This behaviour may be related to the dynamic recovery processes taking place at higher temperatures. This allows uniform softening, so higher ductility and lowers the forces, thus making it harder to generate a localised shear band. This behaviour should be corroborated at higher strain rates to relate it to machining conditions.
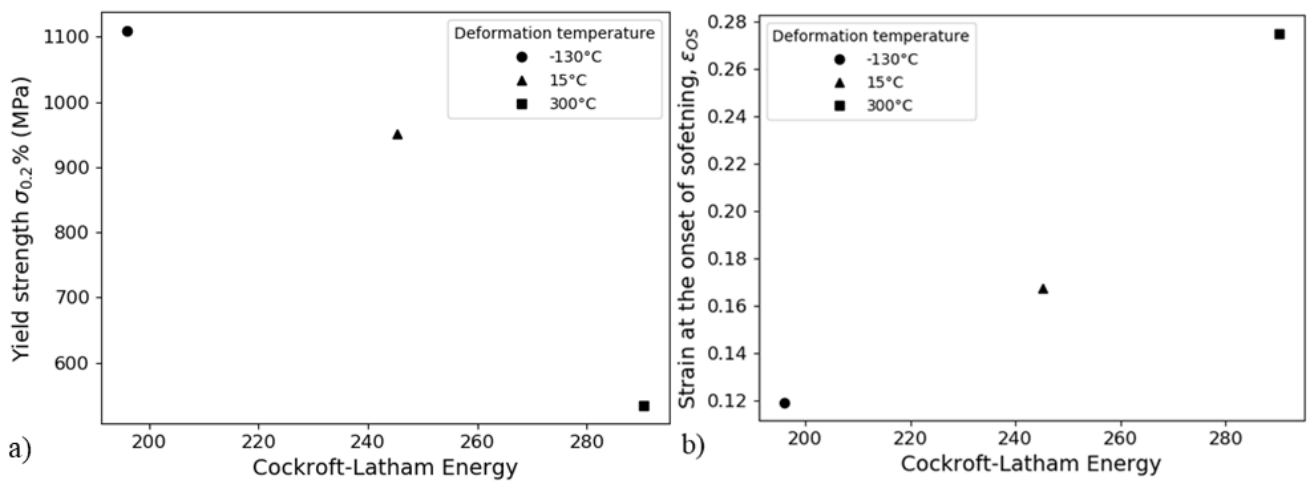
Figure 4-19. Cockcroft-Latham parameter as a function of a) yield strength and b) strain for the onset of thermal softening on specimens deformed at a strain rate of 10^{-1} s^{-1}.

4.10. Zener-Hollomon parameter (Z) influence

The combined effect of deformation temperature and strain rate was investigated through the Zener-Hollomon parameter (Z) as illustrated in Figure 4-20, which shows a behaviour of three different rates between the yield strength and ln(Z). The first stage shows linear behaviour; the second shows a decreasing rate and the last stage, shows an accelerated increase in flow stress. The lower the temperature and the higher the strain rate, the higher the Z value was generated. Whereas at a warm temperature of 300°C, ln(Z) provided the lowest value, near 40, at room temperature ln(Z) values were between 60-80 and at cryogenic temperatures, it provided much higher values between 140-180.

It can be observed that temperature has a higher influence on the ln(Z), which would imply lower the temperature conditions are more prone to grain refinement. That is the case in compression tests of fcc pure copper at high Z values, which show enhanced grain refinement in microstructures. It was found that at lower ln(Z) the grain refinement mechanism is dominated by slip, and at high ln(Z), deformation twinning plays a more critical role. The estimation of recrystallized grain size depends on initial grain size and conditions of strain rate and temperature is shown in Equation (4.5).

$$\frac{d_{recrystalized}}{d_{initial}} = 10^3 Z^{-1/3} = 10^3 \left[\dot{\varepsilon} \exp\left(\frac{Q}{RT}\right) \right]^{-1/3} \tag{4.5}$$

Li et al. [139] attribute the higher yield strength at higher ln(Z) values to the grain refinement as well as the presence of nanoscale twin "bundles". The author considers that the presence of nanoscale deformational twin bundles is the mechanism by which coarse grains refine into nanoscale grain sizes, as Ti-6Al-4V is a low SFE metal which typically develops a fine lamellar subgrain structure composed of microtwins [2].
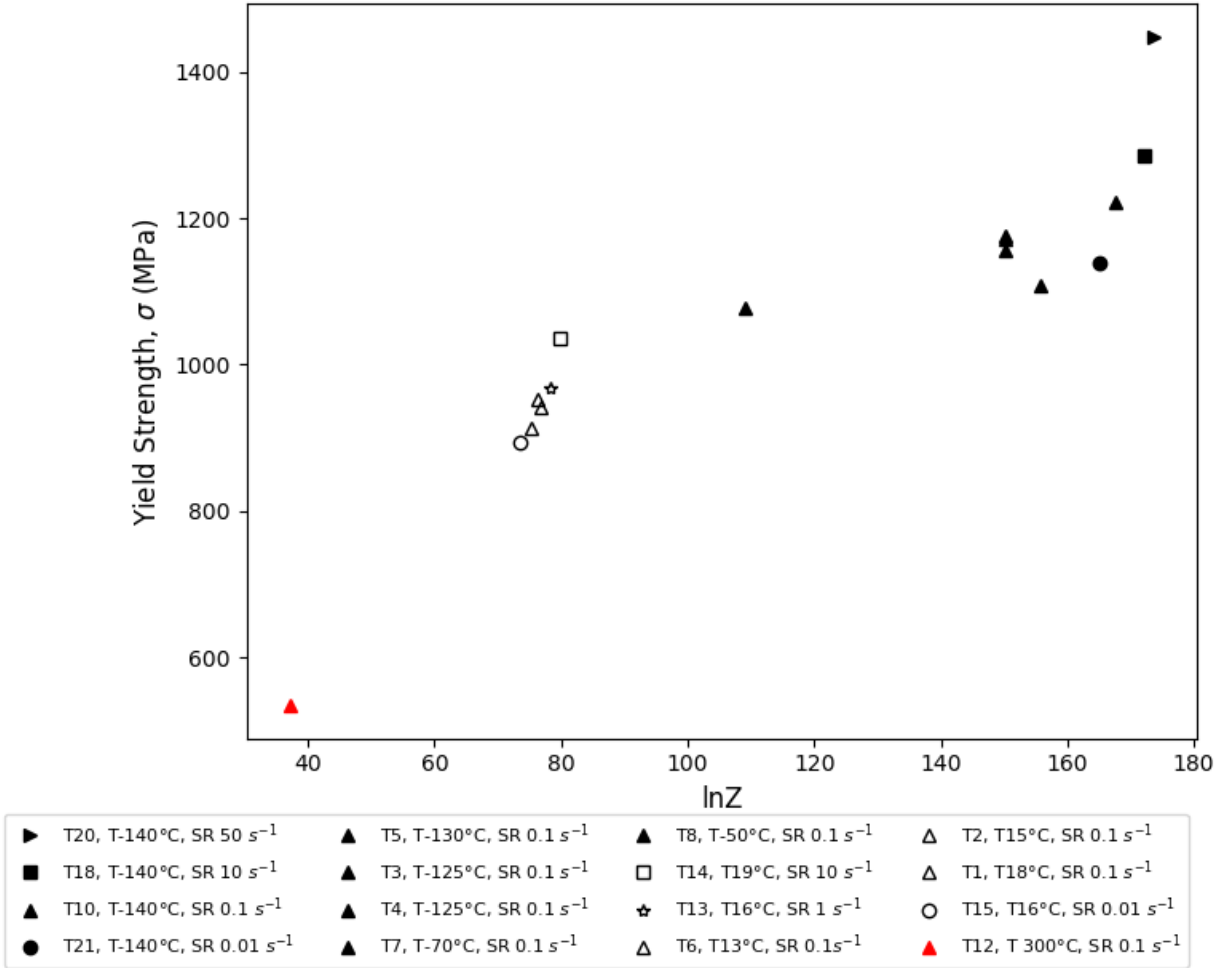
Figure 4-20. Dependence of temperature and strain rate included in the Zener-Hollomon parameter on yield strength on the compression specimens at a true strain $\varepsilon = 0.7$, $\dot{\varepsilon} = 10^{-2}$, 10^{-1}, 10^0, 10^1, 50^1 s^{-1} and cryogenic temperature -140°C, -130°C, -125°C, -70°C, -50°C and room temperature 13 to 19°C.

4.10.1. Effect of Z on the Microstructure Evolution

The process conditions corresponding to higher values of ln(Z) are more likely to undergo dynamic recrystallization. Higher values represent higher dislocation densities in the lattice of the deformed material, as higher forces are required for plastic deformation as seen in Figure 4-20. Cotterill and Mould [53] state that the reduction in temperature during deformation leads to higher dislocation densities, leaving higher strain energy in the lattice with a more uniform distribution of dislocations. This residual energy is retained in the subsurface immediately adjacent to the cutting edge. During cutting, this leads to recrystallization at low strain levels, generating much finer grain sizes. These are beneficial

as they provide higher strength and more ductility, which implies that the components can withstand longer fatigue life and/or operational time.

Under the right conditions of high strain rate and low temperatures, even high SFE materials such as Cu could give rise to recrystallized nanocrystalline grains [140]. Zhang et al. [140] characterised the microstructure on Cu-Al of low SFE samples, and they observed in dynamically deformed samples the dominant deformation mechanism was mechanical twinning at nanoscale which enhanced dynamic recrystallization generating lower equiaxed strain-free grain sizes. At room temperature and quasi-static compression, the leading deformation mechanism was dislocation slip.

In this investigation, at a constant strain rate of 10^{-1} s^{-1}, the reduction in temperature during quasi-static uniaxial compression enhanced the occurrence of deformation twinning, as observed in Figure 4-21. At higher temperatures, dislocation slip was the most common way of accommodating the imparted strain. In low SFE materials, such as titanium alloys, subgrain formation is more stable than in higher SFE materials. These subgrains serve as sinks for dislocations [141]. As more dislocations are accumulated, there is more lattice rotation between subgrains, leading to the formation of HAGB. The shear band region contains a large fraction of fine equiaxed grains, which provide evidence that dynamic recrystallization (DRX) is the dominant restorative mechanism.

The effect of strain rate on the microstructural evolution at constant cryogenic temperature -130°C does not show a marked difference, as shown in Figure 4-22. Two distinctive observations were made. Firstly, at low temperatures deformation twinning is dominant. Secondly, at the highest strain rate tested, 50^{1} s^{-1}, there is evidence of recrystallization in the centre of the shear band after catastrophic shear failure. Higher strain rates may have introduced a higher dislocation density, thus enhancing the degree of higher grain boundary misorientations. There is a high twin density, and these deformation twins traverse completely the prior β grain, with the retained β not being a strong barrier to their growth.

The effect of strain rate at room temperature is shown in Figure 4-23. The higher the strain rate, the higher the number of ASBs generated. The occurrence of dislocation slip and mechanical twinning is observed in all the specimens. The shear band appears to have undergone DRX.

During quasi-static compression at 10^{-1} s^{-1} the increase in temperature from the start of the test to the onset of thermal softening generated a slight difference in temperature (8% or 4.9°C) at low and room temperature as shown in Figure 4-25. This figure also suggests that the increase in temperature started just after the yield point. At low temperatures, an increase of 60°C was reached (-114.5°C to 53.9°C) in only 1.2 sec and at room temperature

an increase of 65.5°C (11.1°C to 76.6°C) in 1.7 sec. This similar increase may be related to the quasi-static deformation at low speed, and the fact that there is sufficient time to conduct the heat to the environment or the tool, deforming on lower friction conditions. Although this difference (only 5.5°C) may seem insignificant, during machining, many chips are formed. As a result of the increase in thermal conductivity and diffusivity of titanium alloys with the increase in temperature (for Ti-6Al-4V it is estimated 0.016 cm^2s^{-1} at -130°C and 0.0255 cm^2s^{-1} at 20°C), heat may be more uniformly distributed during machining at room temperature. This effect could give rise to the activation of softening mechanisms of plastic deformation. This increases ductility and leads to greater energy being needed to reach instability in shear and to, therefore, cause a local fracture. Additionally, this effect may cause tensile residual stresses on the subsurface workpiece, increasing solid-state diffusion mechanisms between the tool, workpiece and chip materials, leading to earlier tool failure. Oxygen or nitrogen pick up in titanium is more rapid at high temperatures. This will cause embrittlement in the freshly created surface, locally reducing its toughness. If dynamic recrystallization has occurred, the grain size in the subsurface layers will be much higher as the temperature may provide energy for grain growth.

Figure 4-24 shows the imparted plastic strain into the specimen in a quasi-static uniaxial compression test in β annealed Ti-6Al-4V ELI at 10^{-1} s^{-1} to a true strain of 0.7 at different temperatures: -150°C, 20°C and 300°C in a 2D model in DEFORM^{TM}. The simulation was fitted to the experimental data through a Norton-Hoff model. The comparison of the imparted strain at different temperatures suggests that at low temperatures, the plastic strain in the specimen is higher in value and area, implying higher strains from machining at cryogenic temperatures. The microstructures of specimens deformed under similar conditions are shown in Figure 4-21.
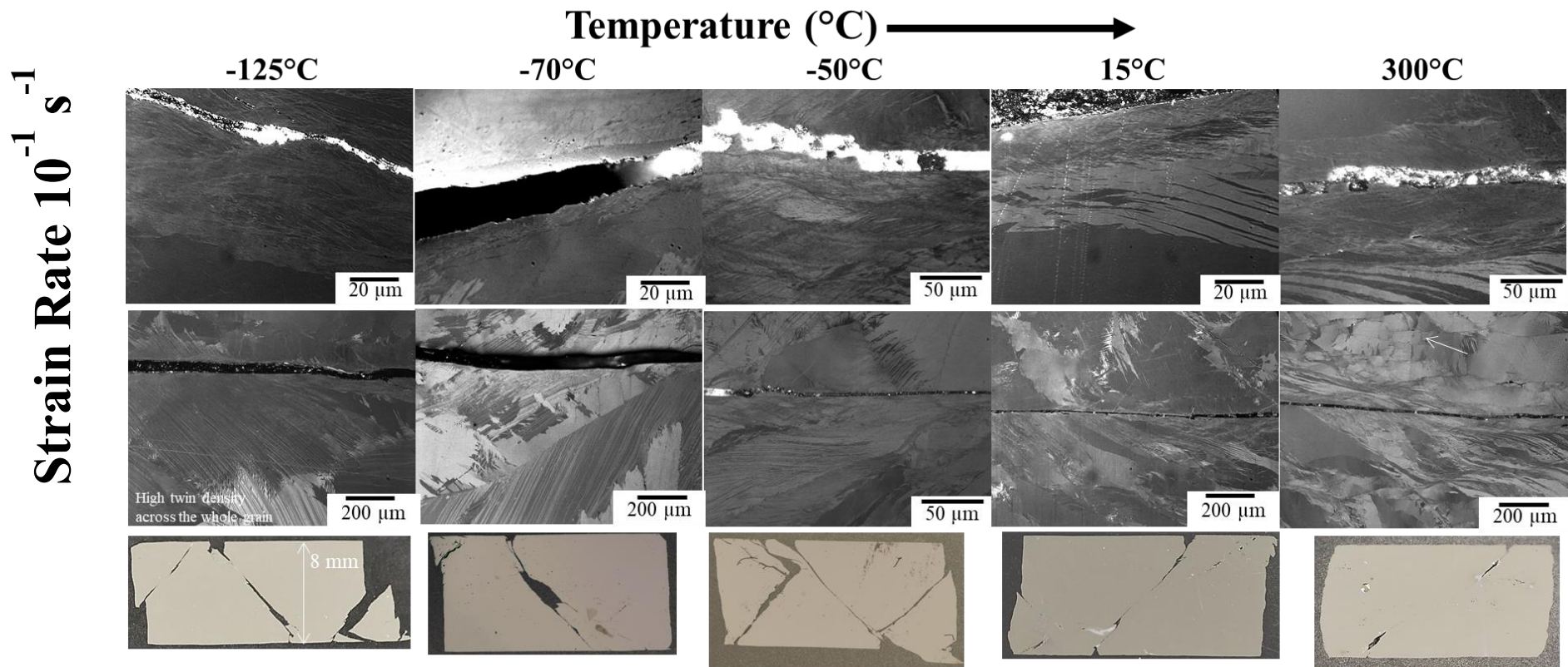
Figure 4-21. Effect of test temperature on uniaxial compression of β annealed Ti-6Al-4V ELI at a strain rate of 10^{-1} s^{-1} to a true strain of 0.7.
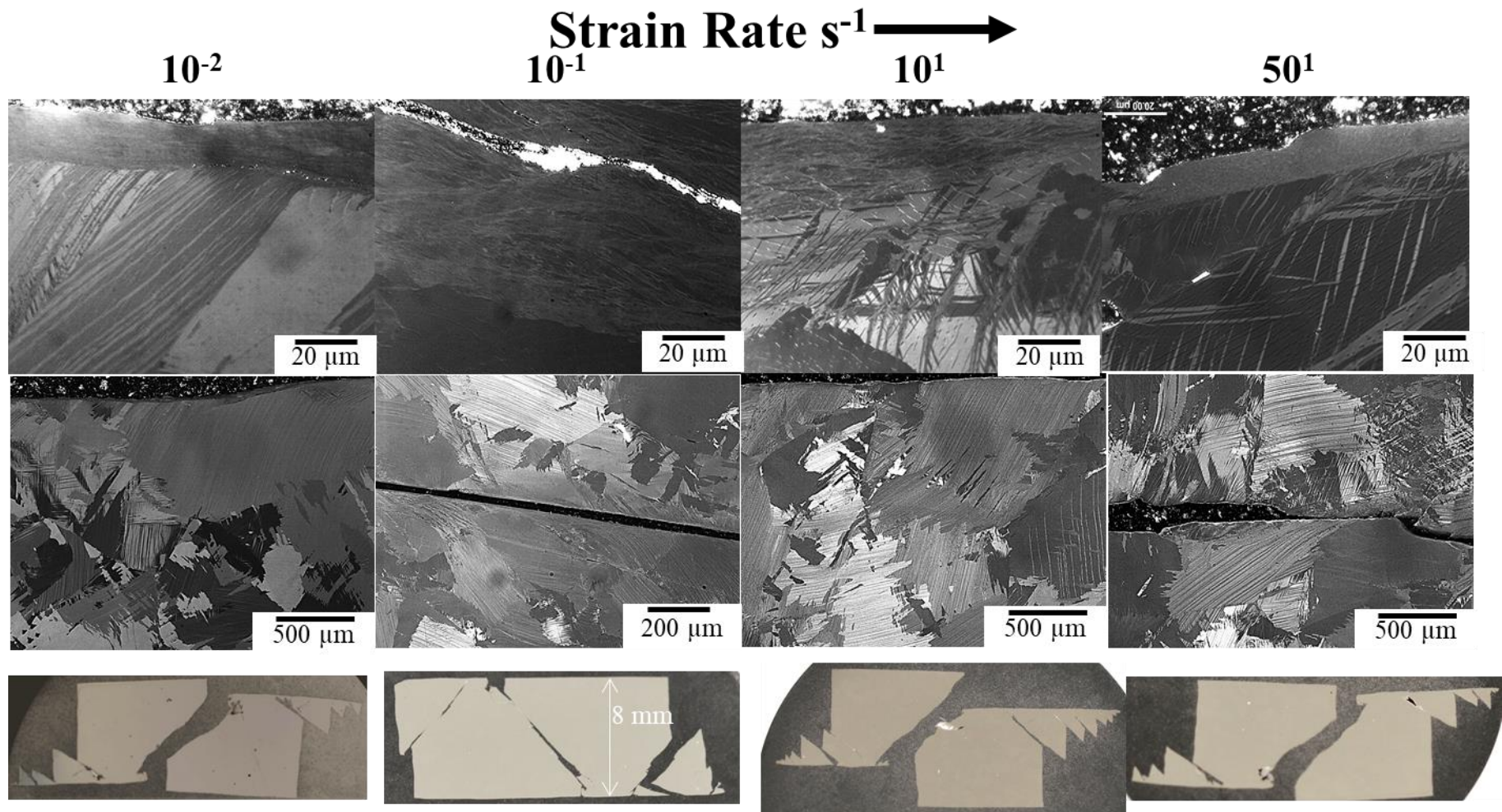
Figure 4-22. Effect of strain rate on plastic deformation of β annealed Ti-6Al-4V at cryogenic temperature ~ -140°C to a true strain of 0.7.
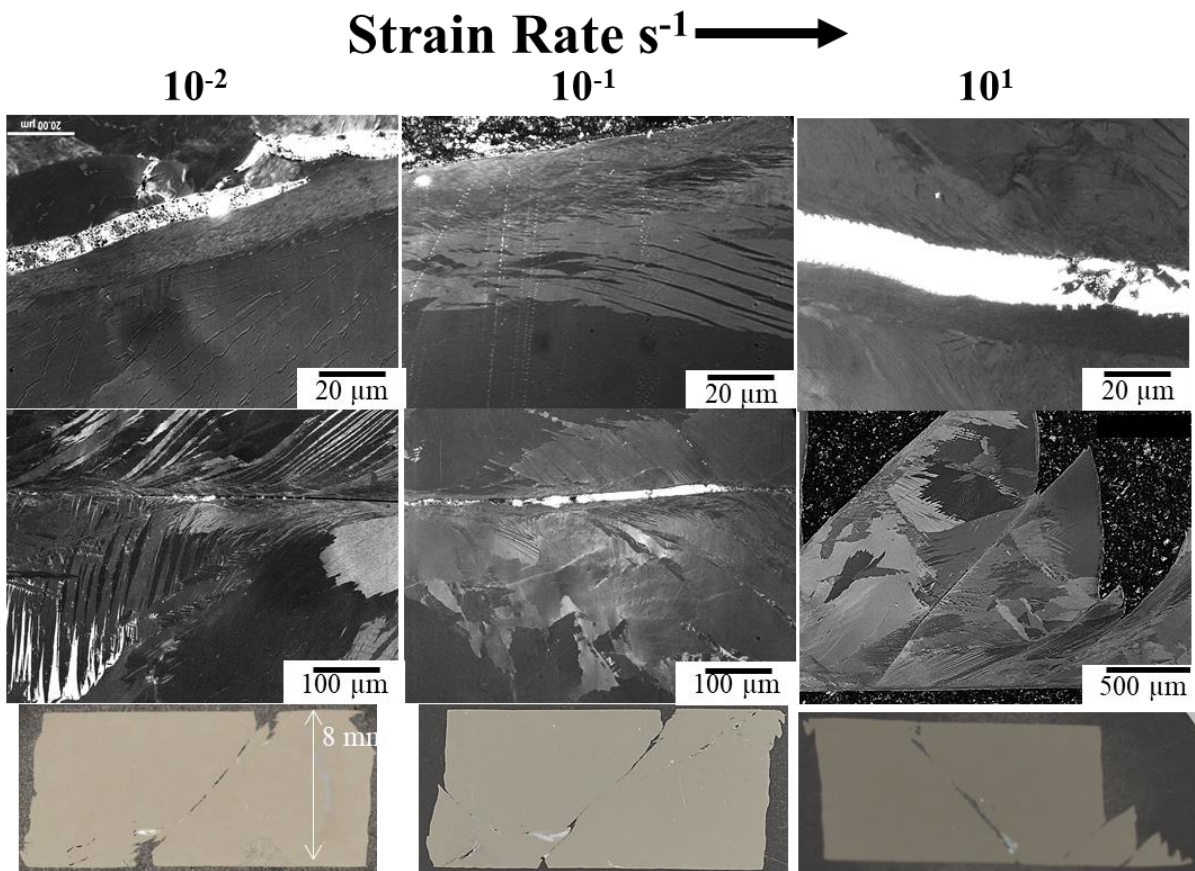
Figure 4-23. Effect of strain rate on room temperature uniaxial compression of β annealed Ti-6Al-4V ELI to a true strain of 0.7.
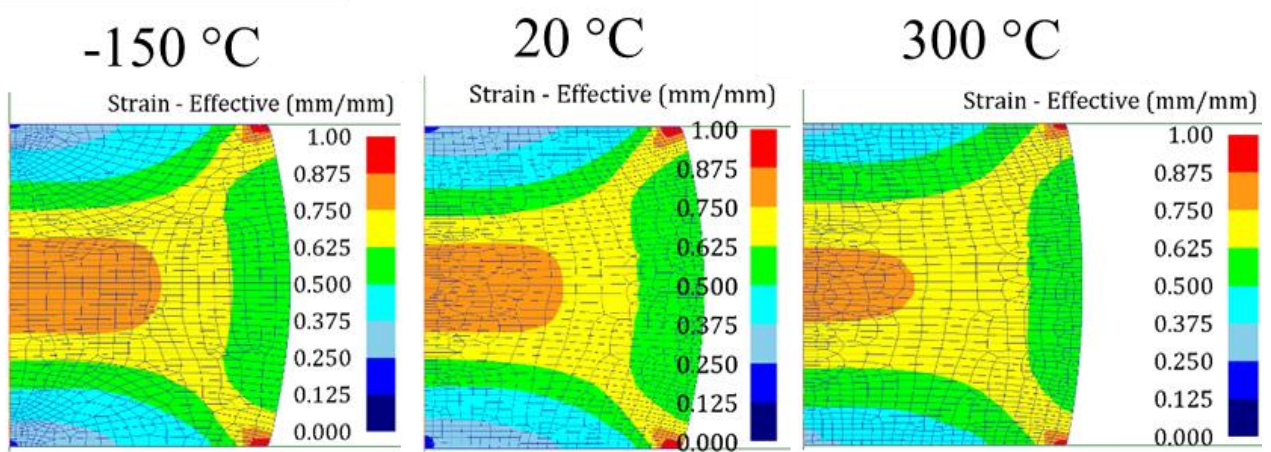
Figure 4-24. Imparted strain in uniaxial compression tests in β annealed Ti-6Al-4V at 10^{-1} s^{-1} to a true strain of 0.7 at temperatures: -150°C, 20°C and 300°C in a DEFORM^{TM} simulation.
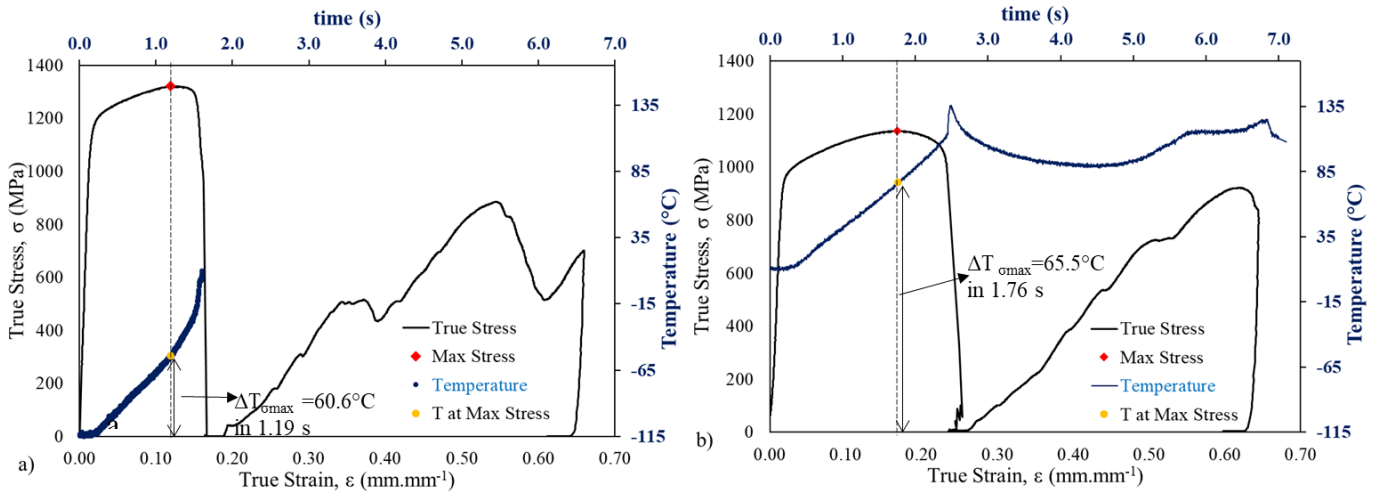
Figure 4-25. Increase of temperature during uniaxial quasi-static compression at 10^{-1} s^{-1}: a) -114.5°C and b) 11°C.

A relationship could be established between the log Z and the DRX grain size, as shown in Figure 4-26. It may help to determine the parameters to engineer the recrystallized grain size in machined components and establish correlations between different alloy chemistries to such parameters.
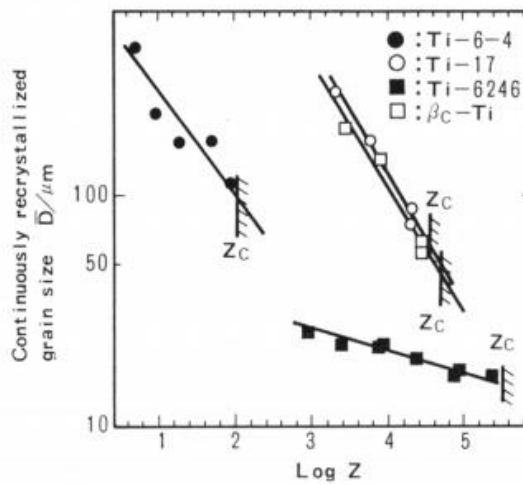
Figure 4-26. A relationship between the log Zener-Hollomon parameter and the dynamically recrystallized grain size [142].

4.11. Microstructural evolution by plastic deformation during axisymmetric compression in the region of intense shear

In order to clearly show the influence of deformation temperature at constant strain rate, only 15°C/room temperature and -130°C/cryogenic temperature will be described in this section. Cross-polarised light micrographs as experimental evidence show that plastic deformation at

156

the lower temperature is governed by mechanical twinning. This fact gives rise to a higher twin density per grain below the shear band, producing needle-like twins. The shear band is observed to be more localised as shown in Figure 4-28 d). This image shows evidence of dynamic recrystallization as the grain size observed is smaller than that at room temperature. In contrast, plastic deformation at higher temperatures, (15°C in Figure 4-28 a) and b)) shows a lower twin density, suggesting a combined mechanism of dislocation slip and mechanical twinning operating at the same time. It shows that mechanical twinning aids plastic deformation through crystal lattice reorientation. It shows lenticular twin morphology. The observed shear band is wider, which makes the development of the shear band more difficult. At -130°C, the recrystallized grain size from the shear band region seems to be smaller than at 15°C. A backscattered electron SEM image corresponding to the shear band of the specimen at -130°C and at $\dot{\varepsilon} = 10^{-1}\,\mathrm{s^{-1}}$ is shown in Figure 4-29. It shows a microstructural graded region. The first 4 μm is constituted of highly elongated retained β with recrystallized nanoscale grains, which could also be thought as a reduction in the spacing of the α phase between the retained β. Below this region, there is a region of higher diameter subgrain boundary, accompained with a higher dislocation density, thus it is a strain-hardened region.

This may be related to the fact that at low temperatures higher shear strains and stresses are generated, leading to greater stored energy and dislocation density accumulation in the subgrains, providing the driving force for increased misorientation in the newly recrystallized grains, in comparison to higher temperatures.

It is hypothesised that the higher yield strength generation at low temperatures may be attributed to the hampering of dislocation motion through the high twin density generated during plastic deformation. This is in agreement with Salem et al. [44] who found an increase in strain hardening at the onset of mechanical twinning.

At low temperatures, localisation of plastic deformation is reached at lower plastic strains. One reason could be due to the atoms being more closely spaced; there are less vibrational forces (phonons) and the CRSS for twinning is lower than for slip. The army movement of atoms which is characteristic of twinning might be able to displace for longer distances and make use of lower energy, which is in good agreement with Glen [62] who reported that CP-Ti needed much lower energy to fracture on a Charpy impact test at cryogenic temperatures (see Figure 2-41).

Figure 4-27 shows different regions of plastic deformation in an uniaxial compression test, with the region in direct contact with the platens showing little deformation, especially if there were high friction conditions. Moderate regions of deformation appear to the side of the cylinder and regions of localised deformation originated from the edges and traversed the whole structure. All images shown in Figure 4-28 correspond to the intense shear region, which had fractured during testing.
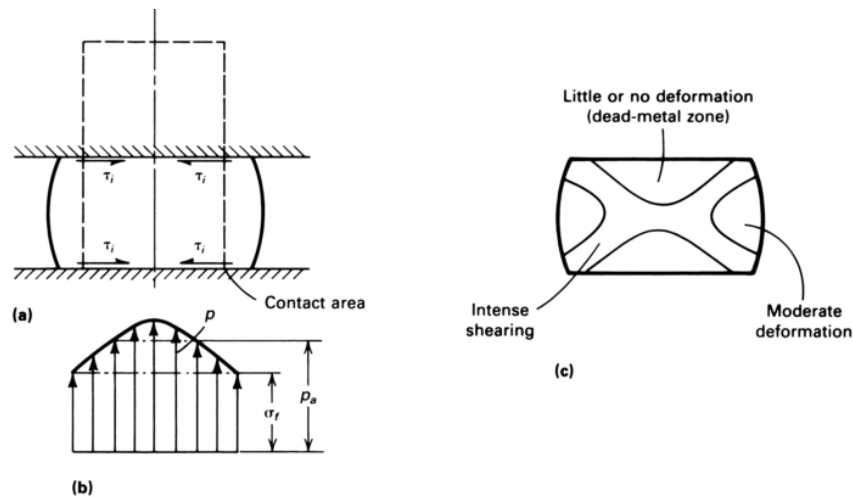
Figure 4-27. Effect of friction during plastic deformation in uniaxial compression of a cylinder a) shear stress direction, b) increase in internal pressure and c) inhomogeneous deformation, localised in narrow bands of concentrated shear [45].
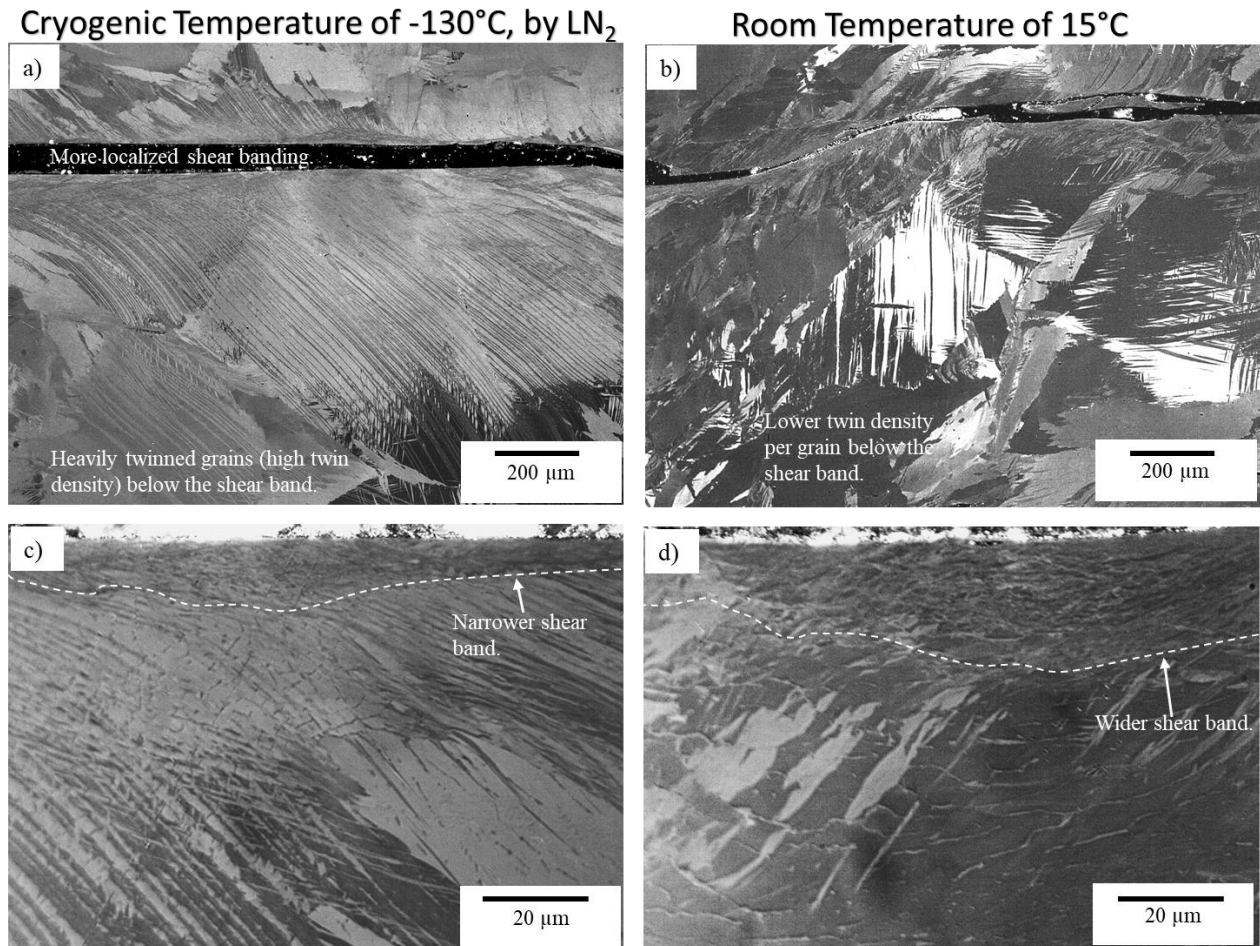
Figure 4-28. Light micrographs corresponding to the cross-sectional microstructure of the principal shear band generated during asymmetrical compression testing to a true strain of 0.7 at a strain rate of 10^{-1} s^{-1}: a) & c) test at a cryogenic temperature of -130°C, cooled by LN$_2$, and b) & d) at room temperature of 15°C.

Figure 4-30 shows a BSE SEM image generated on a uniaxial compression test at 15°C and 10^{-1} s^{-1}. The region corresponds to the intensely localised shear as shown in Figure 4-27. It is observed that a nearby adiabatic shear band divided the specimen into two regions. Each region is composed of similarly graded microstructures. The first region, A, has experienced higher levels of plastic deformation and the second subsurface region, B, lower levels, revealing less damage to the microstructure.

By comparing Figure 4-28, Figure 4-29 and Figure 4-30, it is clear that specimens deformed at low temperatures generated the smallest SPD or dynamically recrystallized region. Figure 4-28 c) at -130°C has an SPD region of 13.6 μm, while Figure 4-28 d) at 15°C has an SPD region of 25.3 μm, nearly twice. However, more measurements would need to be taken to take account of the effect of the crystallographic orientation as this has a significant effect on the accommodation of plastic strain. Projectile impact testing in CP-Ti and Ti-6Al-4V generated shear bands with widths of between 1 and 10 μm [47]. As this work refers to deformation under quasi-static loading, it is likely that the shear band widths are thicker as deformation occurred over lower strain rates. There was more time for the generation of dislocations into the subsurface and the accommodation of plastic deformation.
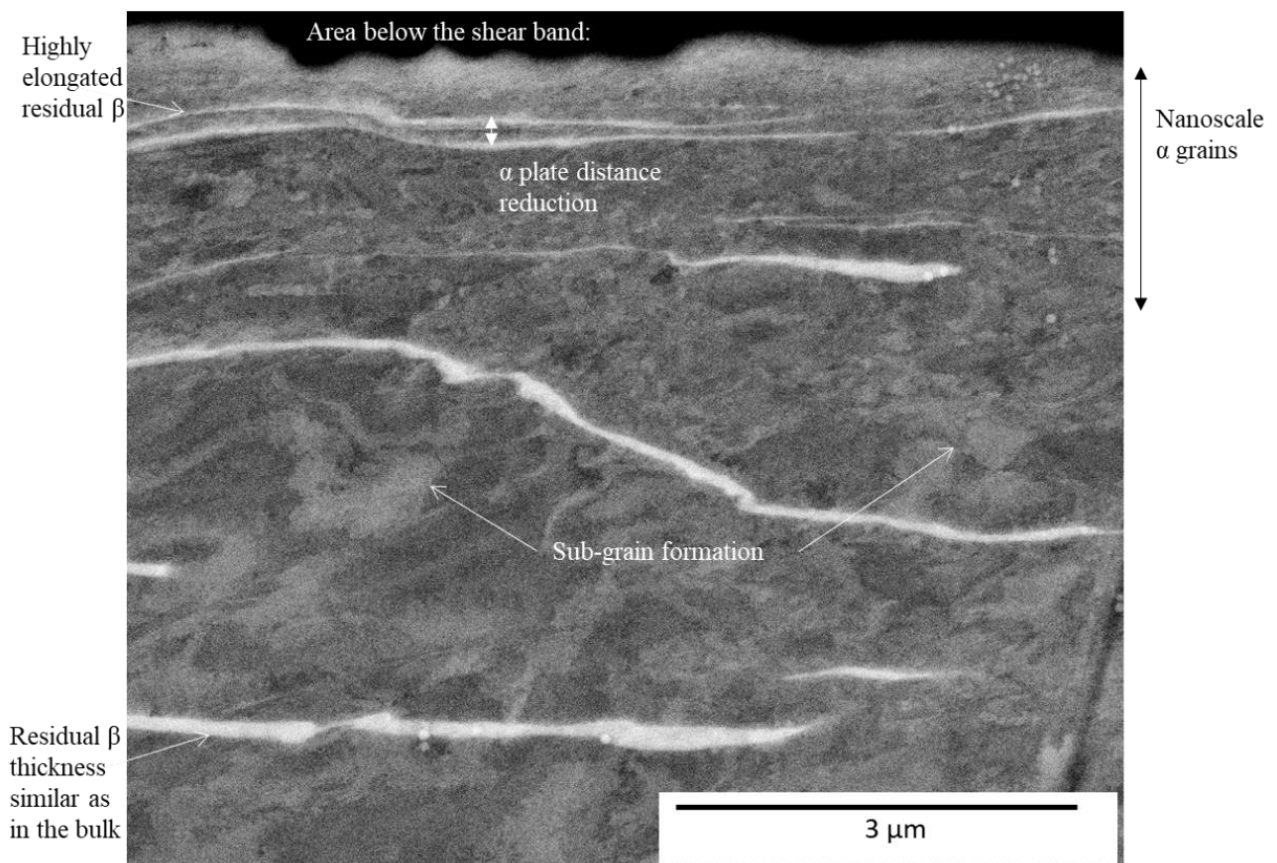
Figure 4-29. Backscatter electron image of small grains formed observed right below the shear band and between the alpha lamellae, corresponding to axisymmetric compression at cryogenic temperature -130°C, at $\dot{\varepsilon} = 10^{-1}$ s^{-1}.

This result is in agreement with Lee et al. [143], who showed a reduction in ASB thickness with lowering the deformation temperature during uniaxial compression in a split-Hopkinson bar of a lamellar Ti-6Al-4V alloy at a high strain rate of 2.5 x 10^3 s^{-1} at 500°C and 1100°C. The ASB thickness at 500°C was 14.7 µm, and at 1100°C was 45 µm. They showed a substantial increase in hardness in the centre of the band with nearly 20% higher harness at 500°C. The author believes that as the β transus for Ti-6Al-4V is near 995°C [21] the ASB formed at 1100°C is from a phase transformation, the lower hardness in the centre may be due to the reduction in the density of defects (dislocations and vacancies) due to restorative mechanisms such as DRV or DRX. The ASB formed at 500°C is severely plastically deformed in shear. They did not provide evidence from high-resolution microscopy.

These results are also in agreement with Song and Gray's results [144], who report that specimens deformed at low temperatures and high strain rates lead to mechanical twins that are homogeneous and have low thickness.

Song and Gray [144] argue that for twins to nucleate, their require the assistance of dislocation slip, however at low temperatures, due to high flow stresses reached, the assistance of dislocation slip is not always required for twin nucleation. This suggests the lower CRSS for twinning at low temperatures than for slip.
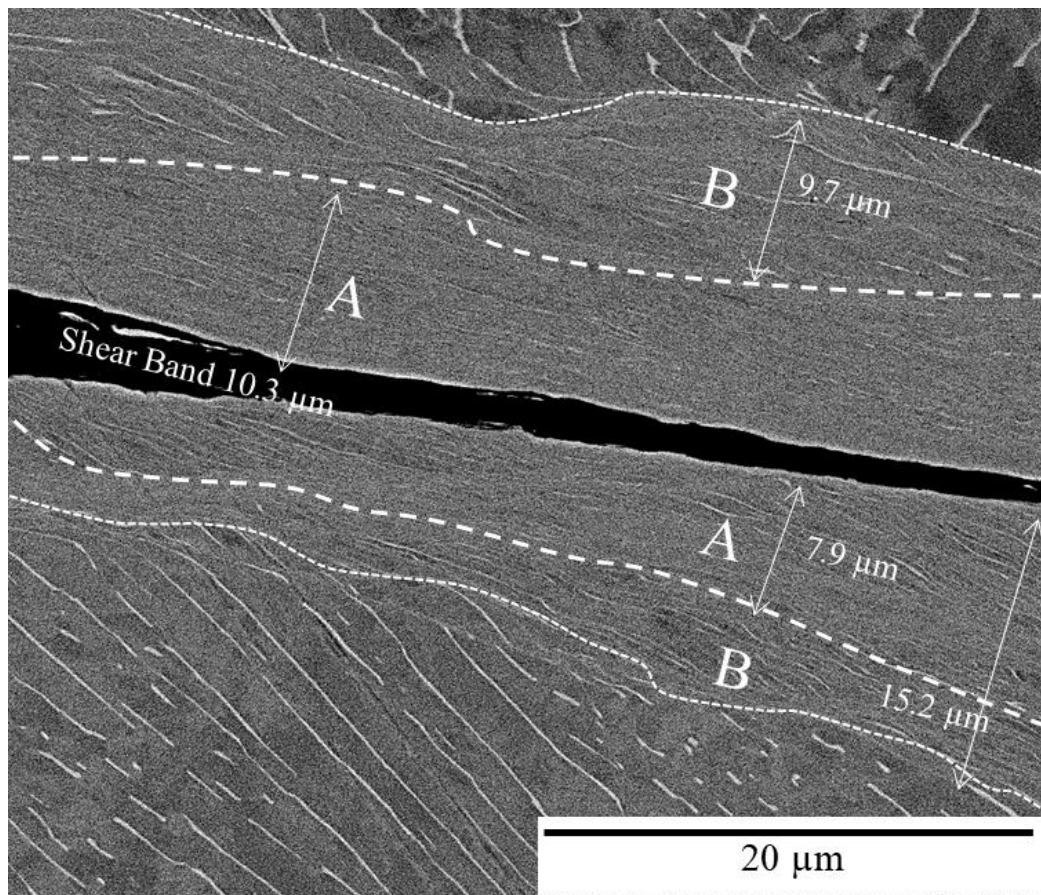
Figure 4-30. BSE Micrograph illustrating the shear band formation in β annealed Ti-6Al-4V ELI under axisymmetric compression at room temperature of 15°C at $\dot{\varepsilon} = 10^{-1}$ s^{-1}.

The effect of temperature on shear band formation in the axisymmetric compression of β annealed Ti-6Al-4V is schematically illustrated in Figure 4-31. Two temperatures are compared: cryogenic -140°C, reached by cooling with LN_2 and ambient temperature. Plastic deformation at low temperatures generated a thinner shear band. This is also shown as an SPD region and the region below the SPD region was heavily twinned. The twins completely traverse the grains, and there is a high density of twins in each grain. The room temperature condition generated a slightly larger SPD region. A distinctive feature at room temperature was the strain localisation in many places along the SPD region. Below this region, mechanical twinning appeared but with a lower twin density inside each grain and of a higher thickness (a lenticular morphology). The uppermost subsurface region shows regions of strain localisation. These may result in a local reduction in load-carrying capacity.
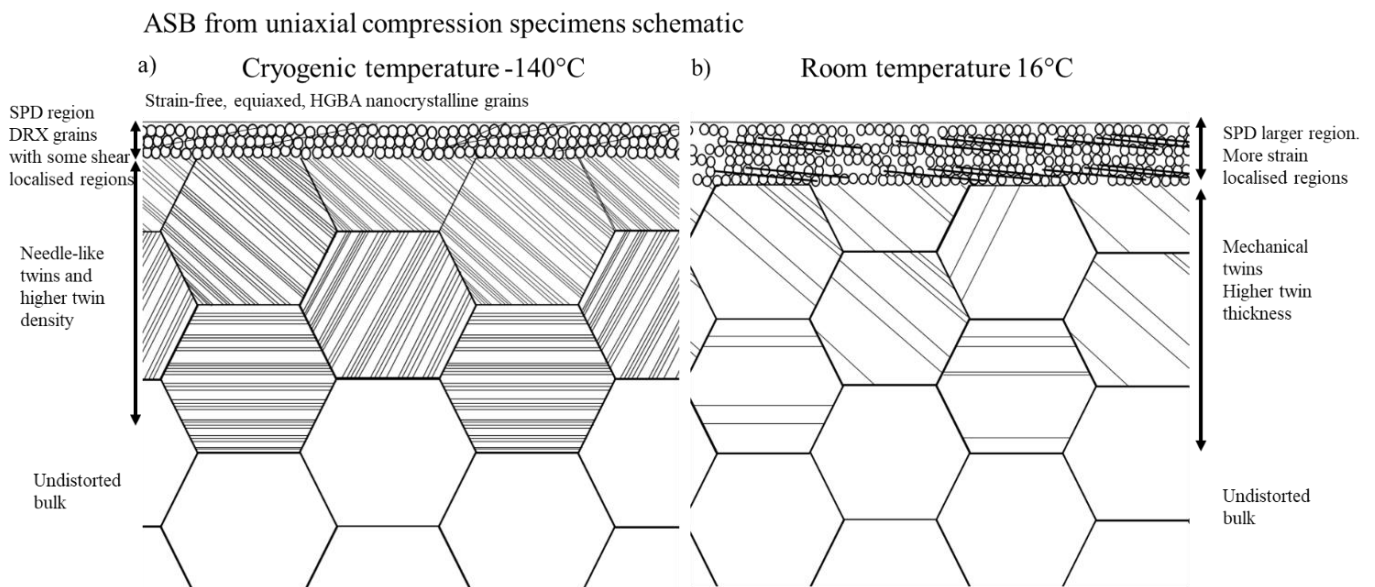
Figure 4-31. Schematic diagram showing the effect of temperature on axisymmetric compression testing at a strain rate of 0.1 s^{-1} of Ti-6Al-4V β annealed a) at a cryogenic temperature provided by LN_2 and b) at room temperature.

Figure 4-32 shows how elliptical voids formed in areas of high strain concentration. The voids reorient with respect to the intense strain localisation flow. Figure 4-32 a) shows how the void tapers to a tip, which may have a strain field around it, and may contribute to localising the deformation further. It shows how, much further from the main crack, a small crack had nucleated in a stress concentration region and elongated in the direction of shear.
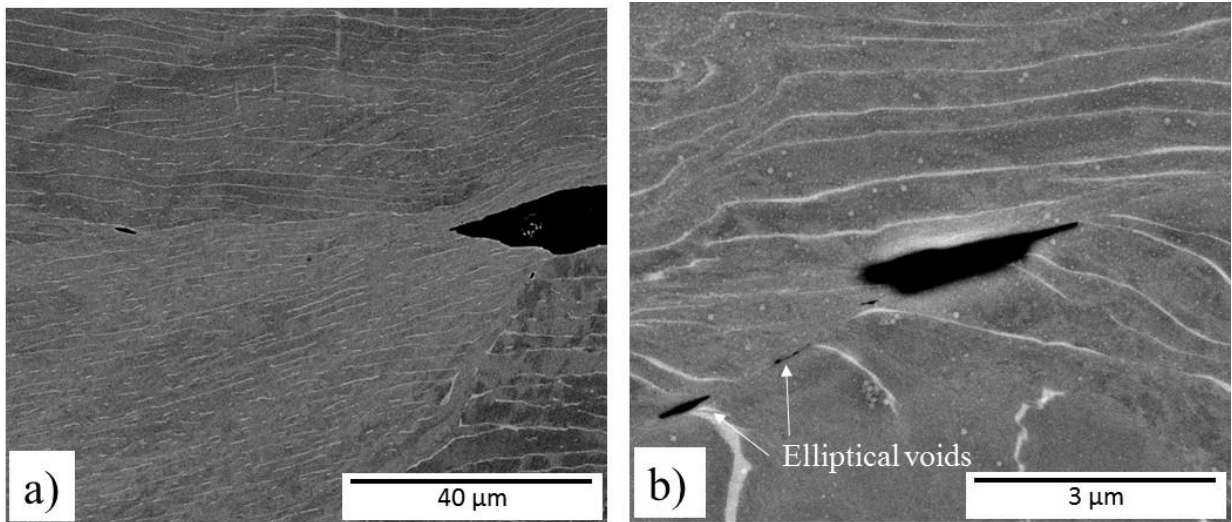
Figure 4-32.A shear band formed by elliptical voids at 10^{-1} s^{-1} at a) cryogenic temperature of -130°C, b) room temperature of 18°C.

Figure 4-33 shows the plastic deformation microstructure of CP-Ti at -130°C at 10^{-1} s^{-1}. Figure 4-33 a) shows grain reorientation towards the direction of flow; however, strain localisation is not observed in this specimen. Figure 4-33 b) shows high elongation assisted by dislocation slip and mechanical twinning.
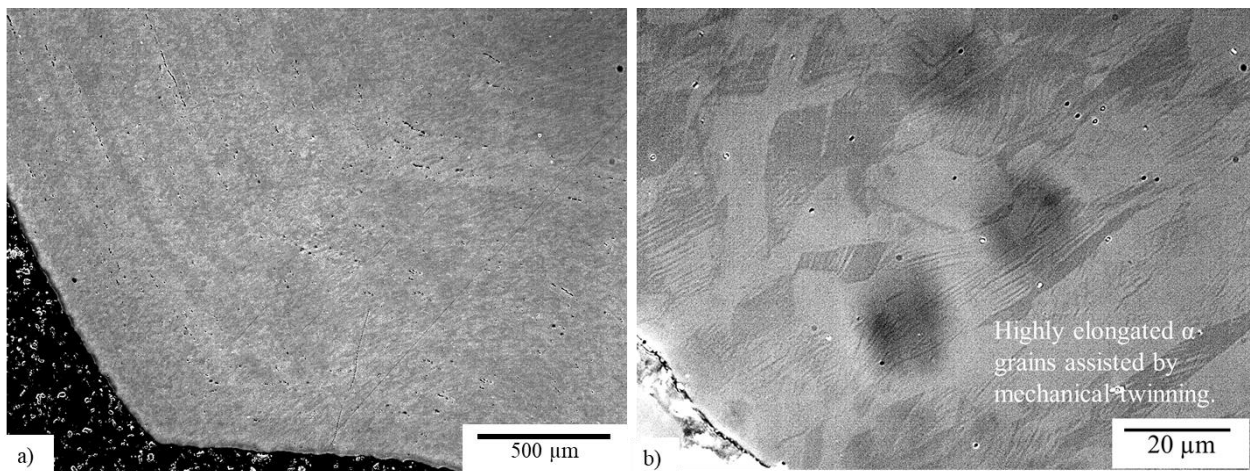
Figure 4-33. CP-Ti -130°C axisymmetric compression at 10^{-1} s^{-1} to a true strain of 0.7. The region of a low imparted plastic strain a) Low magnification at the corner of the specimen, b) Higher magnification.

Figure 4-34 shows the cross section of mill annealed Ti-6Al-4V compressed at 10^{-1} s^{-1} and ambient temperature. The specimen deformed at low temperatures was not available for microstructural observation.
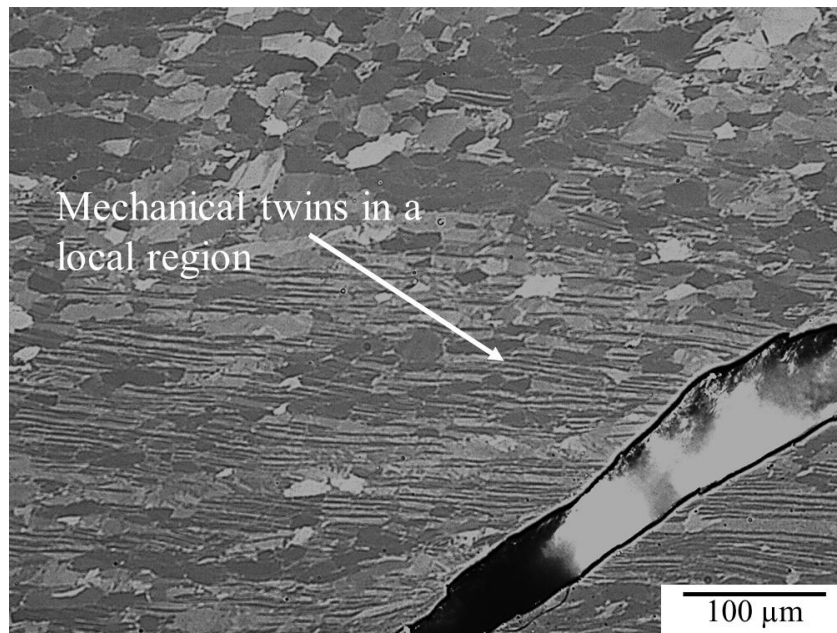
Figure 4-34. Cross-section of the mill annealed Ti-6Al-V compressed specimen at 10^{-1} s^{-1} at ambient temperature to a true strain of 0.7.

4.12. Material Modelling

Flow stress data was used to generate a model to predict load-displacement, stress, strain, and strain rate distribution during orthogonal cutting. The experimental flow stress data at different temperatures and strain rates obtained during uniaxial compression was fitted to a power law model, equation (3.10). The method is described in section 3.4.1. Model parameters are shown in Table 4-1. Three different models were built, one at room temperature, other at two low intermediate temperatures and the third including a wider range of low temperatures. Figure 4-35 displays the room temperature Norton-Hoff model fitting using parameters corresponding to the model A and A_1 in Table 4-1. The damage criterion in A_1 was C&L to a value of 240 and 10% softening. The damage criterion in A was Maximum Principal Stress (MPS) divided over the Ultimate Tensile Stress (UTS) of 0.13 and a MPS of 1333 MPa. Model B corresponds to three tests at low temperatures (-112 °C to -45 °C) and Model C from -63°C to -45°C.

Table 4-1. Material Model parameters corresponding to Norton-Hoff. C&L refers to Cockcroft and Latham damage parameter.

ID	T (°C)	SR (s^{-1})	K	n	m	β	ε_0	Damage	Value	Ratio	Soft. %
A	20	0.1	1150	0.10067	0.0001	44.23	0.02	MPS/UTS	1333	0.13	10
A$_1$	20	0.1	1142	0.08000	0.0001	44.00	0.02	C&L	240	NA	10
B	-112, -63, -45	0.1	1251	0.09700	0	47.63	0.02	C&L	240	NA	10
C	-63, -45	0.1	1010	0.12800	0	115.17	0.02	C&L	240	NA	10
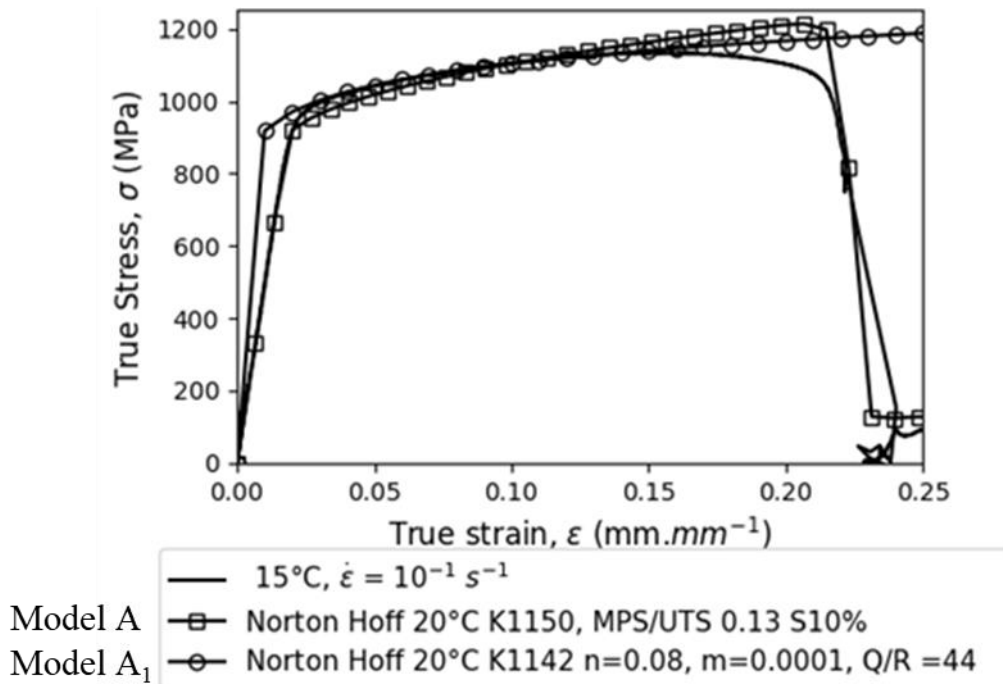
Model A
Model A$_1$

Figure 4-35. Room temperature axisymmetric compression at a strain rate of 0.1 s^{-1} and Norton-Hoff model with a damage criterion maximum principal stress over ultimate tensile stress 1333 to a ratio of 0.13 and C&L 240.

Figure 4-36 shows two models at low temperatures. Figure 4-36 a) depicts the fitting of three uniaxial compression tests (-112°C, -63°, -45°C) at 10^{-1} s^{-1} referred to as model B in Table 4-1. Figure 4-36 b) depicts the fitting of two tests over a narrow temperature range (-63°C, -45°C) referred to as model C in. Model C generated a better fit for the load prediction up to the maximum stress or ultimate compressive stress (UCS).
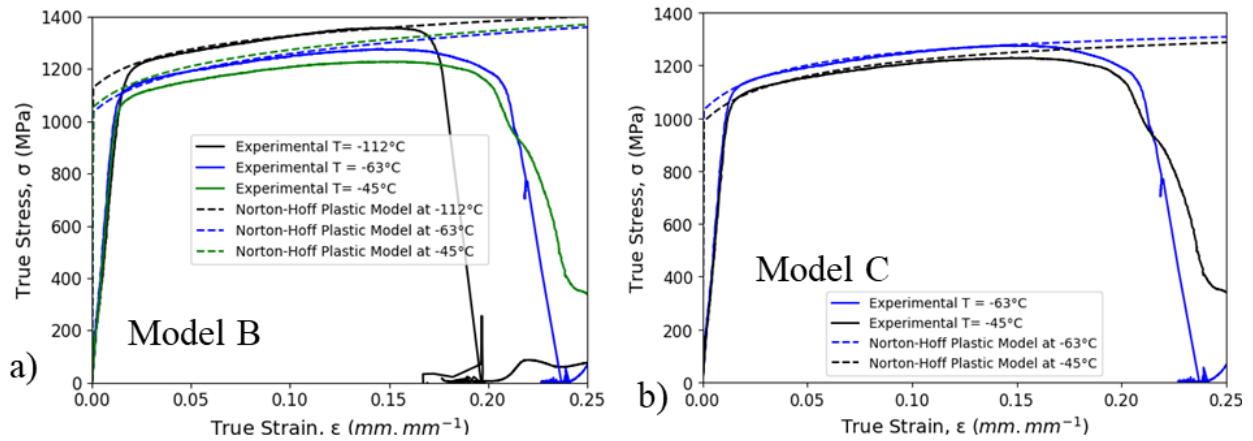
Figure 4-36. Two Norton-Hoff Models at 10^{-1} s^{-1}; a) fitted to three tests at low temperatures (-112°C, -63°, -45°C) and b) fitted to two tests over a narrow temperature range (-63°C and -45°C).

Model C was further improved by generating a closer fit to the first part of the flow curve corresponding to the first part of the strain-hardening region. For this, a Young's Modulus (E) of 90 GPa was introduced in the elasto-plastic simulation during the compression of the cylinder. Ti-6Al-4V has a Youngs Modulus ~ 110 GPa at room temperature and decreases as the deformation temperature increases it. The TMC machine compliance may have been non-calibrated, which gave rise to a high deviation in the E. However, the behaviour is more closely followed in DEFORM^{TM} under this condition.
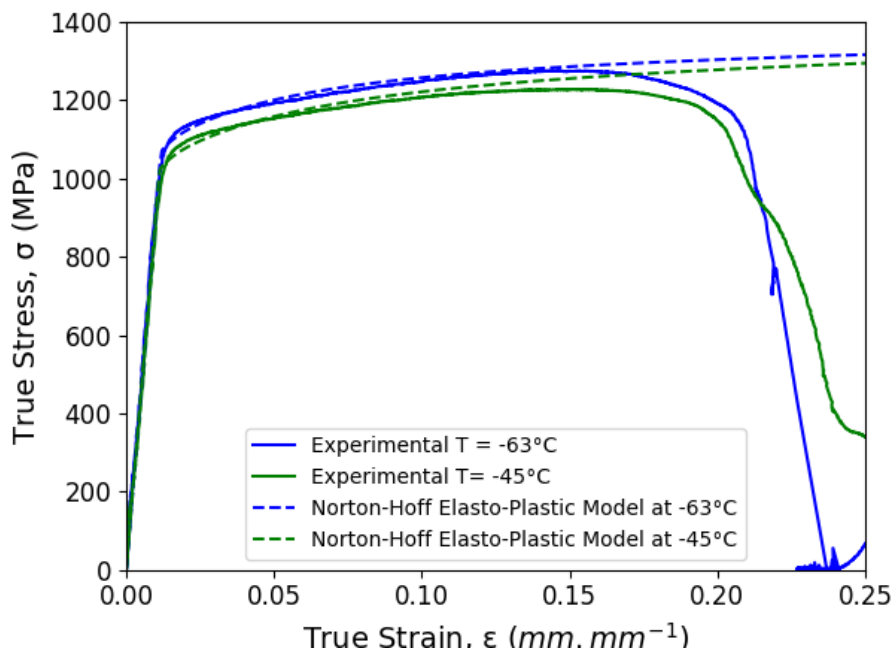
Figure 4-37. Model B fitting in DEFORM^{TM}, using a Modulus of 90 GPa to fit the strain hardening area or the gradient prior to the yield point.

Table 4-2. Parameters used in Deform for simulation of an orthogonal cut.

Variable	Value
Mechanical work converted to heat	0.9
Damage	Cockcroft – Latham 240
Softening of original flow stress (%)	10 %
Tool wear was not studied as it was considered a rigid tool.	
Inter-Object deformation; friction type Shear This applies for contact between workpiece to workpiece, and between the tool and the workpiece.	0.3 Constant
Inter-Object thermal; heat transfer coefficient (N/sec/mm/°C)	45 Constant
Heat capacity (N/mm^2/°C)	2.4
Thermal conductivity (N/s/°C)	7.1
Convection coefficient (N/s/mm/°C)	0.02
Poisson ratio	0.31
Time step (s/step)	0.01
Step increment saving (very No. of steps)	10
Convergence error limit; force (N), vel (mm/s)	0.01, 0.001
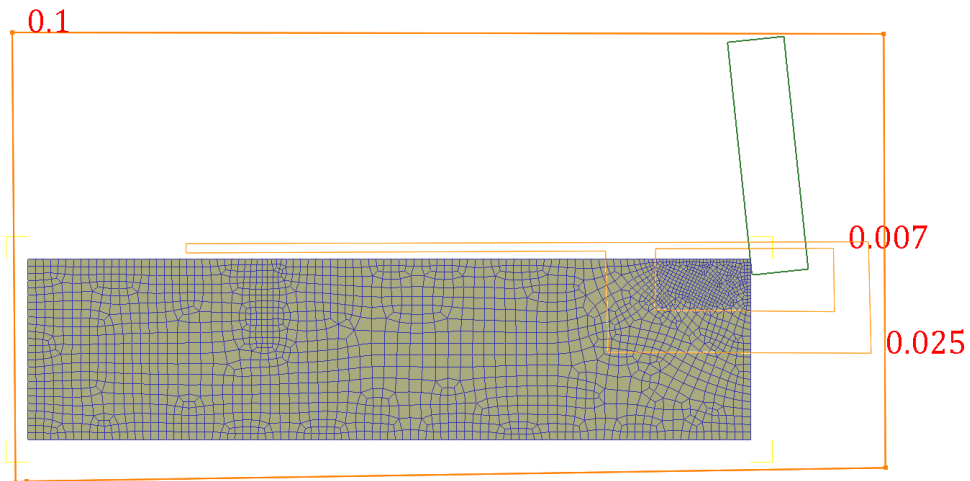
Figure 4-38. Set up for the 2D orthogonal cutting in DEFORM^{TM}.
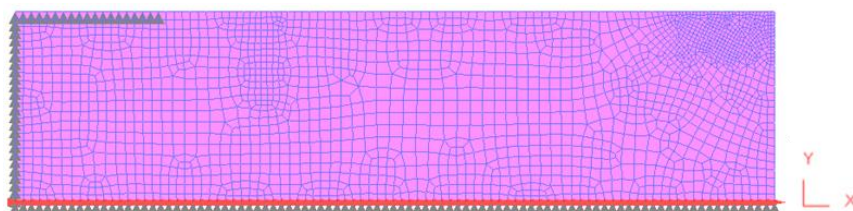
Figure 4-39. Schematic diagram, which shows that the workpiece is allowed to move along the X-axis and restricted along the Y-axis.

An orthogonal or 2D geometry was assumed. A lagrangian incremental methodology with a skyline solver and Newton-Rapson iteration was used. Values of other variables are shown in Table 4-2. The friction coefficient was considered that corresponding to cold forging, a value near 0.3 [2]. The tool geometry was set up in the same way as during the experimental in the ASP (chapter 5). This defined it as a rigid body, preventing the heat transfer between the workpiece and the tool. Three mesh windows with decreasing size as shown in Figure 4-38 were set up (0.1, 0.025 and 0.007 mm). The workpiece moved along the longitudinal direction with a moving mesh in the primary deformation region. The smallest mesh size was 0.007 mm. The mesh was composed of square elements.

Load-displacement data was obtained from an elasto-plastic NH model in DEFORM^{TM}. As it is a 2D simulation, the estimated load on a specific uncut chip thickness (t_1) is given to a basis of 1 mm length of cut (LoC) as depicted in Figure 4-40 near 2 to 3 kN represented as light grey. This load was then multiplied by the experimental LoC (mm), giving a good approximation of the experimental axial load as shown in Figure 4-40 dark grey. This data contained a high noise level. To reduce it, a 0.002 Hz Fourier transformed low band pass filter was applied using IgorPro [145] and the resultant or "cleaned" load (Figure 4-40 black line) generated a good approximation and a similar trend as the experimental data.

The filtered data from the 2D DEFORM^{TM} simulation is presented along with the experimental data of all four conditions in section 5.2 and is presented in Figure 4-41. The modelled data follows similar behaviour as the experimental data with similar values of load peaks and troughs as well as shear band spacing during cutting.
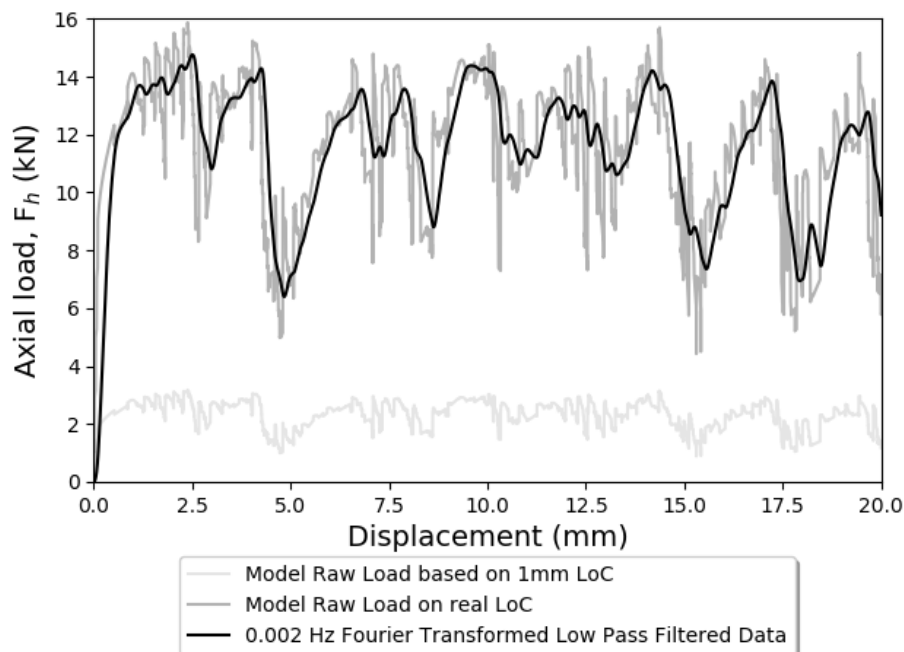
Figure 4-40. DEFORM^{TM} Elasto-Plastic Norton-Hoff model C load-displacement raw data and 0.002 Hz Fourier transformed low band pass filtered data.
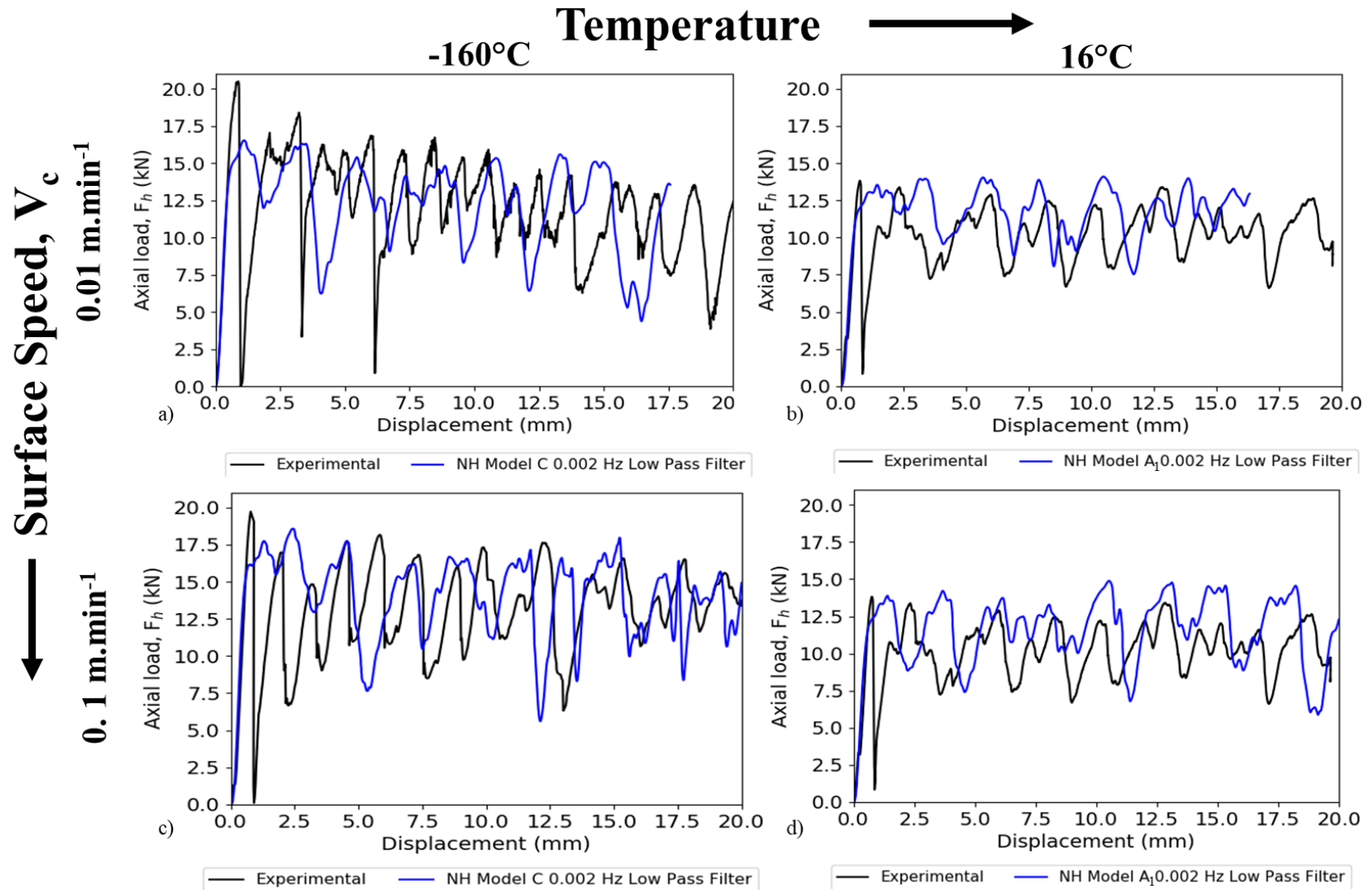
Figure 4-41. Axial load, F_h experimental (black line) and 2D FEM Model (blue line) in t_1 1.3 mm, LoC 5mm; a) & c) Model C at -160°C, b) & d) Model A at 16°C.

Figure 4-42 shows an average peak load on each of the four cutting conditions; at cryogenic temperature -160°C and 16°C at 0.01 and 0.1 m.min^{-1}. It provides a reasonable estimate with a slightly higher error in the data obtained from the simulation. The estimated average trough values are shown in Figure 4-43.
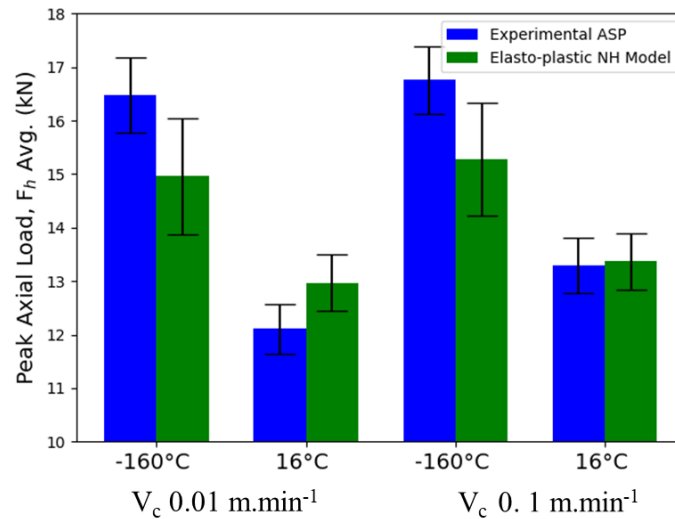
Figure 4-42. Average Peak axial load, F_h, experimental and 2D FEM Modelling at a surface speed of 0.01 m.min^{-1} and 0.1 m.min^{-1} at 16°C and a cryogenic temperature of -160°C provided by LN$_2$, t_1 = 1.3 mm, LoC = 5 mm.
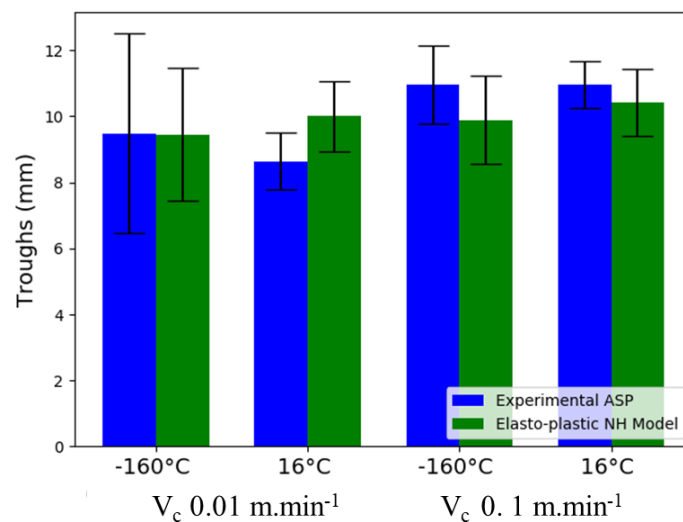
Figure 4-43. Average trough force from axial load in experimental and 2D FEM Modelling at a surface speed of 0.01 m.min^{-1} and 0.1 m.min^{-1} at 16°C and at a cryogenic temperature of -160°C provided by LN$_2$, t_1 = 1.3 mm, LoC = 5 mm.

Figure 4-44 shows the adiabatic shear band spacing, considered as the distance between peak loads. It was examined at that point as it represents the onset of shear instability or thermal softening when the material starts to shear along the tool rake face, as mentioned earlier.
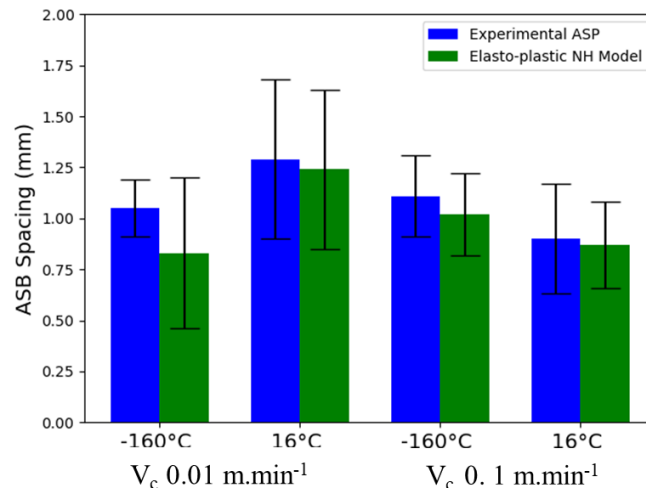
Figure 4-44. Average adiabatic shear band spacing from peak load to peak load in experimental and 2D FEM Modelling at a surface speed of 0.01 m.min^{-1} and 0.1 m.min^{-1} at 16°C and at a cryogenic temperature of -160°C provided by LN$_2$, t$_1$ = 1.3 mm, LoC = 5 mm.

Figure 4-45 shows the modelled and experimental strain imparted into the subsurface and chip during orthogonal cutting at 0.01 m.min^{-1}; a)- d) at -160°C and e)-h) at 16°C. Figure 4-45 a) shows the strain profile generated in the workpiece subsurface and the sheared material in the chip at -160°C. It also shows a region of intense shear or strain concentration in the material, which is in contact with the tool rake face. Shaw [59] reported this behaviour and called it secondary shear. In the microstructure on the experimental workpiece, voids that generated fracture along the secondary shear region start to nucleate. This secondary shearing may be a source of material to create a BUE on the tool rake face. The likelihood of this is enhanced by the high pressure and high temperature in this zone as well as high diffusivity at a high workpiece temperature. The chip formation ahead of the tool tip in Figure 4-45 b) shows the formation of a two-section chip. This is correlated with the characteristic "M" force behaviour in the load-displacement data (Figure 5-3). An average shear band spacing of 822 µm was found in this chip, which is not too different from the model in Figure 4-45 a). However, as the material is anisotropic, and deformation is also influenced by the crystallographic texture, more measurements are needed to precisely establish an estimate of the error in the values obtained. Figure 4-45 c) shows a strain profile of the cut subsurface, obtaining a strain of 0.6 mm.mm^{-1} in the region that experienced the highest levels of strain, strain rate and temperature. The experimental average (Figure 4-45 d) and maximum values have a good fit to the predicted values, showing the effect of plastic deformation in the workpiece's microstructure. Likewise, Figure 4-45 g) shows the strain accommodated in the generated chip on the Model A at 16°C. The shear band spacing of the sheared material from the chip in Figure 4-45 e) has a good

170

correlation with the experimental data, Figure 4-45 g). The strain profile imparted into the subsurface Figure 4-45 h) also shows good agreement with the experimental values in Figure 4-45 h). Twins of lenticular morphology are observed in the subsurface of PSM β annealed Ti-6Al-4V ELI at room temperature, whilst at low temperatures, needle-like twins are shown. Qualitatively, a larger SPD region is observed at room temperature (Figure 4-45 h) than at low temperatures. This agrees with the previous hypothesis (in section 4.11 and in Figure 5-22) of a larger ASB region at higher temperatures.

Figure 4-46 shows the modelled and experimental strain imparted into the subsurface and chip during orthogonal cutting at a 10 times higher surface speed of 0.1 m.min^{-1}; a)- d) at -160°C and e)-h) at 16°C. Figure 4-46 a) shows the levels of imparted strain into the subsurface and the chip. The shear band spacing seems not too dissimilar having only one measurement; 1260 µm (Figure 4-46 a) simulation and 1000 µm (Figure 4-46 b) experimental. The level of subsurface damage shows a good approximation. Figure 4-46 e) shows a closer approximation in the ASB spacing of 850 µm in the model Figure 4-46 e) and the experimental average of 760 µm, Figure 4-46 f). The experimental damage introduced into the subsurface follows a close approximation to the model. This is less than that introduced at lower speeds. Figure 4-46 shows the shear band follows curved behaviour, which may be a source of error in SBA measurements. Figure 4-46 b) shows the chip formation mechanism. It shows that the chip curves gradually. An upward curve is generated; this deviates from the ideal assumption that the shear band is generated at a linear angle.

Figure 4-47 shows a 2D cut in DEFORM^{TM} at room temperature at a surface speed of V_c = 0.01 m.min^{-1}, α = 6°. The axial load is plotted as a function of time. The strain rate during cutting is related to the shear band formation process. These images suggest that the onset of adiabatic heating is during the maximum load or peak load, as indicated by the number 1. Apparently, strain localisation starts approaching the trough load, as indicated by the number 2, where the shear flow is also observed in the chip. With the advancement of the tool, the chip is flowing, and the shear band appears to bifurcate or to transfer the concentrated shear strain to a region ahead of the cutting tool (number 3), to give rise to the next region of concentrated shear. The next adiabatic heating region appears again at the peak load (number 4). This process repeats itself on every formed chip.
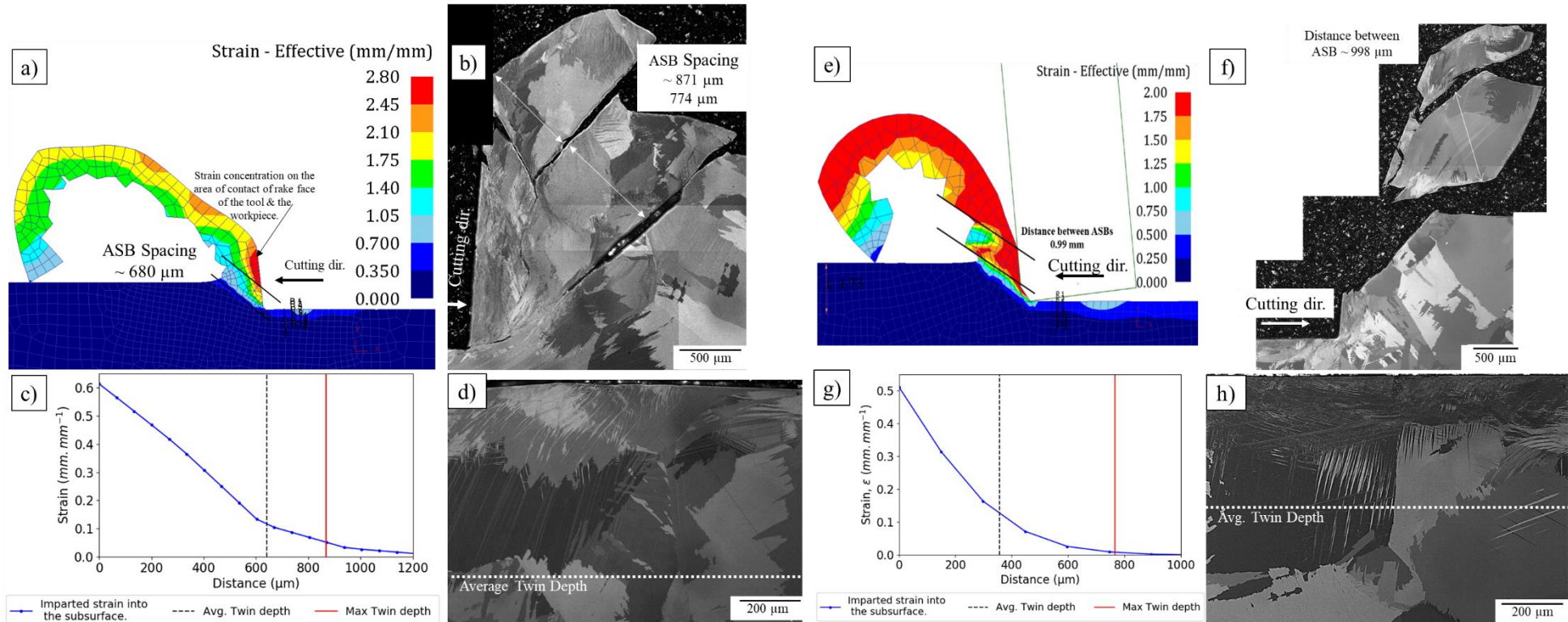
Figure 4-45. 2D FEM at a surface speed of 0.01 m.min^{-1}, uncut chip thickness $t_{1} = 1.3$ mm, rake angle $\alpha = -6°$; a)-d) -160°C model C (Section 4.12, Table 4-1), e)-h) 16°C model A (Table 4-1). The estimated strain imparted into the subsurface as a function of subsurface depth at -160°C in a) is shown in c) and is correlated to subsurface microstructure in d). The estimated strain imparted into the subsurface as a function of depth at 16°C in a) is shown in c) and is correlated to microstructure in d).

172
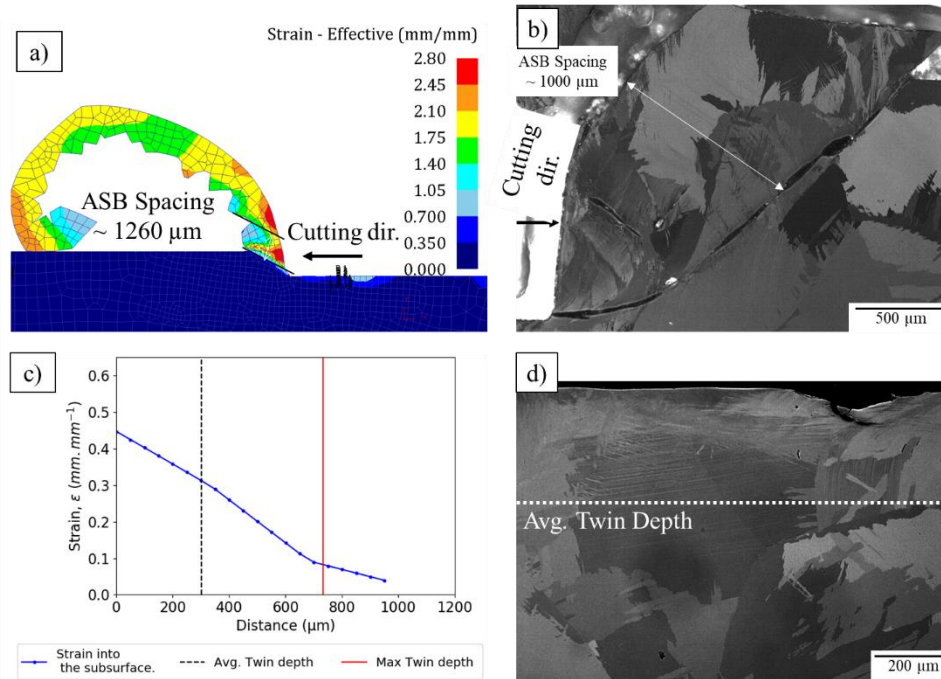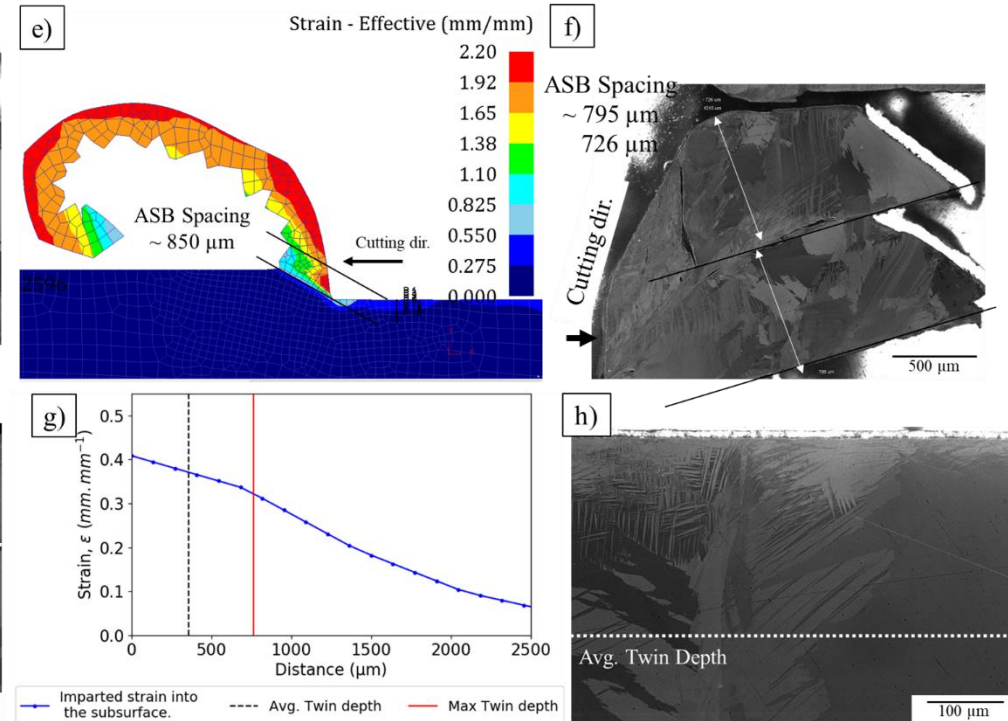
Figure 4-46. 2D FEM at a surface speed of 0.1 m.min^{-1}, uncut chip thickness t$_{1 =}$ 1.3 mm, rake angle α = -6°; a)-d) -160°C model C (Table 4-1), e)-h) 16°C model A (Table 4-1). The estimated strain imparted into the subsurface as a function of subsurface depth at -160°C in a) is shown in c) and is correlated to subsurface microstructure in d). The estimated strain imparted into the subsurface as a function of depth at 16°C in a) is shown in c) and is correlated to microstructure in d).
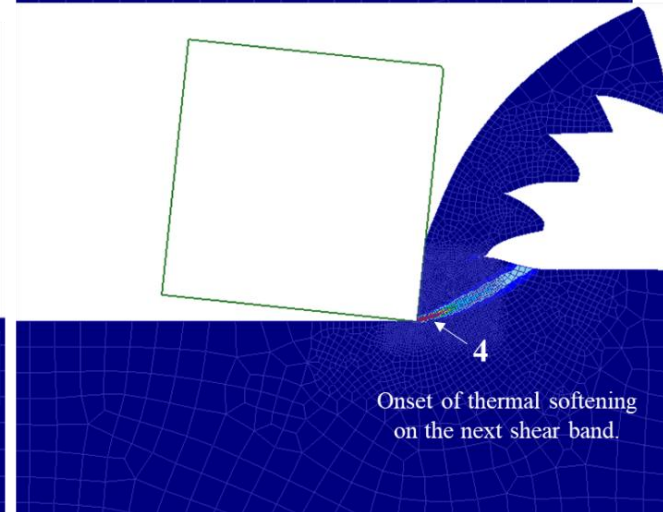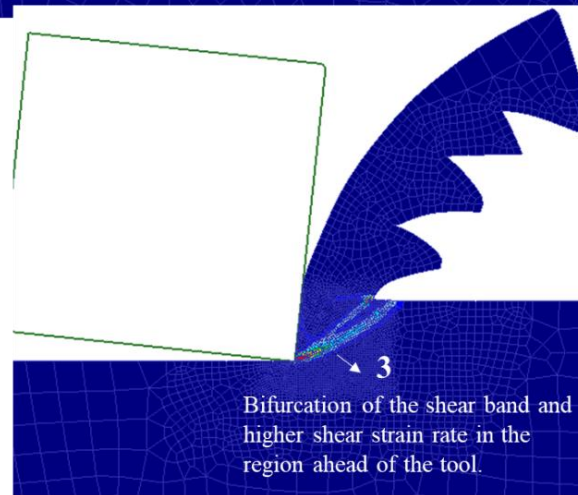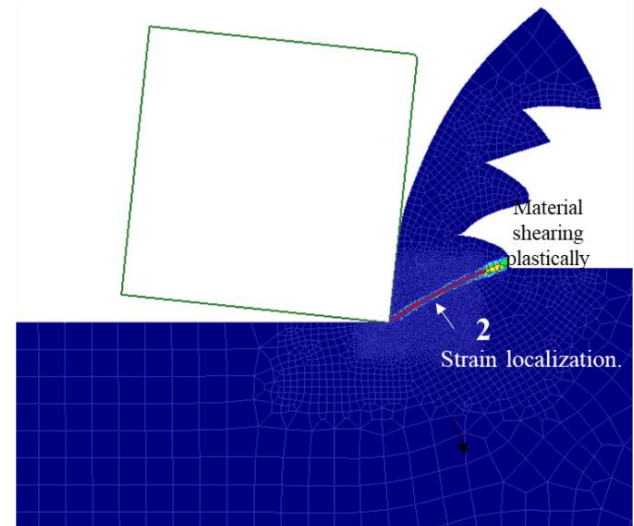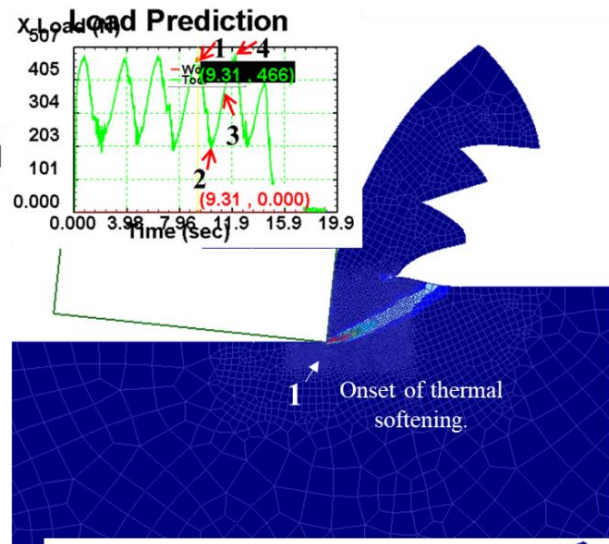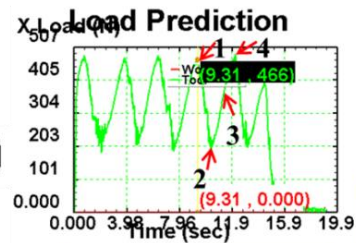
Figure 4-47. Ti-6Al-4V at room temperature, $t_1 = 0.2$ mm, $V_c = 0.01$ m.min^{-1}, $\alpha = -6°$. Axial load relationship to strain rate for chip formation in orthogonal cutting.

4.13. Conclusion

- Cylindrical specimens plastically deformed under uniaxial compression at low temperatures, exhibited:

  (1) Higher compressive yield strength (CYS).

  (2) Higher ultimate compressive strength (UCS).

  (3) Lower true strain to the onset of instability (by thermal softening) and lower strain to failure by catastrophic ASB.

  (4) Lower energy requirement for catastrophic shear failure by void coalescence, in comparison to higher temperatures.

  — For β annealed Ti-6Al4V ELI at 10^{-1} s^{-1}:

    1) CYS at -130°C was over two times that of 300°C (1109 MPa and 535 MPa, respectively) and 16% higher than at 15°C (952 MPa).

    2) The UCS at -130°C was 67% higher than 300°C (1321 MPa and 789 MPa, respectively) and 16% higher than at 15°C (1135 MPa).

    3) The true strain for the onset of thermal softening at -130°C was 30% lower than at 15°C (0.119 and 0.167 respectively). This suggests lower workability under low temperatures.

    4) The energy spent for catastrophic shear failure at -130°C was 30% lower than at 300°C (196 MJ.m^{-3} and 290 MJ.m^{-3} respectively) and 20.1% lower than at 15°C (245 MJ.m^{-3}).

  — For mill annealed Ti-6Al-4V at 10^{-1} s^{-1}:

    1) CYS at -130°C was 35% higher than at 25°C (1467 MPa and 950 MPa, respectively).

    2) The UCS at -130°C was 19% higher than at 25°C (1503 MPa and 1211 MPa, respectively).

    3) The true strain for the onset of thermal softening at -130°C was 73% lower than at 25°C (0.08 and 0.3, respectively).

    4) The energy spent on plastic deformation to the point of catastrophic shear at -130°C was 64% lower than at 25°C (121 MJ.m^{-3} and 342 MJ.m^{-3}, respectively).

  — For CP-Ti at 10^{-1} s^{-1}:

    1) CYS at -150°C was 38% higher than at 15°C. CP-Ti specimens did not catastrophically fail up to a true strain of 0.7; thus the energy spent to failure could not be estimated.

- The strain-hardening rate for β annealed Ti-6Al-4V ELI only increases at very early stages of deformation, up until the yield point. It then decreases at an increasing rate, to a near true strain of 0.03. Then, the rate decreases at a much slower rate. The gradient for the lower

temperature of -140°C was negative and higher than at 15°C and 300°C. This results in a faster decrease in the strain hardening rate. This suggests that, at low temperatures, thermal energy gets more concentrated in a narrower zone due to the low thermal conductivity and its further reduction at low temperatures. This leads to a narrower and concentrated shear region of inhomogeneous plastic deformation. At higher temperatures, the strain hardening rate decreases at a much lower rate. This suggests that plastic deformation is more uniformly distributed and is assisted by restorative processes such as dynamic recovery and easy cross-slip of dislocations. This requires more plastic strain to generate localised heating, followed by strain localisation, and, consequently, failure.

- CP-Ti has three stages of strain hardening: (1) rapid decrease, (2) increase and (3) decrease. (1) and (3) are characterized by dynamic recovery and (2) by the onset of mechanical twinning. CP-Ti exhibits increased strain hardening, as plastic deformation is uniform. This is as CP-Ti has much higher thermal conductivity than titanium alloys (nearly 3 times as much). As a result, during deformation, heat is transported more rapidly through the crystal lattice. This leads to the accumulation of defects, increasing or maintaining the hardening rate. Finally, the decrease in rate up to a true strain of near 0.2 leads to a more rapid decrease at low temperatures, as softening occurs earlier due to the reduction of thermal conductivity at low temperatures.

- Low temperatures generated more localised shear bands than at room temperature (almost half the thickness, 12 µm at -130°C and 23.8 µm at 15°C). Lowering the temperature reduces the already low thermal conductivity of titanium alloys. This causes a more rapid occurrence of thermal softening and earlier strain localisation. Also, low temperatures result in higher density, more uniformly distributed dislocations.

- β annealed Ti-6Al-4V ELI exhibits low strain rate sensitivity (m) values in comparison to fine-grained superplastic forming materials. Higher temperatures lead to higher m values. At -140°C, it was 25% lower, in comparison to 15°C (0.02 and 0.015, respectively).

- The Cockcroft-Latham parameter may be used as a machinability assessment. A linear trend was observed the onset of thermal softening is a function of temperature in terms of yield and strain.

- At low temperatures, higher mechanical twin density and subsurface deformation were exhibited, these were of and of lower thickness than at room temperature.

- The lower the temperature, and the lower the strain rate, the higher the Zener-Hollomon parameter, this resulted in a lower DRX grain size.

- Through 2D simulation in DEFORM^{TM}, fitting the experiment to the simulated flow curve, the strain imparted in the specimen appears higher at -150°C in comparison to 20°C and 300°C.

- Uniaxial compression of β annealed Ti-6Al-4V ELI resulted in a microstructure of high twin density and thin twin thickness. Room temperatures produced a low twin density, a higher

twin thickness, and appear to be strongly assisted by dislocation slip. CP-Ti resulted in highly elongated and reoriented grains, assisted by some mechanical twins but failed to localize to a true strain of 0.7.

- The onset of thermal softening was estimated to be at peak load during cutting, and the onset of strain localisation was at nearly the trough of the load.

- Three simple Norton-Hoff 2D models were built, based on the uniaxial compression data under low and room temperatures. These resulted in a good fit. Thus, an orthogonal cut was simulated using the models, and a good fit was obtained in terms of peak and trough loads, and shear band spacing. This suggests the opportunity to build models to study the deformation characteristics (cutting forces to estimate shear stresses, the energy required and subsurface deformation) of titanium alloys.

5.   Plane Strain Machining

Three alloy chemistries were evaluated on the Arbitrary Strain Path (ASP) machine using near plane strain machining (PSM) or orthogonal cutting. The first alloy under investigation is β annealed Ti-6Al-4V ELI. This alloy is widely used in the aerospace industry due to its enhanced fracture toughness and high strength to low weight ratio. The effect of cutting temperature, speed and the effect of uncut chip thickness on the subsurface deformation was evaluated during PSM. The second alloy evaluated was Ti-6Al-4V in a mill-annealed condition, and the third alloy evaluated was commercially pure titanium (CP-Ti).

5.1.   β annealed Ti-6Al-4V ELI

Four tests simulating a roughing operation were undertaken, two at room temperature and two at cryogenic temperature. Both cooling and lubricating were under liquid nitrogen (LN_2). Two cutting speeds were used, 0.01 m.min^{-1} and 0.1 m.min^{-1}, which correspond to 10 times faster-cutting speed, thus inherently resulting in a higher strain rate. Two additional tests simulating a finishing operation (with much smaller uncut chip thickness) at room temperature were undertaken. These enable comparison of the subsurface damage depth with the roughing operation. Table 5-1 shows all the testing conditions on orthogonal cutting β annealed Ti-6Al-4V.

Table 5-1. Testing conditions for plane strain machining (PSM) of β annealed Ti-6Al-4V ELI in the Arbitrary Strain Path (ASP) machine.

Test	Temp. (°C)	Lubricant/ Coolant	Speed, Vc (m.min^{-1})	Uncut chip thickness, t_1 (μm)	Length (μm)
1	-160	LN_2	0.01	1,329	5,269
2	16	None	0.01	1,248	6,220
3	-160	LN_2	0.1	1,239	5,810
4	16	None	0.1	1,262	5,762
5	16	None	0.01	258	1290
6	16	None	0.01	98.8	494

178

5.2. Load-displacement data

Axial load-displacement data was acquired on the ASP for each testing condition. The effect of cutting temperature and surface speed on axial load during PSM is shown in Figure 5-3. It is clearly observed that the lower temperature testing generated higher loads at both cutting speeds (0.01 and 0.1 m.min^{-1}), as illustrated in Figure 5-1.

At the higher speed and low temperatures, higher peak loads were recorded, see Figure 5-3 c). This finding is in close agreement with the axisymmetric compression testing (Figure 4-1and Figure 4-7) and with the literature [2]. At 0.01 m.min^{-1} and a cryogenic temperature of -160°C an average peak load of 16.47 ± 0.70 kN (with a 95% confidence interval CI) was produced. Whereas at room temperature of 16°C the average peak load was 12.11 ± 0.47 kN (95% CI), corresponding to a 30% higher peak load under cryogenic PSM. At a cutting speed of 0.1 m.min^{-1} (10 times faster), the average peak load under cryogenic cooling with LN$_2$ of -160°C was 16.76 ± 0.63 kN (95% CI). At a room temperature of 16°C, the average peak load was 13.30 ± 0.52 kN (95% CI). This corresponds to a 25% higher peak load at the lower temperature.

The effect of surface speed (implicitly shear strain rate) is smaller. At -160°C, the change from 0.01 m.min^{-1} to 0.1 m.min^{-1}, generated an increase in peak load of 4.8%, whereas at room temperature it was almost double that at low temperatures; it was ~ 9.3%. This implies that β annealed Ti-6Al-4V ELI has higher strain rate sensitivity at higher temperatures.

It was estimated that nearly 4% lower displacement was required to generate an adiabatic shear band and to fracture it under lower temperature. At a speed of 0.01 m.min^{-1} a total of 25 peak loads were counted in a cut distance of 27.8 mm, while at room temperature of 16°C, 17 peak loads were counted in a cut distance of 24.36 mm.

The load-displacement data corresponding to the first chip was different from the rest of the test under all conditions. The reason being that the test started cutting on a full area of contact, or square area, therefore, higher material is being sheared to generate the first chip, thus higher cutting forces and higher shear stresses are required. This is also known as the ploughing effect, which depends on the cutting tool edge radius, discussed in greater detail by Crawforth [3]. After the first chip was generated, the tool edge kept contact with the material at an angle from the previously sheared chip. This increases the force to yielding until maximum stress (or peak load) is reached. This was when the chip started to fracture.

For test 1, under LN$_2$ cryogenic cooling condition, the liquid nitrogen supply was constant up to an 11 mm cut length, supply stopped for 10 seconds as the funnel needed to be refilled, the temperature could not be brought back to -160°C after the 11 mm cut, the sample warmed up to nearly -65°C. Thus, a lower number of data points were used for this test, resulting in a higher error. For test 2, it was easier to maintain the cutting temperature at -160°C as the cut

took less time. It took 166.8 s to cut 27.82 mm at 0.01 m.min^{-1} and 14.61 s to cut 24.36 mm at 0.1 m.min^{-1}.

a) ●— 16°C peak load   -✱- 16°C trough load   b) ●— -160°C peak load   -✱- -160°C trough load
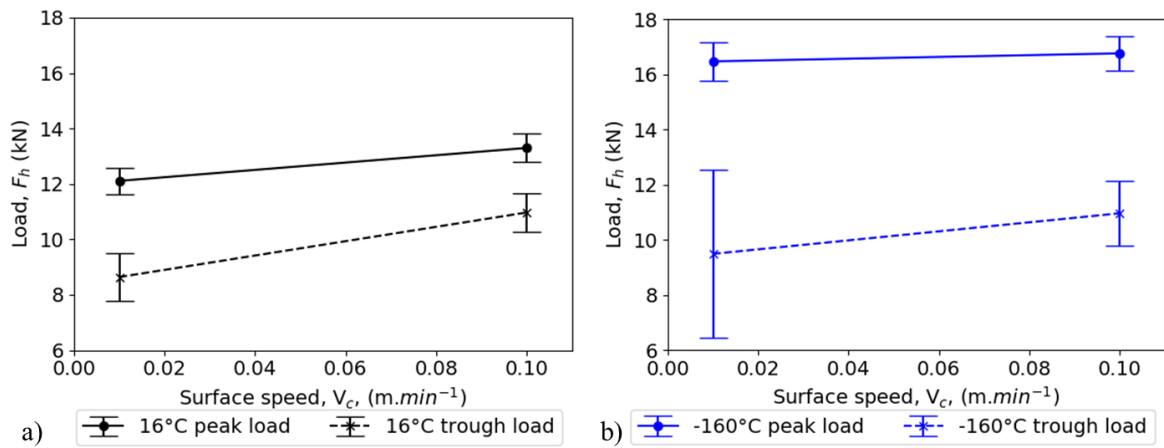
Figure 5-1. Average axial peak load and trough during PSM as a function of surface speed (shear strain rate): a) at 16°C and b) at -160°C. The error bars signify the 95% confidence interval of the average value.

The specific cutting force strongly increases by reducing the uncut chip thickness, as shown in Figure 5-2. This is experienced most strongly in precision or ultra-high precision cuts. This is related to the size effects, which also depend on the cutting edge roundness and grain size. The specific cutting force with an average uncut chip thickness of 0.4 mm for α titanium alloys is 1530 N.mm^{-2} and for α+β annealed alloys is 1675 N.mm^{-2} [66]. The specific cutting force estimated for test 1 was 2470 N.mm^{-2} (uncut chip thickness of 1.3 mm), for test 3, was 2450 N.mm^{-2}, for test 2, K_C 1660 N.mm^{-2} and test 4, K_c was 1931 N.mm^{-2}. The K_c estimated for β annealed Ti-6Al-4V ELI at ambient temperature, and low speed correlates with the previously reported value. However, the low temperature K_c was much higher than the values reported.
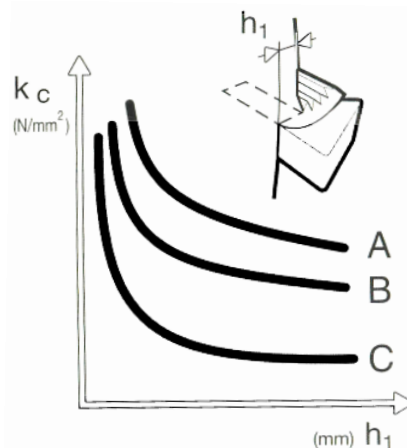
Figure 5-2. Specific cutting force (K_c) and its relationship to the uncut chip thickness. A) corresponds to stainless steel, B) to alloyed steel, and C) to grey cast iron [66]. Titanium alloys follow a closer relationship to that of stainless steels.
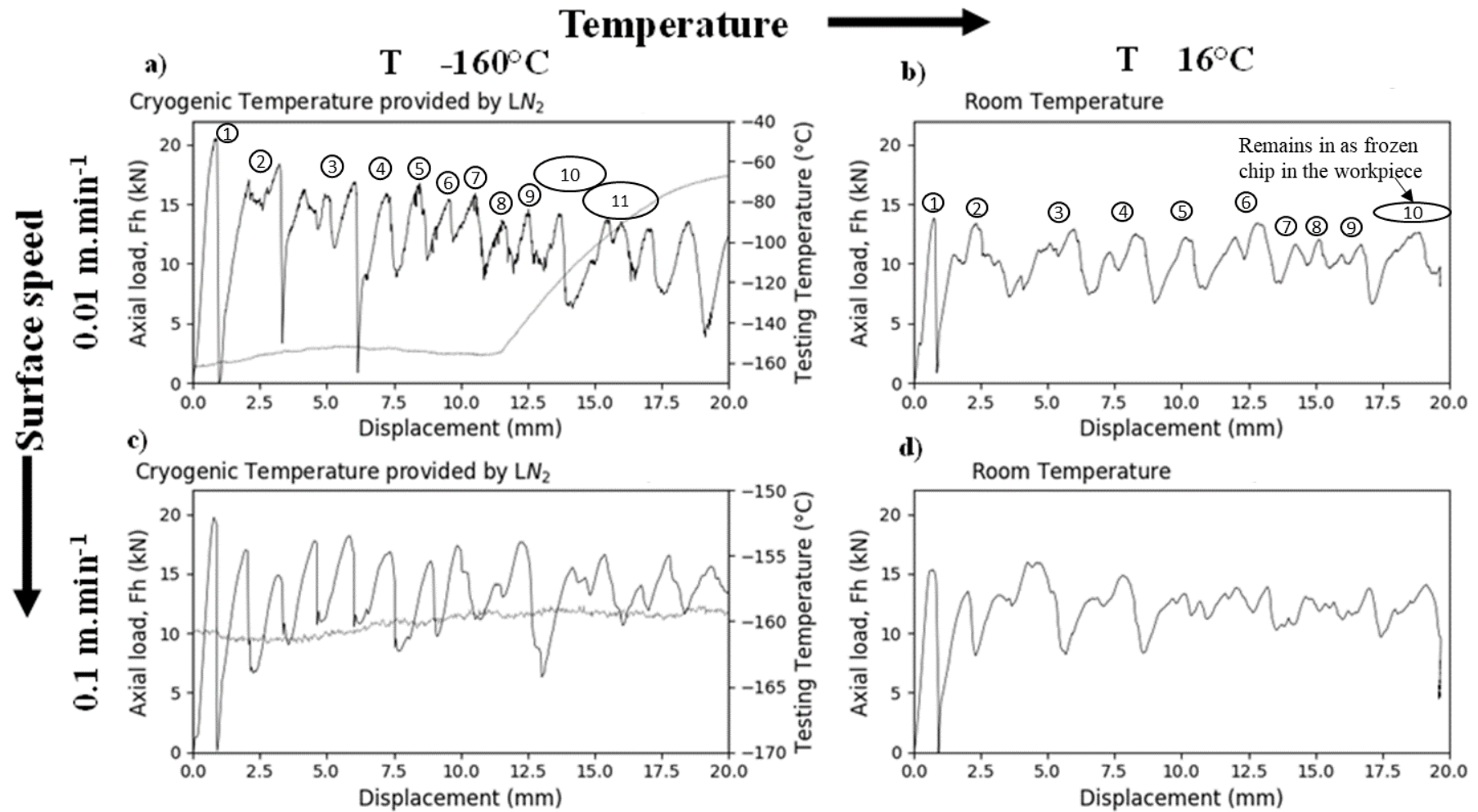
Figure 5-3. Axial load Fh-displacement curves of β annealed Ti-6Al-4V ELI orthogonal cut at a) cryogenic temperature of -160°C provided by LN₂ at a surface speed of 0.01 m.min⁻¹, b) cryogenic temperature of -160°C at a surface speed of 0.1 m.min⁻¹, c) room temperature of 18°C at a surface speed 0.01 m.min⁻¹, d) room temperature of 17°C at a surface speed 0.1 m.min⁻¹. The ovals in a) correspond to the chips in Figure 5-8 and b) correspond to the chips in Figure 5-9.

5.3. Shear Band Angle (SBA)

The shear band angle was measured in order to estimate the tangential forces and shear stresses generated in the shear plane as described in section 3.6.3. It was measured using high-resolution photography at a rate of 5 frames per second. Figure 5-4 a) illustrates how the shear band angle was measured using the software package Image J [146] and Figure 5-4 b) shows the SBA distribution of the measurements.

Cutting of β annealed Ti-6Al-4V ELI at 0.01 m.min^{-1} under a cryogenic temperature of -160°C, by applying LN$_2$ directly to the cutting zone, generated a higher shear band angle in comparison to room temperature of 16°C or dry cutting. The SBA arithmetic average at -160°C was 42.1 ± 4.1 degrees in contrast to 40.9 ± 8.5 degrees at 16°C. This represents a 10% increase in average SBA at -160°C. This is beneficial for the cutting process as schematically illustrated in Figure 5-6, which shows that by increasing the SBA the strain imparted into the chips is lower than at 16°C. This also implies that the shear band distance (A to B1 at 16°C) and (A to B2 in the case of -160°C) is reduced. It, therefore, implies that the energy spent on cutting for a shorter distance should be lower at a lower temperature on the higher SBA generated.
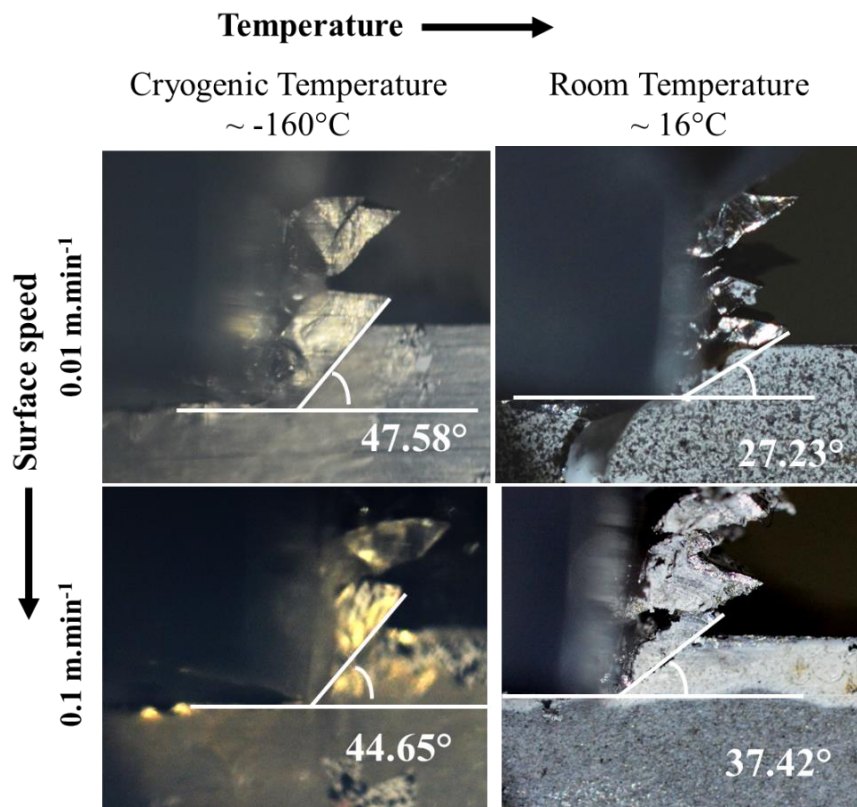
Figure 5-4. Illustration of the measurements of SBA: a) from high-resolution photography during orthogonal cutting.

T (°C)	Vc (m.min^{-1})	SBA (°)		Error
16	0.01	40.9	±	8.5
-160	0.01	42.1	±	4.1
16	0.1	37.6	±	5.0
-160	0.1	39.8	±	4.8
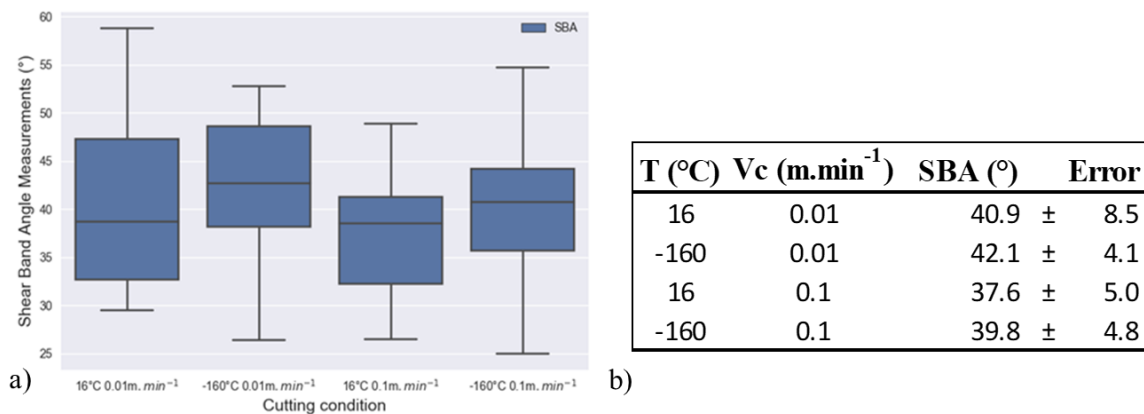
Figure 5-5. Effect of temperature and surface speed on the shear band angle (SBA): a) plot showing the distribution of the measured values, b) average values and their corresponding errors.

The variation on the SBA measurements is related to shear instabilities and to BUE formation. It was observed on the measurements that when a BUE was formed ahead of the cutting tool, the SBA reduced, thus increasing the shearing distance of the generated chip and increasing the energy required to generate a chip.
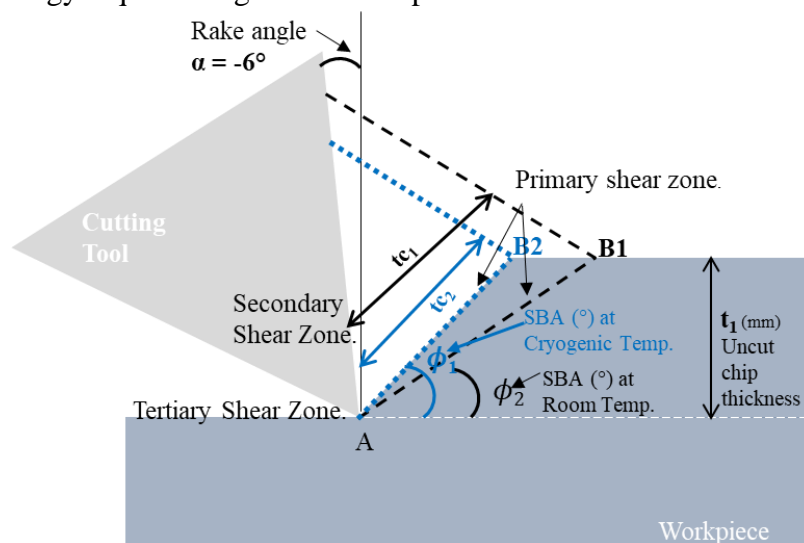
Figure 5-6. The effect of increasing the shear band angle during metal cutting at low temperatures. $\varnothing_1$ corresponds to SBA at a room temperature of 18°C, and $\varnothing_2$ (shown in the colour blue) corresponds to the cryogenic temperature provided by LN$_2$ of -160°C.

Figure 5-14 shows the estimated shear stress experienced on the shear plane during the shearing action. The peak load corresponds to the maximum load or the onset of thermal softening and fracture due to void formation. Higher shear stresses are estimated at lower temperatures, corresponding to the higher axial forces generated under LN$_2$ cryogenic cooling as shown in Figure 5-3. As observed in the prior section 4.9, lower temperatures generate a lower strain rate sensitivity. This is in agreement with the shear stresses observed under both cutting speeds. The higher cutting speed (relating to a higher strain rate) generates slightly

higher shear stresses than that at a lower speed. On the other hand, at room temperature there appears to be a higher strain rate sensitivity as there is a more significant difference in the shear stresses resulting from different cutting speeds. In relation to the segmentation frequency; a higher number of peak loads appear at lower temperatures, which correspond to a higher number of chips forming and are in agreement with the higher SBA and the lower energy needed to cause instability on the shearing plane.

The lower segmentation frequency in Figure 5-14 b) suggests it is more difficult to generate and cause catastrophic fracture of shear bands at room temperature. Figure 5-14 a) shows higher segmentation, with an occasional low trough, suggesting the easier chip formability.

Figure 5-7 shows a relationship between the cutting force and the shear band angle. The present results are at odds with this relationship. Higher SBA was generated at low temperatures and led to higher cutting forces. This may be because this relationship is material dependant as each material has different strain hardening mechanisms, leading to different shearing angles and different cutting forces. This suggests that the energy spent on plastic deformation may be a better way to more accurately estimate the machinability of materials under different cutting conditions, as suggested in chapter 6.
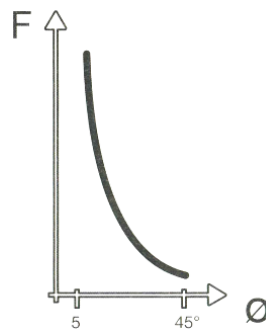
Figure 5-7. Force dependence on the shear band angle [66].

Figure 5-8 shows a sequence of images taken during plane strain machining of β annealed Ti-6Al-4V at 0.01 m.min^{-1} under LN$_2$ cooling. These images correspond to test 1, $t_1 = 1.3$ mm and LoC = 5.2 mm. It shows, first of all, how the first chip corresponds to a higher volume of material removed, which results in a higher peak load and mainly only in the first chip the trough load drops to nearly zero. All other chips resulted in higher trough loads. It also shows how in some chips, such as in chip 3, the imparted strain was not enough to generate total fracture; instead, it generated a fracture in the free surface in more than one region, resulting in a chip with more than one joint segment. In some chips, there was a region of shear stress and strain concentration, which led to a fracture in a direction opposite to the shear angle. This resulted in chips fractured along the secondary shear zone (2° SZ). With the advancing of the cutting tool, a section of the fractured area remained in contact with the rake face of the tool, the high pressures and high temperatures developed in the cutting zone may have led to build up edge (BUE) formation. This BUE changed the shearing angle, and as a result, a chip of

higher volume and of lower shear band angle resulted. Figure 5-9 corresponds to PSM at 16°C and 0.01 m.min^{-1}.
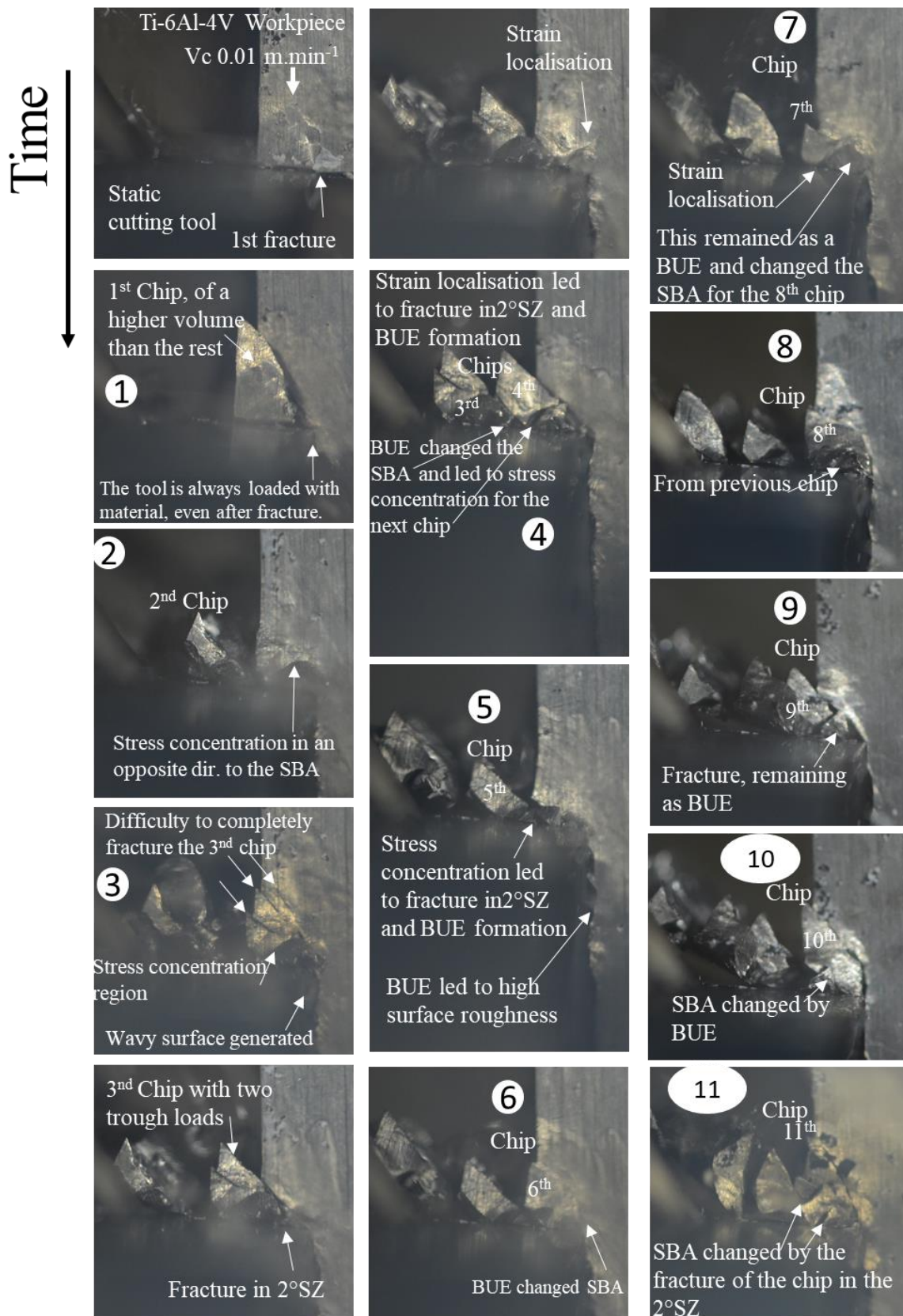
Figure 5-8. Sequence of images during chip formation in orthogonal cutting β annealed Ti-6Al-4V at 0.01 m.min^{-1} under LN$_2$ cooling, t_1 = 1.32 mm and LoC = 5.26 mm using a Seco

tool. The images were taken using a high-resolution camera at 5 frames per second. Ovals correspond to peak load in Figure 5-3 a).
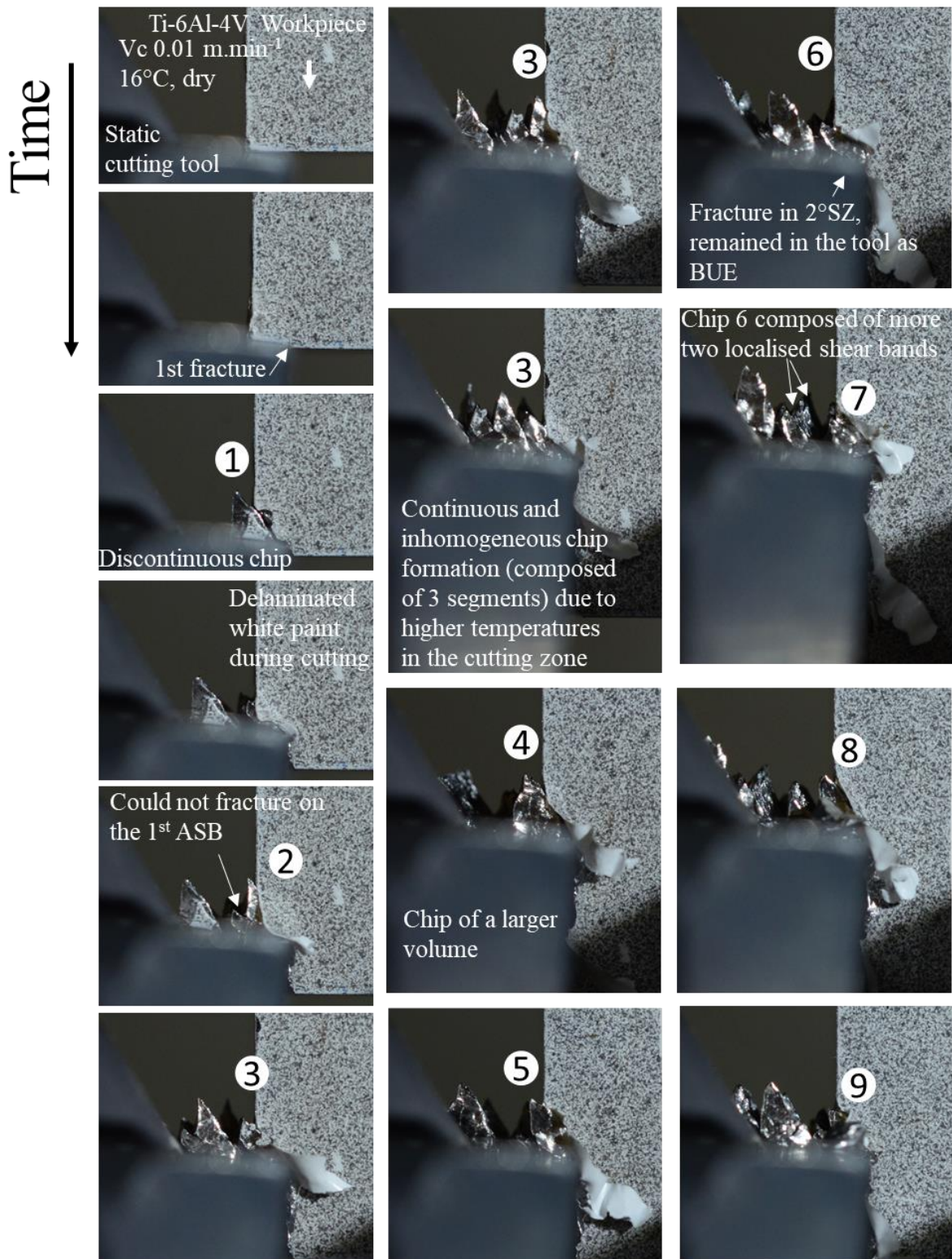
Figure 5-9. Sequence of images during chip formation in orthogonal cutting β annealed Ti-6Al-4V at 0.01 m.min^{-1} at ambient temperature or dry, t_1 = 1.25 mm and LoC = 6.22 mm using a Seco tool. The images were taken using a high-resolution camera at 5 frames per second. The ovals correspond to peak load in Figure 5-3 b).

5.4. Mechanism of chip formation

From Figure 5-10 to Figure 5-13 it is observed that the shear band angle is only a first approximation as the chip formation is through gradual curving of the segment being formed.

Force fluctuation leads to high surface roughness [66]. Force fluctuation also leads to vibration and chatter.

Figure 5-10 shows that strain localisation and the crack initiated ahead of the tool tip. Near the free surface, the material is separated. Also, near the free surface, another curvature appears, suggesting that separation of material in that location was harder to achieve. In the shear direction, closer to the tooltip the material is still united. This suggests that the fracture along the shear direction is not advancing continuously, but it is created first in areas of stress concentration and the regions with lower accommodated strain separate last.

Figure 5-10 to Figure 5-13 support the theory of initial strain localisation leading to fracture and finally the chip is displaced in the shear direction by compression stress. The centre of the ABS is the last region to fracture (as seen in Figure 5-10) and at high speeds, it rewelds to the adjacent segment, leading to a continuous chip.

Although Kommanduri and Turkovich [68] reported almost no deformation on the $2°$ shear zone, the microstructures from Figure 5-10 to Figure 5-12 suggest substantial deformation and periodic fracture of the chip in that region. This may lead to build up edge formation.

At low cutting speeds, the chip formation in titanium alloys is individual chip segments. On the other hand, at high surface speed, the chip is continuous and inhomogeneous giving rise to segmented chips.

Figure 5-10. Chip formation mechanics in near orthogonal cutting β annealed Ti-6Al-4V ELI at 0.01 m.min^{-1}, t_0 1.3 mm, w = 5.2 mm at temperature -160°C by applying LN$_2$ directly to the cutting edge, using a Seco tool with a rake angle, α -6°.

Figure 5-11. Chip formation mechanics in near orthogonal cutting β annealed Ti-6Al-4V ELI at 0.1 m.min^{-1}, t_0 1.24 mm, w =5.81 mm at temperature -160°C by applying LN$_2$ directly to the cutting edge, using a Seco tool with a rake angle, α -6°.

189

Surface speed, $V_c = 0.1$ m.min^{-1}, 16°C dry cutting
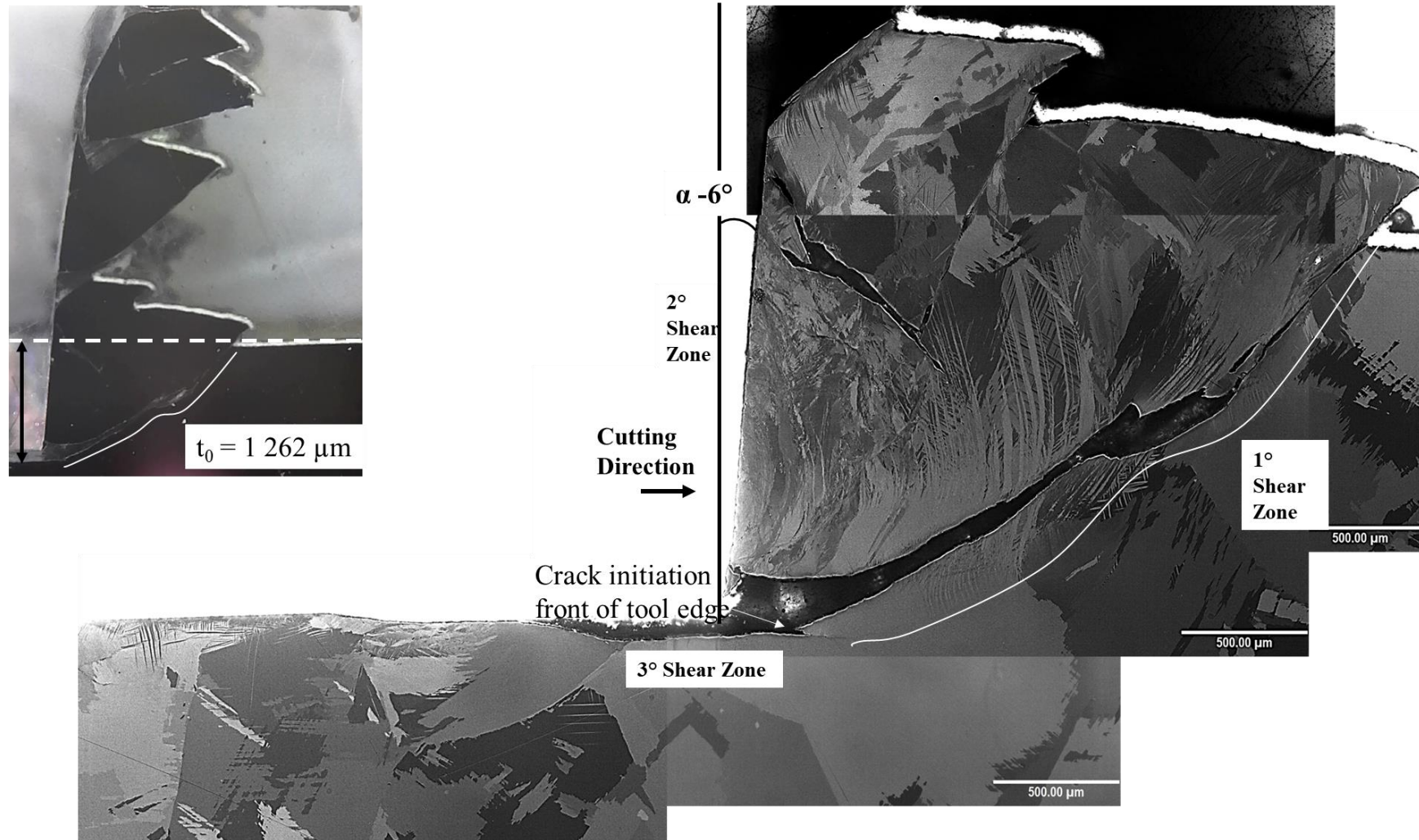
Figure 5-12. Chip formation mechanics in near orthogonal cutting β annealed Ti-6Al-4V ELI at 0.1 m.min^{-1}, t_0 1.262 mm, w =5.762 mm at temperature 16°C dry cutting, using a Seco tool with a rake angle, α -6°.

Surface speed, $V_c = 0.01$ m.min^{-1}, 16°C dry cutting
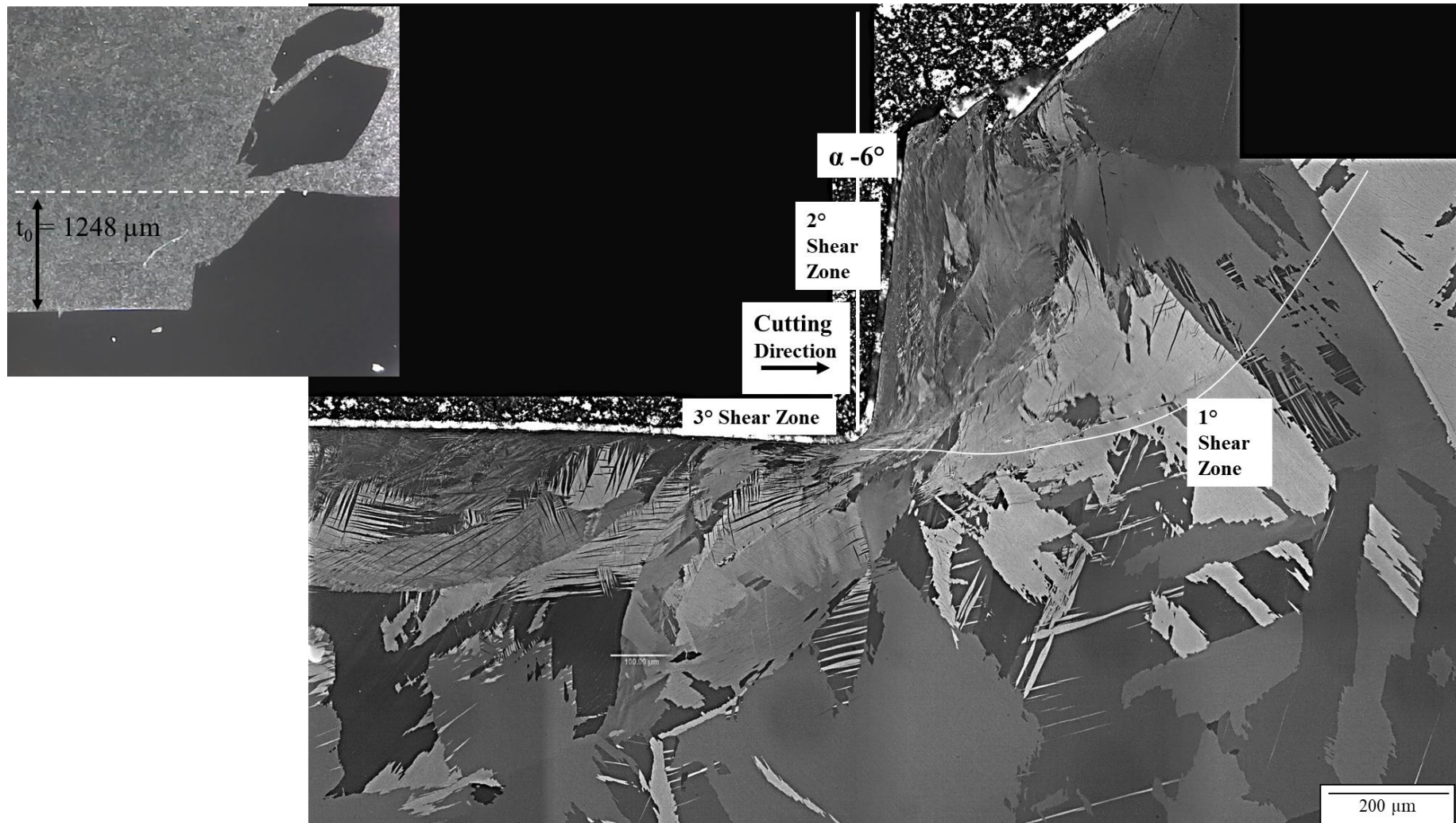
Figure 5-13. Chip formation mechanics in near orthogonal cutting β annealed Ti-6Al-4V ELI at 0.01 m.min^{-1}, t_0 1.262 mm, w =5.762 mm at temperature 16°C dry cutting, using a Seco tool with a rake angle, α -6°.

191

5.5. Estimate of energy spent on shearing and friction

At 0.1 m.min^{-1} under LN$_2$ cryogenic cooling PSM, an estimated 86.4% of energy is spent on the shear band formation, and 13.6% of the energy is spent on friction. At a room temperature of 16°C, an estimation of 67% of the energy was spent on the shearing action, and 33% was spent on overcoming frictional forces. This is also suggested in Figure 4-3, the onset of strain for softening and fracture being higher at high temperatures. Thus, it can be concluded that at a speed of 0.1 m.min^{-1} cutting under cryogenic cooling conditions it was beneficial to the process as more energy was spent on the shearing action. This is fundamental to machining as it leaves only a small fraction of the remaining energy needed to overcome friction. In contrast, at room temperature, a lower percentage of the total energy was spent on the shearing action and a higher portion of the energy was spent on overcoming friction. This implies that lowering the workpiece temperature concentrates more of the energy into the shearing action. Also, the liquid fluid and gas cushion formed by the evaporated gas when in contact with the atmosphere, due to its low boiling point may serve as a lubricating film and may, therefore, reduce friction. Hong et al. [147] estimated a lower friction coefficient at cryogenic temperatures during cutting Ti-6Al-4V 0.3 versus 0.5 for dry cutting.

5.6. Estimation of shear stress for catastrophic shear failure during inhomogeneous plastic deformation

Estimated pseudo shear stress from the PSM trials was performed by applying the methodology described in section 3.6.3. The true strain, which corresponds to the maximum true stress during axisymmetric compression testing, was assigned to the maximum shear stress in PSM. The pseudo shear stress, corresponding to the axial load of one chip was generated and is illustrated in Figure 5-21. It is observed that the lower temperature generated higher shear stresses; however, the onset of failure was generated at a lower strain. Thus by evaluating the Cockcroft-Latham workability parameter, there is less energy spent on both chip formation and the onset of shear band failure. The same behaviour applied under a surface speed of 0.1 m.min^{-1} as well as under slightly higher loads. This was true under both low and ambient temperatures; these were observed due to the higher strain rate implications.
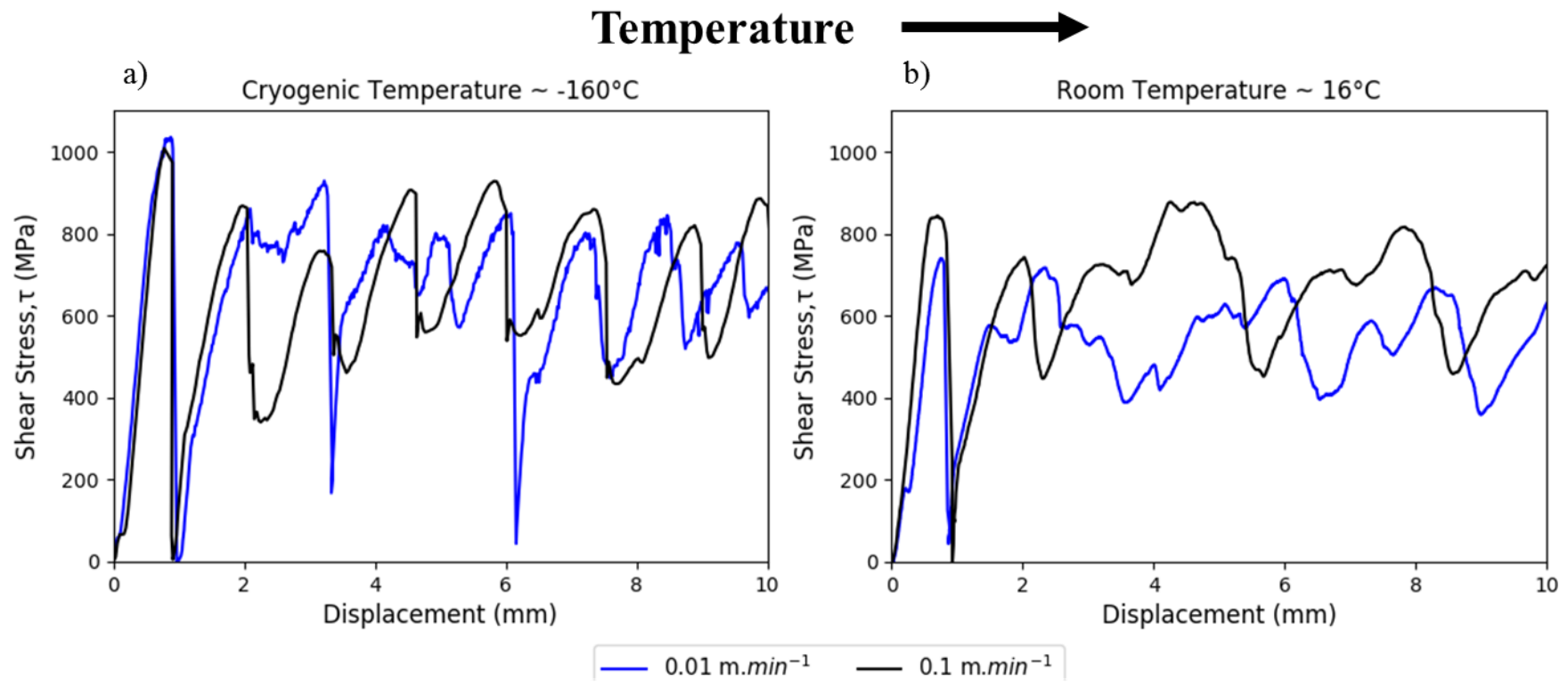
Figure 5-14. Shear stress versus displacement comparing two surface speeds 0.01 m.min-1 and 0.1 m.min-1 at a) room temperature near 16°C and b) cryogenic temperature provided by LN2 reaching near -160°C.

5.1. Strain in the shear band

An attempt to determine the strain locally during shear band formation and therefore chip formation was undertaken using a Digital Image Correlation technique. The workpieces were coated with a micron-sized white and black speckle pattern. During PSM, high-resolution in-plane images were taken at a rate of five frames per second, this being the limit of the available camera. These images were then processed using the package Vic-2D [148] to determine the strain during chip formation and shearing, see Figure 5-15 for a typical result. During the delivery of the LN_2 stream, the coating used was removed from the surface of the workpieces (see Figure 5-8), and for most tests under dry cutting, the white coating delaminated (see Figure 5-9), making it harder to estimate the strain using DIC. Therefore, it was not possible to determine the strain under these conditions. As an alternative, as demonstrated by Shankar [99], the strain was determined from the Model built in DEFORM^{TM}.
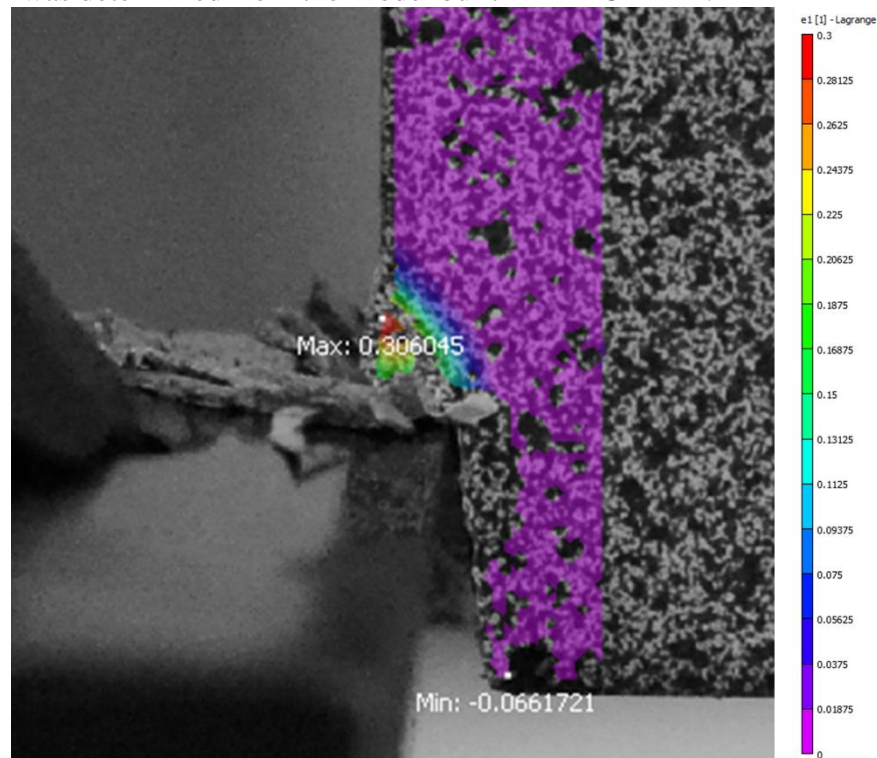
Figure 5-15. Strain determination during plane strain machining using VIC-2D software [148].

The load-displacement data was used as a reference to determine the strain imparted into the shear band. Modelled axial load and strain during cutting was correlated through time. The filtered Model A was used to correlate the peak load, time and strain, see Figure 5-16. Displacement is correlated to time by the surface speed. The strain in the shear band at the maxima was considered to correspond to the maximum shear stress. The strain at the peak through, the strain was considered the end of that specific shear band. At the load maxima in

194

the Model A, a point tracking along the centre of the shear band (Figure 5-17) was used to record time and strain. Then, time and strain were recorded starting from minima to minima of one selected chip. Data points corresponding to the same time were used to estimate shear stress using Merchant's Force Circle Analysis, and the experimentally measured shear band. This was then plotted along the strain, which is correlated through time, see Figure 5-18. In this figure, the Von Mises shear stress in uniaxial compression is also shown for comparison. A close correlation is observed, suggesting that this methodology is a good approximation that can be used to determine the machinability of titanium alloys. In terms of shear stresses, energy and strain generated along the concentrated shear in the ASB and then imparted into the subsurface.

After the first chip formation, the axial load usually remains at an average value of the peak and trough load, as the cutting tool remains loaded with material as a compression operation, building up the next shear band.
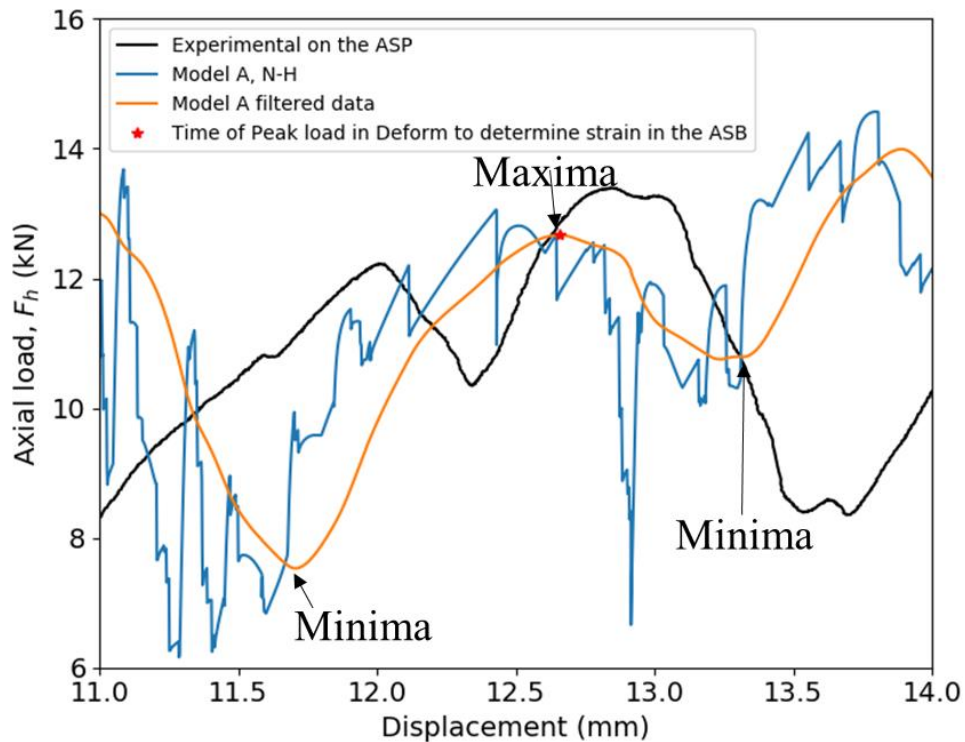
Figure 5-16. Axial load –displacement PSM at 0.01 m.min^{-1} at 16°C; experimental, Norton-Hoff Model A, Filtered Norton Hoff Model A.
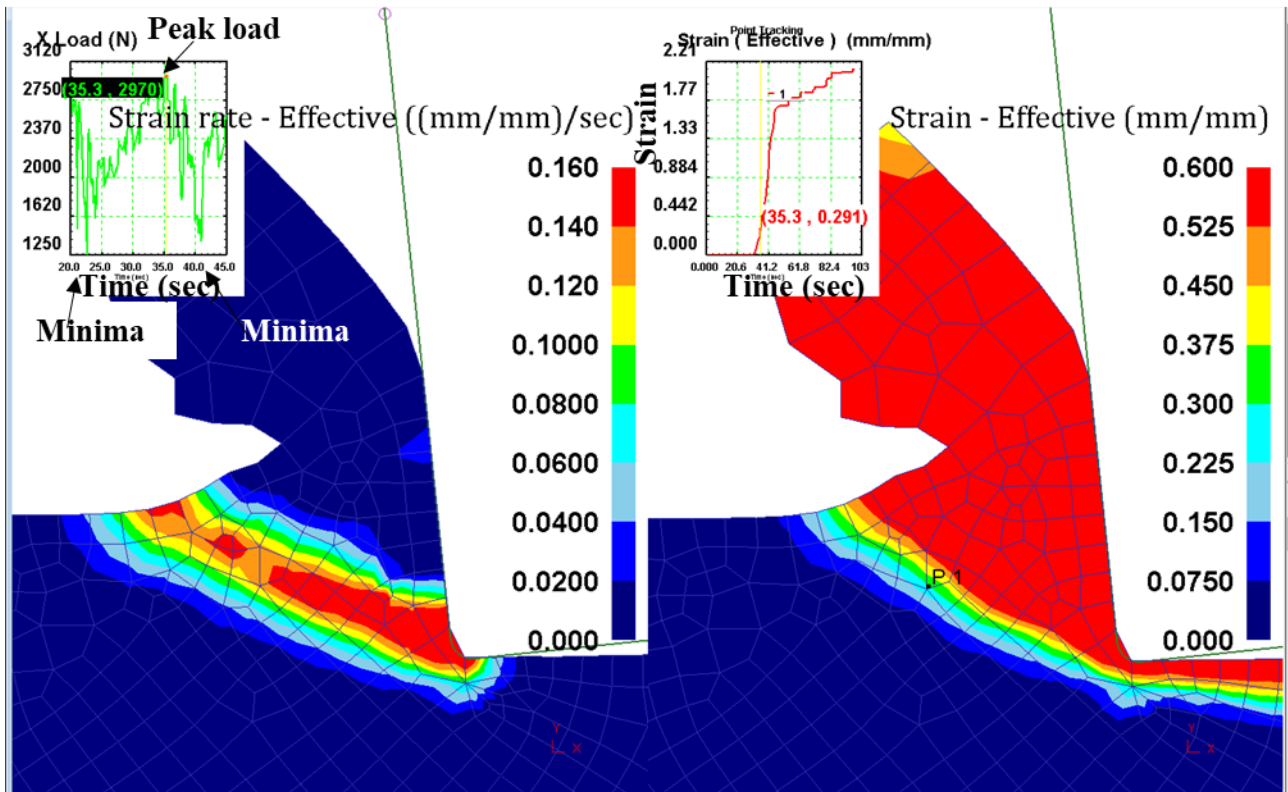
Figure 5-17. Correlation between peak load and strain, using the point-tracking feature in DEFORM™. The point was selected in the centre of the shear band at the time corresponding to peak load. Then the time from min to min load was used to track the strain at the selected point.
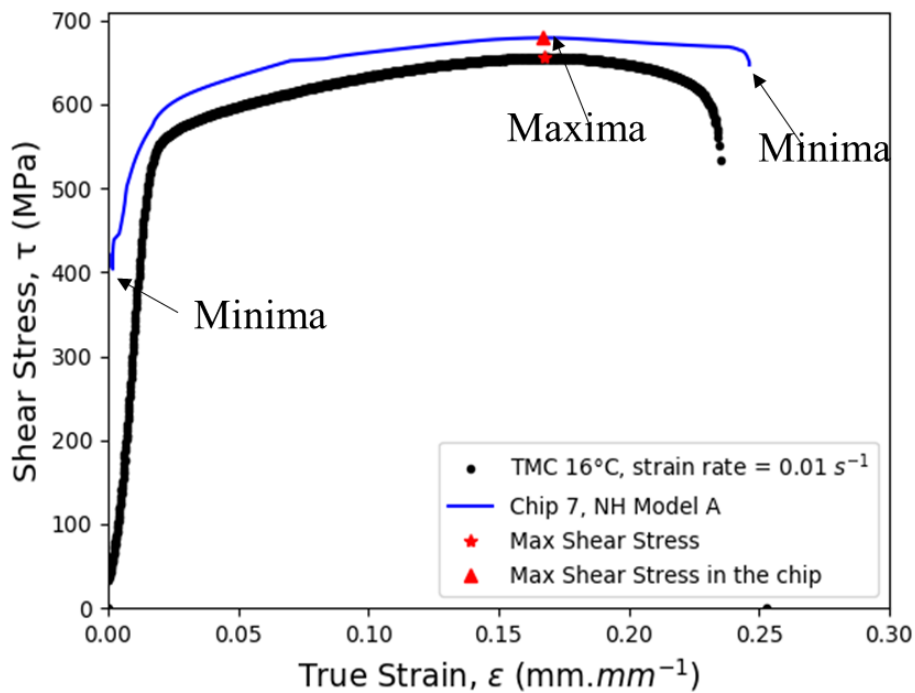
Figure 5-18. Comparison of the shear stress versus strain from the uniaxial compression test to chip No. 7 from the Norton Hoff Model A, linking time, distance, axial load to a point tracking strain along the centre of the ASB.

196

Another method to determine strain along the shear band is that specified by Shankar [99] using a Particle image velocimetry (PIV) technique to determine the imposed strain along a selected trajectory. The measured strain increase along the ASB was done at the time, which corresponds to the load maxima, see Figure 5-19. These values are in agreement with those reported by Shankar [99] and Marshall [5]. Correlated shear stress and strain is shown in Figure 5-20. This curve was compared to the Von Mises shear stress and strain from uniaxial compression testing at the same temperature.

Figure 5-21 shows the shear stress-strain comparison from axisymmetric compression at 10^{-1} s^{-1} and that corresponding to a selected chip under each cutting condition. These graphs show an excellent correlation demonstrating the feasibility and reliability for further testing. With an increase in an order of magnitude in speed, there is an increase in nearly 12% at low temperature and 16% at ambient temperature.
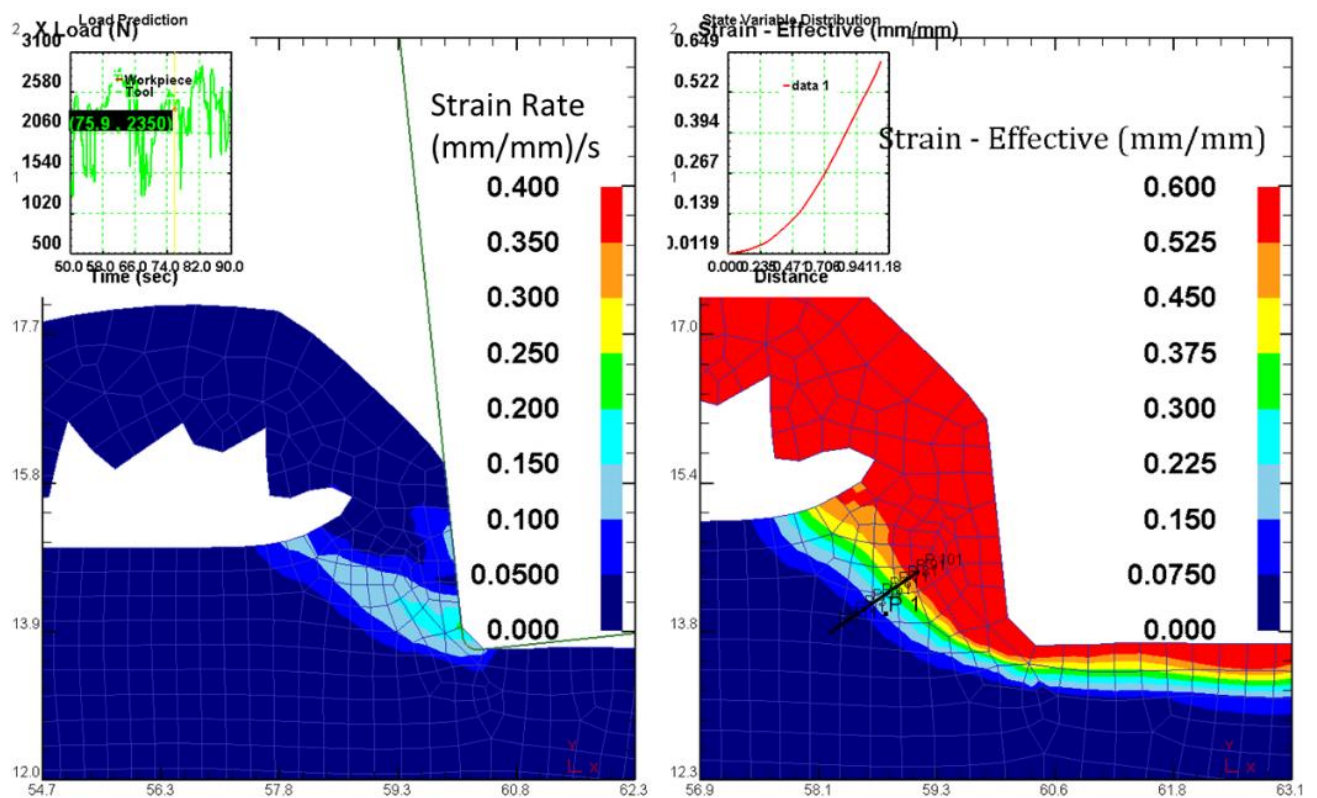
Figure 5-19. Strain along the shear band during orthogonal cutting at room temperature t_1 = 1.3 mm, V_c=0.01 m.min^{-1}, model C Norton-Hoff.
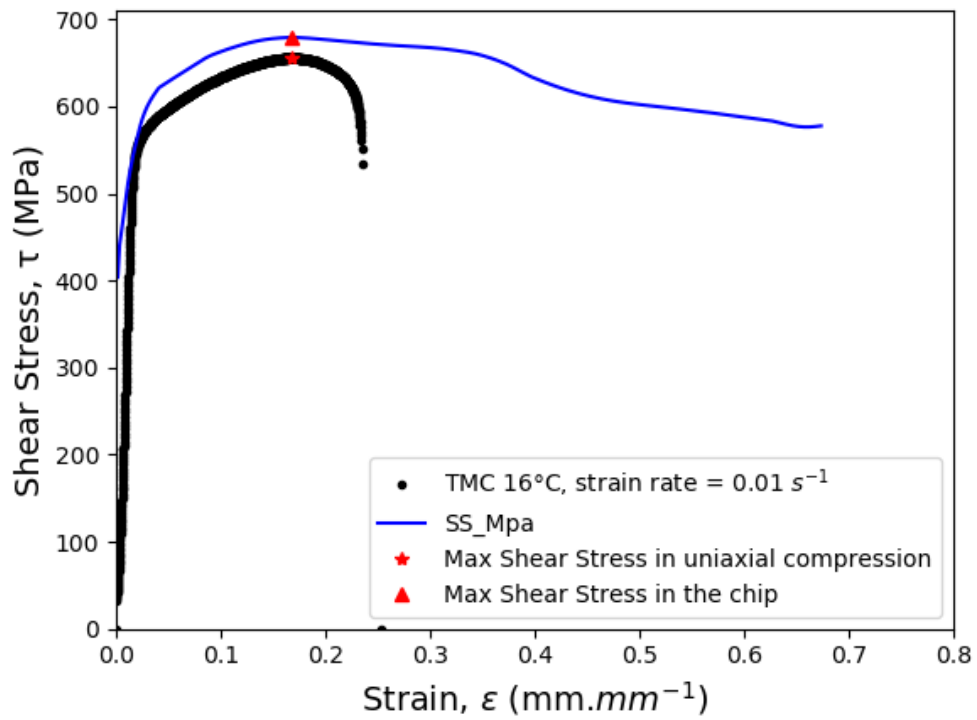
Figure 5-20. Comparison of Shear stress versus strain from uniaxial compression and chip No. 7 from the Norton-Hoff model A, cut at 0.01 m.min^{-1} at 16°C.
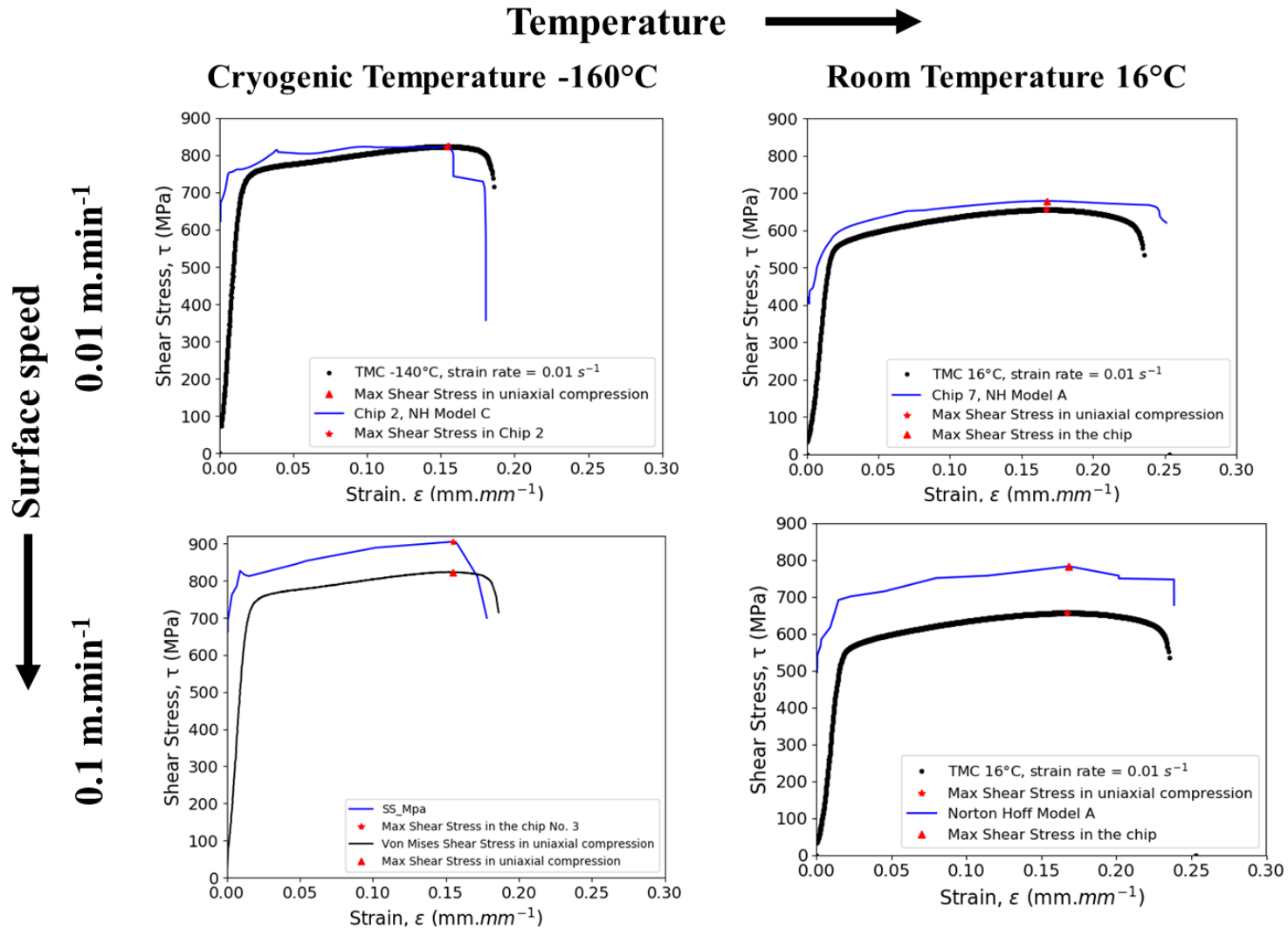
Figure 5-21. Von Mises shear stress versus true strain from axisymmetric compression tests and pseudo shear stress from orthogonal cutting versus strain at a) cryogenic temperature at 0.01 m.min⁻¹, b) cryogenic temperature at 0.1 m.min⁻¹, c) room temperature at 0.01 m.min⁻¹ and d) room temperature at 0.1 m.min⁻¹.

5.2. Severe Plastic Deformation imparted on the subsurface

The surface condition and the subsurface modifications generated during machining have a strong influence on the fatigue resistance [149]. During machining, a graded microstructure is generated originated in the surface and gradually changing in the subsurface. This is the result of the strain rate, stress, strain, and temperature generated local conditions. The severe plastic deformation (SPD) region imparted into the subsurface was measured using high magnification light microscopy using a cross-polarised filter. This is illustrated in Figure 5-22. At a speed of 0.01 m.min^{-1}, the arithmetic average was lower at a cryogenic temperature of -160°C nearly 9 µm. At room temperature of 16°C, it was slightly higher near 15 µm, which corresponds to a 66.6% higher SPD layer at room temperature. This implies that the area that has been recrystallized in the region closest to the subsurface is less deep at lower temperatures. The reason might be as at cryogenic temperatures plastic deformation is more localised, which also has implications in generating a thinner adiabatic shear band. Although the mean seems not too different under both conditions, there is a much higher spread under room temperature. This implies that a thicker SPD layer can be expected on the subsurface of components orthogonally cut at ambient temperatures.

At a speed 10 times faster, 0.1 m.min^{-1} a different behaviour takes place. At a cryogenic temperature of -160°C, an SPD layer of nearly 15µm has been measured. Whilst at room temperature of 16°C an SPD layer of 10 µm was estimated. There is a higher range of deformation under the cryogenic temperature at this speed (Figure 5-22). This might imply that the plastic deformation has been strongly influenced by the strain rate deformation. The higher SPD layer is expected to have a beneficial effect on the subsurface, as grain sizes in the range of ultra-fine or nano grain size have been observed. This SPD layer has enhanced mechanical properties such as higher yield strength (due to the Hall-Petch effect by reducing grain size, thus increasing grain boundary area). The smaller grain size may provide enhanced toughness, enabling plastic deformation to a greater extent.

5.3. Twin depth

At low temperatures, ahead of the cutting tool, mechanical twins appear, introducing a high density of lattice linear and point defects such as dislocations and vacancies as well as a high density of twin boundaries. When the tool approaches, the crystal lattice in the workpiece is forced to bend to allow the accommodation of plastic strain, leading to the introduction of more defects such as secondary twins, dislocations and vacancies. This leads to a higher degree of

misorientation in the lattice. This allows the boundaries to migrate to accommodate in arrays at a lower energy level (more stable).

The twin depth imparted into the subsurface during orthogonal cutting was measured using high magnification light micrographs taken under cross-polarised light, as illustrated in Figure 5-23. The effect of cutting temperature at a constant surface speed of 0.01 m.min^{-1} is that the lower the temperature, the higher cutting forces. This imparts a greater depth of mechanical twins into the subsurface. At a speed of 0.01 m.min^{-1} and at a cryogenic temperature of -160°C, an arithmetic average twin depth of 610 µm was estimated. Whilst at room temperature of 16°C, an arithmetic average of 420 µm was estimated.

It can be clearly observed that the higher the speed, the lower the plastic deformation imparted into the subsurface. This result is in disagreement with observations made by Crawforth et al. [104], who through EBSD micrographs of Ti-834 machined samples at high surface speeds found an increase in subsurface damage depth resulting from the increase in surface speed. Overall, slightly higher twin depths under cryogenic temperatures on both cutting speeds were measured. This comparison may not be directly related because the speeds in this chapter are much smaller than the industrial high-speed machining. Also, the stress state is very different from PSM in comparison to multi-axial stresses in milling.

At a speed 10 times faster, 0.1 m.min^{-1} whilst under a cryogenic temperature of -160°C, an average twin depth of 300 µm was estimated. Most of the data fell in a range of between 190 to 390 µm. At room temperature of 16°C, an average twin depth of 250 µm was estimated with most of the data falling in a range between 180 to 300 µm.

The lower plastic deformation imparted into the subsurface at higher speeds might be related to two factors. (1) Mechanical twinning might be strain rate sensitive during deformation and (2) there is less time available to plastically deform. This means there is less time for the plastic strain to be accommodated into the lattice. Additionally, at higher speeds there might be greater heat generation which concentrates on the shear band; thus, it becomes hotter reaching a near adiabatic condition. Then the shear band becomes more concentrated. A fracture can, therefore, be generated more easily. The faster the cutting speed, the higher the strain rate, so the higher the axial force needed to cut the workpiece orthogonally. This also implies higher stresses both near the cutting edge of the tool and imparted to the workpiece.

At room temperature of 16°C and at a lower speed of 0.01 m.min^{-1}, there is less force required to cut the material, and a higher degree of severe plastic deformation has been imparted into the subsurface. At a 10 times faster speed of 0.1 m.min^{-1}, higher cutting forces are required to yield and fracture the uncut thickness layer, and lower levels of plastic deformation have been imparted into the subsurface.

In terms of twin depth, at a cryogenic temperature of -160°C similar behaviour occurred. At the lower speed of 0.01 m.min^{-1}, lower cutting forces were required to yield and shear the uncut chip thickness layer. Higher levels of subsurface plastic deformation were observed. At a 10

times faster speed of 0.1 m.min^{-1}, slightly higher cutting forces were required, but nearly half the subsurface plastic deformation was measured on light micrographs.

Qualitatively, a much higher twin density is observed at the higher speed of 0.1 m.min^{-1} and at a cryogenic temperature of -160°C.
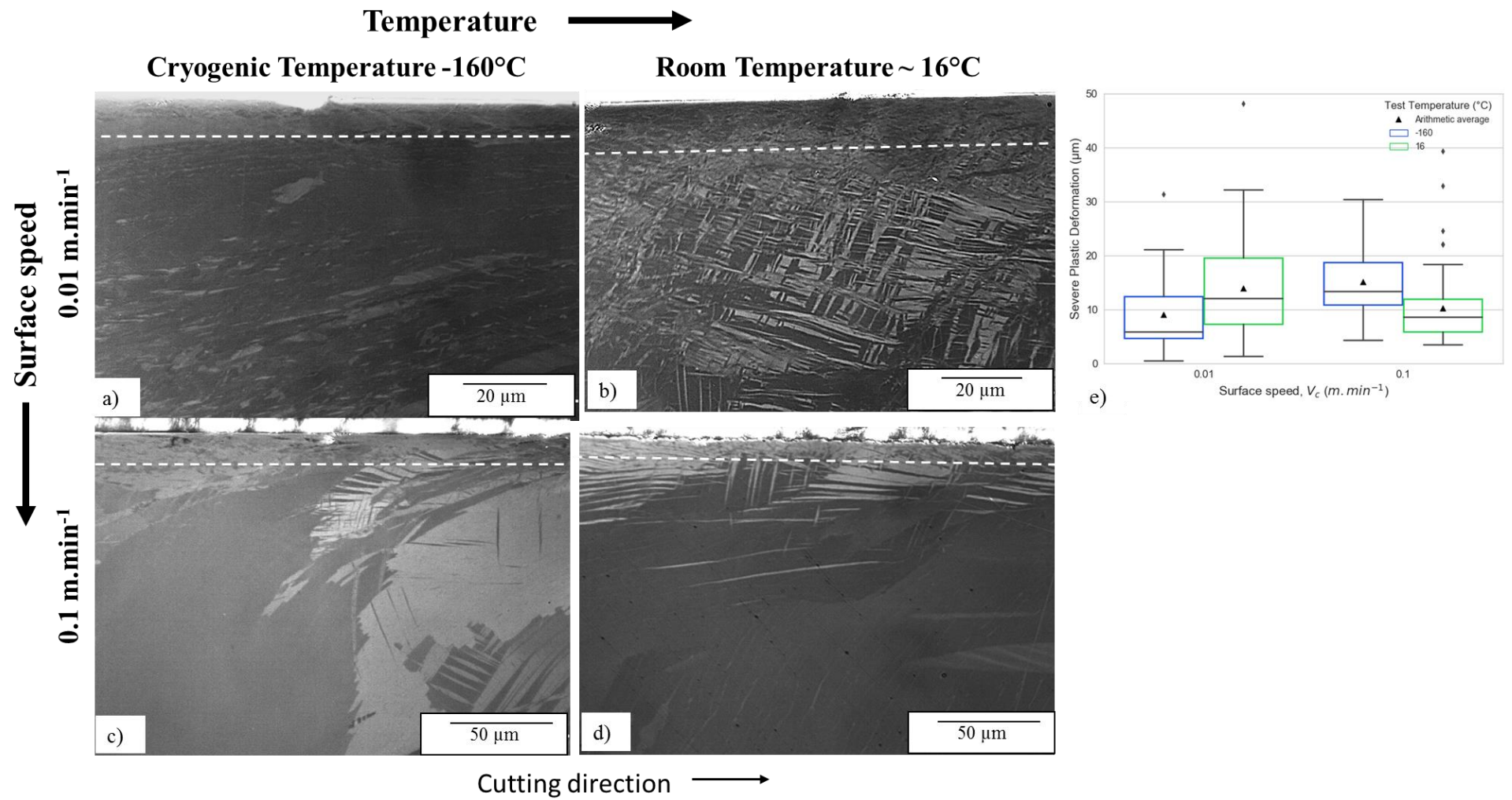
Figure 5-22. a) to d) Cross-sectional high magnification light micrographs of the severely plastically deformed region right below the machined edge: a) of -160°C 0.01 m.min⁻¹, b) of16°C 0.01 m.min⁻¹, c) of -160°C 0.1 m.min⁻¹, d) of 16°C 0.1 m.min⁻¹ and e) bar represent the arithmetic average and the bars represent one standard deviation (68.26% of the spread from the mean).
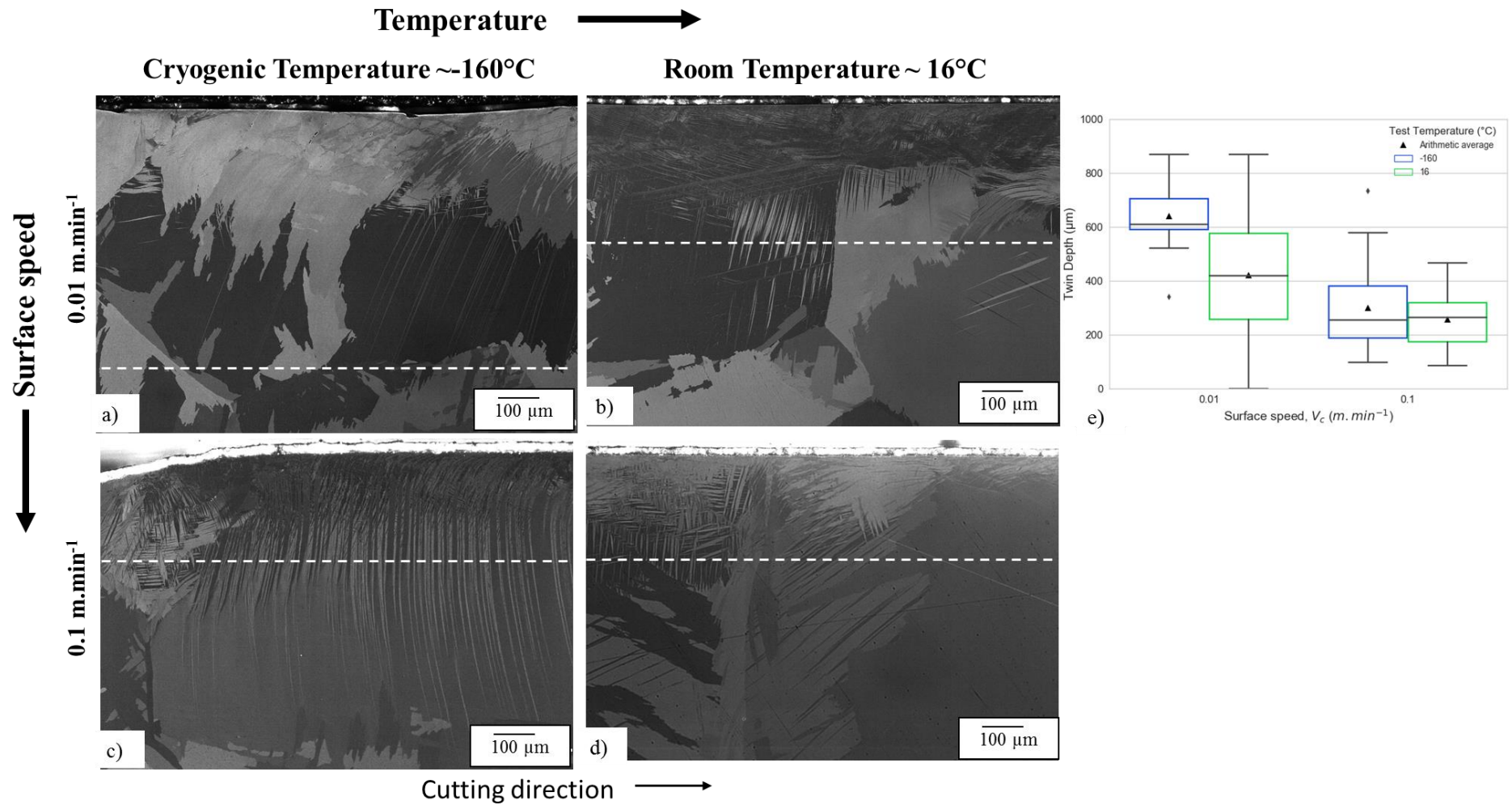
Figure 5-23. a) to d) Cross-sectional high magnification light micrographs of the plastically deformed region right below the machined edge: a) of -160°C 0.01 m.min⁻¹, b) of16°C 0.01 m.min⁻¹, c) of -160°C 0.1 m.min⁻¹, d) of 16°C 0.1 m.min⁻¹ and e) bar represent the arithmetic average and the bars represent one standard deviation (68.26% of the spread from the mean).

5.4. Microstructural defects during PSM

5.4.1. Cryogenic Temperature of -160°C at 0.01 m.min⁻¹

Besides the SPD and TD subsurface measurements, other plastic deformation features have been observed in PSM workpieces' subsurfaces. Figure 5-24 a) shows some cracks generated in the subsurface of a PSM workpiece under cryogenic temperature. A 16.8 µm long crack is found at a 25.7µm distance into the subsurface. This is generated along the boundary of a mechanical twin. This correlates with experimental evidence reported by Partridge [150], Stevenson and Breedis [151] and Beevers and Halliday [152], who reported preferential crack initiation sites the twin boundaries during hcp α Titanium subjected to cyclic loading. Twin boundaries also represent surface energy, however much lower than those of a grain boundary [2] and also are surrounded by areas of high dislocation density (adjacent to the twin boundary). This crack might have nucleated as the strain energy could not be accommodated by the lattice. As a result, the only way to accommodate that plastic strain was through the opening of a crack. Along the twin boundaries, there is a formation of pinning points attributed to dislocation debris, generated during cyclic loading [152]. This results in non-uniform movement of twin boundaries during high shear stresses, leading to twin cracking because of the stress concentration in these pinning points [152]. In Figure 5-24 a) there is another propagating crack at a depth of 57.8 µm in the subsurface, nucleated along a grain boundary. High shear stresses and strains might have been generated in that area, thus crack nucleation is the way in which plastic deformation has been accommodated into the lattice. Figure 5-24 b) shows an example of high surface roughness generated during PSM. This may have occurred due to instability in plastic deformation. The hcp crystal structure is highly anisotropic due to its inherent low symmetry; this causes plastic deformation to be heterogeneous. Another reason might be that BUE formation on the tool tip may have locally changed the SBA. As a result, generating the shear band heterogeneously removing part of it and leaving behind part of it. This part of the chip left on the subsurface could only function as a notch and could represent a site of potentially catastrophic failure.

During PSM under cryogenic cooling conditions, the dominant mode of plastic deformation is mechanical twinning, as the CRSS for slip is much higher at such temperatures. The mechanical twinning generated in the subsurface of the PSM under LN$_2$ appear as needle-like twins. There is a high frequency or density of these features (Figure 5-24 b)). As most of the heat generated during the cutting operation was removed from the cutting zone by the LN$_2$, this might imply that there was less energy available for twin growth. The fact that there is mechanical twinning to a greater subsurface depth might be related to the easier or more

localised formation of shear bands, and the higher forces and shear stresses generated at low temperatures, which may have been imparted to the workpiece microstructure.

Figure 5-24 c) shows voids forming on a localised strain 232.87 µm in length at a depth in the subsurface of 130 µm. In a region nearby, there appear to be some characteristic mechanical twins that usually appear near voids and are harder to detect using light microscopy under cross-polarised light. These types of twins have previously been observed by the author in other conditions under different states of stress (under milling) but without the crack nucleated around it. Detecting these types of twins in machined components may be important as they could be sites of void nucleation under in-service cyclic fatigue. Figure 5-24 d) shows parts of the chip generated, some grains have a high density of twins, these might be "soft" grains, while other nearby grains do not show much plastic deformation. These may be grains with a "hard" orientation with respect to plastic deformation. Different shearing directions are observed; this could be positive. Smaller chips might be generated at low temperatures, thus preventing damage to the workpiece as a result of chip accumulation in the machining zone.
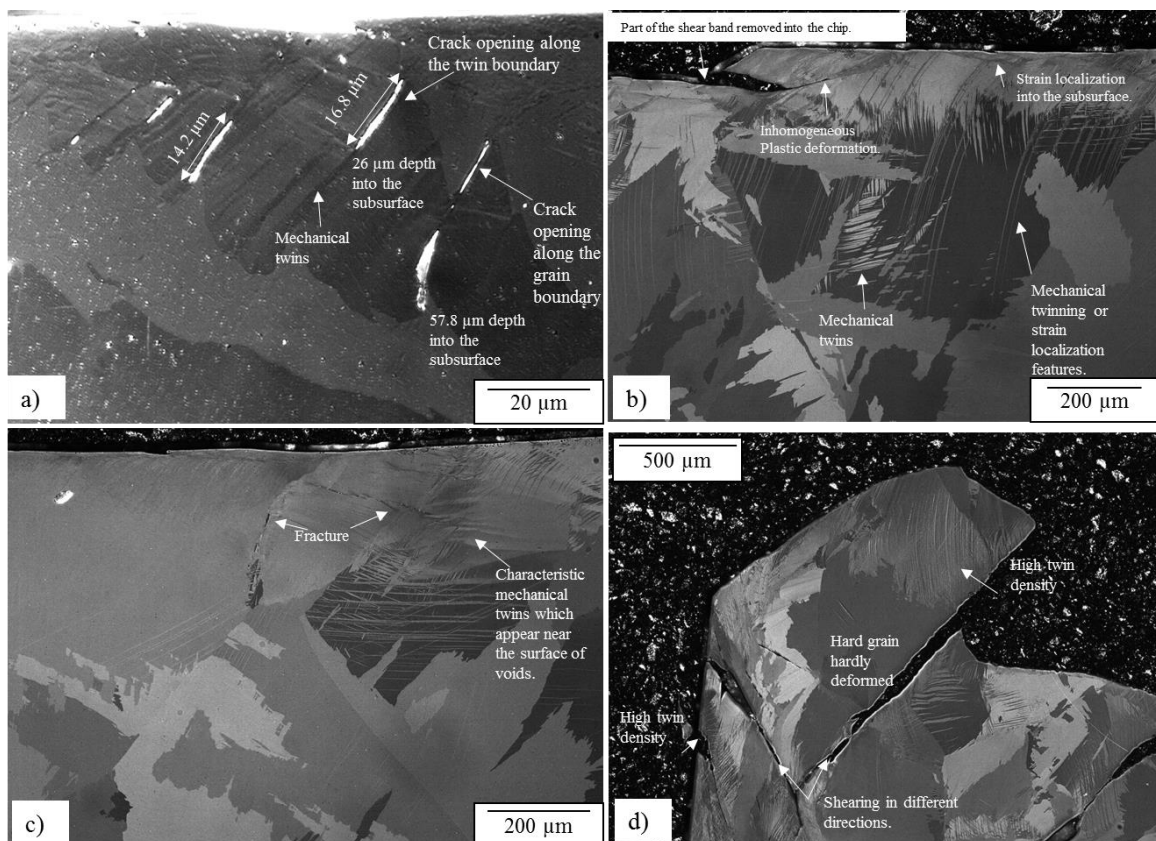
Figure 5-24. a)-c) Cross-sectional, cross-polarised light micrographs showing PSM induced features on the subsurface and d) chip formation in Ti-6Al-4V under a cryogenic temperature of -160°C at 0.01 m.min^{-1}.

5.4.2. Room temperature of 16°C at 0.01 m.min⁻¹

Figure 5-25 illustrates subsurface damage features induced during PSM at ambient temperature whilst being machined at 0.01 m.min^{-1}. Figure 5-25 a) shows a fractured area. The shear band might have been localised in the subsurface and fractured during the pass of the cutting tool. It also shows cracks being formed in a near-normal direction to the cutting direction. Under these features, mechanical twins appear showing a more lenticular morphology. Figure 5-25 b) also shows strain localization in the subsurface but in this area, the subsurface material has not entirely been fractured. Below this, there appears to be a high density of lenticular mechanical twins. Figure 5-25 c) shows other strain localization areas going into the subsurface. Beneath this, there is a high frequency of fractured areas, nearly 60 µm in length. The central features illustrate how intensely localised slip has generated a fracture which displaced the material nearly 5 µm. In Figure 5-25 d) the cutting tool induced mechanical twins of 750 µm ahead of it in the cutting direction and of 645 µm in a normal direction. The average twin depth is smaller than this ND distance, which implies that the twin depth is not influenced by the tertiary cutting zone (flank face of the tool). Nevertheless the flank face of the tool nucleates and distorts the mechanical twins that already exist in the region near to the cutting edge.
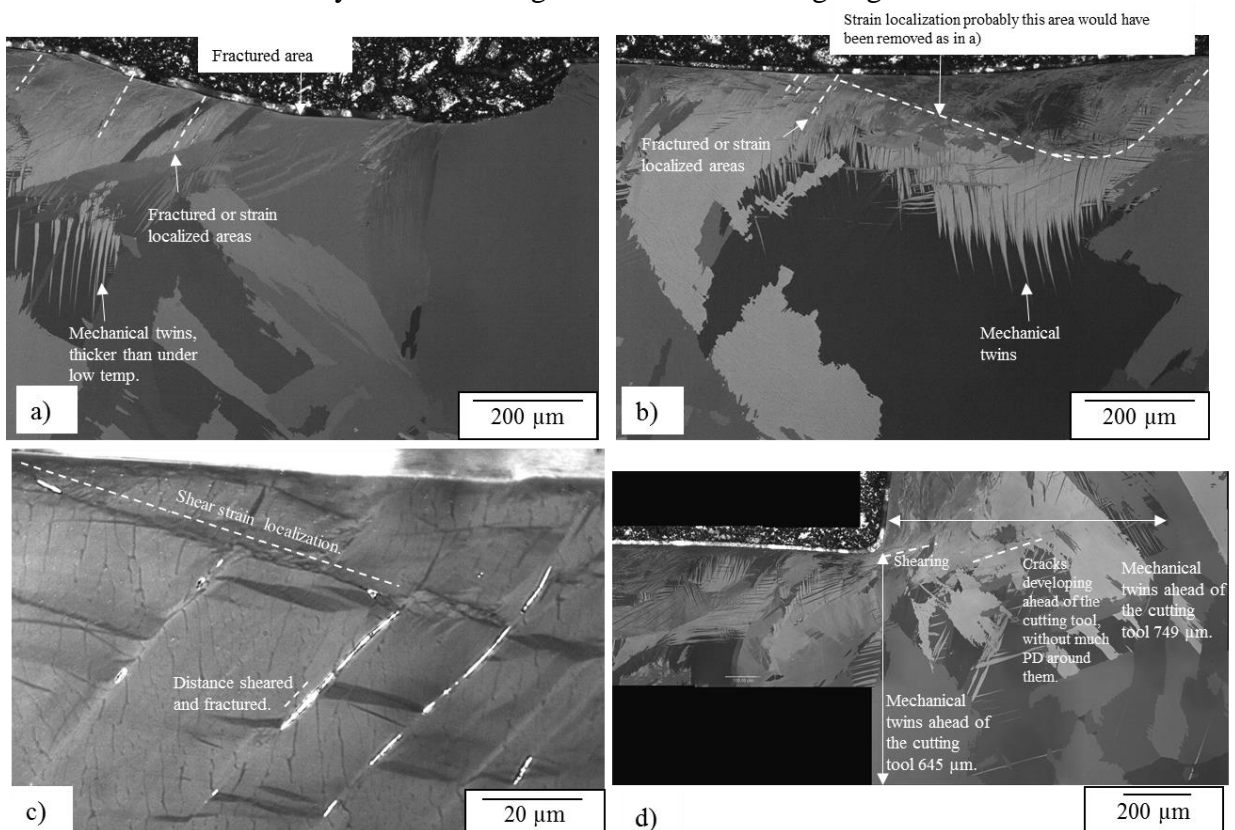
Figure 5-25. Cross-sectional, cross-polarised light images illustrating PSM at 16°C and at 0.01 m.min^{-1} induced deformation features on the subsurface a)-c) and d) area ahead of the cutting tool.

5.5. Deformation Map showing the effect of Temperature and Surface speed on PSM

A deformation map illustrating the effect of cryogenic temperature and ambient temperature as well as different surface speeds (therefore different strain rates) on the machining imparted subsurface plastic deformation during PSM was generated and is shown in Figure 5-26.

Figure 5-26 a) corresponds to a cryogenic temperature of -160°C at a speed of 0.01 m.min^{-1}. It can be observed that ahead of the cutting tool, high strain localisation features appear nearly 800 µm ahead of the rake face of the tool. Behind the cutting tool, the subsurface appears highly deformed with lattice rotation in the cutting direction. There are also new distorted mechanical twins which may have been introduced into the subsurface by the flank face of the tool. A partially fractured chip can be observed with the workpiece still holding the chip in the centre. This implies that the void initiation started ahead of the cutting tool and then followed the primary deformation zone near the tool nose where a higher shear stress is concentrated. This leaves the final fracture to occur in the centre of the shear band. Figure 5-26 c) shows subsurface deformation at -160°C, at a higher speed of 0.1 m.min^{-1}. A lower depth of imparted deformation is observed, nearly 400 µm ahead of the cutting tool, inducing mechanical twinning.

In Figure 5-26 b), ahead of the cutting tool some mechanical twins appear where the lattice is orientated in a consistent direction. After the tool passed the region (via a cut or chip generation), the lattice appears highly distorted. Previously formed mechanical twins underwent secondary twinning or mechanical twinning in different directions — this generated distortion around the area. Figure 5-26 d) shows lower induced subsurface deformation at an ambient temperature of 16°C at 0.1 m.min^{-1}. However, there are voids nucleated nearly vertically into the subsurface and along the cutting direction. As the chip observed has just fractured there is no evidence of deformation features ahead of the cutting tool, only along the fractured shear band on the remaining workpiece material.

Figure 5-27 shows images of the surfaces generated in PSM at 0.01 and 0.1 m.min^{-1} at -160°C and 16°C. At 0.01 m.min^{-1} and 16°C, there were more voids on the surface, suggesting that it was harder to remove the layer of material, the uncut chip thickness. The surface generated at -160°C appears more uniform with qualitatively a lower surface roughness.
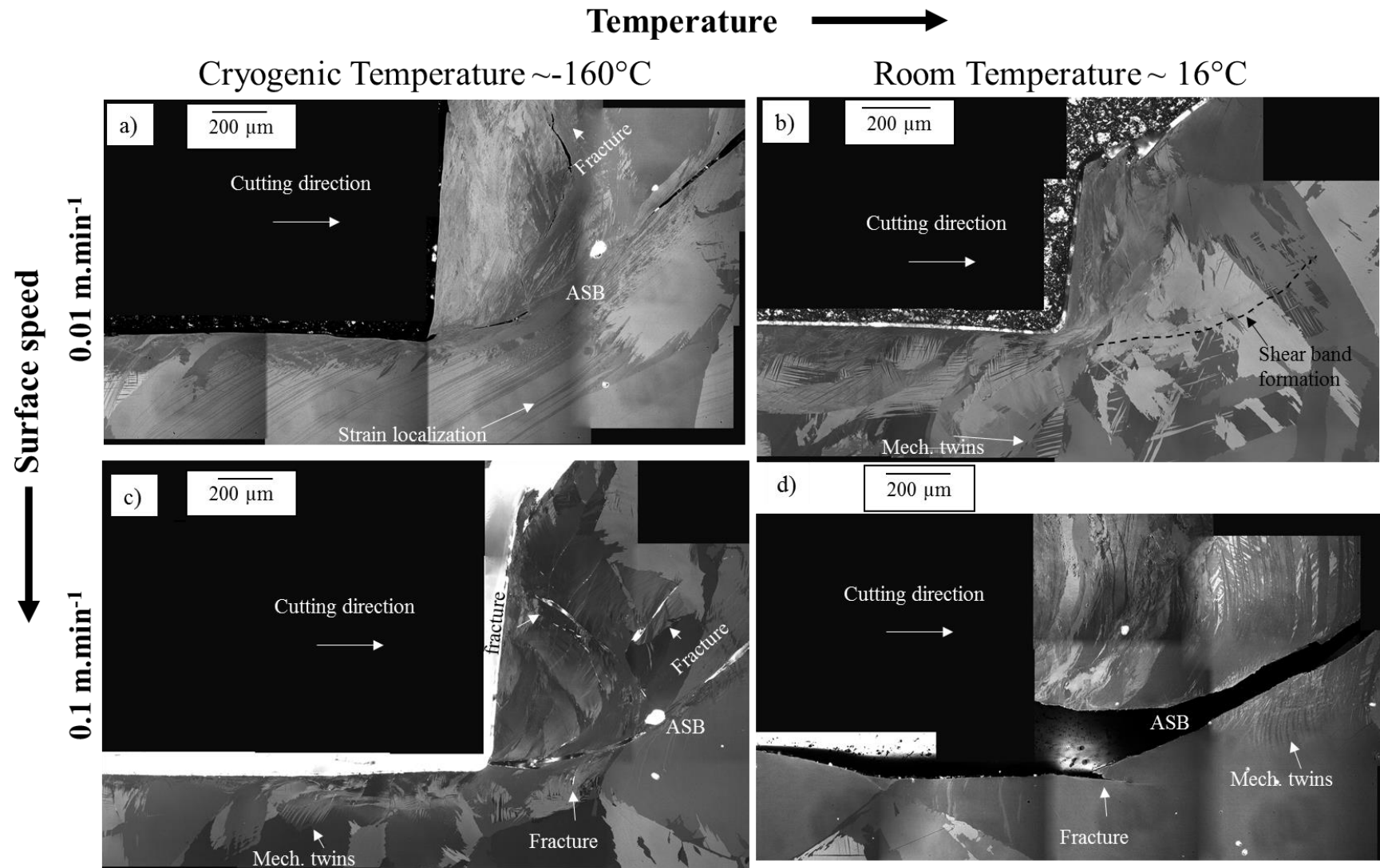
Figure 5-26. Deformation map composed of light micrographs of the region ahead of the tool tip: a) of -160°C at 0.01 m.min^{-1}, b) of 16°C at 0.01 m.min^{-1}, c) of -160°C at 0.1 m.min^{-1}, d) of 16°C at 0.1 m.min^{-1}.

209
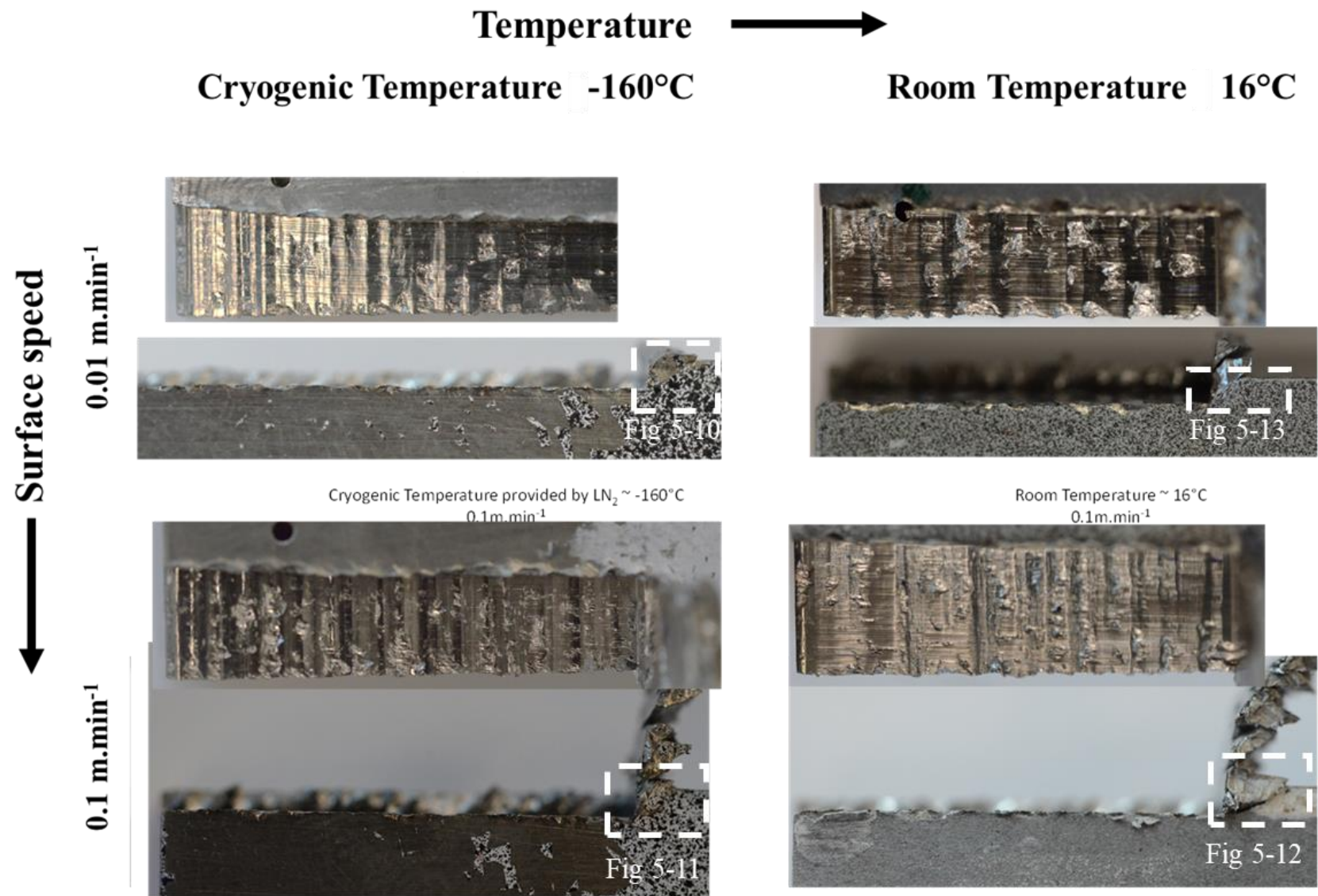
Figure 5-27. Image of the machined workpiece under LN_2 cryogenic cooling and room temperature at 0.01 m.min^{-1} and 0.1 m.min^{-1}.

At low cutting speeds, chips usually result in a discontinuous type. The higher the speed, and the higher heat generation, the chips segments reweld and form continuous chips. At room temperature, at a speed of 0.1 m.min^{-1}, most of the chips were continuous and inhomogeneous, as shown in Figure 5-28. At cryogenic temperature, some of the chips were continuous. This may be the result of a higher heat generation the higher the surface speed.
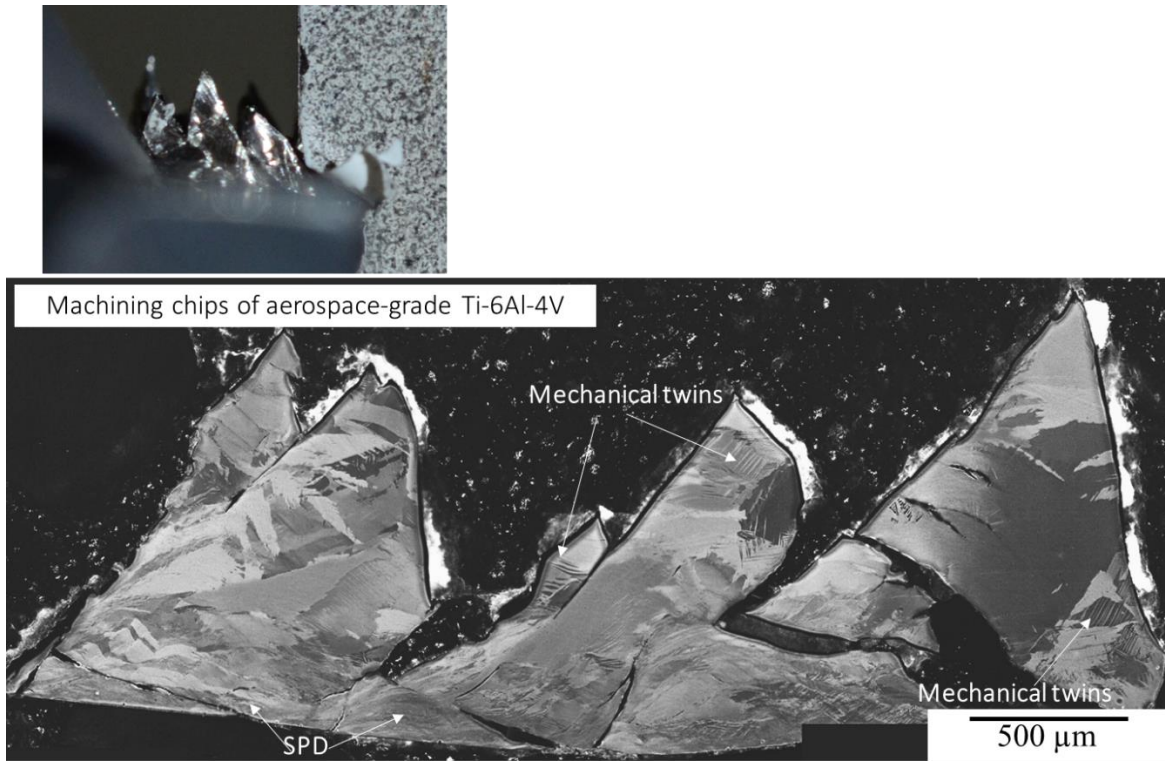
Figure 5-28. Chips generated during PSM of β annealed Ti-6Al-4V ELI at 0.1 m.min^{-1} without coolant (dry) using a Seco tool.

5.6. Severe plastic deformation imparted by the tool edge radius

Figure 5-29 shows the cross-sectional area below the cutting tool edge radius at different temperatures at a surface speed of 0.01 m.min^{-1}. It is observed that at a cryogenic temperature of -160°C a higher area on the subsurface is being refined during the chip formation process. However, the arithmetic average of the SPD layer was smaller at the lower temperature. This implies that a higher amount of grain refinement might be carried away with the chip, leaving behind a smaller refined region within the subsurface component. Another reason may be that the observed subsurface corresponds to different stages of shear band formation; thus different shear stresses have been experienced at that different stages when the tool was being withdrawn from the cutting operation.
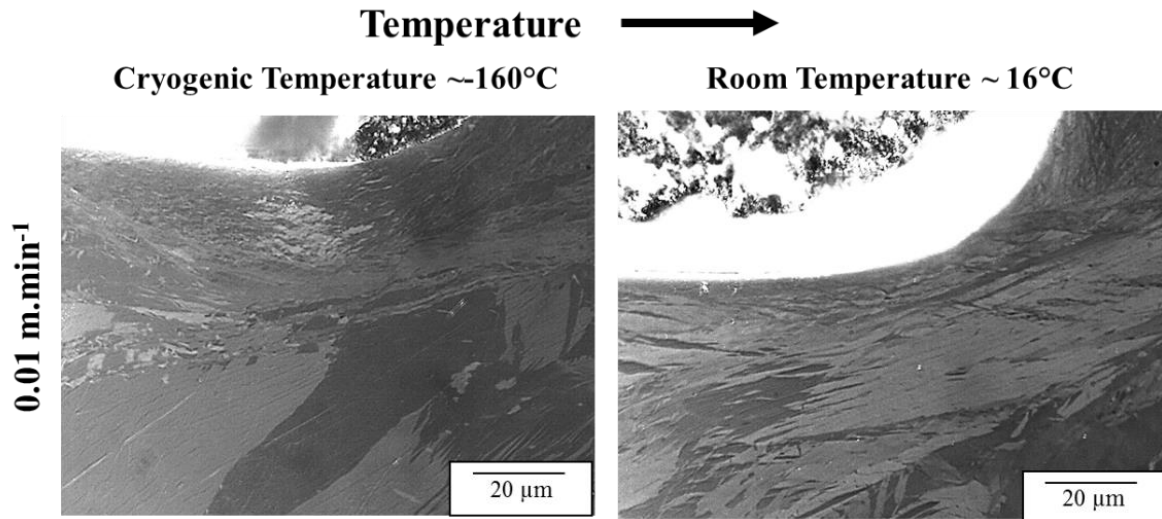
Figure 5-29. Cross-sectional light micrographs of the region below the cutting tool nose.

Figure 5-30 a) shows a BSE micrograph of β annealed Ti-6Al-4V ELI plane strain machined at 0.01 m.min^{-1} at -160°C. A region under a compressive stress state appears just below the crack formed in front of the cutting tool. Behind the tool, a small rounded notch appears on the surface (Figure 5-30 b), from it, a curved ASB with strain localisation develops, branching in the region below and ahead of the cutting tool. The lattice adjacent to the ASB is observed to undergo a high degree lattice reorientation. On other regions of the uppermost subsurface, to a depth of 5.5 μm, the β phase appears elongated but is not continuous (Figure 5-30 d). Below it, the spacing between the retained β phase has reduced, nearly to 0.4 μm, suggesting strain hardening.

At 0.01 m.min^{-1} at room temperature, the subsurface below the advancing cutting tool shows mechanical twins to assist in the lattice reorientation, Figure 5-31 b). Nearly 120 μm in depth on the subsurface, some voids are observed. These may have nucleated due to stress concentration regions imparted by ASB branching.
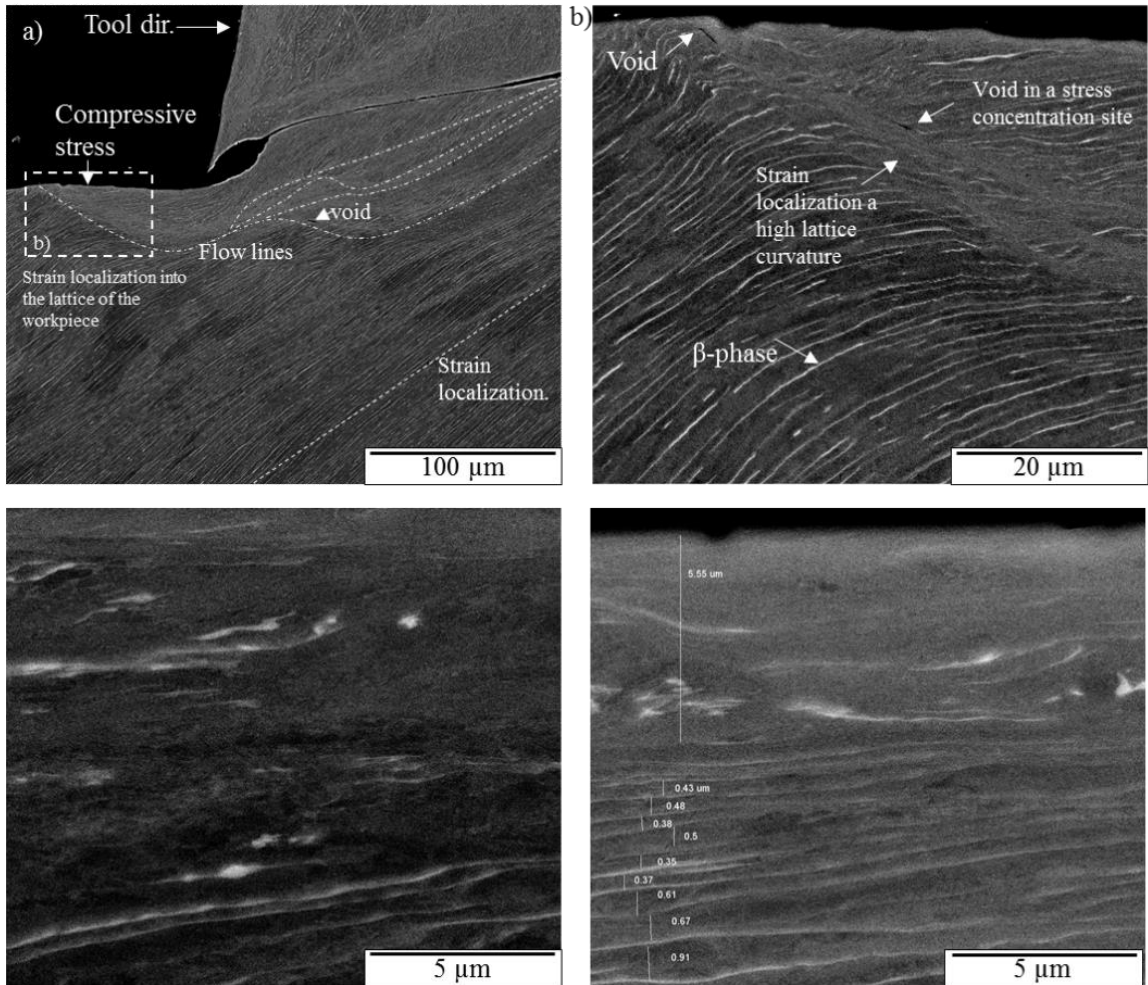
Figure 5-30 Cross-sectional BSE image from β annealed Ti-6Al-4V ELI under LN$_2$ cryogenic cooling conditions at -160°C at a surface speed of 0.01 m.min^{-1}.
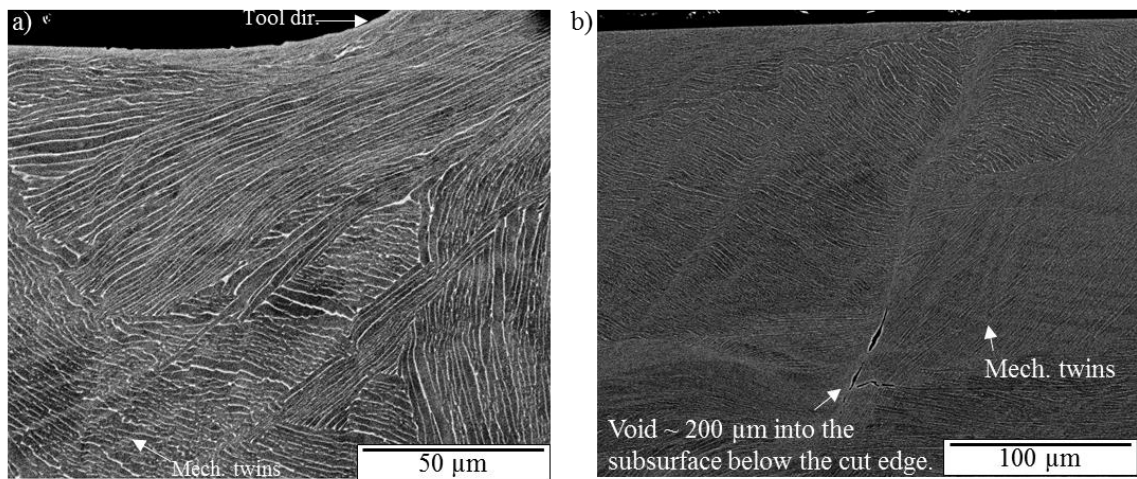
Figure 5-31. Cross-sectional BSE image from Ti-6Al-4V β annealed at room temperature of 16°C, a surface speed of 0.01 m.min^{-1}.

5.7. Effect of the uncut chip thickness t_1 on the imparted subsurface deformation

The effect of uncut chip thickness (t_1) on the machining-induced subsurface plastic deformation was investigated under room temperature conditions. The damage induced on the subsurface is illustrated in Figure 5-32. A slightly higher SPD layer has been observed with an uncut chip thickness which is 13 times wider. Although in the depth of the SPD layer there is not a marked difference, in terms of twin depth there is a significant difference. With a t_1 of 98.8 µm there is an arithmetic average twin depth of 95 µm, and with a t_1 of 1350 µm, there is an arithmetic average of 420 µm. This corresponds to a 4.4 times deeper twin depth deformation. This significant difference stems from the fact that much higher peak loads were generated during cutting larger uncut chip thickness (t_1). Therefore, much higher shear stresses were imparted by the cutting tool on the workpiece near the cutting edge.

From the high magnification light micrographs, it is observed that at the low uncut chip thicknesses, plastic deformation seems more uniformly distributed into the lattice during deformation. On the other hand, under the higher uncut chip thickness, the plastic deformation seems more distorted, giving rise to a gross plastic deformation below the SPD layer and below this gross plastic deformation, there is less distorted twin formation.

The peak load corresponding to 98.8 µm uncut chip thickness is 0.92 kN while for 1350 µm it is 12.8 kN. This 13 times increase in load might have had a significant influence on the twin depth region in the subsurface. An increase from 95 µm to of 420 µm subsurface deformation is related to the higher cutting forces required to cut the higher volume of material whereas there is only a slight difference in the SPD layer. The question remains whether the refined grain size varies under these different conditions. To investigate this further, TEM or high-resolution EBSD is required as light microscopy, and SEM cannot resolve such features.
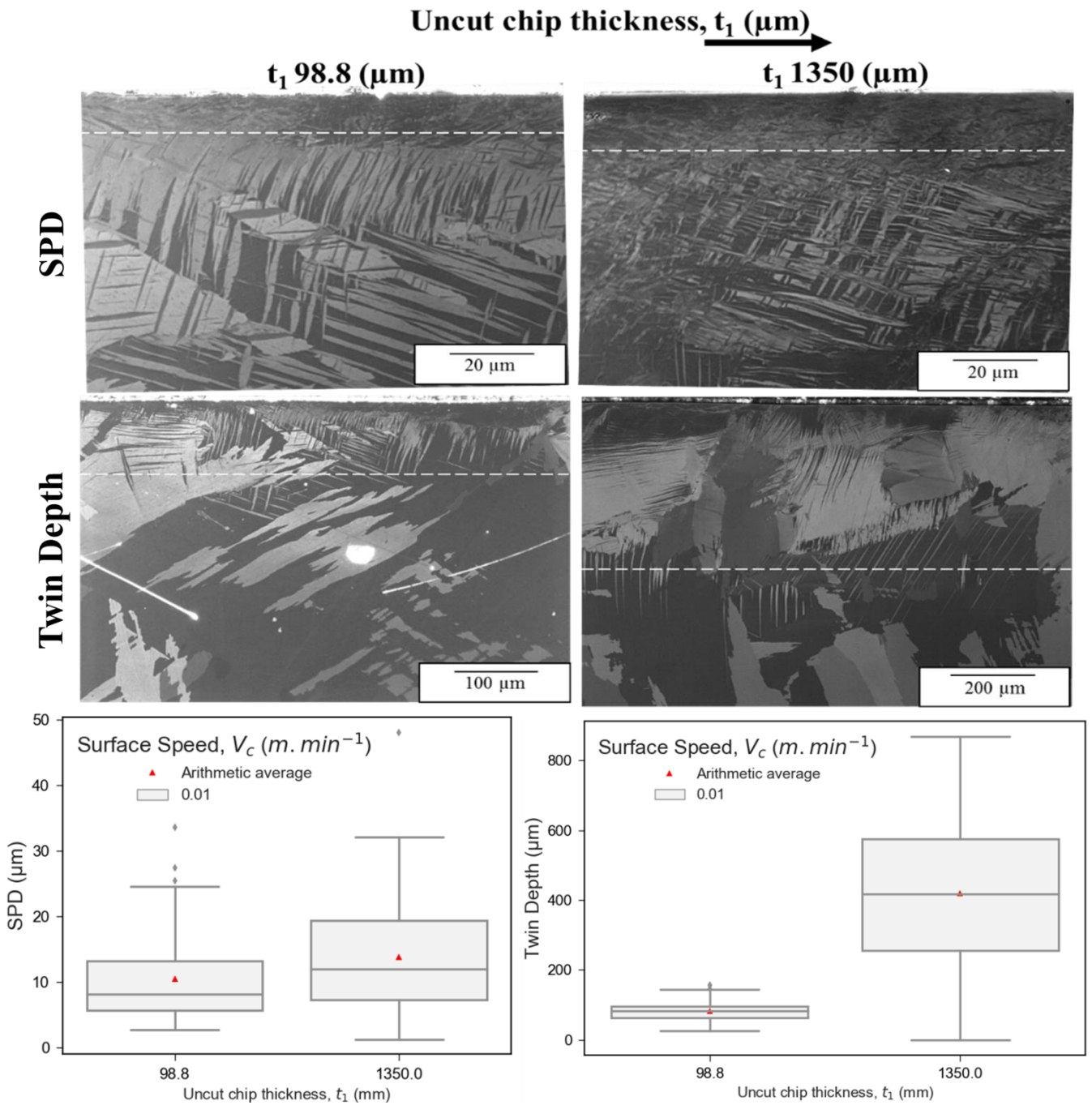
Figure 5-32. Effect of uncut chip thickness on the PSM induced subsurface plastic deformation. The delineated line signifies the arithmetic average twin depth.

According to Pusavec et al. [106], the increase in feed rate resulted in deeper and more compressive residual stresses into the subsurface. Accordingly, this would imply that the subsurface microstructural modification occurred to a deeper level as was the case observed in the microstructures in Figure 5-32, these may have undergone a deeper compressive stress state. The increased volume of material being removed leads to higher cutting forces, resulting in a higher depth of subsurface damage.

5.8. Estimating shear stresses during metal cutting from mechanical tests such as axisymmetric compression

Shear stresses generated during metal cutting operations at higher strain rates can be predicted using this small-scale testing methodology. This correlates to a nearly straight line of $\log_{10}$ strain rate to $\log_{10}$ shear stress [67]. Comparing shear stresses and strain rates during axisymmetric compression testing to higher strain rates obtained during orthogonal cutting exhibited a near linear behaviour. Room temperature testing shows higher strain rate sensitivity, suggested by the higher gradient in Figure 5-33.

Kuhn and Medlin [126] stated that for strain rates up to 10^4 s^{-1}, the yield strength is proportional to the logarithm of strain rate and thermally activated processes control it. This correlates to Figure 5-33. Kuhn and Medlin [126] also stated that for strain rates higher than $10^4 s^{-1}$, the yield is directly proportional to strain rate. It was attributed to a different mechanical response region, controlled by viscous damping.
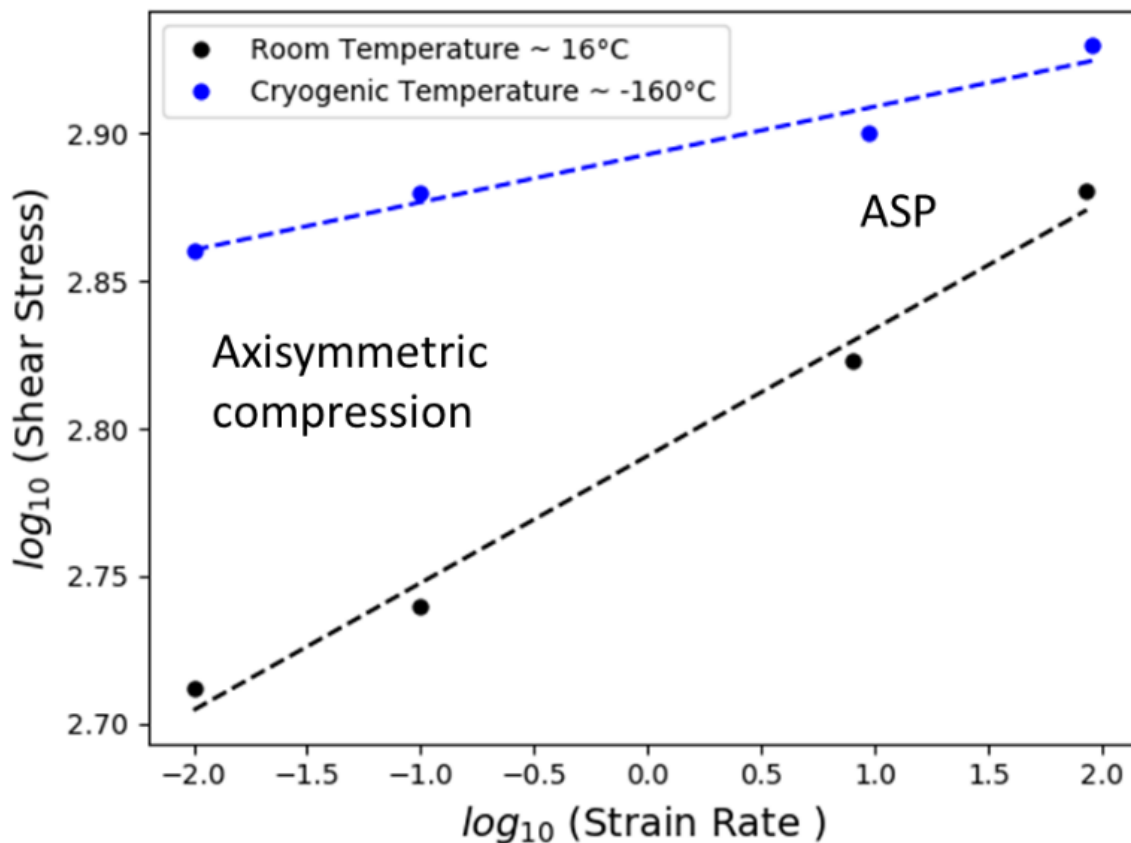
Figure 5-33. Log$_{10}$ strain rate as a function of log$_{10}$ shear stress at cryogenic temperatures during axisymmetric compression testing and orthogonal cutting at 0.01 m.min^{-1} and 0.1 m.min^{-1} β annealed Ti-6Al-4V ELI.

Although cutting forces and shear stresses are higher during cutting at low temperatures, the energy spent on chip formation is lower, see Figure 5-34. The ASB formation is easier to

generate, as the temperature tends to concentrate in a narrower region; thus thermal softening arises at lower imparted plastic shear strains.

After the softening point, the shear band starts to fracture by microvoid nucleation and tearing of the ligaments that join them. Figure 4-3 shows that after the onset of softening, at higher temperatures, there is a higher area before fracture. This suggests that there is a higher ductility and higher friction forces, which need to be overcome to reach fracture in the shear band, or during the transition from ductile to brittle fracture.

The higher the temperature, the higher the strain rate sensitivity, inducing larger forces and allowing it to impart large strains before the onset of instability for ASB formation and chip segmentation. This gives rise to more work done by plastic deformation (MJ.m^{-3}). 90-95% of the mechanical work is converted into heat, the greater the work, the higher the temperatures reached in the cutting zone.
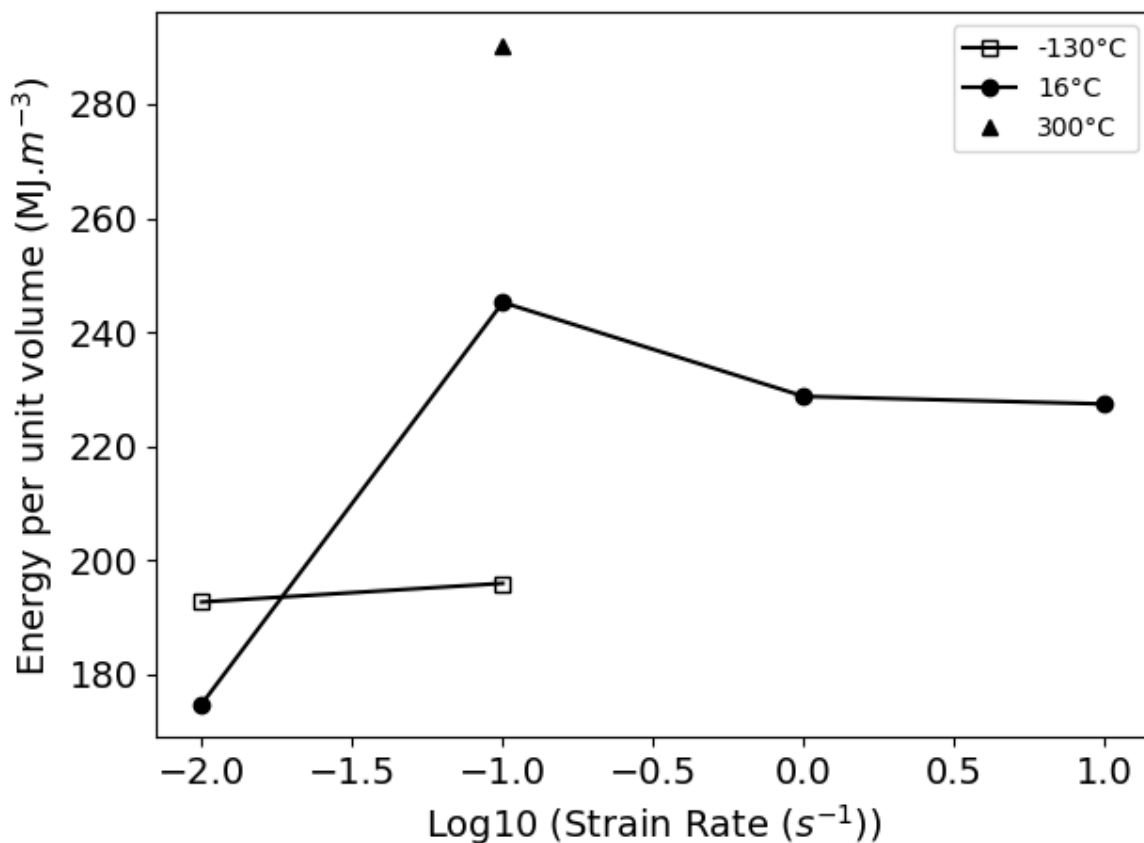
Figure 5-34. The effect of strain rate and temperature of plastic deformation on the energy generation (Cockcroft Latham Energy).

A linear relationship between the twin depth imparted into the workpiece subsurface, and shear strain rate was found, having a more significant impact at cryogenic temperature. It is a well-known fact that the CRSS for slip significantly increases at low temperatures (see Figure 2-10), allowing mechanical twinning to operate as the dominating mechanism of operative plastic deformation. At higher temperatures, slip has a more significant presence during the

accommodation of plastic strain on the lattice of the workpiece. The increase in the shear strain rate (from 0.01 to 0.1 m.min^{-1}) shows a reduction in twin depth imparted into the lattice. Whilst at -160°C it resulted in an almost 50% reduction in twin depth penetration, at 16°C it reduced by nearly 40%. At a high strain rate (corresponding to 0.1 m.min^{-1}) only at 16.6% twin depth penetration does a difference exist between cryogenic, and room temperature machined workpieces. The reduction in machining-induced subsurface damage depth with an increase in strain rate is in agreement with Crawforth [3] who reported a reduction in beta distortion in the subsurface with an increase in surface speed in Ti-834. However, it is in contradiction with the EBSD analysis Crawforth presented. Using this advanced technique, they showed an increase in subsurface damage when surface speed was increased. EBSD enabled the observation of imparted plastic deformation in the primary alpha and the matrix, while BSE in the SEM was based mainly on the deformation of the beta phase (heavily influenced by tool drag during cutting). The number of samples may have been low as EBSD requires a long time to scan an area and to obtain a high percentage of accurate data.
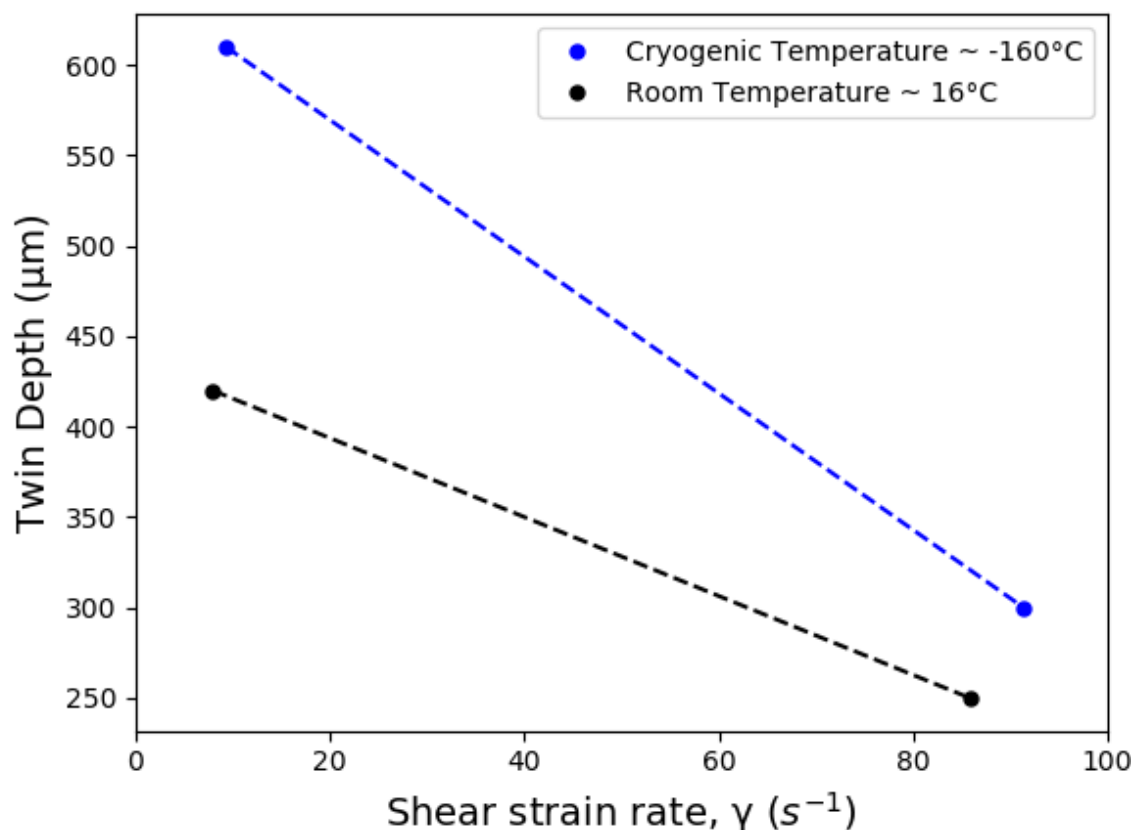
Figure 5-35. Arithmetic average twin depth imparted into the workpiece subsurface as a function of imparted shear strain rate during PSM.
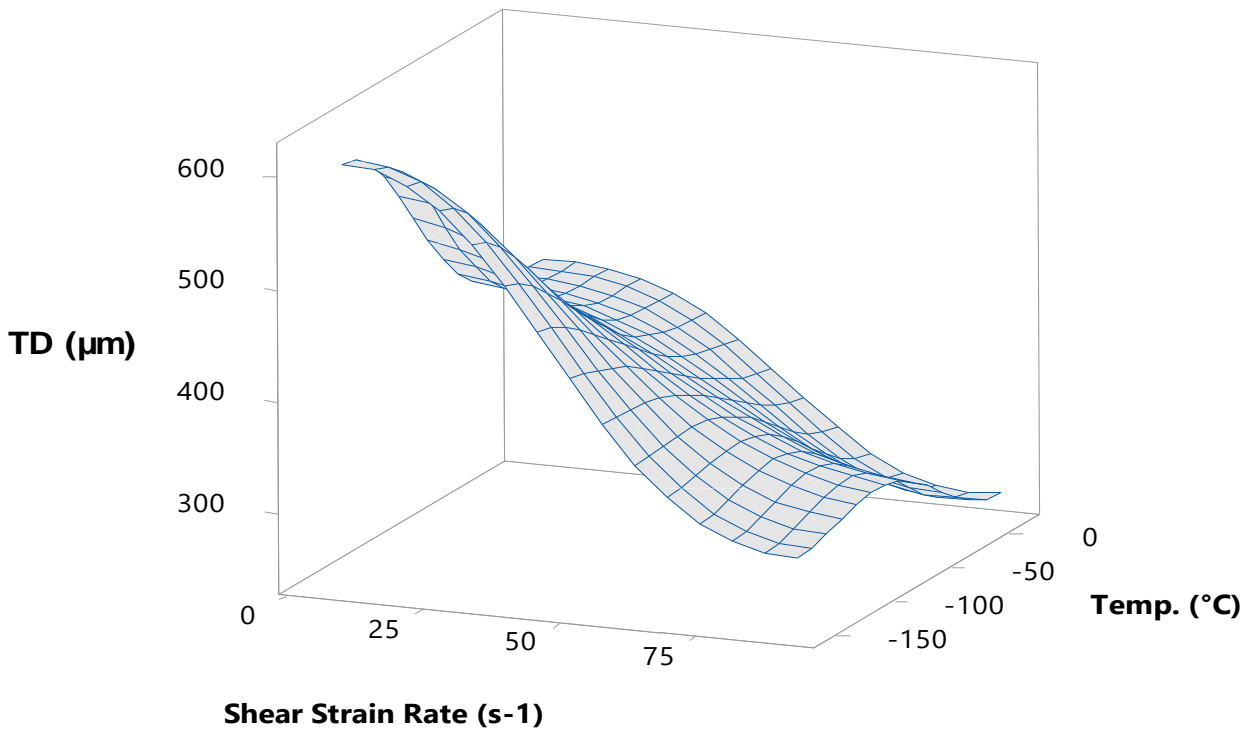
Figure 5-36. Twin depth (µm) in the workpiece's subsurface as a function of shear strain rate and temperature during PSM Ti-6Al-4V in a β annealed condition at 0.01 and 0.1 m.min^{-1} surface speed.

Figure 5-36 shows the relationship between twin depth as a function of shear strain rate (surface speed). The combination of low strain rates and low temperatures generates higher twin depth penetration into the lattice of the workpiece. This clearly shows that both at lower temperatures and low strain rates, a deeper level of subsurface damage is imparted in terms of mechanical twins.

The improvement in tool life from the use of cryogenic coolants has been widely reported [123], [153], [154]. This work was in concurrence with to previously reported results. The LN$_2$ cryogenic coolant generated lower flank wear even when the tool made a longer cut. The flank also showed a fractured area under both conditions. Nevertheless, this area was much smaller during the cryogenic machining. This fact might be due to a reduction of the thermal activation mechanisms for diffusion and the dissolution of tool material alloy additions, which may have adhered to the chip and /or the workpiece material at room temperature.
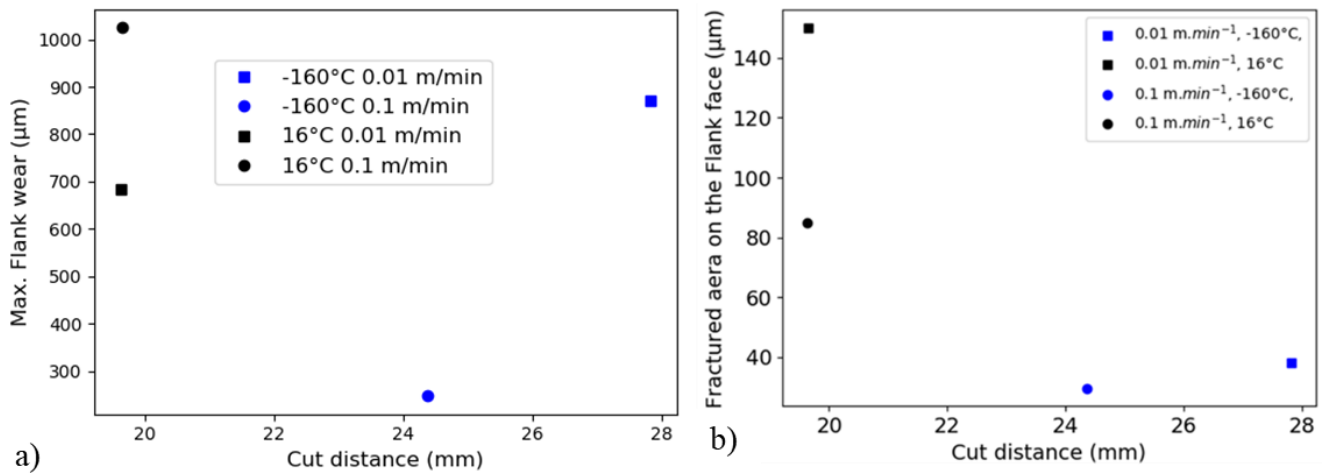
Figure 5-37. Tool wear during PSM at 0.01 m.min^{-1} and 0.1m.min^{-1} under LN$_2$ cryogenic cooling and room temperature: a) Maximum flank wear b) Maximum fractured area on the flank face.

The surface of the Seco tool showing flank wear produced during plane strain machining at low cutting speed under LN$_2$ and dry are observed in Figure 5-38. At a speed of 0.01 m.min^{-1}, the workpiece under LN$_2$ generated lower tool flank wear than at ambient temperature. Also, edge removal was more extensive for the workpiece at 16°C. At 0.1 m.min^{-1}, the difference is more significant at the ambient temperature. Whilst a shallow depth of wear is observed in the tool which was used for cutting at -160°C, a much larger wear depth is observed for the workpiece when it was cut dry or at 16°C. Figure 5-38 d) is a montage using two images at the same magnification. This image also shows a more considerable depth of material removed due to fracture along the cutting edge. The greater affinity of titanium for interstitial oxygen at higher temperatures may have led to the formation of an oxide layer, and this may have also contributed to severe adhesion wear.

Figure 5-38 shows SECO's tool flank surfaces under the four different cutting conditions on the ASP, observed in light microscopy. At 0.01 m.min^{-1}, cutting β annealed Ti-6Al-4V ELI at 16°C, generated slightly higher wear than at -160°C. At 0.1 m.min^{-1}, the difference is more pronounced, generating a much higher depth of wear. This suggests that the chip generated at 16°C was thicker and/or that the higher temperatures generated led to solid-state diffusional mechanisms to be dominant under this condition.

Figure 5-39 shows a rough surface at the back of a chip composed of inhomogeneous fracture. The generation of these rough edges along the titanium oxide layer formed on freshly cut material due to the titanium high affinity for oxygen may lead to higher tool wear rates.

220
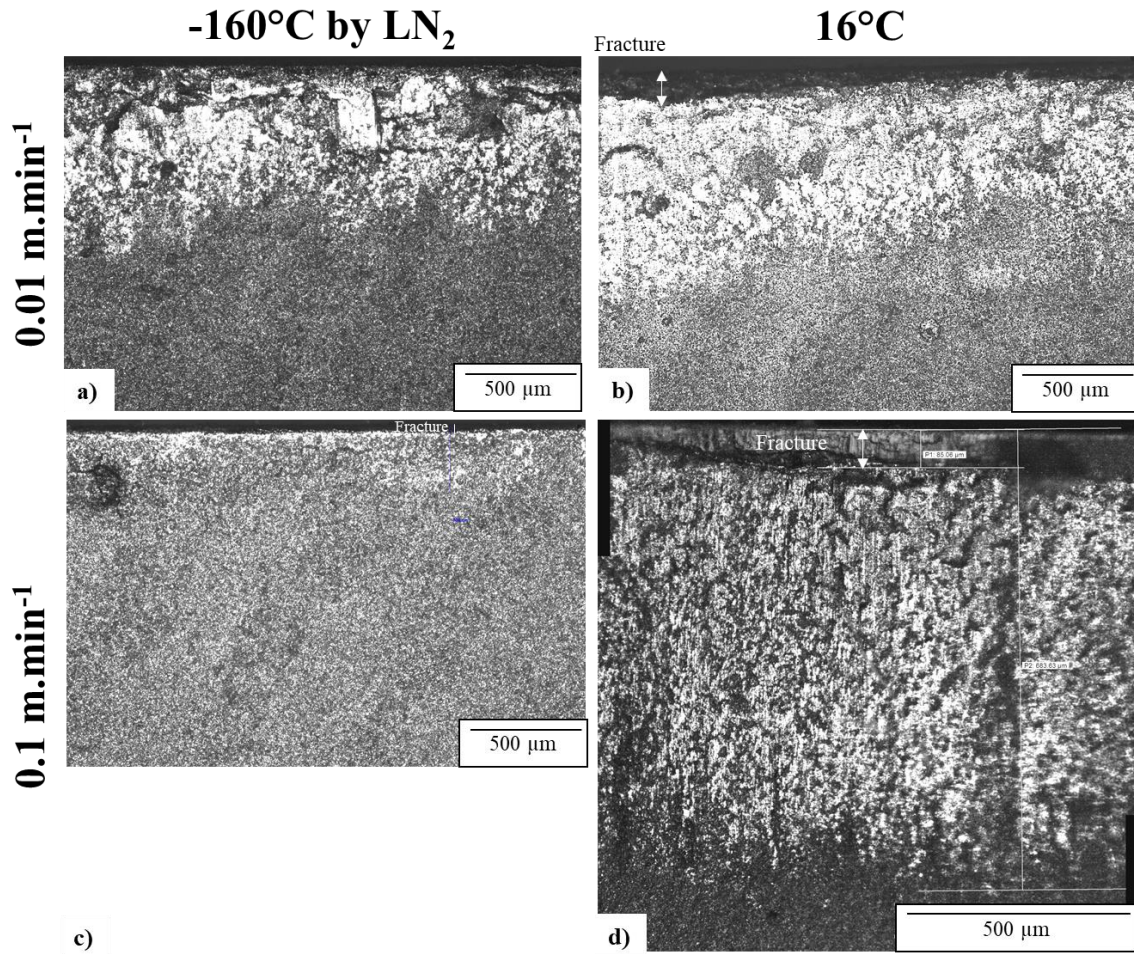
Figure 5-38. Uncoated Seco's tool flank wear during plane strain machining of β annealed Ti-6Al-4V ELI a) at 0.01 m.min^{-1} at -160°C, b) at 0.01 m.min^{-1} at 16°C, c) at 0.1 m.min^{-1} and -160°C and d) 0.1 m.min^{-1} at 16°C.

Figure 5-39. Inhomogeneous fracture on the back of the chip during PSM β annealed Ti-6Al-4V ELI at 0.01 m.min^{-1} at a depth of cut of 259 µm.

5.9. Ti-6Al-4V Mill Annealed

A Sandvik Coromant grade H13 A tool was used to near PSM mill annealed Ti-6Al-4V. Two cutting inserts were used simultaneously for this test, see Figure 3-17. Load-displacement data was acquired from the ASP during orthogonal cutting of Ti-6Al-4V in a mill-annealed condition. This occurred both at room temperature and at cryogenic temperatures achieved through the application of LN_2 directly to the cutting edge. The estimated grain size through the grain intercept method was $18.19 \pm 0.64 \, \mu m$ with a 95% confidence interval. The minimum temperature achieved with LN_2 was -161°C and a maximum of -153°C during metal cutting. This is presented in Figure 5-40. Cutting at cryogenic temperature generated higher peak loads. An arithmetic average of the peak load of 10.33 ± 0.58 kN (95% CI) at -161°C and 8.85 ± 0.36 kN (95% CI) at 21°C was calculated. The trough load average was 5.28 ± 0.63 kN (95% CI) at 21°C and 5.61 ± 1.08 kN (95% CI) at -161°C. An estimation of 13 peak loads at 21°C and 18 peak loads at -161°C over a cutting length of 10 mm was observed. Thus, more chips were generated from the cryogenic temperature-cutting test, or a higher frequency of shear bands was created. It was estimated an average 0.55 mm length between shear bands (per chip generated) at -161°C and 0.77 mm per chip at 21°C. For each test, shear stresses were estimated by the methodology described in section 3.6.3. The pseudo shear stresses obtained from PSM are shown in Figure 5-41. From a macro image of the chip generated at the end of the test, the shear angle was measured at 42.5° for -161°C and 39.4° for 21°C.
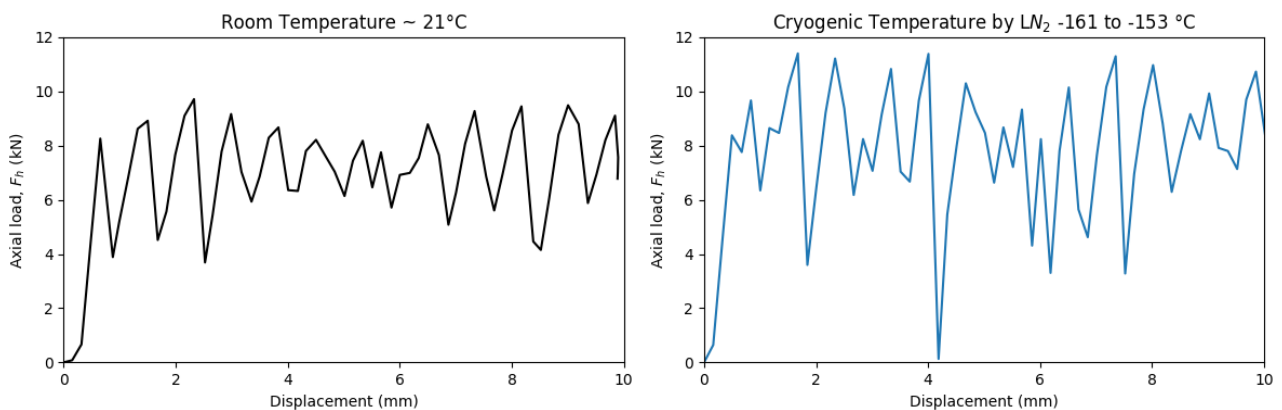
Figure 5-40. Load-displacement from PSM mill annealed Ti-6Al-4V under a) room temperature of 21°C and b) LN_2 cryogenic temperature of -153°C.
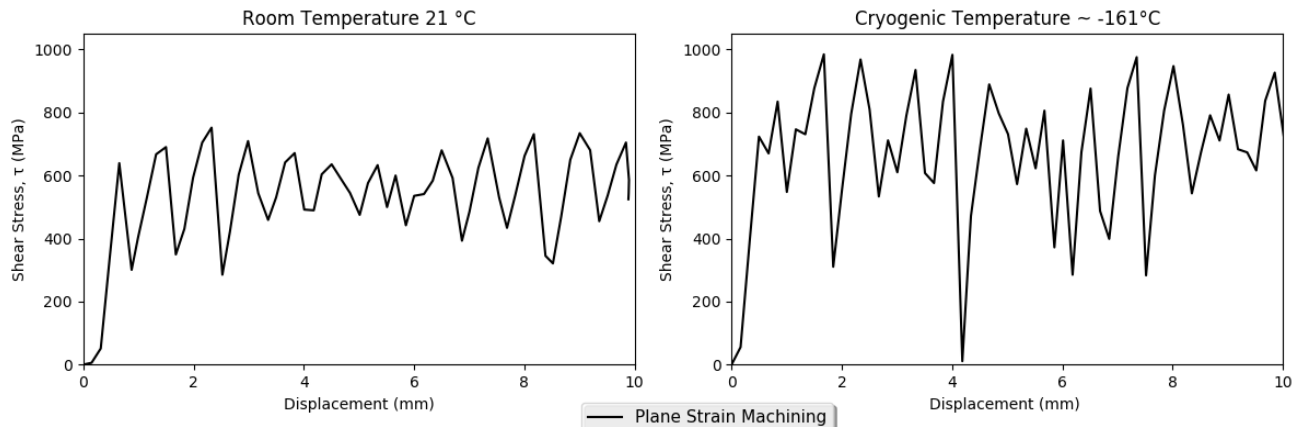
Figure 5-41. Shear stress on PSM versus displacement at a temperature of a) 21°C and b) -161°C.

All the peak loads were registered, and as observed in Figure 5-42, the cryogenic cooling condition generated the highest arithmetic average and higher dispersion of the measurements. On average, mill annealed Ti-6Al-4V cooled to cryogenic temperatures of -160°C generates 1 kN higher peak load (from 9 kN to 10 kN).

Qualitatively, higher trough force and higher segmentation frequency were observed at -161°C, suggesting the ease of chip formation in comparison to 21°C.
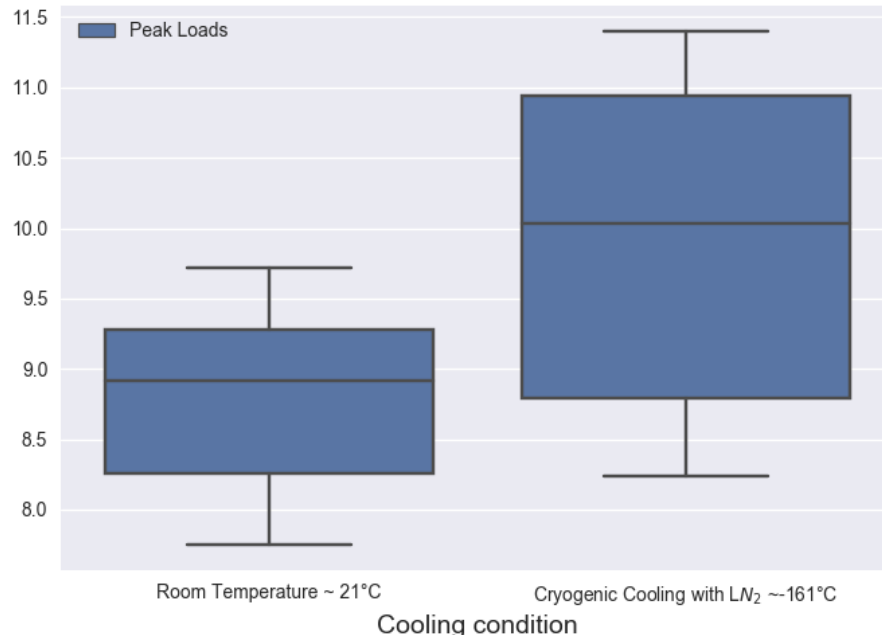
Figure 5-42. Peak loads average and range.

The shear stresses generated during the shear band localisation during PSM coincides with the estimated Von Mises shear strength during axisymmetric compression testing, as illustrated in Figure 5-43. Although the peak load in axisymmetric compression is higher at the cryogenic temperature of -161°C, the true strain to failure generated by localisation (central shear

banding) is lower. This results in less energy for the onset of failure in the uniaxial simple at low temperatures. The maximum stress during axisymmetric compression was reached at a true strain of 0.194 and 0.0717 for 21°C and -161°C respectively. The work done estimated using the Latham-Cockroft approach was 209.14 MJ.m^{-3} for 21°C and as 107.4 MJ.m^{-3} at -161°C. Thus, 94.7 % more energy is required to cut Ti-6Al-4V in a mill annealed condition at 21°C in comparison to -161°C. This implies that the tool is loaded under high stresses for a longer time, and it travels a longer displacement in order to generate a shear band during room temperature cutting. Whereas at cryogenic temperatures, an increased number of chips are generated as there is a lower energy requirement for the shear band generation and the tool spends less time under high stresses. This explains the longer tool life, as the tool is under high stresses for less time, and although higher forces are needed, the onset of the shear band formation is much faster, only briefly putting the tool under high stresses.
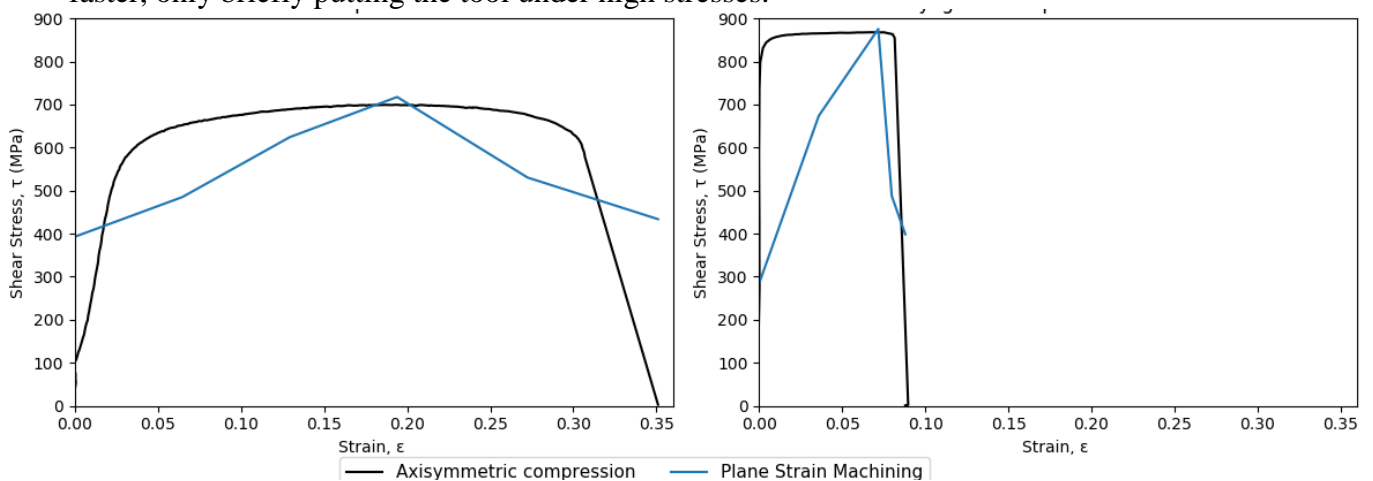
Figure 5-43. Shear stress on axisymmetric compression at a) cryogenic temperature -130°C along with the estimated Von Mises Shear Stress at -161°C and b) axisymmetric shear stress at a room temperature 24°C along with the estimated Von Misses Shear Strength at 21°C during orthogonal cutting.

At a cryogenic temperature of -161°C, it was estimated that 76.4% of the energy required during plastic deformation was used on shear band formation and 23.6% was via friction. At room temperature of 21°C, 70.9% was spent on shear band generation and 29.1% on friction. Thus, it is clear that the cryogenic temperature testing provided by LN$_2$ provided an advantage as a lower fraction of the energy is dissipated by friction (5.5% less energy was spent on friction, which was used to generate the shear band).

Subsurface deformation damage was quantified and analysed by using cross-polarised light and scanning electron microscopy using BSE. This analysis is only from the cryogenically machined sample as the room temperature sample was not available.

Figure 5-44 illustrates the microstructure of Ti-6Al-4V under low magnification light microscopy. It provides an illustration of grain sizes and distribution. The average grain size was estimated as 18.19 ± 0.64 µm. It is also observed that there are macro zones which are

related to thermomechanical processes as this alloy might have been rolled during pre-processing. The texture which developed would have a significant influence on subsequent plastic deformation as the HCP α plastic deformation systems are crystallography dependent.
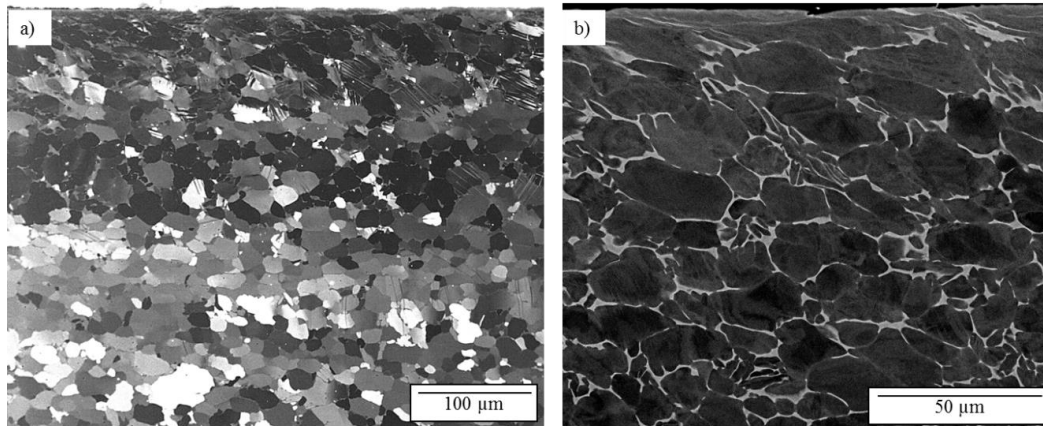
Figure 5-44. Typical microstructure Ti-6Al-4V in a mill annealed condition after being PSM at 0.01 m.min^{-1}at: a) light low magnification and b) BSE.

Figure 5-45 provides high magnification light micrographs of Ti-6Al-4V mill annealed form the PSM at -161°C. The region of severe plastic deformation was measured at an average of 4.15 µm, and twin depth penetration into the subsurface was 114.04 µm.
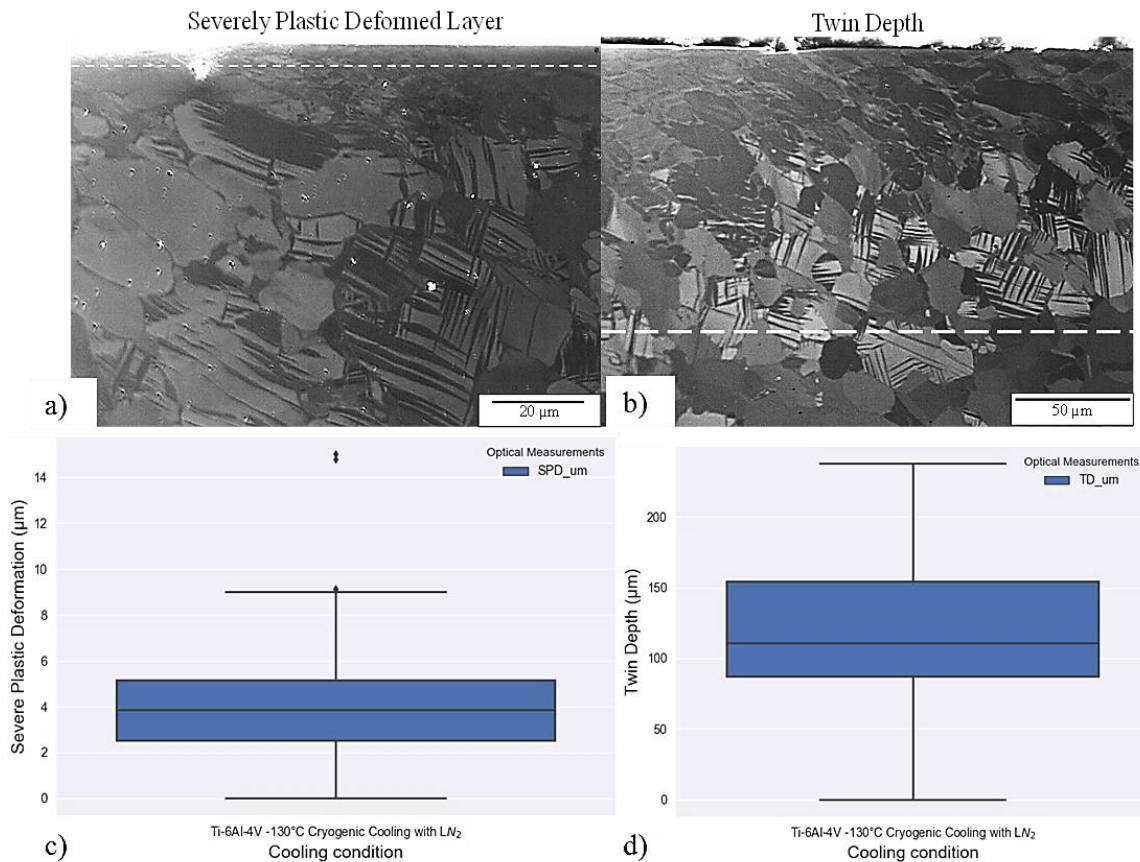
Figure 5-45. Mill annealed Ti-6Al-4V, cryogenic cooling with LN$_2$ to -158°C: a) Severe Plastic Deformation and b) Twin depth penetration into the subsurface measured using light

225

micrographs. The delineating lines signify the corresponding arithmetic average, c) shows a range of SPD layers and d) a range of twin depth distances into the subsurface.

As the CRSS for slip at low temperatures is strongly increased (as shown in Fig 2.8 and Fig 2.9), twinning has a strong presence during plastic deformation. Although cross-polarised light microscopy indicated an arithmetic average twin depth of 114 µm, not much evidence of mechanical twinning was observed in the region closest to the machined edge. High magnification BSE provided evidence of alpha grains which are heavily twinned on the subsurface, right below the SPD layer, below nearly 10 µm. These can be observed in Figure 5-46 a), c) and d). Figure 5-46 c) and d) show a magnification of two alpha grains that have mechanically twinned completely. Figure 5-46 b) shows the SPD layer, which is named by the manufacturing sector as "white layer", however it is the belief of the author that under the machined conditions it does not exist in titanium. The white appearance is due to the high illumination created by the β-phase. As it is Vanadium rich, it appears as white because the heavier elements appear brighter under the BSE. This image also shows that on the subsurface there is a high angle of curvature in that region which generates strain localisation induced by the cutting tool and might be prone to void nucleation under high stresses during operation. Figure 5-46 c) shows that the tool has nucleated a void right on the machined edge; this might be the cause of the strain localisation in this area. Figure 5-46 d) shows subgrain development. This implies that areas above this region, which have experienced higher stresses and strain rates might have undergone continuous dynamic recrystallization during metal cutting.

Heavily twinned alpha grains are not an enhancing microstructural feature in terms of fatigue life during service. The reason is that the ability to plastically deform might exhaust earlier than in a metal that has not undergone as much mechanical twinning; thus damage in terms of void nucleation may develop earlier.
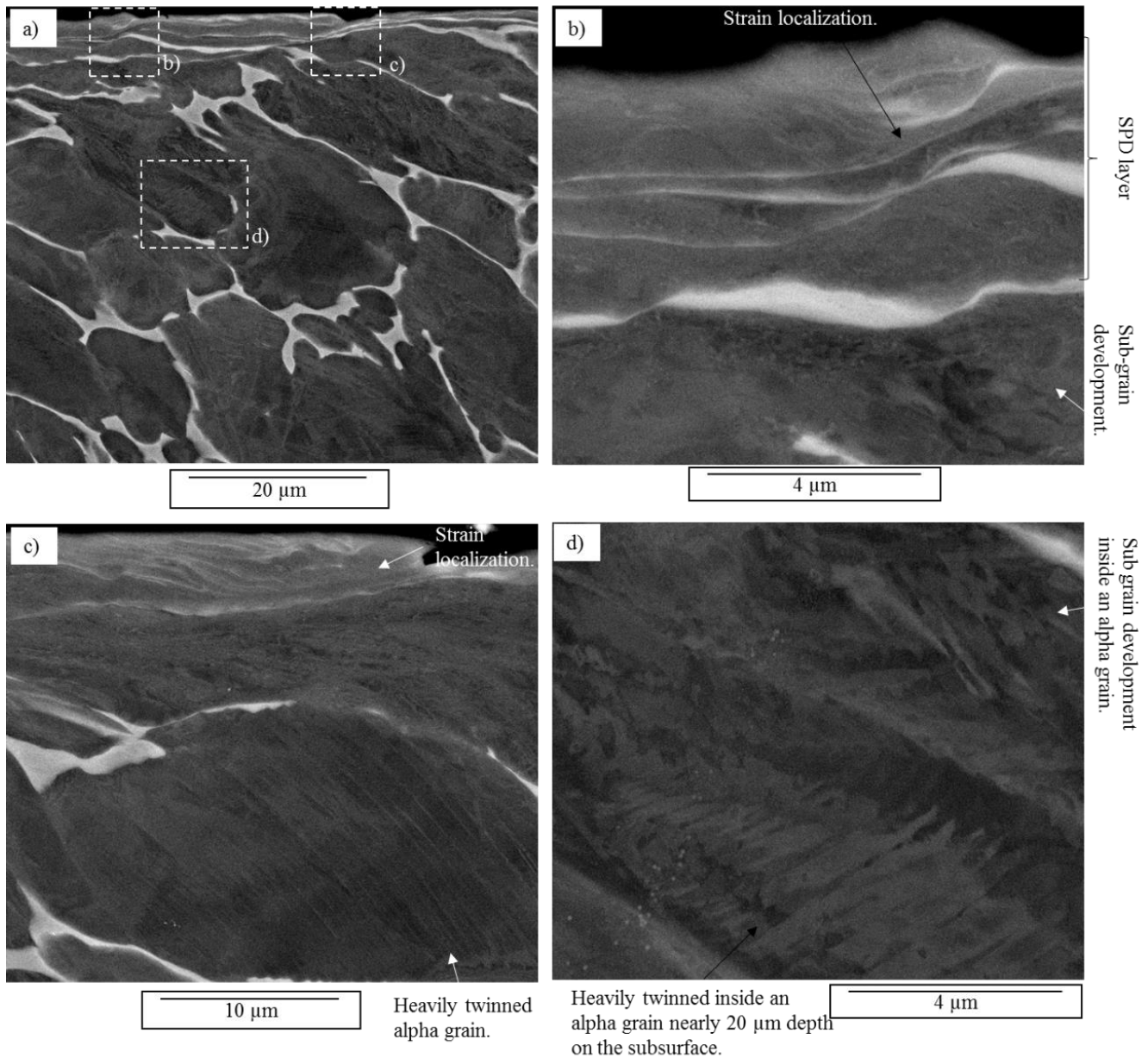
Figure 5-46. BSE subsurface deformation on mill annealed Ti-6Al-4V after PSM under cryogenic cooling with LN$_2$. The first image shows low magnification right below the cutting edge.

Figure 5-47 a), c) and d) illustrate the area ahead of the cutting tool. Figure 5-47 a) shows the initial stage of shear band development. There is a nucleated void almost 120 µm in front of the cutting tool. This may have been generated as a result of an area of stress concentration c) is a higher magnification and it shows two places that started to undergo localisation. Figure 5-47 b) shows the subsurface generated after deformation, it can be observed that at nearly 20 µm another line of localisation was left after the cutting tool pass.

a)

Void on shear direction.

Grain refinement.

b)

100 μm

Strain localization on the subsurface after machining.

b)

Heavily twinned alpha grains.

40 μm

c)

Highly elongated α and β grain.

40 μm
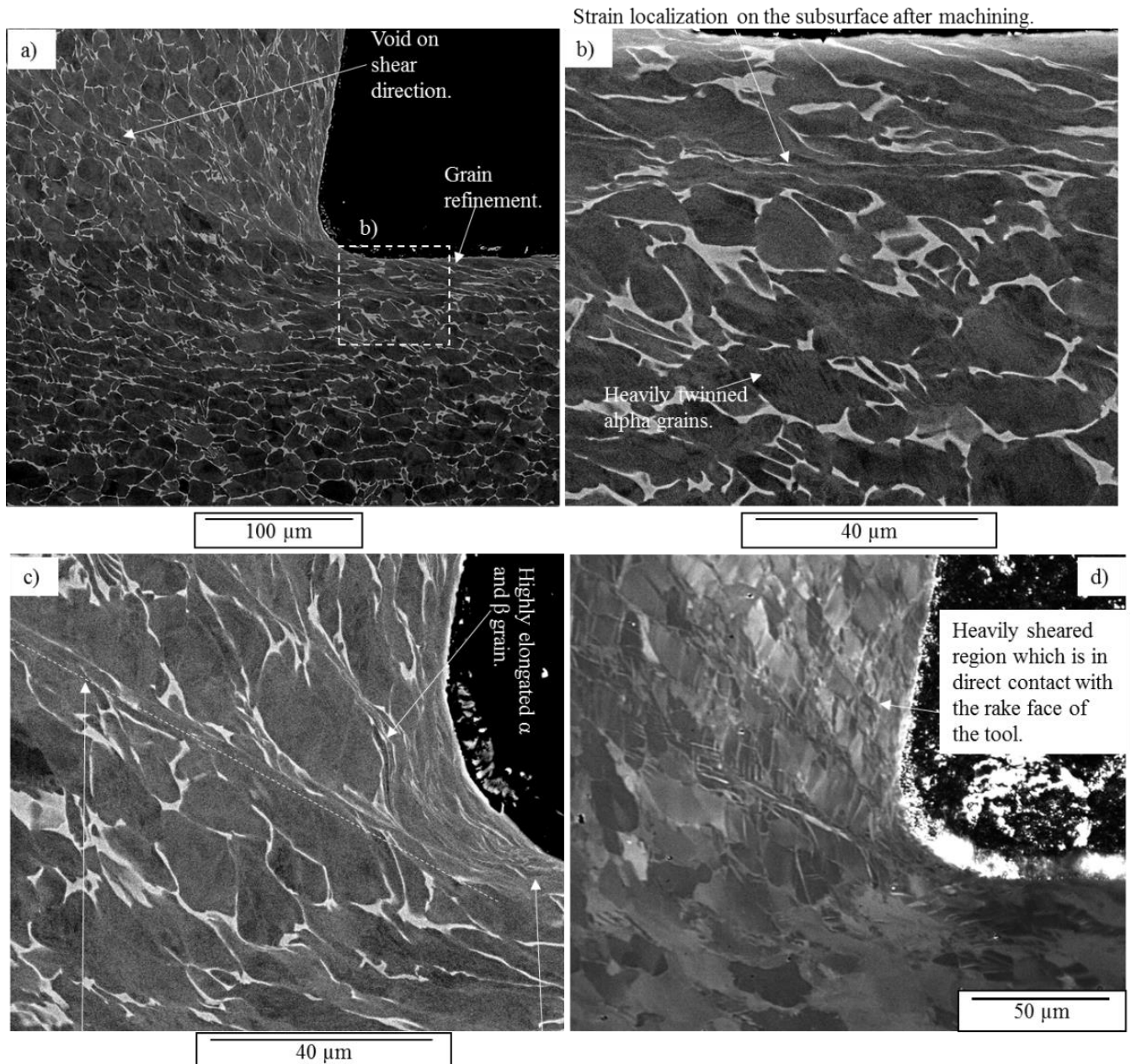
Strain localization, most likely to be the direction of the shear band.

Heavily deformed α and β phase in front of the tool.

d)

Heavily sheared region which is in direct contact with the rake face of the tool.

50 μm

Figure 5-47. a) Low magnification BSE that shows the region ahead of the cutting tool, b) High magnification BSE on the region of subsurface deformation, which shows strain localisation nearly 20 μm below the machined edge, c) BSE showing strain localisation in the direction of shearing and d) light micrograph showing the intensity of deformation on the region in contact with the tool rake face.

228

5.10. Commercially Pure Titanium alloy (CP-Ti)
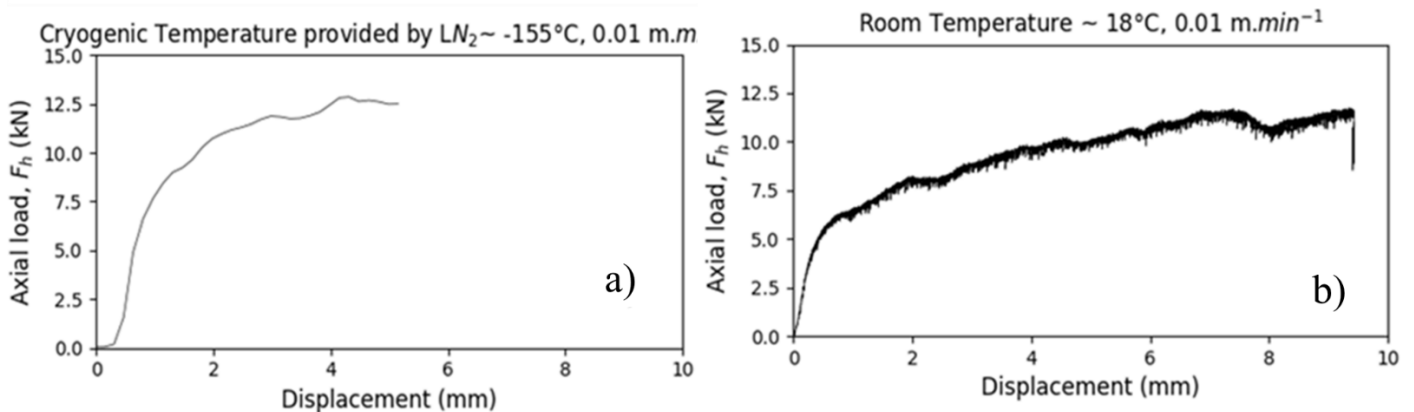
Figure 5-48. Axial load versus displacement during PSM CP-Ti (grade 2) at a) LN$_2$ cryogenic temperature of -155°C and b) room temperature of 20°C.

A Sandvik Coromant grade H13 A tool was used to near PSM CP-Ti. Two cutting inserts were used on the opposite side for cutting, see Figure 3-17. The estimated grain size through a line intercept method was 104.93 ± 5.91 µm with a confidence interval of 95%. As previously shown in section 4.6, the flow stress of CP-Ti shows a strong temperature dependent behaviour. Figure 5-49 shows the microstructural subsurface damage on CP-Ti during orthogonal cutting at a surface speed of $V_c = 0.01$ m.min^{-1} at different temperatures of deformation. The different subsurface damage implies that different operative mechanisms during deformation have taken place. A first observation clearly illustrates that the workpiece deformed at ambient temperature has suffered a higher depth of subsurface damage than the one deformed at cryogenic temperature. Figure 5-49 a) illustrates that at the edge on the subsurface where the cutting tool passed to generate the shear band and separate the material. There is a region that appears to have very small grains, suggesting that dynamic recrystallization may have taken place during the cutting operation. This occurred under cryogenic temperature provided by LN$_2$ of -150°C. When machined at room temperature, it appears that the deformation mechanism is different, heavily influenced by slip with some mechanical twinning occurring. The same observation as in section 4.10 and 4.11. Low temperatures generated a lower twin thickness, whilst room temperature generated larger thickness and lens-shaped twins. The shape of the twins depends on the imparted shear stress.

The mechanical twins at -150°C are much finer, giving a needle-like appearance whereas at 20°C the area deformed is higher and the deformation features seem of a higher thickness. On the other hand, as the mechanical twins are thicker and it seems that the leading plastic deformation mechanism is slip either through glide or climb. On the micrographs shown at 21°C (Figure 5-49 b), all grains appear to have undergone plastic deformation, while at -150°C (Figure 5-49 a) there are more grains that appear to have higher integrity and have undergone little plastic deformation. The LN$_2$ cryogenic coolant may have served as a quenching fluid

after the high temperatures experienced during the cutting operation. This would leave the stored energy in the lattice during plastic deformation only near the surface. As lower energy was required to plastically deform the material at -151°C, higher stresses were imparted into the subsurface. Lower strains were required for the onset of shear failure. As a result, lower levels of residual damage were imparted into the lattice.
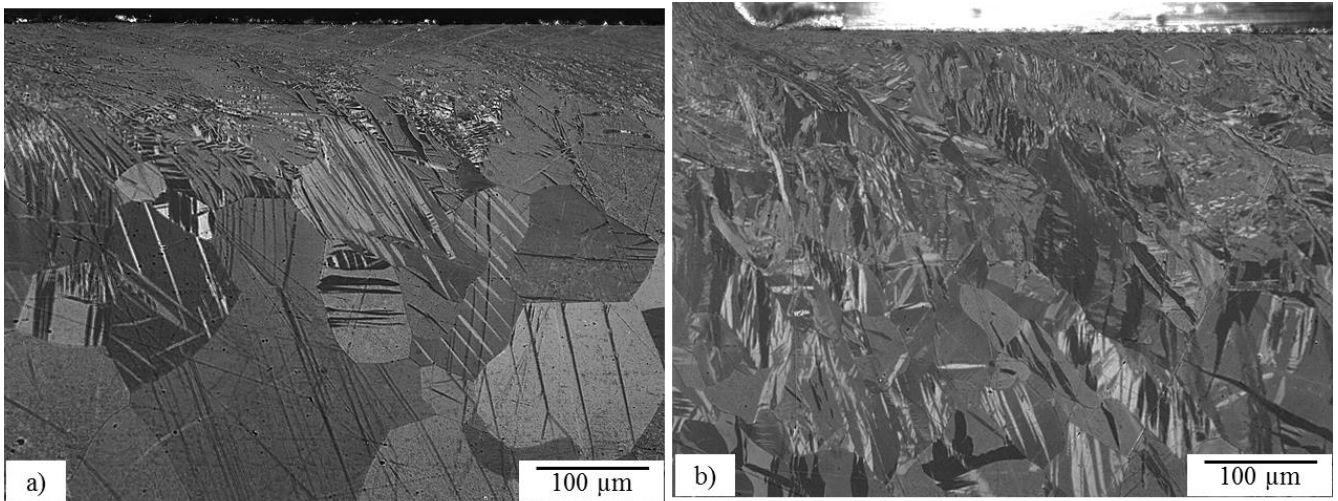
Figure 5-49. Light micrographs of the cross-sectional area below the cutting edge in orthogonal cutting of CP-Ti at a surface speed of 0.01 m.min^{-1}, showing the effect of deformation temperature on the subsurface microstructural damage at a) -150°C provided by LN$_2$ and b) room temperature of 20°C.

The subsurface in the region immediately after the machined edge is shown in Figure 5-50. A much smaller grain size under LN$_2$ cryogenic cooling conditions is observed. It is apparent from Figure 5-50 a) that there is a higher grain boundary area in the immediate subsurface below the machined edge. The subsurface from the room temperature test appears to have experienced higher gross deformation. It is probable that higher slip dislocation activity took place during deformation. The grains near the edge have elongated, but mechanical twinning is also evident. The room temperature sample has local regions of strain localisation into the subsurface as indicated by the arrow in Figure 5-50 b). This may induce earlier strain localisation or void formation during the service life of the component.

CP-Ti at a low temperature appears to have undergone a higher twin density per each grain, thereby increasing the strain hardening in the subsurface more than at ambient temperatures. Low temperatures may have experienced a higher strain and strain rate.
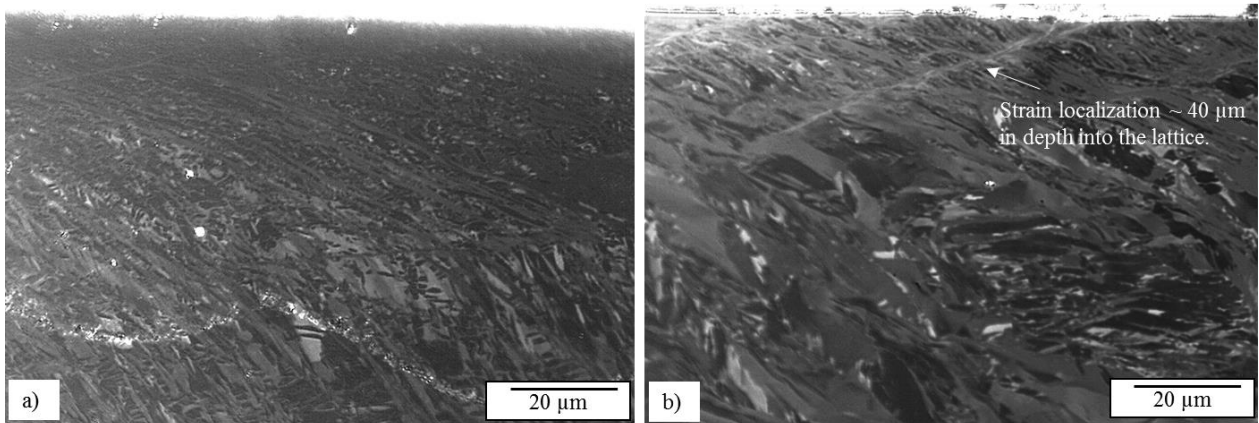
Figure 5-50. High magnification light micrographs of the subsurface from PSM at 0.01 m.min^{-1} a) cryogenic temperature of -150°C by LN$_2$, b) room temperature of 21°C.
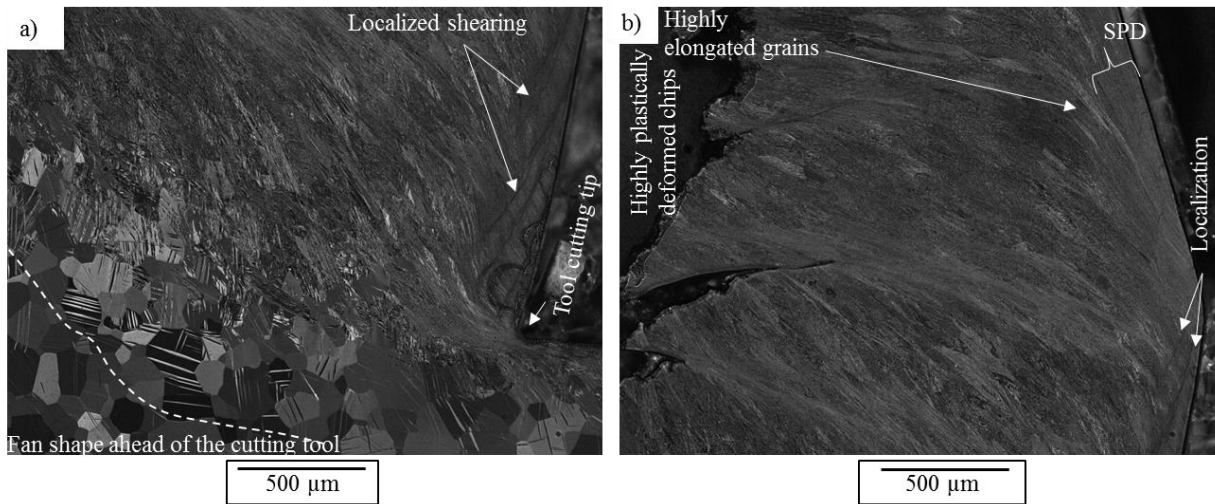
Figure 5-51. CP-Ti cryogenic cooling -150°C PSM a) Region ahead of the tool tip and b) chip highly sheared by PSM
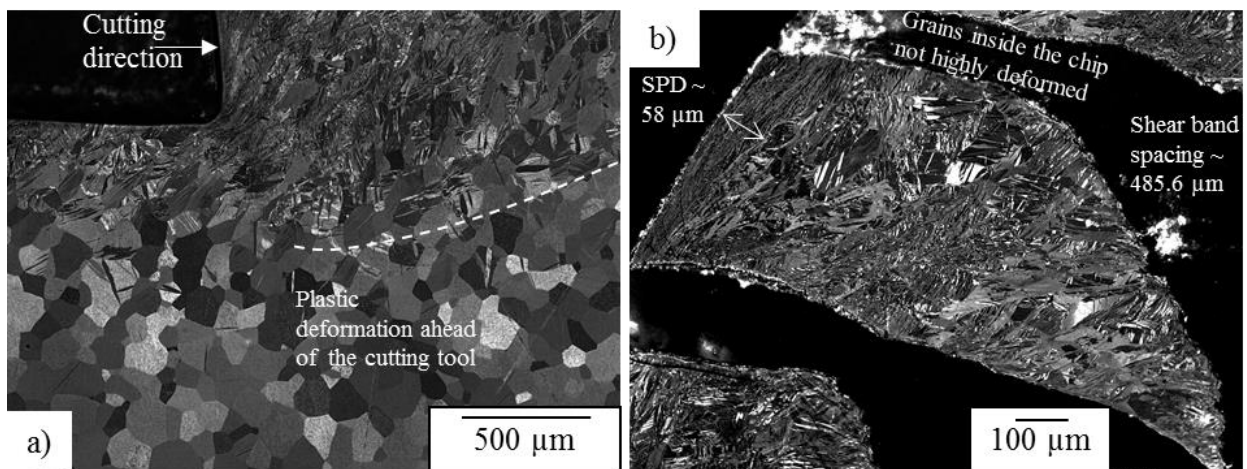
Figure 5-52. CP-Ti room temperature, no coolant/lubricant used a) Region ahead of the tool tip and b) plastic deformation inside the chip.

231

Figure 5-51 shows the zone ahead of the cutting tip, a fan shape, which is in a compressive stress state and it also shows mechanical twins on the area which has experienced lower stresses and strains. However, the chips which experienced much higher stresses, strain rates and strains, appear highly deformed or sheared. This implies that it is easier to plastically deform the workpiece material at cryogenic temperatures. As the shear band is higher at lower temperatures, a higher strain is experienced during cutting at low temperatures. Figure 5-51 a) shows localised shearing. As shearing is easier at lower temperatures, more localised shear marks appear on the edge of the chip as it forms. Figure 5-51 b) shows a region near 100 µm in thickness of SPD. This implies that a fraction of the shear band is carried away on the chip and the other fraction remains on the subsurface just after the machined edge.

Figure 5-52 a) shows the plastic deformation of CP-Ti at room temperature. In Figure 5-52 b) a lower level of grain refinement can be observed. This can be compared to CP-Ti at cryogenic temperature Figure 5-51. Looking at the differences between the micrographs suggests that a higher dislocation density is generated during PSM CP-Ti under cryogenic temperatures. This is in agreement with Cotterill and Mould [53].
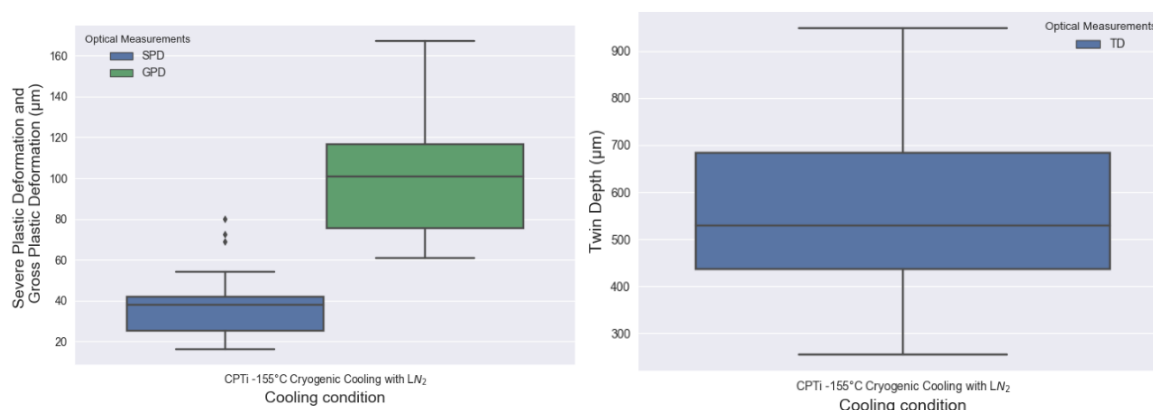
Figure 5-53. Ranges of a) Severe plastic and gross plastic deformation b) twin depth into the lattice at a cryogenic temperature of -150°C.

At a cryogenic temperature of -150°C an average SPD layer of 37 ± 4.6 µm (95% CI), a 100 µm of GPD and 565 ± 60 µm (95%CI) twin depth was estimated, as shown in Figure 5-53. At room temperature, an average SPD layer of 11.98 ± 1.23 µm (95%CI) and an average twin depth of 665 ± 40 µm was estimated. This twin depth penetration into the lattice seems very high in comparison to milling β annealed Ti-6Al-4V ELI. This might be influenced by the high grain size and the much lower temperature reached during plastic deformation under LN_2, in comparison to CO_2. Figure 5-54 shows how the severely plastically deformed region appears featureless under cross-polarised light microscopy. The gross plastic deformation area is where features are distinguishable but highly deformed. These are not as uniformly deformed as undistorted mechanical twins.
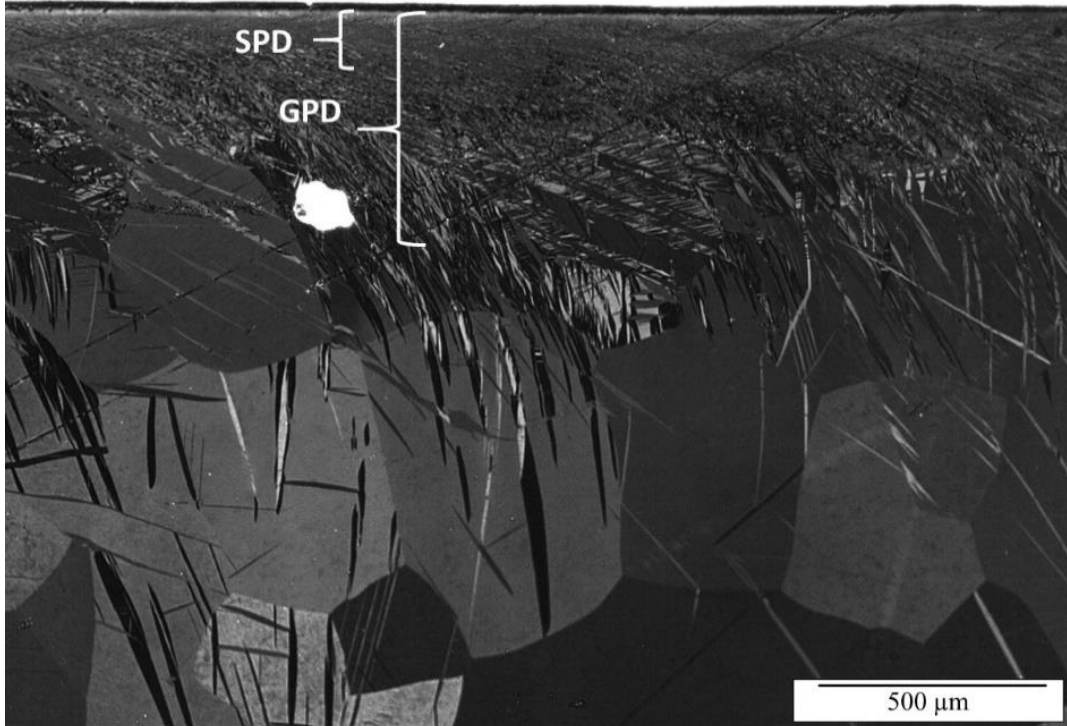
Figure 5-54. Low magnification light micrograph illustrating the extent of the measured features.
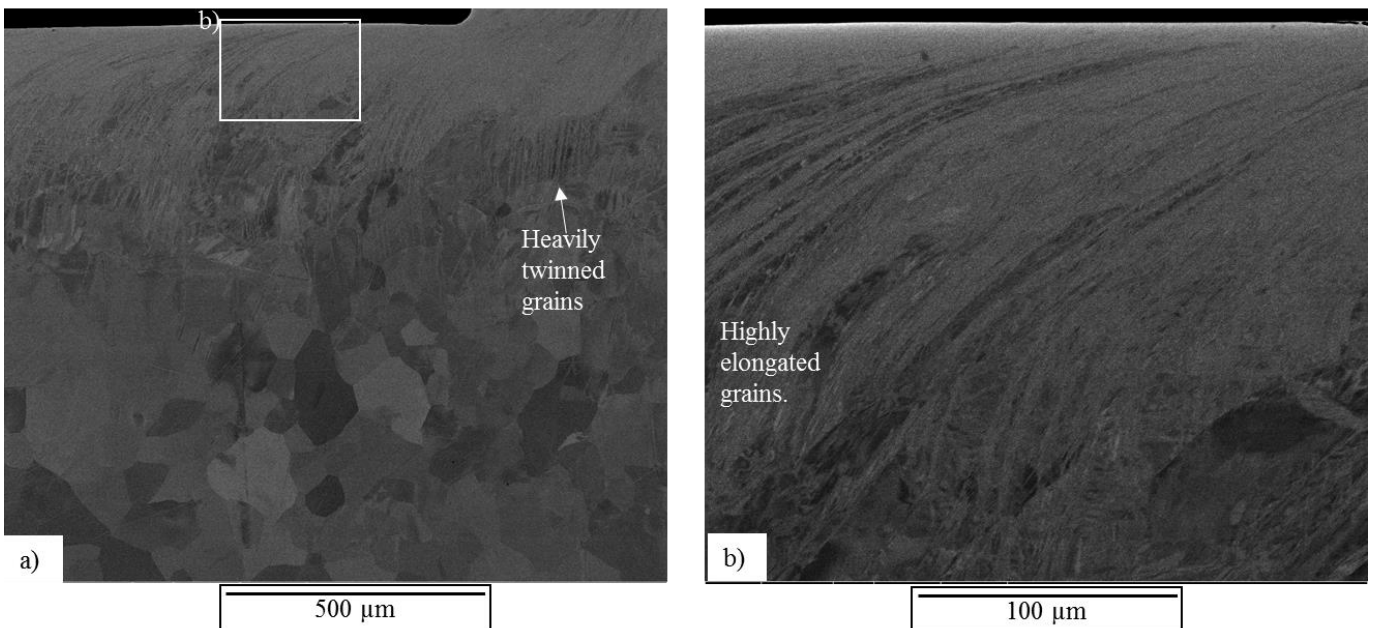
Figure 5-55. Cross section BSE image of CP-Ti PSM at 0.01 m.min^{-1} under LN$_2$ cryogenic cooling condition.

High magnification BSE images of CP-Ti under PSM at 0.01 m.min^{-1} under LN$_2$ cryogenic cooling condition is observed in Figure 5-55 a) shows how the lattice has become more closely spaced. This is either through heavy twinning and/or slip deformation. Figure 5-55 b) shows

233

high elongation grains in the direction of the cutting tool generating a dragged lattice. The upper area closest to the cutting edge appears not to be resolvable under BSE. However, TEM has demonstrated that it possesses a nanocrystalline structure, see (Figure 5-59).
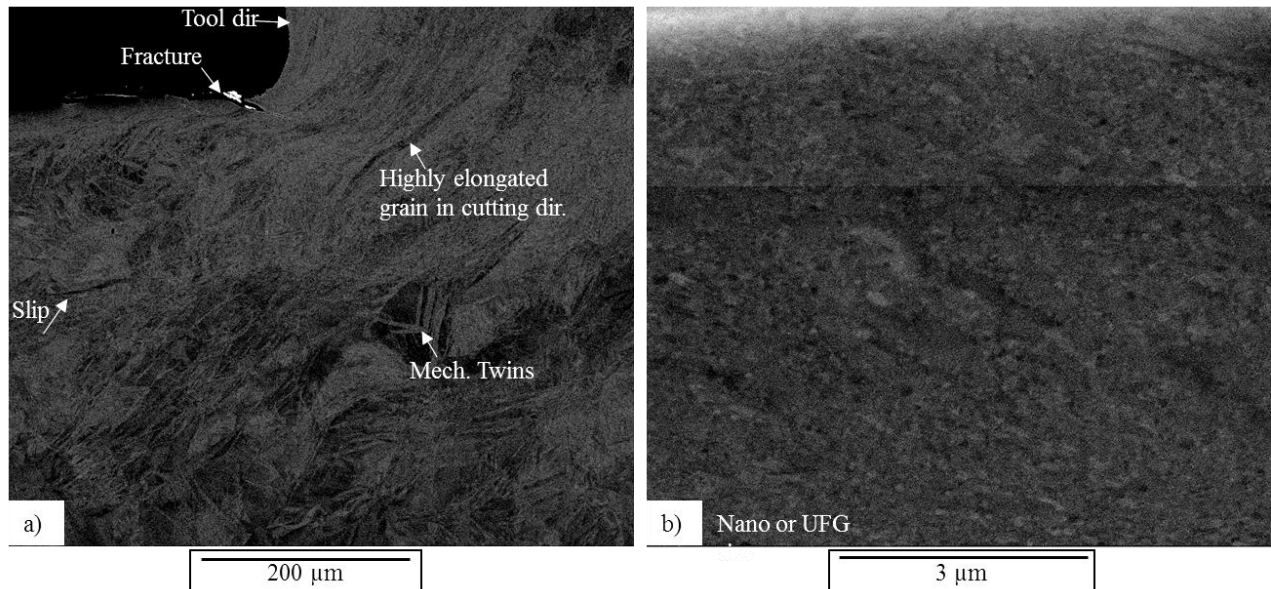
Figure 5-56. Cross-sectional BSE image of CP-Ti PSM at 0.01 m.min^{-1} at room temperature of 21°C.

Figure 5-56 shows the cross-sectional area of PSM CP-Ti at 0.01 m.min^{-1} at room temperature of 21°C. a) Shows grains highly elongated ahead of the cutting tool in the direction of cutting. Below 200 µm in the subsurface where lower shear stresses have been experienced, the lattice has accommodated the plastic strain through mechanical twinning. Nearly 150 µm in depth there is a grain which has possibly experienced slip. The figure shows how the grain has become almost 2 grains. This subdivision of the grains is helpful in plastic deformation as it allows less amount of material easily plastically deformed (require lower stresses). Figure 5-56 b) shows the nearest subsurface from the machined edge. It shows a refined (nano or UFG) structure. However, no further investigation by TEM was undertaken for this specimen.

The shear band angle during cutting CP-Ti appears to be evolving with the advance of the cutting tool. Figure 5-57 a) shows how the SBA in CP-Ti cut at 0.01 m.min^{-1} under LN$_2$ does not occur in one plane, but instead, it gradually increases. The plastic deformation during chip formation appears more homogeneous, in comparison to room temperature. The SBA at room temperature appears to have a lower angle, as shown in Figure 5-57 b).
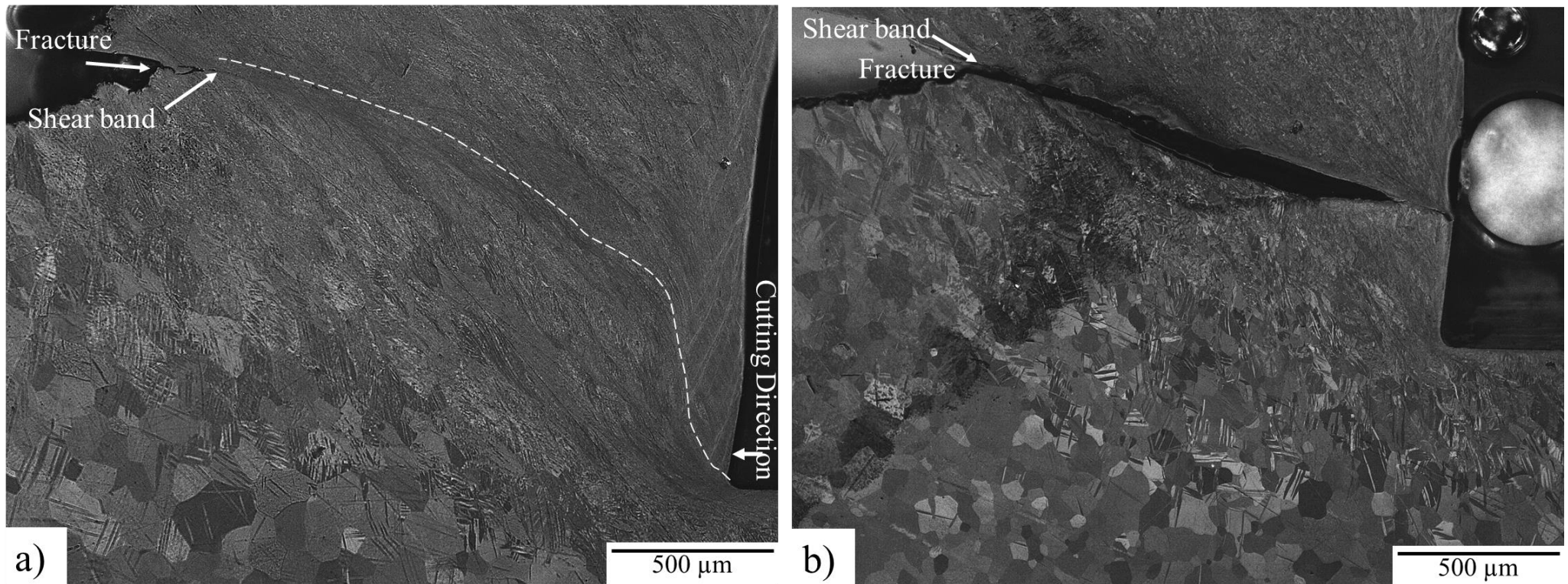
Figure 5-57. Shear band angle development in CP-Ti at 0.01 m.min^{-1} a) at -150°C under LN$_2$ cooling and b) at room temperature of 21°C.

By observation of the chips generated during machining of CP-Ti, the low-temperature workpiece generated chips with a lower degree of fracture. Whilst machining of CP-Ti at room temperature under the same parameters lead to more fractured chips, see Figure 5-58. This can be attributed to the increase in thermal conductivity. This allows the accommodation of more plastic deformation. At room temperature with the advancing cut, temperature increases and this may lead to a reduction in thermal conductivity, thus leading to earlier thermal softening and localising plastic deformation at a lower strain. Therefore, there are more cracks within the chips.
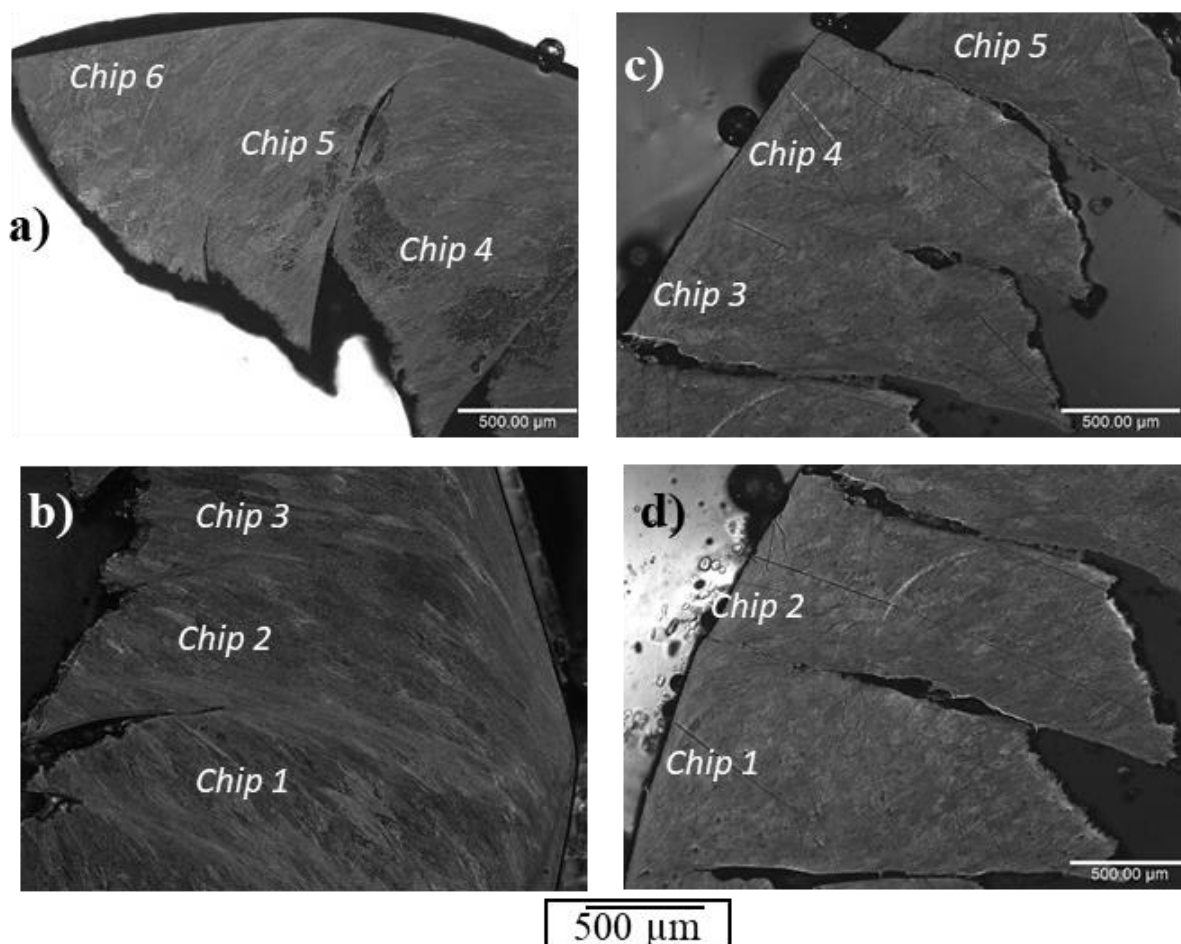
Figure 5-58. Chip formation during machining of CP-Ti at 0.01 m.min^{-1} a)-b) at -150°C by LN$_2$ and c)-d) at room temperature of 21°C.

5.11. Continuous Dynamic Recrystallization during PSM

Bright field TEM images were obtained from the PSM sample machined at a speed of 0.01 m.min^{-1} cooled by LN$_2$ which reached a temperature of -150°C. The methodology to obtain the TEM foils is described in section 3.2.4. The images correspond to the subsurface area at the machined edge (from a foil up to a 5 µm in depth) as illustrated in Figure 5-59. Nanocrystalline grains of high angle grain boundary (HAGB) and strain-free were observed. The grain size was measured from 25 micrographs at a magnification of x175000. The arithmetic average grain size obtained was 77.29 ± 8.2 nm with 95% confidence. The data followed a normal distribution with a standard deviation of 32.06 nm. A 95% confidence interval for the mean ranges from 69.09 to 85.49 nm. Figure 5-60 a) shows a box plot of the distribution of the grain size data and Figure 5-60 b) a histogram of the grain size measurements. The first and third quartile corresponds to 53.02 and 97.41nm respectively.

The near subsurface grain size generation by SPD during metal cutting is in at the nano-scale range. SPD processes such as ECAP and torsion have been used to generate grain sizes in the ultra-fine and nanoscale range. The generation of nano-scale grains enhances the mechanical properties of the material by substantially increasing its yield strength due to the sharp increase of grain boundary area (via the Hall Petch mechanism), and ductility is improved.

During severe plastic deformation processes, nearly 10% of the generated heat is transferred into the lattice of the workpiece material [2]. This energy is stored via the introduction of high dislocation density (each dislocation represents strain energy). When the dislocation density reaches a high level, dislocation annihilation starts to take place through dynamic recovery or dynamic recrystallization. During dynamic recovery, dislocation annihilation may take place giving rise to a recovery of the mechanical properties without a change in the microstructure. If dynamic recrystallization takes place, the generation of new high angle boundary strain-free grains are produced.

The LN$_2$ physical properties allow the heat generated during metal cutting to be removed away from the cutting edge into the atmosphere. This generates a quenching-like effect where the energy for grain growth would have been removed by the coolant. According to this theory, the grain size in an uncooled workpiece is expected to be of a higher size as the energy remains in the lattice, thus allowing grain growth.

Carbon deposition to preserve the machined edge.
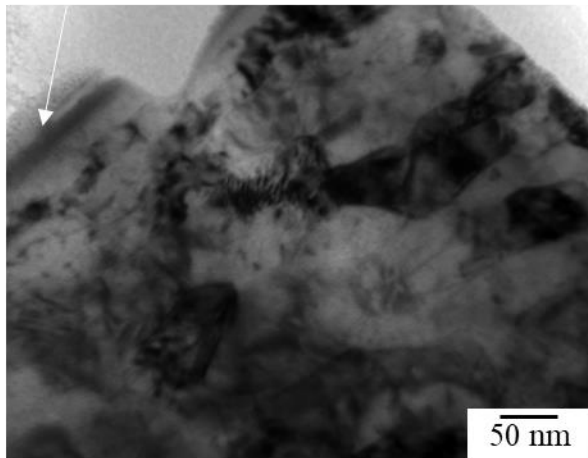
Carbon deposition Smaller grain size area adjacent to the cutting edge.
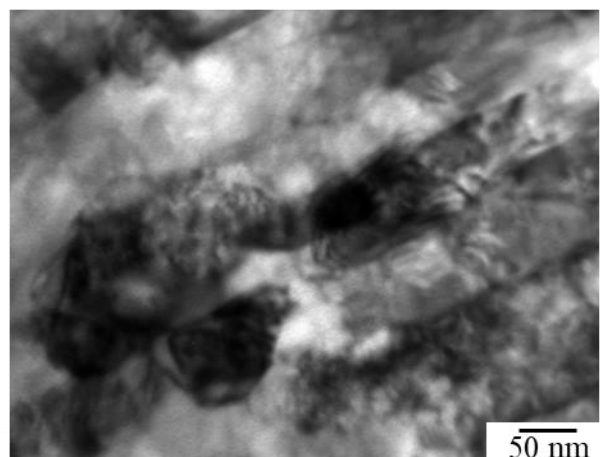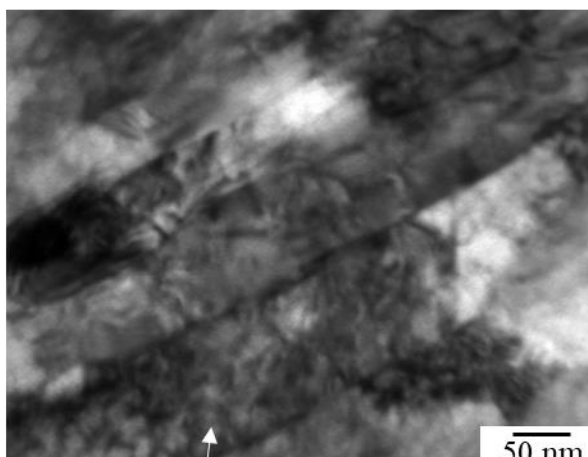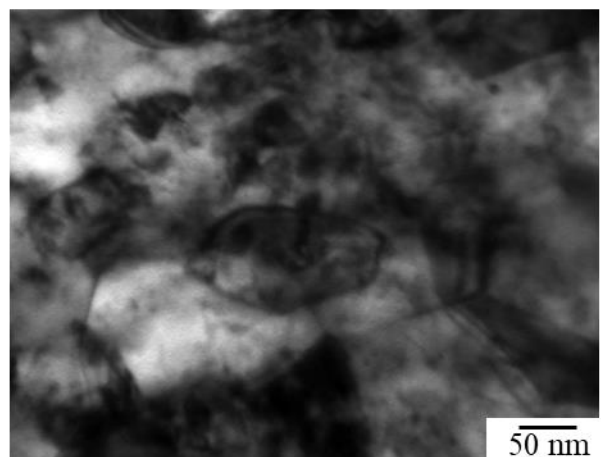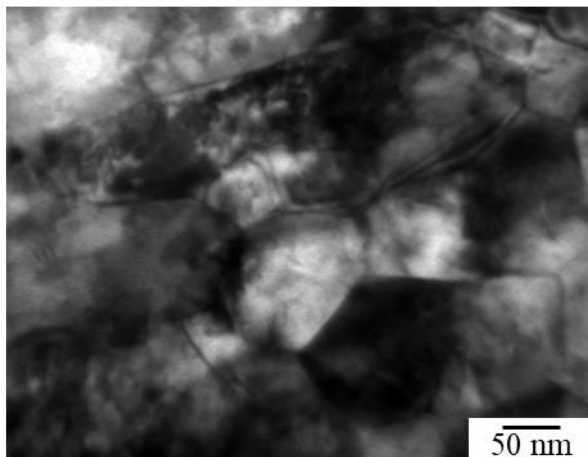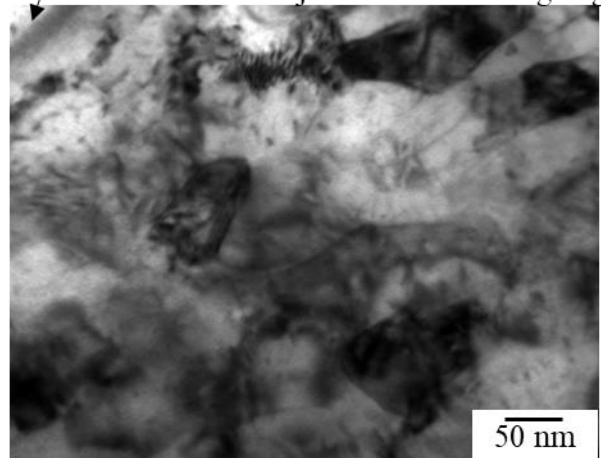
Higher dislocation density below the subsurface ~4 μm depth.

Figure 5-59. Bright field TEM images right below the machined surface on PMS CP-Ti at 0.01 m.min^{-1} cooled under LN$_2$ at a temperature of -150°C at a magnification x175000. Fine lamellar substructure is observed at the bottom of the foil.

238
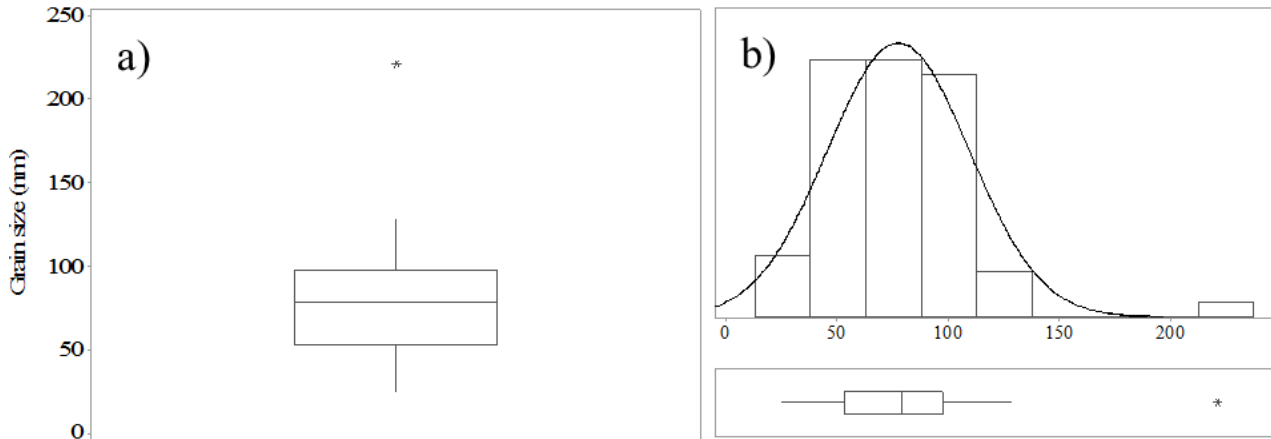
Figure 5-60. Grain size of CP-Ti PSM at 0.01 m.min^{-1} LN$_2$ cooled to a temperature of -150°C a) 25 to 75 percentile and b) distribution of the measured grain sizes from the TEM micrographs.

5.12. Possible causes of errors

Plane strain state was approximated as close as possible. However, the tool is never going to be perfectly sharp as it has an edge radius; thus true plane strain is nearly impossible to replicate.

The shear band angle measured on each chip varied. The anisotropy of the hcp lattice might have heavily influenced this behaviour. However, for analysis of the work, a constant SBA was assumed. This value was obtained from the chip which was employed to compare the shear stress during PSM to the estimated Von Mises Shear stress from the TMC axisymmetric compression tests.

5.13. Chapter Conclusion

Lower strain, therefore lower energy is required to cut (or to generate a shear band) in Ti-6Al-4V under cryogenic cooling conditions. This is due to the fact that a higher shear band angle is generated. The displacement of the material workpiece deformed to generate the chip is reduced. As a result, less shear strain is imparted to generate the chip.

Higher shear stresses were required for the onset of instability of thermal softening in shear β annealed Ti-6Al-4V under cryogenic PSM, which led to the resultant deeper subsurface plastic deformation. However, at 16°C and at 0.01 m.min^{-1} lower shear stresses were generated in comparison to both cryogenic conditions. Higher twin depth penetration resulted (16°C, 0.01 m.min^{-1}, 665 MPa lead to 420 µm twin depth and -160°C 0.1 m.min^{-1} 844 MPa lead to 300 µm). This implies that the twin penetration depth has a high strain rate dependency during

239

plastic deformation. In CP-Ti, a higher twin depth was observed at ambient temperature in comparison to low temperatures (665 µm and 565 µm, respectively).

The effect of deformation temperature on strain-induced mechanical twinning is that the lower the temperature, the deeper the twin is imparted into the subsurface.

The higher the depth of cut, the higher the damage imparted into the subsurface (higher SPD and higher TD).

The peak load has a linear relationship between temperature and strain rate. The lower the deformation temperature and/or the higher the strain rate, the higher the load generated.

A strong relationship between twin depth and the experienced shear strain was observed. The higher the shear strain generated by LN_2, the deeper the twin penetration into the lattice.

CP cut under LN_2 generated a nanocrystalline structure, strain free, of HAGB with a grain size of 77.3 ± 8.2 nm (95% CI) immediately below the cut edge.

- Estimated shear stresses and strains generated in PSM agree with these estimated in uniaxial compression testing using the Von Mises relationship.
- Cutting forces in PSM are highly sensitive to cutting temperature, more so than strain rate (inherently increased by increasing surface speed). For β annealed Ti-6Al-4V ELI: 36% higher loads are reached at -160°C in comparison to 16°C at the same surface speed. PSM at a cryogenic temperature of -160°C leads to higher cutting forces, in comparison with a room temperature of 16°C. For β annealed Ti-6Al-4V ELI, $t_1 = 1.2$ mm, LoC = 5 mm, α = -6°:
  - o At 16°C and at 0.01 m.min^{-1}, the average peak load value was 12.11 ± 0.47 kN, and the average trough value was 8.64 ± 0.87 kN. At 16°C and 0.1 m.min^{-1}, average peak load was 13.30 ± 0.52 kN, and the average trough load was 10.97 ± 0.71 kN.
  - o At -160°C and 0.01 m.min^{-1}, average peak load was 16.47 ± 0.7 kN and the average trough load 9.49 ± 3.03 kN. At -160°C and 0.1 m.min^{-1}, average peak load was 16.76 ± 0.63 kN and the average trough load 10.96 ± 1.17 kN.
- Strain rate sensitivity has a more significant effect at higher temperatures. For β annealed Ti-6Al-4V ELI: at -160°C, a 10 times increase in strain rate leads to 4.8% increase in load, while at 16°C it leads to a 9.3% increase in load.
- The reduction in temperature by applying LN_2 to the cutting edge leads to a reduction of energy spent overcoming friction. This leads to higher energy spent on the shearing process. At 0.1 m.min-1; at 16°C 67% of the total energy was spent on the shearing process, while at -160°C, 86.4%.
- At 16°C, the increase in strain rate generated a smaller distance between peak loads or shear band spacing, nearly - 30% (from 1.29 to 0.90 mm). At -160°C, the increase in strain rate generated an increase in distance between peak loads or ASB spacings of 5.7% (1.05 to 1.11 mm). At the same speed of 0.01 m.min-1, the reduction in temperature generated a 19% reduction in ASB spacing (from 1.29 to 1.05 mm).

- Lower temperatures generated a lower thickness SPD layer. This observation concurs with the previous results in uniaxial compression at lower temperatures, where a reduction in shear band thickness resulted from lowering the temperature.
  - At 0.01 m.min^{-1}: at -160°C, the average SPD layer was estimated as 9 µm, while at 16°C, it was estimated to be 15 µm.
- The twin depth penetrates deeper into the subsurface at lower temperatures. There is a more marked difference at lower surface speeds. At -160°C, the increase in surface speed generated nearly half the twin depth than at lower speeds. At 16°C, there was nearly a 68% reduction in twin depth.
  - At 0.01 m.min^{-1}, PSM at -160°C generated an average of twin depth 45% higher than 16°C (610 µm and 420 µm, respectively). At 0.1 m.min^{-1}, PSM at -160°C generated an average twin depth of 300 µm and at 16°C of 250 µm.
- A deformation map was built showing the subsurface damage imparted during machining at cryogenic temperature by application of LN2 and at room temperature or in dry conditions. At lower temperatures, higher twin density and much lower twin thickness were observed.
- At 16°C, the increase in uncut chip thickness (from 98 µm to 258 µm) generated a marked increase in twin depth penetration (95 µm to 420 µm) and a small increase in the SPD depth.
- A linear correlation of the log of shear stresses and log strain rate was found by plotting the axisymmetric compression test and the PSM values. Titanium has a higher sensitivity to strain rate at room temperature than at cryogenic temperature.
- The twin depth appears to have a negative linear correlation to strain rate with higher effect at lower temperatures (by plotting the log of twin depth and the log of surface speed).
- Flank wear was lower at cryogenic temperatures, even when longer lengths were cut.
- Under all temperatures, increasing surface speed and consequently, strain rate resulted in increased cutting forces. However, cutting at low temperatures exhibited lower strain rate sensitivity.
- Cutting at low temperatures resulted in a higher shear band angle, leading to a lower chip sliding distance (see 5.3Figure 5-4 in section 5.3).
- Regions of strain localisation were observed in the subsurface on PSM mill annealed Ti-6Al-4V at -161°C. α grains below the SPD layer showed heavy deformation twinning with low thickness.
- Qualitatively, chips of LN$_2$ cryogenic PSM accommodated much higher levels of plastic deformation (strain) and introduced a much higher density of dislocations. At -161°C almost no features are discernible, highly elongated and reoriented grains were observed on the chips, while at 21°C, in some sections of the chips, grains are observed, some had undergone mechanical twinning and these are thicker than at lower temperatures.

- In mill annealed Ti-6Al-4V at -161°C, higher levels of grain refinement by DRX, and lower twin depth penetration are observed. At 20°C, thicker regions of plastic deformation were induced, and observed twin thickness is higher than at cryogenic temperatures.

- By observing the trend of the log of shear stresses versus the log of strain rate, the author believes that the prediction of shear stresses on orthogonal cutting and under the same conditions could be predicted for higher surface speeds (such as speeds used in industry).

- Databases of values estimated under PSM tests in conjunct with uniaxial compression tests such as surface speed, rake angle, temperature, shear band angle, energy spent in shear and in friction, etc. may be built to predict titanium alloys machinability.

6. CO₂ Cryogenic milling of β annealed Ti-6Al-4V ELI and its comparison to conventional coolants

β annealed Ti-6Al-4V Extra Low Interstitial (ELI) is characterized by a Widmanstätten or colony microstructure composed of similar crystallographic orientation α laths and retained β in a prior β grain, as shown in Figure 2-46 in section 2.10. The prior β grain size ranges from 600 to 1200 µm with grain boundary α. Ti-6Al-4V is more fracture resistant for structural aerospace applications after a heat treatment in the β-phase field which provides improved fatigue strength, improved resistance to crack growth during high cyclic loading and improved creep resistance [155][116]. This alloy is used for large structural components in aircraft; such as load carrying wing bulkheads and vertical tail stubs [156].

The study of the microstructural evolution or damage generation in the subsurface of machined components is a complex subject as it involves taking into account the interaction of microstructural characteristics of the workpiece (determined by its thermomechanical history), interaction with the coolant/lubricant fluid and the interaction with the surface of the tool and the strain-hardened chip generated during machining. It takes into account the tribology between the surfaces and the thermomechanical response of the workpiece material during the plastic deformation process.

This investigation was dedicated to a roughing operation. The tools used were Walter F2334-6766739, insert type ROHX10T3M0-G67 (Figure 6-1). Only one insert was used for each cutting condition. The process parameters are shown in Table 3-8.

Figure 6-1. F2334 Walter round insert for rough milling difficult to cut alloys [157].

Due to the restriction imposed on the available equipment for experimentation on the high-speed machining trials, the author would have designed the experimental procedure differently, to evaluate the feasibility of extrapolating the low-speed machining shear stresses to those of

high speed (much higher strain rates and at low temperatures). A high-speed orthogonal turning trial would have been done, using the same cutting conditions (same Seco tool geometry of rake angle -6° and LN_2 as a cryogenic coolant, the same uncut chip thickness and width of cut), only varying the surface speed (inherently the strain rate and temperature generation). Therefore, CO_2 was used to study the effect of temperature on the microstructure subsurface deformation; it represents an intermediate value between LN_2 and ambient temperature. The deformation temperature is the independent variable and the subsurface microstructural modification, the dependent. It can thus be compared to subsurface deformation at lower and at higher temperatures than CO_2.

A shoulder milling trial was undertaken evaluating the cooling and lubrication conditions. In this trial, CO_2 was used as the cryogen coolant. The method to compare this condition to low-speed orthogonal cutting is by considering the temperature of the physically low-temperature CO_2 snow and gas. Not only does this fluid only reach a minimum of -78.5°C, but also the cutting mechanics are different. In milling, triaxial stresses are involved during cutting, which prevents the feasibility of using simple approximation such as the Merchant's force circle diagram to study the chip formation process. The only approach available in this case was to compare the effect of temperature on the milling-imparted subsurface deformation. In addition, TMC uniaxial compression tests were undertaken at low strain rates and this intermediate temperature. This allowed only a qualitative comparison of the microstructural modification from PSM and high-speed milling, as a function of plastic deformation temperature.

6.1. Tool wear under CO_2 cryogenic cooling and comparison to conventional coolants/lubricants

Tool wear rates were estimated up to maximum flank wear of 200 µm. The ISO 3685:1993 [158] was used as a reference. The tool wear limit was selected as 200 µm to assure workpiece surface integrity and to reduce subsurface damage. The condition with the best performance is 100% CO_2, followed in order by CO_2 plus Air, conventional flood and CO_2 plus MQL. The worst performing combination is 25% CO_2 and 50% CO_2, which are responsible for the highest tool wear rates.

The increase in the percentage of CO_2 refers to the opening of the delivering flow valve, allowing higher CO_2 mass flow rates at higher percentages. As shown in Figure 6-4, 25% corresponds to 1.9 kg.hr^{-1}, 50% to 10.2 kg.hr^{-1}, 75% to 10.9 kg.hr^{-1} and 100% to 11.84 kg.hr^{-1}. Clearly 25% CO_2 and 50% CO_2 fall within a non-optimal condition for reducing tool wear rates. Although 100% CO_2 represents an increase in mass flow rate over 6 times that applied at 25% CO_2, an increase of more than 3 times in operational cutting time is achieved from 8.4 to

28.5 min. Although this would only represent a marginal increase in the coolants' cost, this leads to a significant increase in productivity (as in material removal rate MRR) and reduction in the incidence of occupational illnesses. It also reduces the cost of hazardous waste disposal and the level of environmental impact. Although the use of CO_2 might imply emission of greenhouse gasses to the environment, it might help assist by reusing CO_2 generated as a by-product in other industries, which currently are released into the environment, thereby, having a less negative impact upon the environment.

Tool wear rates under different cooling/lubricating conditions are shown in Figure 6-2. A clear observation is that all the cooling conditions, with the exception of 25% and 50% CO_2, present a similar wear rate longer than 17 min of cutting. From this point on, different tool wear rates, (influenced by different tool wear mechanisms) are observed. 100% CO_2 has delayed the occurrence of the critical temperature for the onset of solid-state diffusional processes between the tool and workpiece, as shown in Figure 2-58.

Figure 6-3 illustrates the operational lifetime (in minutes) of the tool reaching a maximum of 200 µm flank wear. There is a clear trend in that the increase in the percentage of applied CO_2 prolongs the tool life. A 23% increase in tool life was achieved by only applying an additional 1 kg.hr^{-1} (from 10.9 to 11.8 kg.hr^{-1}). The increase in the CO_2 flow rate is likely to have removed more heat at a faster rate from the cutting edge, reducing the tool/workpiece interface temperature. This gives rise to lower solid-state diffusional processes between the tool material and the chip or the freshly cut edge of the titanium workpiece. According to the PSM investigation referred in section 5.5, friction may be reduced by the application of the LN_2 or CO_2 coolant in this case. A reduction in friction may result from the reduction in fracture toughness, an effect that occurs by exposing the workpiece to low temperatures.
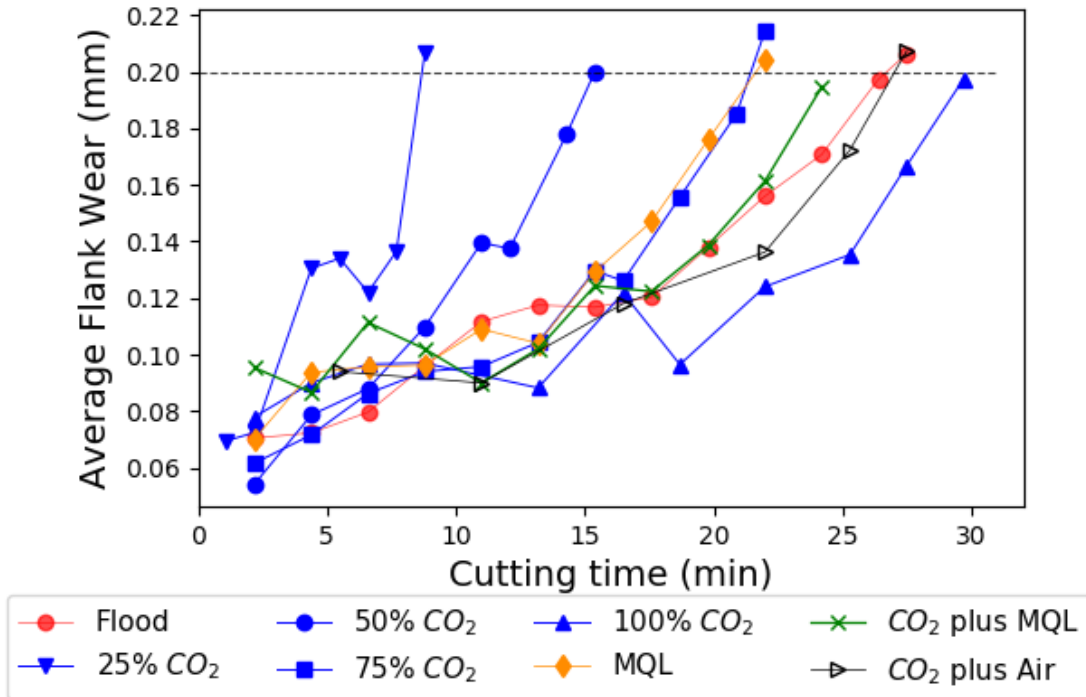
Figure 6-2. Tool wear during milling β annealed Ti-6Al-4V ELI under a varying percentage of CO_2 flowrate compared to conventional flood cooling at a surface speed of 80 m.min^{-1} and a_p = 2 mm, a_e = 10 mm, LoC = 105 mm. Only one cutting insert was used.
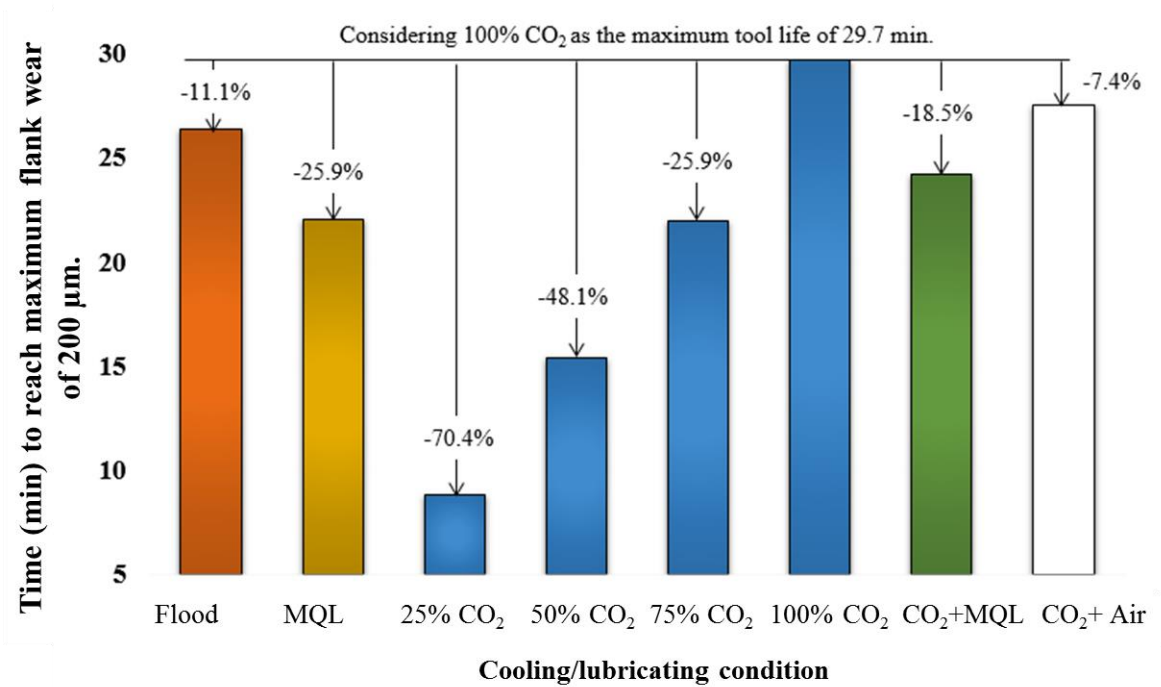
Figure 6-3. Tool life in minutes to reach maximum flank wear of 200 μm at a surface speed of 80 m.min^{-1} and a_p = 2 mm, a_e = 10 mm, LoC = 105 mm.

246
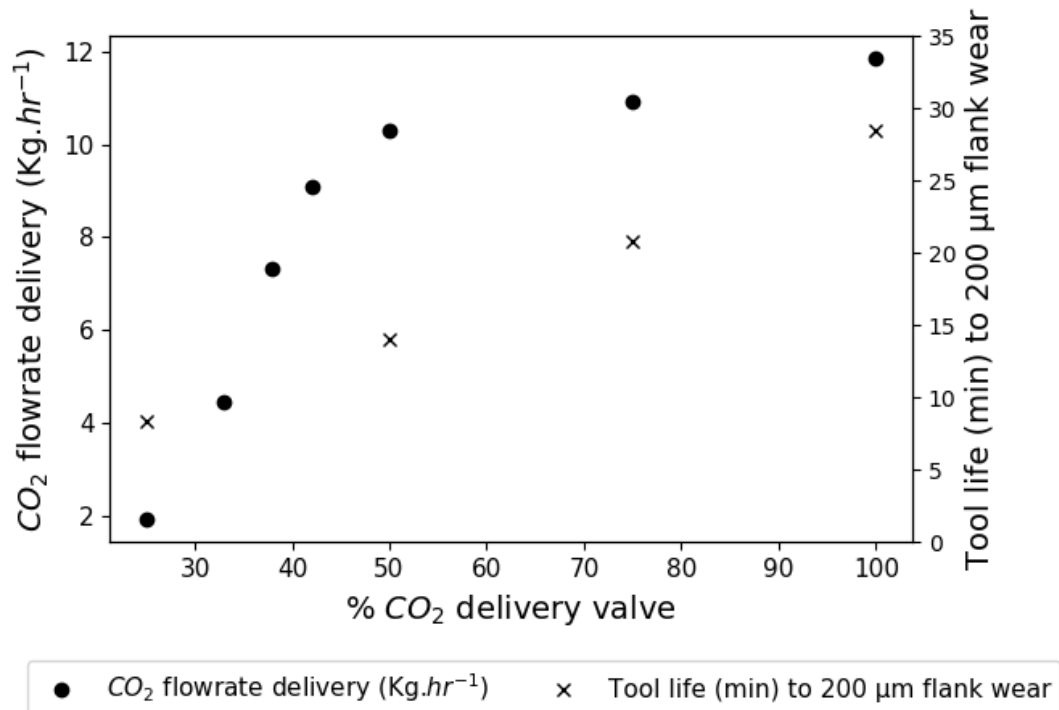
Figure 6-4. Carbon dioxide flowrate in kg.hr^{-1} as a function of CO_2 percentage and the tool life in minutes.

6.2. Subsurface microstructural modification

The surface of components is where fatigue failures commonly originate [159]. The surface is weaker than the interior of the component for three reasons. Firstly, the absence of neighbouring atoms and the resultant constraint leads to lower stress required for plastic flow. Secondly, a surface, which has been machined, has been plastically deformed and as a result, there is a higher number of crystallographic defects (dislocations, twins, point defects, etc.) in the near region to the surface, and this can lead to fatigue damage in that region. Thirdly, there is always a surface roughness generated in machining. These surface irregularities lead to strain and stress concentration, increasing the strain at the surface. Notches left on the surface also represent sites of stress concentration. Additionally, the surfaces are in direct contact with the environment, which may be a hostile environment to the surface integrity. Even air may lead to oxide formation, and if removed, it may lead to abrasive wear. Moisture may lead to a severe attack and degrade the surface faster.

For the measurement of the plastic deformation imparted into the subsurface, more than 30 cross-polarised light micrographs at a magnification of 100x were used, under each cooling condition. A vertical grid with 20 µm spacing was imposed on each micrograph. On each vertical line, a measurement was taken, resulting in an average of 5 measurements per micrograph.

Figure 6-5 illustrates the face milling operation. The type of chip formation was from thick to thin. Using this approach allows introducing less subsurface damage into the workpiece as the damage introduced on the heavier region of the cut leaves with the chip formed.
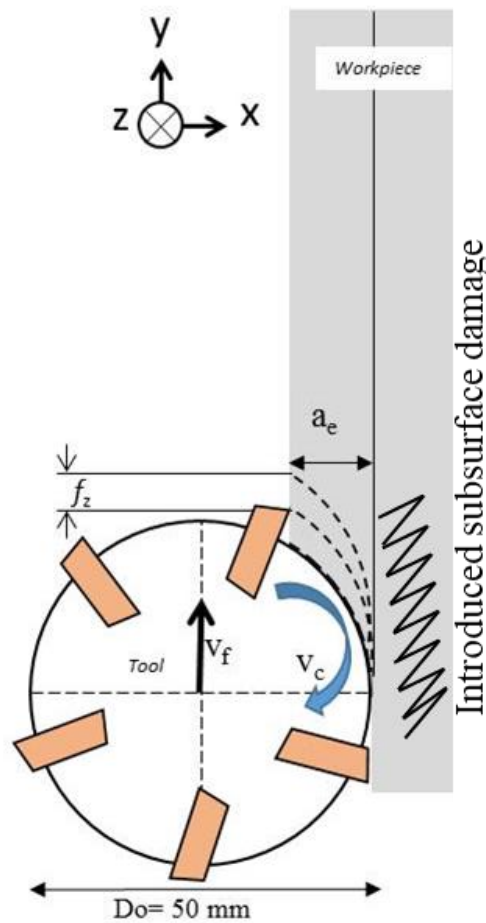
Figure 6-5. Schematic representation of climb milling operation.

As the 100% CO_2 condition enabled the highest operational tool time during cutting, it was compared first of all with the conditions that provided the lowest tool time corresponding to 25% CO_2. Under both extreme conditions, a similar arithmetic average of twin penetration depth was measured, see Figure 6-7. However, under 100% CO_2 the majority of the measurements are nearly 10 µm deeper than the rest of the conditions, and the distribution of the measurements are towards the higher end. Therefore, it is concluded that larger penetration depths are reached with higher flow rates of CO_2, in this case corresponding to 100% CO_2. In terms of SPD, the region appears slightly deeper under 100% CO_2. This could be considered to be an enhancement in mechanical properties as the fine-grained recrystallized region would be more substantial. There would, therefore, be a deeper region providing a larger region with higher strength and higher fracture crack initiation resistance. This would be beneficial during in-service operations as the surface and subsurface would be able to absorb more energy before crack initiation occurs.
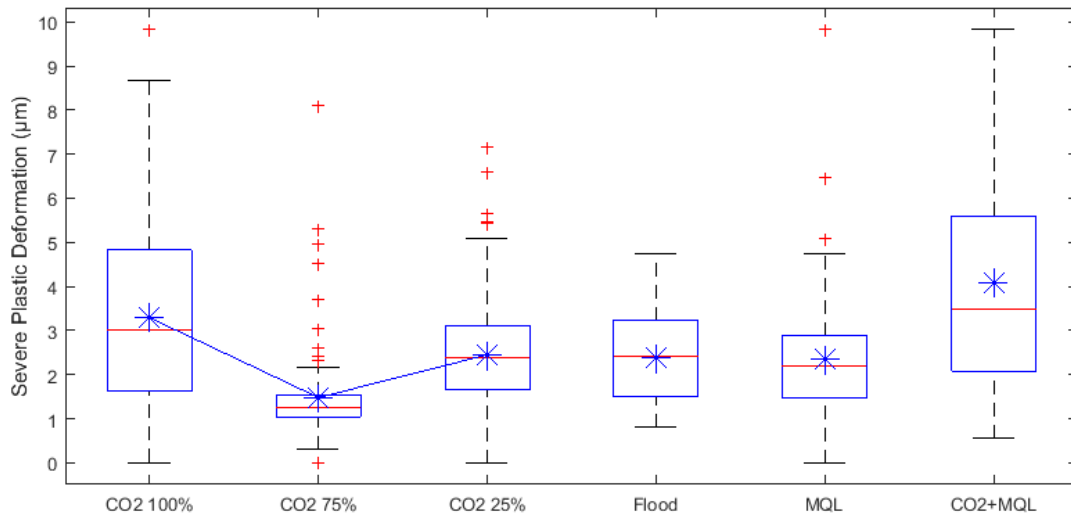
Figure 6-6 Severely Plastically Deformed (SPD) region right below the machined edge heavily influenced by the highest shear strain rate, shear strain and temperature of face milled β annealed Ti-6Al-4V ELI at a surface speed of 80 m.min^{-1} under different cooling/lubricating conditions: 100% CO_2, 75% CO_2, 25% CO_2, conventional flood, MQL and CO_2 plus MQL. The star represents the arithmetic average.
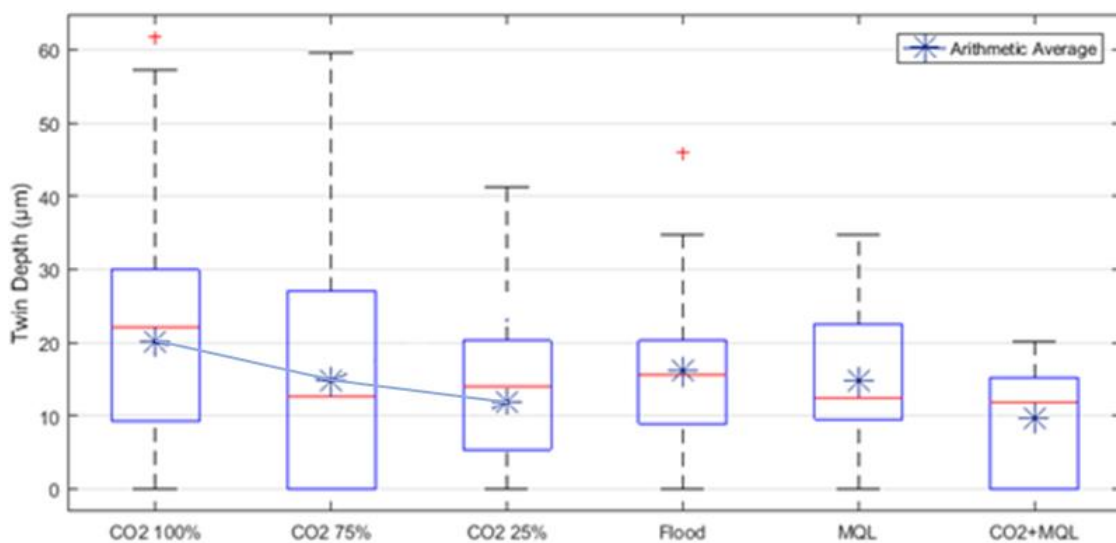
Figure 6-7. Twin depth (TD) below the subsurface of face-milled β annealed Ti-6Al-4V ELI at a surface speed of 80 m.min^{-1} under different cooling/lubricating conditions: 100% CO_2, 75% CO_2, 25% CO_2, conventional flood, MQL and CO_2 plus MQL.

Figure 6-8 is a histogram of the SPD depths measured under the different cooling/lubricating conditions. The range of measurements was between 0 and 10 µm for all cooling conditions. The highest average was under 100% CO_2 with a higher incidence of measurements towards the higher end of the range. CO_2 plus MQL follows a similar behaviour; however, a smaller number of measurements were taken due to more limited sampling availability. The remaining conditions have a similar arithmetic average, and the distribution of the data is also similar. The differences are qualitatively determined from the electron micrographs in section 6.2.1.

Figure 6-9 shows the histogram of the twin depth measurements. The range of measured values was between 0 and 60 μm. The data corresponding to 100% CO_2 distribution is towards the higher end, implying higher twin depth penetration under this condition. CO_2 plus MQL is the condition that generates lower twin depth penetration, followed by conventional flood and MQL, see Figure 6-10, which shows the microstructure modification of the subsurface after milling under each cooling condition.
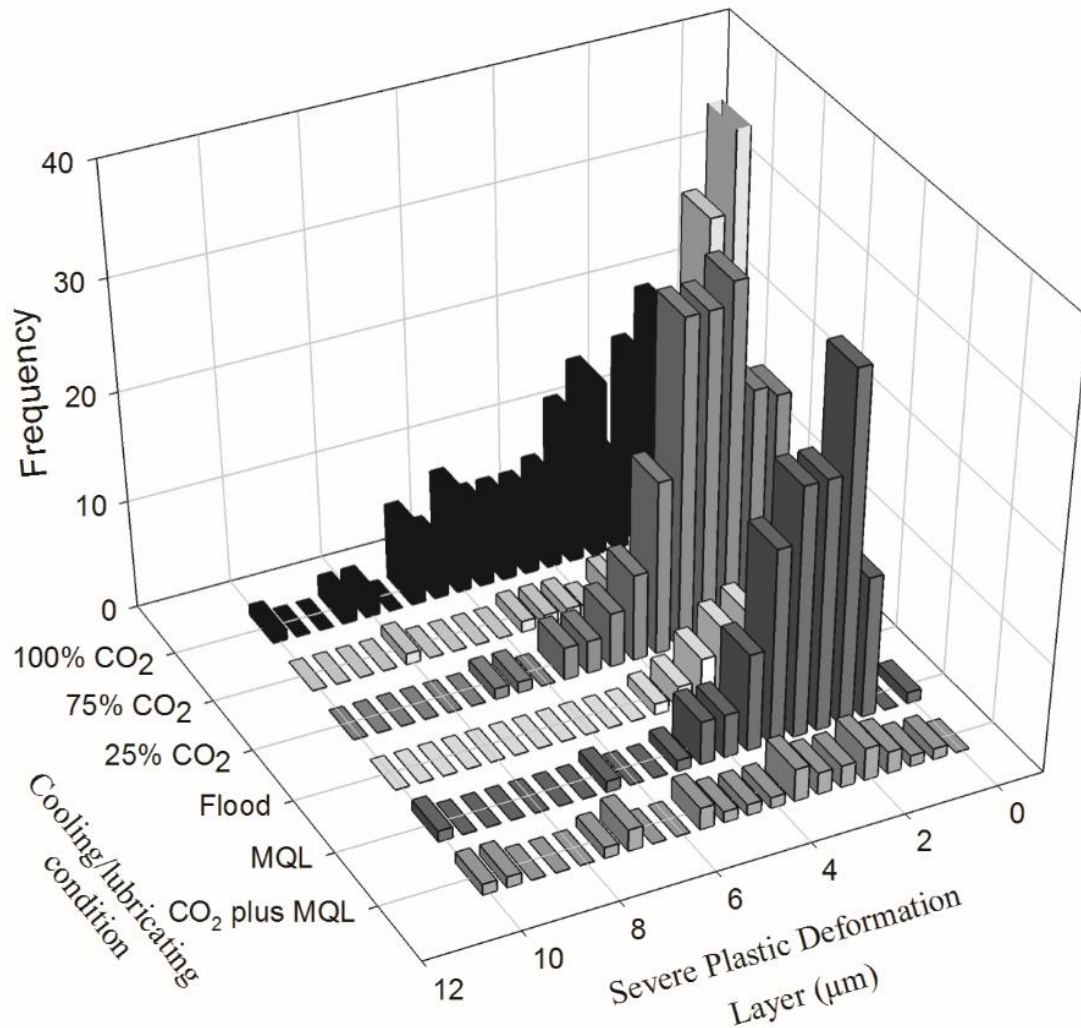
Figure 6-8. Histogram of the measured severe plastic deformation region under different cooling/lubricating conditions during Ti-6Al-4Vface milling at a speed of 80 m.min^{-1}.
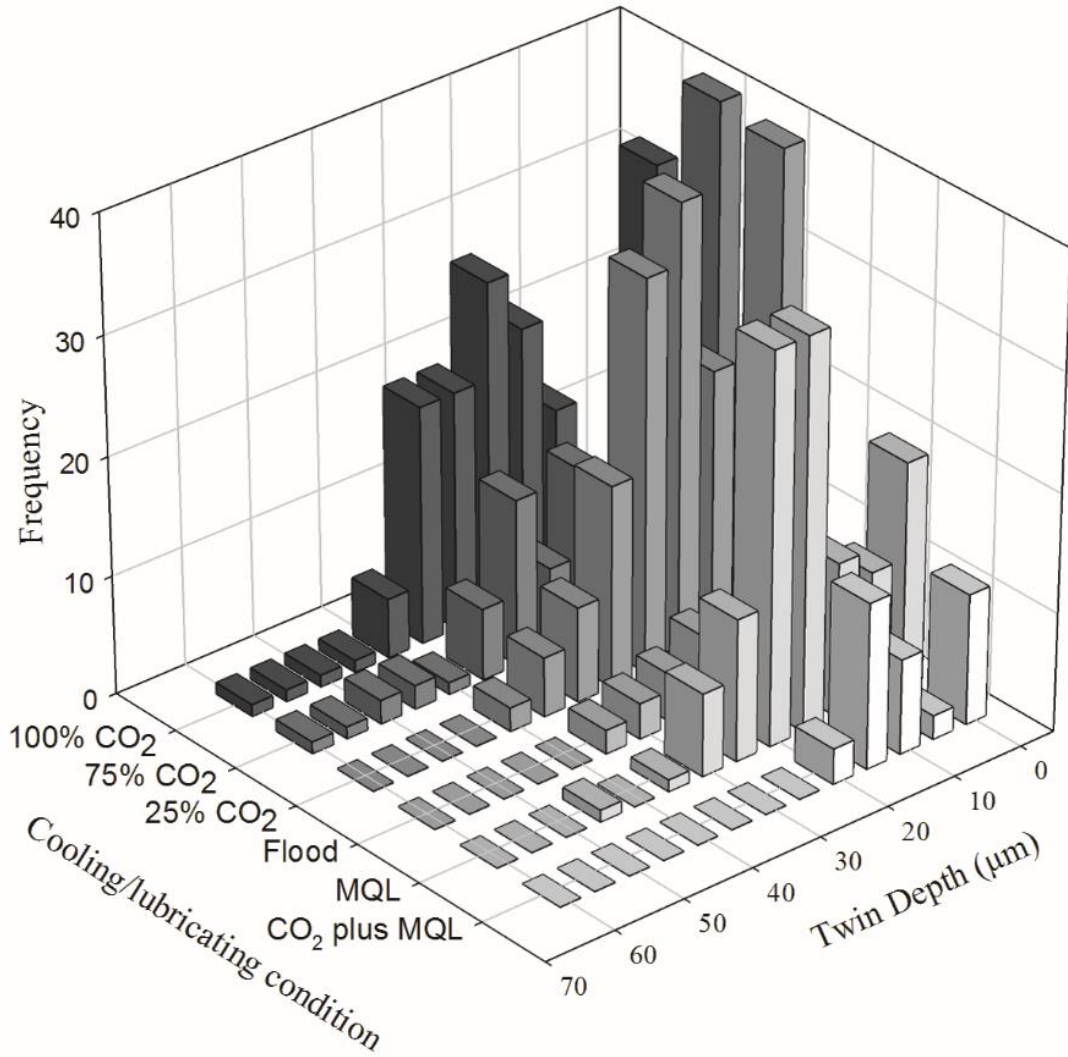
Figure 6-9. Histogram of the measured twin depth region under different cooling/lubricating conditions during Ti-6Al-4V face milling at a speed of 80 m.min^{-1}.
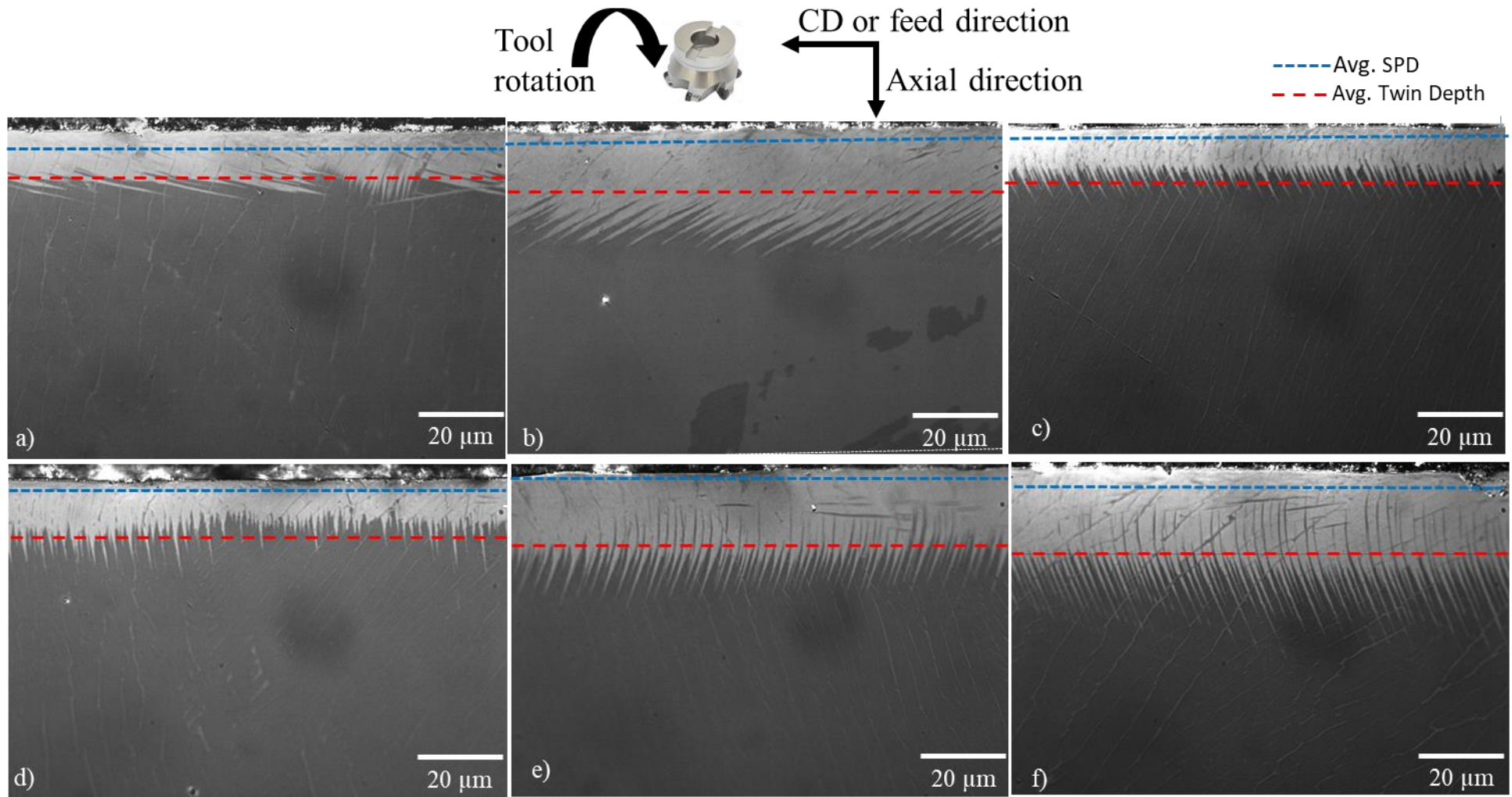
Figure 6-10 Cross-sectional, cross-polarised light micrographs representing the plastic deformation induced during β annealed Ti-6Al-4V ELI face milling at a surface speed of 80 m.min^{-1}, a_p = 2 mm, a_e = 10 mm, LoC = 105 mm with 1 rounded tool tip Walter F2334, under different cooling/lubricating conditions : a) conventional flood cooling, b) MQL, c) CO_2 plus MQL, d) 25% CO_2, e) 75% CO_2 and f) 100% CO_2. The delineated lines correspond to the severely plastic deformed layer and twin depth.

The ability of a grain to mechanically twin depends on the crystallographic orientation of the parent grain. Some grains are crystallographically orientated to allow easy slip; these correspond to soft orientations and grains where slip is unfavourable; thus mechanical twinning or <c+a> slip take place. Figure 6-11 illustrates two grains with different underlying crystallographic orientations. The grains with the darker shade represent those of a hard orientation. Thus the shear generated during machining-induced densely packed mechanical twins. In Figure 6-11 a) the brighter grain shows much less machining-induced plastic deformation as slip is a more favourable deformation mechanism. This represents further evidence that the underlying microstructure and grain orientation is a crucial parameter for generating subsurface damage.
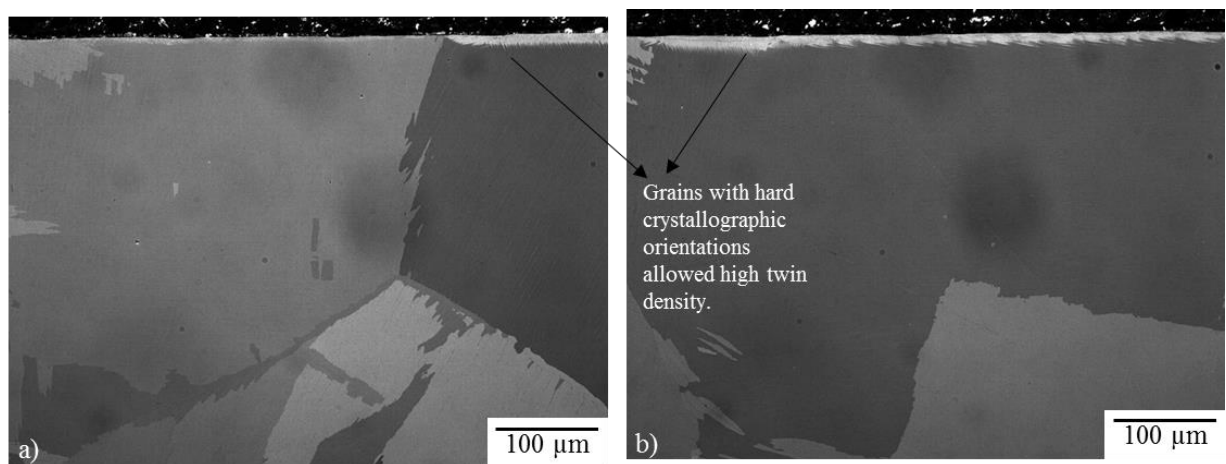
Figure 6-11. Cross-sectional low magnification cross-polarised light corresponding to β annealed Ti-6Al-4V ELI after face milling at a surface speed of 80 m.min^{-1} under CO_2 plus MQL.

Many different types of mechanical twinning for each of the sample conditions have been identified. The type of microstructural feature depends on the relation of the crystallographic orientation to the direction of the applied load. The ability to reach the CRSS for any of the slips modes determines whether slip or mechanical twinning accommodates the plastic strain. This is also dependant on deformation temperature. The relative CRSS for <c+a> slip strongly increases as the temperature is reduced (Figure 2-10); thus the mechanism available to accommodate the imparted strain is mechanical twinning. Twinning does not have a temperature dependency (Figure 2-11). As the temperature reduces, the stress required for slip to operate increases strongly, thus there is a higher probability that mechanical twinning will take place.

Under each of the cooling conditions, there are different operative twin systems during plastic deformation. These strongly depend on the underlying crystallographic orientation of the parent grain and on the stress state generated by the cutting tool. Figure 6-12 shows cross-polarised micrographs corresponding to different twin systems in operation during milling

under 100% CO_2. Figure 6-1 a) only shows an SPD region and the absence of mechanical twins. This grain may be of a "soft" crystallographic orientation, as slip may have easily occurred. Figure 6-12 b) shows a lenticular twin morphology with a thick region of severe plastic deformation. Figure 6-12 c) shows a higher twin depth of needle-like morphology and a very shallow SPD region. Figure 6-12 d) shows mechanical twins in a direction parallel to the cutting/feed direction.
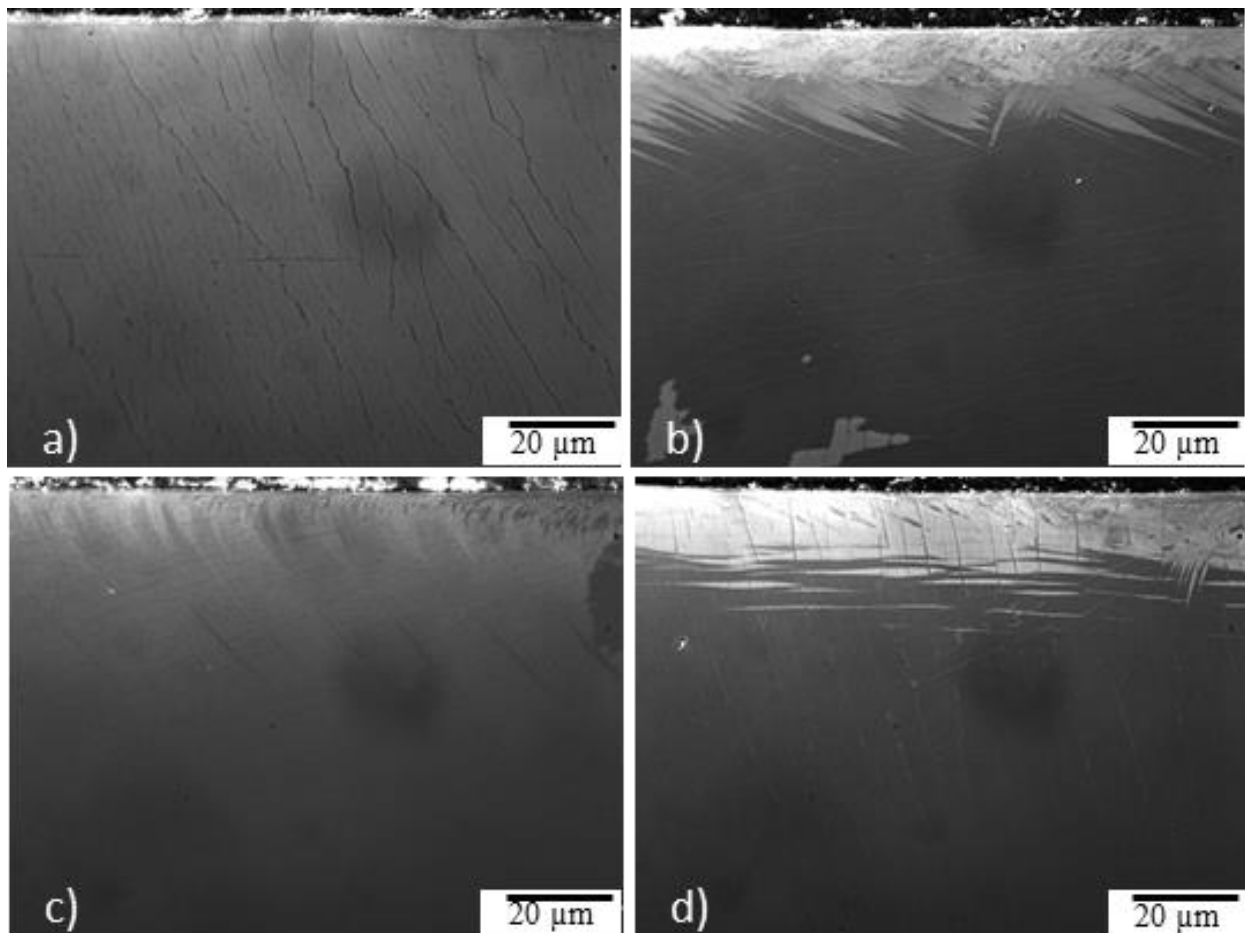
Figure 6-12. Different operative twin systems during milling at 80 m.min^{-1} under 100% CO_2.

6.2.1. Subsurface microstructural evolution under 100% CO_2

Figure 6-13 a) shows a cross-polarised light micrograph under 100% CO_2 cooling condition. It displays a region of nearly 10 µm in depth of a severely plastically deformation. Below this region, there is a mechanical twinning region. This region represents one colony with the α-phase and retained β in the same direction inside of a parent β grain. It shows two different crystallographic orientations for the growth of the mechanical twins. This fact may be related

to a different stress state imparted to the workpiece by the engagement/disengagement of the cutting tool due to the inherently intermittent nature of the milling process.

Figure 6-13 b) shows a backscattered electron micrograph of the area outlined in Figure 6-11 a). Due to channelling contrast in, mechanical twins and other crystallographic defects could be observed. It illustrates how this area has plastically deformed and rotated towards the cutting direction to accommodate the imparted shear strain. A region of 2.2 µm of severely plastically deformed material is shown. The reasoning for this is that the area immediately below the machined edge has experienced the highest shear stress, strain rate and shear strain. The retained β shows a wavy nature characterized by the intense plastic deformation in that region. The retained β thickness appears much less than further in the subsurface, from 0.13 µm to 0.052 µm. This may be due to the elongation of the crystal lattice into the cutting direction during plastic deformation. The thickness of the α-phase lamella has strongly decreased; from 1.36 µm to 0.22 µm. Thus there are a higher number of lamella with α-phase and β-phase boundary. Besides, there is evidence of the presence of dynamically recrystallized nanoscale grains due to the plastic deformation process. Consequently, the increase in strength and hardness is developed in this region. The SPD region may be related to the initial tensile residual stress observed in the machined edge. This region closest to the surface shows a brighter appearance under electron microscopy, resembling a "white layer"; however, its thickness is barely distinguishable as it is nearly 0.38 µm in depth. In this SPD layer, within 10 µm, subgrain development is observed. It also shows a curved notch generated by the cutting tool of nearly 0.6 µm in depth and a small notch to the side. The fact that the white layer represents a stress raiser may be related to the result of the highly distorted lattice and the generation of a precursor to strain localisation. These locations may not be able to withstand the load-capacity better than the bulk of the material. Below the region of mechanical twinning, there is the undistorted bulk material. In this micrograph of this specific colony, it is at 28 µm in depth.

Figure 6-131 c) shows another region from the sample. Three different colonies with different crystal orientations are examined. This factor results in different modes of accommodation of the strain during plastic deformation being observed. In colony 1, the retained β are orientated parallel to the cutting direction, and in colony 2 they are oriented in an orthogonal direction. Thus β lamellae in colony 1 appear uniformly and highly distorted giving the appearance of a wavy structure. In colony 2, retained β have rotated strongly towards the cutting direction with the appearance of intense slip for the accommodation of the plastic strain. Figure 6-13 d) is a higher magnification of the image of the deformation of colony 1 in from Figure 6-13 c). The top layer resembles the "white layer" of nearly 0.34 µm, and no feature is distinguishable under the SEM. Below this layer, there is an SPD layer with the distorted retained β. The α lamellae appear to contain equiaxed nanograins; some observed grains measure between 34 to 46 nm. Mechanical twins appear to different depths and different

crystallographic orientations in the three colonies. This is because the operation of mechanical twinning depends on the crystallographic orientation of the parent grain. In this case, of each of the colonies, but it also depends on the restrictions imposed by the neighbouring colonies as these impose restrictions on strain accommodation and preserve coherency within the sample.

Figure 6-13 e) represents another region of the sample. An SPD layer of nearly 1.5 µm is readily distinguishable where the retained β do not seem to be present. However, upon closer examination in Figure 6-13 f) retained β is observable. There is a significant reduction in the thickness of the β phase, the α lamellae being highly compressed with retained β being strongly elongated. Recrystallized nanograins also appear to be present in this area. Below this region, subgrain development appears to be present, followed by mechanical twinning and, finally, the undistorted bulk material.
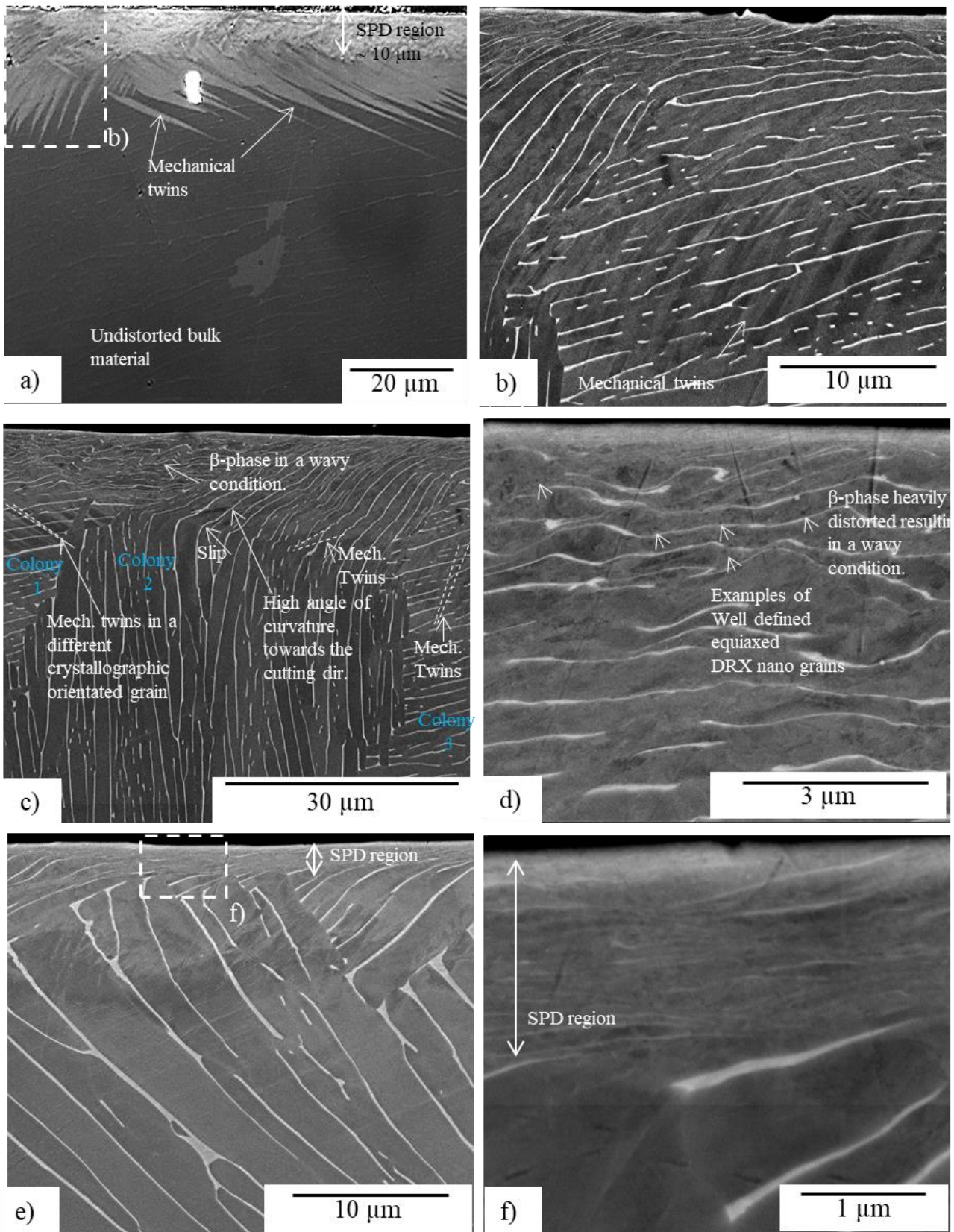
Figure 6-13. Cross-sectional area a) high magnification cross-polarised light b)-f) BSE micrographs corresponding to β annealed Ti-6Al-4V ELI after face milling at a surface speed of 80 m.min^{-1} under 100% CO_2.

6.2.2. Subsurface microstructural evolution under 25% CO_2

Figure 6-14 a) is a light micrograph under 25% CO_2 cooling. It illustrates how cross-polarised light reflects light differently depending upon the orientation difference of the mechanical twins compared to the parent grain. It represents one colony with α and β lamellae or lamella in the same crystallographic orientation, Figure 6-14 b) is a slightly larger magnification BSE micrograph of the same region where mechanical twinning is imaged through channelling contrast in the SEM. Figure 6-14 c) illustrates a similar region to that generated under 100% CO_2 where the retained β appear highly distorted. Subgrain development is observed in the interior of the α lamellae. Figure 6-13 d) shows strain localisation. This implies that lower stresses during in-service may be locally withstood.
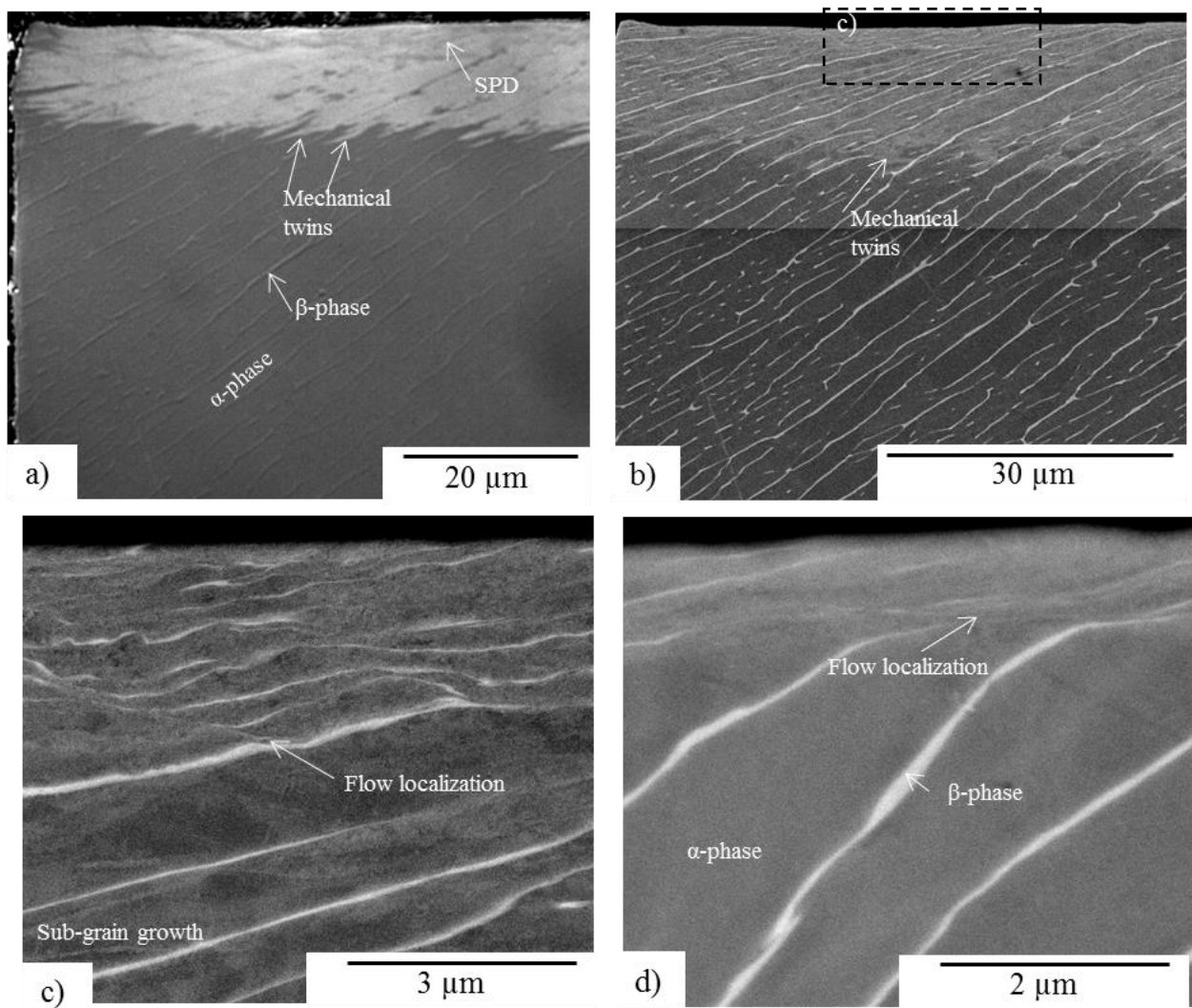
Figure 6-14. Cross-sectional a) high magnification polarised light b)-e) BSE micrograph corresponding to Ti-6Al-4V β annealed after face milling at the surface speed of 80 m.min^{-1} under 25% CO_2.

6.2.3.   Subsurface microstructural evolution under conventional flood coolant

Figure 6-15 a) shows the milling induced subsurface damage under conventional flood cooling. A high frequency of micron size v-notches is observed. In the first part of the colony, a mechanical twin of ~ 4.7 µm is observed and β phase reorientation at a depth of 2.5 µm. In the alpha lamellae, between the two β-lamellae of the first v-notch appears to have suffered slip. The v-notch fractured the retained β partitioning it into two sections. The mechanical twin appears to have extended across the colony, however non-uniformly. A slightly deeper twin appears close to the second v-notch. In terms of topography, under cross-polarised light micrographs the workpiece presented many surface irregularities such as micron size peaks, troughs and notches as shown in Figure 6-15 a). Some small size and thick mechanical twins are observed with a twin tip that has not penetrated through the parent grain. Two colonies of different crystallographic orientation appear in Figure 6-15 b) where minimal retained β drag is shown. The colony with the orientation orthogonal to the cutting direction shows a mechanical twin that tapers to a sharp edge. The immediate area under the edge on the first colony shows subgrain development. In contrast to what was observed in Figure 6-15 a) and Figure 6-15 b), Figure 6-15 c) shows microstructural grain refinement in the SPD layer with high lattice reorientation in the retained β and α lamellae. Image Figure 6-15 d) also shows microstructural refinement in the SPD layer with a small amount of mechanical twinning.

It is believed that warm temperatures were reached during milling with conventional coolants. As the load is significantly influenced by higher temperatures (~300°C), as previously observed in the TMC testing in chapter 5, lower stresses may have been imparted into the lattice of the workpiece, consequently generating lower mechanical twin depths. Additionally, thermal fluctuations generated by higher temperatures may assist plastic flow in overcoming short-range obstacles. Therefore plastic deformation occurs at lower shear stresses. Also, at lower temperatures such as in cryogenic cooling, higher dislocation densities are imparted into the subsurface of deformed components as evidenced in section 5.10, Figure 5-51, and stated by Cottrelli and Mould [53]. That difference in dislocation density content may be the source of mechanical twin growth deeper in the subsurface.
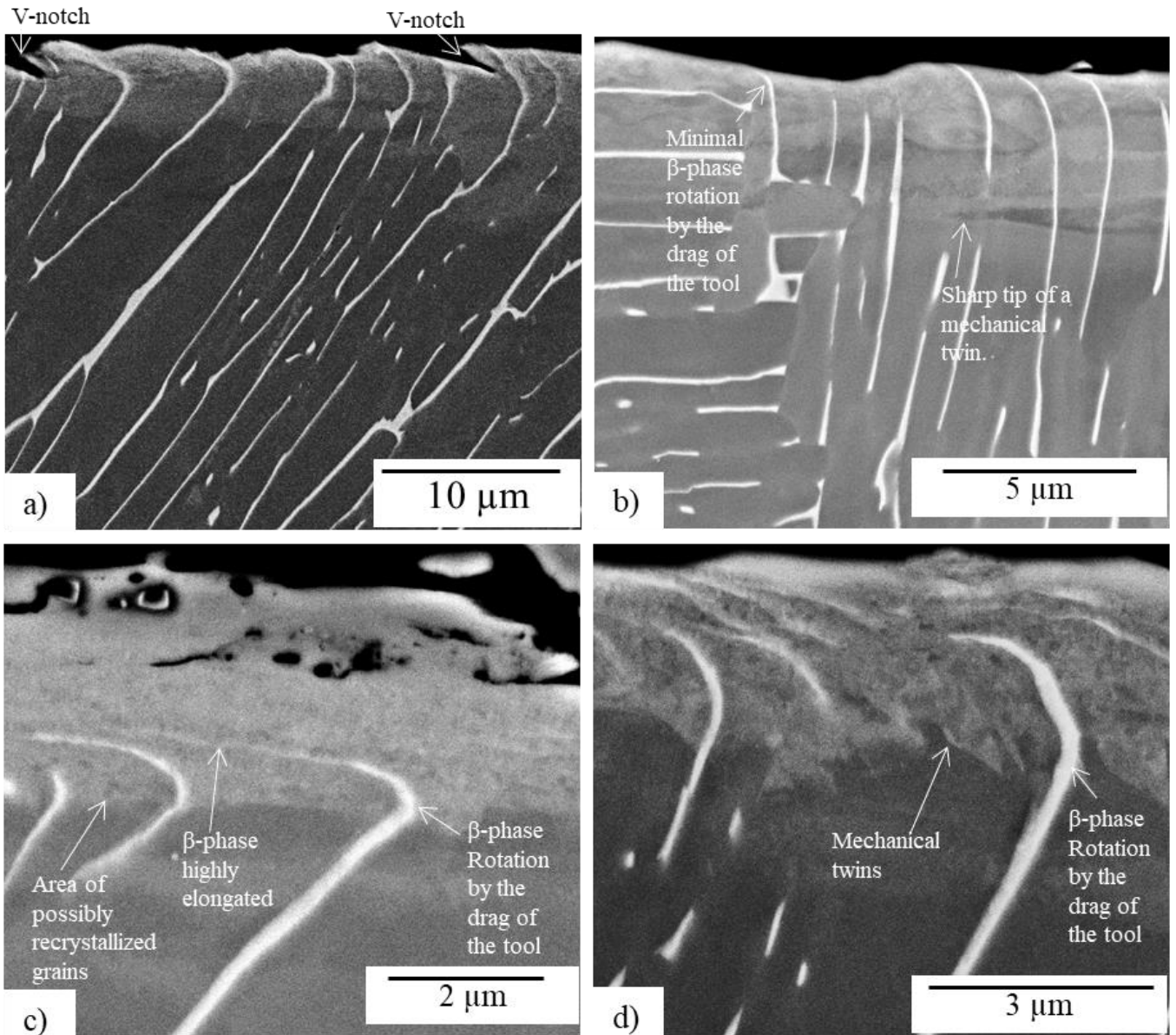
Figure 6-15. Cross-sectional a)-e) BSE micrograph corresponding to β annealed Ti-6Al-4V ELI after face milling at a surface speed of 80 m.min^{-1} under conventional flood coolant.

6.2.4. Subsurface microstructural evolution under MQL

Although the application of a lubricant reduces the friction generated during machining, at high speeds the coolant is necessary to prevent a build-up of high temperatures leading to detrimental tool wear, primarily by solid state diffusion. Solid state diffusion promotes crater wear [66]; thus tool wear failure may result in the development of a crater on the rake face of the tool. When the tool is not sharp and is becoming dull, higher stresses are imparted into the workpiece, enabling plastic deformation to take place. At 200 µm tool wear, higher shear stresses may have been imparted to plastically deform the uncut chip thickness. This means the similarity in the subsurface twin depth with the low temperatures was generated by the CO_2.

Surface topographical features such as v-notches of fractions of a micron in size were observed in some micrographs. As the temperature built up in the tool (due to the lack of coolant), it is believed that the high temperature generated during MQL cutting may have given rise to tensile residual stress in the subsurface immediately below the machined edge.

Nanograins are observed in the alpha lamellae right below the machined edge; see Figure 6-16 d). Below this region, subgrain development is observed in Figure 6-16 c) and Figure 6-16 d). Below the SPD region, a heavily mechanically induced region is observed. The growth of some twins to similar depths as in cooler conditions implies that twin growth depends on the parent grain's crystallographic orientation and the higher stresses imparted by the tool, which is probably dull or crater worn.
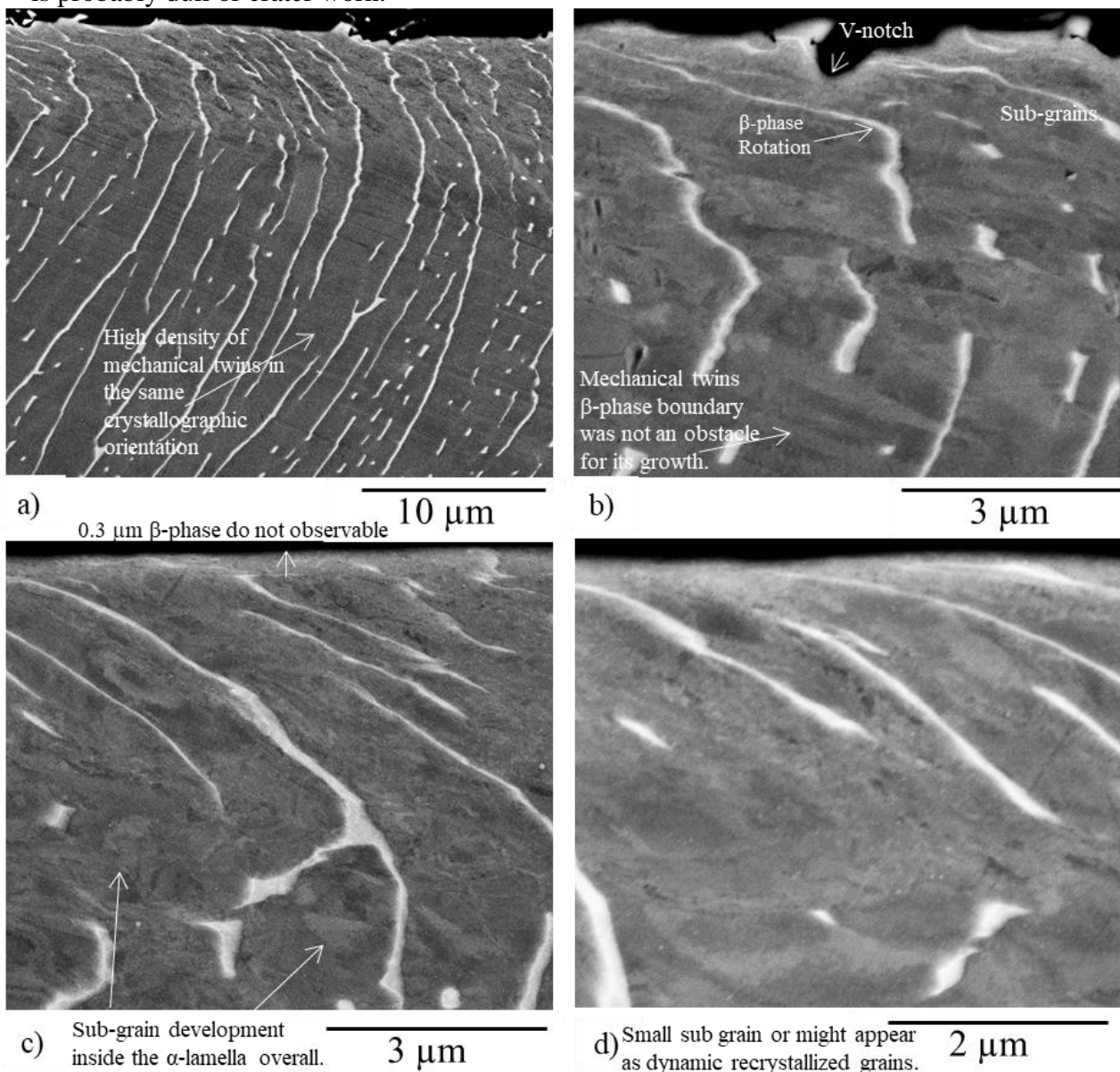
Figure 6-16. Cross-sectional a) high magnification polarised light b)-e) BSE micrograph corresponding to β annealed Ti-6Al-4V ELI after face milling at a surface speed of 80 m.min^{-1} under MQL.

261

V-notches represent stress raisers due to the introduction of triaxial stresses, locally increasing the stresses, sites of higher strain hardening and a local increase in the strain rate thus creating sites for crack initiation. The generation of v-notches has been observed on machined surfaces, close to the recrystallized area. Thus, it may not be wise to etch the top surface as the nanograined surface is beneficial in terms of an increase in yield strength. The development of a nanograin structure also increases the grain boundary volume fraction, and this implies that a high number of dislocation barriers will exist on the immediate layer below the machined surface. This might counteract the v-notch effect preventing it from becoming a crack initiation site.

According to Reed-Hill [34], the parameter with the highest significance to determine the plastic deformation mode is the stacking fault energy. Low stacking fault energy materials, such as titanium alloys, are characterized by difficulty in cross slipping and a low ability to change shape by slip alone, favouring twinning. The dissociation into partials leads to more planar dislocation arrays.

### 6.2.5.	Subsurface microstructural evolution under CO$_2$ plus MQL

CO$_2$ plus MQL provided the lowest average twin depth. Figure 6-17 shows cross-polarised light micrographs of the subsurface below the machined edge. Figure 6-17 a) constitutes one prior β grain and it appears to be only one colony. As the α and β laths have the same crystallographic orientations, the same depth of deformation twins is observed. A cyclical behaviour is apparent; this may be related to the feed rate or the tool's number of revolutions per second. Figure 6-17 b) shows how the plastic deformation mode changes in a small colony that is inside a larger one. In the larger colony, there is a high twin density, closely spaced and it is related to the underlying parent grain. Figure 6-17 c) shows a colony where the dominant mode of plastic deformation is slip and an SPD layer was generated. Figure 6-17 d) shows needle-like twins, oriented towards the cutting direction. In this micrograph, a minimal SPD region is apparent.

a) Mechanical twins reoriented towards cutting direction — 50 μm

b) High density deformation twins in the crystallographic orientation of this colony — No deformation twinning in this colony — 20 μm

c) Severely plastically deformed region — 20 μm

d) Low density deformation twins (needle like) — 20 μm
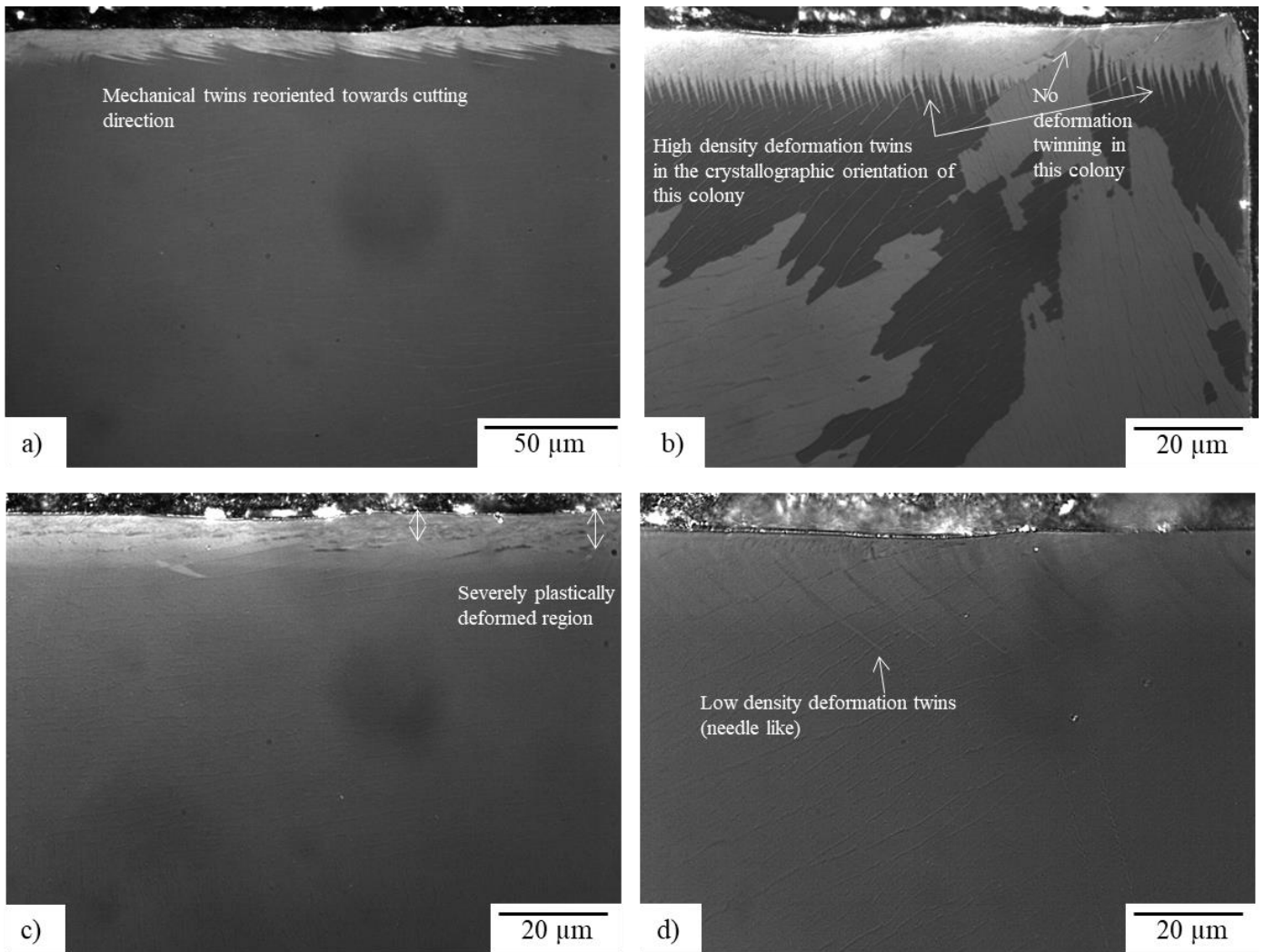
Figure 6-17. Cross-polarised light micrographs of β annealed Ti-6Al-4V ELI after face milling at a surface speed of 80 m.min^{-1} under CO_2 plus MQL.

6.3. Damage imparted leading to void nucleation

Low-temperature plastic deformation is achieved by application of cryogenic liquefied gas CO_2 which drove mechanical twinning as the dominant deformation mechanism. Thus mechanical twins accommodated the majority of the imposed plastic shear strain. This suggests a similar behaviour as in Zirconium, an HCP metal; twinning generated during room temperature deformation was linearly related to the imparted strain contributing with <15%, however, at -196°C twinning ($\{11\bar{2}1\}$ and $\{10\bar{1}2\}$) accounted for the majority of the strain accommodated during plastic deformation [160]. The effect of twinning during plastic deformation at low temperatures represents an increase in strength, strain hardening rate and ductility [160]. On the other hand, cracks in twin interfaces have been observed in many HCP metals [1]. Other

slip systems could be generated by the influence of twinning: by the generation of localised high stresses or by its interaction with dislocations.

Avery and Backofen [161] reported that cracking occurred along traces of slip planes in iron during fatigue. Persistent slip bands may grow during cyclic fatigue as the site of crack initiation [161]. Surface irregularities: slip band intrusions and extrusions — factors which influence the mode of plastic deformation [160]. Below ambient temperatures, the increase in interstitials leads to an increase in flow stress, and it is strongly dependent on impurity content [162].

6.4. Continuous Dynamic Recrystallization

The driving force for dynamic recrystallization is the energy stored in the lattice during plastic deformation. During machining, plastic deformation, recovery and recrystallization take place simultaneously and continuously. The plastic deformation response of the microstructure is similar to a cold worked structure, where a high dislocation density is introduced into the lattice, dislocation loops, tangles and networks are generated. During recrystallization, strain-free grains are generated in regions where there is sharp lattice curvature by rearranging their orientation and generating high grain boundary angles. Preferred nucleation places for DRX are regions of the small volume where the crystal lattice is highly distorted [141]. In these regions, the critical size of a stable nucleus is small and to form a HAGB it only requires a short distance of growth [141]. In DRX, a change in texture occurs that can be attributed to the high angle boundary migration [141].

If the dynamic recrystallization process occurs in the presence of localised deformation heating or adiabatic heating, strain localisation leading to catastrophic failure may occur [2]. The application of a cryogenic coolant is beneficial in the sense that it may enhance locally adiabatic heating, softening a localised region, and therefore, allowing easier ABS formation or chips in machining. This leads to lower heat generation during plastic deformation.

Figure 6-18 shows bright field transmission electron micrographs of a thin generated foil through focused ion beam milling (FIB). Section 3.2.4 describes the methodology to obtain the TEM's specimens. Figure 6-18 a) shows a low magnification micrograph of a ~ 6 µm in depth. The top area represents the subsurface immediately below the machined area. It depicts two different regions: one of the highly refined grains or nanostructured layer of nearly 2.9 µm in depth and a second appearing as subgrain development region. The measured average grain size with 95% confidence limits is 48.9 ± 5.2 nm. Figure 6-18 b) and Figure 6-18 c) are higher magnification micrographs and they exhibit many equiaxed dynamically recrystallized grains uniformly spread through the region. Figure 6-18 d) and Figure 6-18 e) represents the region closer to the bottom of the foil. Some recrystallized grains are observed, but the main feature

appears to be α lamellar substructure with arrays of clustered dislocations and elongated grains. The reason that the region did not recrystallize is that not enough dislocations were accumulated into the lattice. Consequently, it has not stored the required driving force to enable the process to occur.

Electron micrographs from Figure 6-13 show subgrain development within and below the SPD layer. This suggests that new grain boundaries were generated through subgrain low angle development in regions of sharp lattice curvature. This lattice curvature may have been imparted into the lattice of the workpiece by the cutting tool. New recrystallized strain-free equiaxed nanograins of HAGB may have been mainly developed through subgrain rotation and coalescence. The pre-existing grain boundary may have contributed to the dynamic recrystallization process through polygonization. However, there is no experimental evidence from the existing foil image. Recovery and recrystallization are competitive processes, and usually, some recovery takes place before recrystallization initiates.

Cutting at low temperatures implies that a higher dislocation and defect density would be introduced into the lattice of the workpiece as well as the corresponding strain fields surrounding dislocations. As each defect represents stored energy, the higher the number of dislocations, the higher the internal energy or driving force available for dynamic recrystallization to take place. Cotterill et al. [53] report that while an annealed alloy contains 10^6-10^8 dislocations.cm^{-2} and a heavily deformed alloy contains 10^{10}-10^{12} dislocations.cm^{-2}. There is more than four orders of magnitude difference in the dislocation density of the lattice. Factors which influence the structure of deformed metals are stacking faults, solute atoms, temperature, second phase particles, strain rate and the type of shear process. Metals with low stacking fault energies such as titanium or copper produce wide stacking faults creating partial dislocations. This hampers the ability to cross slip; thus the dislocations slip only short distances. This generates higher internal energy in the lattice. Also, the dislocations will be more uniformly spread out. Cell-wall formation is not likely to occur as it depends on the capacity of screw dislocations to cross-slip to other planes and to arrange themselves into high localisation regions. The increase in solute content results in higher dislocation generation and, as a result, higher internal energy which would be available for DRX. The effect of temperature influences the dislocation density, dislocation distribution through the lattice and the internal energy. At low temperatures, the dislocation distribution is more uniform (as shown in Figure 2-15 and Figure 2-16), and there is a lower propensity for the formation of cell walls [35]. The retained β in α-β alloys represent sources of more dislocation creation and act as barriers to its movement. However, in the case of this alloy β-phase does not seem to be a strong barrier to the growth of mechanical twinning. The increase in strain rate increases the number of dislocations, as a consequence of the increase in internal energy and there is a higher tendency to generate a uniform distribution of dislocations. Metal cutting is a localised process; therefore there will be a gradient in the intensity of experienced stresses, strains and temperature. This

will generate a graded microstructure in the subsurface. As a result, dislocation generation will also be graded, with higher energy in the regions close to the cutting edge. Under high strain rates such as these, generated in metal cutting, the near adiabatic heating condition is enough to lead to dynamic recrystallization [53]. Thus the cryogenic coolant may function as a "quenching fluid" preventing the growth of the newly recrystallized grains. Cotterill et al. [53] report that shear bands are nucleation sites for recrystallization. It is in these regions where the adiabatic temperature is reached and where the highest shear strains and strain rates are experienced. Additionally, there is some sort of "shear band partitioning" by the plastic instability developed due to strain localisation and the predominance of thermal softening over strain hardening in that region. This causes the nucleation of microcracks, and the ligaments that connect the voids are broken. Two SPD areas are generated, one is left in the subsurface of the cut workpiece and the other is on the bottom of the chip.

Figure 6-18 f) is a micrograph from the top of another location on the foil. In the top region, new strain-free recrystallized grains are observed. Additionally, there are some regions with clusters of dislocations, regions where more internal energy was probably required to generate new HAGB grains. The bottom region of the micrograph seems to contain mechanical nanotwins, which could lead to the theory that nano-mechanical twins were operative during shear band generation.
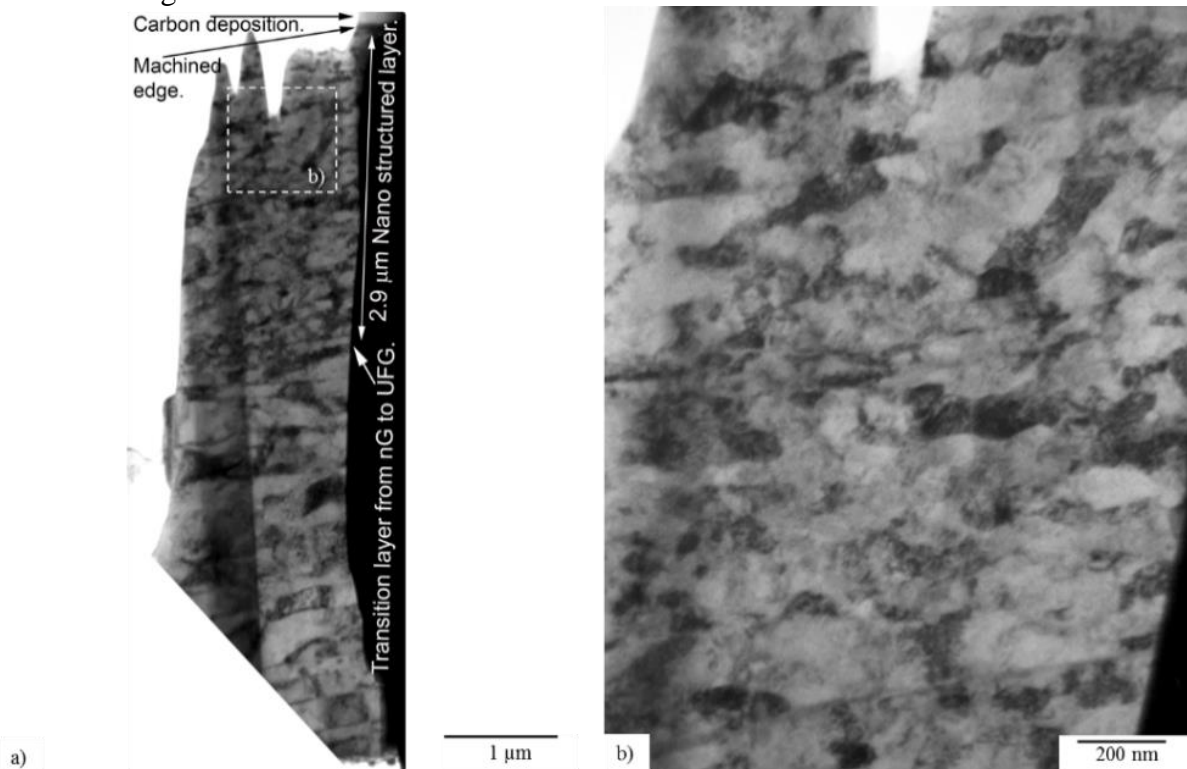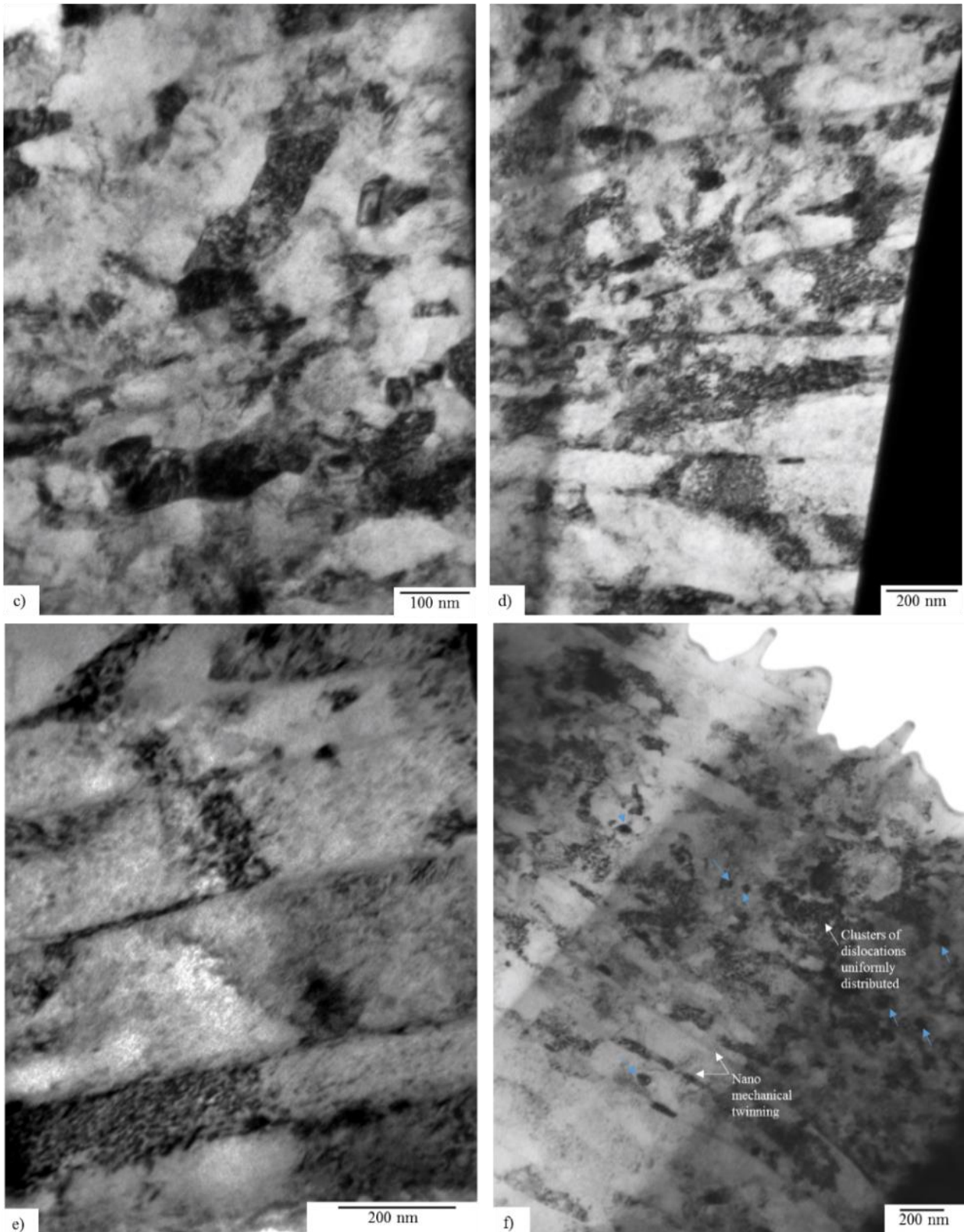
Figure 6-18. Bright field transmission electron micrograph from a β annealed Ti-6A1-4V ELI face milled at 100 m.min^{-1} under CO_2 cryogenic cooling using one Walter ADGT10T3PER-D67 insert: a) full-length foil and scanned area, b) magnification of a), c)

deeper area ~ 2 µm, d) ~ 3 µm in depth e) bottom of the foil showing alpha phase elongated subgrains.

Bright field transmission electron micrographs from face-milled samples at 80 m.min^{-1} under conventional flood cooling are shown in Figure 6-19. This represents experimental evidence of dynamically recrystallized grains in the subsurface, however at a depth approx. of only 400 nm as shown in Figure 6-19 a) and Figure 6-19 b). The estimated mean grain size in Figure 6-19 b) is 27.7 ± 2.36 nm with 95% confidence limits. At nearly 0.5 µm in depth in Figure 6-19 a) dislocation clusters appear. This suggests that not enough strain energy was introduced into the lattice during deformation to stimulate grain boundary migration to initiate dynamic recrystallization. As the closest area to the machined edge has locally experienced the highest shear stresses and shear strains, it is a highly distorted region and a place where higher dislocation density was generated to allow the accommodation of the imparted plastic strain. There is evidence of nanometre mechanical twins taking place at a depth to approx. 3 µm as observed in Figure 6-19 c). Figure 6-19 d) exhibits highly elongated subgrains with high dislocation density, implying that the strain energy imparted during metal cutting under conventional flood cooling was not enough to activate dynamic recrystallization at a deeper level as in 100% CO_2. This experimental evidence suggests that conventional flood cooling has generated a very narrow area of recrystallized grains on the subsurface. By comparing the depth of the recrystallized grains in the subsurface of 100% CO_2, only 11% of the subsurface depth was achieved by flood cooling.

The presence of mechanical twinning in the machined subsurface under flood cooling implies that there is the presence of mechanical twinning under CO_2 and LN_2 cryogenic cooling as it is the leading deformation mechanism at lower temperatures. Mechanical nanotwins might not have been observed in Figure 6-18. This is due to lower magnification achieved with that foil in comparison to the foil corresponding to flood cooling.

The more uniform distribution of dislocations prevents dislocation rearrangement or their annihilation. The stored energy is available for DRX once sufficient thermal energy is supplied or stored in the crystal lattice. In low stacking fault energy (LSFE) materials, planar arrays of dislocations are generated, and as the subgrains are more stable than high stacking fault energy (HSFE) materials, more dislocations are retained leading to a higher increase in misorientations [141]. In LSFE materials there is little dynamic recovery (DRV) prior to dynamic recrystallization (DRX) [141].
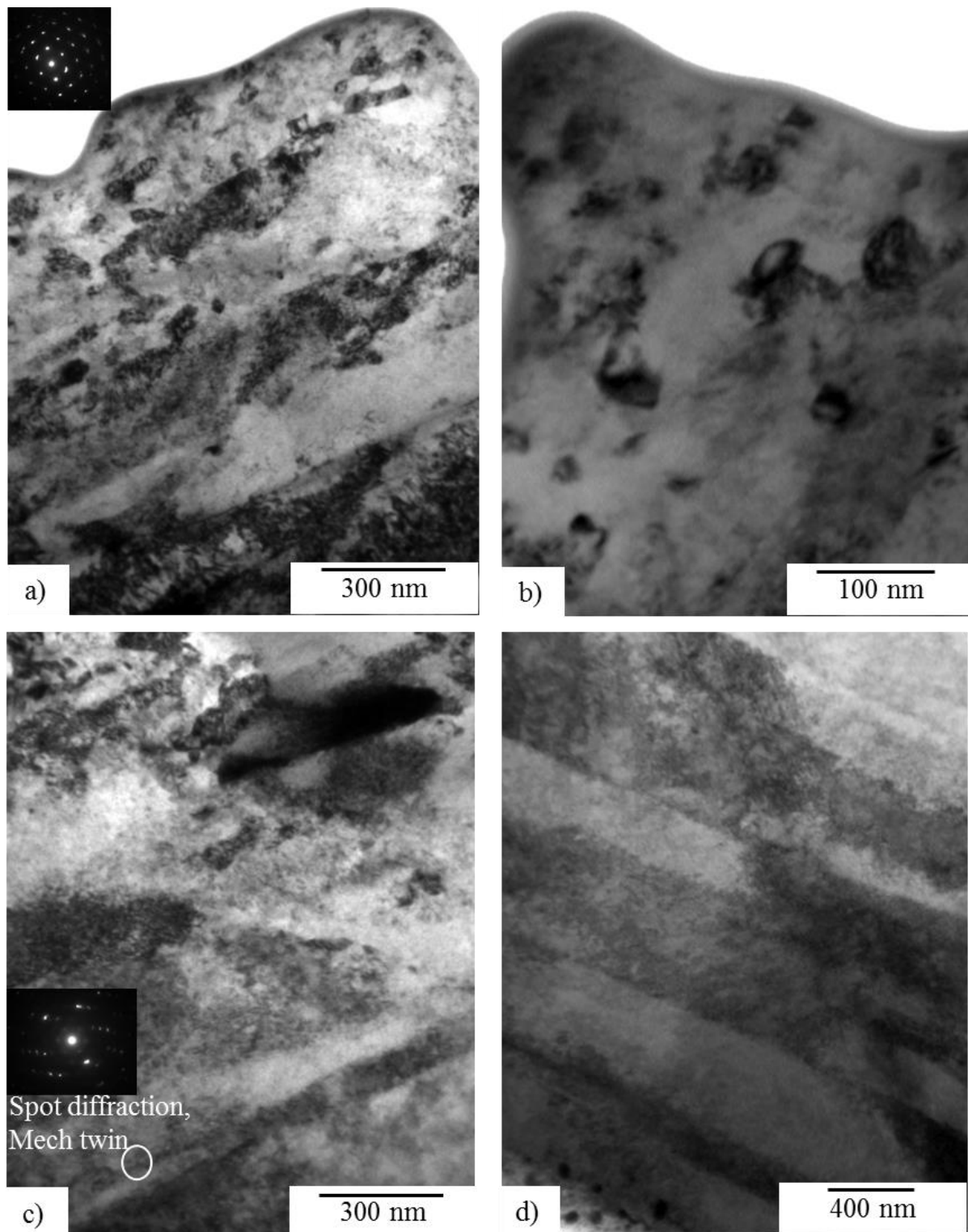
Figure 6-19. Bright field transmission electron micrograph from a β annealed Ti-6A1-4V ELI face milled at 80 m.min^{-1} under conventional flood cooling: a) top part of the foil, b) higher magnification of a section of the top part of the foil, c) centre of the foil d) at the end of the foil where lower strain and strain rate were imparted.

A schematic representation of subsurface deformation damage introduced during high-speed machining of β annealed Ti-6Al-4V ELI under CO_2 cryogenic cooling condition is

269

illustrated in Figure 6-20. The immediate layer below the machined edge represents the SPD region and the recrystallized equiaxed nanograin size. This area is likely to have a high yield strength and enhanced ductility due to the high volume fraction of the grain boundary area introduced by the recrystallized strain-free nanograins [54], [163]. Even though this area represents an increase in yield strength, it also represents a reduction in fracture toughness K_{IC} as observed in Figure 6-21. This is due to the change in grain morphology from lamellar to equiaxed. Once a crack has been nucleated, it grows quickly, easily traversing the nanocrystalline grains. Therefore, a balance in mechanical properties should be sought. The retained β phase has been dragged by the cutting tool and shows a bent appearance towards the cutting direction. Below this area, there is subgrain development inside the alpha phase lamellae. The area that contains the retained β and subgrain development are regions of high strain hardening due to the introduction of high dislocation density and the interaction between dislocations and their corresponding strain fields. A deeper region is followed by significant mechanical twinning; their penetration depth depends on the crystallographic orientation of the parent grain. According to experimental evidence in section 5.5 and Figure 5-26, the initial mechanical twins were introduced ahead of the cutting tool. In many microstructures, secondary twinning appears. This is hypothesized to have nucleated and grown when the tool passes and leaves that area behind. Finally, there is the undeformed bulk microstructure with initial mechanical properties.
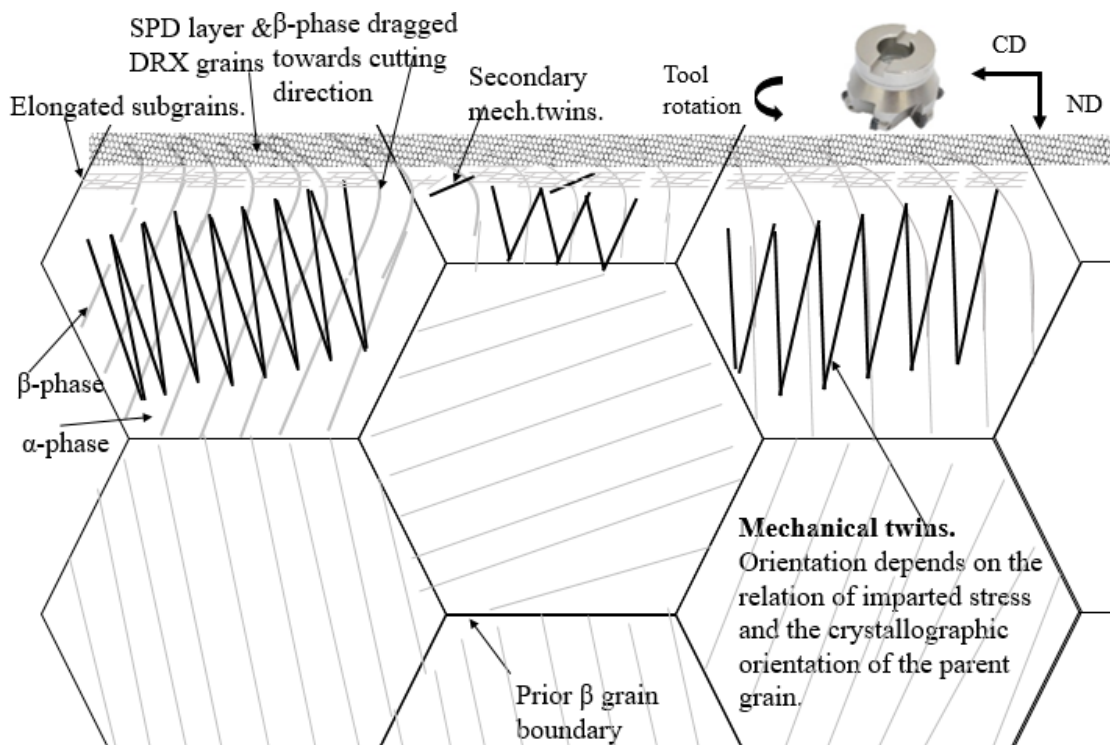
Figure 6-20. Schematic diagram illustrating the microstructural evolution during milling at high speed under cryogenic coolants.
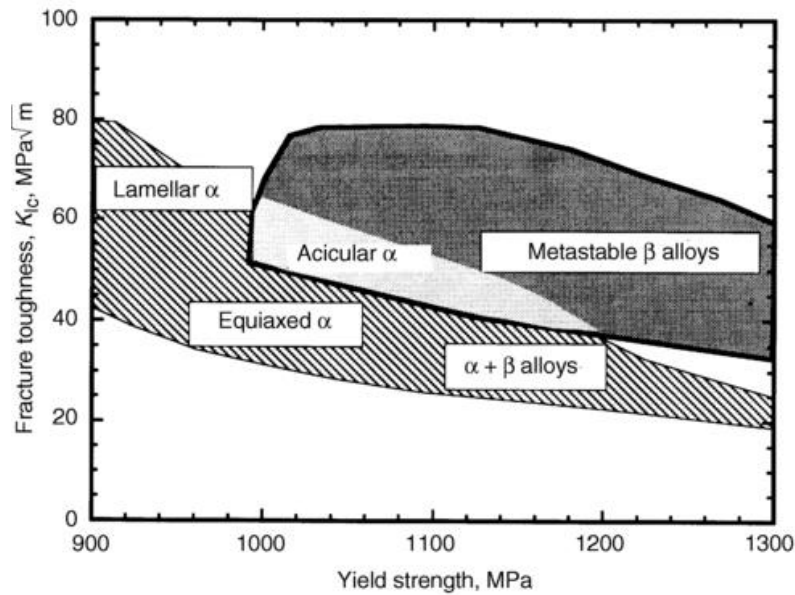
Figure 6-21. Fracture toughness and yield strength dependency of the underlying microstructure of titanium alloys [164].

6.5. White layer

The sample of β annealed Ti-6Al-4V ELI under 100% CO_2 machined with a worn tool of 200 μm wear land was chemically etched to investigate the existence of a "white layer", as reported in the literature. The author's typical way of examining the subsurface is under cross-polarised light as shown in Figure 6-22 d). Under this condition, it is possible to observe the severe plastic deformation region closest to the machined edge and the mechanical twins, as they are orientated in different crystallographic direction and reflect light differently than the bulk material. Chemically etching a sample, attacks the grain boundaries preferentially; in this case, the lamellae boundaries or the retained β phase as they possess higher energy. Figure 6-22 c) shows an etched sample under cross-polarised light. It is observed that the retained β phase is not being attacked in the region closest to the machined edge. This may be because the retained β boundary thickness is reduced by the strong elongation (as the β is more ductile than the α phase), giving them lower energy levels than the boundary in the bulk. Many authors report the appearance of a "white layer" on an etched sample machined with a worn tool. In this case, only a very shallow "white layer" was observed of 0.43 μm in depth under secondary electron (SE), see Figure 6-22 a). Under BSE, an etched sample does not show a "white layer". It shows microstructure refinement and subgrain structure. Under both SE and BSE, an SPD layer of 3.84 μm in depth and a region of strain localisation in the transition between the SPD and the twinned region is observed. The author believes this strain localisation feature on the uppermost subsurface may reduce the load carrying capacity during dynamic loading in

271

service, as it is a region of stress and strain concentration. This may allow the nucleation of microvoids, and consequently to fracture.

In face milling, the residual stress is tensile in the surface and changes into compression in the subsurface [117]. This tensile residual stress may correspond to this "white layer" and may affect fatigue properties. As observed in Figure 6-18, the uppermost region of the machined edge under CO_2 is composed of an equiaxed nanocrystalline grain size α phase, and as observed by electron microscopy, it contains highly elongated retained β phase. Once a crack has nucleated at the surface, this recrystallized grain morphology most likely will not arrest it, or there will be low energy required to grow the crack until it reaches the strain-hardened region or the colony structure. The colony structure will not allow a crack to continue growing along the same path, a direction change should occur, and this requires energy.

Figure 6-23 shows other regions of the polished and etched workpiece machined under 100% CO_2. A "white layer" appearance is shown under SE, but it does not appear under BSE. The SPD layer is composed of highly elongated retained β and dynamically recrystallized α phase. Figure 6-23 a) - b) also show strain localisation as evidenced by the displacement of the upper part of the retained β. This also may lead to the nucleation of a crack during dynamic loading. Figure 6-23 c) – d) show mechanical twins below the SPD layer, which are chemically etched, as they are sites of high energy.

"White layer" in SE

Severely Plastically Deformed layer

Strain localization

Retained β observed in both "white layer" and SPD layer

Highly elongated β

Retained β thickness same as in the bulk

a)

3 μm

b)

3 μm

Etch does not attack the uppermost subsurface layer; may be due to the significant reduction in retained β thickness

c)

20 μm

d)

20 μm
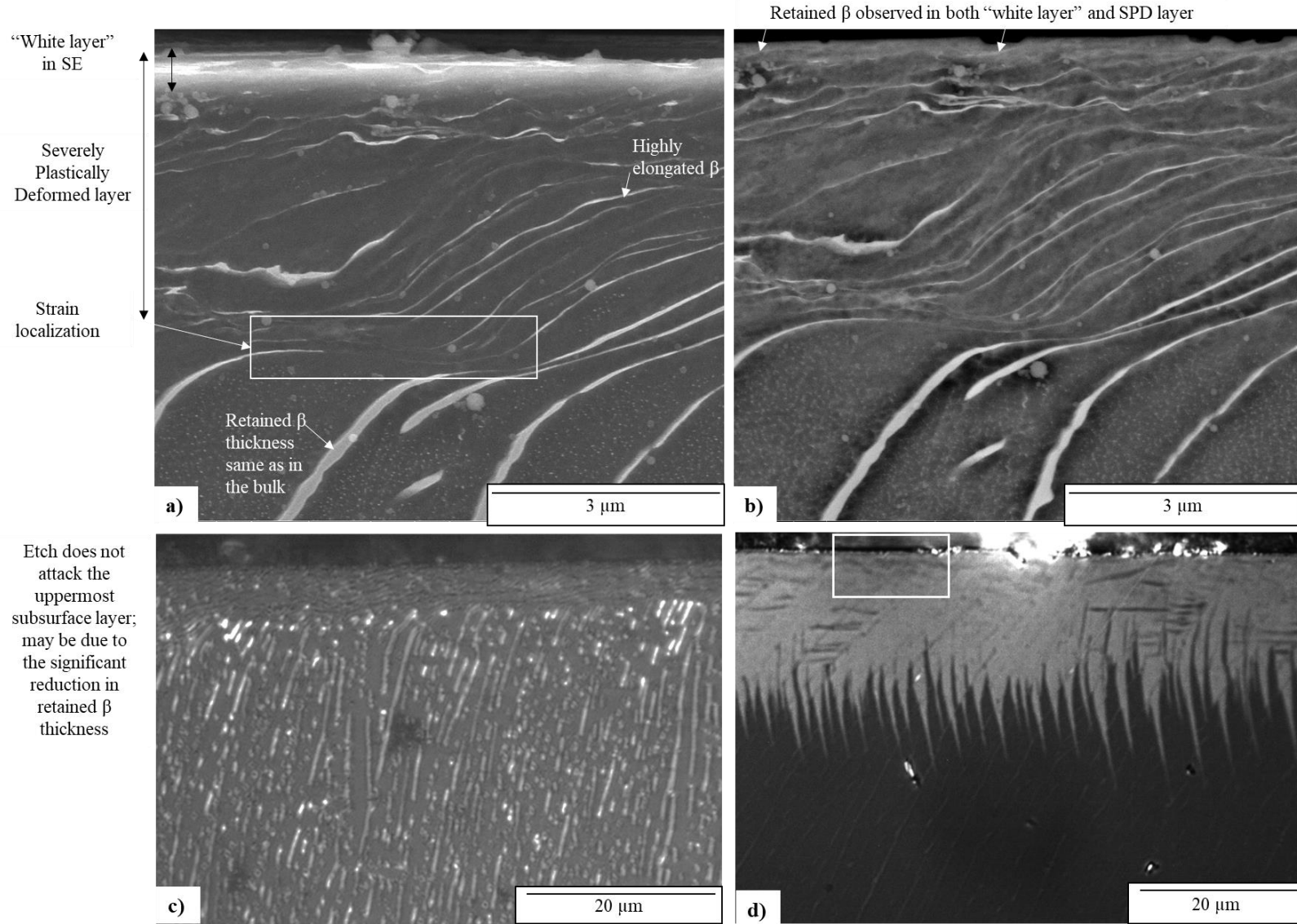
Figure 6-22. 100% CO_2 a) SE etch sample, b) BSE etch sample, c) cross-polarised light etch, d) cross-polarised-light.
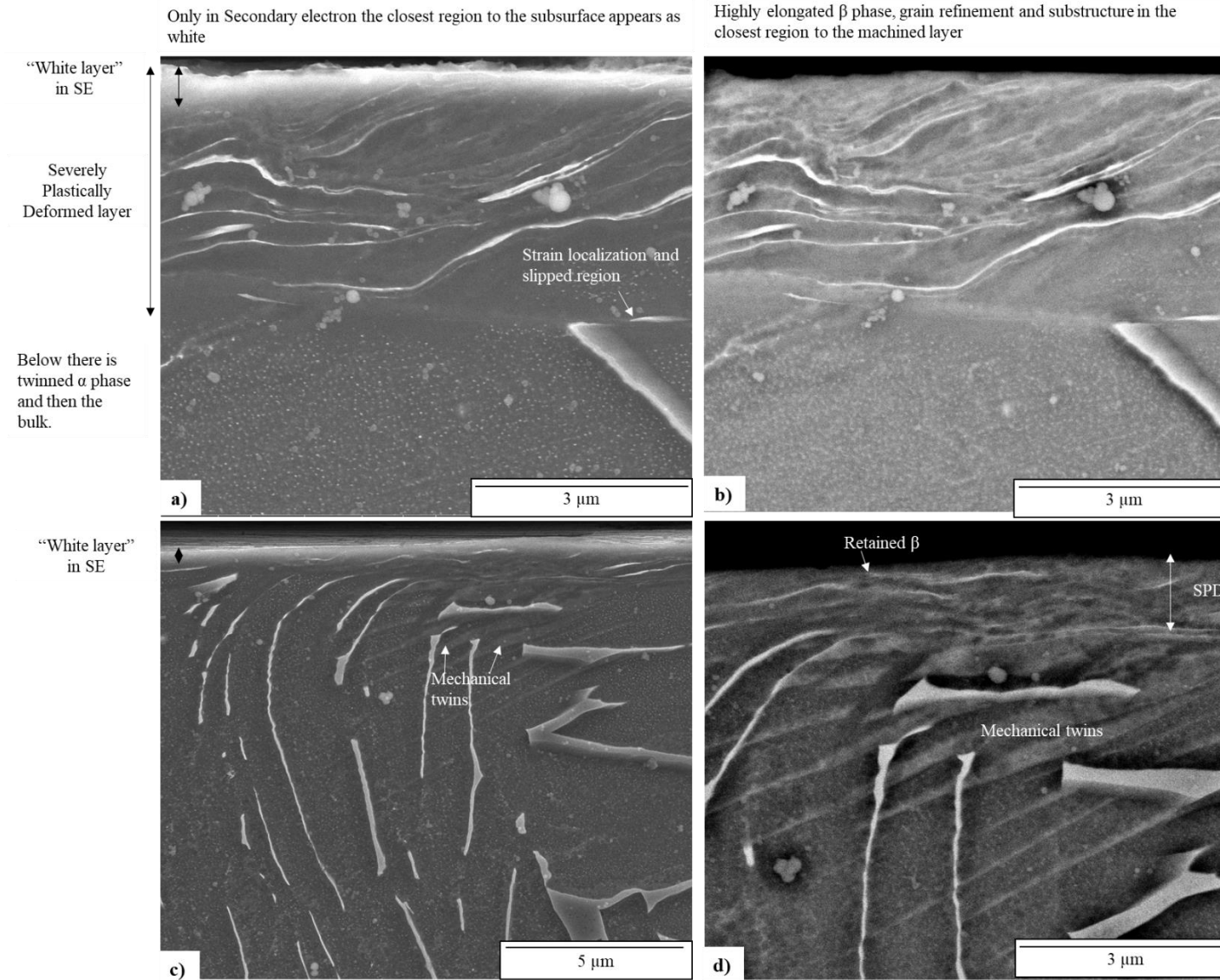
Figure 6-23. BSE cross section of the subsurface of machined under 100% CO_2 etch sample: a) &c) SE, b) & d) BSE.

6.6. Chip morphology of β annealed Ti-6Al-4V ELI under different cooling and lubrication conditions

An essential problem related to metal cutting involves the type of chip generation as it concerns four main aspects. The first is the personal safety for the operators handling sharp and hot chips. The second is damage to the workpiece or the machine. The third its handling and disposal. The final is related to vibration, temperatures generated, cutting forces and tool life. Titanium alloys are ductile and, as such, they tend to generate long, continuous and segmented/inhomogeneous chips which are difficult to manipulate. These long continuous chips tend to entangle with the machine spindle, especially in turning operations, which pose a risk to the machined workpiece and/or the machine (see Figure 1-4). Thus they are usually manually removed from the machining area, leading to a decline in productivity. This suggests that shorter chips are better because in smaller sizes, these can leave the cutting area more efficiently, thus reducing damage or safety risks. This also emphasizes the importance of cooling/lubrication fluid in assisting the removal of chips from the cutting area. Chip curvature plays a crucial role in the breaking of the chips as the imparted strain increases with an increase in curvature and leads to fracture. During fracture, a critical local strain is reached. In the previous section (Figure 4-3) during cryogenic uniaxial compression, a lower strain was reached for fracture in comparison to a room and warm temperature (~300°C), leading to ~ 25% lower energy for fracture at low temperatures as referenced in section 4.2 and figure Figure 4-5.

During metal cutting, extensive microstructural modification results not only from the interaction of thermomechanical parameters such as strain, strain rate and temperature on the flow stress of the material. Also due to the geometric restrictions imposed by the tool geometry. The mechanical operation and the friction generated in the cutting zone between the tool material and its interaction with the workpiece material affects the microstructure. The microstructural evolution of a sample of chips generated under each cooling condition was characterized through cross-polarised light and BSE in the SEM. Chip formation during climb milling is complex because the uncut chip thickness varies dynamically. Therefore, a considerable variation or an amount of inhomogeneity is expected. This also applies to the subsurface damage imparted during climb milling. There is a high degree of variability within the same chip suggesting that catastrophic shear failure is a complex process, which involves the operation of different mechanisms simultaneously. Chip formation in titanium alloys is undertaken through inhomogeneous deformation or formation of highly localised narrow bands of adiabatic shear (also known as shear instabilities), giving rise to a high frequency of segmentation. Titanium alloys have a high propensity for the formation of ASB, primarily

owing to their low thermal conductivity and low specific heat, which leads to self-propagating instability or thermal softening [47], [165]. When the competing mechanism of thermal softening is preferred over the strain hardening on the primary shear zone, it leads to the onset of shear instability. It is followed by localisation, starting at areas of stress concentration or microstructural inhomogeneities. Mechanical twinning has been observed to assist the reorientation of the chip lattice, found in the material adjacent to the secondary shear band and many aligned twins traverse the distance from shear band to shear band as seen in Figure 6-24c), Figure 6-26 a) and Figure 6-26 b). The growth of cracks in the secondary shear zone was observed to behave as per the classical theory of catastrophic shear failure [166]: microvoid nucleation, void growth, void reorientation, void elongation (elliptical shape) and tearing of the ligaments that separate the elliptical voids as in Figure 6-24 f).

Figure 6-24 shows a sample of the chips generated during milling at 80 m.min^{-1} under 100% CO_2. A continuous chip with non-uniform segmentation (inhomogeneous plastic deformation) is observed. Figure 6-24 b) shows a continuous chip where first a wider segmentation took place related to inhomogeneous chip formation, followed by homogeneous shear banding. This is followed by inhomogeneous segmentation with a consistent frequency until the end of the chip where the size of the peak and troughs are continuously decreasing to a very small value. This may be related to the type of milling operation that goes from thick to thin chip formation, which clearly shows a decrease in the chip thickness in Figure 6-24 a). Strain localisation has occurred due to the high level of reorientation of the crystal lattice during shearing. This high level of reorientation has taken place via the cooperative mechanisms of both slip and twinning. Microvoid nucleation might have started at the highest lattice curvature sites which were heavily strained and could no longer support the load or continue to re-orientate. Strain localisation is also assisted by the heavily elongated and reoriented grains towards the cutting tool, and it concentrates in a narrow band ~ 20 µm, see Figure 6-24 b). This part of the chip shows a wide variation in shear band spacing; an average of 38.0 ± 16.11 µm with a 95% confidence limit was estimated, a maximum of 108.6 µm and a minimum of 7.7 µm was found.

Figure 6-24 c) shows that during the shearing in the secondary zone, mechanical twinning has taken place allowing accommodation of the lattice reorientation in the chip to form the segmented parts of the chip. It also shows that the shear band formation is originated and transferred from the primary shear zone. The whole segment has to be reoriented which may experience compressive, tensile and shear stresses. During this reorientation, a microcrack would have emerged at the edge of the chip. Crack growth in the secondary shear area (where peak segments are generated) is not constant. It may be influenced by the stress state experienced locally and imparted local strain.

Figure 6-24 d) depicts a continuous and non-uniform segmentation. It has an average ASB spacing of 52.9 µm, consistent with the average from Figure 6-24 c). Figure 6-24 d) is at higher magnification and it shows a heavily strained area but appears to be more difficult to

concentrate the strain for the shear band formation. Figure 6-24 e) agrees with the fact that microcracks corresponding to the secondary shear zone started on the surface of the material, then continued downwards towards the primary shear zone. It shows an elliptical void orientated towards the shearing direction and also shows that the crack grows when the ligaments that separate the voids is broken. It depicts some mechanical twins aiding in reorienting the lattice of the chip, for local straining. The reoriented area seems to have profoundly distorted β and appears as a wavy morphology (the same as in the subsurface in Figure 6-13 b) and Figure 6-13 c)). Figure 6-24 g) depicts elliptical voids and shows how the ligament between the voids is highly sheared and has joined them, causing a fracture. In the primary shear zone, a highly refined area appears. This corresponds to primary shear band formation. Retained β is not readily visible. This suggests that recrystallization has taken place at this location also corresponds to the area that separated from the freshly generated edge.

a) Chip thickness reduction, related to type of cut: thick to thin chip formation.

Inhomogeneous plastic deformation.

First segment usually consist o higher vol. of material

Homogeneous plastic deformation.

500 μm

b) Mechanical twins assisting shape changes during reorientation in the chip.

High variability in distance between ASBs. Avg.~ 38.0 ± 16.1 μm (95% confidence limits)

Distance between ASBs

100 μm

c) Avg. distance between ASBs ~ 53.7 μm

Mech. twins

SB bifurcation

50 μm

d) Different levels of fracture depth.

Avg. distance between ASBs ~ 52.9 μm

2° ASB

Mech. Twins assisting the reorientation of the lattice in the chip

100 μm

e) 20 μm

f) Mech. Twins assisting the reorientation of the lattice between shear bands.

Elliptical void in the shear band.

Retained β different orientation.

SPD layer from the primary shear band

20 μm

g) Grain refinement in the 1° ASB.

Void coalesced in the shear band dir.

Ligament broken between micro voids, leading to fracture.

50 μm

Figure 6-24. Cross-polarised light micrograph of a continuous chip with inhomogeneous or catastrophic shear of β annealed Ti-6Al-4V ELI face-milling at 80 m.min^{-1} under 100% CO_2.

278

Chip formation under 25% CO_2 displays a similar behaviour. Figure 6-25 a) shows a continuous and inhomogeneous shear deformed chip. This change in segmentation frequency may be related to different stress states generated during the pass of the complex tool geometry which, in turn, creates a complex stress state. The distance between ASBs was estimated as an average of 42.9 µm. Figure 6-25 b) shows an average distance between ASBs ~ 39.9 µm. By comparing this value to 100% CO_2, it is nearly 10 µm or 23% smaller. This suggests that a higher number of ASBs were formed under a lower percentage of CO_2 (or at slightly higher temperature). This is in agreement with PSM at 0.01 m.min^{-1} at -160°C, see Figure 4-43. The generation of a higher number of ABSs implies a concentration of higher temperatures, promoting the occurrence of solid-state diffusional processes. Figure 6-25 c) shows that the direction of the material between shear bands is different from the actual shear band. The area closest to the shear band is reoriented horizontally and appears as a high frequency of closely spaced lamellae or mechanical twins, whereas the shear band appears vertically. Figure 6-25 d) shows slightly more uniform shear banding or smaller differentiation between peaks and troughs.
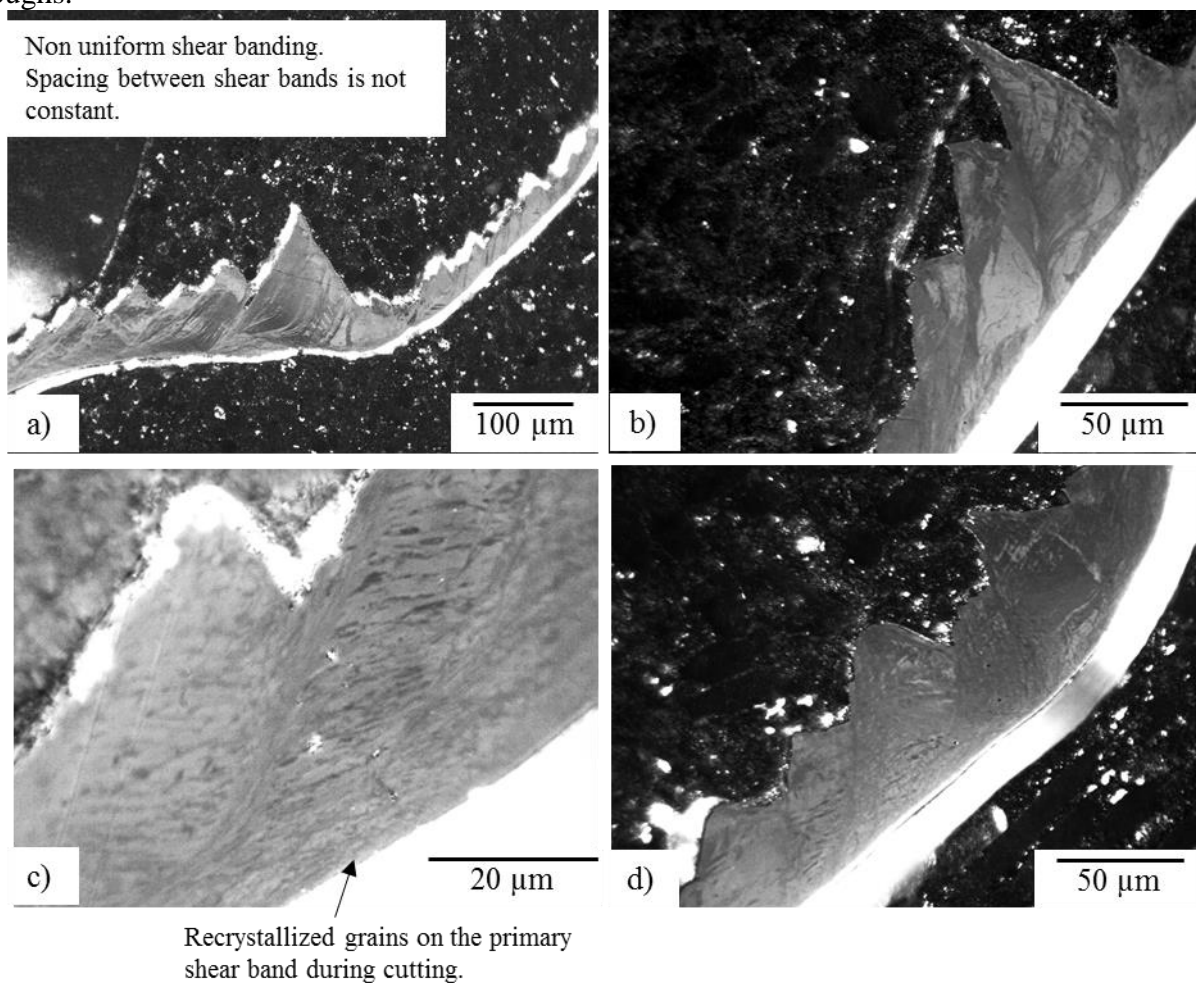
Figure 6-25. Cross-polarised light micrograph of a continuous chip with inhomogeneous shear of β annealed Ti-6Al-4V ELI face-milled at 80 m.min^{-1} under 25% CO_2.

279

The chip generated under CO_2 plus MQL was continuous and inhomogeneous. The segmentation frequency varied widely. Figure 6-26 a) shows a distance between shear bands of ~ 66.3 µm whereas Figure 6-26 b) shows a distance of only 16.4 µm with a secondary shear band thickness approximately 1.15 µm. Figure 6-26 a) and b) show a high density of mechanical twins in the area adjacent to the shear band, orientated orthogonally to the shear band direction and completely traversing the area between the shear bands. Figure 6-26 a) illustrates how these twins help to reorientate the crystal lattice of the chip locally. The retained beta below these twins appears to be distorted and shows a wavy appearance the same as in the immediate subsurface of the machined workpiece as in Figure 6-13 b). This is because of the catastrophic failure in the primary shear zone. This initiates, grows and fails in the centre of the ASB, generating two areas of the severely plastically deformed region and similar characteristics in the subsurface. Figure 6-26 c) -d) shows different shear band formation mechanisms. Figure 6-26 c) shows a wide shear band spacing ~ 43.7 µm, with some twins but not heavily deformed. On the other hand, Figure 6-26 d) shows a smaller shear band distance ~ 22.5 µm and the microstructure inside appears highly plastically deformed with much smaller grain size than the original α lamellae. This part of the chip might have experienced much higher shear stresses and strains during plastic deformation.
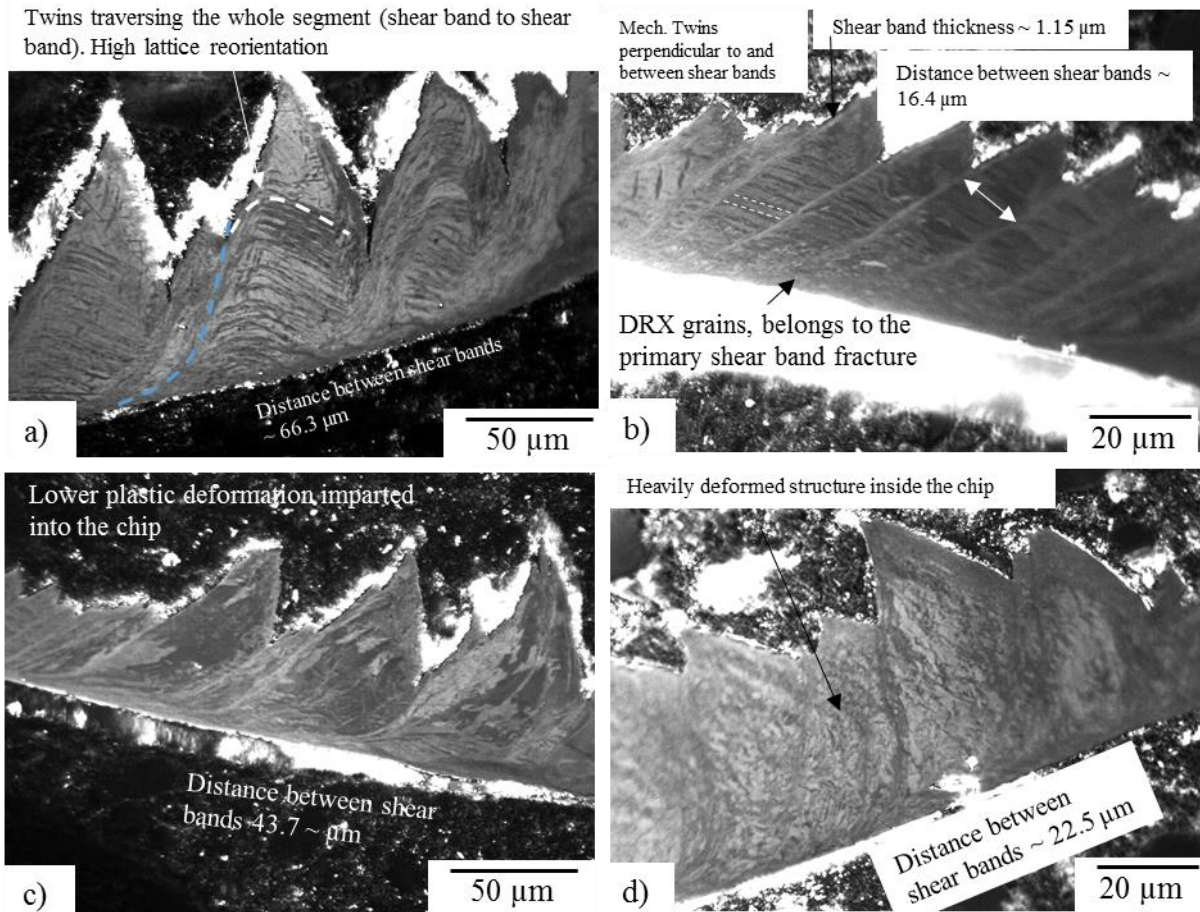
Figure 6-26. Cross-polarised light micrograph of a continuous chip with inhomogeneous shear of β annealed Ti-6Al-4V ELI face-milled at 80 m.min^{-1} under CO_2 plus MQL.

A sample of one chip generated under conventional flood cooling is shown in Figure 6-27 a). An important observation is the segmentation frequency within one chip. The two selected rectangles in Figure 6-27 a) show the sharp contrast in the distance between shear bands from a high value ~ 33.4 µm as depicted in Figure 6-27 b) and the low value ~ 1 to 4 µm in Figure 6-27 c) and within the same chip it transitions to a lower segmentation frequency shear banding. However, at a further section within the same chip, a reduction in chip segmentation frequency appears again. While Figure 6-27 a) shows an inhomogeneous chip, Figure 6-27 b) shows a more homogeneous chip formation. The shear bands formed in the secondary shear zone are accompanied by mechanical twinning. It appears that twins have allowed crystallographic reorientation; this leads to shear band formation. Figure 6-27d) shows a rather wide shear band spacing ~ 55.9 µm and the mechanical twins are aligned in the direction of the shear band (in contrast to Figure 6-27 b), and these twins are thin, appearing to be detrimental to cyclic fatigue life because they concentrate higher stresses in the region surrounding the twin boundaries. Indeed, Figure 6-27 d) shows them as nearly orthogonal to the ASB direction. Near these twins, a small fracture ~ 30 µm appears. Figure 6-27 e) shows a chip with shorter shear band distances ~ 13.5 µm but heavily plastically deformed. This leads to the conclusion that shear band

formation is strongly influenced by the stress state during cutting which is complex and three dimensional in a milling operation. It also is influenced by the friction conditions between the cutting tool, the workpiece material and the chip. This is influenced by the cooling and lubrication application applied to the cutting interface. Flood cooling generated both homogeneous and inhomogeneous chip formation during high-speed milling.
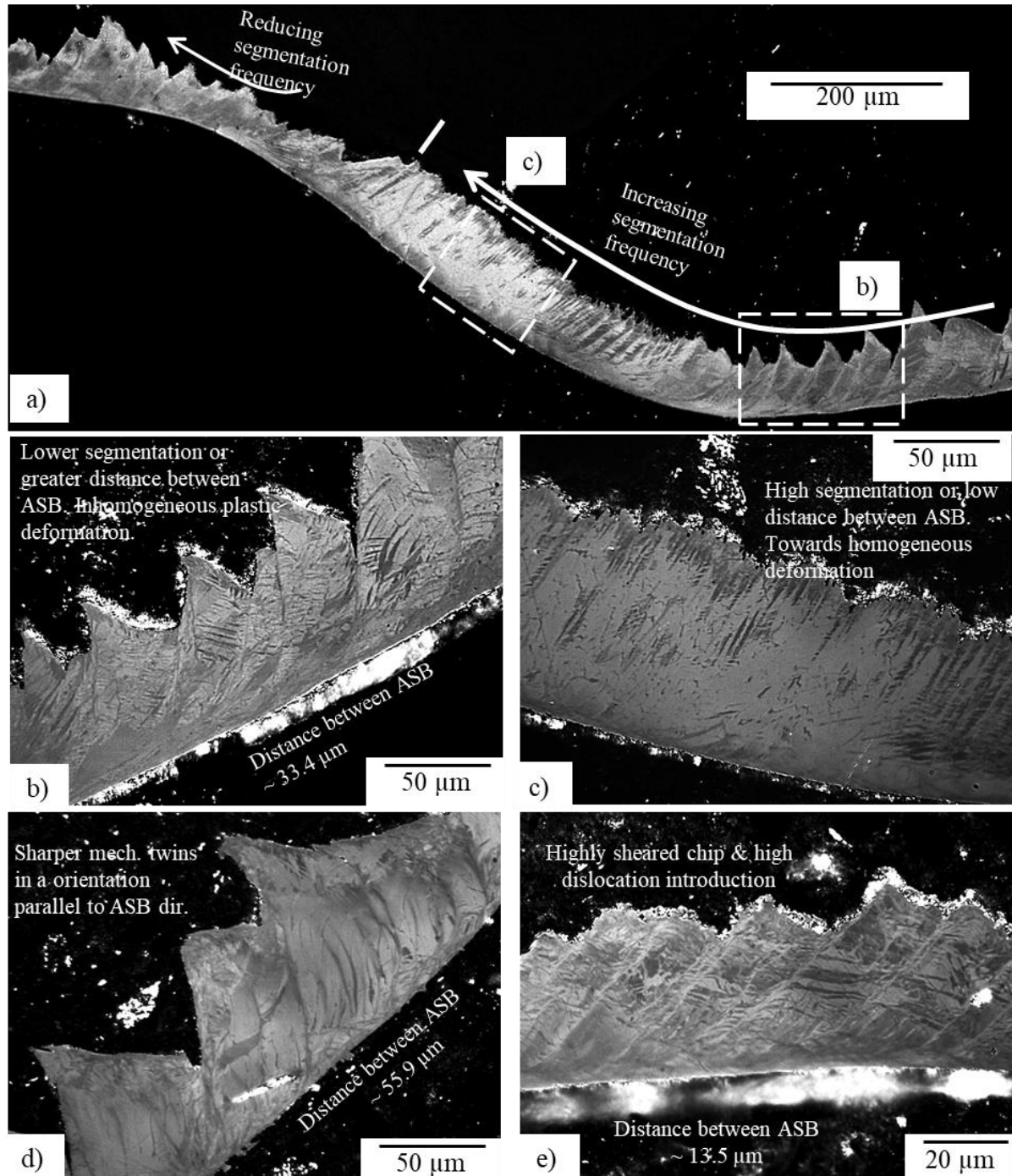
Figure 6-27. Cross-polarised light micrograph of a continuous chip with inhomogeneous shear of β annealed Ti-6Al-4V ELI face-milled at 80 m.min^{-1} under conventional flood cooling.

The effect of tool wear on the plastic deformation features of climb milling β annealed Ti-6Al-4V ELI at 80 m.min^{-1} under MQL conditions is shown in Figure 6-28.

At early stages of plastic deformation with a new cutting tool, the shear band concentrates in a narrow band as shown in Figure 6-28 a), thus facilitating the shearing process and allowing for chips to form more easily. When the tool is worn, material from the tool may have been removed, leading to a more rubbing than cutting action. As a result, it makes it harder for local plastic deformation to occur. Therefore harder chips are formed as shown in Figure 6-28 b) (where thicker shear band formation appears towards the end of the tool life). Also, the chip-segments appear highly plastically deformed (they have elongated more). This may indicate a higher energy requirement for chip generation with a worn tool.
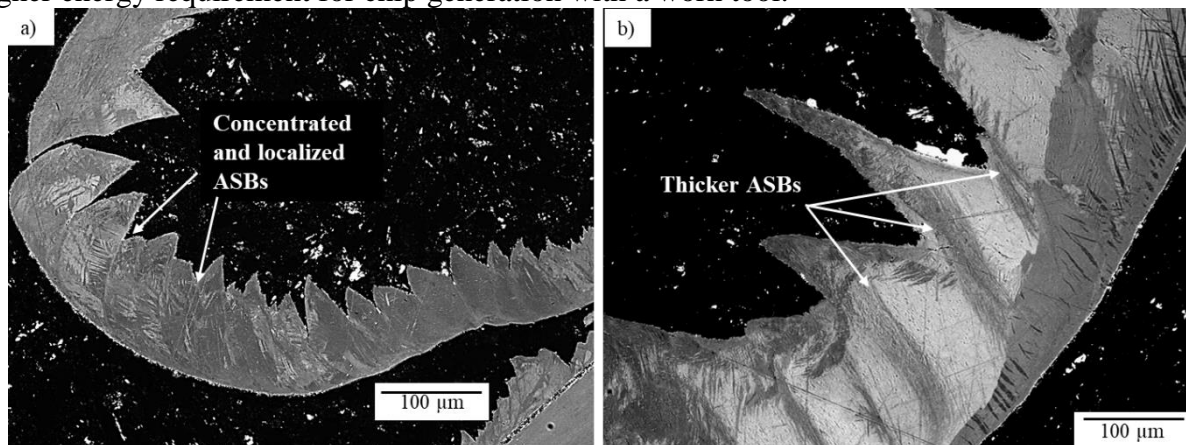
Figure 6-28. Chip microstructural characteristics during climb milling at 80 m.min^{-1}, $a_p = 1$ mm, $a_e = 6$ mm, LoC = 10 mm, under MQL lubricating conditions: a) new tool, b) worn tool at the end of tool life (pass 264).

6.7. High-temperature diffusion couple test

A vacuum weight (VW) diffusion couple test, designed by Hatt [167], was undertaken, using a 20X20X5 mm specimen of β annealed Ti-6Al4V ELI and a tool composed of WC-6%wt. Co. A drop of the oil used for MQL trials was placed in between the materials. This VW couple was placed in a vacuum oven for 2 hours at 1100°C. It then was mounted in Bakelite and sectioned in half for X-EDS scanning.

The SEM image form the scanned area is shown in Figure 6-29. A strong diffusion bond of nearly 28 μm, composed of TiC, was generated between the tool and the workpiece. The counts of the main elements are shown in Figure 6-30. Figure 6-30 a) shows all the elements, and Figure 6-30 b) shows a close up of the elements of lower values. It is observed that the carbon strongly diffused from the tool material to the workpiece material. This suggests the formation of a TiC layer in the tool during machining β annealed Ti-6Al-4V ELI. This layer may retard the wear processes in the tool, allowing them to be operational for longer cutting times. This

also suggests the strong adhesion of the chip to the tool material, generating BUE. The BUE will consequently alter the SBA. However, the effect on the SBA is unknown to the author. Blazynski [168] reported that when machining with carbide tools and the temperature reached exceeds 800°C, the primary wear mechanism is a temperature dependent process: diffusion. In diffusion wear, the log of tool wear rate is typically expected to be inversely proportional to temperature.

Reaching a critical temperature, as observed in Figure 2-58, the tool wear strongly accelerates from the point of the start of diffusion processes. This suggests that the BUE generates the fracture of the tool material as the bond between the chip and the tool is strong, and the fracture may occur on a deeper level of the tool material, causing a loss of integrity in it and finally, failure.
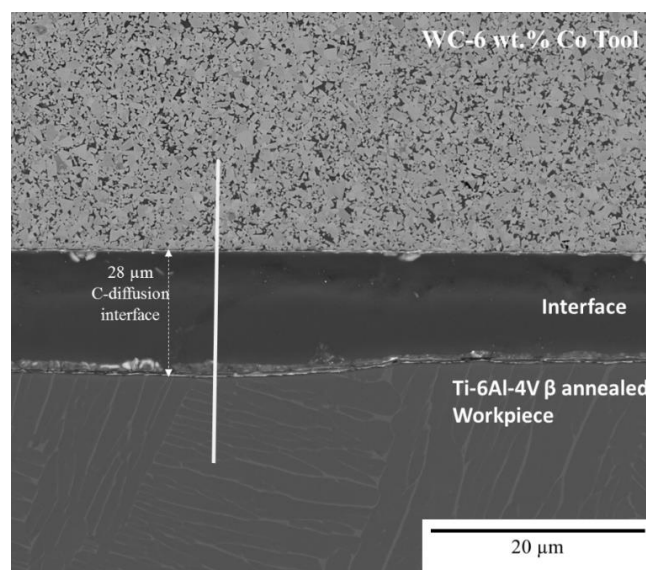
Figure 6-29. Diffusion couple test between WC-6 wt.% Co and β annealed Ti-6Al-4V ELI in a vacuum furnace at 1100°C for 2 hours.
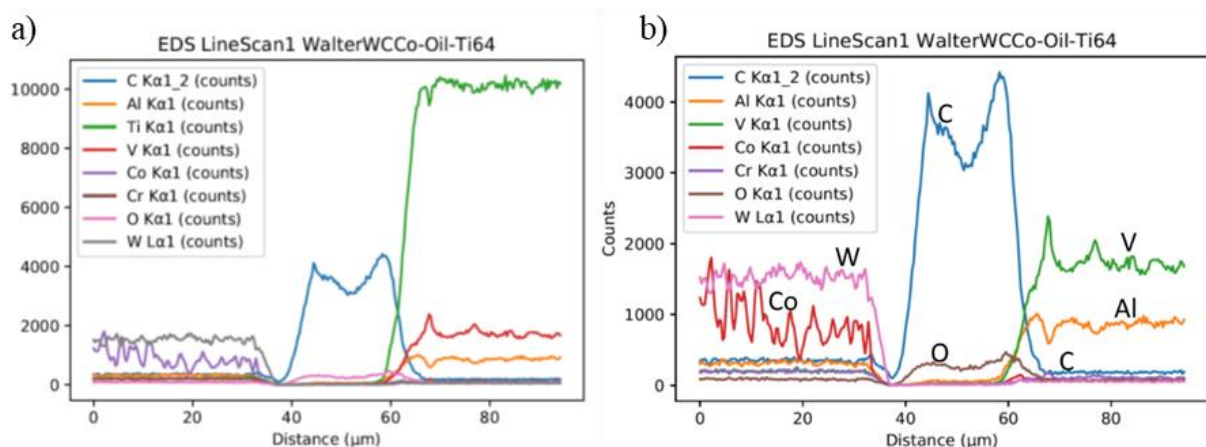
Figure 6-30. XEDS line scan corresponding to the white line in Figure 6-29 of β annealed Ti-6A4V ELI, a drop of MQL oil and WC- 6%wt. Co: a) full profile and b) Ti element removed to illustrate other elements more clearly.

6.8. Conclusions

The CO_2 flow rate has a substantial effect on the tool life. This is related to the ability of the cryogenic fluid to remove the generated heat from the cutting zone during metal cutting and, as it was observed in section 5.5 to reduce friction. In addition, there is probably a reduction in heat generation during cutting. It also helps to localise the imparted strain, forming the ASB easily, reaching the softening and localisation point earlier.

The temperature during plastic deformation has a significant effect on the mechanical properties and the subsurface microstructural evolution. The lower the temperature in the cutting zone, the higher the SPD layer formed and the smaller the recrystallized grain size in this region. Also, the higher twin depth imparted is the leading mechanism for the accommodation of imparted shear strain.

Although lubrication has led to a slight reduction in twin depth in MQL (in the absence of a coolant), diffusional processes may have taken place, which had generated crater wear in the tool surface, thus creating a dull tool edge. As the tool gets dull, it applies higher stresses to plastically shear the material in the chip; therefore it is hypothesised that a greater twinning depth will be imparted into the subsurface.

The condition which generated the best subsurface microstructural evolution or which might have the best performance during in-service in cyclic loading is CO_2 plus MQL. The reason is that a high SPD layer with potentially a high depth of recrystallized grains in the nanoscale range was generated. It also created a lower depth of mechanical twins. This implies that a lower twin boundary area was generated under that condition. The CO_2 supported the removal of the heat from the cutting edge. This would have lower solid-state diffusional processes to operate, therefore enhancing the strength of the tool structure. It has also lead to the introduction of a higher dislocation density, providing the driving force for recrystallization. Moreover, there is a lower number of potential sites for crack nucleation due to the reduction of the high-energy twin boundary area, which concentrates stresses in the regions adjacent to it.

The condition that generated the best tool life is 100% CO_2 (three times that of the 25% CO_2). It generated the largest area of severe plastic deformation, which was composed of a nanocrystalline structure. This region has shown to be a graded microstructure starting from equiaxed nanocrystalline grains to elongated subgrains up to a 5 µm in depth. It generated a grain depth of 2.9 µm with an average grain size of 48.9 nm. This localised microstructure will have a strong and positive influence on the material's mechanical properties giving much higher strength and ductility. However, it has generated the deepest twin penetration into the lattice in the subsurface of the machined component or the highest twin boundary volume fraction, which during in-service operation may provide sites for crack nucleation.

The condition with the shortest tool life was 25% CO_2. It implies that the mass flow rate was not enough to remove the heat generated during cutting which accelerates the solid diffusion of substitutional elements from the tool material to the chip or workpiece material, or the temperature in the subsurface was not low enough to locally reduce the fracture toughness. A low SPD layer and low twin depth penetration were generated. The increase in heat generation allowed a high temperature in the cutting zone, introducing a lower amount of dislocations into the lattice due to the restorative dislocation annihilation processes during dynamic recovery. Thus, a lower dislocation density may generate lower SPD and a lower twin depth.

Flood cooling generated one of the best tool life conditions, only 11.1% lower than 100% CO_2 (as shown in Figure 6-2 and Figure 6-3). However, it generated a smaller SPD layer. As the conventional flood coolant is soluble oil water-based, the water has much higher ability to remove the generated heat especially the latent heat (transforming the liquid to gas). Flood coolant also contains chemical additives, which aid in reducing friction thus generating lower forces and lower heat generation. The fact that the lower SPD layer was generated might be related to the annihilation of dislocations due to higher thermal energy. Also, a lower twin depth penetration was generated. It is believed that more slip systems will be operational at the temperatures experienced under this cooling/lubricating condition.

The imparted damage introduced into the subsurface of the workpiece may represent potential sites of crack initiation during dynamic loading. Areas of pre-strain localisation (as observed in Figure 6-14 c) might act as stress raisers. These will locally reduce the load-carry capacity and accelerate microvoid nucleation during cycle fatigue.

Relating the deformation mechanisms observed in the simple orthogonal cutting experiment to high-speed machining subjected to multiaxial stresses under both cooling/lubricating condition is analysed in Figure 6-31. A plot of the imparted microstructural subsurface deformation damage (twin depth penetration) versus the logarithm of the surface speed has been proposed and is illustrated. This figure shows that at lower surface speed (inherently relating to a lower strain rate) there is a significant difference in the imparted subsurface damage. There is a much greater depth at low temperatures. Substantially increasing the surface speed and consequently, the strain rate results in a significant reduction in the levels of subsurface damage and a smaller difference between the low temperatures and room temperature. However, low-temperature deformation consistently generates higher twin depth penetration levels than at room temperature. Additionally, the tool geometry is different from high-speed milling to low speed, approximating an orthogonal cut. It would be ideal to test at turning process at high speed using the same cutting tool geometry and the same cooling/lubrication conditions to find out whether the twin subsurface penetration depths follow a trend as observed in Figure 6-31.
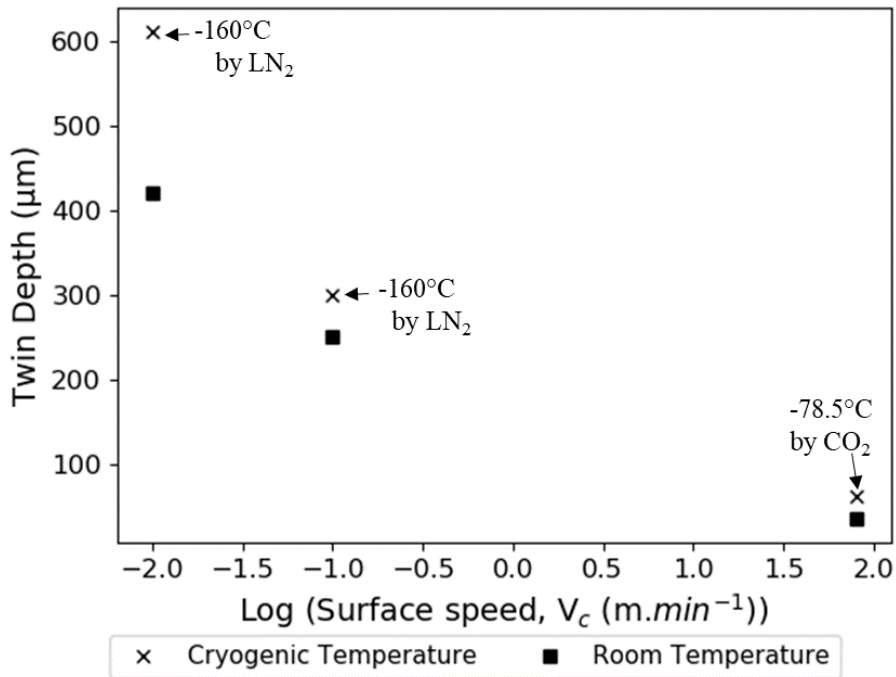
Figure 6-31. Twin depth (µm) as a function of $\log_{10}$ (Vc) of β annealed Ti-6Al-4V ELI during metal cutting. The square marker refers to the lower cutting speed of 0.01 m.min^{-1} on the ASP. The triangles show a higher cutting speed of 0.1 m.min^{-1} on the ASP and circles show high-speed cutting, markers in blue represent low temperatures and red ambient temperature.

Machining is a complex system where many processes take place simultaneously as illustrated in Figure 6-32. It shows how the new cut surface is generated through void coalescence in the primary shear zone, while strain is concentrated in a narrow zone that is adiabatically heated. The grains in that local straining area become extremely elongated and mechanical twinning assists in lattice reorientation for catastrophic shearing [21], [31], [169]. It shows the mechanical twins generated ahead of the cutting tool in a fan shape. It illustrates the microstructural evolution in the subsurface of the workpiece. DRX equiaxed nanocrystalline grains are formed in the immediate layer of the cut edge. Below this area, there is evidence of elongated subgrain, and below this area, there are mechanical twins. The retained β is highly bent towards the cutting direction.
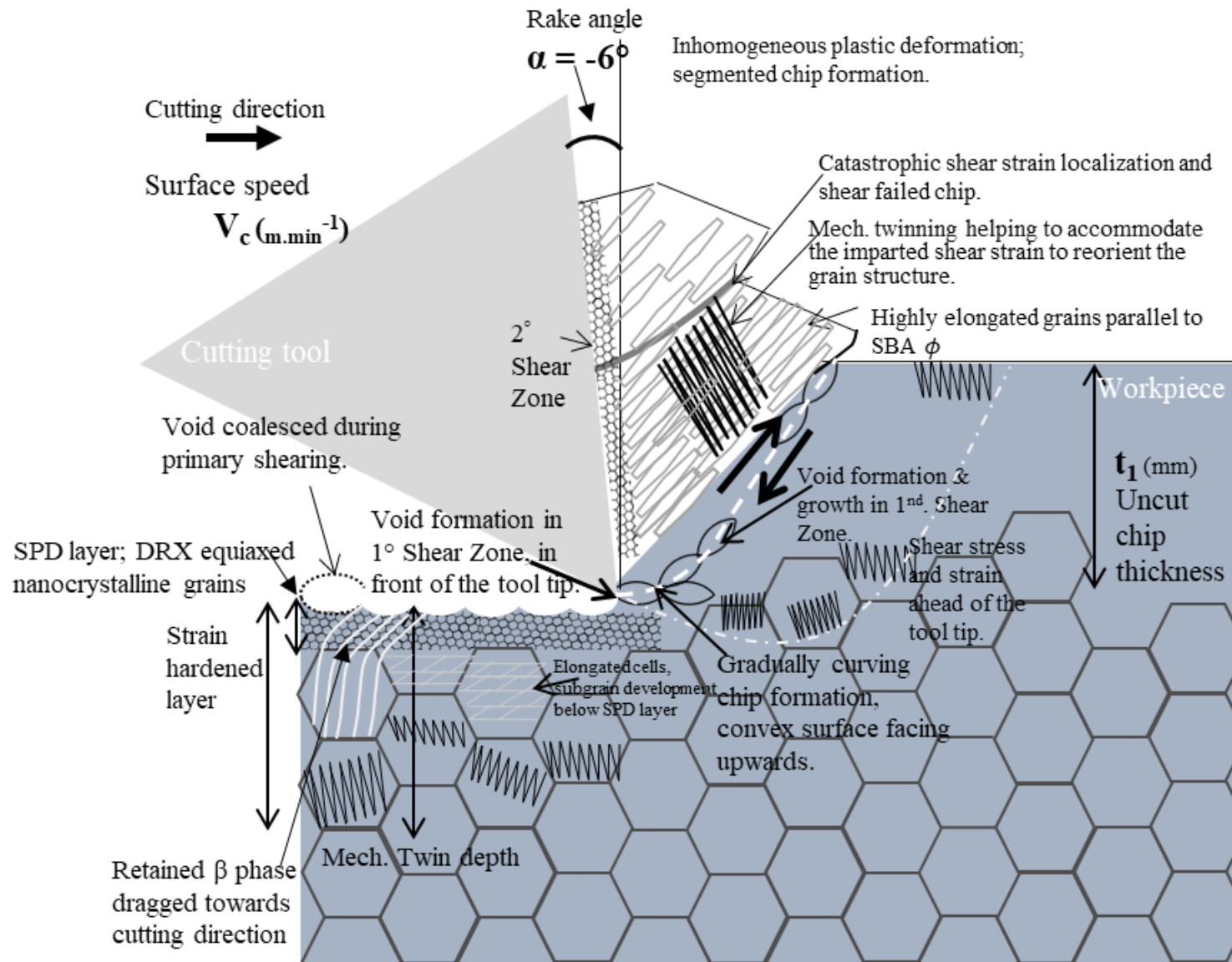
Figure 6-32. Schematic representation of the mechanisms taking place during Ti-6Al-4V orthogonal cutting.

7. Conclusions

This novel small-scale testing methodology, which consists of undertaking both a laboratory-scale plane strain machining (PSM) test and a uniaxial compression test, successfully enabled the evaluation and prediction of the mechanical and microstructural behaviour during machining of titanium alloys at low surface speeds.

Shear stresses imparted in uniaxial compression testing were correlated to the shear stresses in plane strain machining by a linear relationship with the logarithm of strain rate. Low temperatures resulted in higher shear stresses in comparison to ambient temperature. Although higher shear stresses were obtained at low temperatures, lower energy was required for segmented chip formation. This was obtained by estimating the area under the flow stress curve, a parameter also known as Cockcroft-Latham parameter. This lower energy led to a reduced temperature increase in the cutting zone, during chip formation, and consequently, delaying the critical temperature for solid-state diffusional processes, which gives rise to accelerated tool wear. This delta of temperature was predicted taking into account the thermal properties of the material as well as the Cockcroft-Latham parameter and resulted in an excellent correlation to the experimental value.

The shear stress-strain behaviour obtained from chip formation in PSM followed a close correlation to the estimated Von Mises shear stress-true strain in uniaxial compression testing. The strain for chip formation was estimated through a 2D-FEM model correlating time, displacement, load and strain using a point track method in the centre of the ASB.

This test is beneficial for the machining community as it allows prediction of the fundamental material behaviour of "difficult to machine alloys" in a simple testing methodology. Subsurface deformation generated under different parameters could be predicted. In this case, in β annealed Ti-6Al-4V ELI, the low strain rate and low temperatures led to a higher subsurface damage depth in terms of twin depth. It shows a linear correlation to the logarithm of strain rate. In addition, parametric studies of a broader range of conditions could be performed. For example, different cutting geometries could be used. This allows imparting different levels of strain into the workpiece and examining its behaviour mechanically and microstructurally into the generated subsurface. Different tool coatings, coolants and lubricants may be investigated. In this work, only an uncoated tool was used. Different heat treatments with their corresponding variation in grain morphology, size, volume phase content and distribution could be investigated.

Using this testing methodology could allow the study of the effect of a more extensive range of parameters, and thus enable determination of mechanical and microstructural effects. It will allow the determination of the best conditions to generate the best surface and subsurface. This will lead to enhanced reliability and in-service behaviour of machined components.

The uniaxial compression test allowed determination of the fundamental plastic deformation behaviour of each alloy at specific levels of strain, strain rate and temperature. Compressive yield strength, ultimate compressive strength, strain for the onset of thermal instability, strain for fracture, energy per unit volume for catastrophic shear, and strain hardening behaviour were determined. The shear stress was estimated using the Von-Mises, Tresca and Octahedral relationships. For β annealed Ti-6Al-4V ELI, compressive yield strength followed linear correlation to the deformation temperature, resulting in higher flow stress at low temperatures. The following equation gives the effect of temperature at a constant strain rate of 10-1s-1: Flow stress = -1.35 Temp. (°C) + 948.63 with an R^2 = 0.995, meaning a reduction of flow stress accompanies an increase in temperature. Temperature has a stronger effect on the flow stress than strain rate.

The strain for fracture was smaller at low temperatures, resulting in less energy per unit volume for plastic deformation, up to catastrophic shear. There is a 20% lower energy for fracture needed at -130°C in comparison to room temperature and 30% lower than at 300°C. The strain-hardening coefficient was at a low value and was lower for low temperatures. This is in agreement with the literature [170], which correlates it indirectly to the extent of uniform plastic deformation until plastic instability or strain for fracture. Strain rate sensitivity was lower at low temperatures; this is also correlated to the lower strain required for catastrophic shear. At low temperatures, the initial strain- hardening rate was at a higher level. With the increase in imparted strain, the rate decreases acceleratedly until yield; it then decreases at a lower linear rate. At low temperatures, the strain-hardening rate decreases more rapidly, leading to a smaller strain for fracture. The estimated peak load, trough load and segmentation frequency (spacing) correlated well with the ASP experimental results. With the uniaxial compression tests flow stress data, a Norton-Hoff phenomenological equation was used to determine the constants to predict the flow stress behaviour during plastic deformation. With this model, the strain imparted into the chip and subsurface was estimated. It was assumed correct because of the close relationship between the experimental and model load data.

Examination of the deformed specimens shows a higher number of adiabatic shear bands and cracks at low temperatures. This suggests easier segmented chip formation at low temperatures. Plastic deformation of titanium alloys at low temperatures is more prone

to adiabatic shear band formation. The adiabatic shear band is more concentrated at low temperatures. Upon examination of the microstructure, it revealed an ASB thickness of 13.6 µm at -140°C, whilst at 16°C, it was 25.3 µm. This is attributed to the low thermal conductivity and its reduction by lowering temperature, its low thermal capacity and its low density. Fracture along the shear band occurs by microvoid nucleation, growth and coalescence. The morphology of the voids was elongated, meaning they were generated under shear. The subsurface below the ASB revealed uniform nucleation of needle-like mechanical twins at low temperatures. At room temperature, a lower volume fraction of mechanical twins of larger width and lens-shaped boundaries were observed.

From the PSM test, a deformation map correlating the surface speed (inherently the strain rate) and the temperature were built. It shows the different underlying plastic deformation mechanisms during cutting, the chip formation and the plastic deformation mechanisms ahead of the cutting tool.

Plastic deformation behaviour was examined under cross-polarised light and scanning electron microscopy, and the chip formation mechanisms were determined. The strain imparted into the chip was thoroughly examined. The chip formed was of an inhomogeneous type, with shear strain concentration in narrow bands, where the temperatures strongly increase.

7.1. Plane Strain Machining Tests

For PSM of β annealed Ti-6Al-4V ELI at 0.01 m.min^{-1}, representing a semi-finishing operation:

Chips formed resulted in inhomogeneous and discontinuous type. The chip formation mechanism was correlated with Komanduri and Von Turkovich's results [68]. The chip first starts to build up by a compression process. When the strain is localised, the first crack appears ahead of the cutting tool tip and grows gradually with an upward curvature. This suggested that the use of Merchant's force circle analysis is only a first approximation for the determination of the shear stresses as the shear band angle is not a plane as assumed in this methodology. The second series of cracks appeared on the free surface, leaving the centre of the shear band to fracture at the end. The increase of an order of magnitude of speed also generated an inhomogeneous type of chip formation with the gradual curvature upwards, but some of the chips were continuous. This is attributed to the higher heat generation at higher speeds.

The temperature had a stronger effect than strain rate on the load for plastic deformation; resulting in higher peak loads at low temperatures. At -160°C, 36% higher peak loads were measured in comparison to 16°C. At low temperatures, an increase in an order of magnitude in speed led to a 1.7 % increase in peak load. At room temperature, the same increase in speed led to a 9.8% increase in peak load. This leads to the conclusion that strain-rate sensitivity has a higher impact at higher temperatures.

A higher shear band angle was obtained at low temperatures. This suggested a lower strain was imparted to generate a chip.

A higher twin depth was generated at low temperatures. This correlated with high-speed machining trials at low temperatures under CO_2.

A crack in the subsurface, which was observed under cross-polarised light, revealed that it was nucleated and grew along a twin boundary. This was correlated to previous results reported by Partridge [150], Stevenson and Breedis [151] and Beevers and Halliday [152].

At 0.01 m.min^{-1} at -160°C, some chips were broken into sections in the 2°SZ. A piece of the previous chip remained adhered to the cutting tool as a built up edge, and it changed the shear band angle for the next chip formation. This resulted in higher surface roughness, and even some of the surface showed a fracture.

At ambient temperature, the increase in uncut chip thickness led to a higher subsurface damage depth; (t_1 of 98.8 µm led to 95 µm in damage depth, whilst t_1 of 1350 µm led to 420 µm damage depth). This was the result of higher shear stresses imparted into the subsurface by the cutting tool.

For mill annealed Ti-6Al-4V, low temperatures also resulted in higher peak loads in comparison to ambient temperatures. Microstructural examination at high-resolution, under scanning electron microscopy, revealed alpha grains to be plastically deformed by a high density of mechanical twins, showing mechanical twinning as the dominant plastic deformation mechanism at low temperatures.

Near orthogonal cutting of CP-Ti at low temperatures led to a more homogeneous chip formation. The strain was imparted uniformly in the chip, showing a highly refined microstructure. The dominant plastic deformation mechanism was mechanical twinning of a needle-like thickness. CP-Ti chips orthogonally cut at room temperature were heavily fractured, while those cut at low temperatures showed cracks mainly at the free surface. This was attributed to the increase in thermal conductivity by lowering the deformation temperatures. Also, higher purity titanium possesses higher thermal conductivity, nearly three times higher than that of alloys. Cutting at ambient temperature or increasing the deformation temperatures shows a decrease in thermal conductivity. This leads to thermal

softening dominating over a narrow zone, the shear band, and allows easy strain localisation and fracture, therefore resulting in more fractured chips.

A subsurface composed of nanocrystalline, equiaxed, high angle grain boundary grains (grain size = 77.28 ± 8.2 nm with a 95% CI) was generated during near PSM of CP-Ti at a cryogenic temperature of -150°C at a surface speed of 0.01 m.min^{-1}. This is a significant advantage in terms of strength, which increases significantly by increasing the volume fraction of the grain boundary via a Hall-Petch relationship. Whilst ductility is also increased, fracture toughness may decrease slightly. However, this may have a lesser impact as the deeper subsurface most likely remains strain-hardened; this would counteract the reduction in K_{IC}.

The surface generated during machining is of utmost importance because it has been recognised as the region where fatigue fractures initiate most frequently. There are positive and negative effects of a machined workpiece. The large strain imparted during metal cutting in a single pass leads to a dynamic recrystallization process, which results in the uppermost surface layer being composed of nanocrystalline or ultra-fine grain size. This strongly increases the local strength and ductility. On the other hand, features such as notches in the surface are frequently generated and they represent sites of stress and strain concentration. Subsurface microstructural modification features such as mechanical twins and dislocations are correlated to crack initiation sites, thus reducing fatigue strength.

Machining of titanium alloys leads to very high rates of heat generation and, consequently high tool wear rates. This is because approximately 90% of the mechanical energy spent on plastic deformation is converted to thermal energy. The remaining 10% is stored in the crystal lattice as crystal defects such as point (vacancies) and linear (dislocations) defects. This is the driving energy for dynamic recrystallization. As titanium alloys have low thermal properties, they cannot conduct the heat generated, and it concentrates in the cutting zone. It is mainly transferred to the cutting tool, which has a higher thermal conductivity. Maintaining high temperatures in the cutting zone leads solid-state diffusion processes to dominate, and these lead to accelerating tool wear. There is TiC formation, and this weakens the tool, leading it to fracture more easily.

7.2. High-speed machining tests

High-speed milling (using a round insert) of β annealed Ti-6Al-4V ELI at low temperatures (by cooling with CO_2) led to high twin depths. The mass flow rate applied directly to the cutting zone (though tool spindle) has a substantial effect on tool wear rates

and tool life. The higher the mass rate, the longer the cutting time. At 80 m.min^{-1}, a_e 2 mm, a_p 10 mm, LoC 105 mm and at 100% opening of the CO_2 delivery valve resulted in over three times the tool life to that of 25% CO_2 (29.7 min and 8.5 min, respectively) with more than 6 times mass rate (1.9 and 11.84 Kg.hr^{-1}, respectively. However, the higher the percentage increase of the opening valve, the higher the twin depth (20.5 µm versus 13.7 µm, respectively). The combined effect of CO_2 and MQL is an excellent strategy, not only for increasing cutting time, but also reducing the subsurface damage imparted in terms of twin depth. This condition generated a damage depth similar to the 25% CO_2. The severely plastically deformed (SPD) layer was in a range of between 0-10 µm with only a hardly noticeable differentiation between all the cooling methodologies.

Microstructures generated in high-speed machining (under all conditions) generated a graded microstructure in the subsurface. This suggests different levels of imposed strain, strain rate and temperature, being highest in the centre of the ASB, which corresponds to the surface with strain reducing as it goes deeper into the subsurface.

Mechanical twinning is strongly dependent on the underlying crystallographic orientation of its parent grain or local texture. If the parent grain has a "soft" orientation, slip operated easily, and twins were not observed in the subsurface. As the grain size in β annealed Ti-6Al-4V ELI is high, there were "hard" oriented grains. These were twinned entirely all along the surface (the grain with the same crystallographic orientation), where twinning had stopped at the grain boundary until a different orientation was met.

The critical resolved shear stress (CRSS) for slip strongly increased at low temperatures, especially for the <c+a> pyramidal systems. As mechanical twinning is temperature insensitive, it was the dominating operative mechanism for plastic deformation. It is easier for twins to operate at low temperatures because low temperatures generate higher stresses, and mechanical twins nucleate at sites of stress concentration.

The severely plastically deformed (SPD) region was composed of a highly elongated beta phase, which was bent towards the cutting direction. This represents strain hardening in the subsurface. The alpha phase uppermost subsurface could not be observed under SEM. Therefore, TEM was used to observe its crystallographic structure. Below the subsurface, subgrain development was observed under SEM. This revealed how the subgrains served as sinks for dislocations during plastic deformation. Bright field transmission electron micrographs of β annealed Ti-6Al-4V ELI face milling at 100 m.min^{-1} under CO_2 revealed a nanocrystalline grain size in the uppermost subsurface (48.9 ± 5.2 nm with 95% CI). This resulted in an increase in strength and ductility via the Hall-Petch relationship.

Reducing temperatures during machining could lead to a reduction in tensile residual stresses, which are mainly encountered on the surface. This may also enhance the compressive residual stresses in the subsurface. This will allow improving fatigue strength during in-service dynamic loading by counteracting tensile stresses and causing crack closure or not allowing microvoid growth.

In a machining operation, knowledge of the chip formation process is critical. Conditions, which generate a homogeneous type of chip, should be sought. This will allow more uniform distribution of heat, and will not let it concentrate on the narrow zone (ASB). This will result in lower temperatures, and will; therefore, allow the tool to cut for longer, maintaining its surface integrity and sharpness. The reduction in temperature is beneficial because solid-state diffusion is reduced, resulting in lower diffusional tool wear mechanisms. These are the cause of accelerated tool wear. This may be achieved by modifying the surface speed and uncut chip thickness.

Important findings are summarised in the following paragraphs:

- Cryogenic machining is beneficial in terms of reduction in tool wear rates and tool wear damage. A high shear band angle is generated leading to a lower strain, and consequently, lower energy for chip formation. The ASB formation is easier and more localised (narrower) at low temperatures, attributed to the low thermal properties of titanium alloys. The ASB is thinner and is composed of nanocrystalline grains of HAGB due to DRX. This leads to a local increase in strength. However, it leads to higher levels of subsurface damage depths. The dominating mode of plastic deformation is mechanical twinning, and its morphology is of a smaller thickness, and they are nucleated more homogeneously, in comparison to room temperature. This may lead to lower fatigue life under in-service dynamic loading. A crack was nucleated along a twin boundary, confirming that they are considered as damage for cyclic fatigue.

- The application of CO_2 plus MQL is highly recommended as it results in a reduction in subsurface damage depth, to similar levels as the conventional flood or high-pressure coolants. The oil dispersed as micron-sized particles lead to a reduction in the friction forces. The cooling effect of CO_2 causes a reduction in the temperature of the tool material, keeping it sharper for longer cutting time.

- To take advantage of the physical properties of low temperature coolants such as CO_2 and LN_2, a heat management approach should be considered to remove heat from the cutting tool. The entire workpiece material should not be allowed to reach a low temperature. Low temperatures should be allowed to reach the uncut chip thickness depth level to reduce the energy required during plastic deformation for chip formation. This would reduce the subsurface damage imparted to the workpiece and maintain the tool integrity longer.

7.3. Future work / Perspectives

This thesis described the development of a new and simple testing technique, which was successfully applied to determine the mechanical and microstructural response to the conditions imposed during metal cutting. To advance this testing technique, the following methods are suggested:

- A plastic deformation mechanisms map can be built, correlating the effect of plastic deformation (strain, strain rate, temperature and uncut chip thickness) on the underlying microstructural mechanisms operative during metal cutting. This can be developed by examining the microstructure at high magnification under transmission electron microscopy. This may also allow building a database with the machinability parameters of titanium alloys.
- Undertake a fatigue testing of titanium alloys, which were cryogenically machined. It would be valuable, as it would corroborate the extent of the damage introduced during low temperatures machining (a high needle-like twin density) on the fatigue life during in-service applications. Also to determine if the recrystallized grains in the ASB region yielded a higher strength, allowing higher fatigue strength.
- A test where the cryogenically machined specimens are thermally exposed in air to determine if the subsurface damage introduced to the utmost subsurface layer has an effect in the diffusional processes, such as those observed by Thomas [4] where easy diffusion paths allowed interstitial pick up, thus causing embrittlement and evidence of silicide precipitation which would reduce the fatigue life.
- A high-speed machining 2D simulation using the same cutting tool, tool geometry, cooling and lubricating conditions and workpiece material would be beneficial in ascertaining if higher speeds agree with the linear correlation in the log of shear stress versus log strain rate. Additionally, microstructural features such as SPD,

twin depth, SBA, shear band spacings would be beneficial in identifying if they follow the same trend as in the uniaxial compression test and the PSM.

- Localised strain rates during the shear band formation could be estimated through models such as these presented by Bai and Dood [47]. For this, FEM simulation would need to be carried out to estimate the local shear strain on the shear band. This would help correlate the strain rates achieved during specific cutting conditions. This value could be correlated to grain sizes measured through TEM.

- It would be useful to compare parameters such as grain refinement and shear band segmentation obtained from modelling to experimental high-speed values. Thus, it would be certain that accurate predictions can be obtained from modelling and mechanical testing might be performed more efficiently.

- Determination of the nature of mechanical twinning, which occur in workpieces machined under cryogenic coolants would give an insight of the specific operating systems in the subsurface and corroborate if twins allowed a contraction or an extension of the c-axis.

- It would be beneficial to identify the twin type(s), which grew cracks along the twin boundary. Thus, the occurrence of this type of twin in other tests may lead to crack nucleation.

- An EBSD analysis could reveal the nature of the microstructural features identified in this work as strain localisation or mechanical twinning. It would provide the crystallographic orientations where nearly zero subsurface deformation was found. Thus, trough thermomechanical processing, this crystallographic orientation may be engineered to reduce damage introduced during machining.

- Study of the effect of supercritical CO_2 and MQL on subsurface deformation. Theoretically, there should be lower subsurface deformation as the oil dissolves into the $scCO_2$; therefore, the oil is directly transported into the cutting zone by the CO_2, reducing friction forces. A lower subsurface damage depth represents fewer potential sites for crack nucleation. The supercritical CO_2 ($scCO_2$) has a slightly higher temperature than liquid CO_2, and oils are soluble in it. This allows it to transport the lubricant oil directly to the cutting zone, generating lower sticking and sliding friction.

- It would be beneficial to improve the rigidity of the workpiece holder to prevent workpiece deflection during cutting, especially when generating a single chip.

- Obtain TEM images of the dislocation distribution after machining under both dry and low temperatures.

- It would be interesting to compare the cutting forces and energy generated in multiaxial deformation processes and compare it to uniaxial to see if it could be approximated.
- A graph of the log Z and the DRX grain size may be developed by analysing the uniaxial compression specimens.
- Determine if mechanical twins observed at low temperatures, (needle-like) show a higher degree of reorientation than room temperature lenticular twins.
- High strain chips may be used through powder consolidation techniques [171]. Shankar et al. corroborated the thermal stability of Al6061 chips exposed to thermo-mechanical processing. In titanium alloys, the chip formation is inhomogeneous, imparting large strains in localised regions and the rest of the chip is characteristic of a lower strain. This may lead to a non-uniform distribution of mechanical properties in consolidated titanium chips specimens.
- Model a high-speed turning operation. With the estimated strain, strain rate and temperature then undertake a double hat shape shear test in a split-Hopkinson bar at simulated high strain rates, strain and temperatures. Develop a constitutive equation to model flow behaviour under these conditions.
- Determine the effect of underlying crystallographic texture on the shear band formation. It would be important to establish certain types of textures that are more prone to ASB and failure and to determine if there is a correlation between texture and the thickness of these concentrated shear/ narrow bands.
- If a camera with the capability of acquisition of a higher number of frames per second is available, the strain evolution during shear band formation in cutting should be closely examined. This may provide clues or relations of the shear band initiation characteristics.
- Model the grain size after refinement from the imparted strain during metal cutting.
- The grain size has an effect on ASB thickness [172], which also influences the temperature distribution along the plastic deformation zone. A study of the effect of grain size on the thickness of ASB is beneficial in determining conditions where ASB do not represent a high risk of crack initiation or fracture.

References

[1]   P. G. Partridge, "Effect of cyclic stresses on the microstructures of hexagonal close-packed metals," *Czech. J. Phys.*, vol. 19, no. 3, pp. 323–332, 1969.

[2]   G. E. Dieter, *Mechanical Metallurgy, SI edition*. McGraw-Hill Higher Education, 1989.

[3]   P. Crawforth, "Towards a micromechanistic understanding of imparted subsurface deformation during machining of titanium alloys," Ph.D thesis, The University of Sheffield, Sheffield, UK, 2014.

[4]   M. Thomas, "On the characterisation of subsurface deformation microstructures in aerostructural titanium alloys," Ph.D thesis, The University of Sheffield, Sheffield, UK, 2012.

[5]   L. A. Marshall, "The influence of aluminium additions on titanium during machining through the application of a novel orthogonal cutting test method," Ph.D thesis, The University of Sheffield, Sheffield, UK, 2014.

[6]   M. E. Merchant, "Mechanics of the metal cutting process. II. Plasticity conditions in orthogonal cutting," *J. Appl. Phys.*, vol. 16, no. 6, pp. 318–324, 1945.

[7]   "Titanium: Global industry markets and outlook 2018," *Roskill*, 2018. [Online]. Available: https://roskill.com/market-report/titanium-metal/. [Accessed: 20-Jan-2018].

[8]   F. Froes, "Current and emerging opportunities in titanium's expanding market," *JOM*, p. 27, 2007.

[9]   R. A. Rahman Rashid, S. Sun, G. Wang, and M. S. Dargusch, "Machinability of a near beta titanium alloy," *Proc. Inst. Mech. Eng. Part B J. Eng. Manuf.*, vol. 225, no. 12, pp. 2151–2162, 2011.

[10]   ITA, "Titanium USA 2018, International Titanium Association," 2018. [Online]. Available: https://cdn.ymaws.com/titanium.org/resource/resmgr/02_jens_folder/titanium_usa_2018_executive_.pdf. [Accessed: 03-Dec-2018].

[11]   Airbus, "Global market forecast-Airbus 2018-2037," 2018. [Online]. Available: https://www.airbus.com/content/dam/corporate-topics/publications/media-day/GMF-2018-2037.pdf. [Accessed: 02-Jan-2019].

[12]   "Committee on Climate Change," 2018. [Online]. Available: https://www.theccc.org.uk/. [Accessed: 21-Jan-2018].

[13] "Air Transport Action Group." [Online]. Available: https://www.atag.org/component/factfigures/?Itemid=. [Accessed: 08-Aug-2018].

[14] S. Morkavuk, U. Köklü, M. Bağcı, and L. Gemi, "Cryogenic machining of carbon fiber reinforced plastic (CFRP) composites and the effects of cryogenic treatment on tensile properties: A comparative study," *Compos. Part B Eng.*, vol. 147, no. April, pp. 1–11, 2018.

[15] J. Turner, R. J. Scaife, and H. M. El-Dessouky, "Effect of machining coolant on integrity of CFRP composites," *Adv. Manuf. Polym. Compos. Sci.*, vol. 1, no. 1, pp. 54–60, 2015.

[16] "The National Institute for Occupational Safety and Health (NIOSH)." [Online]. Available: https://www.cdc.gov/niosh/index.htm. [Accessed: 10-Feb-2018].

[17] A. F. Clarens, K. F. Hayes, and S. J. Skerlos, "Feasibility of metalworking fluids delivered in supercritical carbon dioxide," *J. Manuf. Process.*, vol. 8, no. 1, pp. 47–53, 2006.

[18] M. Zhang and S. E. Mason, "The effects of contamination on the mechanical properties of carbon fibre reinforced epoxy composite materials," *J. Compos. Mater.*, vol. 33, no. 14, pp. 1363–1374, Jul. 1999.

[19] V. P. Astakhov and S. Joksch, *Metalworking Fluids (MWFs) for Cutting and Grinding*. Cambridge UK: Woodhead Publishing Limited, 2012.

[20] M. S. Najiha, M. M. Rahman, and A. R. Yusoff, "Environmental impacts and hazards associated with metal working fluids and recent advances in the sustainable systems: A review," *Renew. Sustain. Energy Rev.*, vol. 60, pp. 1008–1031, 2016.

[21] G. Lütjering and J. C. Williams, *Titanium*, 2nd ed. Springer, 2007.

[22] M. Donachie, *Titanium. A Technical Guide*. ASM International, Materials Park, OH, 2000.

[23] F. Pusavec, D. Kramar, P. Krajnik, and J. Kopac, "Transitioning to sustainable production - Part II: Evaluation of sustainable machining technologies," *J. Clean. Prod.*, vol. 18, no. 12, pp. 1211–1221, 2010.

[24] M. I. Sadik, S. Isakson, A. Malakizadi, and L. Nyborg, "Influence of coolant flow rate on tool life and wear development in cryogenic and wet milling of Ti-6Al-4V," *Procedia CIRP*, vol. 46, pp. 91–94, 2016.

[25] M. J. Bermingham, J. Kirsch, S. Sun, S. Palanisamy, and M. S. Dargusch, "New observations on tool life, cutting forces and chip morphology in cryogenic machining Ti-6Al-4V," *Int. J. Mach. Tools Manuf.*, vol. 51, no. 6, pp. 500–511, Jun. 2011.

[26]   H. M. Flower, "Microstructural development in relation to hot working of titanium alloys," *Mater. Sci. Technol.*, vol. 6, no. 11, pp. 1082–1092, 1990.

[27]   D. R. Chichili, K. T. Ramesh, and K. J. Hemker, "The high strain rate response of alpha-titanium: Experiments, deformation mechanisms and modeling," *Acta mater.*, vol. 46, no. 3, pp. 1025–1043, 1998.

[28]   V. Mises, "Mechanik der plastischen formänderung von kristallen," *ZAMM - Zeitschrift für Angew. Math. und Mech.*, vol. 8, no. 3, pp. 161–185, 1928.

[29]   M. A. Meyers, O. Vöhringer, and V. A. Lubarda, "The onset of twinning in metals: A constitutive description.," *Acta Mater.*, vol. 49, no. 19, pp. 4025–4039, 2001.

[30]   S. Kibey, J. B. Liu, D. D. Johnson, and H. Sehitoglu, "Predicting twinning stress in fcc metals: linking twin-energy pathways to twin nucleation," *Acta Mater.*, vol. 55, no. 20, pp. 6843–6851, 2007.

[31]   E. O. Hall, *Twinning and diffusionless transformations in metals*. London: Butterworth's Scientific Publications, 1954.

[32]   S. Di Iorio, L. Briottet, E. F. Rauch, and D. Guichard, "Plastic deformation, damage and rupture of PM Ti-6Al-4V at 20 K under monotonic loading," *Acta Mater.*, vol. 55, pp. 105–118, 2007.

[33]   S. Di Iorio, L. Briottet, C. Cayron, E. F. Rauch, and D. Guichard, "Damage mechanisms at microscopic scale during machining PM Ti-6Al-4V at 20K," *J. Mater. Sc. Technol.*, vol. 20, 2004.

[34]   R. Reed-Hill and R. Abbaschian, *Physical metallurgy principles*, 3rd ed. Boston, Mass.: International Thomson Publishing, 1994.

[35]   D. Hull, *Introduction to dislocations*, 4th ed. Oxford: Butterworth Heinemann, 2001.

[36]   J. R. Davis and S. Semiatin, *ASM Handbook, Volume 14: Forming and Forging*, 9th ed., vol. 14, no. 3. Ohio: ASM International, 1993.

[37]   J. C. Williams, J. C. Williams, R. G. Baggerly, R. G. Baggerly, N. E. Paton, and N. E. Paton, "Deformation behavior of HCP Ti-Al alloy single crystals," *Metall. Mater. Trans. A*, vol. 33, no. 13, pp. 837–850, 2002.

[38]   J. C. Williams, A. W. Sommer, and P. P. Tung, "The influence of oxygen concentration on the internal stress and dislocation arrangements in alpha titanium," *Metall. Trans.*, vol. 3, no. 11, pp. 2979–2984, 1972.

[39]   F. H. Froes, *Titanium- Physical Metallurgy Processing and Application*. Materials Park, OH, US: ASM International, 2015.

[40]   H. Conrad, "The cryogenic properties of metals," in *Proc Berkeley Intern Mater*

301

Conf, 2nd., 1964, vol. 16, no. 3, pp. 437–509.

[41] McQuillan and McQuillan, *Metallurgy of the rarer metals-4 Titanium*. London: Butterworths Scientific Publications, 1956.

[42] D. N. Williams and D. S. Eppelseheimer, "A theoretical investigation of the deformation textures of titanium," *J. Inst. Met.*, vol. 81, pp. 553–561, 1952.

[43] F. D. Rosi, F. C. Perkins, and L.L. Seigle, "Mechanism of plastic flow in titanium at low and high temperatures," *Trans. AIME*, vol. 115, 1956.

[44] A. Salem, S. R. Kalidindi, and R. D. Doherty, "Strain hardening of titanium : role of deformation twinning," vol. 51, pp. 4225–4237, 2003.

[45] G. E. Dieter, H. Kuhn, and S. L. Semiatin, *Handbook of Workability and Process Design*. Materials Park, OH: ASM International, 2003.

[46] M. A. Meyers, G. Subhash, B. K. Kad, and L. Prasad, "Evolution of microstructure and shear-band formation in α-hcp titanium," *Mech. Mater.*, vol. 17, pp. 175–193, 1994.

[47] Y. Bai and B. Dodd, *Adiabatic shear localization, frontiers and advances*, 2nd ed. London, Great Britain: Elsevier, 2012.

[48] M. A. Meyers and H. Pak, "Observation of an adiabatic shear band in titanium by high-voltage transmission electron microscopy," *Acta Metall.*, vol. 34, no. 12, pp. 2493–2499, 1986.

[49] D. Sagapuram and K. Viswanathan, "Viscous shear banding in cutting of metals," *J. Manuf. Sci. Eng.*, vol. 140, no. 11, p. 111004, 2018.

[50] J. Peirs *et al.*, "Microstructure of adiabatic shear bands in Ti6Al4V," *Mater. Charact.*, vol. 75, pp. 79–92, 2013.

[51] P. Shewmon, *Transformations in Metals*. New York: Mc Graw-Hill, 1969.

[52] P. B. Prangell, Y. Huang, M. Berta, and P. J. Apps, "Mechanisms of formation of submicron grain structures during spd," *Mater. Sci. Forum*, vol. 50, pp. 159–168, 2007.

[53] P. Cotterill and P.R. Mould, *Recrystallization and Grain Growth in Metals*. London, UK: Surrey University Press: International Textbook Co., 1976.

[54] S. H. Whang, *Nanostructured Metals and Alloys: processing, microstructure, mechanical properties and applications*. Cambridge, UK: Woodhead Pub. Ltd., 2011.

[55] G. Welsch, R. Boyer, and E. Collings, *Materials Properties Handbook: Titanium*

Alloys. ASM International, 1994.

[56] H. Conrad, "Plastic flow and fracture of titanium at low temperatures," *Cryogenics.*, vol. 24, no. 6, pp. 293–304, 1984.

[57] R. H. Van Stone, J. R. Low, and J. L. Shannon, "Investigation of the fracture mechanism in Ti-5Al-2.5Sn at cryogenic temperatures," Washington, D. C., 1977.

[58] D. R. Salomon, *Low Temperature Data Handbook Titanium and Ti alloys*. National Physical Laboratory (NPL), 1979.

[59] M. Shaw, *Metal cutting principles*, 2nd ed. New York ; Oxford : Oxford University Press, 2005.

[60] M. Donnachie, *Titanium: a technical guide*, 2nd ed. Materials Park, OH : ASM International.

[61] H. M. Rosenberg, *Low temperature solid state physics*. Oxford: Oxford University Press, 1963.

[62] G. W. Geil and N. Carwile, "Effect of low temperatures on the mechanical properties of a commercially pure titanium," *J. Res. Natl. Bur. Stand.*, vol. 54, no. 2, pp. 91–101, 1955.

[63] P. Duthil, "Material properties at low temperature," *Inst. Phys. Nucléaire d'Orsay, IN2P3-CNRS*, pp. 77–95, 2013.

[64] C. F. Hickey Jr, "Mechanical properties of titanium and aluminum alloys at cryogenic temperatures," Watertown Arsenal Laboratories, Watertown MA, USA, Technical Report TR 340, 1962.

[65] K. Nagai, K. Hiraga, T. Ogata, and K. Ishikawa, "Cryogenic temperature mechanical properties of β-annealed Ti-6Al-4V alloys," vol. 26, no. 6, pp. 405–413, 1985.

[66] S. Idereklam, *Modern Metal Cutting Handbook*, First. Sweden: Tofters Tryckeri AB, 1994.

[67] D. Stephenson and J. Agapiou, *Metal Cutting Theory and Practice*, 3rd ed. Boca Raton, Florida: CRC Press Taylor and Francis Group, LLC, 2016.

[68] R. Komanduri and B. Turkovich, "New observations on the mechanism when machining titanium alloys of chip formation," *Wear*, vol. 69, no. 2, pp. 179–188, 1981.

[69] D. Sagapuram *et al.*, "Geometric flow control of shear bands by suppression of viscous sliding," *Proc. R. Soc. A Math. Phys. Eng. Sci.*, vol. 472, no. 2192, 2016.

[70] A. E. Bayoumi and J. Q. Xie, "Some metallurgical aspects of chip formation in

cutting Ti-6wt.%Al-4wt.%V alloy," *Mater. Sci. Eng. A*, vol. 190, no. 1–2, pp. 173–180, 1995.

[71]   M. C. Shaw, S. O. Dirke, P. A. Smith, N. H. Cook, E. G. Loewen, and C. T. Yang, *Machining titanium*. Department of Mechanical Engineering. Massachusetts Institute of Technology, 1954.

[72]   S. L. Semiatin and S. B. Rao, "Shear localization during metal cutting," *Mater. Sci. Eng.*, vol. 61, pp. 185–192, 1983.

[73]   S. Joshi, P. Pawar, A. Tewari, and S. S. Joshi, "Influence of β phase fraction on deformation of grains in and around shear bands in machining of titanium alloys," *Mater. Sci. Eng. A*, vol. 618, pp. 71–85, Nov. 2014.

[74]   V. Astakhov, *Tribology of metal cutting*. Oxford, United Kingdom: Elsevier, 2006.

[75]   E. O. Ezugwu and Z. M. Wang, "Titanium alloys and their machinability—a review," *J. Mater. Process. Technol.*, vol. 68, no. 3, pp. 262–274, 1997.

[76]   S. Pervaiz, A. Rashid, I. Deiab, and M. Nicolescu, "Influence of tool materials on machinability of titanium- and nickel-based alloys: a review," *Mater. Manuf. Process.*, vol. 29, no. 3, pp. 219–252, 2014.

[77]   R. Komanduri, "Some clarifications on the mechanics when machining titanium alloys of chip formation," *Wear*, vol. 76, pp. 15–34, 1982.

[78]   M. C. Shaw, S. O. Dirke, P. A. Smith, N. H. Cook, E. G. Loewen, and C. T. Yang, *Machining titanium*. Department of Mechanical Engineering. Massachussetts Institute of Technology, 1954.

[79]   H. Singh and A. Singh, "An enhancement of properties of material SAE 1045 steel," *Imp. J. Interdiscip. Res.*, vol. 3, no. 2, pp. 1678–1685, 2017.

[80]   F. Klocke, *Manufacturing processes 1: Cutting*. Aachen, Germany: Werkzeugmaschinenlabor (WZL) Springer Berlin Heidelberg, 2011.

[81]   S. D. Supekar, A. F. Clarens, D. A. Stephenson, and S. J. Skerlos, "Performance of supercritical carbon dioxide sprays as coolants and lubricants in representative metalworking operations," *J. Mater. Process. Tech.*, vol. 212, no. 12, pp. 2652–2658, 2012.

[82]   "OSHA, Metalworking fluids." [Online]. Available: https://www.osha.gov/SLTC/metalworkingfluids/mwf_finalreport.html. [Accessed: 01-Feb-2018].

[83]   P. Davim, *Machining of titanium alloys*. Aveiro Portugal: Springer, 2014.

[84]   I. S. Jawahir *et al.*, "Cryogenic manufacturing processes," *Manuf. Technol.*, vol. 65,

no. 2, pp. 713–736, 2016.

[85] C. Machai and D. Biermann, "Machining of β-titanium-alloy Ti–10V–2Fe–3Al under cryogenic conditions: Cooling with carbon dioxide snow," *J. Mater. Process. Technol.*, vol. 211, no. 6, pp. 1175–1183, Jun. 2011.

[86] G. White, *Experimental techniques in low temperature physics*, 3rd ed. Oxford: Clarendon Press, Oxford Science Publications, 1979.

[87] F. Pusavec *et al.*, "Sustainable machining of high temperature Nickel alloy - Inconel 718: Part 1 - Predictive performance models," *J. Clean. Prod.*, vol. 81, pp. 255–269, 2014.

[88] A. Stoll, K. Busch, C. Hochmuth, and B. Pause, "Modern cooling strategies for machining of high-temperature materials," in *3rd ICMC, Hybrid Processes*, 2014, pp. 299–315.

[89] T. Lu, "A metrics-based sustainability assessment of cryogenic machining using modeling and optimization of process performance," 2014.

[90] L. S. Tong and Y. S. Tang, *Boiling heat transfer and two phase flow*, 2nd Editio. Taylor & Francis, New York, 1997.

[91] C. Bates, G. Totten, and R. Brennan, "Quenching of steel," in *ASM Handbook Vol 4 Heat treating*, 1991.

[92] J. Stahl and P. De Vos, *Metal cutting theories in practice*. Lund-Fagersta, Sweden: Seco tools AB, 2014.

[93] J. P. Holman, *Heat transfer*, 10th ed. Boston Mass. ; London: McGraw-Hill, 2010.

[94] Y. Su, L. Gong, B. Li, Z. Liu, and D. Chen, "Performance evaluation of nanofluid MQL with vegetable-based oil and ester oil as base fluids in turning," *Int. J. Adv. Manuf. Technol.*, vol. 83, no. 9–12, pp. 2083–2089, 2016.

[95] A. R. Jha, *Cryogenic Technology and Applications*. Butterworth-Heinemann, 2006.

[96] D. Ulutan and T. Ozel, "Machining induced surface integrity in titanium and nickel alloys: A review," *Int. J. Mach. Tools Manuf.*, vol. 51, no. 3, pp. 250–280, Mar. 2011.

[97] M. Dhananchezian and M. Pradeep Kumar, "Cryogenic turning of the Ti–6Al–4V alloy with modified cutting tool inserts," *Cryogenics (Guildf).*, vol. 51, no. 1, pp. 34–40, Jan. 2011.

[98] B. D. Jerold and M. P. Kumar, "The influence of cryogenic coolants in machining of Ti–6Al–4V," *J. Manuf. Sci. Eng.*, vol. 135, no. 3, 2013.

305

[99]   M. R. Shankar, B. C. Rao, S. Lee, S. Chandrasekar, A. H. King, and W. D. Compton, "Severe plastic deformation (SPD) of titanium at near-ambient temperature," *Acta Mater.*, vol. 54, no. 14, pp. 3691–3700, 2006.

[100]   Z. Pu, J. C. Outeiro, a. C. Batista, O. W. Dillon, D. a. Puleo, and I. S. Jawahir, "Enhanced surface integrity of AZ31B Mg alloy by cryogenic machining towards improved functional performance of machined components," *Int. J. Mach. Tools Manuf.*, vol. 56, pp. 17–27, 2012.

[101]   N. R. Tao, X. L. Wu, M. L. Sui, J. Lu, and K. Lu, "Grain refinement at the nanoscale via mechanical twinning and dislocation interaction in a nickel-based alloy," *J. Mater. Res.*, vol. 19, no. 6, pp. 1623–1629, 2004.

[102]   I. S. Jawahir *et al.*, "Surface integrity in material removal processes: Recent advances," *CIRP Ann. - Manuf. Technol.*, vol. 60, no. 2, pp. 603–626, Jan. 2011.

[103]   J. I. Hughes, A. R. C. Sharman, and K. Ridgway, "The effect of cutting tool material and edge geometry on tool life and workpiece surface integrity," *Proc. Inst. Mech. Eng. Part B J. Eng. Manuf.*, vol. 220, no. 2, pp. 93–107, 2006.

[104]   P. Crawforth, B. Wynne, S. Turner, and M. Jackson, "Subsurface deformation during precision turning of a near-alpha titanium alloy," *Scr. Mater.*, vol. 67, no. 10, pp. 842–845, Nov. 2012.

[105]   M. S. Dargusch, M. X. Zhang, S. Palanisamy, A. J. M. Buddery, and D. H. StJohn, "Subsurface deformation after dry machining of grade 2 titanium," *Adv. Eng. Mater.*, vol. 10, no. 1–2, pp. 85–88, 2008.

[106]   F. Pusavec, H. Hamdi, J. Kopac, and I. S. Jawahir, "Surface integrity in cryogenic machining of nickel based alloy—Inconel 718," *J. Mater. Process. Technol.*, vol. 211, no. 4, pp. 773–783, 2011.

[107]   D. Umbrello, F. Micari, and I. S. Jawahir, "The effects of cryogenic cooling on surface integrity in hard machining: A comparison with dry machining," *CIRP Ann. - Manuf. Technol.*, vol. 61, no. 1, pp. 103–106, 2012.

[108]   F. Klocke, L. Settineri, D. Lung, P. Claudio Priarone, and M. Arft, "High performance cutting of gamma titanium aluminides: Influence of lubricoolant strategy on tool wear and surface integrity," *Wear*, vol. 302, no. 1–2, pp. 1136–1144, 2013.

[109]   Y. Kaynak, H. Tobe, R. D. Noebe, H. E. Karaca, and I. S. Jawahir, "The effects of machining on the microstructure and transformation behavior of NiTi Alloy," *Scr. Mater.*, vol. 74, pp. 60–63, 2014.

[110]   D. M. R. Taplin and a L. W. Collins, "Fracture at High Temperatures Under Cyclic Loading," *Annu. Rev. Mater. Sci.*, vol. 8, no. 1, pp. 235–268, 1978.

[111] D. Hull, "Fracture of solids," in *Proceedings of an International Conference at the Institute of Metals Division and American Institute of Mining, Metallurgical and Petroleum Engineers*, 1962.

[112] Z. W. Wyatt, W. J. Joost, D. Zhu, and S. Ankem, "Deformation mechanisms and kinetics of time-dependent twinning in an α-titanium alloy," *Int. J. Plast.*, vol. 39, pp. 119–131, 2012.

[113] T. Xiaoli and G. Haicheng, "Fatigue crack initiation in high-purity titanium crystals," *Int. J. Fatigue*, vol. 18, no. 5, pp. 329–333, 1996.

[114] D. Hull, D. Drucker, and J. Gilman, "Fracture in solids," *Acta Met.*, vol. 9, pp. 417–453, 1963.

[115] D. Hull, "Effect of grain size and temperature on slip, twinning and fracture in 3% silicon iron," *Acta Metall.*, vol. 9, no. 3, pp. 191–204, 1961.

[116] R. J. H. Wanhill and S. A. Barter, *Fatigue of β processed and β heat-treated titanium alloys*. Amsterdam, The Netherlands: Springer, 2012.

[117] M. Field and J. F. Kahles, "Review of surface integrity of machined components," *Ann. CIRP*, vol. 20, no. 2, pp. 153–157, 1971.

[118] E. Henriksen and Ithaca, "Residual Stresses in Machined Surfaces," *Trans. ASME*, vol. 73, pp. 69–74, 1951.

[119] Field M. and Kahles J.F., "The surface integrity of machined and ground high strength steels," *DMIC Rep.*, vol. 210, pp. 54–77, 1964.

[120] P. Crawforth, C. M. Taylor, and S. Turner, "The influence of alloy chemistry on the cutting performance and deformation kinetics of titanium alloys during turning," vol. 45, pp. 151–154, 2016.

[121] Y. Kaynak, T. Lu, and I. S. Jawahir, "Cryogenic machining-induced surface integrity: a review and comparison with dry, MQL, and flood-cooled machining," *Mach. Sci. Technol.*, vol. 18, no. 2, pp. 149–198, 2014.

[122] R. M. Arunachalam, M. A. Mannan, and A. C. Spowage, "Residual stress and surface roughness when facing age hardened Inconel 718 with CBN and ceramic cutting tools," *Int. J. Mach. Tools Manuf.*, vol. 44, no. 9, pp. 879–887, 2004.

[123] I. S. Jawahir *et al.*, "Cryogenic manufacturing processes," *Manuf. Technol.*, vol. 65, no. 2, pp. 713–736, 2016.

[124] S. Zabeen, M. Preuss, and P. J. Withers, "Evolution of a laser shock peened residual stress field locally with foreign object damage and subsequent fatigue crack growth," *Acta Mater.*, vol. 83, pp. 216–226, 2015.

[125] G. Rotella, O. W. Dillon, D. Umbrello, L. Settineri, and I. S. Jawahir, "The effects of cooling conditions on surface integrity in machining of Ti6Al4V alloy," *Int. J. Adv. Manuf. Technol.*, vol. 71, no. 1–4, pp. 47–55, 2014.

[126] H. Kuhn and D. Medlin, "High strain rate shear testing," in *Asm Handbook vol 8: Mechanical Testing and Evaluation*, 2000, pp. 447–461.

[127] H. Kuhn and D. Medlin, "High strain rate tension and compression tests," *ASM Handbook, Vol. 8 Mech. Test. Eval.*, vol. 8, pp. 429–446, 2000.

[128] J. Peirs, P. Verleysen, J. Degrieck, and F. Coghe, "The use of hat-shaped specimens to study the high strain rate shear behaviour of Ti-6Al-4V," *Int. J. Impact Eng.*, vol. 37, no. 6, pp. 703–714, 2010.

[129] M. S. Loveday *et al.*, "Measurement of flow stress in hot plane strain compression tests," *Mater. High Temp.*, vol. 3409, no. July, 2016.

[130] B. Roebuck, J. D. Lord, M. Brooks, M. S. Loveday, C. M. Sellars, and R. Evans, "Measurement of flow stress in hot axisymmetric compression tests," *Mater. High Temp.*, vol. 3409, no. July, 2016.

[131] Y. Guo, R. M'Saoubi, and S. Chandrasekar, "Control of deformation levels on machined surfaces," *CIRP Ann. - Manuf. Technol.*, vol. 60, pp. 137–140, 2011.

[132] J. T. Black, *ASM Handbook Machining*. .

[133] S. Group, "LX 051-5-axis blade machining center." [Online]. Available: https://www.starrag.com/en-us/machine-361?machineId=29. [Accessed: 22-Jul-2016].

[134] "Digital measuring microscope." [Online]. Available: http://www.insize.com/products/tools/pdf/digital microscope/ISM-PM200SB.pdf. [Accessed: 22-Jul-2016].

[135] R. F. Recht, "Catastrophic thermoplastic shear," *J. Appl. Mech.*, vol. 31, pp. 189–93, 1964.

[136] M. G. Cockroft and D. J. Latham, "Ductility and Workability of Metals," *J. Inst. Met.*, vol. 96, pp. 33–39, 1968.

[137] D. Wigley, *Mechanical properties of materials at low temperatures*. New York, US: Springer, 1971.

[138] H. Conrad, "Effect of interstitial solutes on the strength and ductility of titanium," *Prog. Mater. Sci.*, vol. 26, pp. 123–403, 1981.

[139] Y. S. Li, Y. Zhang, N. R. Tao, and K. Lu, "Effect of the Zener – Hollomon parameter on the microstructures and mechanical properties of Cu subjected to plastic

deformation," *Acta Mater.*, vol. 57, no. 3, pp. 761–772, 2009.

[140] Y. Zhang, N. R. Tao, and K. Lu, "Effects of stacking fault energy , strain rate and temperature on microstructure and strength of nanostructured Cu – Al alloys subjected to plastic deformation," vol. 59, pp. 6048–6058, 2011.

[141] S. L. Semiatin, *ASM Handbook: Vol 14A Metalworking: Bulk Forming*, vol. 14A. Materials Park, OH: ASM International, 2005.

[142] M. Nishimoto, W. Takahashi, and Y. Shida, "Examination of high temperature deformation behaviours in titanium alloys by means of Zener-Hollomon parameter," *J. Iron Steel Inst. Japan*, vol. 78, no. 8, pp. 1398–1405, 1992.

[143] W.-S. Lee and C.-F. Lin, "Plastic deformation and fracture behaviour of Ti–6Al–4V alloy loaded with high strain rate under various temperatures," *Mater. Sci. Eng. A*, vol. 241, no. 1–2, pp. 48–59, 1998.

[144] S. Song and G. T. Gray, "Structural interpretation of the nucleation and growth of deformation twins in Zr and Ti-II. TEM Study of twin morphology and defect reactions during twinning.," *Acta Metall. Mater.*, vol. 43, no. 6, pp. 2339–2350, 1995.

[145] "IgorPro." Wave Metrics Inc., IGOR Pro (version 5.3.0) [software program].

[146] W. S. Rasband, "Image J." http://imagej.nih.gov/ij/: U.S National Institutes of Health, Bethesda, Maryland, USA., 1977.

[147] S. Hong, Y. Ding, and W. Jeong, "Friction and cutting forces in cryogenic machining of Ti–6Al–4V," *Int. J. Mach. Tools Manuf.*, vol. 41, no. 15, pp. 2271–2285, Dec. 2001.

[148] "Correlated Solutions Inc., VIC 2D (version 2009.1.0, build 738:744M) [computer package]." .

[149] D. R. Tobergte and S. Curtis, "ASM Handbook Volume 19 - Fatigue and Fracture," *J. Chem. Inf. Model.*, vol. 53, no. 9, pp. 1689–1699, 2013.

[150] P. G. Partridge, "Cyclic twinning in fatigued close-packed hexagonal metals," *Phil. Mag.*, vol. 12, no. 119, pp. 1043–1054, 1965.

[151] R. Stevenson and J. E. Breedis, "Cyclic deformation of commercially-pure Titanium," *Acta Met.*, vol. 23, no. 1419, 1975.

[152] C. J. Beevers and M. D. Halliday, "The role of twinning in the fatigue behaviour of alpha-titanium," vol. 19, 1969.

[153] S. Hong, I. Markus, and W. Jeong, "New cooling approach and tool life improvement in cryogenic machining of titanium alloy Ti-6Al-4V," *Int. J. Mach.*

Tools Manuf., vol. 41, no. 15, pp. 2245–2260, Dec. 2001.

[154] N. Tapoglou, M. I. Aceves Lopez, I. Cook, and C. M. Taylor, "Investigation of the influence of CO2 cryogenic coolant application on tool wear," *Procedia CIRP*, vol. 63, pp. 745–749, 2017.

[155] M. Halliday and C. Beevers, "Non-closure of cracks and fatigue crack growth in beta heat treated Ti-6Al-4V," *Int J. Fract.*, vol. 15, no. 1, pp. R27–R30, 1979.

[156] R. Wanhill and S. Barter, *Fatigue of Beta Processed and Beta Heat-treated Titanium Alloys*. Dordrecht, The Netherlands: Springer Briefs in applied sciences and Technology, 2012.

[157] "Walter F2334 round insert cutter." [Online]. Available: https://www.walter-tools.com/en-gb/tools/standard_products/milling/overview/copy_milling/contour_mill/pages/default.aspx. [Accessed: 02-Feb-2018].

[158] "ISO, Tool life testing with single-point turning tools," *Int. Stand. No. 3685*, 1993.

[159] S. Manson and G. R. Halford, "Mechanisms of fatigue," in *Fatigue and durability of structural materials*, 2006, pp. 237–266.

[160] P. G. Partridge, "The crystallography and deformation modes of hexagonal close-packed metals," *Int. Mater. Rev.*, vol. 12, no. 1, pp. 169–194, 1967.

[161] D. Avery and W. Backofen, "Nucleation and growth of fatigue cracks.," in *Fracture of Solids AIMME*, 1963.

[162] V. S. Sarma, W. W. Jian, J. Wang, H. Conrad, and Y. T. Zhu, "Effect of rolling temperature on the evolution of defects and properties of an Al – Cu alloy," pp. 4846–4850, 2010.

[163] M. Zehetbauer and R. Valiev, *Nanomaterials by Severe Plastic deformation*. 2004.

[164] K. A. Ravichandran and A. K. Vasudevan, "Fracture resistance of structural alloys," in *ASM Handbook Vol 19: Fatigue and Fracture*, 1996, pp. 381–392.

[165] S. P. Timothy and I. M. Hutchings, "The structure of adiabatic shear bands in a titanium alloy," *Acta Metall.*, vol. 33, no. 4, pp. 667–676, 1985.

[166] M. A. Meyers, G. Subhash, B. K. Kad, and L. Prasad, "Evolution of microstructure and shear-band formation in a-hcp titanium," *Mech. Mater.*, vol. 17, pp. 175–193, 1994.

[167] O. Hatt, "On the mechanism of tool crater wear during titanium alloy machining," Ph.D thesis, The University of Sheffield, Sheffield, UK, 2017.

[168] T.Z. Blazynski, *Plasticity and modern metal forming technology*. Elsevier Applied Science.

[169] J. W. Christian and S. Mahajan, "Deformation twinning," *Prog. Mater. Sci.*, vol. 39, pp. 1–157, 1995.

[170] H. Kuhn and D. Medlin, "Mechanical Testing for Metalworking Processes," in *ASM Handbook, Volume 8: Mechanical Testing and Evaluation*, vol. 8, 2000, pp. 70–78.

[171] M. R. Shankar, S. Chandrasekar, A. H. King, and W. D. Compton, "Microstructure and stability of nanocrystalline aluminum 6061 created by large strain machining," *Acta Mater.*, vol. 53, no. 18, pp. 4781–4793, 2005.

[172] Z. Zhang, D. E. Eakins, and F. P. E. Dunne, "On the formation of adiabatic shear bands in textured HCP polycrystals," *Int. J. Plast.*, vol. 79, pp. 196–216, 2016.